

SYNTHESIS, CHARACTERIZATION, AND APPLICATIONS OF PYRIDINE-
AND PYRIDOL-BASED AZAMACROCYCLIC TRANSITION METAL COMPLEXES

by

HANNAH MAY JOHNSTON

Bachelor of Science, 2013
Abilene Christian University
Abilene, TX

Submitted to the Graduate Faculty of the
College of Science and Engineering
Texas Christian University
in partial fulfillment of the requirements
for the degree of

Doctor of Philosophy

May 2018

SYNTHESIS, CHARACTERIZATION, AND APPLICATIONS OF PYRIDINE-
AND PYRIDOL-BASED AZAMACROCYCLIC TRANSITION METAL COMPLEXES

by

Hannah May Johnston

Dissertation approved:

Kayla Green

Major Professor

Paul G. Jewell

John F. Coff

R. W. Nelson

[Signature]

For the College of Science and Engineering

Acknowledgements

I've put off writing these acknowledgements for as long as possible, but the time has finally come. This is not because I didn't want to write them (quite the contrary really) but because there are so many people I must thank that I cannot possibly put everything I want to say into words. These past five years have been an incredible journey and I could not have made it to the finish line without the help of a small army of people. I will do my best to express my gratitude within these few pages, but to all those who've helped me along the journey I want to say thank you, truly I would not be where I am today without you.

Firstly, to Dr. Green I would like to say thank you, from the bottom of my heart. Thank you for taking a chance on me five years ago when I needed an escape from an impossible situation. Joining the Green group was the best decision I could have made, and I haven't looked back since. I would not be where I am today without your leadership, guidance, and the countless hours you've put in during my graduate career helping me grow and develop as a scientist. You've been such an incredible mentor and I've learned so much from you. You've helped me become a better student, teacher, scientist, and person. When I look back at grad school, I'll remember all our 'life-talks' and how you didn't always tell me what I wanted to hear, but you always told me what I needed to hear. Truly, you are an incredible mentor and I know how much you care about your students, both in class and in the lab. This attribute shines through in everything you do, from Chem. Club, to extra help sessions for students, to group meetings, to time spent in the lab helping us. I count myself blessed to have been a part of the Green group, and I will do my best to go forth into the world and make you proud as an advisor.

To the rest of the members of the Green group, past, present, and honorary, thank you for making my time at TCU incredible. You all are an amazing group of people that I am lucky to have as colleagues and as friends. To Kimberly Lincoln, thank you for teaching me synthesis and for giving me the tools I needed to continue the work we started together.

To Kyrallyssa Hauger (a founding member of the three musketeers), thank you for helping me to come out of my shell. I still remember how nervous and shy I was asking if I could eat lunch with you for the first time. You were kind and understanding and I am blessed to count you as one of my closest friends. You are a patient listener, incredible scientist, amazing teacher, and lifelong friend. My time at TCU would not have been the same without you. Thank you for helping me come out of my shell and for being one of my first friends in grad school.

To Marianne Burnett (another founding member of the three musketeers), I'm so lucky that you decided to join the Green group those three years ago. You are an amazing friend, colleague, and scientist. Thank you for all the wonderful things you've brought to the Green lab, from super organizational skills, to expert level biochemistry and electrochemistry knowledge, to your generous helping attitude. We've made some wonderful memories in grad school that I will never forget. As Dorothy said to the Scarecrow in *The Wizard of Oz*, "I think I'm going to miss you most of all". Truly, your friendship means the world to me and you are going to be an amazing scientist wherever you go.

To Samantha Brewer, you are an incredibly hard worker and generous person. Your dedication to scientific discovery is inspiring. I've looked up to you ever since joining the Green group, because you lead through example. Your love for what you are doing shines through in dedicated hours you work. I also count myself lucky to call you a friend. Thank you for always being a great listener and for all the wonderful words of encouragement. We've been through so much together and you've always been there for me no matter what. Your time is coming soon, and I cannot wait to see where you end up after grad school; no matter where it is I know you will be successful.

To all the undergrads in the lab, past and present, I've loved getting to know each and every one of you. To Matthew Canipe, Jack Parker, Ryan Itoh, and Nhan Pham, thank you for allowing me to teach you (even if it was only for a short while). To Maddie Barnett, thank you for being such a big help with my

project, I am truly grateful for all the hard work you've put in to telling the story of **L4**. Also, thanks for being such a fun person to hang out with, I've loved getting to know you first in Quant and now in lab. To Brian Niebuhr and Tim Schwartz, thanks for always bringing a little joy to the lab, no matter how gloomy it is that day; never stop being rays of sunshine. To Magy Mekhail, I know you're not an undergrad, but I just wanted to thank you for your words of encouragement this semester. I wish you every success in your grad school career.

Additionally, I have some faculty members I'd like to thank. To Dr. Fry, you are without a doubt the reason I chose to pursue a career in chemistry and a large part of why I ended up at TCU. Your passion and love for the subject were infectious in high school. I chose to become a chemistry major at ACU because of you and I've never looked back. Thank you for your dedication to teaching this incredible subject to young minds. I'm so lucky that I've gotten to know you in high school and beyond, and that you've allowed me to TA and teach for you; I am blessed to call you a mentor and friend. To Dr. Bob, thank you for the insight and knowledge you offered through each step of my grad school career. You are inspiring as a professor, because I see how much you care about your students. I'm also going to miss sitting in front of you during seminar and the wonderful comments that you make. To Dr. Coffer, thank you for sharing the sacred knowledge with me; your transition metal class was so much fun and I'm glad I got to have you as a professor. To Page Kimbrell, thanks for always being such a good listener and for all the hard work you do to keep the department running smoothly. To Jerry, thanks for always being around to help fix things so we can do science; you keep the departmental instrumentation running smoothly! To Drs. Dzyuba and Janesko, thank you for helping me navigate all the graduate school requirements, both at the beginning and end of my time at TCU. For contributions to the project, I'd also like to thank Dr. Brad Pierce and Philip Palacios, at UTA, for running all the EPR experiments for us and allowing use to use their instrument. To Dr. Eric Reinheimer at Rigaku, thank you for your help solving that particularly tricky crystal structure. To Dr. Akkaraju and Olivia Kinsinger, thank you for running cell studies with my compounds.

To Dr. Gyula Tircsó thank you for being such a wonderful collaborator and for running pH-potentiometric titrations on our ligands.

Finally, thank you to all my family and friends who've supported me on this journey. To my parents, I could not have done this without you. Thank you for your love, support, and unwavering faith in me to get the job done. Thank you for allowing me to live at home during grad school; I don't think I could've done it without such an incredible support system! I love you and am so lucky to have you as parents. This dissertation, this degree is for you.

Table of Contents

Acknowledgments	ii
List of Figures	xii
List of Schemes	xvii
List of Tables	xix
List of Equations.....	xxi
List of Abbreviations	xxv
Chapter 1: Introduction to macrocyclic chemistry	1
1.1. Classification of macrocycles	1
1.2. A brief history of macrocyclic chemistry	2
1.2.1. Origins of macrocyclic chemistry.....	2
1.2.2. Development of modern day macrocyclic chemistry	4
1.3. Properties of azamacrocycles	5
1.3.1. Determining the cavity size/ring size of macrocyclic ligands.....	6
1.3.2. The <i>macrocyclic</i> effect.....	11
1.3.2.1. Thermodynamic considerations	13
1.3.2.2. Kinetic considerations	17
1.3.2.2.1. Formation kinetics	17
1.3.2.2.2. Dissociation kinetics	20
1.4. Synthesis of macrocycles	22
1.4.1. Direct/Non-template synthetic methods	23
1.4.2. Metal-directed/template synthetic methods.....	26
1.5. Applications of macrocyclic ligands	28
1.6. Macrocyclic chemistry of the Green group	29
Chapter 2: Synthesis, characterization, and applications of a novel bis-pyridol-based tetraazamacrocycle (L4).....	33
2.1. Introduction	33
2.1.1. The pathology of neurodegenerative diseases	33
2.1.2. Current therapeutic approaches	36
2.1.3. Using a rational design approach to design L1	39
2.1.4. Using a rational design approach to design L2 and L3	41

2.1.5. Synthetic methodology for L1-L3	43
2.2. A rational design approach to L4 : a novel bis-pyridol-based tetraazamacrocyclic	44
2.3. Synthetic methodology for L4	45
2.4. Protonation and stability constants of L4 with various divalent transition metals	49
2.4.1. An introduction to equilibrium constants	49
2.4.2. Relevant equations for the expression of the protonation and stability constants of L4	51
2.4.3. Determination of protonation constants for L4	53
2.4.4. Determination of formation (stability) constants for L4	56
2.5. L4 complexes with biologically relevant transition metals, Cu(II) and Zn(II)	60
2.5.1. Complexes of L4 with Cu(II) and Zn(II)	60
2.5.2. Solid state structures of L4Cu and L4Zn	62
2.5.3. Electronic spectrum of L4Cu in aqueous and organic solvents	67
2.5.4. Electrochemistry of L4Cu	68
2.5.5. ¹ H NMR spectrum of L4Zn	71
2.6. Biological assays with L4	72
2.6.1. DPPH radical quenching assay performed with L1 , L2 , and L4	72
2.6.2. CCA redox cycling assay performed with L2 and L4	74
2.7. The therapeutic window of L4	76
2.8. Conclusions	77
2.9. Experimental (methods and materials)	78
2.9.1. Physical measurements	78
2.9.2. Preparation of 1,4,7-tris(2-nitrobenzenesulfonyl)-1,4,7-triazaheptane (2.1)	78
2.9.3. Preparation of 1,4,7,10-tetraza-2,6-pyridinophane trishydrochloride (L1)	79
2.9.4. Preparation of 1,4,7,10-tetraaza-2,6-pyridinophane-14-ol trishydrochloride (L2)	81
2.9.5. Preparation of 1,4,7,10-tetraaza-2,6-pyridinophane-13-ol trishydrochloride (L3)	84
2.9.6. Preparation of 1,4,11,13-tetraaza-bis(2,6-pyridinophane)-8,17-ol (L4)	88
2.9.7. Preparation of [L4Cu ^{II} Cl] ₂ [Cl] ₂ (L4Cu)	90
2.9.8. Preparation of [L4Zn ^{II} Cl] ₂ [Cl] ₂ (L4Zn)	91
2.9.9 X-ray crystallography	91
2.9.9.1. [C ₄₂ H ₄₀ N ₄ O ₆ S ₂] (2.14) structure determination	92
2.9.9.2. [L4Cu ^{II} Cl] ₂ [Cl] ₂ (L4Cu) structure determination	92
2.9.9.3. [L4Zn ^{II} Cl] ₂ [Cl] ₂ (L4Zn) structure determination	93

2.9.10. Electrochemical measurements	94
2.9.11. Equilibrium measurements	94
2.9.12. DPPH radical quenching assay.....	96
2.9.13. CCA redox cycling assay	96
2.9.14. Cell studies	97
2.9.15. Experimental acknowledgments	97
Chapter 3: Spectroscopic and solid state evaluations of tetraazamacrocyclic cobalt complexes with parallels to the classic cobalt(II) chloride equilibrium	98
3.1. Introduction	98
3.1.1. Werner complexes: the foundation of coordination chemistry	99
3.1.2. Illustration of Le Châtelier's Principle using the classic CoCl_2 equilibrium.....	101
3.1.3. Macrocyclic Co(III) complexes with parallels to the classic CoCl_2 equilibrium.....	102
3.2. Synthesis of L1Co , L2Co , L3Co and equilibrium behavior in organic and aqueous solvents.....	103
3.3. Electronic absorption spectroscopy of L1Co , L2Co , and L3Co	104
3.4. Solid state evaluation of L1Co1 , L2Co1 , L3Co1 , and L1Co2	107
3.5. Equilibrium behavior L1Co , L2Co , L3Co	113
3.6. Electrochemistry of L1Co , L2Co , and L3Co	114
3.7. Ion exchange reactions with L1Co , L2Co , and L3Co	115
3.8. Exploration of catalytic activity	116
3.8.1. Michael-Addition C-C coupling.....	116
3.8.2. Suzuki-Miyaura type C-C coupling.....	117
3.9. Conclusions	118
3.10. Experimental (methods and materials).....	119
3.10.1. Physical measurements.....	119
3.10.2. Preparation of $[\text{L1Co}^{\text{III}}\text{ClX}]^{n+}$ (L1Co)	120
3.10.3. Preparation of $[\text{L2Co}^{\text{III}}\text{ClX}]^{n+}$ (L2Co)	120
3.10.4. Preparation of $[\text{L3Co}^{\text{III}}\text{ClX}]^{n+}$ (L3Co)	121
3.10.5. Preparation of $[\text{L1Co}^{\text{III}}\text{Cl}(\text{DMF})][\text{BF}_4]_2$ (L1Co3)	122
3.10.6. Preparation of $[\text{L2Co}^{\text{III}}\text{Cl}(\text{DMF})][\text{BF}_4]_2$ (L2Co3)	123
3.10.7. Preparation of $[\text{L3Co}^{\text{III}}\text{Cl}(\text{DMF})][\text{BF}_4]_2$ (L3Co3)	123

3.10.8. X-ray crystallography.....	123
3.10.8.1. [L1Co ^{III} Cl ₂] ₃ [ClO ₄] ₃ (L1Co1) structure determination.....	124
3.10.8.2. [L2Co ^{III} Cl ₂][ClO ₄][Cl] (L2Co1) structure determination.....	124
3.10.8.3. [L3Co ^{III} Cl ₂][ClO ₄] (L3Co1) structure determination	125
3.10.8.4. [L1Co ^{III} Cl(DMF)][Co ^{II} Cl ₄] (L1Co2) structure determination.....	126
3.10.9. Electrochemical measurements	127
3.10.10. X-band EPR spectroscopy and quantitative simulations	127
3.10.10.1. EPR results of L1Co in H ₂ O and DMF	128
3.10.11. Michael-Addition C-C coupling.....	129
3.10.12. Suzuki-Miyaura type C-C coupling.....	130
3.10.13. Experimental acknowledgements	130
Chapter 4: Synthesis and characterization of novel manganese monomer and dimers with tetraazamacrocyclic ligands	131
4.1. Introduction	131
4.2. History of Mn(III,IV) di-μ-oxo bridged dimer complexes	136
4.2.1. Photosystem II and water oxidation	136
4.2.2. The oxygen evolving complex (OEC)	137
4.2.3. Schemes and tables related to historic Mn(III,IV) dimers.....	139
4.2.4. Bipy and phen Mn(III,IV) dimers.....	146
4.2.4.1. Catalytic ability of bipy and phen Mn(III,IV) dimers	148
4.2.5. Bispicen Mn(III,IV) dimers	150
4.2.6. Tmpa Mn(III,IV) dimers	153
4.2.7. Tren Mn(III,IV) dimer.....	158
4.2.8. Cyclam and cyclen Mn(III,IV) dimers	159
4.2.9. Terpy Mn(III,IV) dimers	163
4.2.10. Additional macrocyclic Mn(III,IV) dimers with pyclen and isocyclam.....	165
4.3. History of mononuclear Mn(III) complexes.....	166
4.3.1. Description of tetraazamacrocyclic ligands discussed.....	167
4.3.2. Mn(III) mononuclear complexes with tetraazamacrocycles.....	169

4.4. Novel library of high valent manganese complexes derived from pyridine- and pyridol-based tetraazamacrocyclic ligands	176
4.4.1. Synthesis of novel Mn(III) monomers and Mn(III,IV) dimers.....	177
4.4.2. UV-visible spectroscopy of Mn(III) monomers and Mn(III,IV) dimers	180
4.4.3. Solid state structures of Mn(III) monomers and Mn(III,IV) dimers.....	183
4.4.4. Electrochemical studies of Mn(III) monomers and Mn(III,IV) dimers	190
4.4.5. Infrared spectroscopy of Mn(III,IV) dimers	193
4.4.6. Conclusions	194
4.5. Experimental (methods and materials).....	195
4.5.1. Physical measurements.....	195
4.5.2. Preparation of [L1MnO]₂[ClO₄]₃ (L1Mn1)	195
4.5.3. Preparation of [L2MnO]₂[ClO₄]₂ (L2Mn1)	196
4.5.4. Preparation of [L1MnCl₂][ClO₄] (L1Mn2)	196
4.5.5. Preparation of [L2MnCl₂][ClO₄] (L2Mn2)	197
4.5.6. Preparation of [L3MnCl₂][ClO₄] (L3Mn2)	197
4.5.7. X-ray crystallography.....	197
4.5.7.1. [L1MnO]₂[ClO₄]₃ (L1Mn1) structure determination	197
4.5.7.2. [L2MnO]₂[ClO₄]₂ (L2Mn1) structure determination	198
4.5.7.3. [L1MnCl₂][ClO₄] (L1Mn2) structure determination	199
4.5.8. Electrochemical measurements	199
Chapter 5: Synthesis, characterization, and applications of a novel 30-membered pyridine/piperazine-based decaazamacrocycle (L5)	201
5.1 Introduction	201
5.1.1. Magnetic resonance imaging (MRI) and use of contrast agents (CA).....	201
5.1.2. Alternatives to the paramagnetic Gd(III) metal ion	202
5.1.3. Previously designed frameworks for Mn(II)-based contrast agents	204
5.1.4. Designing an ultra-rigid ligand framework for Mn(II)-based contrast agents.....	206
5.2. Synthesis of a novel 30-membered decaazamacrocycle (L5)	207
5.2.1. Procedure modifications for the attempted isolation of 15-anePyN₅Pip	213

5.3. Overview of large macrocyclic and/or piperazine-containing ligands.....	215
5.3.1. Applications of large polyazamacrocycles.....	216
5.3.1.1. Large polyazamacrocycles as metalloenzyme models.....	217
5.3.1.2. Large polyazamacrocycles as catalysts.....	217
5.3.1.3. Large polyazamacrocycles as anion receptors.....	218
5.3.2. Azamacrocyclic piperazine-containing ligands and corresponding metal complexes	219
5.3.2.1. A piperazine-containing macrocycle similar to 15-anePyN₅Pip	220
5.3.2.2. Piperazine-containing macrocycles similar to L5	222
5.4. Complexation studies of L5 with Cu(II)	224
5.5. Protonation and stability constants of L5 with various divalent transition metals	226
5.5.1. Relevant equations for the expression of the protonation and stability constants of L4	226
5.5.2. Determination of protonation constants for L5	229
5.5.3. Determination of stability (formation) constants for L5 with various divalent transition metal ions	231
5.6. Conclusions.....	238
5.7. Experimental (methods and materials).....	239
5.7.1. Physical measurements.....	239
5.7.2. Preparation of L5	240
5.7.3. X-ray crystallography.....	244
5.7.3.1. [C ₃₀ H ₅₀ N ₁₀] (L5) structure determination.....	244
5.7.4. Preparation of L5Cu	245
5.7.5. Equilibrium measurements	249
Chapter 6: Conclusions	252
Appendix.....	256
References	272
Vita	
Abstract	

List of Figures

1.1. Examples of different types of macrocycles.....	2
1.2. Common examples of naturally occurring macrocyclic ligands.....	3
1.3. Synthetic phthalocyanine macrocycle, and corresponding metal complexes.....	4
1.4. Series of cyclam congeners with ring sizes ranging from 12- to 16-members	8
1.5. Geometries adapted by mismatched metal-ligand complexes	11
1.6. An example of the <i>chelate effect</i> which is observed when comparing the reactions of monodentate vs. bidentate ligand set. The equilibrium constant (<i>K</i>) of the bidentate reaction is significantly larger than the monodentate reaction.....	12
1.7. Tetraazamacrocycles, open-chain noncyclic analogues, and di- <i>N</i> -methylated noncyclic analogues used in the comprehensive study conducted by Clay <i>et al.</i>	15
1.8. Thermodynamic parameters vs. increasing size/length of ligands for Cu(II) complex formation	16
1.9. Possible transition states prior to formation of second metal-nitrogen bond during ligand coordination (S = solvent molecule)	19
1.10. General mechanism for formation of a <i>trans</i> -tetraazamacrocyclic metal complex (S = solvent molecule)	20
1.11. Chemical structures of macrocyclic ligands synthesized by the Green group	29
2.1. The ‘pathological trifecta’ which are hallmarks of neurodegenerative diseases	33
2.2. Current neurotherapeutic molecules relevant to this discussion. (R group examples include 8-hydroxyquinoline and propylpyridine-4-yl)	36
2.3. L1 and metal chelating ligands studied by the Green group	39
2.4. L1-L3 ligands synthesized and studied by the Green group	42
2.5. Rational design approach of L4 , based off successes of L1 and L2	45
2.6. Common conformations of pyridinophanes and the solid state conformation of (2.14).....	49
2.7. pH-potentiometric titration curve of a solution containing 1.897 mM of H ₄ L ₄ ²⁺ titrated with 99.78 mM NaOH (<i>I</i> = 0.15 M NaCl, <i>T</i> = 25 °C) over pH range 1.6 – 12.0. (H ₄ L ₄ ²⁺ represents fully protonated L4).54	
2.8. Species distribution diagram for 10.00 mM L4 at <i>I</i> = 0.15 M NaCl and 25.0 °C	56
2.9. pH-potentiometric titration curve of a solution containing 2.041 mM H ₄ L ₄ ²⁺ in the presence of 1.975 mM Zn(II) (<i>I</i> = 0.15 M NaCl, <i>T</i> = 25 °C); titrated with a 0.09978 M standardized NaOH solution.....	59
2.10. Species distribution diagram for 10.00 mM Zn(II) and 10.00 mM L4 at <i>I</i> = 0.15 M NaCl and 25.0 °C.	60

2.11. Orientations of nitrogen atom lone pairs in common pyridinophane conformers and example of metal-ligand complex in the <i>syn</i> boat-boat orientation (for L4 , R = OH and X = Cl)	61
2.12. Asymmetric units and symmetry generated solid state structures of L4Cu and L4Zn	63
2.13. Solid state structure of L1-L4Cu and L1-L4Zn (Hydrogen atoms have been omitted for clarity).....	64
2.14. The electronic spectra of L4Cu in H ₂ O (pH = 5.00) and DMF. Molar Absorptivity: [λ_{\max}/nm ($\epsilon/\text{M}^{-1} \text{cm}^{-1}$)] in H ₂ O: 758 (23); in DMF: 873 (49)	68
2.15. Cyclic voltammogram recorded in 3.0 mL of DMF containing 3 mg L4Cu + 0.1 M TBAP with a glassy carbon working electrode, Ag wire quasi-reference electrode, and a platinum wire auxiliary electrode. Arrow indicates direction of scans, all scans performed at 100 mV/s.....	69
2.16. Measured distances between pyridol ring planes in L4Cu	70
2.17. ¹ H NMR spectrum of L4 in D ₂ O.....	71
2.18. ¹ H NMR of L4Zn in D ₂ O.....	72
2.19. DPPH radical quenching assay showing the antioxidant character of L1 , L2 , and L4 compared to the standard antioxidant BHT ($n = 3$).....	74
2.20. Fluorescence intensity of 7-hydroxy-CCA after incubation of CCA [100 μM] and ascorbate [300 μM] with Cu(II) [10 μM]. Compound L2 [5 μM ; 10 μM] and L4 [5 μM ; 10 μM] were combined prior to addition of ascorbate. No fluorescence was observed with CCA co-incubated with samples of: (1) ascorbate [300 μM] only or (2) Cu(II) [10 μM]. All solutions except CuSO ₄ •6H ₂ O (MilliQ water only) were dissolved and diluted in 7.4 pH 1X KH ₂ PO ₄ /NaCl buffer containing Desferal [1 μM]. Final volume = 3 mL. ($n = 3$).....	75
2.21. (a) Cell survival vs. log conc. of MCF-7 cells dosed with L2 or L4 ; (b) cell survival vs. log conc. of HT22 cells dosed with L2 or L4	76
2.E1. pH-potentiometric titration curves of L4 with and without the presence of an M(II) transition metal (Ca(II), Mn(II), Co(II), and Zn(II)). ($I = 0.15 \text{ M NaCl}$, $T = 25 \text{ }^\circ\text{C}$).....	95
3.1. (a) <i>cis</i> and <i>trans</i> isomers of Werner complexes; (b) Werner's carbon-free optically active compound	101
3.2. Images of the complexation reaction of Co(II) + ligand in DMF. Co(ClO ₄) ₂ is bright pink when dissolved in DMF, upon addition of L1 , L2 , or L3 the solution color changes to deep blue (L1 : R = H, R' = H; L2 : R = OH, R' = H; L3 : R = H, R' = OH).....	104
3.3. Comparison of the electronic absorption spectra of (a) L1Co1 , L2Co1 , and L3Co1 with (b) L1Co2 , L2Co2 , and L3Co2 in water vs. DMF. The observed species in (a) and (b) are noted in (c) and (d), respectively (L1 : R = H, R' = H; L2 : R = OH, R' = H; L3 : R = H, R' = OH)	105
3.4. Comparison of the electronic absorption spectra of (a) CoCl ₂ and (b) L1Co1 and L1Co2 in DMF vs. water. The conversion process observed for (a) and (b) are noted in (c) and (d), respectively	106

3.5. Comparison of L1Co1 , L2Co1 , L3Co1 , and L1Co2 growth methods, crystal morphology, and solid state structures (ORTEP views 50% probability; hydrogen atoms were omitted for clarity).....	108
3.6. Comparison of solid state structure of L1Co1 , L2Co1 , L3Co1 , L1Co2 , and 3.1 (hydrogen atoms have been omitted for clarity)	113
3.7. Comparison of the electronic absorption spectra of (a) CoCl₂ and (b) L1Co2 in concentrated hydrochloric acid; both contain the anionic species [Co ^{II} Cl ₄] ²⁻	114
3.8. Cyclic voltammograms recording in 10 mL of DMF containing 10 mg (L1Co , L2Co , or L3Co ; 0.01 mmol) + 0.1 TBAP with a glassy carbon working electrode, Ag wire <i>quasi</i> -reference electrode, and platinum wire auxiliary electrode. All voltammograms were referenced to Fc/Fc ⁺ (E _{1/2} = 0.00 V). Arrows indicated direction of scans performed at 100 mV/s; (a) scanning from cathodic to anodic potentials and (b) scanning from anodic to cathodic potentials.....	115
3.9. Electronic absorption spectra of L1Co3 , L2Co3 , and L3Co3 in (a) H ₂ O and (b) DMF. No characteristic [CoCl ₄] ²⁻ absorbance band is present	116
3.10. (a) L1Co isolated as a blue powder; (b) L1Co dissolved in H ₂ O exists as L1Co1 ; (c) L1Co dissolved in DMF exists as L1Co2 (this solvent dependent behavior is also observed for L2Co and L3Co).....	118
3.E1. 10 K X-band EPR spectra of L1-Co and in water (1) and DMF (2). Quantitative simulations (<i>dashed lines</i>) for each spectrum are included for comparison. Instrumental parameters: microwave frequency, 9.643 GHz; microwave power, 100 μW for each spectrum arc; 0.9 mT; temperature, 10 K. Simulation parameters for each ⁵⁹ Co(II) S = 3/2 (I = 7/2) site: S1 , g _{x,y,z} (2.01, 2.69, 2.15), σg _{x,y,z} (0.09, 0.08, 0.09), A _{iso} , (250 MHz), D = 10 ± 5 cm ⁻¹ , E/D = 0.05; S2 (i) , g _{x,y,z} (2.38, 2.34, 2.17), σg _{x,y,z} (0.05, 0.05, 0.05), A _{iso} , (250 MHz), D = 10 ± 5 cm ⁻¹ , E/D = 0.09; (ii) , g _{x,y,z} (2.46, 2.48, 2.04), σg _{x,y,z} (0.01, 0.02, 0.03), A _{iso} , (230 MHz), D = 10 ± 5 cm ⁻¹ , E/D = 0.23, 0.1 mT. All simulations utilize a uniform line width (σ _B) of 0.1 mT	129
3.E2. Michael-Addition reaction <i>sans</i> catalyst monitored by ¹ H NMR; product formation is observed without catalyst present (at RT)	130
3.E3. GC-MS data for C-C coupling product of the Michael-Addition reaction (without catalyst)	131
3.E4. Michael-Addition reaction with L1Co3 , monitored by ¹ H NMR.....	131
3.E5. GC-MS data for C-C coupling product of the Michael-Addition reaction with L1Co3 catalyst	131
3.E6. ¹ H NMR spectra of control and catalyst reactions of Suzuki-Miyaura type C-C coupling. Starting materials were conserved with no product formation observed by ¹ H NMR.....	132
4.1. Electronic spectra of <i>cis</i> -Mn(III) complexes of L1Mn2 , L2Mn2 , and L3Mn2	181
4.2. Electronic spectra of di-μ-oxo bridged Mn(III,IV) complexes of L1Mn1 , L2Mn1 , and L3Mn1	182
4.3. Solid state structures of complexes L1Mn1 , L2Mn1 , and L1Mn2 (hydrogen atoms have been omitted for clarity).....	183
4.4. Comparison of the solid-state structures of L1Mn2 and 4.19a	184

4.5. Cyclic voltammograms of <i>cis</i> -Mn(III) complexes L1Mn2 , L2Mn2 , L3Mn2 . CV recording in 10.0 mL of DMF containing 10 mg complex + 0.1 M TBAP with a glassy carbon working electrode, Ag wire <i>quasi</i> -reference electrode, and a platinum wire auxiliary electrode.	191
4.6. Cyclic voltammograms of Mn(III,IV) dimer complexes L1Mn1 , L2Mn1 . CV recorded in 3.0 mL of H ₂ O containing 3 mg complex + 0.1 M NaClO ₄ with a glassy carbon working electrode, Ag/AgCl reference electrode, and a platinum wire auxiliary electrode	193
5.1. (a) Ligand framework for only clinically approved Mn(II)-based contrast agent; (b) Common ligand frameworks used in Gd(III)-based contrast agents.	204
5.2. Ligand frameworks designed by Tóth and coworkers for Mn(II)-based contrast agents (names have previously been used in literature)	206
5.3. Novel ultra-rigid pentaazamacrocyclic ligand frameworks for Mn(II)-based contrast agents.....	206
5.4. (a) Mass spectrum of predicted 15-anePyN₅Pip ; (b) ¹ H NMR spectrum of predicted 15-anePyN₅Pip with resonance assignments; (c) ¹³ C NMR spectrum of predicted 15-anePyN₅Pip with resonance assignments.	209
5.5. Solid state structure of L5 ; the asymmetric unit and grown structure are pictured above (hydrogen atoms have been omitted for clarity)	210
5.6. (a) Mass spectrum of L5 ; (b) ¹ H NMR spectrum of L5 with resonance assignments; (c) ¹³ C NMR spectrum of L5 with resonance assignments.....	211
5.7. Conformational changes of piperazine in solution eventually leading to inversion, which is reminiscent of cyclohexane. (R = H for piperazine; R = CH ₂ CH ₂ NH ₂ for (5.3))	213
5.8. Modifications to reaction conditions of metal-template synthetic procedure for L5	215
5.9. Selected large polyazamacrocyclic ligands.....	216
5.10. Ligand set, and metal complex designed and synthesized by Alcock <i>et al.</i>	221
5.11. Positions of nitrogen atom lone pairs dependent on the conformation of piperazine	221
5.12. Hexaazamacrocyclic ligand 5.17 and related solid state structures	222
5.13. Ligand 5.10 and related solid state structures	223
5.14. Mass spectrum of L5 complexation reaction with 2 equivalents of Cu(II).....	225
5.15. pH-potentiometric titration curve of H ₆ L ⁶⁺ titrated with NaOH (<i>I</i> = 0.15 M NaCl, <i>T</i> = 25 °C) over pH range 2.0 – 12.0. (H ₆ L ⁶⁺ represents the fully protonated L5).....	230
5.16. pH-potentiometric titration of solutions containing 1:1 equivalents of H ₆ L ⁶⁺ in the presence of M(II) (<i>I</i> = 0.15 M NaCl, <i>T</i> = 25 °C). (M(II) is a divalent transition metal ion; M(II) was introduced in the form of a MCl ₂ stock solution). *For Mn(II) and Fe(II) the titrations were halted due to formation of metal hydroxide species	232

5.17. pH-potentiometric titration of solutions containing 1:1 and 1:2 equivalents of H_6L^{6+} in the presence of Cu(II) ($I = 0.15$ M NaCl, $T = 25$ °C). Cu(II) was introduced in the form of a $CuCl_2$ stock solution..	233
5.18. Plot of the first stability constants for 1:1 complex of L5 with M(II) ions. Log K_{ML} values follow the Irving-Williams series (Mn(II) < Fe(II) < Co(II) < Ni(II) < Cu(II) > Zn(II))	234
5.19. Species distribution diagram for the L5 : Cu^{2+} : H^+ system ($[Cu^{2+}] = [L5] = 2.0$ mM; $pK_{30} = L5$)	237
5.20. Species distribution diagram for the L5 : Cu^{2+} : H^+ system ($[Cu^{2+}] = 4.0$ mM, $[L5] = 2.0$ mM; $pK_{30} = L5$)	237
5.21. Solid state structure of L5 , showing preferred <i>chair</i> conformation of piperazine rings and <i>trans</i> orientation of nitrogen atom lone pairs. (Hydrogen atoms have been omitted for clarity)	239
5.E1. MS of L5 with assignments and zoomed in isotopic envelopes of $[L5+2H^+]^{2+}$ and $[L5+H^+]^+$	243
5.E2. Overall MS spectrum of L5Cu dissolved in H_2O (originally shown as figure 5.14	246
5.E3. Found vs. theoretical isotopic distribution of $[L5+2Cu^{2+}-2H^+]^{2+}$ fragment	246
5.E4. Found vs theoretical isotopic distribution of $[L5+2Cu^{2+}+2Cl^-]^{2+}$ and $[\frac{1}{2}L5+Cu^{2+}+Cl^-]^+$ fragments.....	247
5.E5. Found vs theoretical isotopic distribution of $[L5+Cu^{2+}-H^+]^+$ fragment	247
5.E6. Found vs theoretical isotopic distribution of $[L5+Cu^{2+}+Cl^-]^+$ fragment.....	248
5.E7. Found vs theoretical isotopic distribution of $[L5+2Cu^{2+}+3Cl^-]^+$ fragment.....	248
5.E8. Found vs theoretical isotopic distribution of $[L5+2Cu^{2+}+2Cl^-+ClO_4^-]^+$ fragment	249
5.E9. pH-potentiometric titration curves of L5 with and without the presence of 1 equiv. of transition metal M(II) (M(II) = Mn(II), Fe(II), Cu(II), or Zn(II)). ($I = 0.15$ M NaCl, $T = 25$ °C). Titrations in the presence of Mn(II) and Fe(II) were halted upon precipitation of metal-hydroxide species.	250
5.E10. pH-potentiometric titration curve of L5 with and without the presence of 1 or 2 equiv. of Cu(II). ($I = 0.15$ M NaCl, $T = 25$ °C)	251
6.1. Macrocyclic ligands synthesized by the Green group	252
6.2. Pyridinophane-metal complexes that have been tested as catalysts in a variety of different reactions; the ligand framework and metal-binding modalities are similar to L4	255

List of Schemes

1.1. The original proposed products of the condensation reaction between $[\text{Ni}(\text{en})_3]^{2+}$ and acetone (1960) and the actual products reported in 1966, now known as 'Curtis macrocycles'	5
1.2. Representative reaction for the Richman-Atkins synthetic method using tosyl groups	24
1.3. Representative reaction for the modified Richman-Atkins synthetic method using nosyl groups.....	25
1.4. Representative example of a metal-template reaction between a di-carbonyl and di-primary amine in the presence of a metal salt; imine bonds are chemically reduced to yield the saturated cyclic amine complex.....	27
2.1. Redox cycling of copper in the presence of oxygen and ascorbate to produce hydroxyl radicals	41
2.2. General methodology for the synthesis of L1-L3 ; (Ns = nosyl).....	44
2.3. Synthetic methodology for the isolation of L4	46
2.4. Cyclization reaction with 2 equivalents of TsNHNa resulting in macrocycle formation	47
2.5. Solid state structure of (2.14); the asymmetric and grown structure are pictured above (hydrogen atoms have been omitted for clarity)	48
2.6. Protonation events for ligands L1-L4 based on pH-potentiometric titrations.....	55
2.7. Complexation reaction of L4 with Cu(II) and Zn(II).....	62
2.8. Mechanism of the DPPH radical quenching assay and corresponding color change associated with reduction of the DPPH radical.....	73
2.E1. Protection of triethylamine with nosyl groups.....	78
2.E2. Macro-cyclization and nosyl group removal for L1	79
2.E3. Synthesis of alkyl halide precursor for macro-cyclization of L2	81
2.E4. Macro-cyclization and nosyl group removal for L2	83
2.E5. Synthesis of alkyl halide precursor for macro-cyclization of L3	84
2.E6. Macro-cyclization and nosyl group removal for L3	86
2.E7. Preparation of TsNHNa salt.....	88
2.E8. Synthetic methodology for the preparation of cyclized/protected L4	88
2.E9. Synthetic methodology for the deprotection and isolation of L4	89
3.1. Equilibrium reaction between cobalt(II) hexahydrate and cobalt(II) tetrachloride used to demonstrate Le Châtelier's Principle	102
3.2. Synthesis of L1Co , L2Co , and L3Co ; equilibrium of L1Co1/L1Co2 , L2Co1/L2Co2 , and L3Co1/L3Co2 in aqueous and organic solvents (L1 : R = H, R' = H; L2 : R = OH, R' = H; L3 : R = H, R' = OH	104

3.3. Metathesis reaction with AgBF ₄ and subsequent complexation reaction to form L1Co3 , L2Co3 , and L3Co3 (L1 : R = H, R' = H; L2 R = OH, R' = H; L3 : R = H; R' = OH)	116
3.4. Michael-Addition C-C- coupling reaction between nitrostyrene and dimethyl malonate	117
3.5. Suzuki-Miyaura type catalyzed C-C coupling reaction.....	117
4.1. Water splitting redox reactions (water oxidation + proton reduction)	136
4.2. (a) Proposed model of OEC published in 1994; (b) Crystal structure of OEC at resolution of 1.9 Å, published in 2011	138
4.3. Parent ligands for Mn(III,IV) dimer complexes.....	139
4.4. Historically significant di-μ-oxo bridged Mn(III,IV) dimers	139
4.5. Synthesis timeline of Mn(III,IV) di-μ-oxo bridged dimers.....	140
4.6. Oxidation and reduction values for various di-μ-oxo bridged Mn(III,IV) dimers in literature	145
4.7. Bispicen and derivatized ligands	151
4.8. Tmpa and derivatized ligands	155
4.9. Tetraazamacrocyclic ligands described in table 4.8	169
4.10. Different methods for synthesis and isolation of Mn(III) monomers vs. Mn(III,IV) dimers	177
4.11. Asymmetric units and symmetry generated dimers for the solid-state structure of 4.9a , L1Mn1 , L2Mn1 (Hydrogen atoms omitted for clarity)	187
5.1. (a) Synthesis of 15-anePyN₃O₂ published by Tóth and coworkers; (b) Predicted intermediate and products of the template reaction with (5.1), (5.3), and Mn(II).....	208
5.2. Mn(II) Schiff base complex and resulting product (L5) from the template reaction between (5.1) and (5.3)	212
5.3. (a) Original starting material order of addition, resulting in isolation of L5 ; (b) Hypothesized isolation of 15-anePyN₅Pip upon reversal of starting material order of addition	214
5.4. Proposed protonation sequence of L5 (for visualization purposes only)	231
5.E1. Synthesis of (5.1) using activated MnO ₂	240
5.E2. Synthesis of piperazine-based amine precursor (5.3) for cyclization	240
5.E3. Template synthesis of L5 ligand using MnCl ₂	241
6.1. Oxygen atom transfer catalytic reaction to be studied with Mn(III) complexes	254
6.2. Hydrogen atom abstraction catalytic reaction to be studied with Mn(III) complexes	254

List of Tables

1.1. Spectrochemical parameters for complexes <i>trans</i> -[Co ^{III} ([13-16]aneN ₄)Cl ₂] ⁺ and <i>trans</i> -[Ni ^{II} ([13-16]aneN ₄)Cl ₂].	9
1.2. Ideal M-N bond lengths and planarity of a series of macrocyclic ligands.	10
1.3. Stability constants for the 1:1 complexes of tetraamines with Cu(II).	13
1.4. Thermodynamic parameters for Cu(II) complex formation with tetraaza ligands at 298 K	15
1.5. Rates of formation of Cu(II) complexes with tetraazamacrocycles in acidic aqueous solution	18
1.6. First-order dissociation rate constants of 1:1 Cu(II) complexes in 6.1 M HCl at 25.0 °C.	21
1.7. Rates of dissociation of Ni(II) complexes in 0.3 M HClO ₄ at 25 °C	22
1.8. Typical classification of ring sizes	24
2.1. Crystal data, intensity collections, and structure refinement parameters for (2.14)	47
2.2. Protonation constants (pK) of the species formed during titration of L1, L2, L3, L4, and cyclen (I = 0.15 M NaCl, T = 25 °C)	54
2.3. Overall stability constants (log β) of M(II) ligand complexes (I = 0.15 M NaCl and T = 25 °C)	57
2.4. Crystal data, intensity collections, and structure refinement parameters for L4Cu and L4Zn	63
2.5. Selected bond lengths (Å) for L1-L4Cu and L1-L4Zn	66
2.6. Selected bond angles (°) for L1-L4Cu and L1-L4Zn	67
2.7. Electrochemical values related to L4Cu	69
2.8. A comparison of electrochemical values for L1Cu-L4Cu	70
3.1. Comparison of Blomstrand's Chain Theory and Werner's Coordination Theory	100
3.2. Electronic absorption bands and transition assignment for L1Co in DMF and H ₂ O, λ _{max} /nm(ε/M ⁻¹ cm ⁻¹)	107
3.3. Crystal data, intensity collections, and structure refinement parameters for L1Co1 , L2Co1 , L3Co1 , and L1Co2	109
3.4. Selected bond lengths (Å) and angles (°)	111
3.E1. Reaction conditions for Michael-Addition experiments	130
3.E2. Reaction conditions for Suzuki-Miyaura type experiments	132
4.1. Di-μ-oxo bridged Mn(III,IV) dimers reported in literature	141
4.2. Mn – Mn bond distances within di-μ-oxo bridged Mn(III,IV) dimers	142
4.3. Mn ₂ O ₂ vibrational frequencies of di-μ-oxo bridged Mn(III,IV) dimers.	142

4.4. Electronic spectra of di- μ -oxo bridged Mn(III,IV) dimers	143
4.5. Electrochemistry of di- μ -oxo bridged Mn(III,IV) dimers.....	144
4.6. Bispicen derived Mn(III,IV) dimer complexes.....	151
4.7. Tmpa derived Mn(III,IV) dimer complexes	154
4.8. Mn(III) monomeric complexes with various tetraazamacrocyclic ligands.....	168
4.9. Electronic spectra of selected monomeric <i>cis</i> -Mn(III) tetraazamacrocyclic complexes in CH ₃ CN	181
4.10. Selected bond distances (Å) for complexes 4.9a , L1Mn1 , L2Mn1 , 4.19a , and L1Mn2	185
4.11. Selected bond angles (°) for complexes 4.19a and L1Mn2	185
4.12. Selected bond angles (°) for 4.9a , L1Mn1 , L2Mn1	186
4.13. Crystal data, intensity collections, and structure refinement parameters for L1Mn1 , L2Mn1 , and L1Mn2	189
4.14. Electrochemical data for complexes synthesized by the Green group (all reported vs. NHE).....	190
5.1. Crystal data, intensity collections, and structure refinement parameters for L5	210
5.2. Protonation constants for L5 (<i>I</i> = 0.15 M NaCl, 25 °C).....	229
5.3. Protonation constants (log <i>K</i>) for various large polyazamacrocycles (T = 25 °C).....	231
5.4. Stability constants of the complexes formed with L5 and various metal ions (<i>I</i> = 0.15 M NaCl, 25 °C)	233
5.5. Overall stability constants and protonation constants of various polyazamacrocyclic M(II) complexes	235

List of Equations

1.1. $\Delta G^\circ = -RT \ln K$	12
1.2. $\Delta G^\circ = \Delta H^\circ - T\Delta S^\circ$	12
1.3. $[ML_{\text{noncyclic}}]^{n+}(\text{aq}) + L_{\text{macrocyclic}}(\text{aq}) \rightarrow [ML_{\text{macrocyclic}}]^{n+}(\text{aq}) + L_{\text{noncyclic}}(\text{aq})$	14
1.4. $M^{n+}(\text{aq}) + L(\text{aq}) \rightarrow ML^{n+}(\text{aq})$ (where L is either macrocyclic or noncyclic).....	14
1.5. $M^{n+} + L \rightleftharpoons_{k_d}^{k_f} ML^{n+}$	17
1.6. $K_{ML} = \frac{[ML^{n+}]}{[M^{n+}][L]} = \frac{k_f}{k_d}$	17
1.7. $MS_6 + L \xrightleftharpoons{K_{OS}} MS_6 \cdots L$ (OS=outersphere).....	18
1.8. $MS_6 \cdots L \xrightleftharpoons{k_1} MS_5L$	18
1.9. $MS_5L \xrightarrow{k_2} \xrightarrow{k_3} \cdots \xrightarrow{k_n} ML$	18
2.1. $O_2^{\bullet-} + H_2O_2 \rightarrow OH^- + OH^\bullet + O_2$ (Haber-Weiss reaction)	35
2.2. $M^{n+} + H_2O_2 \rightarrow M^{(n+1)+} + OH^- + OH^\bullet$ (Fenton Reaction; M = Fe (n = 2) or Cu (n = 1))	35
2.3. $aA + bB \leftrightarrow cC + dD$ $K_{eq} = \frac{a^c_C \times a^d_D}{a^a_A \times a^b_B}$	50
2.4. $aA + bB \leftrightarrow cC + dD$ $K_{eq} = \frac{[C]^c[D]^d}{[A]^a[B]^b}$	50
2.5. $K_1^H = \frac{[HL^-]}{[H^+][L^{2-}]}$	52
2.6. $K_2^H = \frac{[H_2L]}{[H^+][HL^-]}$	52
2.7. $K_3^H = \frac{[H_3L^+]}{[H^+][H_2L]}$	52
2.8. $K_4^H = \frac{[H_4L^{2+}]}{[H^+][H_3L^+]}$	52
2.9. $\theta_{HL} = K_1^H$	52
2.10. $\theta_{H_2L} = K_1^H K_2^H$	52
2.11. $\theta_{H_3L} = K_1^H K_2^H K_3^H$	52
2.12. $\theta_{H_4L} = K_1^H K_2^H K_3^H K_4^H$	52
2.13. $\beta_{HL} = \frac{[HL^-]}{[H^+][L^{2-}]}$	52
2.14. $\beta_{H_2L} = \frac{[H_2L]}{[H^+]^2 [L^{2-}]}$	52

2.15.	$\beta_{H_3L} = \frac{[H_3L^+]}{[H^+]^3 [L^2]}$	52
2.16.	$\beta_{H_4L} = \frac{[H_4L^{2+}]}{[H^+]^4 [L^2]}$	52
2.17.	$K_{ML}^M = \frac{[ML]}{[M^{2+}][L^2]}$	53
2.18.	$K_{MHL}^H = \frac{[MHL^+]}{[H^+][ML]}$	53
2.19.	$K_{MH_2L}^H = \frac{[MH_2L^{2+}]}{[H^+][MHL^+]}$	53
2.20.	$K_{MH_3L}^H = \frac{[MH_3L^{3+}]}{[H^+][MH_2L^{2+}]}$	53
2.21.	$\beta_{ML} = K_{ML}^M$	53
2.22.	$\beta_{MHL} = K_{ML}^M K_{MHL}^H$	53
2.23.	$\beta_{MH_2L} = K_{ML}^M K_{MHL}^H K_{MH_2L}^H$	53
2.24.	$\beta_{MH_3L} = K_{ML}^M K_{MHL}^H K_{MH_2L}^H K_{MH_3L}^H$	53
2.25.	$\beta_{ML} = \frac{[ML]}{[M^{2+}][L^2]}$	53
2.26.	$\beta_{MHL} = \frac{[MHL^+]}{[H^+][M^{2+}][L^2]}$	53
2.27.	$\beta_{MH_2L} = \frac{[MH_2L^{2+}]}{[H^+]^2 [M^{2+}][L^2]}$	53
2.28.	$\beta_{MH_3L} = \frac{[MH_3L^{3+}]}{[H^+]^3 [M^{2+}][L^2]}$	53
3.1.	$\hat{H} = \mathbf{D} \left(\hat{S}_Z^2 - \frac{S(S+1)}{3} \right) + \mathbf{E} \left(\hat{S}_X^2 + \hat{S}_Y^2 \right) + \beta \mathbf{B} \cdot \mathbf{g} \cdot \mathbf{S} + \mathbf{S} \mathbf{A} \mathbf{I}$	127
5.1.	$K_1^H = \frac{[HL^+]}{[H^+][L]}$	226
5.2.	$K_2^H = \frac{[H_2L^+]}{[H^+][HL^+]}$	226
5.3.	$K_3^H = \frac{[H_3L^{3+}]}{[H^+][H_2L^{2+}]}$	226
5.4.	$K_4^H = \frac{[H_4L^{4+}]}{[H^+][H_3L^{3+}]}$	227
5.5.	$K_5^H = \frac{[H_5L^{5+}]}{[H^+][H_4L^{4+}]}$	227
5.6.	$K_6^H = \frac{[H_6L^{6+}]}{[H^+][H_5L^{5+}]}$	227
5.7.	$\beta_{HL} = K_1^H$	227
5.8.	$\beta_{H_2L} = K_1^H K_2^H$	227

5.9. $\beta_{H_3L} = K_1^H K_2^H K_3^H$	227
5.10. $\beta_{H_4L} = K_1^H K_2^H K_3^H K_4^H$	227
5.11. $\beta_{H_5L} = K_1^H K_2^H K_3^H K_4^H K_5^H$	227
5.12. $\beta_{H_6L} = K_1^H K_2^H K_3^H K_4^H K_5^H K_6^H$	227
5.13. $\beta_{HL} = \frac{[HL^+]}{[H^+][L]}$	226
5.14. $\beta_{H_2L} = \frac{[H_2L^{2+}]}{[H^+]^2 [L]}$	226
5.15. $\beta_{H_3L} = \frac{[H_3L^{3+}]}{[H^+]^3 [L]}$	226
5.16. $\beta_{H_4L} = \frac{[H_4L^{4+}]}{[H^+]^4 [L]}$	227
5.17. $\beta_{H_5L} = \frac{[H_5L^{5+}]}{[H^+]^5 [L]}$	227
5.18. $\beta_{H_6L} = \frac{[H_6L^{6+}]}{[H^+]^6 [L]}$	227
5.19. $K_{ML}^M = \frac{[ML^{2+}]}{[M^{2+}][L]}$	228
5.20. $K_{MHL}^H = \frac{[MHL^{3+}]}{[H^+][ML^{2+}]}$	228
5.21. $K_{MH_2L}^H = \frac{[MH_2L^{4+}]}{[H^+][MHL^{3+}]}$	228
5.22. $K_{MH_3L}^H = \frac{[MH_3L^{5+}]}{[H^+][MH_2L^{4+}]}$	228
5.23. $K_{MH_4L}^H = \frac{[MH_4L^{6+}]}{[H^+][MH_3L^{5+}]}$	228
5.24. $\beta_{ML} = K_{ML}^M$	228
5.25. $\beta_{MHL} = K_{ML}^M K_{MHL}^H$	228
5.26. $\beta_{MH_2L} = K_{ML}^M K_{MHL}^H K_{MH_2L}^H$	228
5.27. $\beta_{MH_3L} = K_{ML}^M K_{MHL}^H K_{MH_2L}^H K_{MH_3L}^H$	228
5.28. $\beta_{MH_4L} = K_{ML}^M K_{MHL}^H K_{MH_2L}^H K_{MH_3L}^H K_{MH_4L}^H$	228
5.29. $\beta_{ML} = \frac{[ML^{2+}]}{[M^{2+}][L]}$	228
5.30. $\beta_{MHL} = \frac{[MHL^{2+}]}{[H^+][M^{2+}][L]}$	228

5.31.	$\beta_{\text{MH}_2\text{L}} = \frac{[\text{MH}_2\text{L}^{4+}]}{[\text{H}^+]^2 [\text{M}^{2+}] [\text{L}]}$	228
5.32.	$\beta_{\text{MH}_3\text{L}} = \frac{[\text{MH}_3\text{L}^{5+}]}{[\text{H}^+]^3 [\text{M}^{2+}] [\text{L}]}$	228
5.33.	$\beta_{\text{MH}_4\text{L}} = \frac{[\text{MH}_4\text{L}^{6+}]}{[\text{H}^+]^4 [\text{M}^{2+}] [\text{L}]}$	228
5.34.	$K_{\text{M}_2\text{L}}^{\text{M}} = \frac{[\text{M}_2\text{L}^{4+}]}{[\text{M}^{2+}]^2 [\text{ML}^{2+}]}$	229
5.35.	$K_{\text{M}_2\text{HL}}^{\text{H}} = \frac{[\text{M}_2\text{HL}^{5+}]}{[\text{H}^+] [\text{M}_2\text{L}^{4+}]}$	229
5.36.	$K_{\text{M}_2\text{H}_2\text{L}}^{\text{H}} = \frac{[\text{M}_2\text{H}_2\text{L}^{6+}]}{[\text{H}^+] [\text{M}_2\text{HL}^{5+}]}$	229
5.37.	$\beta_{\text{M}_2\text{L}} = K_{\text{M}_2\text{L}}^{\text{M}}$	229
5.38.	$\beta_{\text{M}_2\text{HL}} = K_{\text{M}_2\text{L}}^{\text{M}} K_{\text{M}_2\text{HL}}^{\text{H}}$	229
5.39.	$\beta_{\text{M}_2\text{H}_2\text{L}} = K_{\text{M}_2\text{L}}^{\text{M}} K_{\text{M}_2\text{HL}}^{\text{H}} K_{\text{M}_2\text{H}_2\text{L}}^{\text{H}}$	229
5.40.	$\beta_{\text{M}_2\text{L}} = \frac{[\text{M}_2\text{L}^{4+}]}{[\text{M}^{2+}]^2 [\text{L}]}$	229
5.41.	$\beta_{\text{M}_2\text{HL}} = \frac{[\text{M}_2\text{HL}^{2+}]}{[\text{H}^+] [\text{M}^{2+}]^2 [\text{L}]}$	229
5.42.	$\beta_{\text{M}_2\text{H}_2\text{L}} = \frac{[\text{M}_2\text{H}_2\text{L}^{6+}]}{[\text{H}^+]^2 [\text{M}^{2+}]^2 [\text{L}]}$	229

List of Abbreviations

Å	Angstrom (1.0×10^{-10} m)
δ	Chemical shift
λ	Wavelength (typically reported in nm)
7-hydroxy-CCA	7-hydroxy-coumarin-3-carboxylic acid
[12]aneN ₄	1,4,7,10-tetraazacyclododecane
[13]aneN ₄	1,4,7,11-tetraazacyclododecane
[14]aneN ₄	1,4,8,11-tetraazacyclododecane
[15]aneN ₄	1,4,8,12-tetraazacyclododecane
[16]aneN ₄	1,5,9,13-tetraazacyclododecane
ABTS	2,2'-azino-bis(3-ethylbenzothiazoline-6-sulphonic acid)
AD	Alzheimer's disease
APP	Amyloid precursor protein
BBB	Blood-brain barrier
BHT	Dibutylhydroxytoluene; 2,6-Di- <i>tert</i> -butyl-4-methylphenol
Bipy	2,2-bipyridine
Bispicbn	<i>N,N'</i> -bis(2-pyridylmethyl)-2,3-butanediamine
Bispicen	<i>N,N'</i> -bis(2-pyridylmethyl)-1,2-diaminoethane
Bispichxn	<i>N,N'</i> -bis(2-pyridylmethyl)-1,2-cyclohexanediamine
Bispicpn	<i>N,N'</i> -bis(2-pyridylmethyl)-1,2-propanediamine
CA	Contrast agent
CCA	Coumarin-3-carboxylic acid
CCDC	Cambridge crystallographic data center
CQ	Clioquinol; iodochlorhydroxyquin,5-chloro-7-iodo-8-hydroxyquinoline
CV	Cyclic voltammetry
Cy	Cyclohexane
Cyclen	1,4,7,10-tetraazacyclododecane

Cyclam	1,4,7,11-tetraazacyclododecane
Cyclal	1,4,8,12-tetraazacyclododecane
DMEM	Dulbecco's Modified Eagle's Medium
DMF	<i>N,N</i> -dimethyl formamide
DNA	Deoxyribonucleic acid
DOTA	1,4,7,10-tetraazacyclododecane-1,4,7,10-tetraacetic acid; tetraxetan
DPPH	2,2-diphenyl-1-picrylhydrazyl
DPDP	<i>N,N'</i> -diprydoxylethylenediamine- <i>N,N'</i> -diacetate-5,5'-bis(phosphate)
DTBBQ	3,5-di- <i>t</i> -butyl-1,2-benzoquinone
DTBSQ	3,5-di- <i>t</i> -butyl-1,2-semiquinonato
DTPA	Diethylenetriaminepentacetate; gadopentetic acid
EDTA	Ethylenediaminetetraacetic acid
En	Ethylenediamine
EPR	Electron paramagnetic resonance
ETC	Electron transport chain
Etcyclam	4,11-dimethyl-1,4,8,11-tetraazabicyclo[6.6.2]hexadecane
Etcyclen	4,10-dimethyl-1,4,8,11-tetraazabicyclo[5.5.2]tetradecane
EXAFS	Extended X-ray absorption fine structure
Fc	Ferrocene
HD	Huntington's disease
HEC	Hydrogen evolution catalyst
H ₂ PDC	Pyridinedicarboxylic acid
H ₂ (2,6-PDC)	2,6-pyridinedicarboxylic acid
Imcyclam	5-imidazole-1,4,8,11-tetraazacyclotetradecane
ⁱ Pr	<i>iso</i> -propyl
IR	Infrared spectroscopy
Isocyclam	1,4,7,11-tetraazacyclotetradecane
IT	Intervalence transfer
IUPAC	International union of pure and applied chemistry

k_{ex}	Water exchange rate
L1	1,4,7,10-tetraaza-2,6-pyridinophane
L2	1,4,7,10-tetraaza-2,6-pyridinophane-14-ol
L3	1,4,7,10-tetraaza-2,6-pyridinophane-13-ol
L4	1,4,11,13-tetraaza-bis(2,6-pyridinophane)-8,17-ol
LMCT	Ligand-to-metal charge transfer
MCF-7	Michigan cancer foundation-7
Me ₂ bispicen	<i>N,N'</i> -bis(1-(2-pyridyl)ethyl)-1,2-ethanedimine
Me ₂ bispictrn	<i>N,N'</i> -bis(1-(2-pyridyl)ethyl)-1,3-propanediamine
MEMRI	Manganese enhanced magnetic resonance imaging
Mep	<i>N,N'</i> -dimethyl- <i>N,N'</i> -bis(2-pyridylmethyl)ethane-1,2-diamine
Mepmea1	(1-(2-pyridyl)ethyl)(2-(2-pyridyl)ethyl)(2-pyridylmethyl)amine
Mepmea2	((6-methyl-2-pyridyl)methyl)(2-(2-pyridyl)ethyl)(2-pyridylmethyl)amine
Mepmea3	((6-methyl-2-pyridyl)methyl)bis(2-pyridylmethyl)amine
MLCT	Metal-to-ligand charge transfer
Mpp	<i>N,N'</i> -dimethyl- <i>N,N'</i> -bis(2-pyridylmethyl)propane-1,3-diamine
MRI	Magnetic resonance imaging
MS	Mass spectrometry
MTT	3-(4,5-dimethylthiazol-2-yl)-2,5-diphenyltetrazolium bromide
NHE	Normalized hydrogen electrode
NEt ₃	Triethylamine
<i>N,N</i> bispicen	<i>N,N</i> -bis(2-pyridylmethyl)-1,2-diaminoethane
NMR	Nuclear magnetic resonance
NOTA	1,4,7-triazacyclononane-1,4,7-triacetic acid
Ns	Nosyl; 2-nitrobenzenesulfonyl
NSF	Nephrogenic systemic fibrosis
[O]	Oxidant
OEC	Oxygen-evolving complex
ORTEP	Oak Ridge Thermal Ellipsoid Plot

PBT2	5,7-dichloro-2-2[(dimethylamino)methyl]quinoline-8-ol
PCTA	Pyridine-containing triaza macrocyclic triacetate
PD	Parkinson's disease
Phen	1,10-phenanthroline
Pmap	Bis[2-(2-pyridyl)ethyl]-2-pyridylmethylamine
Pmea	(2-(2-pyridyl)ethyl)bis(2-pyridylmethyl)amine
PSI	Photosystem I
PSII	Photosystem II
Pyclen	1,4,7,10-tetraaza-2,6-pyridinophane
q	Hydration number
r_1	Proton relaxivity
ROS	Reactive oxygen species
SMON	Subacute myelo-optic neuropathy
SOD	Superoxide dismutase
T_1	Longitudinal relaxation time (of water protons)
T_2	Transverse relaxation time (of water protons)
T_{ie}	Electron spin relaxation
τ_M	Residence time
τ_R	Rotational correlation time
TBAP	Tetrabutylammonium perchlorate
TBAPF ₆	Tetrabutylammonium hexafluorophosphate
^t Bu	<i>Tert</i> -butyl
Terpy	2,6:6',2''-terpyridine
Tet <i>a</i>	<i>Meso</i> -5,5,7,12,12,14-hexamethyl-1,4,8,11-tetraazacyclotetradecane
Tet <i>b</i>	<i>Rac</i> -5,5,7,12,12,14-hexamethyl-1,4,8,11-tetraazacyclotetradecane
THF	Tetrahydrofuran
Tmpa	Tris(2-methylpyridyl)amine
TOF	Turnover frequency
TON	Turnover number

Tren	Tris(2-aminoethyl)amine
Ts	Tosyl; <i>p</i> -toluenesulphonyl
TsNH ₂	<i>p</i> -toluenesulphonylamide
TsNHNa	Tosylamide monosodium
UV-vis	UV-visible spectroscopy
WOC	Water oxidation catalyst
XRD	X-ray diffraction

Chapter 1: Introduction to macrocyclic chemistry

1.1. Classification of macrocycles

Macrocycles represent a broad family of unique ligands that can be utilized across many different chemical fields. Although macrocycles have many of the same attributes as their noncyclic counterparts, these ligands have exceptional coordination behavior (such as the *macrocyclic effect*) that places them in a unique ligand class.¹ The IUPAC defines a macrocycle as a cyclic macromolecule or a macromolecular cyclic portion of a molecule.² Although this term does describe macrocycles, a more relevant definition in terms of coordination chemistry is that a macrocycle is a cyclic molecule with three or more potential donor atoms in ring of at least nine atoms.^{1,3} In other words, macrocycles have the intrinsic ability to bind metal ions within a central cavity, forming a variety of coordination complexes. The ambiguity of the definitions pertaining to macrocycles means that there is a large pool of ligands which are considered “macrocyclic”. Donor atoms within macrocycles usually consist of nitrogen or oxygen, but “softer” analogues also exist, such as sulfur, selenium, and phosphorous (Figure 1.1).¹ Furthermore, the macrocyclic ring can be a variety of different sizes, as long as at least 3 donor atoms are present and ring is no smaller than nine atoms. Polyamine or imine macrocycles, also referred to as azamacrocycles, are a family of nitrogen containing cyclic molecules with varying degrees of saturation (Figure 1.1).¹ Cyclic polyethers or crown ethers are another family of macrocyclic ligands, which contain oxygen atoms and cyclic rings of various sizes (Figure 1.1).¹ Other examples of macrocyclic ligands include mixed donor-atom macrocycles, encapsulating macrocycles known as cryptands, dinucleating macrocycles, and linked macrocycles (Figure 1.1).^{1,3} Although many different types of macrocycles exist, the remaining discussion of macrocyclic ligands will be focused on azamacrocycles for the purpose of this dissertation.

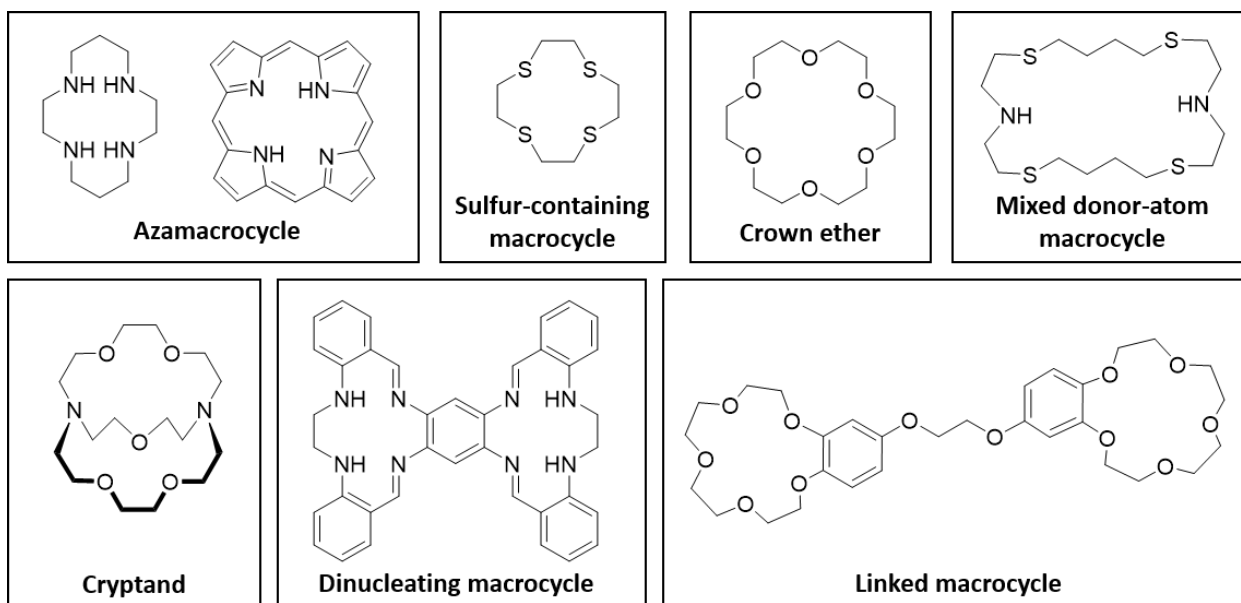


Figure 1.1. Examples of different types of macrocyclic ligands.^{1,3}

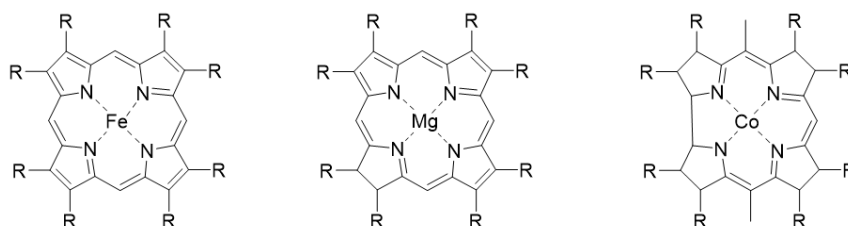
1.2. A brief history of macrocyclic chemistry

1.2.1. Origins of macrocyclic chemistry

The unusual properties of macrocyclic ligands and their corresponding metal complexes have garnered the attention of researchers for many years. Scientists are particularly interested in the unique structural, kinetic, thermodynamic, spectral, and electrochemical properties of macrocyclic complexes.³ The exceptional physical properties that entice scientists to study macrocycles also make them ideal for biological applications. The following discussion focuses/describes the evolution of macrocycles in the chemical literature.

In nature, macrocyclic complexes are utilized in numerous fundamental biological systems due to the enhanced kinetic and thermodynamic stability offered by the cyclic ligand frame. Metal ions that would otherwise demetallate from open-chain ligands under mild to moderate conditions are held firmly within the cyclic cavity during biological functions.³ Common examples of naturally occurring macrocyclic complexes include the iron-bound porphyrin ring contained in the active site of hemoglobin, the chlorin complex of magnesium in chlorophyll, and the cobalt-bound corrin ring of vitamin B₁₂ (Figure 1.2).^{1, 3-5}

Early in the development of macrocyclic chemistry, researchers studied naturally occurring macrocyclic complexes to investigate the unusual coordination properties. Scientists hoped that by studying the physical properties of these naturally occurring complexes they could synthesize model complexes to further understand the structure and functions of biological macrocyclic complexes.^{1,3-4} This fundamental approach to understanding naturally occurring macrocyclic complexes helped form the foundation for the field of macrocyclic chemistry.



Biological Complex	Hemeprotein	Chlorophyll	Cobalamin
Macrocycle type	Porphyrin	Chlorin	Corrin
Metal ion present	Fe(II)	Mg(II)	Co(I), Co(II), or Co(III)
Function	O ₂ transport in blood	Light absorption in Photosynthesis	Coenzyme for Isomerases and Methyltransferases/Enzymes

Figure 1.2. Common examples of naturally occurring macrocyclic ligands.^{1,3-4,6}

The field of modern macrocyclic chemistry began in 1960 when Curtis and coworkers pioneered a template reaction to synthesize tetraaza macrocyclic Ni(II) complexes.^{3,7} Prior to this, phthalocyanine and its derivatives were the only type of synthetic macrocyclic ligand.^{1,3,5,8} Phthalocyanines are highly conjugated cyclic ligands which strongly resemble naturally occurring porphyrin rings (Figure 1.3).^{1,3,5} In 1928, the first phthalocyanine complex was discovered serendipitously during the industrial preparation of phthalimide from phthalic anhydride and ammonia.^{3,9} During the reaction, the glass vessel housing the chemicals cracked to expose the outer steel casing. As a result, a dark-blue material formed, which was later identified as an extremely stable Fe(II) phthalocyanine complex. Since the initial discovery, phthalocyanine complexes have been prevalent in the chemical literature.^{3,9} These chemically interesting macrocycles have been investigated for use as semiconductors, catalysts, and biological model

complexes.³ In addition, due to phthalocyanine's highly conjugated nature and ability to form highly stable metal complexes, resulting in rich hues, it was (and still is) used as a coloring agent.^{3, 10-11} Copper phthalocyanine or phthalocyanine blue is used extensively as a blue/blue-green pigment with the color dependent upon what substituents are present within the complex (Figure 1.3).³ Phthalocyanines were the first class of synthetic macrocyclic ligands and they continue to be used for many different applications.

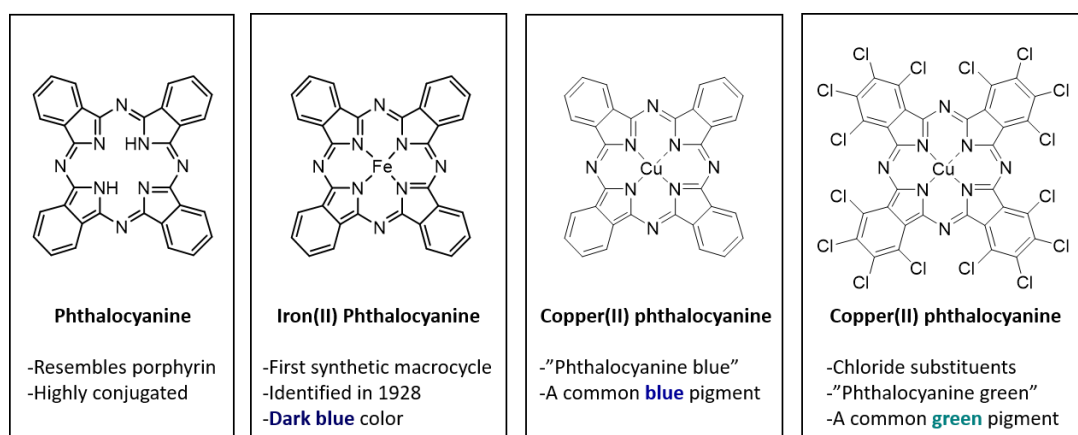
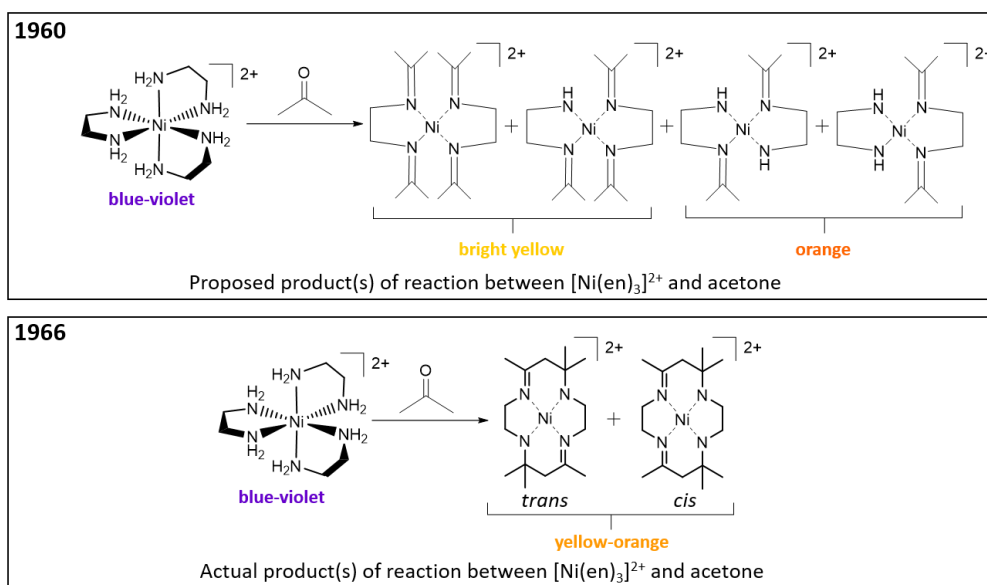


Figure 1.3. Synthetic phthalocyanine macrocycle, and corresponding metal complexes.^{1, 3, 9-11}

1.2.2. Development of modern day macrocyclic chemistry

The pioneering synthesis of isomeric tetraazamacrocyclic Ni(II) complexes and subsequent studies by Curtis and coworkers between 1960-1966 marks the inception of modern-day macrocyclic chemistry.^{7, 12-20} This new branch of chemistry was discovered fortuitously when Curtis combined tris(ethylenediamine)nickel(II) perchlorate with dry acetone to yield both the *cis* and *trans* isomers of a Ni(II) macrocyclic imine complex.^{3-4, 7, 12-20} Initially, Curtis was attempting to prepare a series of aliphatic Schiff bases according to previously established procedures.^{3-4, 7, 13} He proposed that the product(s) formed when the Ni(II) salt and dry acetone were combined was a series of yellow and orange bis-imine coordination complexes (Scheme 1.1).^{7, 13} Interestingly, upon boiling in acidic and alkaline conditions, the proposed Ni(II) imine complex exhibited unusual chemical inertness inconsistent with type of ligand

present within the complex.⁷ The imine ligands were expected to decompose under such harsh chemical conditions, but the complex remained intact. In several subsequent reports, Curtis used extensive characterization techniques to determine that the yellow and orange products were a mixture of isomeric Ni(II) macrocyclic imine complexes formed by the condensation of acetone molecules (Scheme 1.1).^{3-4, 12, 14-15, 17-20} Following Curtis's groundbreaking work an immense number of synthetic macrocyclic ligands and complexes have been reported in the chemical literature.



Scheme 1.1. The original proposed products of the condensation reaction between $[\text{Ni}(\text{en})_3]^{2+}$ and acetone (1960) and the actual products reported in 1966, now known as 'Curtis macrocycles'.^{3-4, 7, 12-20}

1.3. Properties of azamacrocycles

Azamacrocyclic ligands contain nitrogen donor atoms, but the number of donor atoms can vary greatly. The most heavily studied type of azamacrocyclic ligand are tetraazamacrocycles, which contain four nitrogen atoms and have rings sizes varying from 12- to 17-members.^{1, 3} Although tetraazamacrocycles are the most common type of azamacrocyclic ligand, and will be a focus of this dissertation, many more variations exist. The smallest triazamacrocycles contain just 3 nitrogen donor atoms dispersed in a ring containing 9 to 13 atoms.³ Pentaazamacrocycles contain five donor nitrogen atoms with ring sizes between 15- and 21-members and hexaazamacrocycles contain six donor atoms

with eighteen to twenty-five membered rings.³ Azamacrocycles with more than six donor atoms exist as well, these types of large rings can often bind multiple metal ions or even large anions.^{1,3}

Although all azamacrocycles contain nitrogen donor atoms, this class of macrocycles has many diverse coordination properties influenced by a variety of factors. The number of donor atoms an azamacrocycle contains is obviously a factor that contributes to coordination properties, but there are many others including: cavity size, degree of unsaturation, ligand denticity, and the presence of substituents.³⁻⁴ Although all of the factors listed above are important, the concept of cavity size is integral to the field of macrocyclic chemistry and is one of the most influential structural parameters that effects the properties of resultant macrocyclic metal complexes.³ For the purpose of this dissertation, discussion of influential factors of the coordination properties of macrocyclic ligands will be limited to cavity size, which is directly influenced by the number of donor atoms present within a macrocycle.

1.3.1. Determining the cavity size/ring size of macrocyclic ligands

In simple terms, the cavity of a macrocyclic ligand is the hole surrounded by donor atoms that is occupied by a metal ion upon coordination complex formation.¹ Unfortunately, the cavity size of a macrocyclic ligand is a deceptively simple concept, which is remarkably difficult to quantify. Cavity size is influenced by many different factors, including number of donor atoms, type of donor atoms, ligand flexibility, and ligand confirmation.

Perhaps the most easily determined parameter with regards to cavity size is the radius of the macrocyclic cavity.¹ Scientists often match the ligand cavity radius with known metal ion radii when selecting suitable combinations of metal ions and ligands to form macrocyclic coordination complexes.¹ Early approaches to determining the radius of a macrocyclic cavity involved measuring the distance between the nuclei of diagonally oriented donor atoms.¹ The distances were either generated from computer models or taken directly from solid state structures of the ligands and/or their coordination

complexes.¹ This rudimentary method generally works for predicting the cavity sizes of relatively simple macrocycles such as tetraazamacrocyclic ligands. However, when predicting the cavity size of a macrocycle it is necessary to give a range of values due to conformational changes within the flexible macrocyclic ligand. Therefore, it is only meaningful to compare the cavity radii between ligands with similar conformations.¹ Additionally, the concept of unambiguous hole size is only effective when discussing ligands that are planar or nearly planar, such as tetraazamacrocyclic ligands.

Unfortunately, predicting the cavity size of a macrocycle based on estimating hole radius is a rather rudimentary method for matching metal ions with an ideal macrocyclic host. In the 1960s-1970s several groups conducted in-depth studies of the relationship between metal ions and optimum macrocyclic hole sizes utilizing a series of fully-saturated tetraazamacrocycles.^{5, 21} Beginning in the mid-1960s, Bosnich *et al.* synthesized and characterized two novel tetraazamacrocyclic metal complexes with Ni(II) and Co(III).²²⁻²⁴ The ligand utilized in the studies was 1,4,8,11-tetraazacyclotetradecane ([14]aneN₄ or cyclam) which is a saturated 14-membered tetraazamacrocyclic. Cyclam is large enough to fit a range of first-row transition metal ions within its cavity and investigations of metal-cyclam complexes are ubiquitous in the chemical literature. Following this initial investigation of cyclam and its corresponding metal complexes, several cyclam congeners ranging from 12- to 16-membered rings were synthesized (Figure 1.4).^{5, 21, 25} Busch and coworkers considered cyclam and its congeners the 'ultimate prototypic macrocyclic ligand' because of several key features (i) they were the 'cyclic counterparts' of common noncyclic ligands like ethylenediamine (en); (ii) they were saturated ligands, ensuring that only sigma bonding was present between the metal ion and ligand; and (iii) they had properties that were similar to classic coordination complexes with noncyclic ligands.⁵ Utilizing these prototypical macrocyclic ligands ([12-16]aneN₄), a high-spin Ni(II) ion, and a low-spin Co(III) ion, Busch and coworkers evaluated the effects that ring size (i.e. cavity size) had on metal donor interactions. The materials listed above were used to synthesize complexes with the general formula, *trans*-[Ni^{II}([13-16]aneN₄)Cl₂] and *trans*-[Co^{III}([13-

[16]aneN₄)Cl₂]⁺. It is interesting to note that [12]aneN₄ was not used in this study, due to its inability to fully encapsulate the metal ions; this important consideration will be discussed later. To evaluate the relationship between ring size and metal donor interaction, Busch applied the ligand field model to electronic spectral data for each complex.⁵ By doing this, he obtained the important spectrochemical parameters Dq^{xy} and Dq^z , where Dq^{xy} is a measure of the ligand field strength of a tetradentate transition metal complex and Dq^z provides information about the axial ligand-metal ion interaction.⁵ Using previously determined Dq^{xy} values for other macrocyclic Ni(II) and Co(III) complexes, Busch determined that the donor atoms found in ligands [13-16]aneN₄ should exhibit 'normal' or ideal ligand field strengths of around 1200 cm⁻¹ (for the Ni(II) complexes) and 2530 cm⁻¹ (for the Co(III) complexes).

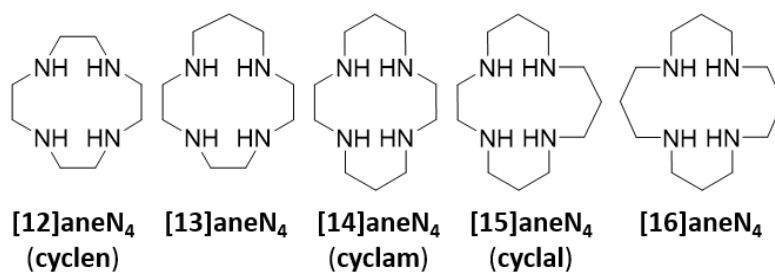


Figure 1.4. Series of cyclam congeners with ring sizes ranging from 12- to 16-members.^{5, 21, 25}

In a typical noncyclic coordination complex, it could be expected that the ligand field strength (Dq^{xy}) remains constant with a constant donor set, such as N₄Cl₂.⁵ Busch and coworkers discovered this was not the case with tetraazamacrocyclic complexes. They found that ligand field strength was strongly dependent on ring size (Table 1.2). In their report, they used the analogy of a stiff rubber band encircling a metal ion to describe the phenomenon. A stiff rubber band (i.e. the tetraazamacrocycle) has a natural radius, when the ring fits the metal ion precisely, there is no deviation from its normal shape, leading to a 'normal' or ideal ligand field strength.⁵ If the rubber band is 'too small' it must stretch to accommodate the metal ion; when it distorts from the normal shape this enhances the metal-donor interaction, increasing the Dq^{xy} parameter.⁵ The opposite is true if the rubber band is too large, the metal-donor bonds will stretch to try and compress the ring, which leads an abnormally low Dq^{xy} parameter.⁵ Based on a

comparison of the Dq^{xy} parameters for both the Ni(II) and Co(III) macrocyclic complexes with their ideal reference Dq^{xy} values, Busch found that Ni(II) fit best within the 15-membered ring [15]aneN₄ and Co(III) fit best within the 14-membered ring [14]aneN₄.^{5, 21}

Table 1.1. Spectrochemical parameters for complexes $trans$ -[Co^{III}([13-16]aneN₄)Cl₂]⁺ and $trans$ -[Ni^{II}([13-16]aneN₄)Cl₂].^{4-5, 21}

Ligand	Co(III) Dq^{xy} , cm ⁻¹ 'Normal' = 2530 cm ⁻¹	Ni(II) Dq^{xy} , cm ⁻¹ 'Normal' = 1200 cm ⁻¹
[13]aneN ₄	2750	*---
[14]aneN ₄	2480	1480
[15]aneN ₄	2360	1250
[16]aneN ₄	2250	1110

*The [13]aneN₄ ligand was not large enough to encompass the Ni(II) ion; only the *cis*-complex was isolated.

After interpreting these results, Busch sought the help of a colleague to develop a strain energy model for saturated tetraazamacrocycles.⁵ Utilizing this model Busch was able to derive the metal-nitrogen bond distance with the least strain in any given saturated tetraazamacrocycle. He coined the term *ideal M-N distance* to describe this calculation. The concept of an *ideal M-N distance* was validated with experimental data obtained in the studies regarding Ni(II) and Co(III) tetraazamacrocyclic complexes previously conducted by Busch.^{5, 21} In fact, a pattern was observed: the *ideal M-N distance* differs by regular increments of 0.10-0.15 Å as the number of members in a macrocyclic ring is changed by one (Table 1.3).^{3, 5} To this day, scientists still utilize the concept of *ideal M-N distance* to determine the best combination of ligand and metal ion when synthesizing macrocyclic complexes.

Table 1.2. Ideal M-N bond lengths and planarity of a series of macrocyclic ligands.^{3, 5, 21}

Ring Size	Avg. ideal bond length (Å)	Avg. deviation from ideal N ₄ plane (Å)
[12]	1.83	0.41
[13]	1.92	0.12
[14]	2.07	0.00
[15]	2.22	0.14
[16]	2.38	0.00

Until this point the discussion of cavity size has been focused on matching a metal ion to the ideally sized ligand cavity, but what happens when the metal ion is too large or too small for the macrocyclic cavity? Fortunately, macrocyclic ligands are usually flexible and can accommodate metal ions that are larger than the macrocyclic cavity, so that complexation occurs. When a metal ion is too large for the cavity the macrocycle can either fold around the metal ion and/or displace it from the donor plane (Figure 1.5).³⁻⁴ For example, 12- and 13-membered tetraazamacrocycles are usually too small to house most transition metals within the N₄ donor planes, so these macrocycles adopt *cis*-folded geometries around the metal ion; additional ligands complete the coordination sphere in equatorial positions around the metal center.³⁻⁴ It is perhaps most important to note that just because there is a mismatch between the macrocyclic cavity and the metal ion, this does not mean that complexation will not occur. In fact, many times when there is a mismatch between the metal ion and cavity the resulting macrocyclic metal complex exhibits unusual properties. These unusual properties, such as unique electrochemical and spectral behavior, are ubiquitous in the chemical literature.³ One such example is the ‘entatic state’ hypothesis proposed by Vallee and Williams.²⁶ This hypothesis suggests that the reactivity of many metalloenzymes is a result of the unusual coordination geometries of metal ions within the active site.²⁶

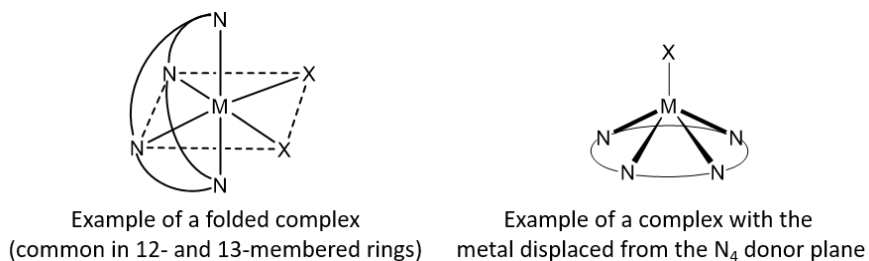


Figure 1.5. Geometries adapted by mismatched metal-ligand complexes.³

1.3.2. The *macrocyclic effect*

It has been well established that the coordination complexes of macrocyclic ligands exhibit unique and unusual behavior. Factors that imbue macrocyclic complexes with these exceptional spectral and electrochemical behaviors have been discussed in the previous sections, but a very important concept remains to be discussed, the *macrocyclic effect*. In the following section the origins of the *macrocyclic effect* will be discussed, as well as thermodynamic and kinetic considerations for this fundamental concept.

Prior to the discovery of the *macrocyclic effect* in 1969, scientists had defined and studied the *chelate effect*. The well-documented *chelate effect* states that a complex with a bidentate or multidentate ligand set is more thermodynamically stable than a complex with the equivalent number of monodentate ligands.^{1, 3-4, 27-30} An example of the *chelate effect* is directly observed when comparing the complexation of Cd(II) with monodentate methylamine vs. bidentate ethylenediamine (en) (Figure 1.6).²⁹⁻³⁰ The complex $[\text{Cd}(\text{en})_2(\text{H}_2\text{O})_2]^{2+}$ has a much larger equilibrium constant (by over four orders of magnitude) than its monodentate counterpart, $[\text{Cd}(\text{CH}_3\text{NH}_2)_2(\text{H}_2\text{O})_2]^{2+}$ (Figure 1.6). The equilibrium constants of each reaction can be related back to Gibbs free energy (ΔG°) using equation [1.1].²⁷ Additionally, Gibbs free energy is related the enthalpic and entropic terms through equation [1.2], where R is the universal gas constant, T is the temperature (in K), K is the equilibrium constant, ΔH° is change in enthalpy, and ΔS° is change in entropy.²⁷

$$\Delta G^{\circ} = -RT \ln K \quad [1.1]$$

$$\Delta G^{\circ} = \Delta H^{\circ} - T\Delta S^{\circ} \quad [1.2]$$

For each reaction the difference in the enthalpic terms is relatively small, but the entropic terms are vastly different. Therefore, it can be concluded that the *chelate effect* is largely influenced by entropy, while enthalpy is variable.²⁷⁻³⁰ This makes sense, because the monodentate reaction resulted in no net increase of molecules; whereas, the bidentate reaction had a net increase of two molecules. Generally, an increase in chelation (polydentate vs. monodentate) corresponds to an increasingly positive ΔS° term and therefore a larger equilibrium constant.^{27, 29}

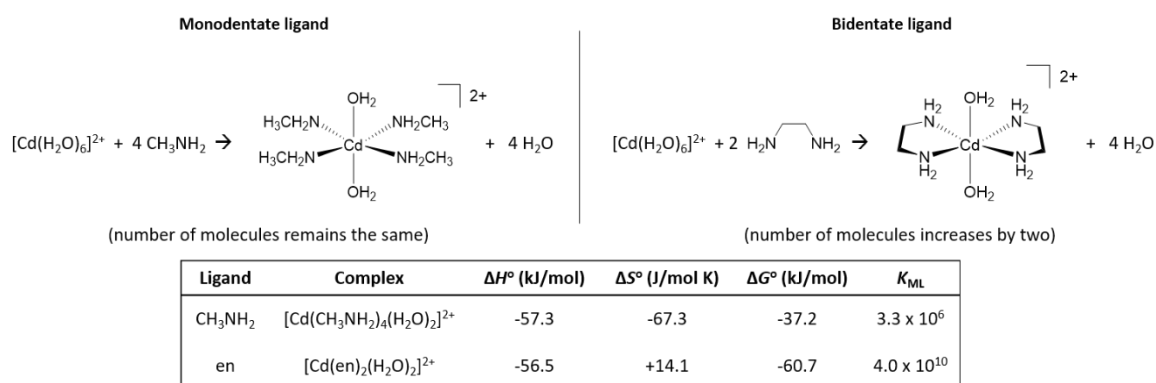


Figure 1.6. An example of the *chelate effect* which is observed when comparing the reactions of a monodentate vs. bidentate ligand set. The equilibrium constant (K) of the bidentate reaction is significantly larger than the monodentate reaction.²⁹⁻³⁰

In the pioneering study conducted by Margerum and Cabiness in 1969, the stability of cyclic tetra-amine Cu(II) complexes (tetraazamacrocycle complexes) were compared to several reference noncyclic Cu(II) tetra-amine complexes (Table 1.3).^{1, 3-4, 31-32} Using potentiometric methods, Margerum and Cabiness determined the stability constants of these complexes. The authors compared the stabilities of the noncyclic Cu(II) 2,3,2-tet complex ($\log K_{ML} = 23.9$) with the red macrocyclic Cu(II) tet *a* complex ($\log K_{ML} = 28$), because both complexes had a similar sequence of chelate rings (5,6,5 vs. 5,6,5,6).^{1, 3-4, 31-32} They discovered that the Cu(II) macrocyclic complex was about 10⁴ times more stable than its noncyclic analogue.^{1, 3-4, 31-32} This marked increase in stability could not be explained by the *chelate effect* alone, and

was about an order of magnitude larger than predicted, hence Margerum and Cabiness termed it the *macrocyclic effect*.^{1, 3-4, 31-32} The *macrocyclic effect* states that a complex with macrocyclic ligands is more stable than a complex with the equivalent number of open-chain (noncyclic) ligands.^{1, 3-4}

Table 1.3. Stability constants for the 1:1 complexes of tetraamines with Cu(II).³¹⁻³²

Type	Noncyclic					Macrocyclic	
Name	tpt	3,3,3-tet	tren	trien	2,3,2-tet	tet α (blue complex)	tet α (red complex)
Ligand							
Log K_{ML}	13.1	17.3	18.8	20.1	<u>23.9</u>	20	<u>28</u>
Ring Sequence	6,6,6	6,6,6	5,5,5	5,5,5	<u>5,6,5</u>	5,6,5,6	<u>5,6,5,6</u>

1.3.2.1 Thermodynamic considerations

Since the groundbreaking studies of the *macrocyclic effect* conducted by Margerum and Cabiness, many other groups have investigated this phenomenon. Initially, studies were conducted to learn more about the thermodynamic origins of the *macrocyclic effect*. Was the enhanced stability of macrocyclic metal complexes dependent on entropic factors, enthalpic factors, or both? Based on evidence presented earlier regarding the *chelate effect*, it might be tempting to assume that both the *chelate effect* and the *macrocyclic effect* originate from the entropic term, but the *macrocyclic effect* is more complex than the *chelate effect*.¹ Early analysis of thermodynamic considerations for the *macrocyclic effect* were often contradictory.^{1, 3-4} Groups would investigate specific ligand sets and claim that the *macrocyclic effect* was either exclusively enthalpic in nature³³, or exclusively entropic in nature.^{1, 3-4, 34-36} These contradictions were the result of inconsistencies in solvent or ionic strength conditions used to determine thermodynamic parameters.¹ Additionally, discrepancies arose because in many studies the temperature dependence of complex stability constants were utilized to derive the enthalpy term (ΔH°).^{3, 36} These inconsistencies were eventually resolved when the enthalpic terms for a large range of noncyclic and macrocyclic ligand complexes were determined using calorimetric methods.^{3, 36-38} Several studies utilized this newly acquired experimental data to determine enthalpy values for the *macrocyclic effect*, which can

be represented by the general metathetic reaction [1.3].^{1, 3, 36, 39} If the enthalpy terms (of the related macrocyclic and noncyclic complexes) associated with the formation reaction [1.4] are subtracted, this gives the macrocyclic enthalpy for the metathetic reaction [1.3].^{3, 36, 39-41}



More recent studies, utilizing experimentally determined enthalpy values, seem to indicate that the entropy term associated with the *macrocyclic effect* is generally favorable.^{1, 3, 40} In contrast, the enthalpy term associated with this effect can vary significantly and is very dependent on matching the cavity size of the macrocycle with a suitable metal ion.⁴⁰

Continued investigation of the thermodynamic origins of the *macrocyclic effect* led several groups to explore other factors influencing the enthalpic term. Obviously, the size of the macrocyclic cavity vs. the metal ion was an important factor to the variability of enthalpy.^{3, 40} Another concern was the role that ligand solvation may play in certain cases.³ Noncyclic reference ligands such as those depicted in series 2 of figure 1.7 have two terminal -NH₂ groups where solvent may interact more strongly than with the macrocyclic ligand (which only contains secondary amines). Could differences in solvation energy between the reference noncyclic ligands vs. the macrocyclic ligands play a role in determining enthalpic influence? Clay *et al.* conducted a study to answer this question, utilizing di-*N*-methylated amine groups.^{36, 39-40} In the study, three different series of ligand types were synthesized. Series 1 consisted of 12-16 membered tetraazamacrocycles, series 2 consisted of the noncyclic unsubstituted linear polyamines of series 1, and series 3 consisted of the di-*N*-methylated analogues of series 2 (Figure 1.7).³⁶ Clay hypothesized that the di-*N*-methylated noncyclic ligands would be better suited for comparison with the analogous macrocycles, due to minimized differences in solvation energies.^{36, 39-40} In this comprehensive study, Clay compared log K_{ML} , ΔG° , ΔH° , and ΔS° terms for 13 different ligands (Table 1.4).

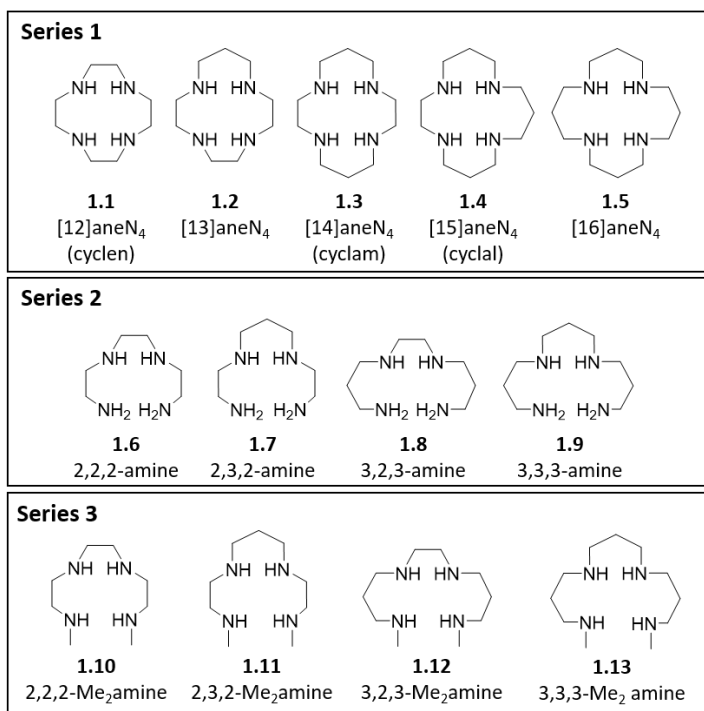


Figure 1.7. Tetraazamacrocycles, open-chain noncyclic analogues, and di-*N*-methylated noncyclic analogues used in the comprehensive study conducted by Clay *et al.*^{36, 39-40}

Table 1.4. Thermodynamic parameters for Cu(II) complex formation with tetraaza ligands at 298 K.^{36, 39}

Ligand	log K_{ML}	$-\Delta G^\circ$ (kJ mol ⁻¹)	$-\Delta H^\circ$ (kJ mol ⁻¹)	$T\Delta S^\circ$ (kJ mol ⁻¹)
1.1	24.8	141.5	95.0	46.5
1.2	29.1	166.0	107.1	58.9
1.3	27.2	155.2	135.6	19.6
1.4	24.4	139.2	110.9	28.3
1.5	20.9	119.3	83.7	35.6
1.6	20.2	115.3	90.4	24.9
1.7	23.9	135.4	115.9	20.5
1.8	21.8	124.5	108.4	16.1
1.9	17.3	98.8	81.6	17.2
1.10	20.9	119.3	88.3	31.0
1.11	21.9	124.9	108.4	16.6
1.12	18.5	105.6	93.1	12.5
1.13	14.6	83.4	62.3	21.5

Based on a comparison of the thermodynamic parameters for each series of tetraaza ligands, Clay concluded that the di-*N*-methylated noncyclic ligands were appropriate reference ligands and offered a better parallel to macrocyclic ligands.^{1, 3, 36, 39-40} This trend is easily observed when the log K_{ML} , ΔH° , or $T\Delta S^\circ$

terms vs. increasing size/length of the ligand are graphed (Figure 1.8). These plots show that the di-*N*-methylated ligands and macrocyclic ligands tend to parallel one another, while the -NH₂ ligands eventually converge with the macrocycles.³⁶

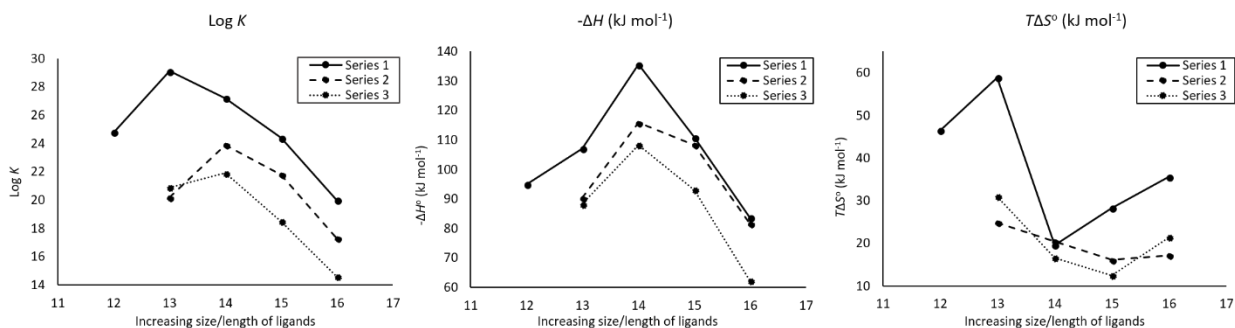


Figure 1.8. Thermodynamic parameters vs. increasing size/length of ligands for Cu(II) complex formation.^{36, 39-40}

Another conclusion made by Clay *et al.* based on the above data, was that the magnitude of the macrocyclic effect seems to be independent of ring size of the macrocycle as long as an appropriate noncyclic reference ligand is chosen.^{36, 39-40} Although Clay determined that the di-*N*-methylated noncyclic ligands were more appropriate reference ligands for quantifying the *macrocyclic effect*, he made one very important observation concerning previously chosen reference ligands. In a report published in 1982, he discusses that the choice to utilize nonsubstituted linear polyamines as reference ligands to macrocycles is still completely appropriate and that it was not necessary to modify previous interpretations of the *macrocyclic effect*.³⁹

Thermodynamic considerations of the *macrocyclic effect* are complex. Numerous studies have been conducted to try and determine thermodynamic origins, but it is not possible to assign a single source to the *macrocyclic effect*.^{1, 3} Generally, studies have found that the entropic term associated with the *macrocyclic effect* tends to be energetically favorable.^{1, 3, 36} Whereas, the enthalpic term associated with the *macrocyclic effect* is more variable and can either be energetically favorable or unfavorable

depending on the system.^{1, 3, 36} Of course, each ligand system studied is unique, hence it is hard to generalize specific thermodynamic origins to the *macrocyclic effect*.

1.3.2.2. Kinetic considerations

In the previous section, the exceptional thermodynamic stability of macrocyclic complexes was discussed. In addition to this enhanced thermodynamic stability, macrocycles experience a kinetic component of the *macrocyclic effect* as well. Numerous studies have shown that both the formation and dissociation reactions of macrocyclic complexes tend to be significantly slower than noncyclic analogues.^{1, 3} Of course, the kinetic behavior of macrocycles is a broad area of research; it is often difficult to determine a kinetic mechanism that is widely applicable, due to metal ion variability and differences in ligand structural features.^{1, 3} In this section several representative formation and dissociation reactions will be discussed, which apply to most tetraazamacrocyclic ligand complexes.³

1.3.2.2.1. Formation kinetics

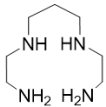
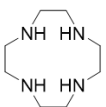
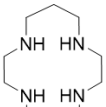
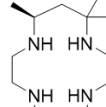
The equilibrium constant, K_{ML} , for the formation of a complex can generally be related to two separate equations [1.5] and [1.6].^{1, 3} K_{ML} is directly related to the ratio of the second-order formation constant (k_f) to the first-order dissociation rate constant (k_d) (equation [1.6]).³



$$K_{ML} = \frac{[ML^{n+}]}{[M^{n+}][L]} = \frac{k_f}{k_d} \quad [1.6]$$

For macrocyclic complexes, the rate of formation (k_f) is generally much slower than noncyclic analogues. These slower rates of formation can be observed when comparing several macrocyclic complexes with an open-chain noncyclic analogue (Table 1.5).¹ The Cu(II) complex with 2,3,2-tet (an open-chain polydentate ligand) forms much faster than with macrocyclic ligands. Additionally, from the rates of formation presented in table 1.5, it can be observed that macrocycles with more steric bulk (i.e. additional methyl groups) tend to exhibit slower formation kinetics.¹

Table 1.5. Rates of formation of Cu(II) complexes with tetraazamacrocycles in acidic aqueous solution.¹

$\text{Cu}^{2+}(\text{aq}) + \text{L} \rightarrow [\text{CuL}]^{2+}$				
	2,3,2-tet	[12]aneN ₄ (cyclen)	[14]aneN ₄ (cyclam)	tet <i>a</i> (red complex)
Ligand (L)				
$k_f (\text{M}^{-1} \text{s}^{-1})$	10^8	10^6	$\approx 10^4$	$\approx 10^6$

The effects of pH must be accounted for when studying the kinetics of tetraazamacrocyclic ligands.^{1, 3} Although it is possible to conduct kinetic studies in aqueous media, this is complicated by the presence of protonated ligands species which need to be taken into consideration.¹ In contrast, when studies are conducted in basic solution the ligands are not protonated, but the metal ions do tend to exist as hydroxy species.¹ Several groups have conducted in depth studies of the formation kinetics of tetraazamacrocyclic ligands under basic conditions to prevent such ligand protonation.^{1, 3, 32, 42-43}

By summarizing a collection of meticulous studies, a general kinetic mechanism for the coordination of macrocyclic ligands starts to take shape.¹ The formation rate of macrocyclic ligands is influenced by solvation. The formation of a macrocyclic ligand complex from a fully solvated metal species, MS_6 ($S = \text{solvent}$) generally follows the *Eigen-Wilkins* mechanism (equations [1.7], [1.8], [1.9]).^{1, 3, 44}



The first step, denoted in equation [1.7], involves the rapid formation of an ‘outersphere’ complex with the stability constant K_{OS} , which can either be determined experimentally or estimated.^{1, 3} Equation [1.8], represents the second step of the *Eigen-Wilkins* mechanism, where this newly formed ‘outersphere’ complex is converted by an interchange process into an ‘innersphere’ complex; in this step a metal-ligand bond is formed.^{1, 3} Finally, equation [1.9] represents the subsequent formation of metal-ligand bonds until all (or most) metal-solvent interactions are replaced by coordination to the ligand.^{1, 3}

For the *Eigen-Wilkins* mechanism, any of the steps could be rate determining. Referring to table 1.5, for 2,3,2-tet the rate determining step is found to be the formation of the first metal-ligand bond.^{1, 3,}
⁴³ In contrast, for cyclam the rate determining step does not occur until the second metal-ligand bond formation.^{1, 3, 43} Cyclam and its macrocyclic analogues, are slower to coordinate to metal ions due to steric constraints and reduced flexibility, as compared to noncyclic polydentate ligands.^{1, 3} This concept can be illustrated by comparing the formation of the second metal-ligand bond of 2,3,2-tet and cyclam. 2,3,2-tet can freely rotate to position another nitrogen donor atom for subsequent coordination to the solvated metal ion. Whereas, cyclam must be forced into a high energy conformation to position another nitrogen donor atom for coordination (Figure 1.9).^{1, 3}

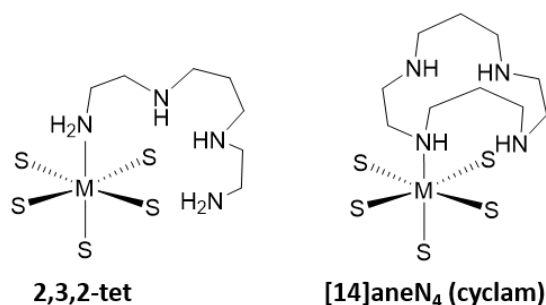


Figure 1.9. Possible transition states prior to formation of second metal-nitrogen bond during ligand coordination. (S = solvent molecule).¹

As stated earlier, several in depth kinetic studies of tetraazamacrocyclic ligands were conducted under basic conditions.^{32, 42-44} In one such study, Lin *et al.* investigated the formation kinetics of a Cu(II) tetraazamacrocyclic complex in basic media. In basic environments, Cu(II) ions exist as hydroxy species, $[\text{Cu}(\text{OH})_3]^-$ or $[\text{Cu}(\text{OH})_4]^{2-}$.⁴³ This comprehensive study led to the development of a general mechanism for the formation of a *trans*-macrocyclic metal complex under basic conditions (Figure 1.10).⁴²⁻⁴³ The mechanism follows the previously discussed *Eigen-Wilkins* mechanism in which an ‘outersphere’ complex is formed and is then subsequently converted into the ‘innersphere’ complex. The macrocycle forms sequential metal-ligand coordination bonds, although it must adapt various high energy conformations to ‘wrap’ around the metal ion.

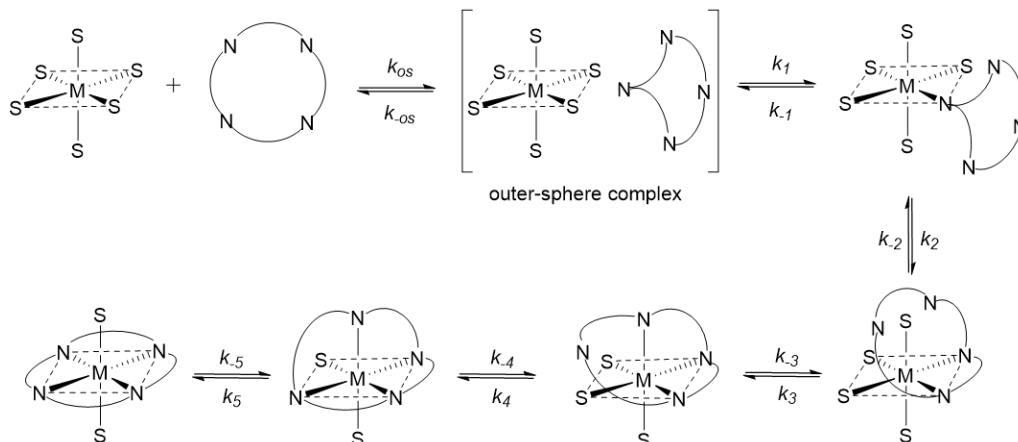


Figure 1.10. General mechanism for formation of a *trans*-tetraazamacrocyclic metal complex. (S = solvent molecule).^{3, 42-43}

In summary, the rate of formation of macrocyclic complexes is usually much slower than the rates of formation for open-chain noncyclic polydentate ligands.^{1, 3} Macrocyclic ligand coordination generally follows the *Eigen-Wilkins* mechanism and the rate determining step for the formation reactions is usually designated to the second coordination step or later.^{1, 3} Additionally, macrocyclic complexes are slower to form due to steric constraints and reduced flexibility of the cyclic ligand vs. a noncyclic polydentate ligand.^{1, 3}

1.3.2.2.2. Dissociation Kinetics

In addition to having relatively slow formation kinetics, macrocyclic ligands tend to have very high stabilities due to extremely sluggish dissociation reactions.^{1, 3-4} Referring to equations [1.5] and [1.6] defined in the previous section, the dissociation constant (k_d) values for macrocyclic complexes are very small (sometimes 10^5 - 10^7 times smaller than noncyclic analogues).^{1, 3} In fact, the dissociation of macrocyclic metal complexes (especially tetraazamacrocycles) is so slow that detailed kinetic studies in neutral solutions are impossible, because dissociation is unmeasurable using conventional methods.¹ Dissociation kinetic studies of tetraazamacrocycles are usually conducted in acidic solutions. Even under strongly acidic conditions, dissociation of macrocyclic complexes can be extremely slow. For example, in acidic conditions the complex of $[\text{Ni}(\text{cyclam})]^{2+}$ has a half-life of around 30 years!^{3, 45} The high stability of

macrocyclic complexes brought about by slow dissociation rates is an expression of the kinetic component of the *macrocyclic effect*.³

Several studies have compared dissociation rates of macrocyclic ligand complexes with noncyclic analogues (Table 1.6).^{3-4, 32} The data in table 1.6 shows a significant difference between the dissociation constants and resulting half-lives of the 2,3,2-tet complex compared to the red tet α complex. The macrocyclic tet α complex has a half-life upwards of twenty-two days in highly acidic conditions; whereas, the 2,3,2-tet complex only has a half-life of fractions of a second. Additional kinetics studies compare the rates of dissociation for tetraazamacrocycles with different cavity sizes (Table 1.7).⁴⁴ In a previous section the concept of cavity size was discussed, which is exemplified in the rates of dissociation of Ni(II) complexes shown in table 1.7. When Ni(II) is bound to 15- or 16-membered macrocycles this leads to a high-spin Ni(II) complex.⁴⁴ In contrast, a low-spin square planar Ni(II) complex results if Ni(II) is bound to 13- or 14-membered macrocycles.⁴⁴ Data shown in table 1.7 exemplifies that low-spin Ni(II) fits best within the 14-membered macrocycle [14]aneN₄ (cyclam); this Ni(II) complex has an unmeasurable dissociation constant, implying a half-life of years. Whereas, the high-spin Ni(II) fits best within the 15-membered macrocycle [15]aneN₄, this complex has a much smaller dissociation constant than the 16-membered macrocyclic complex. The kinetic *macrocyclic effect* is most prominent when the size of the metal ion and cavity size match. As discussed previously, a mismatch between metal ion and cavity size does not mean that a complex will not form, but the stability of such a complex may decrease slightly.

Table 1.6. First-order dissociation rate constants of 1:1 Cu(II) complexes in 6.1 M HCl at 25.0 °C.^{3-4, 32}

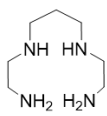
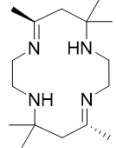
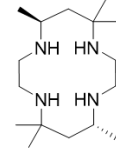
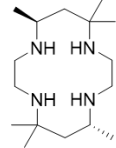
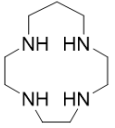
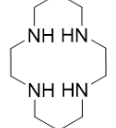
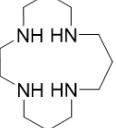
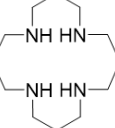
	2,3,2-tet	<i>trans</i> -[14]-diene	tet α (blue complex)	tet α (red complex)
Ligand				
k_d (s ⁻¹)	4.1	1.2×10^{-3}	3.8×10^{-3}	3.6×10^{-7}
Half-life	0.16 s	9.6 m	3.0 m	22 d

Table 1.7. Rates of dissociation of Ni(II) complexes in 0.3 M HClO₄ at 25 °C.⁴⁴

	[13]aneN ₄	[14]aneN ₄	[15]aneN ₄	[16]aneN ₄
Ligand				
k_d (s ⁻¹)	2.0 x 10 ⁻⁵	--	6.4 x 10 ⁻⁵	1.9 x 10 ⁻¹
Half-life	9.6 h	--	3.0 h	3.6 s

Macrocyclic dissociation kinetics studies have also revealed that the mechanism for complex dissociation follows a stepwise removal of the cyclic ligand from the coordination sphere. Dissociation of a macrocyclic complex into its metal and ligand components is a more intricate process than an open-chain polydentate ligand, because a macrocycle is just that, a cycle. The cyclic ligand has no end and as a result the macrocycle may have to fold into unfavorable conformations before dissociation of the complex can occur.

1.4. Synthesis of macrocycles

Macrocyclic chemistry is a diverse field with far reaching applications, but one important concept left to be discussed is the synthesis of these unique cyclic ligands. The synthesis of macrocycles is a complex process and procedures describing how to isolate macrocycles are ubiquitous in the chemical literature.^{7, 25, 46-49} Despite an extensive number of procedures pertaining to macrocyclic ligand synthesis, two overarching synthetic categories exist. The first category involves the 'direct' or non-templated synthesis of macrocycles. Direct synthesis involves cyclization of the ligand using conventional organic reactions without dependence on a metal ion.^{1, 3} The second category encompasses metal-directed or metal-templated reactions. Metal-directed reactions utilize a metal ion to generate a cyclic product.^{1, 3} In other words, a metal ion acts as a 'template' for the cyclization reaction to occur. Although the synthetic routes are broken in to broad categories, the process of synthesizing macrocyclic ligands involves many intricate steps, which probably include aspects of both direct and metal-directed reactions.³ A common

goal for both templated and non-templated reactions is to maximize yields by choosing strategies that will minimize side-reactions and polymerization of the ligand components.³ The following section will discuss the two synthetic categories for the synthesis of macrocyclic ligands. A general overview of several exemplifying synthetic strategies will also be discussed.

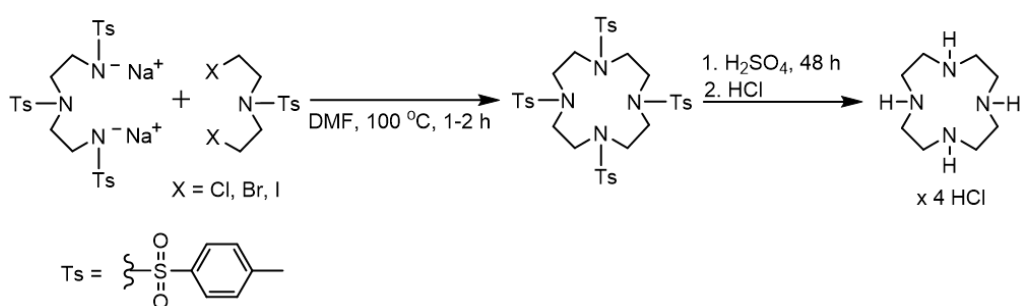
1.4.1. Direct/Non-template synthetic methods

The direct method of synthesizing macrocycles involves using conventional organic methods. Many direct synthetic methods for obtaining macrocyclic ligands involve intramolecular or intermolecular nucleophile-electrophile reactions.¹ In terms of organic chemistry, macrocycles having 12 or more members are considered large rings (Table 1.8).¹ Compared to smaller rings, macrocycles have very little ring strain, because the ligands are flexible enough to obtain ideal bond lengths and angles.¹ When synthesizing large rings, such as macrocycles, the main controlling factor tends to be entropic.¹ Regardless of the synthetic pathway, the final step in a cyclization procedure usually involves bringing two reactive moieties together so that a 1:1 condensation occurs and a ring-forming bond is generated.^{1, 3} Unfortunately, there are many alternative pathways that can also occur, which do not lead to formation of a macrocycle. Polymerization and oligomerization, a result of the entropic constraint, can occur if the appropriate moieties do not find one another to generate a macrocyclic ring.^{1, 3} Polymerization side-reactions can be prevented by performing cyclization reactions under high-dilution conditions. These conditions can involve milligram amounts of reactants and solvent amounts upwards of liters.¹ Additionally, it is usually necessary to ensure reactants are mixed slowly; this can be achieved by using special equipment that adds reactants dropwise over several hours or days (i.e. an addition funnel).¹ These special reaction conditions help to decrease the chance of two reactive moieties meeting in solution that could result in undesired polymerization.^{1, 3}

Table 1.8. Typical classification of ring sizes.¹

Ring Size	
3-4	small
5-7	normal
8-11	medium
≥ 12	large

High-dilution procedures are useful for preventing polymerization of reactants, but other non-template strategies exist. Successful cyclization reactions have been conducted under moderate to low dilution conditions. The Richman-Atkins cyclization represents a widely used strategy for the synthesis of polyazamacrocycles.^{3, 48, 50} This synthetic method can be used to prepare 9- to 21-membered rings containing 3 to 7 donor atoms in moderate to good yields (40-90%).^{3, 48} In the Richman-Atkins cyclization, a tosyl-protected amine (tosyl or Ts = *p*-toluenesulphonyl) is combined with a dihalide, under basic conditions, to yield a tosylated-macrocycle (Scheme 1.2).^{1, 3, 48, 50} The tosyl-protected macrocycle is then deprotected by stirring the resulting compound in concentrated sulfuric acid for several days (Scheme 1.2).^{1, 3, 48, 50} A work-up of the deprotected compound in hydrochloric acid yields the macrocycle as a hydrochloride salt (Scheme 1.2).⁴⁸

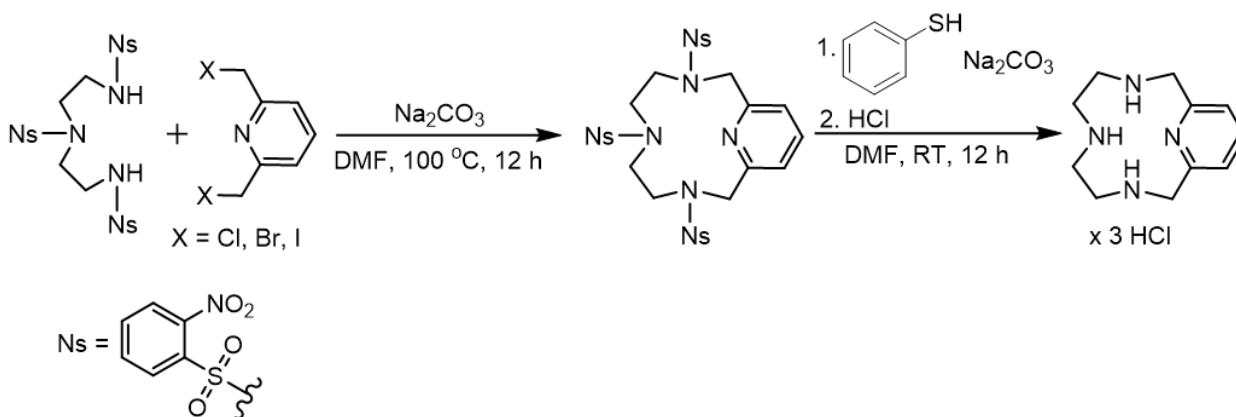


Scheme 1.2. Representative reaction for the Richman-Atkins synthetic method using tosyl groups.⁴⁸

Tosyl groups play several important roles in the Richman-Atkins reaction. They protect the secondary amine groups on the polyamine and also serve to increase the acidity of the remaining N-H bonds; this allows deprotonation to occur even under weakly basic conditions.^{1, 50} Additionally, the bulky

tosyl groups generally reduce the number of conformational degrees of freedom of reactants and intermediates.^{1, 3} This reduction is thought to help prevent polymerization products usually observed when cyclization occurs under low dilution conditions.^{1, 3, 48, 50} Another contribution to the high-yields of the Richman-Atkins reaction may involve influence from the base source. Typically, in these reactions a weak inorganic base, like Na₂CO₃ or K₂CO₃, is utilized.^{3, 25, 50-52} It has been suspected and reported that the presence of these alkali metal ions may also serve a template for cyclization.^{1, 3}

The Richman-Atkins procedure has many advantages, but one disadvantage is the set of harsh conditions needed for the deprotection of the tosyl groups.⁵⁰ Deprotection in concentrated sulfuric acid can be problematic when other functional groups are present within the macrocyclic structure or if the macrocycle contains relatively labile C-N bonds.⁵⁰ Fortunately, an alternative protecting group can be used. In 1995, Fukuyama *et al.* published a report describing the use of nosyl (nosyl or Ns = 2-nitrobenzenesulfonamide) groups as protective moieties.⁵³ Since this report, numerous groups have utilized nosyl groups for N-donor protection during cyclization reactions (Scheme 1.3).^{4, 50, 54-58} Nosyl groups offer the same synthetic advantages as tosyl groups, but the conditions necessary to remove them are much milder. Generally, nosyl groups can be removed with thiophenol under basic conditions (Scheme 1.3).^{4, 50, 53, 55-56, 58-59}



Scheme 1.3. Representative reaction for the modified Richman-Atkins synthetic method using nosyl groups.⁵⁴

The direct or non-template method of synthesizing macrocycles is a very broad category, with many representative procedures. General synthetic strategies within this category include high dilution conditions and/or bulky protecting groups. These synthetic methods are often time consuming, but generally the free-ligands are obtained in good yields. Although direct synthetic methods allow for synthesis of many kinds of macrocycles, this is not always the best synthetic strategy. If organic procedures come up short, template synthesis or metal-directed reactions may be necessary.

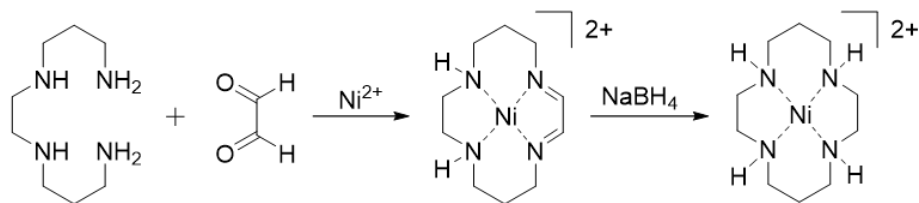
1.4.2. Metal-directed/template synthetic methods

Metal-directed or metal-template reactions depend on the influence of a metal ion to act as a 'template' for the cyclization of macrocyclic ligand. As discussed in the previous section, an entropic constraint of macrocyclic ligand synthesis is the possibility of two different moieties reacting to form a polymer. However, with the metal-template strategy, this problem is circumvented.¹ Generally, in a metal-template reaction a metal ion will coordinate to several donor atoms of a reactant or intermediate and pre-organize the components into a conformation that will yield the desired cyclic product. There are advantages and disadvantages to the metal-directed synthesis of macrocycles, as with any synthetic method. Advantages of metal-template synthesis include good yields, direct synthesis of a metal complex, and relatively mild reaction conditions. Unfortunately, one of the major disadvantages of metal-directed synthesis is that it is often an imprecise art. Not all metal ions serve as good templating agents and finding the correct metal ion for a specific type of template reaction can be difficult. Additionally, it is not always possible to predict the resulting product of a template synthesis (an exemplary case is presented in chapter 5).

Needless to say, the metal ion plays an integral role in template reactions and two possible roles of the metal ion have been described.^{1, 3, 60} Thompson and Busch designate both a kinetic and thermodynamic *template effect* in a fundamental article pertaining to the metal-directed synthesis of macrocyclic complexes.^{1, 3, 60} In the kinetic *template effect* the metal ion helps to control the

stereochemistry of the intermediates so that cyclization is the favored reaction pathway; the same macrocycle would not be formed using the same reactants in the absence of the metal ion.^{1, 3, 60} In contrast, the thermodynamic *template effect* involves the sequestration of a macrocycle by the metal ion from an equilibrium mixture containing products and reactants. The macrocycle is formed as the macrocyclic coordination complex and the metal ion is involved in shifting the equilibrium.^{1, 3, 60} Examples of both types of *template effect* have been well documented in the chemical literature. While these two types are useful conceptionally, in reality many template reactions involve aspects of both the kinetic and thermodynamic *template effect*.³ Additionally, mechanistic studies of metal-template syntheses are rare and details of the role a metal ion might play in template reactions still remain to be elucidated.^{1, 3}

The first template reaction of modern macrocyclic chemistry was reported by Curtis in 1960, followed by a series of subsequent reports pertaining to this pioneering synthesis.^{3, 7, 12-20} This reaction involving the condensation of acetone molecules to form a macrocyclic Ni(II) complex was detailed in section 1.2.2. Following this groundbreaking synthesis many other reports of template syntheses were reported. One of the most common types of template reactions involves the reaction between a di-carbonyl molecule and an appropriate di-primary amine in the presence of a metal salt (Scheme 1.4).^{1, 3, 61} This results in the formation of metal complex containing imine bonds. The imine bonds can be subsequently reduced either chemically (ex: NaBH₄), catalytically (ex: H₂ and Pd/C), or electrochemically to yield the saturated amine complex.³ The resulting reduced ligand can then be separated from the metal ion using numerous procedures.³



Scheme 1.4. Representative example of a metal-template reaction between a di-carbonyl and di-primary amine in the presence of a metal salt; imine bonds are chemically reduced to yield the saturated cyclic amine complex.^{1, 3, 61}

Metal-directed synthesis offers a synthetic strategy for using metal ions to influence formation of a macrocyclic ligand/complex. This strategy is useful for directly obtaining metal complexes, or synthesizing macrocycles that cannot be made using conventional organic methods. While this method offers the advantage of high yields and mild reaction conditions, finding the ideal metal ion for obtaining the desired macrocyclic complex is often a complex and imprecise art.

1.5. Applications of macrocyclic ligands.

In previous sections the properties of macrocycles were discussed. Researchers have long studied the unique structural, kinetic, thermodynamic, spectral, and electrochemical properties of macrocyclic complexes.^{1, 4, 56, 62-63} These exceptional complexes can be utilized for various applications across many different fields. In the early days of modern macrocyclic chemistry, a major driving force for the synthesis of these complexes was merely to develop highly efficient synthetic routes for large ring ligands.¹ Since then, many important and far reaching applications have been discovered. One of the largest applications is the use of macrocycles as biomimetic models for the active sites of metalloproteins.^{1, 3-4} Naturally occurring macrocyclic complexes are prevalent in biology. Important examples include the iron-bound porphyrin ring contained in the active site of hemoglobin, the chlorin complex of magnesium in chlorophyll, and the cobalt-bound corrin ring of vitamin B₁₂ (Figure 1.2).^{1, 3-4} Scientists have long studied these naturally occurring complexes and have designed and synthesized macrocyclic complexes to study the structure and function of metalloproteins. Macrocyclic complexes also have applications in organic chemistry, specifically as redox catalysts.^{4, 64-66} Macrocycles can stabilize a variety of different metal oxidation states⁶⁷, making these complexes ideal for use as redox catalysts. Various catalytic studies have been performed using macrocyclic ligands and their corresponding metal complexes.⁶⁸ Macrocycles also have many applications in the field of biochemistry; complexes can be used as both therapeutic and diagnostic agents. For example, if a macrocyclic ligand is functionalized its paramagnetic metal complex may be used as a diagnostic MRI contrast agent.⁶⁹⁻⁷⁰ Additionally, a macrocyclic ligand may be used as a

therapeutic agent to sequester misregulated metal ions in various neurodegenerative disorders.⁷¹⁻⁷³ These are just a few of the many applications of macrocyclic complexes.

1.6. Macrocyclic chemistry in the Green group

One of the main research focuses within the Green group is the synthesis, characterization, and applications of azamacrocyclic ligands (**L1-L9**) (Figure 1.11) and their corresponding transition metal complexes. The first generation of ligands consist of 12-membered pyridine- and pyridol-based tetraazamacrocycles (**L1-L3**) (Figure 1.11).^{55-56, 62, 72-73} Generation two includes a 12-membered bis-pyridol based tetraazamacrocycle and a large 30-membered decaazamacrocycle (**L4-L5**) (Figure 1.11). Finally, the third generation encompasses several *para*-functionalized pyridine-based tetraazamacrocycles (R = CN, NO₂, Cl, or NH₂) (**L6-L9**) (Figure 1.11). This library of azamacrocycles has been built over several years and is a result of the culmination of many different studies including: (i) the optimization of synthetic methods (for both free-ligands and metal complexes)^{55-56, 72-73}; (ii) the analysis of unique structural, spectral, and electrochemical features of first-row late transition metal macrocyclic complexes^{55-56, 62}; (iii) the examination of enhanced antioxidant, amyloid disaggregation, and metal sequestration capabilities exhibited by these macrocycles for use as therapeutics to combat neurodegenerative disorders⁷²⁻⁷³; (iv) the exploration of the catalytic abilities of macrocyclic metal complexes; (v) the investigation of modified macrocycles and macrocyclic complexes for use as novel MRI contrast agents; and (vi) the inspection of functional group influence on ligand induction and resonance.

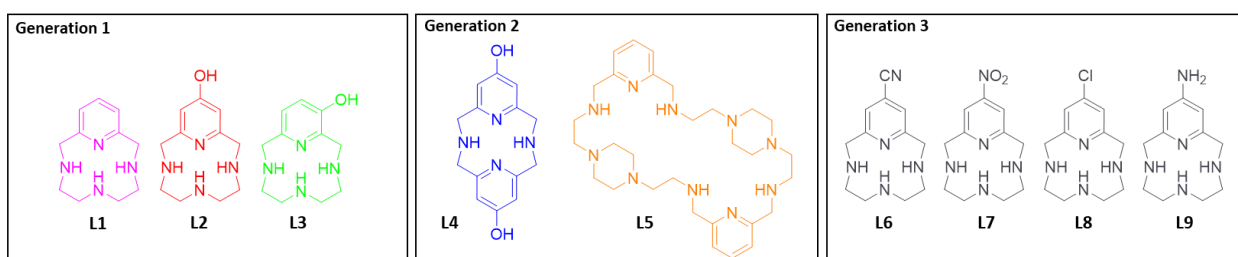


Figure 1.11. Chemical structures of macrocyclic ligands synthesized by the Green group.^{55-56, 72-73}

The first generation of ligands (**L1-L3**) serve as a foundation for rest of the macrocyclic ligand library. **L1** was first reported by Stetter and coworkers, in 1981, and inspired the development of **L2** and **L3** as therapeutic agents for the treatment of neurological disorders.⁷²⁻⁷³ The exact mechanism leading to neurodegenerative disorders, such as Alzheimer's Disease (AD) and Parkinson's Disease (PD), is not fully understood. One leading hypothesis is that a 'pathological trifecta' is responsible for many hallmarks of neurodegenerative disorders.^{71, 74-83} This trifecta encompasses metal ion misregulation, oxidative stress from reactive oxygen species (ROS), and amyloid aggregation.^{71, 74-83} Based on this pathological hypothesis the Green group designed and synthesized several therapeutic agents (**L1-L3**). The rationale behind the design for these therapeutic agents was based off cyclen ([12]aneN₄) which has been shown to decrease amyloid beta aggregation by sequestering metal ions from amyloid plaques.⁸⁴ Pyridine and pyridol moieties were added to increase the radical scavenging abilities of these novel therapeutic agents. Several studies conducted by the group have shown that addition of these moieties does increase radical scavenging capacity, particularly in the case of pyridol.⁷² Additionally, macrocyclic metal complexes were synthesized using biologically relevant metals such as Cu(II), Zn(II), and Ni(II) to ensure that the macrocyclic cavity could sequester metal ions.⁵⁶

L1-L3 complexes with Cu(II), Zn(II), and Ni(II) were the first to be synthesized and characterized spectroscopically.⁵⁶ Solid state structures of these metal complexes revealed the binding modality of the 12-membered tetraazamacrocycles **L1-L3**. Despite slight differences in bond lengths and bond angles, it was revealed that first-row late transition metals bind to these 12-membered tetraazamacrocyclic ligands in a *cis*-fashion, due to the inability of the macrocyclic cavity to fully encompass the metal ion (Figure 1.5). All metal ions investigated by the Green group bind to **L1-L3** in this fashion. After initially complexing biological metals, these three ligands were complexed with a range of first-row late transition metal ions such as: Co(III), Mn(III)/Mn(IV), and Fe(III). Each metal complex exhibited unique structural, spectral, and electrochemical features. Complexes of **L1-L3** with Fe(III) have been extensively characterized and applied

as redox catalysts for the Suzuki-Miyaura type C-C coupling reaction between pyrrole and phenylboronic acid by colleague Samantha Brewer.⁸⁵⁻⁸⁶

After the foundational work with the first macrocyclic ligand generation **L1-L3**, another macrocycle was designed and synthesized. **L4**, and the related first-generation ligands, **L1-L3**, will be discussed in chapter 2. **L4** encompasses two pyridol moieties within a tetraazamacrocyclic ring. The rationale behind this ligand design was to further enhance the radical scavenging ability **L2** exhibited by doubling the pyridol moieties present within the molecule. This second-generation macrocycle is another proposed neurodegenerative therapeutic agent, like **L1-L3**. **L4** has been complexed to several biologically relevant metals, including Cu(II) and Zn(II). The protonation and stability constants for **L4** were obtained using pH-potentiometric methods. Additionally, cell toxicity studies have been conducted and the antioxidant activity has been probed using several relevant assays.

Chapter 3 focuses on the Co(III) complexes with **L1-L3**, which exhibit a solvent dependent equilibrium that parallels the CoCl_2 equilibrium used to illustrate Le Châtelier's principle.⁶² Additionally, the macrocyclic Co(III) complexes were explored for used as catalysts in several organic reactions. Chapter 4 will discuss two different manganese complexes, a monomeric Mn(III) complex and a dimeric Mn(III,IV) complex. One of these complexes encompasses two ligand-bound manganese ions connected through a di- μ -oxo bridge; incidentally these types of di- μ -oxo bridged dimers have historically been used to model the active site of photosystem II in plants. The beginning half of chapter 4 encompasses a full review of most known dimeric Mn(III,IV) and monomeric Mn(III) complexes synthesized to date.

Chapter 5 focuses on **L5**, which is a bit of an anomaly, and was originally designed to be utilized as a Mn(II)-based MRI contrast agent. The proposed structure was a 15-membered pyridine and piperazine containing macrocycle with 5 nitrogen donor atoms. It has been shown that Mn(II) complexes of rigid 15-membered N5 macrocycles exhibit high relaxivity, which is a strongly desired feature for contrast agents.⁸⁷⁻⁹² In our design, the piperazine moiety was incorporated into the macrocycle to increase

the rigidity of the complex. Typical templating procedures were used to synthesize this hypothetical macrocycle, but the presence of a piperazine ring within the di-primary amine, lead to an unexpected result. A 30-membered decaazamacrocyclic 'dimer' of the originally designed macrocycle was synthesized instead. The resulting **L5** ligand has been analyzed using, X-ray diffraction and pH-potentiometric methods, to give its protonation and stability constants.

The last generation of macrocyclic ligands **L6-L9** have only recently been synthesized in collaboration with Akop Yepremyan at TCU. Future work with this new set of ligands includes analysis of how different R groups effect ligand and metal complex properties.

Chapter 2: Synthesis, characterization, and applications of a novel bis-pyridol-based tetraazamacrocyclic (L4)

2.1. Introduction

2.1.1. The pathology of neurodegenerative diseases

AD is the most common neurodegenerative disease, affecting millions of people worldwide.^{73, 93-}
⁹⁴ A widely accepted hypothesis for the pathogenesis of this disease is termed the metal hypothesis of AD. This hypothesis, proposed by Bush and coworkers, suggests that the hallmarks of AD (oxidative stress and amyloid plaques) are a result of a cascade of events beginning with the misregulation of metal ions.⁹⁴⁻¹⁰¹ Metal ion misregulation, oxidative stress, and amyloid aggregation are all interrelated. Misregulation of metal ions can lead to the formation of protein aggregates through metal-protein interactions and free metal ions can also catalyze ROS generating reactions leading to oxidative stress. This 'pathological trifecta' (metal ion misregulation, oxidative stress, and amyloid aggregation) has been implicated in various neurodegenerative diseases, including AD (Figure 2.1). The following discussion will dissect the factors involved and rational for developing small molecules to target the disease.

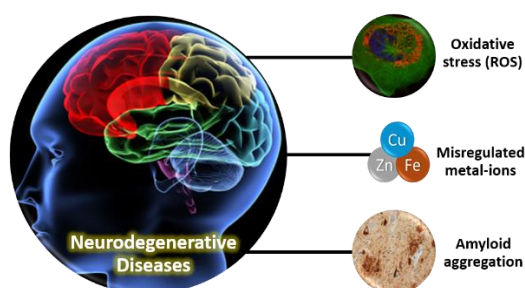


Figure 2.1. The 'pathological trifecta' which are hallmarks of neurodegenerative diseases.

The human body utilizes metal ions for a variety of different processes. Na(I) and K(I) are utilized for electrical conditions in the nervous system, Zn(II) and Cu(II) are present in metalloregulatory proteins that play a central role in DNA signaling, and Fe(II/III) and Cu(II) are implicated in electron transfer.^{94, 102} Not only are metal ions required for general cellular processes, but they are also essential to neuronal

processes in the brain.¹⁰³ Zn(II), Cu(II), and Fe(III) ions all play important roles in the brain. These transition metal ions help regulate neuronal activity within the synapses, are essential components of several metalloproteins, and are required for mitochondrial function and neurotransmission.¹⁰³ Although Zn(II), Cu(II), and Fe(III) ions are essential to neuronal processes, concentrations within the brain must be tightly regulated because aberrations can lead to cell death and a variety of disease states.¹⁰³ The brain has many intricate homeostatic mechanisms to maintain metal ion homeostasis. Metal ions crossing through the blood-brain barrier (BBB) are tightly regulated via transporters and chaperones, which strictly control the metal uptake and delivery to specific domains.¹⁰³⁻¹⁰⁴ When the brain is in a healthy state, the free metal ion concentration is maintained at very low values (between 70-300 μ M) by homeostatic mechanisms.¹⁰⁵⁻¹⁰⁶ Unfortunately, these mechanisms can sometimes become impaired, which leads to metal ion misregulation. An increase in the free metal ion concentration due to misregulation can lead to protein aggregation and oxidative stress.¹⁰³ The formation of protein aggregates and reactive oxygen species by misregulated metal ions has been implicated in a variety of neurodegenerative diseases such as: Huntington's disease (HD), Alzheimer's disease (AD), Parkinson's disease (PD), and Lou Gehrig's disease.^{95,}

104, 106-115

Amyloid- β ($A\beta_{1-42}$) is a normal protein present within the brain and is derived from the cleavage of the amyloid precursor protein (APP) by β - and λ -secretases.^{4, 106} Unfortunately, $A\beta_{1-42}$ can aggregate to form insoluble $A\beta$ -plaques.^{4, 106} Recent evidence suggests misregulation of metal ions in the brain also contributes to $A\beta$ aggregation.¹⁰⁶ The accumulation of $A\beta$ -plaques has been implicated in AD.¹⁰⁶ For example, in the case of AD patients, $A\beta$ plaques are observed to contain increased amounts of Zn(II), Cu(II), and Fe(III) (Zn(II): 1055 μ M, Cu(II): 390 μ M, Fe(III): 940 μ M compared with normal age-matched neuropil where Zn(II): 350 μ M, Cu(II): 70 μ M, Fe(III): 340 μ M), while intracellular transition metal stores are deficient.^{73, 94, 106} $A\beta_{1-42}$ contains a histidine rich region that is proposed to effectively bind free metal ions such as Cu(II) and Zn(II).^{4, 73} Although the exact pathology leading to the development of AD has not been

elucidated, the formation of A β plaques is central to many hypotheses.^{73, 95-101} A β plaques are hypothesized to lead to the progression of AD by oxidizing DNA, protein, and lipids, impairing synaptic and axonal communication, and disrupting mitochondrial membrane potentials.⁴

In addition to protein aggregation, oxidative stress brought about by the metal-mediated generation of ROS is also implicated in the development of neurodegenerative diseases. The brain produces billions of free radicals daily, which are a natural consequence of oxygen metabolism.¹⁰⁴ The molecules produced during the metabolism of oxygen, both radical and nonradical, are known as reactive oxygen species (ROS).¹⁰⁴ In the body, molecular oxygen (O₂) is reduced to water in the electron transport chain (ETC) followed by the addition of four electrons in a stepwise fashion; through this process several hydrogen based ROS are formed: the hydroperoxyl radical (OOH[•]), superoxide radical (O₂^{•-}), and hydroxyl radical (OH[•]).¹⁰⁴ Elevated oxygen consumption leads to an increased concentration of the superoxide radical, which is particularly concerning in the brain because it accounts for approximately 20% of the total oxygen consumed by the body.^{72, 93, 103, 116} The superoxide radical cannot cross cell membranes, but the dismutation of superoxide forms hydrogen peroxide, which can easily cross cell membranes.¹⁰⁴ When superoxide and hydrogen peroxide react, they yield highly reactive hydroxyl radicals via the Haber-Weiss reaction, shown in equation [2.1].¹⁰⁴ Additionally, if metal ions (like Fe or Cu in low oxidation states) are present hydroxyl radicals can also be generated via Fenton reactions, shown in equation [2.2].^{74-78, 95, 103-104, 106, 113, 117-131}



ROS are produced during normal cellular functions and many antioxidant homeostatic mechanisms are in place, but ROS levels exceeding normal cellular production are potentially dangerous.¹⁰⁴ Oxidative stress occurs when the homeostasis of ROS is disrupted, allowing for initiation of

radical chain reactions, such as the ones described above.¹⁰⁴ ROS, like the hydroxyl radical, can cause lipid peroxidation, DNA base hydroxylation, and protein modification.^{74, 77, 103-104, 120, 129, 131} Unfortunately, the brain's elevated demand for oxygen makes it particularly susceptible to oxidative stress, hence the BBB and increased levels of metal transporters and chaperones.^{72, 93} For instance, if the homeostasis of redox active transition metal ions (Cu(II) and Fe(III)) is disrupted, this can lead to generation of excess ROS via Fenton reactions previously described^{74-78, 95, 103, 106, 113, 117-131} Conditions of oxidative stress often develop when metal ion misregulation occurs because the production of ROS species due to these reactions exceeds cellular antioxidant defense mechanisms.⁴

2.1.2. Current therapeutic approaches

There are many different approaches to treating AD presented in the chemical literature; strategies range from vaccinating against A β ₁₋₄₂, treatment with known antioxidants, or using strong metal chelators to sequester aberrant metal ions.^{107-108, 132-144} Many therapeutic strategies are designed around the metal hypothesis of AD, proposed by Bush and coworkers. As discussed previously, this hypothesis suggests that metal ion misregulation causes the cascade of events, such as amyloid aggregation in conjunction with oxidative stress, that leads to the development of AD.^{94-101, 109, 132, 145-147} There are thousands of proposed strategies for treating neurodegenerative disorders and are reviewed elsewhere.^{75, 107, 133-139, 141, 148-149} For the purpose of this dissertation, the following section will be limited to several current therapeutic molecules relevant to controlling ROS and metal ions (Figure 2.2).

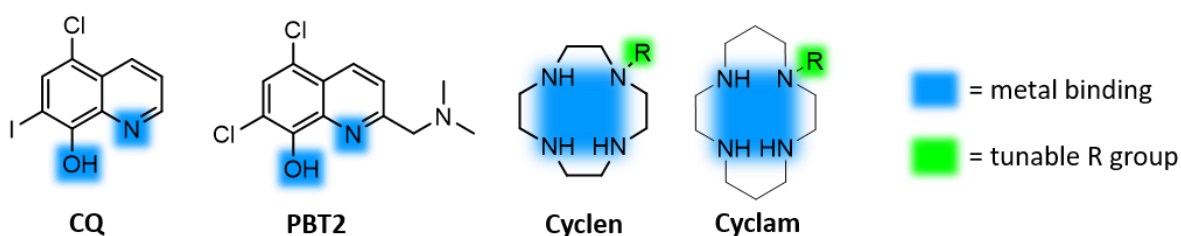


Figure 2.2. Current neurotherapeutic molecules relevant to this discussion. (R group examples include 8-hydroxy-quinoline and propylpyridine-4-yl)^{107, 133-134, 137, 149-151}

Clioquinol (CQ) has been used as an antifungal and antiprotozoal drug in the past, but recently it has garnered attention by researchers as a possible neurotherapeutic agent (Figure 2.2).^{132, 134, 152-153} CQ is derived from 8-hydroxyquinoline, which is a monoprotic bidentate metal chelator. CQ binds metals in a bidentate fashion and exhibits a higher affinity for Zn(II) and Cu(II) ions over Mg(II) or Ca(II) ions; Zn(II) and Cu(II) bind to A β and cause aggregation, making this a highly desirable feature.¹⁵⁰ CQ is also a hydrophobic molecule and easily crosses the blood-brain barrier. In 2001, Cherny *et al.* reported that the oral treatment of CQ on aged APP2576 Tg mice (with advanced A β deposition) markedly inhibited A β deposition after 9 weeks.¹⁵⁰ The changes in A β deposition were not accompanied by any adverse effects and the mice exhibited improved cognition after the treatment.^{4, 72-73, 150} Additionally, CQ treatment exhibited encouraging results in a phase II clinical trial involving moderately severe AD patients.¹⁵⁴⁻¹⁵⁵ Despite these successes, CQ has also been shown to redistribute copper ions and increase the level of biological copper within the brain.¹⁴⁹ CQ was also taken off the US market as an antifungal agent in 1971, due to its link with the development of subacute myelo-optic neuropathy (SMON), which leads to paralysis, blindness, and death.^{154, 156} Notwithstanding the negative health effects of CQ in large doses, scientists were encouraged by successful animal studies and clinical trials with this potential neurotherapeutic. The positive results shown by CQ testing encouraged researchers to pursue the development of metal chelators for treatment of metal ion misregulation associated with neurodegenerative diseases.⁷³

The promising results of CQ phase II clinical trials, lead researchers to develop a second-generation congener, PBT2 (Figure 2.2).^{107, 132, 134, 137, 150, 153, 155} PBT2, like CQ, is derived from 8-hydroxyquinoline; but in contrast to CQ it contains an additional tertiary amine in the *ortho* position of the pyridine ring (Figure 2.2). PBT2 has been shown to restore cognitive abilities of AD transgenic mice to the same level as cognitively healthy mice.^{73, 107, 153} In addition, phase II clinical trials of PBT2 have exhibited improved cognition in patients with mild AD.^{73, 107, 153} PBT2 was originally designed to combat AD by modulating aberrant metal ions bound to A β , but studies have shown that PBT2 can also function

as an ionophore and has the additional ability to chaperone metal ions across the plasma membrane into cells.^{73, 107, 153} The metal ions involved in the deposition of A β are salvaged by chaperones (such as PBT2), activities in communication pathways are restored, and A β dissolution is increased.^{73, 107, 132, 137, 151, 153} The ability of PBT2 to act as both an ionophore and metal chelator further encouraged researchers to continue pursuing the strategy of modulating metal ion misregulation in combating AD disease.

CQ and PBT2 are bidentate metal chelators being tested as therapeutic agents for the treatment of AD, but many more variations of metal chelating ligands exist. Macrocyclic polyamine compounds or polyazamacrocycles have a strong affinity for metal ions and their denticity can be modified depending on the number of donor atoms within the cyclic ring.¹⁴⁹ Polyazamacrocycles have been utilized for many biological applications from diagnostic imaging (MRI contrast agents) to the treatment of metal overload disorders.¹⁴⁹ Several physical properties make polyazamacrocycles ideal for biological applications including: low molecular weights, neutral charges, amphiphilic solubility and low toxicities.^{141, 149, 154} These favorable physical properties have lead scientists to investigate polyazamacrocycles as potential therapeutics for neurodegenerative disorders.

In 2009, Guo and coworkers investigated the effects of cyclen (a 12-membered tetraazamacrocycle) and cyclam (a 14-membered tetraazamacrocycle) on Zn(II) and Cu(II) induced A β aggregation.¹³³ In this study, the authors observed the ability of cyclen and cyclam to dissolve A β aggregates and protect A β plaques from forming in the presence of Cu(II) and Zn(II). Additionally, both cyclen and cyclam exhibited the ability to inhibit the production of H₂O₂ induced by metal-amyloid aggregation.¹³³ These results show the ability of cyclen and cyclam to act as potential therapeutic agents for AD and are encouraging for the development of additional metal sequestration strategies for the treatment of neurodegenerative disorders (Figure 2.2). Indeed, several other groups have adapted cyclen and cyclam to even further enhance their therapeutic abilities.^{138, 149, 154} Modifications include the addition of tunable R groups attached to the nitrogen atoms.^{138, 149, 154} By strategically choosing R groups

researchers have developed bimodal therapeutic agents. The macrocyclic core (which includes the nitrogen donor atoms) acts as a metal chelator to sequester aberrant metal ions, but addition of tunable R groups instills synergistic properties to the macrocycle to further combat neurodegeneration.^{78, 82-83, 157} Pendant arms that increase the lipophilicity or antioxidant properties of the macrocycle can be added via simple alkylation and acylation reactions.^{78, 82-83, 149, 157-158} Unfortunately, derivatization of macrocyclic nitrogen atoms can lead to reduced reactivity or metal binding ability, thus decreasing the applicability of N-based modified azamacrocycles.¹⁵⁹

2.1.3. Using a rational design approach to design L1

Inspired by the work of Guo and coworkers, the Green group developed a series tetraazamacrocyclic ligands for the multimodal treatment of AD.¹³³ The initial design, synthesis, and analysis of the macrocyclic pyridinophane **L1** (and eventually **L2** and **L3**) was completed by colleagues Kimberly Lincoln, Paulina Gonzalez, and collaborators.^{55-56, 72-73} **L1**, also known as pyclen (a tetraaza macrocyclic pyridinophane), was repurposed using a rational design approach and contains a 12-membered tetraazamacrocyclic ring with an additional pyridine moiety (Figure 2.3).^{4, 72-73} **L1** combines the metal binding affinity of cyclen with the built-in antioxidant functionality of a pyridine ring to offer a bimodal molecule for the treatment of AD.^{4, 72-73} This ligand design was chosen for several reasons: (i) it is the backbone to the compound PCTA (Pyridine-Containing Triaza Macrocylic TriAcetate) which is a well-studied MRI contrast agent^{4, 89, 160-161}, (ii) it contains a 12-membered ring system similar to cyclen, which has a high binding affinity for Cu(II) and Zn(II)^{4, 133}, and (iii) the pyridine ring contained within the ligand offers antioxidant functionality.^{4, 162}

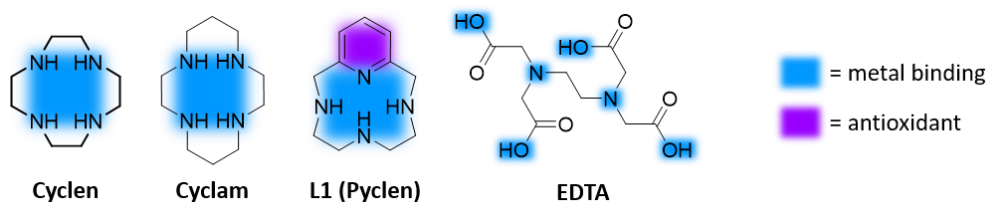


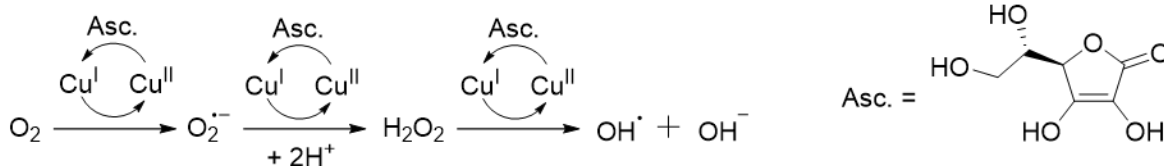
Figure 2.3. L1 and metal chelating ligands studied by the Green group.^{4, 73}

Initially, several key features of **L1** were compared with cyclen, cyclam, and EDTA, which are all known chelating ligands (Figure 2.3). When biological metal ions such as Cu(II) and Zn(II) bind to A β they can form insoluble aggregated plaques, which are a hallmark of AD.^{4, 72-73} Amyloid (A β) aggregation can be followed spectroscopically using turbidity^{83, 132-133, 149, 157, 163-164} and tyrosine fluorescence^{132, 165-168} studies.^{4, 73} These methods were used to investigate the ability of the metal chelators (listed above) to dissociate and prevent amyloid aggregation by sequestering metal ions within A β plaques. Results of both turbidity and tyrosine fluorescence studies indicated that **L1**, cyclen, cyclam, and EDTA all possess the ability to dissolve amyloid aggregates and prevent formation of aggregates when co-incubated with amyloid.^{4, 73}

In addition to A β aggregation, oxidative stress, caused by increased levels of ROS, has also been implicated in AD.^{4, 73} **L1** was designed to have an increased antioxidant capacity compared to other chelating agents such as cyclen; this additional antioxidant capacity was tested using several relevant assays. The ABTS decolorization assay is a spectroscopic method that can be used to measure the antioxidant capability of a molecule (ABTS = 2,2'-azino-bis(3-ethylbenzothiazoline-6-sulphonic acid)).^{80, 169-170} The ability of a compound to quench the ABTS^{•+} radical (monitored spectroscopically) is often normalized against Trolox, which is a well-known antioxidant.^{80, 169-170} When performed by the Green group, this assay showed that **L1** was able to quench the ABTS^{•+} radical more effectively than cyclen or cyclam.⁷³ Because cyclen and cyclam both lack a pyridine moiety, it was concluded that the enhanced antioxidant capability of **L1** was due to the presence of the pyridine ring; confirming the importance of the presence of the pyridine group within the molecule.

As stated previously, increased oxidative stress is implicated in the pathology of AD. One of the proposed pathways for producing ROS involves the redox cycling of metal ions such as Cu(II).⁷³ A good model for redox cycling in the brain, where high levels of oxygen and ascorbate are present, is the Cu-ascorbate redox system (Scheme 2.1).^{73, 171-172} This redox cycling model was used to determine if chelating ligands, such as **L1**, could halt Cu based redox cycling under aerobic conditions. To quantify the ability of

L1 to halt Cu based redox cycling a CCA (Coumarin-3-carboxylic acid) assay was used.^{73, 171-172} In the presence of hydroxyl radicals, CCA is converted into fluorescent 7-hydroxy-CCA.^{73, 171-172} The change in fluorescence intensity of 7-hydroxy-CCA can be used to quantify a ligands ability to halt redox cycling.^{73, 171-172} Studies performed by the Green group indicated that both **L1** and cyclam are capable of completely halting copper-based redox cycling by metal complexation.⁷³



Scheme 2.1. Redox cycling of copper in the presence of oxygen and ascorbate to produce hydroxyl radicals.^{73, 171}

2.1.4. Using a rational design approach to design **L2** and **L3**

In initial studies, **L1** exhibited the ability to disrupt metal-induced A β plaques, quench ROS species, and protect cells against ROS induced cell death.⁷³ Given the success of these studies, **L1** was modified to improve its neurotherapeutic abilities. Due to the increasing interest in the role that oxidative stress play in the development of AD, the Green group set out to further enhance the antioxidant capabilities of **L1**.⁷² As discussed previously, making modifications to the nitrogen atoms of azamacrocyclic ligands is an easy way to add multimodal functionality to potential therapeutic agents.^{149, 154} Although, this strategy can lead to a decrease in ligand reactivity and metal binding ability.¹⁵⁹ In contrast to other cyclen or cyclam based therapeutic agents, **L1** contains a pyridine ring that can easily be modified in the C3 (*para*) or C4 (*meta*) positions.⁷² Additional substituents can be added to the pyridine ring without altering the chelating ability of the core nitrogen atoms.^{4, 72} The pyridine ring within **L1** was converted to a pyridol ring, with a hydroxyl moiety in the *para* position, to yield **L2** (Figure 2.4).^{4, 72} Pyridols are known to react with hydroxyl radicals via addition at the C2 or C4 position.¹⁷³ The products of these reactions are similar to tannins, which are known antioxidants.¹⁷⁴ It was hypothesized that the addition of the hydroxyl functional group on the

pyridine ring of **L2** would further enhance the antioxidant capabilities exhibited by **L1**.^{4,72} Several different studies were conducted by the Green group to test the enhanced radical scavenging/antioxidant ability of **L2** vs. **L1**.⁷²

To test the radical scavenging ability of **L2** a DPPH (2,2-diphenyl-1-picrylhydrazyl) radical quenching assay was used.^{72, 132, 149, 175} DPPH is a stable radical with a maximum absorbance at 520 nm. When the DPPH radical is quenched by a radical scavenger the color of the solution changes from purple to yellow and this change can be measured spectroscopically.^{72, 175} Although both **L1** and **L2** exhibit the ability to reduce free radicals, **L2** displayed a greater radical reducing ability at higher concentrations.⁷² These results led to the conclusion that the enhanced radical reducing ability exhibited by **L2** was due to the pyridol ring, because this feature is absent in **L1**.⁷² Furthermore, a CCA assay was performed with **L1** and **L2**; both ligands exhibited the ability to halt the redox cycling of copper.⁷²

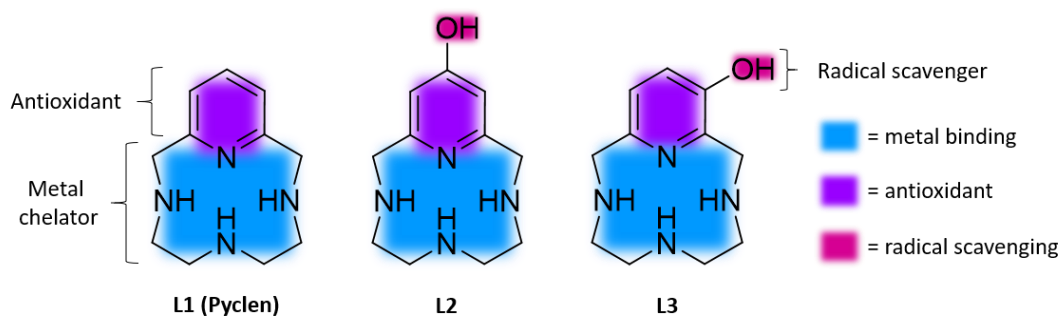


Figure 2.4. L1-L3 ligands synthesized and studied by the Green group.^{55-56, 72-73}

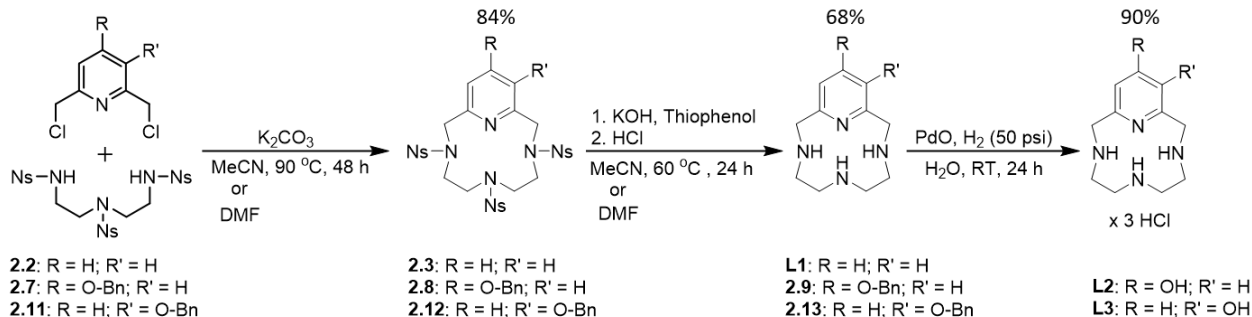
L2 was made by adding a hydroxyl group in the *para* position of the pyridine ring contained in **L1**.^{55, 72} In addition to **L2**, another congener was synthesized. **L3** was made by adding a hydroxyl group in the *meta* position of the pyridine ring contained in **L1** (Figure 2.4).⁵⁶ Originally, **L1** and **L2** were synthesized as potential therapeutic agents for the treatment of AD; studies pertaining to their therapeutic abilities are discussed above. **L3** was synthesized to investigate how changing the position of hydroxyl group, from *para* (**L2**) to *meta* (**L3**), would affect the antioxidant activity of the pyridol system. Another DPPH radical scavenging assay was used to determine the radical scavenging abilities of **L1-L3**.⁵⁶ Once again it was

observed that pyridol ring contained in **L2** and **L3** engendered these ligands with enhanced antioxidant capabilities compared to **L1**.^{56, 72} It was also observed that both **L2** and **L3** exhibited equivalent radical scavenging abilities.⁵⁶ Finally, studies were conducted to determine if the electronic nature of **L2** and **L3** could be distinguished from one another. Ligand-metal complexes were made using Ni(II), Cu(II), and Zn(II) and these were subsequently analyzed using spectroscopic and electrochemical methods.⁵⁵⁻⁵⁶

2.1.5. Synthetic methodology for L1-L3

In chapter 1 (section 1.4.1), two overarching categories for the synthesis of azamacrocyclic ligands were discussed. The direct or non-templated synthesis of macrocycles involves cyclization using conventional organic reactions without dependence on a metal ion.^{1, 3} In contrast, the metal-directed or metal-templated synthesis of macrocycles involves a metal ion acting as a 'template' to generate a cyclic product.^{1, 3} When developing the methodology for the synthesis of **L1-L3** both synthetic routes (direct and metal-directed) were tested.⁴ After extensive of experimentation, it was determined that the direct method worked best for the isolation of the ligands **L1-L3**.⁴

Kimberly Lincoln and coworkers developed the synthetic pathways for the preparation of **L1-L3** by adapting the Richman-Atkins method and several other published procedures.^{4, 55-56, 72-73, 176} These ligands can be isolated in good yields using a variation of the Richman-Atkins synthetic method, which involves the 1:1 condensation of a nosyl-protected amine with a dihalide molecule to yield a cyclic product.^{3, 48, 50} Traditionally, the Richman-Atkins method utilizes tosyl groups to protect the nitrogen atoms in the amine, but the conditions needed to remove the tosyl groups are harsh (involving concentrated sulfuric acid).^{48, 176} A slight variation to this method involves the use of nosyl protected groups, which can be removed under much milder conditions.^{53-54, 57-58, 176} In subsequent years, the Green group has made slight modifications to optimize these procedures.



Scheme 2.2. General methodology for the synthesis of **L1-L3**; (Ns = Nosyl).^{4, 54-57, 59, 176-182}

The first step for producing **L1-L3** involves the 1:1 condensation of a nosyl protected amine with the corresponding dihalide (synthetic methodology for both the nosyl protection and dihalide synthesis can be found in the experimental section of this chapter).^{4, 54-57, 59, 176} First, the nosyl protected amine is deprotonated with a weak inorganic base, K_2CO_3 , followed by dropwise addition of the halide to initiate the condensation reaction to yield a cyclic product (Scheme 2.2).⁵⁴⁻⁵⁵ After stirring for several days, the nosyl protected macrocycle is obtained in good yields (typically 80-90%).⁵⁵ Following the cyclization step, the nosyl groups are removed using the strong base KOH and thiophenol (Scheme 2.2); this forms potassium thiolate which acts a nucleophile to perform a nucleophilic substitution on the nosyl groups.^{55, 176, 181} The nosyl groups are eliminated from the macrocycle and SO_2 is evolved in the process.¹⁸¹ In the subsequent work-up, the free macrocycle is acidified with hydrochloric acid and thereby isolated as the HCl salt (with yields of 60-70%).⁴ The removal of the nosyl groups is the last step in the synthesis of **L1**, but **L2** and **L3** both require an additional step to remove the benzyl protecting group on the pyridine ring. The deprotection of benzyl is achieved by a palladium-catalyzed hydrogenation to yield **L2** or **L3** in good yields (typically 90%; Scheme 2.2).¹⁷⁶

2.2. A rational design approach to **L4**: a novel bis-pyridol-based tetraazamacrocycle

Pyridol-based **L2** and **L3** both exhibited enhanced radical scavenging abilities compared to their pyridine-based congener, **L1**.⁵⁶ Given the success of antioxidant studies with **L2** and **L3**, an additional pyridol moiety was added to **L2** to even further enhance its radical scavenging abilities, resulting in the

bis-pyridol-based tetraazamacrocycle **L4** (Figure 2.5). It was hypothesized that doubling the pyridol moieties would result in an increase the radical scavenging ability and antioxidant capabilities of the molecule (**L4**) thus increasing potency and lowering the effective dosage. To test this hypothesis, several relevant assays have been performed with **L4**, including the CCA redox cycling assay and DPPH radical quenching assay; both of which have previously been utilized to determine the antioxidant capabilities of **L1-L3**.⁷²⁻⁷³ Cell studies performed with **L4** give insight into the possible therapeutic window of this molecule for the treatment of neurodegenerative disorders. In addition to these assays and cell studies, **L4** has been complexed to several biologically relevant metals (Cu(II) and Zn(II)) associated with the development of AD. These complexes were characterized using X-ray diffraction (XRD), nuclear magnetic resonance (NMR), mass spectrometry (MS), UV-visible spectroscopy (UV-vis), and cyclic voltammetry (CV). Finally, pH-potentiometric titrations were performed with **L4** to determine the protonation and stability constants, which were compared to generation 1 ligands **L1-L3**.

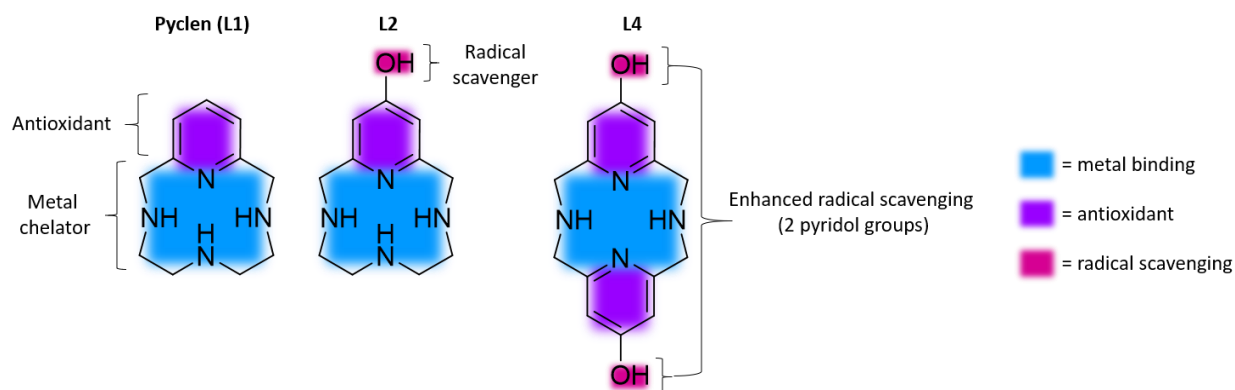
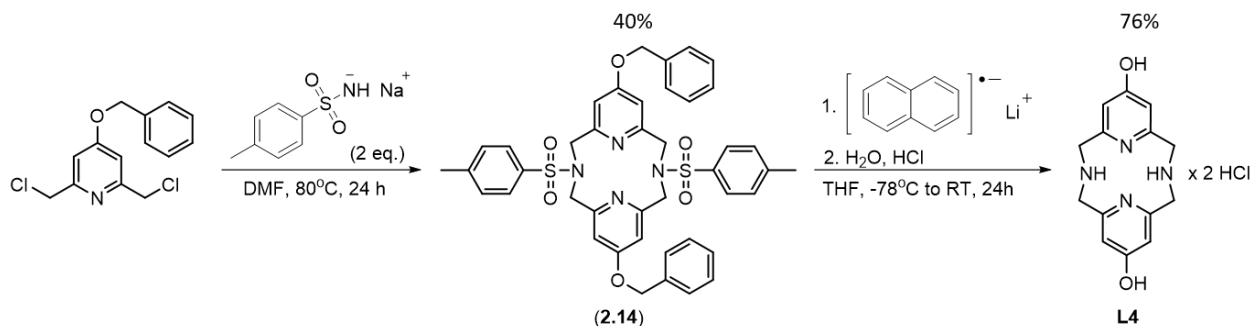


Figure 2.5. Rational design approach of **L4**, based off successes of **L1** and **L2**.

2.3. Synthetic methodology for **L4**

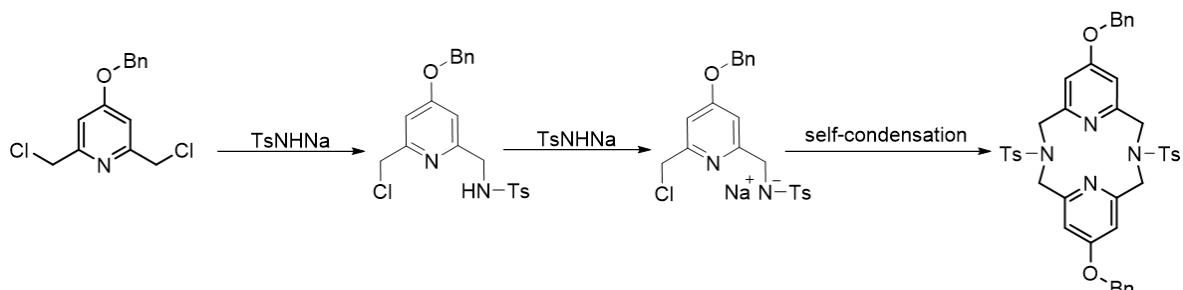
L1-L3 were synthesized using a variation of the Richman-Atkins synthesis in which traditional tosyl protecting groups are replaced with nosyl protecting groups followed by deprotection with thiophenol and subsequent acidification to obtain the ligands as hydrochloride salts.^{4, 48, 54-57, 59, 176-182} A slightly different variation of the Richman-Atkins synthesis was used to obtain **L4** in moderate to good yields. The

first step in the synthesis of **L4** involves the simultaneous formation of a cyclized and tosyl-protected tetraazamacrocycle (**2.14**) (Scheme 2.3). Following the cyclization step the ligand is deprotected and acidified to yield **L4** as a hydrochloride salt (Scheme 2.3).



Scheme 2.3. Synthetic methodology for the isolation of **L4**.

The cyclization of novel molecule **L4** is accomplished using a procedure originally published by Bottino *et al.* that describes the one-pot 1:1 condensation of tosylamide monosodium (TsNHNa) with a dihalide molecule to produce a symmetrical *N*-tosyl aza macrocycle.¹⁸³ Before the cyclization step, TsNHNa is generated by reacting *p*-toluenesulfonylamide (TsNH₂) with sodium ethoxide (NaOEt) in absolute ethanol.¹⁸³⁻¹⁸⁵ The electron-withdrawing tosyl protecting group in TsNH₂ serves two roles: (i) it enhances the acidity of the hydrogen atoms, and (ii) it protects the nitrogen atoms from substitution by electrophilic reagents.¹⁸³ Once the TsNHNa is generated, 2 equivalents are combined with the corresponding dihalide molecule in DMF under reflux conditions to produce the cyclized and tosyl-protected product (**2.14**).¹⁸³⁻¹⁸⁶ In the case of **L4**, the dihalide is the same one utilized in the synthesis of **L2**, (**2.7**). DMF is used as the solvent because it helps to minimize side reactions and oligomerization.¹⁸⁴ Additionally, the amount of TsNHNa used (2 equivalents) in the synthesis is crucial, because TsNHNa is acting as both the nitrogen source and as the base.¹⁸³⁻¹⁸⁴ This cyclization reaction can be visualized by proceeding through a monoalkylated-intermediate followed by self-condensation in the presence of excess TsNHNa, which acts as a base, to yield the desired macrocyclic product (Scheme 2.4).¹⁸⁴

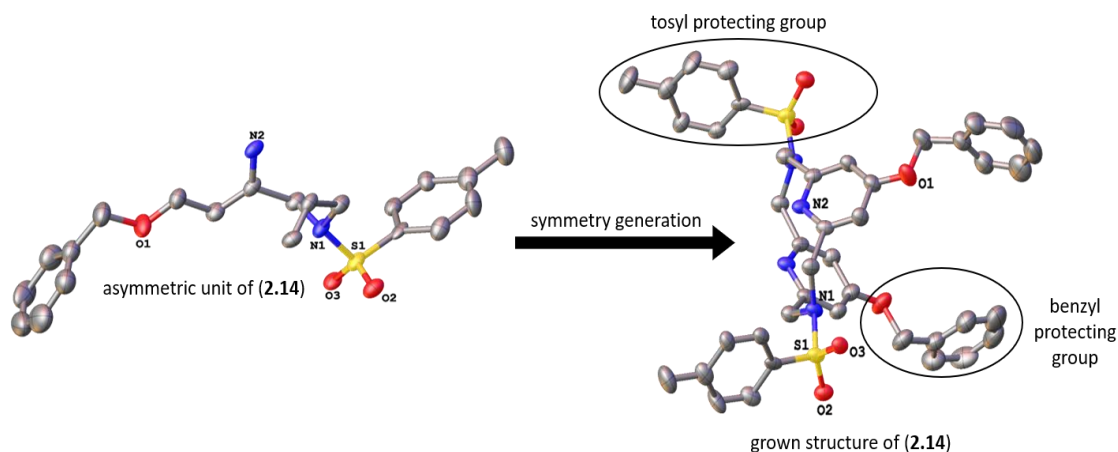


Scheme 2.4. Cyclization reaction with 2 equivalents of TsNHNa resulting in macrocycle formation.¹⁸⁴

The protected macrocycle (**2.14**) was characterized using X-ray crystallography. Crystallizations of the protected macrocycle were carried out in a DMF/CH₃OH mixture yielding X-ray quality crystals of (**2.14**), respectively. The solid state structure of (**2.14**) offered insights into its confirmation compared to other pyridinophanes.^{184-185, 187}

Table 2.1. Crystal data, intensity collections, and structure refinement parameters for (**2.14**).

Complex	(2.14)
Empirical formula	C ₂₁ H ₂₀ N ₂ O ₃ S
Formula weight	380.45
Temperature/K	99.97
Crystal system	Tetragonal
Space group	I4 ₁ /a
a/Å	21.742(2)
b/Å	21.742(2)
c/Å	16.3228(19)
α/°	90
β/°	90
γ/°	90
Volume/Å ³	7715.8(19)
Z	16
ρ _{calc} /cm ³	1.310
μ/mm ⁻¹	0.191
F(000)	3200.0
Radiation	MoKα (λ = 0.71073)
2θ range for data collection/°	6.15 to 55.136
Index ranges	-23 ≤ h ≤ 28, -28 ≤ k ≤ 27, -21 ≤ l ≤ 21
Reflections collected	54710
Independent reflections	4437 [R _{int} = 0.3703, R _{sigma} = 0.2501]
Data/restraints/parameters	4437/0/245
Goodness-of-fit on F ²	1.071
Final R indexes [I >= 2σ (I)]	R ₁ = 0.1263, wR ₂ = 0.1621
Final R indexes [all data]	R ₁ = 0.2975, wR ₂ = 0.2042
Largest diff. peak/hole / e Å ⁻³	0.40/-0.28



Scheme 2.5. Solid state structure of **(2.14)**; the asymmetric and grown structure are pictured above (hydrogen atoms have been omitted for clarity).

Off-white needle-like crystals of **(2.14)** suitable for X-ray analysis were obtained from solvent diffusion of DMF and CH₃OH. The asymmetric unit of **(2.14)** consists of half of the macrocyclic molecule; the remaining half of the macrocycle can be visualized by symmetry generation (Scheme 2.5). The resulting structure of **(2.14)** is derived from a tetragonal $I4_1/a$ system (Table 2.1). In the solid state **(2.14)** crystallizes in a *syn* chair-chair conformation where the tosyl-protected nitrogen atoms are oriented away/outward from the macrocyclic ring (Figure 2.6).^{184-185, 187} Three common conformations of macrocyclic pyridinophanes (and their corresponding metal complexes) have been observed in solution and in the solid state: *syn* chair-chair, *syn* boat-chair, and *syn* boat-boat (Figure 2.6).^{184-185, 187} The three conformers arise from the CH₂NCH₂ bridges flipping between the boat and chair conformations.¹⁸⁷ In solution there is a conformational equilibrium between the three conformers, but in the solid state one conformation is generally preferred.¹⁸⁷ The *syn* chair-chair conformation is the lowest energy conformer and has been observed for several other free/uncoordinated macrocyclic pyridinophane derivatives in the solid state, including **(2.14)**.^{184-185, 187} Additionally, this conformation is most likely adopted by the protected macrocycle **(2.14)** due to the steric bulk of the tosyl and benzyl protecting groups present within the molecule.

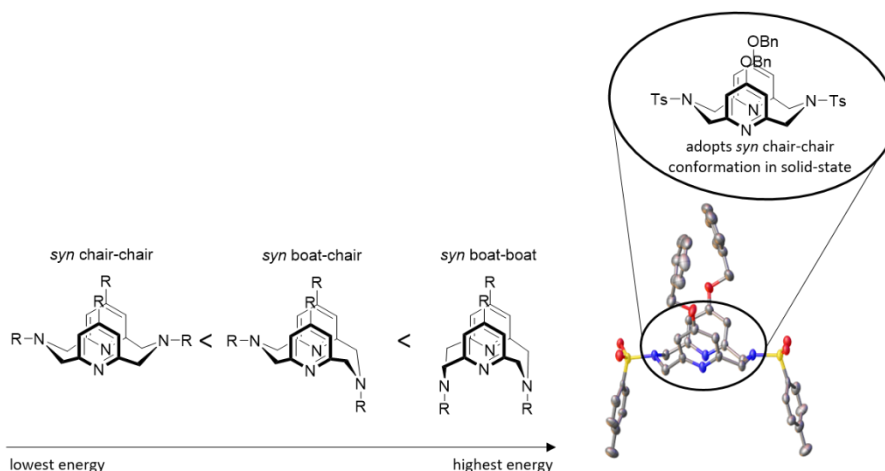


Figure 2.6. Common conformations of pyridinophanes and the solid state conformation of **(2.14)**.

The second step in the synthesis of **L4** involves the deprotection of **(2.14)**. For **L1-L3** precursors (**2.3**, **2.8**, and **2.12**; see Scheme 2.2) deprotection is performed in two separate steps. First, the nosyl groups are removed using KOH and thiophenol. After removal of the nosyl groups and acidification of the deprotected ligand, the benzyl group is removed using a palladium-catalyzed hydrogenation. This methodology works well for obtaining the hydrochloride salts of **L1-L3** in good yields. A slightly different route must be taken to deprotect **(2.14)** due to the presence of tosyl-protecting groups. The deprotection of both the benzyl and tosyl groups is accomplished in one-step by using a naphthalene-catalyzed lithiation (Scheme 2.4).^{176, 188} The lithium naphthalenide radical is generated by combining lithium metal and naphthalene in THF; upon agitation the dark green radical species is formed. **(2.14)** is added dropwise to the radical containing solution at $-78\text{ }^{\circ}\text{C}$ and stirred overnight. The reaction mixture is then hydrolyzed and followed by an acid work-up to isolate **L4** as the hydrochloride salt. Elemental analysis of the white solid indicates a composition of **L4**•3HCl•CH₃OH•H₂O (MW = 406.75).

2.4. Protonation and stability constants of **L4** with various divalent transition metals

2.4.1. An introduction to equilibrium constants

The equilibrium constant (K) for a chemical reaction is the reaction quotient related to the concentrations or activities of chemical species at equilibrium.¹⁸⁹ This constant can be defined as the ratio

of the product of the activities a for the reaction products (raised to the appropriate power), to the product of the activities of the reaction reactants (raised to the appropriate power).¹⁸⁹ Equation [2.3] shows how K is related to the reaction quotient; a , b , c , and d are stoichiometric coefficients of the solution species A, B, C, and D, respectively.¹⁸⁹



The equilibrium constant is directly related to the Gibbs free energies (ΔG°) of the products and reactants in their standard states through equation [1.1].¹⁸⁹ K is therefore a measure of the difference between the reactivities of the reactants vs. the products.¹⁸⁹

Determining the activities (a , shown in equation [2.3]) of complex ionic species is an intricate and time-consuming process, which is sometimes disregarded by scientists.¹⁸⁹ Many early determinations of equilibrium constants were filled with discrepancies due to inconsistencies in ionic strength.¹ A solution to this problem was discovered in 1905, when Grossman utilized a non-reacting electrolyte (KNO_3) to keep the ionic strength constant.¹⁸⁹⁻¹⁹⁰ However, the concept of maintaining constant ionic strength was not formally introduced until 1921 by Lewis *et al.*^{189,191} Since the formal introduction of constant ionic strength in 1921, it has become common practice to measure the equilibrium constants of various coordination compounds at constant ionic strength (maintained by a non-reactive supporting electrolyte) and temperature.¹⁸⁹ Concentrations parallel the activities of ionic solutes when the ionic strength is controlled by a non-reactive (spectator) electrolyte (such as NaCl or KNO_3) present in large excess compared to the ionic species under investigation. Therefore, at constant ionic strength the equilibrium constant can be expressed by equation [2.4].



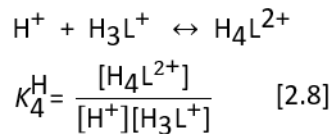
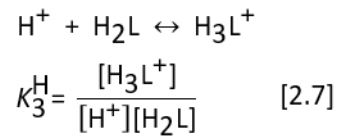
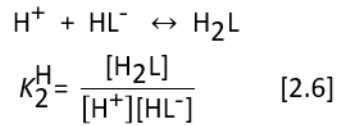
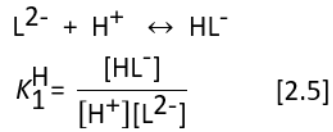
There are many different types of equilibrium constants, including: association constants, dissociation constants, stability constants, binding constants, formation constants, protonation constants, etc. Generally, for ligands and corresponding coordination complexes researchers are concerned with observing the protonation and complex formation equilibria.¹⁸⁹ The most commonly used expressions for reporting results of protonation and complex formation equilibria in the current literature are: stepwise protonation constants for the ligand and either overall metal complex formation constants (also known as stability constants) or stepwise formation constants for the coordination complex.¹⁸⁹ Stability constants of metal complex formation are often used to measure the affinity of a ligand for a metal ion (in solution).¹⁸⁹ In other words, these stability constants can serve as an indication for the success (or failure) of a ligand design.¹⁸⁹

2.4.2. Relevant equations for the expression of the protonation and stability constants of L4

The protonation and stability constants of **L4** (and related ligands) will be described in terms of Lewis acids (hydrogen ions and metal ions) and Lewis bases (ligands). Two different types of constants will be used to describe the protonation and complex formation equilibria, stepwise constants (K) and overall constants (β).¹⁸⁹ **L4** is represented as L in the following equilibrium expressions. In solution and in the absence of metal ions, **L4** can be modulated between five different species: H_4L^{2+} , H_3L^+ , H_2L , HL^- , and L^{2-} , based on pH. The five-different species are related by four successive stepwise protonation constants, which are represented by equations [2.5]-[2.8]. Additionally, the stepwise protonation constants (K^H) are related to the overall protonation constants (β) through equations [2.13]-[2.16], where the overall protonation constants are the cumulative product of the stepwise protonation constants in equations [2.9]-[2.12].

The complex formation equilibria can be expressed in a similar manner to the protonation equilibria. For the metal complexes that form with **L4** up to five different species are possible: ML , MHL^+ , MH_2L^{2+} , and MH_3L^{3+} (where M represents a divalent metal ion); although not all species listed above are

experimentally observed for each type of metal. The five-different species are related by four successive stepwise formation/protonation constants, which are represented by equations [2.17]-[2.20]. The stepwise formation/protonation constants (K^M and K^H) are related to the overall formation/protonation constants (β) through equations [2.25]-[2.28], where the overall formation/protonation constants are the cumulative product of the stepwise formation/protonation constants in equations [2.21]-[2.24]. It should be noted that some of the species appearing in equations [2.5]-[2.8] and [2.17]-[2.20] are not present (not formed) within the system over various pH ranges (or in the absence of a metal ion), but a complete set of equations [2.5]-[2.28] are necessary to describe the equilibria in the pH range where hydrogen ion concentrations are measured.¹⁸⁹ In addition to the species listed within the equations [2.5]-[2.28], there can also be H^+ , M^{2+} , and OH^- ions present within the solution.¹⁸⁹

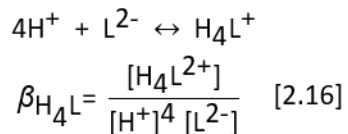
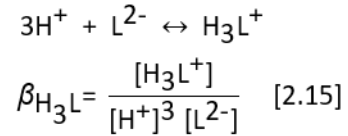
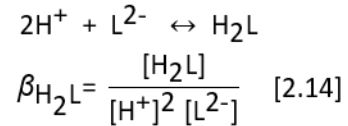
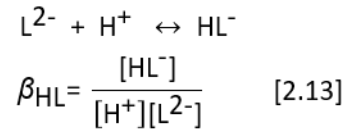


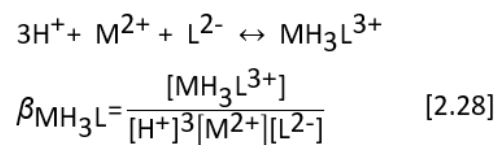
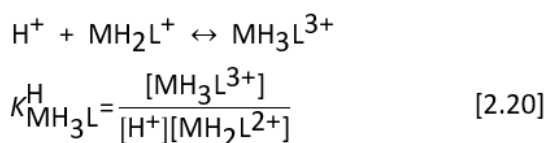
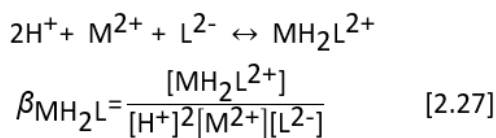
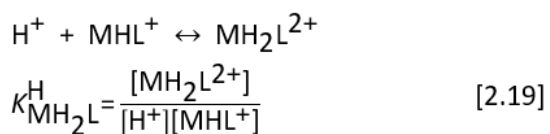
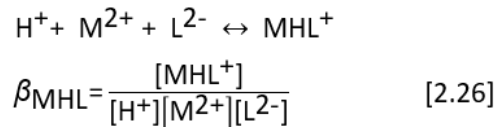
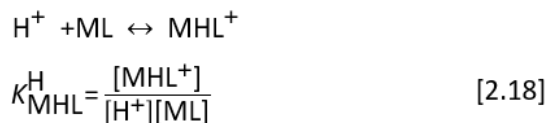
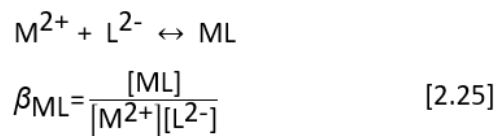
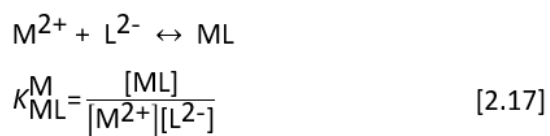
$$\beta_{HL} = K_1^H \quad [2.9]$$

$$\beta_{H_2L} = K_1^H K_2^H \quad [2.10]$$

$$\beta_{H_3L} = K_1^H K_2^H K_3^H \quad [2.11]$$

$$\beta_{H_4L} = K_1^H K_2^H K_3^H K_4^H \quad [2.12]$$





$$\beta_{ML} = K_{ML}^M \quad [2.21]$$

$$\beta_{MHL} = K_{ML}^M K_{MHL}^H \quad [2.22]$$

$$\beta_{MH_2L} = K_{ML}^M K_{MHL}^H K_{MH_2L}^H \quad [2.23]$$

$$\beta_{MH_3L} = K_{ML}^M K_{MHL}^H K_{MH_2L}^H K_{MH_3L}^H \quad [2.24]$$

2.4.3. Determination of protonation constants for L4

The step-wise protonation constants, $\log K_n^H$ ($n=1, 2, 3, \text{ or } 4$), of **L4** as defined in equations [2.5]-[2.8] were determined by pH-potentiometric titrations at constant ionic strength (I) and temperature ($I = 0.15 \text{ M NaCl}, 25 \text{ }^\circ\text{C}$) (Figure 2.7). The results are compiled in table 2.2 along with the protonation constants of **L1-L3** (previously determined by collaborator Gyula Tircs6)¹⁹² and other relevant ligands from literature (cyclen).¹⁹²⁻¹⁹³ **L1-L3** contain three secondary amines in the macrocyclic core and one tertiary amine in the pyridine/pyridol moieties. In contrast, **L4** contains two secondary amines in the macrocyclic core and two tertiary amines in the pyridol moieties. For **L1-L4** all the amines can undergo protonation equilibria. Furthermore, ligands **L2-L4** also contain hydroxyl groups (on the *para* or *meta* positions of the pyridine

ring) which can undergo protonation equilibria. The protonation constants of **L1-L3** were all previously determined by pH-potentiometric titrations (in collaboration with Gyula Tircsó), while the protonation constants for **L4** were only recently acquired. Determination of the protonation constants and speciation curves (**L4** only) for **L1-L4** gave insights into ligand structural differences and optimization of metal complexation conditions (i.e. which pH is optimum for metal complexation to occur).

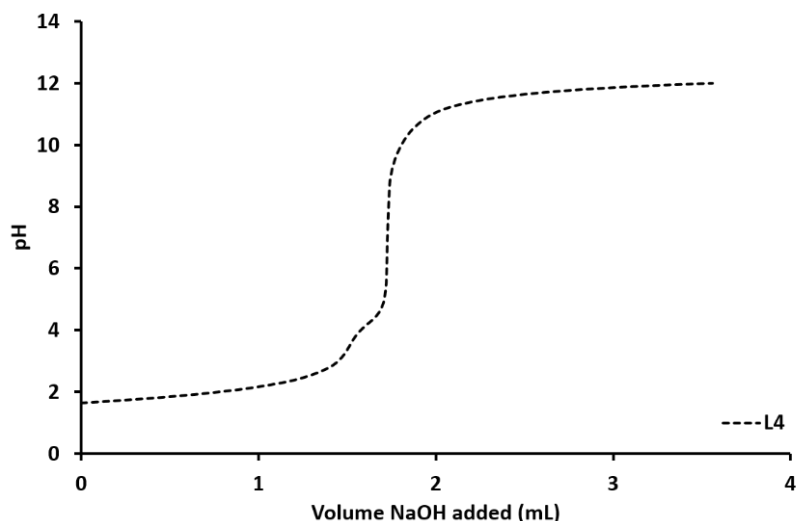


Figure 2.7. pH-potentiometric titration curve of a solution containing 1.897 mM of $H_4L_4^{2+}$ titrated with 99.78 mM NaOH ($I = 0.15$ M NaCl, $T = 25$ °C) over pH range 1.6 – 12.0. ($H_4L_4^{2+}$ represents fully protonated **L4**).

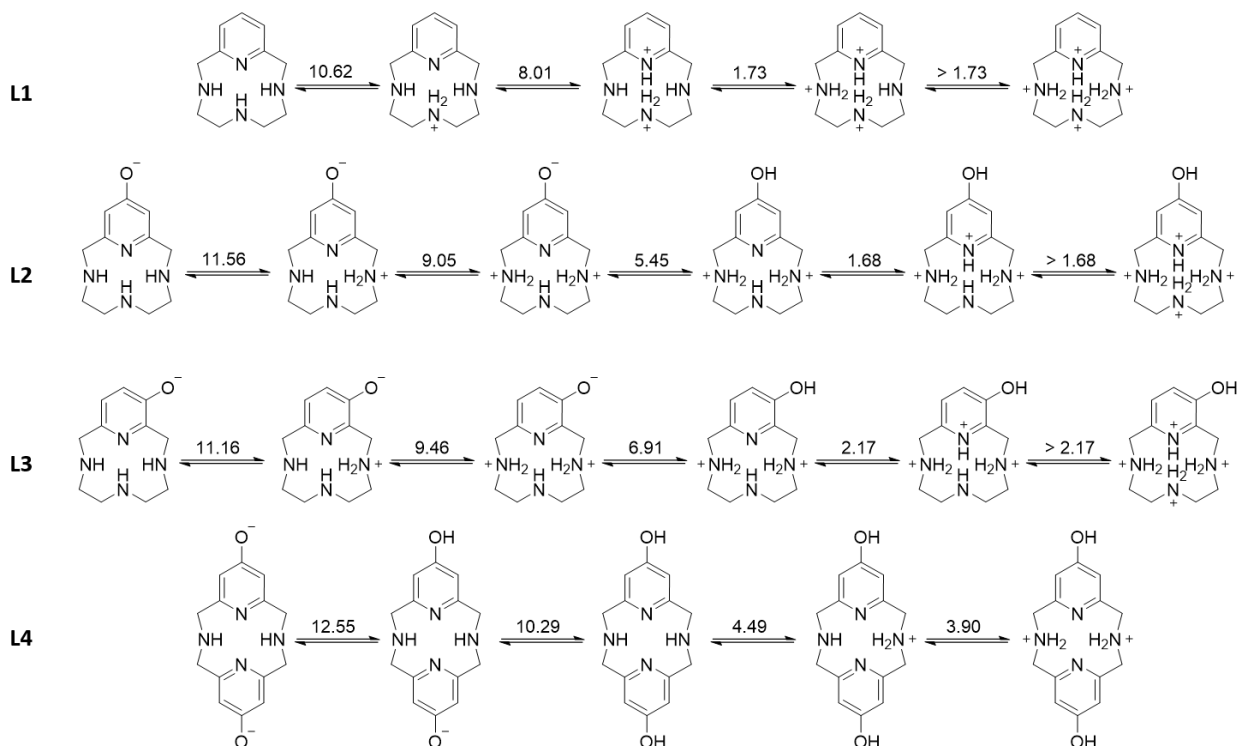
Table 2.2. Protonation constants (pK) of the species formed during titration of **L1**, **L2**, **L3**, **L4**, and **cyclen** ($I = 0.15$ M NaCl, $T = 25$ °C).

Ligand	$\log K_1^H$	$\log K_2^H$	$\log K_3^H$	$\log K_4^H$	$\sum \log K_{1-4}^H$
L1 ^a	10.62	8.01	1.73	x	20.36
L2 ^a	11.56(3) ^b	9.05(5)	5.45(6)	1.68(5)	27.79 (16.18)
L3 ^a	11.16(1) ^b	9.46(2)	6.91(2)	2.17(3)	29.70
L4	12.46(2) ^b	10.28(3) ^b	4.49(6)	3.90(4)	31.13
Cyclen ^c	10.66	9.69	1.73	0.94	21.76
Pyridine	5.2	x	x	x	x
Pyridol	11.2	3.2	x	x	x

(a) from ref. ¹⁹²; (b) assigned to the deprotonation of the phenolic OH; (c) ¹⁹⁴ = 0.15 M NaClO₄ from ref. ¹⁹³; (x) species not observed.

Three protonation constants ($\log K^H$) were determined for **L1** at 10.62, 8.01, and 1.73; which are assigned to the protonations of one secondary amine within the macrocyclic ring (*trans* to the pyridine ring) followed by the protonation of the nitrogen atom within the pyridine ring and then the other

secondary amine (*cis* to the pyridine ring) (Scheme 2.6).¹⁹² The last protonation constant for **L1** was lower than the experimental limit (at > 1.73).¹⁹² Four protonation constants were measured for **L2-L4** (Scheme 2.6). With the addition of each pyridol moiety (one pyridol moiety for **L2** and **L3**; two pyridol moieties for **L4**) the ligands exhibited a marked increase in the values measured for $\log K_1^H$ and $\log K_2^H$ compared to **L1**.¹⁹² This indicates that the presence of a hydroxyl group on the pyridine ring increases the basicity of the ligands. An increase in ligand basicity can be used to predict the formation of thermodynamically stable metal-complexes.¹⁹⁴ **L4** is the most basic ligand due to the presence of two hydroxyl groups, followed by **L2**, then **L3**. For **L2** and **L3** the third protonation event is assigned as the protonation of the oxygen atom on the pyridol ring (Scheme 2.5).¹⁹² In contrast, the first and second protonation event for **L4** are tentatively assigned as the protonation of the oxygen atoms on both pyridol rings (Scheme 2.6).¹⁸⁹ Although, more titration data is necessary to make concrete protonation assignments for **L4**.



Scheme 2.6. Protonation events for ligands **L1-L4** based on pH-potentiometric titrations.¹⁹²

Finally, a species distribution diagram was generated, by co-worker Kristóf Póta, for **L4** (Figure 2.8, where $L_4 = \mathbf{L4}$). Species distribution diagrams are a good tool for visualizing species present in solution and their concentrations as a function of pH.¹⁸⁹ As the pH is varied from 0 – 14 the solution components change from majority $H_4L_4^{2+}$ (at pH = 0 – 3), to $H_3L_4^+$ (at pH = 4), to H_2L_4 (at pH = 5 – 9), to HL_4^- (at pH = 10 – 12), and finally L_4^{2-} (at pH = 13 – 14) (Figure 2.8).

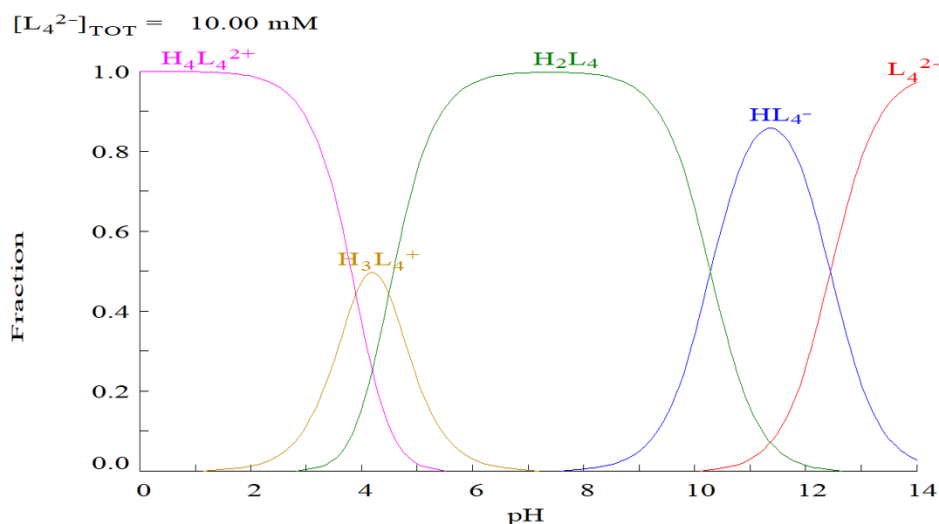


Figure 2.8. Species distribution diagram for 10.00 mM **L4** at $I = 0.15 \text{ M NaCl}$ and $25.0 \text{ }^\circ\text{C}$.

2.4.4. Determination of formation (stability) constants for **L4**

As previously stated, the applications of tetraaza macrocyclic ligands and their corresponding metal complexes is broad, from catalysis, to diagnostics and therapeutics. To assess the thermodynamic stability and applicability of **L1-L4**, the metal binding constants were determined for biologically and/or catalytically relevant metal ions including: Mg(II), Ca(II), Mn(II), Ni(II), Cu(II), and Zn(II).¹⁹² The results of these studies, shown in table 2.3, indicate that metal ion preference is modulated by the presence and position of the hydroxyl moiety on the pyridine ring of the macrocycle.¹⁹² The stability constants of **L1-L3** were all previously determined by pH-potentiometric titrations¹⁹², while the stability constants for **L4** were recently acquired (pH-potentiometric titration of **L4** in the presence of Zn(II) is shown in figure 2.9).

Table 2.3. Overall stability constants ($\log \beta$) of M(II) ligand complexes $I = 0.15$ M NaCl and $T = 25$ °C.

Metal ion	Equation*	Cyclen	L1	L2	L3	L4
Mg(II)	$\beta_{ML} = [ML]/[M][L]$	2.25 ^a	–	4.96(1)	5.17 (1)	–
	$\beta_{MHL} = [MHL]/[M][L][H^+]$	–	–	13.53(2) (1.97)	13.18(2)	–
Ca(II)	$\beta_{ML} = [ML]/[M][L]$	3.12 ^b	–	4.17(3)	4.46(1)	4.81(5)
	$\beta_{MHL} = [MHL]/[M][L][H^+]$	–	–	13.66(5) (2.10)	12.99(2)	15.56(10) (3.10)
Mn(II)	$\beta_{ML} = [ML]/[M][L]$	–	8.81	10.96(4)	10.14(4)	12.98(9)
	$\beta_{MHL} = [MHL]/[M][L][H^+]$	–	–	17.36(7) (5.80)	17.33(4)	20.54(10) (8.08)
	$\beta_{MH_2L} = [MH_2L]/[M][L][H^+]^2$	–	–	x	x	27.30(7)
	$\beta_{MH_3L} = [MH_3L]/[M][L][H^+]^3$	–	–	x	x	31.76(3)
	$\beta_{ML(OH)} = [ML]/[M][L][OH^-]$	–	–	0.78(6)	-0.83(4)	2.60(10)
	$\beta_{ML_2} = [ML_2]/[M][L]^2$	–	–	15.70(15) ^h	x	x
Co(II)	$\beta_{ML} = [ML]/[M][L]$	–	–	–	–	18.01(8)
	$\beta_{MHL} = [MHL]/[M][L][H^+]$	–	–	–	–	24.65(8) (12.19)
	$\beta_{MH_2L} = [MH_2L]/[M][L][H^+]^2$	–	–	–	–	30.05(2)
	$\beta_{MH_3L} = [MH_3L]/[M][L][H^+]^3$	–	–	–	–	31.89(11)
	$\beta_{ML(OH)} = [ML]/[M][L][OH^-]$	–	–	–	–	6.82(9)
Ni(II)	$\beta_{ML} = [ML]/[M][L]$	16.4 ^c	17.05	10.41(4)	10.98(4)	‡
	$\beta_{MHL} = [MHL]/[M][L][H^+]$	–	–	17.72(4) (6.16)	18.14(2)	‡
	$\beta_{MH_2L} = [MH_2L]/[M][L][H^+]^2$	–	–	23.75(7)	24.25(10)	‡
	$\beta_{ML(OH)} = [ML]/[M][L][OH^-]$	–	–	-1.83(5)	-1.06(5)	‡
	$\beta_{ML_2} = [ML_2]/[M][L]^2$	–	–	13.32(11) ^h	–	‡
Cu(II)	$\beta_{ML} = [ML]/[M][L]$	23.3 ^d	20.14 ^e	19.16(11)	22.66(4)	‡
	$\beta_{MHL} = [MHL]/[M][L][H^+]$	–	x	25.79(3) (14.34)	29.04(4)	‡
	$\beta_{MH_2L} = [MH_2L]/[M][L][H^+]^2$	–	x	28.38(5) ^f	30.53(5) ^f	‡
	$\beta_{ML(OH)} = [ML]/[M][L][OH^-]$	–	7.48 ^e	8.55(13)	12.67(4)	‡
Zn(II)	$\beta_{ML} = [ML]/[M][L]$	16.2 ^g	14.40	17.18(7)	16.83(6)	16.34(4)
	$\beta_{MHL} = [MHL]/[M][L][H^+]$	–	x	23.02(3) (11.46)	23.82(3)	23.61(4) (11.15)
	$\beta_{MH_2L} = [MH_2L]/[M][L][H^+]^2$	–	x	25.72(7)	27.04 (5)	29.67(1)
	$\beta_{MH_3L} = [MH_3L]/[M][L][H^+]^3$	–	x	x	x	32.21(3)
	$\beta_{ML(OH)} = [ML]/[M][L][OH^-]$	–	8.50	8.92(9)	7.99(7)	x

(*) all values in table reported as $\log \beta$ (a) from ref. ¹⁹⁵; (b) from ref. ¹⁹⁶; (c) from ref. ¹⁹⁷; (d) from ref. ¹⁹⁸; (e) determined using competition titration; (f) determined using direct UV-vis titration; (g) from ref. ¹⁹⁹; (h) the titration data for these systems indicate formation of $[ML_2]$ type complexes at high pH when the ligand is present in excess; (–) species not measured; (x) species not observed; (‡) species could not be measured accurately using pH-potentiometric techniques.

Potentiometric titrations were used to measure the formation (stability) constants of **L2-L4** with alkaline earth metals Mg(II) and Ca(II) (Table 2.3). The formation constants ($\log \beta_{ML}$) for Ca(II), were determined to be 4.17(3) for **L2**, 4.46(1) for **L3**, and 4.81(5) for **L4**.¹⁹² For all three ligands (**L2-L4**) the formation constants for Ca(II) were largely increased from cyclen ($\log \beta_{ML} = 3.12$).^{192, 196} The increase in formation constants is consistent with an increase in ligand rigidity; **L2** and **L3** both contain one pyridol moiety, while **L4** contains two pyridol moieties and has the highest formation constant.

Formation constants were also determined with several catalytically and biologically relevant transition metals: Mn(II), Co(II), Ni(II), Cu(II), and Zn(II) (Table 2.3). Complexation with **L1-L4** was observed for all transition metals tested, lending validity to the ligand design for use as metal chelating neurotherapeutic agents. Table 2.3 provides a full comparison of formation (stability) constants determined for **L2-L4** as well as values reported in the literature for **L1** and cyclen. When comparing the formation constants between each ligand some general trends were observed and will be discussed in the following paragraph.

For **L2** and **L3**, the formation constants observed with several different metals are different between the two ligands; this supports previous studies indicating that the position of the hydroxyl moiety on the pyridine ring provides differences to the donor character of each ligand (*meta*- vs. *para*-hydroxy). Additionally, the formation constants of both **L2** and **L3** with different transition metals are observed to follow the Irving-Williams series (Table 2.3). The Irving-Williams series refers to the relative stabilities of complexes formed with divalent first-row transition metal ions.²⁰⁰ In this series the stabilities of transition metal complexes generally increases across the period to a maximum stability at copper: Mn(II) < Fe(II) < Co(II) < Ni(II) < Cu(II) > Zn(II).²⁰⁰ The formation constants of **L2** and **L3** with Mn(II), Ni(II), Cu(II), and Zn(II) are observed to generally follow the trend discussed above; the largest formation constant is Cu(II), followed by Zn(II), Ni(II), and finally Mn(II) (Table 2.3) (the order of Mn(II) and Ni(II) are flipped for **L2**). Finally, **L4** was complexed with the transition metals: Co(II), Mn(II), and Zn(II) (Table 2.3). The formation

constants were largest for Co(II) followed by Zn(II), then Mn(II). The order of these stability constants may offer insight to the size of the macrocyclic cavity of **L4**. Since the formation constant with Co(II) was largest it can be hypothesized that this metal ion has the best fit within the macrocyclic cavity. Most importantly though, stable transition metal complexes are formed with **L4** in aqueous solutions. This is particularly encouraging for Zn(II), which is involved in the pathogenesis of AD. The pH-potentiometric titration curve of **L4** in the presence of Zn(II) ions is shown below in figure 2.8.

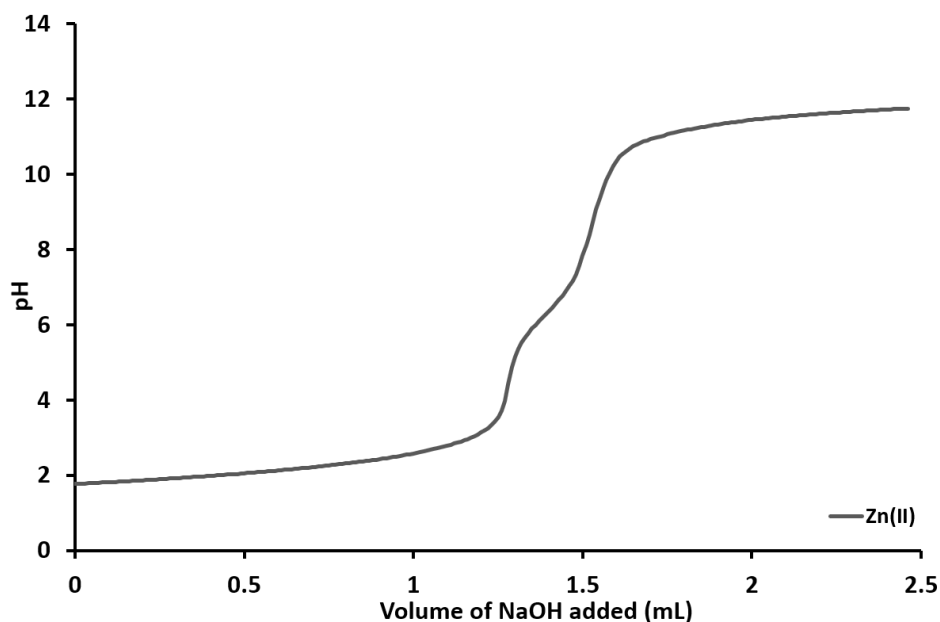


Figure 2.9. pH-potentiometric titration curve of a solution containing 2.041 mM $H_4L_4^{2+}$ in the presence of 1.975 mM Zn(II) ($I = 0.15$ M NaCl, $T = 25$ °C); titrated with a 0.09978 M standardized NaOH solution.

Finally, a species distribution diagram was generated, by co-worker Kristóf Póta, for the pH-potentiometric titration of **L4** (where $L_4 = \mathbf{L4}$) in the presence of Zn(II) (Figure 2.10). As the pH is varied from 0 – 14 the solution components change from a majority of uncomplexed Zn(II) (at pH = 1), to $ZnH_3L_4^{3+}$ (at pH = 1.5 – 2.5), to $ZnH_2L_4^{2+}$ (at pH = 3 – 6), to $ZnHL_4^+$ (at pH = 6.5 – 7), and finally ZnL_4 (at pH = 7 – 9).

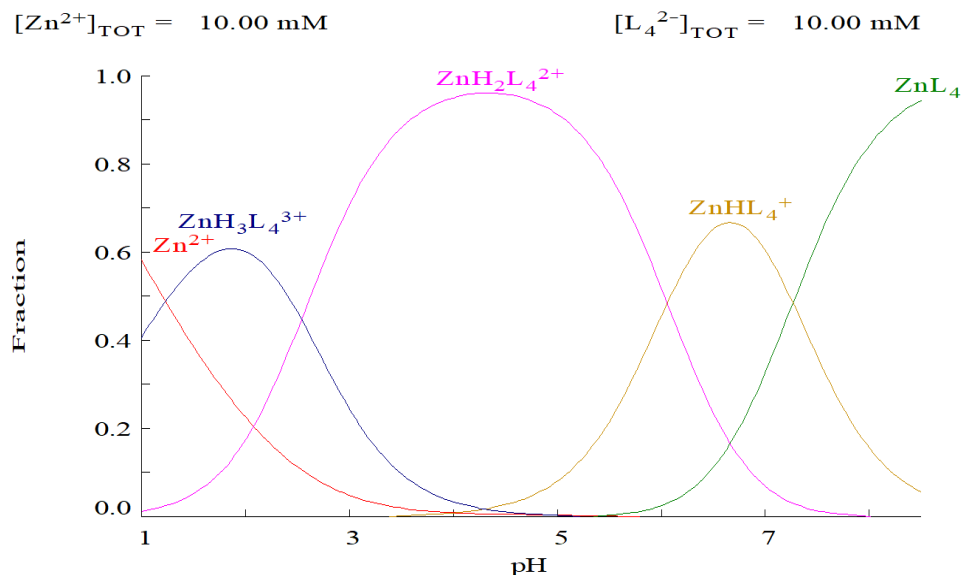


Figure 2.10. Species distribution diagram for 10.00 mM Zn(II) and 10.00 mM **L4** at $I = 0.15 \text{ M NaCl}$ and $25.0 \text{ }^\circ\text{C}$.

2.5. L4 complexes with biologically relevant transition metals, Cu(II) and Zn(II)

2.5.1. Complexation of L4 with Cu(II) and Zn(II)

After performing pH-potentiometric titrations determine to the protonation and stability constants **L4** was complexed with two biologically relevant metals, Cu(II) and Zn(II). As discussed earlier, there are three common conformations of macrocyclic pyridinophanes (like **L4**) observed in solution and in the solid state: *syn* chair-chair, *syn* boat-chair, and *syn* boat-boat (Figure 2.6); although, there is a conformational equilibrium between all three forms in solution^{184-185, 187} The lone pairs on each of the nitrogen atoms are oriented very differently in each conformer (Figure 2.11).^{185, 187, 201} For example, in the *syn* chair-chair conformation two of the four nitrogen lone pairs are oriented away from the macrocyclic cavity (Figure 2.10). Contrastingly, in the *syn* boat-boat conformation all four of the nitrogen lone pairs are oriented toward the macrocyclic cavity. When complexation with a metal ion occurs, this conformer is adopted, because all the nitrogen atom lone pairs are oriented in the same direction toward the macrocyclic cavity. The resulting metal complex also adopts a *syn* boat-boat conformation, as shown in figure 2.11.¹⁸⁵

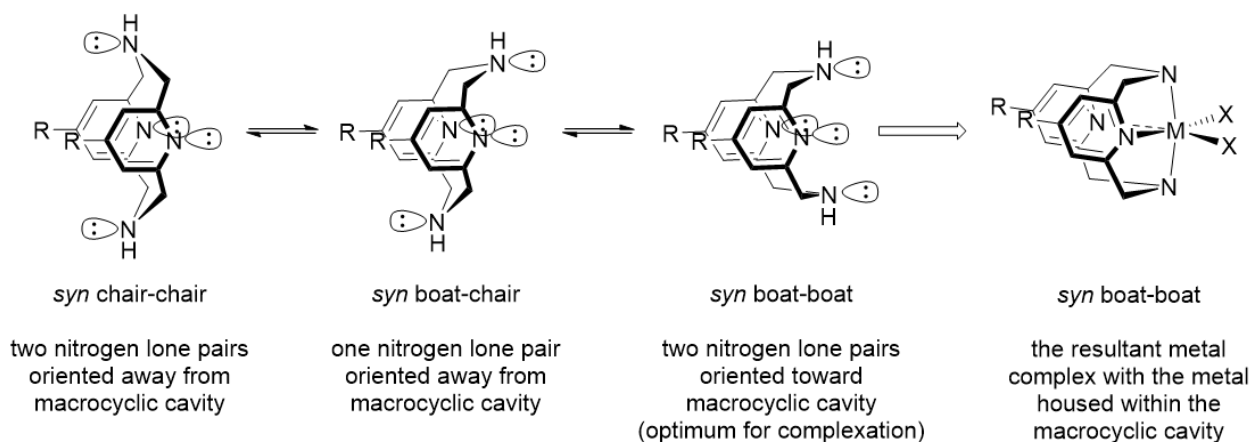
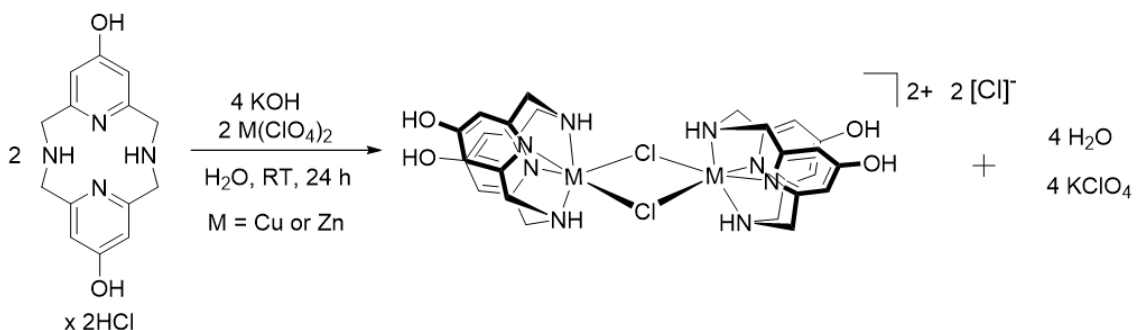


Figure 2.11. Orientations of nitrogen atom lone pairs in common pyridinophane conformers and example of metal-ligand complex in the *syn boat-boat* orientation (for **L4**, R = OH and X = Cl).^{184-185, 201}

Complexation reactions of **L4** with Cu(II) and Zn(II) were performed in water using methodology previously reported by the Green group (Scheme 2.7).⁵⁶ The first step in the complexation reaction is to dissolve the ligand in a small amount of water and adjust the pH to around 6 -7. **L4** is isolated as the hydrochloride salt and upon dissolution the major species present is fully protonated ($H_4L_4^{2+}$); therefore, the pH must be adjusted to deprotonate the nitrogen atoms, so they can bind to a metal ion. As shown in the distribution diagram of **L4** (Figure 2.8), the major species present in solution between the pH of 6 and 7 is the neutral doubly deprotonated species H_2L_4 , which is ideal for complexation. After the pH adjustment, one equivalent of the corresponding metal perchlorate salt ($Zn(ClO_4)_2$ or $Cu(ClO_4)_2$) was added dropwise to the ligand solution. Upon addition of the Cu(II) salt the solution color changed from pale yellow to light blue. In contrast, no color change occurred upon the addition of the Zn(II) salt. These solutions stirred for several hours to ensure complete complexation. After filtration and drying, the crude solids were dissolved in a minimal amount of CH_3OH . Water was added to the CH_3OH solution until only salts were left undissolved; these solutions were then filtered and set out for crystallizations via slow evaporation. After several days more salts precipitated out of solution, these were subsequently removed by filtration and the solutions were set out for slow evaporation crystallization again. After several cycles of filtering the solution and setting it out for slow evaporation, X-ray quality crystals of both the Cu(II) and

Zn(II) ligand complex developed. The metal complexes exist as dimeric species in the solid state; $[\mathbf{L4Cu}^{\text{II}}\text{Cl}]_2[\text{Cl}]_2$ (**L4Cu**) exists as a light-green block-like crystalline species and $[\mathbf{L4Zn}^{\text{II}}\text{Cl}]_2[\text{Cl}]_2$ (**L4Zn**) exists as a light-yellow block-like crystalline species. Both **L4Cu** and **L4Zn** were confirmed using mass spectrometry and X-ray diffraction. Additionally, the crystalline material of **L4Cu** was characterized using UV-visible spectroscopy and cyclic voltammetry and the crystalline material of **L4Zn** was characterized using ^1H NMR.



Scheme 2.7. Complexation reaction of **L4** with Cu(II) and Zn(II).

2.5.2. Solid state structures of **L4Cu** and **L4Zn**

Light-green crystals of **L4Cu** and light-yellow crystals of **L4Zn** were evaluated using X-ray diffraction and the data provided resulted in the structures shown in figure 2.12. The solid state structures of both **L4Cu** and **L4Zn** are structurally analogous, despite the difference in metal centers. In each complex, two separate **L4** molecules are bound to two metal ions (either Cu(II) or Zn(II)) in a *cis*-fashion, each with two pyridol-based nitrogen atoms bound in the equatorial plane and two nitrogen atoms bound in the axial plane. The coordination environment is completed by two bridging chloride ions ($\mu\text{-Cl}_2$) bound in a *cis*-fashion, which connect the two-separate metal-bound **L4** complexes (Figure 2.12). Each dimeric complex contains two 5-5-5 ring structures (for each metal-bound **L4**); this is a typical coordination environment adopted by 12-membered tetraaza macrocyclic complexes. Both **L4Cu** and **L4Zn** were modeled in the monoclinic $P2_1/c$ space group (Table 2.4). Interestingly, the asymmetric unit of each

complex contains only one half of the dimeric structure; therefore, the second half of the dimeric complexes are symmetry generated (Figure 2.12).

Table 2.4. Crystal data, intensity collections, and structure refinement parameters for **L4Cu** and **L4Zn**.

Complex	L4Cu	L4Zn
Simplified formula	[L4Cu ^{II} Cl] ₂ [Cl] ₂ •2CH ₃ OH	[L4Zn ^{II} Cl] ₂ [Cl] ₂ •2CH ₃ OH
Empirical formula	C ₁₅ H ₂₀ Cl ₂ CuN ₄ O ₃	C ₁₅ H ₂₀ Cl ₂ ZnN ₄ O ₃
Formula weight	438.79	440.62
Temperature/K	293.15	293.15
Crystal system	Monoclinic	Monoclinic
Space group	P2 ₁ /c	P2 ₁ /c
a/Å	11.375(7)	11.346(5)
b/Å	12.294(7)	12.280(5)
c/Å	12.815(8)	13.065(5)
α/°	90	90
β/°	90.49(2)	92.509(13)
γ/°	90	90
Volume/Å ³	1792.2(18)	1818.6(12)
Z	4	4
ρ _{calc} /g/cm ³	1.626	1.609
μ/mm ⁻¹	1.539	1.667
F(000)	900.0	904.0
Crystal size/mm ³	0.279 × 0.160 × 0.126	0.469 × 0.244 × 0.176
Radiation	MoKα (λ = 0.71076)	MoKα (λ = 0.71076)
2θ range for data collection/°	5.808 to 60.268	5.886 to 60.198
Index ranges	-15 ≤ h ≤ 16 -17 ≤ k ≤ 17 -18 ≤ l ≤ 18	-15 ≤ h ≤ 16 -17 ≤ k ≤ 17 -18 ≤ l ≤ 18
Reflections collected	45954	45536
Independent reflections	5217 [R _{int} = 0.0499, R _{sigma} = 0.0350]	5341 [R _{int} = 0.0285, R _{sigma} = 0.0173]
Data/restraints/parameters	5217/0/236	5341/0/230
Goodness-of-fit on F ²	1.169	1.096
Final R indexes [I ≥ 2σ (I)]	R ₁ = 0.0517, wR ₂ = 0.0891	R ₁ = 0.0259, wR ₂ = 0.0511
Final R indexes [all data]	R ₁ = 0.0656, wR ₂ = 0.0944	R ₁ = 0.0307, wR ₂ = 0.0530
Largest diff. peak/hole / e Å ⁻³	0.62/-0.56	0.46/-0.29

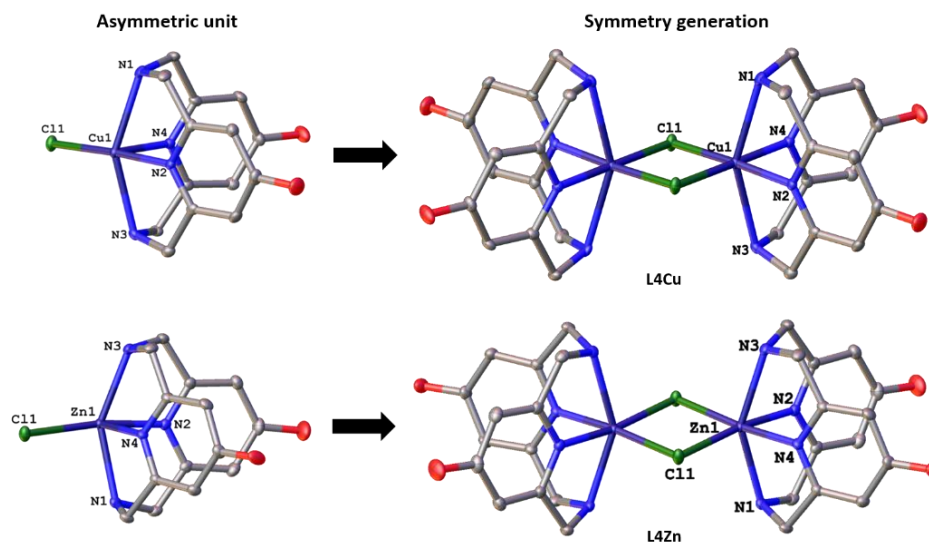


Figure 2.12. Asymmetric units and symmetry generated solid state structures of **L4Cu** and **L4Zn**.

The solid state structures of **L4Cu** and **L4Zn** were compared with the solid state structures of related tetraazamacrocyclic complexes previously published by the Green group (**L1Cu**, **L2Cu**, **L3Cu**, **L1Zn**, **L2Zn**, and **L3Zn**) (Figure 2.13).⁵⁶ Upon comparison of this series of pyridine and pyridol-based tetraazamacrocyclic metal complexes, some interesting similarities and differences were observed. The most obvious difference between **L1-L3Cu/L1-L3Zn** and **L4Cu/L4Zn** is that both **L4Cu** and **L4Zn** crystallize as dimeric structures in the solid state, while **L1-L3Cu** and **L1-L3Zn** are monomeric in the solid state (Figure 2.13). Additionally, **L1-L3Cu/L1-L3Zn** all contain 5-coordinate metal centers, whereas **L4Cu** and **L4Zn** both contain 6-coordinate metal centers. It is hypothesized that the different coordination geometries associated with **L1-L3Cu/L1-L3Zn** vs. **L4Cu/L4Zn** are related to the completely symmetric nature of **L4** and its corresponding metal complexes. **L4Cu/L4Zn** crystallize and pack differently than the metal complexes of **L1-L3**, presumably because they are more symmetric than **L1-L3Cu/L1-L3Zn**. For instance, metal complexes with **L4** are symmetric with respect to the axial and equatorial planes, whereas metal complexes with **L1-L3** are only symmetric with respect to the equatorial plane.

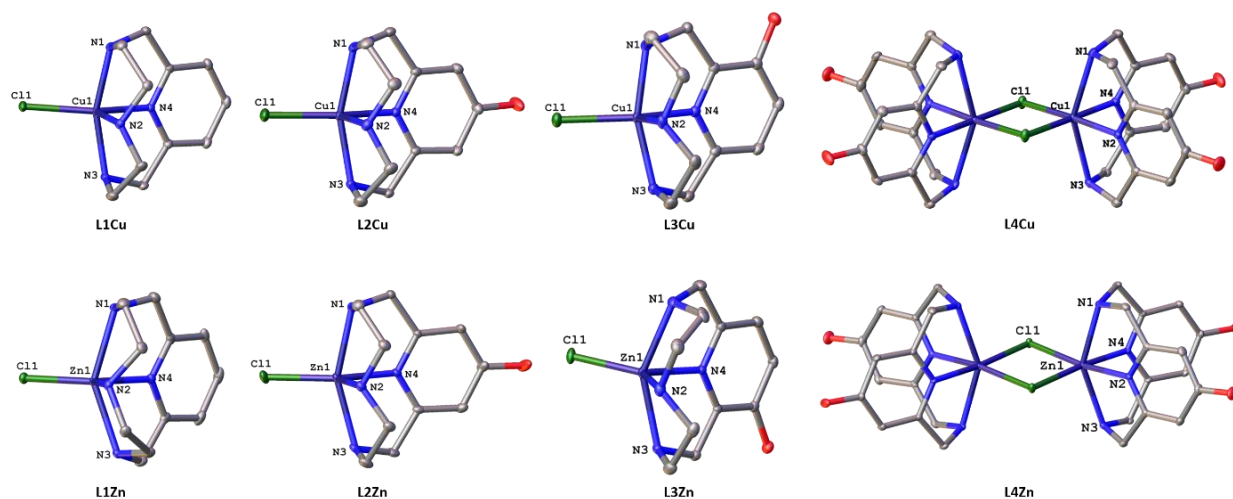


Figure 2.13. Solid state structure of **L1-L4Cu** and **L1-L4Zn** (Hydrogen atoms have been omitted for clarity).⁵⁵⁻⁵⁶ (CCDC #s **L1Cu**: 101808; **L2Cu**: 950045; **L3Cu**: 911993; **L1Zn**: 628572; **L2Zn**: 950047; **L3Zn**: 947495)

Additional comparisons can be made between the bond lengths and angles of **L1-L3Cu/L1-L3Zn** vs. **L4Cu/L4Zn** (Tables 2.5, 2.6). Most of the bond lengths for complexes **L1-L4Cu/L1-L4Zn** follow the expected periodic trends, increasing from Cu(II) and Zn(II). It is interesting to note that M-N bonds between the pyridine or pyridol nitrogen atom and the metal center (M(1)-N(4) for **L1-L4** and additional M(1)-N(2) bond for **L4**) are the shortest M-N bonds within the complexes. This is due to the additional electron density from the pyridine or pyridol ring stabilizing the bonding interactions, thus shortening those bond distances. Additionally, a very pronounced difference between the axial and equatorial M-N bond lengths is observed for both **L4Cu** and **L4Zn**. In both complexes the M(1)-N_{ax}(1)/M(1)-N_{ax}(3) bond lengths are significantly longer (by 0.16 to 0.30 Å) than the corresponding M(1)-N_{eq}(2)/M(1)-N_{eq}(4). The difference can be explained once again by the placement of the two pyridol rings. Both equatorial nitrogen atoms (N(2) and N(4)) are part of the pyridol ring systems. The additional electron density provided by the pyridol ring stabilizes the bonding interactions between the metal and nitrogen atom and these bonds are significantly shorter than the corresponding axial M-N bonds. Moreover, in **L4Cu** the differences between the M-N_{ax} and M-N_{eq} bond distances is even more pronounced due to Jahn-Teller distortion. Cu(II) is a d⁹ ion and in an octahedral complex the two degenerate e_g orbitals are unequally occupied by three electrons, leading to a doubly degenerate electronic ground state. Jahn-Teller distortions arise due to the degenerate e_g orbitals being unequally occupied by electrons. Often complexes distort along the z-axis (oriented along M(1)-N(1) and M(1)-N(3) in complex **L4Cu**), which removes electronic degeneracies and lowers the overall energy of the complex. The physical manifestation of the Jahn-Teller effect is the lengthening of axial bond distances vs. equatorial bond distances. Therefore, the lengthening of bond M-N_{ax} bond distances within complex **L4Cu** is enhanced compared to **L4Zn** because of Jahn-Teller distortion experienced by the Cu(II) d⁹ metal ion.

Table 2.5. Selected bond lengths (Å) for **L1-L4Cu** and **L1-L4Zn**

Selected Bond Lengths (Å)	L1Cu	L2Cu	L3Cu	L4Cu	L1Zn	L2Zn	L3Zn	L4Zn
M(1)-N(1)	2.068(9)	2.082(16)	2.060(2)	2.313(3)	2.245(2)	2.207(17)	2.214(5)	2.2407(13)
M(1)-N(2)	2.151(9)	2.173(19)	2.137(2)	2.007(3)	2.048(1)	2.087(19)	2.060(5)	2.0899(14)
M(1)-N(3)	2.079(9)	2.079(16)	2.063(2)	2.309(3)	2.212(2)	2.209(19)	2.226(5)	2.2520(14)
M(1)-N(4)	1.956(8)	1.939(16)	1.952(2)	2.010(2)	2.055(2)	2.041(17)	2.059(4)	2.0866(13)
M(1)-Cl(1)	2.247(4)	2.226(9)	2.264(7)	2.3152(14)	2.245(6)	2.214(6)	2.234(5)	2.4022(8)
M(1)-Cl(1) ^{1,2}	-	-	-	2.3347(12)	-	-	-	2.4258(8)

(1) for Cu(II) : -X, 1-Y, 2-Z; (2) for Zn(II) : 1-X, +Y, +Z

Finally, after observing selected bond angles within complexes **L1-L4Cu** and **L1-L4Zn** several more comparisons can be made. As discussed previously, the metal complexes of **L1-L3** have a different geometry than those made with **L4**. **L1-L3Cu/L1-L3-Zn** are all 5-coordinate with respect to the metal center, while **L4Cu/L4Zn** are 6-coordinate octahedral complexes. Obviously, the change in coordinate geometry results in differences between bond angles; most notably the equatorial bond angles: N(2)-M(1)-Cl(1), N(4)-M(1)-Cl(1), and N(4)-M(1)-N(2) (Table 2.6). In complexes **L4Cu/L4Zn** these equatorial bond angles have little deviation from octahedral geometry (180° and 90°), whereas in complexes **L1-L3Cu/L1-L3Zn** these angles align more to trigonal bipyramidal/square pyramidal geometries (120° and 90°) (Table 2.6). Another interesting observation can be made about the bond angles with respect to the different metal centers present within the complexes and is most easily observed when looking at the N(1)-M(1)-N(3) bond angles. In complexes **L1-L4Cu** the N(1)-M(1)-N(3) bond angles are all slightly larger (2.24-14.07° larger) than the same angle in the corresponding **L1-L4Zn** complexes. The difference in bond angles agrees with periodic trends, with metal ion size increasing from Cu(II) to Zn(II). In **L1-L4Zn** the larger Zn(II) ions sits farther outside the macrocyclic cavity than the corresponding Cu(II) complexes **L1-L4Cu**.

Table 2.6. Selected bond angles (°) for **L1-L4Cu** and **L1-L4Zn**

Selected Bond angles (°)	L1Cu	L2Cu	L3Cu	L4Cu	L1Zn	L2Zn	L3Zn	L4Zn
N(1)-M(1)-Cl(1)	102.94(3)	100.69(5)	98.95(7)	105.04(7)	104.27(5)	101.96(5)	104.34(9)	94.78(4)
N(2)-M(1)-Cl(1)	112.51(3)	106.94(5)	108.93(7)	176.23(7)	126.80(5)	119.04(5)	128.79(9)	172.52(3)
N(3)-M(1)-Cl(1)	102.95(3)	100.07(5)	101.31(7)	97.30(7)	109.96(5)	104.69(5)	108.57(9)	109.80(4)
N(4)-M(1)-Cl(1)	125.65(3)	154.20(5)	147.59(6)	94.18(7)	119.85(5)	143.46(5)	119.84(8)	95.16(4)
N(2)-M(1)-N(1)	86.50(3)	84.44(7)	85.84(9)	78.17(9)	84.46(6)	83.96(7)	84.00(13)	77.81(5)
N(2)-M(1)-N(3)	86.84(4)	84.49(7)	85.40(9)	78.99(9)	84.05(6)	84.37(7)	83.38(13)	77.47(5)
N(3)-M(1)-N(1)	153.87(3)	158.57(6)	159.60(9)	149.36(8)	145.15(7)	153.31(7)	145.53(11)	147.12(4)
N(4)-M(1)-N(1)	81.95(4)	81.87(6)	81.87(9)	78.76(10)	77.78(7)	79.22(6)	77.48(11)	78.38(5)
N(4)-M(1)-N(2)	121.83(4)	98.89(6)	103.45(9)	84.45(9)	113.32(7)	97.47(7)	111.33(12)	84.49(5)
N(4)-M(1)-N(3)	80.21(4)	81.79(6)	82.31(9)	78.95(9)	76.87(6)	78.62(7)	77.54(11)	77.98(5)
Cl(1)-M(1)-Cl(1) ^{1,2}	-	-	-	87.82(3)	-	-	-	87.33(2)
N(1)-M(1)-Cl(1) ^{1,2}	-	-	-	99.54(7)	-	-	-	105.59(4)
N(2)-M(1)-Cl(1) ^{1,2}	-	-	-	93.63(7)	-	-	-	93.59(4)
N(3)-M(1)-Cl(1) ^{1,2}	-	-	-	102.03(7)	-	-	-	97.28(4)
N(4)-M(1)-Cl(1) ^{1,2}	-	-	-	177.65(7)	-	-	-	175.16(3)
M(1)-Cl(1)-M(1) ^{1,2}	-	-	-	92.18(3)	-	-	-	92.67(2)

(1) for Cu(II) : -X, 1-Y, 2-Z; (2) for Zn(II) : 1-X, 1-Y, 2-Z

The solid state structures of **L4Cu** and **L4Zn** offer insight into the coordination geometry of these unique complexes compared to structurally similar complexes such as **L1-L3Cu** and **L1-L3Zn**. Additionally, the solid state structures offer absolute proof that **L4** can easily bind to biologically relevant metal ions, such as Zn(II) and Cu(II). Chelation of these metal ions is essential if **L4** is to be used as a therapeutic agent for neurodegenerative diseases. Finally, the X-ray quality crystals utilized to determine the solid state structure of **L4Cu** and **L4Zn** were analyzed using additional characterization methods to further understand these metal complexes, this will be discussed in the following sections.

2.5.3. Electronic spectrum of **L4Cu** in aqueous and organic solvents

After obtaining the solid state structure of **L4Cu** using X-ray diffraction, the crystals were dissolved in both H₂O and DMF to investigate the electronic spectrum of **L4Cu**. In water, the solution is light blue with one absorbance band observed at 758 nm and an extinction coefficient of 22.66 M⁻¹ cm⁻¹. Contrastingly, in DMF the solution is light yellow-green with one absorbance band at 873 nm and an extinction coefficient of 48.61 M⁻¹ cm⁻¹ (Figure 2.14). Generally, Cu(II) complexes are blue or green.^{30, 202}

The observed blue or green color of these complexes is due to d-d transitions incorporated into a single absorption band in the 600-900 nm region.^{30, 202} This single broad absorption band encompasses several overlapping transitions, but actual assignments are difficult to make.³⁰ The three components can generally be assigned as the transitions from the $d(xy)$, $d(z^2)$, or $d(xz)/d(yz)$ pair to the σ anti-bonding half-filled $d(x^2-y^2)$ orbital.²⁰² The order of the transitions is situational and dependent on the axial metal-ligand interaction.²⁰² Commonly the molar intensities (or extinction coefficients) vary from 20 – 50 $M^{-1} \text{ cm}^{-1}$ for symmetric molecules to several hundred $M^{-1} \text{ cm}^{-1}$ for nonsymmetric molecules. Therefore, for **L4Cu** absorbance bands in two different solvents are assigned to the d-d transitions of Cu(II), with the understanding that the single absorbance band encompasses the overlapping transitions discussed above. Additionally, a slight difference in the absorption maxima was observed in the two different solvents, indicating solvent dependent behavior (Figure 2.14). This may be due to the dimeric species breaking apart in solution and weakly coordinating to the solvent molecules.

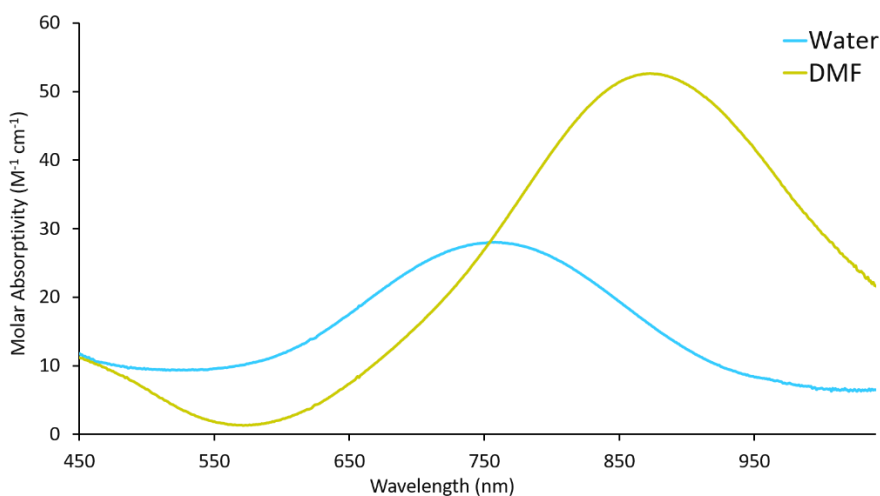


Figure 2.14. The electronic spectra of **L4Cu** in H_2O (pH = 5.00) and DMF. Molar Absorptivity: [λ_{max}/nm ($\epsilon/M^{-1} \text{ cm}^{-1}$)] in H_2O : 758 (23); in DMF: 873 (49).

2.5.4. Electrochemistry of **L4Cu**

Cyclic voltammetry was used to characterize the redox behavior of **L4Cu** in solution. The electrochemical activity of **L4Cu** was studied in DMF with 0.1 M tetrabutylammonium perchlorate as the supporting electrolyte and the system was referenced to the Fc/Fc^+ redox couple; these conditions have

previously been utilized by the Green group to study similar ligand-Cu(II) complexes.^{55-56, 72} Two redox events (reduction and oxidation) were observed for this complex when scanning from cathodic to anodic potentials (Figure 2.15, solid trace). Investigation into the two redox events revealed that they are related; the oxidation event only appears after the reduction event has occurred (Figure 2.15, dashed trace). Although the two events are related, the oxidation and reduction events are considered irreversible based on a separation of roughly 1.30 V (Table 2.7, Figure 2.15). It is hypothesized that in solution the dimeric complex breaks apart into separate $[\text{L4Cu}^{\text{II}}\text{Cl}]^+$ species; therefore, the cathodic event (= -816 mV) is assigned as the reduction of Cu(II) to Cu(I) and the anodic event (= 47 mV) is assigned as the oxidation of Cu(I) to Cu(II). Reduction of the metal center from Cu(II) \rightarrow Cu(I) could result in the loss of *cis*-bound ligand (Cl⁻) in a weakly coordinating solvent, such as DMF.²⁰³ Upon reversal of the scan directions the resulting Cu(I) 4-coordinate complex is re-oxidized to Cu(II) at much higher potentials and the 5-coordinate Cu(II) complex is reformed in quick succession.²⁰³ The presence of a single Cu(II/I) couple supports the hypothesis that the dimers break apart upon solvation. Additionally, similar redox events are observed for **L1Cu**, **L2Cu**, and **L3Cu** with a Cu(II)/Cu(I) at comparable potentials (Table 2.8). The Cu(II) complexes with **L1-L3** are 5-coordinate, thus further supporting the hypothesis that **L4Cu** breaks apart in solution.

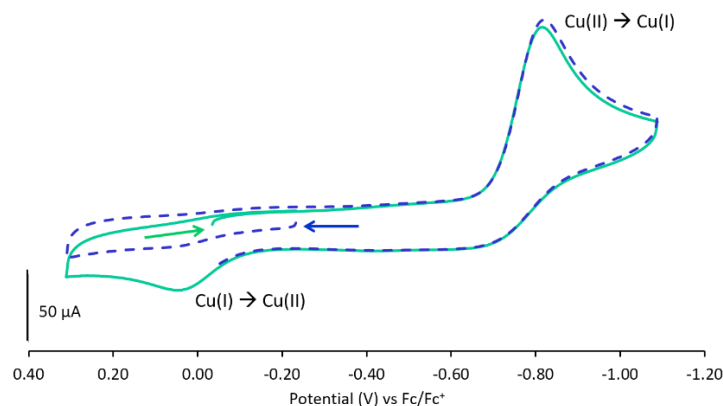


Table 2.7. Electrochemical values related to **L4Cu**

	E_{pc} (mV)	E_{pa} (mV)	$E_{1/2}$ (mV)	ΔE_p (mV)
L4Cu	-816	47	-385	863

Figure 2.15. Cyclic voltammogram recorded in 3.0 mL of DMF containing 3 mg **L4Cu** + 0.1 M TBAP with a glassy carbon working electrode, Ag wire quasi-reference electrode, and a platinum wire auxiliary electrode. Arrow indicates direction of scans, all scans performed at 100 mV/s.

When the E_{pc} value for **L4Cu** is compared to Cu(II) complexes previously synthesized by the Green group (**L1Cu**, **L2Cu**, and **L3Cu**), some interesting trends are observed (Table 2.8). Generally, the more negative the E_{pc} potential, the more electron density the ligand donates to the Cu(II) metal center. Based on this correlation the electron donating capacity (E_{pc} potentials only) of the ligands is **L2** > **L3** > **L1** > **L4**. This may seem surprising since **L4** has double the pyridol moieties of any other ligand and is thus expected to be a stronger donor; however, inspection of the structure provides insight. The two pyridol rings of **L4** may be interacting with one another (Figure 2.16). We postulate that this interaction is responsible for **L4Cu**'s more positive E_{pc} potential. **L4** is a 12-membered macrocycle so it must bind to the Cu(II) metal in a *cis*-folded fashion; which could allow the pyridol rings within **L4** to interact with one another. It is hypothesized that if these two rings interact through interactions more of the electron density stays within the pyridol rings and less electron density is donated to the Cu(II) center, compared to macrocycles containing one pyridine or pyridol ring. Thus, the E_{pc} for **L4Cu** is the most positive when compared to **L1Cu**-**L3Cu** due to structural interactions within the ring itself.

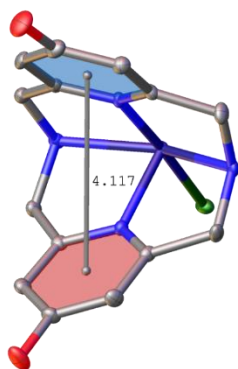


Figure 2.16. Measured distances between pyridol ring planes in **L4Cu**.

Table 2.8. A comparison of electrochemical values for **L1Cu**-**L4Cu**.

Metal Complex	E_{pc} (mV)
L1Cu	-960
L2Cu	-1030
L3Cu	-970
L4Cu	-816

*GC electrode; 2 mM complex + 0.1 M TBAP in DMF; E_{pc} values referenced to Fc/Fc⁺ couple

2.5.5. ^1H NMR spectrum of L4Zn

Due to the diamagnetic nature of the Zn(II) metal ion, ligand complexes containing Zn(II) were not characterized using UV-visible spectroscopy or cyclic voltammetry. Zn(II) complexes are not expected to exhibit d-d transitions due to the complete filling of the t_{2g} and e_g orbitals; they do not undergo any redox activity for the same reason. Although Zn(II) ligand complexes cannot be characterized using these traditional techniques adopted for analyzing transition metal complexes, they can be characterized using NMR, due to the diamagnetic nature of Zn(II) . In addition to mass spectrometry and X-ray diffraction, L4Zn was also characterized with ^1H NMR. The ^1H NMR spectrum of **L4** contains only two resonances due to the absolute symmetry of the molecule (Figure 2.17). Contrastingly, when **L4** is complexed to Zn(II) , more resonances appear, and splitting is observed. In solution, the L4Zn complex adopts a *cis*-folded geometry which causes resonance splitting, assignments have been made in figure 2.18. The Zn(II) ion locks the ligand into a *cis*-folded orientation, thus making the H-atoms on the bridging ethyl groups, non-equivalent. The differences between the two spectra offer more evidence to the complexation of the biologically relevant metal ion Zn(II) .

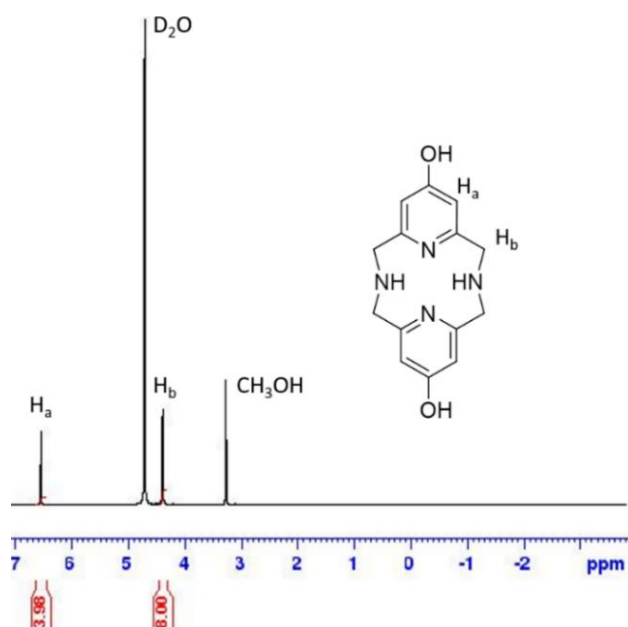


Figure 2.17. ^1H NMR spectrum of **L4** in D_2O .

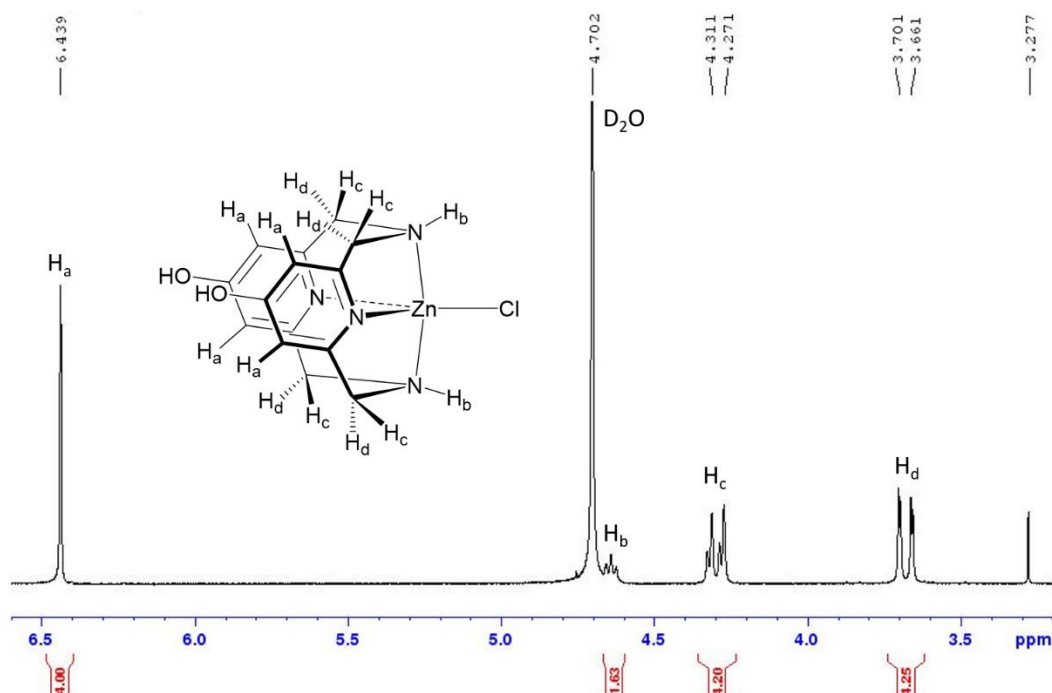


Figure 2.18. ¹H NMR of L4Zn in D₂O.

2.6. Biological assays with L4

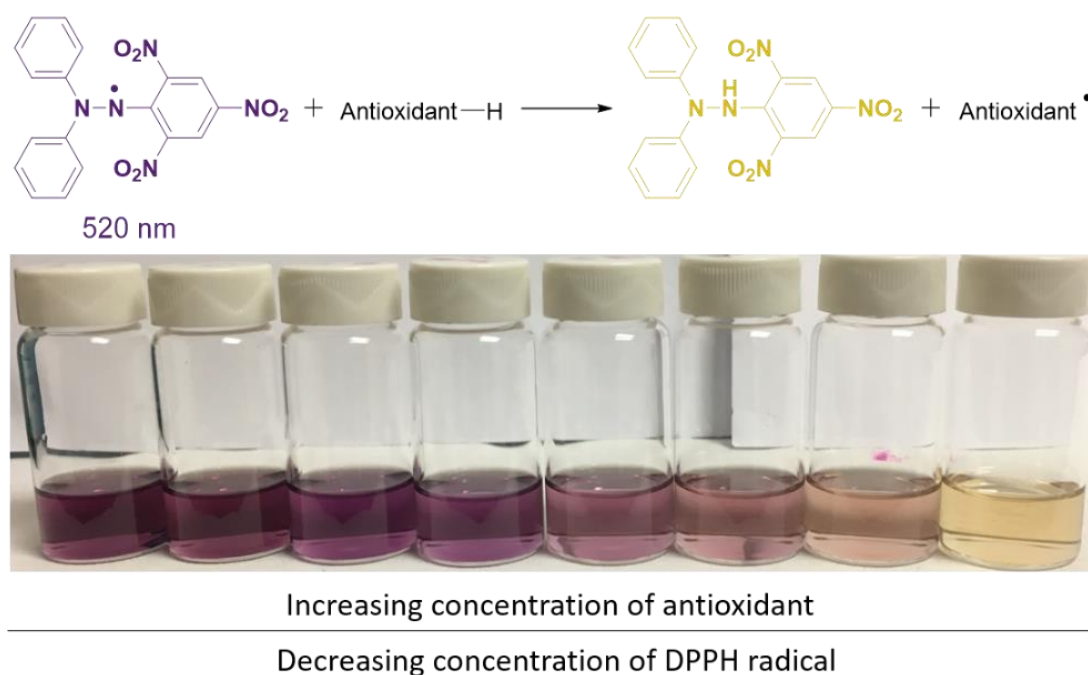
When designing **L4** it was hypothesized that by doubling the pyridol moieties present within the molecule this would further enhance the radical scavenging abilities exhibited by **L2**. As noted in section 2.1.2. earlier in this chapter, increasing the radical scavenging abilities is desirable for a potential neurotherapeutic agent designed to combat ROS in the brain. Following the full characterization of **L4** and the corresponding metal complexes **L4Cu** and **L4Zn**, two relevant assays were performed on **L4** to evaluate antioxidant activity: the DPPH radical quenching assay and the CCA redox cycling assay. The results of both assays performed on **L4** will be discussed in the following section. Additionally, assay results from **L4** and **L2** will be compared to determine the validity of the design hypothesis.

2.6.1. DPPH radical quenching assay performed with L1, L2, and L4

The radical scavenging ability of **L4** compared to **L1-L2** was tested using a DPPH radical quenching assay. As discussed in section 2.1.4., DPPH is a stable radical with a maximum absorbance at 520 nm.^{4, 72, 149, 175} When a radical scavenging molecule is added to a solution of DPPH the radical is quenched, leading

to a decrease in the absorption maximum and a corresponding color change from purple to yellow (Scheme 2.7).^{4, 72, 149, 175} The depletion of the absorbance band at 520 nm is directly related to the reduction in DPPH radical concentration (Scheme 2.8).⁴

Typically, when performing the DPPH assay a well-known antioxidant molecule is used as a positive control; in this study BHT (dibutylhydroxytoluene) was utilized.^{4, 72} Recently, the DPPH radical quenching assay was performed on BHT, **L1**, **L2**, and **L4**; at concentration ranging from 0.060 μM to 500 μM (Figure 2.19). The results indicate that at higher μM concentrations (starting at 31.25 μM) **L4** exhibits an enhanced radical-scavenging ability compared to both **L1** and **L2**. In fact, at very high μM concentrations (250 and 500 μM) the radical-scavenging ability of **L4** is comparable to BHT. The results of the DPPH radical quenching assay provide evidence to support the hypothesis that doubling the pyridol moieties on **L4** leads to enhanced radical scavenging abilities compared to **L2**.



Scheme 2.8. Mechanism of the DPPH radical quenching assay and corresponding color change associated with reduction of the DPPH radical.

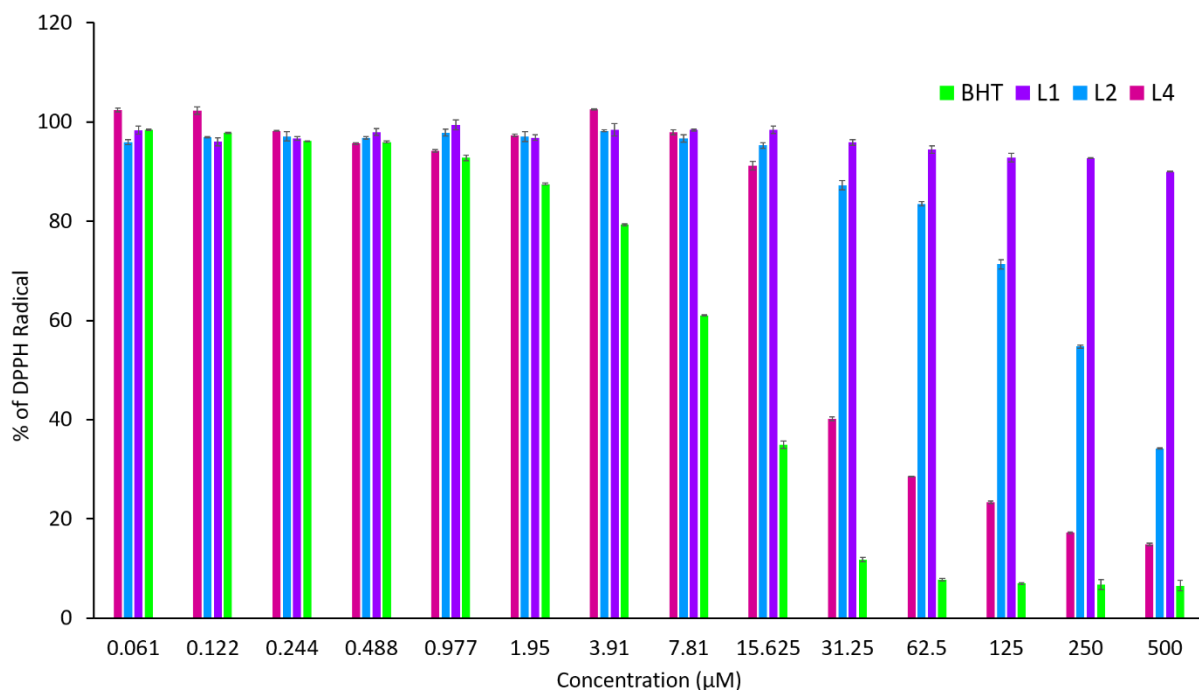


Figure 2.19. DPPH radical quenching assay showing the antioxidant character of **L1**, **L2**, and **L4** compared to the standard antioxidant BHT ($n = 3$).

2.6.2. CCA redox cycling assay performed with **L2** and **L4**

In section 2.1.3., the implications of the redox cycling of metal ions such as Cu(II) and Zn(II) were discussed.⁷² ROS can be produced by the redox cycling of such metal ions. The overproduction of ROS is hypothesized to lead to the development of neurodegenerative diseases.^{93, 116, 132, 204} A good model for redox cycling in the brain is the Cu-ascorbate redox system (Scheme 2.1).^{72, 171-172} This system has been used by the Green group and others, in recent publications, to determine if chelating ligands, such as **L1** and **L2**, can halt the Cu based redox cycling under aerobic conditions.^{72, 171-172} One way to quantify this is to use the CCA redox cycling assay.¹⁷¹ In this assay, CCA is stoichiometrically converted to the fluorescent 7-hydroxy-CCA species in the presence of hydroxyl radicals generated by copper in the presence of ascorbate and oxygen.¹⁷¹⁻¹⁷² The CCA assay was recently performed on **L2** and **L4** and redox cycle halting abilities of the two chelating ligands were compared.

Figure 2.20 shows the results of the CCA redox cycling assay performed with **L2** and **L4**. The addition of a full equivalent of **L2** or **L4** (vs. Cu(II) concentration) results in almost complete inhibition of CCA conversion to fluorescent 7-hydroxy-CCA (Figure 2.20). The addition of ½ equivalents of **L2** or **L4** result in a marked decrease in fluorescence compared to the negative control (shown in the graph inset); the stoichiometric decrease in fluorescence is thereby attributed to the chelation of Cu(II) ions. Interestingly, the results shown in figure 2.20 indicate that **L4** is slightly better than **L2** at halting the redox cycling of Cu(II) and ascorbate. This enhanced ability of **L4** to halt redox cycling is most likely due to the additional pyridol moiety, which may quench hydroxyl radicals produced during redox cycling. Most importantly, both **L2** and **L4** exhibit the ability to halt the redox cycling of Cu(II) and ascorbate in an aerobic environment making both these molecules good candidates for use as future neurotherapeutic agents to combat the production of excess ROS in the brain.

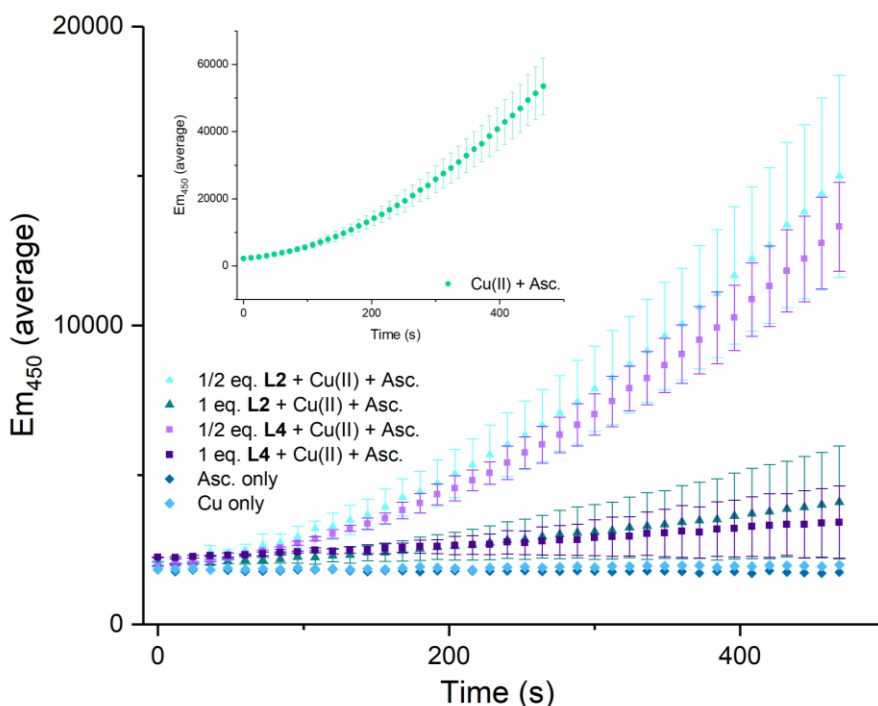


Figure 2.20. Fluorescence intensity of 7-hydroxy-CCA after incubation of CCA [100 μ M] and ascorbate [300 μ M] with Cu(II) [10 μ M]. Compound **L2** [5 μ M; 10 μ M] and **L4** [5 μ M; 10 μ M] were combined prior to addition of ascorbate. No fluorescence was observed with CCA co-incubated with samples of: (1) ascorbate [300 μ M] only or (2) Cu(II) [10 μ M]. All solutions except CuSO₄·6H₂O (MilliQ water only) were dissolved and diluted in 7.4 pH 1X KH₂PO₄/NaCl buffer containing Desferal [1 μ M]. Final volume = 3 mL. (n = 3)

2.7. The therapeutic window of L4

L4 was designed to be utilized as a therapeutic agent for the treatment of neurodegenerative diseases. In the previous section radical scavenger and redox focused assays were performed to determine the antioxidant capacity of L4. Additionally, because L4 is a potential therapeutic agent, it is important to understand how this molecule impacts the viability of cells. To accomplish this, cell studies were conducted to establish the cell toxicity and therapeutic window for L4 as well as L2, for comparison. The cell studies were performed by Olivia Kinsinger at TCU. Two different cell lines were used in these studies, HT22 (mouse hippocampal, neuronal) and MCF-7 (breast cancer, for comparison). For the HT22 cell line, L4 was observed to be toxic in the low mM range, with an EC₅₀ value of 2.200 mM±0.006, meaning that the therapeutic window for L4 is in the nM to low μM range, respectively (Figure 2.21). Similar results were observed for the MCF-7 cell line, both L2 and L4 were shown to be toxic in the low mM range, with EC₅₀ values of 8.374±0.01 mM (L2) and 1.714±0.01 mM (L4), respectively (Figure 2.21). Additionally, the therapeutic window for both L2 and L4 is in the μM range for the MCF-7 cell line, respectively. These results suggest that the observed toxicity is not cell line specific and that the addition of the pyridol moiety to L4 renders little change to the biological tolerance of pyridine containing macrocycles.

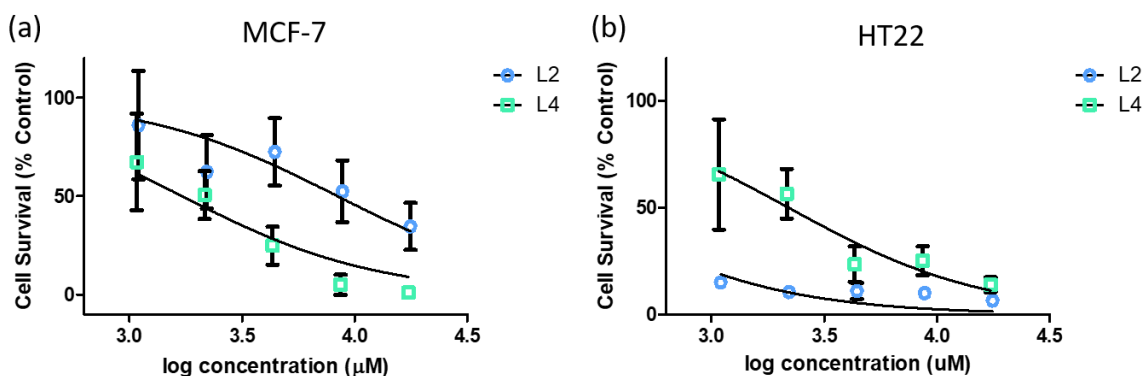


Figure 2.21. (a) Cell survival vs. log conc. of MCF-7 cells dosed with L2 or L4; (b) cell survival vs. log conc. of HT22 cells dosed with L2 or L4. (Cell studies performed by Olivia Kinsinger)

2.8. Conclusions

L4 was designed to enhance the antioxidant abilities exhibited by **L2** by adding another pyridol moiety. It was hypothesized that doubling the pyridol moieties would result in an increase in the radical scavenging and antioxidant capabilities of **L4** compared to **L2**. This novel bis-pyridol-based tetraazamacrocycle was synthesized using a variation of the Richman-Atkins synthesis for making symmetrical *N*-tosyl aza macrocycles. The first step in the two-step synthesis of **L4** involves simultaneous cyclization and protection of nitrogen and oxygen atoms with tosyl and benzyl groups, respectively. The cyclization step is then followed by a single deprotection step in which both the tosyl and benzyl groups are removed using a naphthalene-catalyzed lithiation.

Following the complete synthesis of **L4**, its protonation and stability constants were determined by pH-potentiometric titrations; four protonation steps were observed. Additionally, **L4** forms stable metal complexes with several biologically relevant metals, including Zn(II). Solid state structures of **L4Cu** and **L4Zn** confirmed metal complexation. In the solid state, the complexes of **L4Cu** and **L4Zn** crystallize as dimeric species with two metal-complexed ligands connected through a μ -Cl₂ bridge. **L4Cu** was also characterized with UV-visible spectroscopy and cyclic voltammetry; both techniques offered insight into the electronic properties of the Cu(II) metal center. Contrastingly, **L4Zn** was characterized with ¹H NMR and XRD analysis due to the diamagnetic nature of the Zn(II) ion.

Finally, the enhanced antioxidant capacity of **L4** was probed with several relevant assays: the DPPH radical quenching assay and the CCA redox cycling assay. The results of the DPPH assay are consistent with the hypothesis that the two pyridol moieties contained within **L4** offer enhanced radical scavenging abilities compared to **L2**. The ability of **L4** to halt the redox cycling of Cu(II) with ascorbate was also confirmed using the CCA assay. A decrease in the fluorescence of 7-hydroxy-CCA was observed upon addition of both ½ eq. and 1 eq. of **L4**. Finally, the therapeutic window for **L4** was also determined to be

in the μM range for both MCF-7 and HT22 cells. Altogether, these results validate the rational design hypothesis of **L4**.

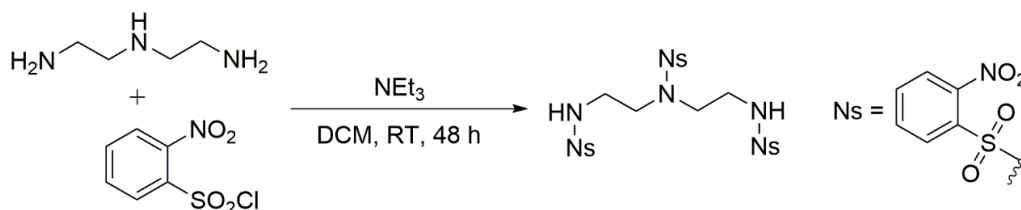
2.9. Experimental (methods and materials)

Caution! Perchlorate salts are explosive and should be handled with care; such compounds should never be heated as solids. All chemical reagents were purchased from either Millipore Sigma or Alfa Aesar and used without further purification. The 12-membered tetraazamacrocycles **L1**, **L2**, **L3**, and **L4** were isolated as the hydrochloride salts prior to metal ion complexation in accordance with standard practices. The yields reported for **L4Cu** and **L4Zn** were calculated based on elemental analysis results; each reaction was carried out in H_2O . Elemental analyses were performed by Canadian Microanalytical Services Ltd.

2.9.1 Physical measurements

ESI mass spectral analysis were obtained on an Agilent 1200 series 6224 TOF LC/MS spectrometer at 175 V (positive ESI scan) in H_2O , CH_3OH , CHCl_3 , or CH_2Cl_2 . ^1H NMR and ^{13}C NMR spectra were carried out in deuterated solvents at 25°C . All spectra reported were obtained on a Bruker Avance III (400 MHz) High Performance Digital NMR Spectrometer. Electronic absorption spectra were collected between 190 nm and 1100 nm using an 8453 UV-vis spectrophotometer (Agilent) and a 3-mL quartz cuvette with a path length of 1.0 cm. Molar extinction coefficients were calculated utilizing the Beer-Lambert law ($A = \epsilon bc$).

2.9.2. Preparation of 1,4,7-tris(2-nitrobenzoylsulfonyl)1,4,7-triazaheptane (**2.1**):

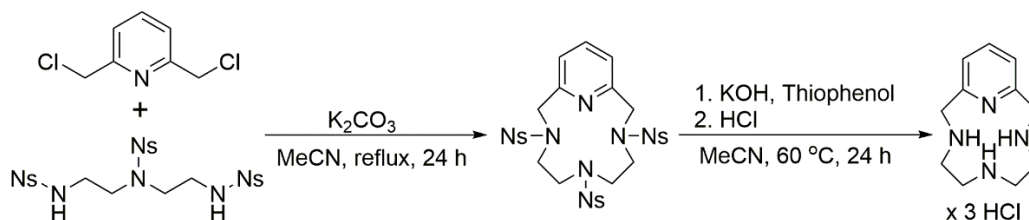


Scheme 2.E1. Protection of triethylamine with nosyl groups.

Synthesis of 1,4,7-tris(2-nitrobenzenesulfonyl)-1,4,7-triazaheptane (**2.1**):

A sample of 2-nitrobenzenesulfonyl chloride (25.00 g, 112 mmol) was dissolved in dichloromethane (125 mL) and put under N₂. Diethylenetriamine (3.80 mL, 35 mmol) and triethylamine (17.00 mL, 122 mmol) were dissolved in dichloromethane (100 mL) and added dropwise, over 1 h, via addition funnel to the protecting group. The reaction stirred under an N₂ atmosphere until a white solid precipitated out of the dichloromethane. Upon observing the white solid, chloroform (150 mL) was added to the reaction mixture and this was placed in the refrigerator for several hours. After cooling, the reaction mixture was filtered using reduced pressure and washed with chloroform (3 x 50 mL). The product (**2.1**) was isolated as a pure white solid. Yield: 15.00 g (65%). ¹H NMR (400 MHz, DMSO, 23 °C): δ = 7.98-7.86 (m, 12H), δ = 3.37 (t, 4H), δ = 3.06 (t, 4H); ¹³C NMR (101 MHz, DMSO, 23 °C): δ = 148.0, 135.2, 134.6, 132.9, 129.9, 125.1, 48.5, 41.8. ESI-MS (m/z): Found: 659.0513 [M+H]⁺ (100%) Theoretical: 659.0536 [M+H]⁺ (100%).^{4, 54, 57, 176}

2.9.3. Preparation of 1,4,7,10-tetraaza-2,6-pyridinophane (**L1**)



Scheme 2.E2. Macro-cyclization and nosyl group removal for L1.

Synthesis of 4,7,10-tris(2-nitrobenzenesulfonyl)-1,4,7,10-tetraaza-2,6-pyridinophane (**2.3**):

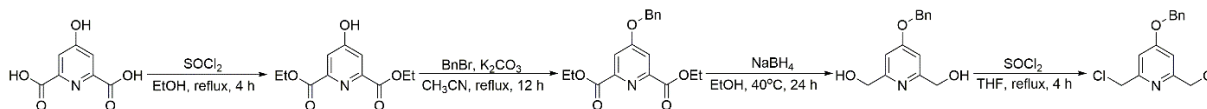
A sample of 2,6-bis(chloromethyl)pyridine (**2.2**) (2.99 g, 17 mmol) was dissolved in CH₃CN (80 mL). This solution was added drop-wise, via addition funnel, to an off-white solution of (**2.1**) (11.3g, 17 mmol) and K₂CO₃ (7.09 g, 51 mmol) in CH₃CN (200 mL), under reflux conditions (100 °C) and under nitrogen. The reaction mixture stirred under reflux conditions for 24 h and under nitrogen, to allow maximum cyclization. The solvent of the resulting bright yellow solution was subsequently removed under reduced

pressure. The chalky residue was rinsed with water (4 x 50 mL) and filtered using reduced pressure. The resulting pale-yellow solid was then rinsed further with CH₃CN (1 x 15 mL), CH₃OH (3 x 15 mL), and diethyl ether (3 x 15 mL), in that order. Finally, the solid was dried on a Schlenk line to afford **(2.3)** as a pale-yellow solid. Yield: 11.7 g (90 %). ¹H NMR (400 MHz, DMSO, 22 °C): δ = 8.07-7.35 (m, 12H), δ = 7.35-7.34 (d, 3H), δ = 4.62 (s, 4H), δ = 3.76, (s, 4H), δ = 3.53, (s, 4H); ¹³C NMR (101 MHz, DMSO, 25 °C): δ = 156.2, 148.3, 147.7, 139.0, 135.2, 135.1, 133.1, 132.6, 131.0, 130.2, 129.9, 125.1, 124.8, 122.9, 55.4, 49.7, 46.6. ESI-MS (m/z): Found: 762.0903 [M+H]⁺ (100%), Theoretical: 762.0958 [M+H]⁺.^{4, 55, 59}

Synthesis of 1,4,7,10-tetraaza-2,6-pyridinophane trishydrochloride (L1):

KOH (3.54 g, 63 mmol) was dissolved in a minimum amount of water and added, along with CH₃CN (100 mL) to a one-neck reaction flask. The flask was covered with a septum and thiophenol (6.40 mL, 54 mmol) was cautiously added, via syringe, to the stirred solution. Finally, **(2.3)** (11.7 g, 16 mmol) was added all at once to the flask. After the addition of **(2.3)**, the reaction mixture was put under N₂, heated to 60°C, and left to stir overnight. The solvent was removed under reduced pressure to give a dark yellow oily residue. This oily residue was acidified to pH 1 using concentrated HCl (10 mL). The acidic solution was extracted with diethyl-ether (3 x 50 mL) until the organic layer was no longer colored. Next, the aqueous layer was basified to pH 14 using solid KOH. The solvent was removed using reduced pressure. The resulting yellow solid was dissolved in CH₃OH (50 mL) and dried over sodium sulfate. This solution was filtered, and the solvent was removed under reduced pressure to yield dark yellow oil. To this oil, CH₃CN (50 mL), concentrated HCl (5 mL), and diethyl-ether (60 mL) were added to give a yellow powdery precipitate. This precipitate was filtered off and then immediately boiled in absolute ethanol (50 mL). Upon cooling the solution was filtered to afford **L1** a pale off-white powder. Yield: 5.85 g (50%). ¹H NMR (400 MHz, D₂O, 25 °C): δ= 7.94-7.90 (t, 1H), 7.46-7.44 (d, 2H), 4.57 (s, 4H), 3.33-3.31(t, 4H), 3.21-3.19 (t, 4H); ¹³C NMR (101 MHz, D₂O, 25 °C): δ = 149.7, 140.2, 123.6, 49.2, 44.6, 43.5. ESI-MS (m/z): Found: 207.2238 [**L1**+H]⁺ (100%), Theoretical: 207.1610 [**L1**+H]⁺.^{4, 55}

2.9.4. Preparation of 1,4,7,10-tetraaza-2,6-pyridinophane-14-ol trishydrochloride (L2):



Scheme 2.E3. Synthesis of alkyl halide precursor for macro-cyclization of L2.

Synthesis of diethyl-4-hydroxypyridine-2,6-dicarboxylate (2.4):

A sample of chelidamic acid (5.0 g, 27 mmol) was dissolved in absolute EtOH (200 mL) in a one-neck reaction flask. The flask was covered with a septum and put on ice; thionyl chloride (4.00 mL, 55 mmol) was added cautiously, via syringe, to the stirred solution. The ice bath was removed, and the reaction stirred under reflux conditions for 4 h. The solvent was removed using reduced pressure. The resulting clear pale-yellow oil was rinsed with toluene (2 x 100 mL), each time the toluene was removed under reduced pressure. To the resulting oil, H_2O (30 mL) and diethyl ether (30 mL) were added and this mixture was shaken vigorously until a white powder developed between the two solvent layers. The resulting mixture was filtered and rinsed with diethyl ether (3 x 25 mL) to afford (**2.4**) as a white crystalline powder. Yield: 4.76 g (73%). ^1H NMR (400 MHz, CDCl_3 , 25°C , TMS): δ = 9.20 (s, 1H), 7.34 (s, 2H), 4.51-4.46 (q, 4H), 1.46-1.43 (t, 6H); ^{13}C NMR (101 MHz, CDCl_3 , 25°C) δ = 162.5, 119.0, 63.2, 14.1.^{4, 180}

Synthesis of diethyl-4-(benzyloxy)pyridine-2,6-dicarboxylate (2.5):

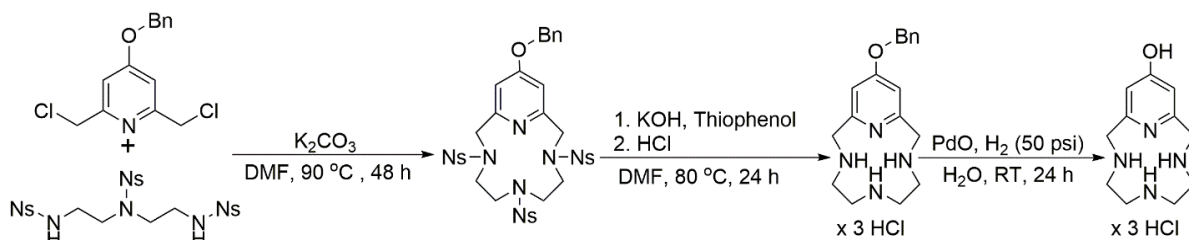
A sample of compound (**2.4**) (4.76 g, 20 mmol) was dissolved in CH_3CN (200 mL) followed by sequential addition of K_2CO_3 (5.5 g, 40 mmol) and benzyl bromide (2.6 mL, 22 mmol). This reaction mixture was put under inert atmosphere and stirred under reflux conditions for 12 h. The reaction was cooled to room temperature and filtered to remove the inorganic salts. The supernatant was evaporated to dryness under reduced pressure. The resulting colorless oil was re-crystallized from hot hexanes (100 mL) to afford (**2.5**) as a white powder. Yield 5.9 g (90%). ^1H NMR (400 MHz, CDCl_3 , 25°C , TMS): δ = 7.88 (s, 2H), 7.46-7.28 (m, 5H), 5.25 (s, 2H), 4.50-4.48 (q, 4H), 1.49-1.46 (t, 6H); ^{13}C (101 MHz, CDCl_3 , 25°C): δ = 166.6, 614.7, 150.3, 134.8, 128.9, 128.8, 127.8, 114.7, 70.8, 62.5, 14.21.^{4, 180}

Synthesis of 4-(benzyloxy)-2,6-bis(hydroxymethyl)pyridine (2.6):

A sample of compound (2.5) (5.86 g, 18 mmol) was dissolved in absolute EtOH (500 mL) and NaBH₄ (3.44 g, 90 mmol) was added portionwise. The mixture was heated to 40 °C and stirred for 24 h. After reaction completion, the mixture was quenched with H₂O and the pH of the solution was adjusted to 1 with concentrated HCl. The resulting solution was filtered, and the supernatant was evaporated to dryness under reduced pressure. The resulting solid was re-dissolved in absolute EtOH (100 mL), dried with Na₂SO₄, and filtered. The supernatant was evaporated to dryness under reduced pressure to afford (2.6) as a tacky white solid. Yield: 3.75 g (86%). ¹H NMR (400 MHz, DMSO, 24 °C): δ = 7.46-7.41 (m, 5H), 7.00 (s, 2H), 5.47 (br, 2H), 5.23 (s, 2H), 4.50 (s, 4H); ¹³C (101 MHz, DMSO, 24 °C): δ = 171.1, 158.7, 135.1, 129.2, 128.8, 108.9, 72.0, 59.6.^{4,178}

Synthesis of 4-benzyloxy-2,6-bis(chloromethyl)pyridine (2.7):

A sample of (2.6) (3.74 g, 15 mmol) was dissolved in THF (30 mL) in a one-neck reaction flask. The flask was covered with a septum and put on ice; thionyl chloride (3.6 mL, 50 mmol) was added cautiously, via syringe, to the stirred solution. The ice bath was removed, and the reaction stirred under reflux conditions for 4 h. The reaction mixture was neutralized with a saturated solution of NaHCO₃. The neutralized solution was evaporated to dryness under reduced pressure. The resulting crusty brown solid was dissolved in chloroform (150 mL) and this mixture was filtered using reduced pressure. The supernatant was dried over Na₂SO₄ and subsequently filtered. The resulting clear brown solution was evaporated to dryness under reduced pressure to afford (2.7) as a light brown solid. Yield 3.10 g (72%). ¹H NMR (400 MHz, CDCl₃, 25 °C, TMS): δ = 7.45-7.44 (m, 5H), 7.06 (s, 2H), 5.17 (s, 2H), 4.63 (s, 4H); ¹³C NMR (101 MHz, CDCl₃, 25 °C): δ = 166.6, 158.1, 135.3, 128.8, 128.6, 127.7, 108.8, 70.24, 46.47.^{4,179}



Scheme 2.E4. Macro-cyclization and nosyl group removal for L2.

Synthesis of 14-benzyloxy-4,7,10-tris(2-nitrobenzenesulfonyl)-1,4,7,10-tetraaza-2,6-pyridinophane (2.8):

A solution of **(2.7)** (3.00 g, 11 mmol) in anhydrous DMF (90 mL) was added dropwise, under N₂, to a stirred solution of **(2.1)** (7.00 g, 11 mmol) and K₂CO₃ (4.50 g, 33 mmol) in anhydrous DMF (200 mL) at 100 °C. The resulting dark yellow-brown solution was stirred under N₂ at 100 °C for 48 h. The solvent was removed under reduced pressure to give a dark yellow-orange powder. The resulting solid was dissolved in dichloromethane, this solution was filtered using reduced pressure. The yellow filtrate was subsequently washed with 0.1 M NaOH (4 x 50 mL), H₂O (2 x 100 mL), and diethyl ether (2 x 100 mL) to afford **(2.8)** as a pale-yellow powder. Yield: 7.26 g (80%). ¹H NMR (400 MHz, DMSO, 23 °C): δ = 8.01-7.94 (m, 12H), 7.46-7.41 (m, 5H), 7.01 (s, 2H), 5.19 (s, 2H), 4.55 (s, 4H), 3.76 (t, 4H), 3.52 (t, 4H); ¹³C (101 MHz, DMSO, 25 °C): δ = 156.6, 134.2, 132.3, 131.5, 131.1, 129.0, 128.7, 128.0, 124.6, 124.4, 111.2, 70.6, 54.9, 46.3, 31.2. ESI-MS (m/z) Found: 868.1517 [M+H]⁺ (100%). Theoretical: 868.1377 [M+H]⁺.^{4, 56, 59}

Synthesis of 14-benzyloxy-1,4,7,10-tetraaza-2,6-pyridinophane tris-hydrochloride (2.9):

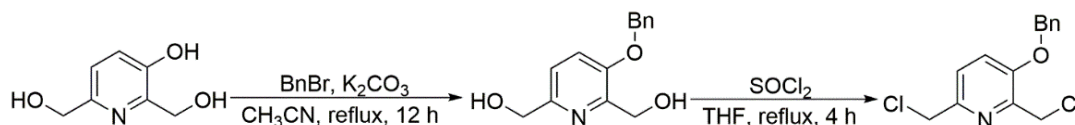
KOH (1.77 g, 33 mmol) was dissolved in a minimum amount of water and added, along with anhydrous DMF (100 mL) to a one-neck reaction flask. The flask was covered with a septum and thiophenol (3.40 mL, 32 mmol) was cautiously added, via syringe, to the stirred solution. Finally, **(2.8)** (6.83 g, 8 mmol) was added all at once to the flask. After the addition of **(2.8)**, the reaction mixture was put under N₂, heated to 80 °C, and left to stir overnight. The solvent was removed under reduced pressure to give a yellow oily residue. This oily residue was dissolved in a mixture of 1.0 M HCl and concentrated HCl (250 mL, ratio of 3:1). The acidic solution was extracted with diethyl ether (3 x 50 mL) until the organic

layer was no longer colored. Next, the aqueous layer was basified to pH 14 using solid KOH. The solvent was removed using reduced pressure to give a light-yellow solid. This solid was dissolved in dichloromethane (200 mL) and dried with Na₂SO₄. The resulting solution was filtered using reduced pressure and the filtrate was evaporated to dryness under reduced pressure. A dark yellow-orange oily substance was isolated. This oil was made solid by adding a specific ratio of CH₃CN, concentrated HCl, and diethyl ether. This mixture was filtered and **(2.9)** was isolated as a dark yellow powder. Yield: 2.60 g, (79%).
¹H NMR (400 MHz, D₂O, 23 °C): δ = 7.37-7.33 (m, 5H), 7.09 (s, 2H), 5.17 (s, 2H), 4.49 (s, 4H), 3.51-3.46 (q, 8H); ¹³C (101 MHz, D₂O, 25 °C): δ = 167.2, 151.6, 135.2, 129.0, 128.8, 128.0, 110.6, 70.7, 49.11, 44.2, 43.3.
 ESI-MS (m/z): Found: 313.2569 [M+H]⁺ (100%), Theoretical: 313.2028 [M+H]⁺.^{4, 56, 59}

Synthesis of 1,4,7,10-tetraaza-2,6-pyridinophane-14-ol trishydrochloride (**L2**):

A sample of compound **(2.9)** (2.57 g, 6 mmol) was dissolved in H₂O (100 mL) and filtered. To the filtered solution solid PdO (0.75 g, 6 mmol) was added. This suspension was exposed to H₂(g) (50 psi) using a Parr hydrogenator system for 24 h. The resulting clear solution was filtered and evaporated to dryness under reduced pressure, an off-white solid resulted. This solid was further treated with a small amount of absolute ethanol (20 mL), concentrated HCl (2 mL), and diethyl ether (40 mL). The product precipitated out of this solution and the reaction mixture was filtered to afford **L2** as a pure white powder. Yield: 1.74 g (87%). ¹H NMR (400 MHz, D₂O, 25 °C): δ = 6.89 (s, 2H), 4.44 (s, 4H), 3.34-3.37 (m, 4H), 3.30-3.29 (m, 4H); ¹³C (101 MHz, D₂O, 25 °C): δ = 166.2, 151.5, 111.4, 48.9, 44.0, 43.2. ESI-MS (m/z): Found: 223.1834 [**L2**+H]⁺ (100%), Theoretical: 223.1559 [**L2**+H]⁺.^{4, 56, 182}

2.9.5. Preparation of 1,4,7,10-tetraaza-2,6-pyridinophane-13-ol trishydrochloride (**L3**):



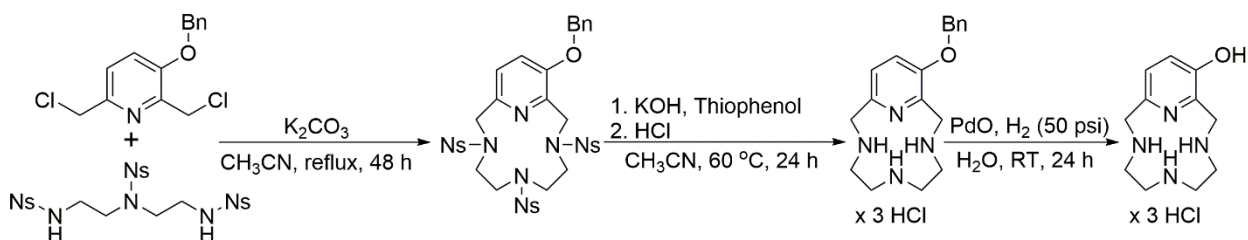
Scheme 2.E5. Synthesis of alkyl halide precursor for macro-cyclization of **L3**.

Synthesis of 2-benzyloxy-2,6-(hydroxymethyl)pyridine (**2.10**):

A sample of 3-hydroxy-2,6-bis(hydroxymethyl)pyridine hydrochloride (5.00 g, 26 mmol) was dissolved in CH₃CN (200 mL), followed by subsequent addition of K₂CO₃ (10.85 g, 79 mmol) and benzyl bromide (3.42 mL, 29 mmol). The reaction mixture was stirred under reflux conditions in an inert atmosphere for 12 h. The reaction mixture was cooled and filtered to remove the inorganic salts. The supernatant was evaporated to dryness under reduced pressure. The resulting oil was recrystallized from hot hexanes (100 mL) to afford (**2.10**) as a white powder. Yield: 6.39 g (99%). ¹H NMR (400 MHz, CDCl₃, 25 °C, TMS): δ = 7.42-7.36 (m, 5H), 7.31-7.28 (d, 2H), 5.15 (s, 2H), 4.88 (s, 2H), 4.76 (s, 2H); ¹³C (101 MHz, DMSO, 25 °C): δ = 152.5, 150.9, 148.6, 137.3, 128.9, 128.3, 127.8, 120.4, 120.2, 69.8, 64.1, 60.2.^{4, 56-57}

Synthesis of 2-benzyloxy-2,6-bis(chloromethyl)pyridine (**2.11**):

A sample of (**2.10**) (6.39 g, 26 mmol) was dissolved in THF (40 mL) in a one-neck reaction flask. The flask was covered with a septum and put on ice; thionyl chloride (5.8 mL, 80 mmol) was added cautiously, via syringe, to the stirred solution. The ice bath was removed, and the reaction stirred under reflux conditions for 4 h. The reaction mixture was neutralized with a saturated solution of NaHCO₃. The neutralized solution was evaporated to dryness under reduced pressure. The resulting crusty brown solid was dissolved in chloroform (200 mL) and this mixture was filtered using reduced pressure. The supernatant was dried over Na₂SO₄ and subsequently filtered. The resulting clear brown solution was evaporated to dryness under reduced pressure to afford (**2.11**) as a light brown solid. Yield: 6.02 g (82%). ¹H NMR (400 MHz, CDCl₃, 24 °C, TMS): δ = 7.48-7.41 (m, 5H), 7.30 (s, 2H), 5.21 (s, 2H), 4.82 (s, 2H), 4.68 (s, 2H); ¹³C NMR (101 MHz, CDCl₃, 23 °C): δ = 152.5, 147.9, 145.9, 135.7, 128.8, 128.4, 127.2, 124.1, 120.3, 70.4, 46.3, 42.3.^{4, 179}



Scheme 2.E6. Macro-cyclization and nosyl group removal for L3.

Synthesis of 13-benzyloxy-4,7,10-tris(2-nitrobenzenesulfonyl)-tetraaza-2,6-pyridinophane (2.12):

A solution of (**2.11**) (3.00 g, 11 mmol) in CH₃CN (100 mL) was added dropwise, under N₂, to a stirred solution of (**2.1**) (7.00 g, 11 mmol) and K₂CO₃ (4.40 g, 33 mmol) in CH₃CN (250 mL) at 90 °C. The resulting dark yellow solution was stirred under N₂ under reflux conditions for 48 h. The solvent was removed under reduced pressure to give a dark yellow-orange foamy solid. This solid was dissolved in dichloromethane and dried over Na₂SO₄. This mixture was filtered under reduced pressure. The clear dark orange-brown supernatant was evaporated to dryness under reduced pressure to give a foamy yellow solid. The solid was dissolved in an equal parts mixture of hot absolute ethanol and hot ethyl acetate (combined 150 mL), this mixture was left to stir for several hours. After several hours of stirring a powdery yellow solid had developed in the flask, this mixture was filtered and (**2.12**) was isolated as bright yellow powder. Yield: 7.56 g (82%). ¹H NMR (400 MHz, DMSO, 23 °C): δ = 7.97-7.88 (m, 12H), 7.61-7.58 (d, 2H), 7.43-7.33 (m, 5H), 5.20 (s, 2H), 4.69 (s, 2H), 4.53 (s, 2H), 4.36 (s, 2H), 3.53 (s, 2H), 3.46-3.43 (m, 4H). ESI-MS (m/z): Found: 867.9835 [M+H]⁺ (100%), Theoretical: 867.1298 [M+H]⁺.^{4, 59}

Synthesis of 13-benzyloxy-1,4,7,10-tetraaza-2,6-pyridinophane trishydrochloride (2.13):

KOH (1.90 g, 35 mmol) was dissolved in a minimum amount of water and added, along with CH₃CN (250 mL) to a one-neck reaction flask. The flask was covered with a septum and thiophenol (3.48 mL, 30 mmol) was cautiously added, via syringe, to the stirred solution. Finally, (**2.12**) (7.35 g, 8 mmol) was added all at once to the flask. After the addition of (**2.12**), the reaction mixture was put under N₂, heated to 60°C, and left to stir overnight. The solvent was removed under reduced pressure to give a yellow oily residue.

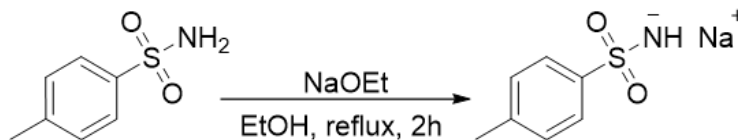
This oily residue was dissolved in a mixture of 1.0 M HCl and concentrated HCl (250 mL, ratio of 3:1). The acidic solution was extracted with diethyl ether (3 x 50 mL) until the organic layer was no longer colored. Next, the aqueous layer was basified to pH 14 using solid KOH. The solvent was removed using reduced pressure to give a bright yellow solid. This solid was dissolved in dichloromethane (200 mL) and dried with Na₂SO₄. The resulting solution was filtered using reduced pressure and the filtrate was evaporated to dryness under reduced pressure. A dark yellow-orange oily substance was isolated. This oil was made solid by adding a specific ratio of hot absolute EtOH, concentrated HCl, and diethyl ether. This mixture was filtered and **(2.13)** was isolated as a dark yellow powder. Yield: 2.63 g (74%). ¹H NMR (400 MHz, D₂O, 25 °C): δ = 7.63-7.60 (d, 1H), 7.46-7.37 (m, 6H), 5.23 (s, 2H), 4.53 (s, 2H), 4.48 (s, 2H), 3.31-3.10 (m, 8H). ESI-MS (m/z): Found: 313.2089 [M+H]⁺ (100%), Theoretical: 313.2028 [M+H]⁺.^{4, 56, 59}

Synthesis of 1,4,7,10-tetraaza-2,6-pyridinophane-13-ol trishydrochloride (L3):

A sample of compound **(2.13)** (2.63 g, 6 mmol) was dissolved in H₂O (100 mL) and filtered. To the filtered solution solid PdO (0.76 g, 6 mmol) was added. This suspension was exposed to H₂(g) (50 psi) using a Parr hydrogenator system for 24 h. The resulting clear solution was filtered and evaporated to dryness under reduced pressure, an off-white solid resulted. This solid was further treated with a small amount of absolute ethanol (20 mL), concentrated HCl (2 mL), and diethyl ether (40 mL). The product precipitated out of this solution and the reaction mixture was filtered to afford **L3** as a pure white powder. Yield: 1.92 g (93%). ¹H NMR (400 MHz, D₂O, 23 °C): δ = 7.38 (s, 2H), 4.51 (s, 2H), 4.45 (s, 2H), 3.39-3.22 (m, 8H); ¹³C NMR (101 MHz, D₂O, 25 °C): δ = 151.5, 139.7, 138.2, 125.9, 125.3, 48.6, 45.6, 44.4, 43.4, 43.1, 42.5. ESI-MS (m/z): Found: 223.1615 [**L3**+H]⁺ (100%), Theoretical: 223.1481 [**L3**+H]⁺.^{4, 182}

2.9.6. Preparation of 1,4,11,13-tetraaza-bis(2,6-pyridinophane)-8,17-ol (L4)

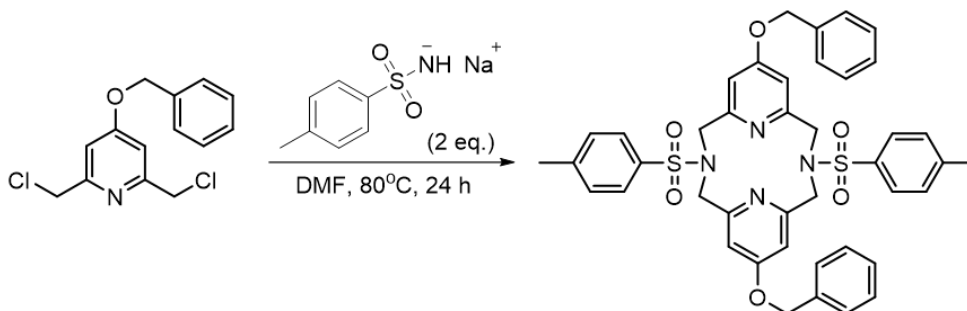
Synthesis of tosylamide monosodium salt (TsNHNa):



Scheme 2.E7. Preparation of TsNHNa salt.^{183, 185}

TsNHNa was prepared according to literature procedures.^{183, 185} Under reflux conditions solid *p*-toluenesulfonamide (60.0 g, 35 mmol) was added to freshly prepared NaOEt (23.8 g, 35 mmol) in absolute EtOH (400 mL). This mixture was stirred under reflux conditions for 2 h then cooled. The insoluble TsNHNa salt was collected via vacuum filtration and subsequently washed with absolute EtOH. The isolated white solid (TsNHNa) was dried in vacuo to give >90% yield. The tosylamide monosodium salt was used without further purification and can be stored indefinitely.^{183, 185}

Synthesis of protected 8,17-benzyloxy-4,13-bis-(*p*-toluenesulfonyl)-1,4,11,13-tetraaza-bis(2,6-pyridinophane) (2.14):

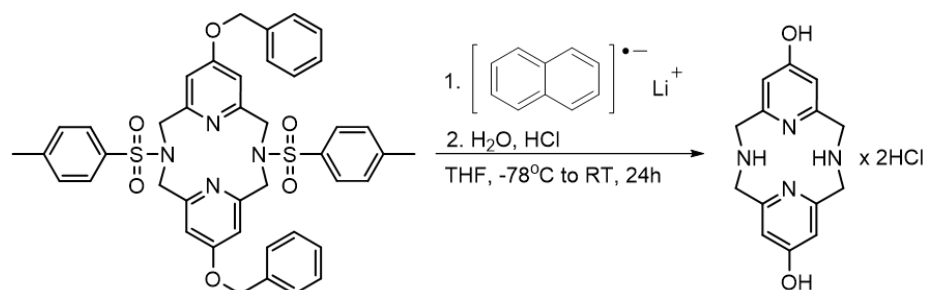


Scheme 2.E8. Synthetic methodology for the preparation of cyclized/protected L4.

1 equivalent of TsNHNa (1.93 g, 10 mmol) was dissolved in 200 mL of DMF, put under N₂, and heated to 80°C. (2.7) (2.82 g, 10 mmol) was dissolved in 50 mL of DMF and added dropwise to the above solution via addition funnel. Upon complete addition of TsNHNa, the reaction mixture was stirred for 1 hour. After 1 h, a second equivalent of TsNHNa (1.93 g, 10 mmol) was added (as a solid) to the reaction all at once. The reaction stirred for an additional 12 h at 80°C and under N₂. Upon reaction completion,

the solvent was pumped off under reduced pressure. Toluene was added to help azeotrope the mixture. When about 5 mL of the solvent remained an excess of cold methanol was added; **(2.14)** precipitated out as an off-white powder. This mixture was placed in the refrigerator for 12 h. Afterwards, the mixture was vacuum filtered and the collected solid was washed with cold methanol. **(2.14)** was isolated as an off-white powder (3.11 g, 4 mmol, 40% yield).¹⁸³⁻¹⁸⁵ Crystals suitable for X-ray analysis were obtained via solvent diffusion of DMF and CH₃OH.

Synthesis of 1,4,11,13-tetraaza-bis(2,6-pyridinophane)-8,17-ol (L4):



Scheme 2.E9. Synthetic methodology for the deprotection and isolation of **L4**.

Lithium metal (1.3 g, 187 mmol) was cautiously weighed out and cut into small pieces to expose unoxidized Li metal. These small pieces of Li were added to a flask with 150 mL of dry THF. Naphthalene (3.0 g, 23 mmol) was weighed out and added all at once to the flask. To produce the lithium naphthalenide radical the solution was stirred and then sonicated until a dark green color developed, indicating formation of the radical species. The resulting dark green solution was cooled to -78°C in a dry ice/acetone bath. **(2.14)** (2.6 g, 3.4 mmol) was dissolved in 100 mL of THF to form a brown slurry. This slurry was added dropwise to the lithium naphthalenide solution in the flask. After complete addition of **(2.14)** the reaction mixture was allowed to come up to room temperature slowly, by letting the dry ice/acetone bath evaporate. The reaction was stirred at room temperature for 12 h. Afterwards the reaction mixture was placed on ice and hydrolyzed with water, a precipitate developed, and the solution was a light brown color. Upon quenching with water, a combination of 1 M and 6 M HCl was added to the reaction until there was no longer a discernable layer between the water and THF, and no additional color change was

observed. This aqueous solution was washed several times with diethyl ether. After extraction with diethyl ether the aqueous layer was evaporated under reduced pressure until about 15 mL of solution were present. The remaining yellow solution was transferred to a falcon tube and evaporated using a lyophilizer. The resulting semi-dry solid was dissolved in a minimal amount of methanol. To this solution an excess of ether and additional methanol was added until an off-white solid precipitated out of solution. This mixture was left stirring for several hours. The solution was vacuum filtered and the collected solid was washed with diethyl ether. **L4** was isolated as an off-white solid and was characterized with ^1H and ^{13}C NMR. Yield: 0.502 g (54%). ^1H NMR (400 MHz, D_2O , 25 °C): δ = 6.54 (s, 4H), 4.38 (s, 8H); ^{13}C NMR (101 MHz, D_2O , 25°C): δ = 165.5, 151.3, 111.7, 52.1.¹⁸⁸ Electronic absorption, $\lambda_{\text{max}}/\text{nm}$ ($\epsilon/\text{M}^{-1} \text{cm}^{-1}$); H_2O : 255 (4400,sh). Elemental Analysis for **L4**; **L4**•3HCl•H₂O•CH₃OH Found (Calculated): C, 41.51 (41.73); H, 5.64 (5.84); N, 12.38 (12.98) %.

2.9.7. Preparation of [**L4Cu**Cl]₂[Cl]₂ (**L4Cu**)

L4 (42.5 mg, 0.123 mmol) was weighed out and dissolved in 5 mL of water to give a clear light-yellow solution. The pH of the ligand solution was adjusted to 5.5 using a 1.0 M solution of KOH. $\text{Cu}(\text{ClO}_4)_2 \cdot 6 \text{H}_2\text{O}$ (45.6 mg, 0.123 mmol) was subsequently weighed out and dissolved in 1 mL of H_2O . The metal solution was slowly added dropwise to the pH adjusted ligand solution to initiate the metalation. Immediately the solution color changed from light yellow to light blue; this solution stirred at room temperature, open to air, for 12 h. The reaction mixture was subsequently pumped down under reduced pressure to afford a light green solid. The solid was dissolved in a minimum amount of CH_3OH (1 mL) and a very small amount of H_2O was added (0.8 mL). Any remaining salts left undissolved were filtered out of the solution; the filtered solution was set out for crystal growth. After several days more salts precipitated out of solution, these were subsequently removed by filtration and the solutions were set out for slow evaporation crystallization again. After several cycles of filtering the solution and setting it out for slow evaporation, light green X-ray quality crystals of **L4Cu** were isolated (15.1 mg, 0.017 mmol, 28% yield).

Electronic absorption, $\lambda_{\text{max}}/\text{nm}$ ($\epsilon/\text{M}^{-1} \text{cm}^{-1}$); H₂O: 758 (23); DMF: 873 (49). Elemental Analysis for **L4Cu**; [L4Cu^{II}Cl]₂[Cl]₂•3KCl•H₂O•2CH₃OH Found (Calculated): C, 32.09 (32.19); H, 3.57 (3.78); N, 10.44 (10.01) %.

2.9.8. Preparation of [L4Zn^{II}Cl]₂[Cl]₂ (L4Zn)

L4 (37.4 mg, 0.108 mmol) was weighed out and dissolved in 5 mL of water to give a clear-light yellow solution. The pH of the ligand solution was adjusted to 5.5 using a 1.0 M solution of KOH. Zn(ClO₄)₂•6 H₂O (39.4 mg, 0.106 mmol) was subsequently weighed out and dissolved in 1 mL of H₂O. The metal solution was slowly added dropwise to the pH adjusted ligand solution to initiate the metalation. No color change occurred upon addition of the Zn(II) salt; this solution stirred at room temperature, open to air, for 12 h. The reaction mixture was subsequently pumped down under reduced pressure to afford an off-white solid. The solid was dissolved in a minimum amount of CH₃OH (1 mL) and a very small amount of H₂O was added (0.4 mL). Any remaining salts left undissolved were filtered out of the solution; the filtered solution was set out for crystal growth. After several days more salts precipitated out of solution, these were subsequently removed by filtration and the solutions were set out for slow evaporation crystallization again. After several cycles of filtering the solution and setting it out for slow evaporation, pale yellow X-ray quality crystals of **L4Zn** were isolated (7.7 mg, 0.009 mmol, 16% yield). ¹H NMR (400 MHz, D₂O, 25°C): δ = 6.44 (s, 4H), 4.60-4.68 (d, 2H), 4.31-4.27 (dd, 4H), 3.70-3.66 (dd, 4H). Elemental Analysis for **L4Zn**; [L4Zn^{II}Cl]₂[Cl]₂•KCl•CH₃CN•4CH₃OH Found (Calculated): C, 38.51 (38.49); H, 4.45 (4.85); N, 11.62 (11.88) %.

2.9.9. X-ray crystallography

A Leica MZ 75 microscope was used to identify samples suitable for analysis. A Bruker APEX-II CCD diffractometer was employed for crystal screening, unit cell determination, and data collection; which was obtained at 100 K. The Bruker D8 goniometer was controlled using the APEX3 software suite, v1.²⁰⁵ The samples were optically centered with the aid of video camera so that no translations were observed

as the crystal was rotated through all positions. The X-ray radiation employed was generated from a MoK α sealed X-ray tube ($\lambda = 0.71076$) with a potential of 50 kV and a current of 30 mA; fitted with a graphite monochromator in the parallel mode (175 mm collimator with 0.5 mm pinholes).

2.9.9.1. [C₄₂H₄₀N₄O₆S₂] (**2.14**) structure determination

Crystals of (**2.14**) suitable for X-ray analysis were obtained by solvent diffusion of DMF and CH₃OH. Solvent diffusion of this solution at 4 °C afforded a translucent colorless crystal of (**2.14**), which was mounted on a 100 μ m cryo-loop and used for X-ray crystallographic analysis. The crystal-to-detector distance was set to 50 mm, and the exposure time was 20 s per degree for all data sets at a scan width of 0.5°. A total of 1,092 frames were collected, and the data collection was 99% complete. The frames were integrated with the Bruker SAINT Software package²⁰⁶ using a narrow frame algorithm. The integration of the data used a tetragonal unit cell yielding a total of 54,710 reflections to a maximum ϑ angle of 27.57° (0.77 Å resolution) of which 4,437 reflections were independent with the $R_{\text{int}} = 37.0\%$. Data were corrected for absorption effects using the multi-scan method SADABS.²⁰⁷ Using Olex2²⁰⁸ the structure was solved with the ShelXS²⁰⁹ structure solution program using Direct Methods and refined with the SHELXL²¹⁰ refinement package using Least Squares minimization. All hydrogen and non-hydrogen atoms were refined using anisotropic thermal parameters. The thermal ellipsoid molecular plots (50%) were produced using Olex2.²⁰⁸

2.9.9.2. [L4Cu^{II}Cl]₂[Cl]₂ (**L4Cu**) structure determination

Crystals of **L4Cu** suitable for X-ray analysis were obtained by dissolving several mg of light green powder of **L4Cu** in a mixture of CH₃OH/H₂O to provide a light green solution. Slow evaporation of this solution at room temperature afforded a translucent light green block-like crystal of **L4Cu** (0.279 x 0.160 x 0.126 mm³), which was mounted on a 150 μ m cryo-loop and used for X-ray crystallographic analysis. The crystal-to-detector distance was set to 50 mm, and the exposure time was 10 s per degree for all data sets

at a scan width of 0.5°. A total of 2,180 frames were collected, and the data collection was 99% complete. The frames were integrated with the Bruker SAINT Software package²⁰⁶ using a narrow frame algorithm. The integration of the data used a monoclinic unit cell yielding a total of 45,954 reflections to a maximum ϑ angle of 30.13° (0.71 Å resolution) of which 5,217 reflections were independent with the $R_{\text{int}} = 4.99\%$. Data were corrected for absorption effects using the multi-scan method SADABS.²⁰⁷ Using Olex2²⁰⁸ the structure was solved with the ShelXS²⁰⁹ structure solution program using Direct Methods and refined with the SHELXL²¹⁰ refinement package using Least Squares minimization. All hydrogen and non-hydrogen atoms were refined using anisotropic thermal parameters. The thermal ellipsoid molecular plots (50%) were produced using Olex2.²⁰⁸

2.9.9.3. [L4Zn^{II}Cl]₂[Cl]₂ (L4Zn) structure determination

Crystals of **L4Zn** suitable for X-ray analysis were obtained by dissolving several mg of white powder of **L4Zn** in a mixture of CH₃OH/H₂O to provide a light-yellow solution. Slow evaporation of this solution at room temperature afforded a translucent light-yellow block-like crystal of **L4Zn** (0.469 x 0.244 x 0.176 mm³), which was mounted on a 150 µm cryo-loop and used for X-ray crystallographic analysis. The crystal-to-detector distance was set to 50 mm, and the exposure time was 10 s per degree for all data sets at a scan width of 0.5°. A total of 1,830 frames were collected, and the data collection was 100% complete. The frames were integrated with the Bruker SAINT Software package²⁰⁶ using a narrow frame algorithm. The integration of the data used a monoclinic unit cell yielding a total of 45,536 reflections to a maximum ϑ angle of 30.10° (0.71 Å resolution) of which 5,341 reflections were independent with the $R_{\text{int}} = 2.85\%$. Data were corrected for absorption effects using the multi-scan method SADABS.²⁰⁷ Using Olex2²⁰⁸ the structure was solved with the ShelXS²⁰⁹ structure solution program using Direct Methods and refined with the SHELXL²¹⁰ refinement package using Least Squares minimization. All hydrogen and non-hydrogen atoms were refined using anisotropic thermal parameters. The thermal ellipsoid molecular plots (50%) were produced using Olex2.²⁰⁸

2.9.10. Electrochemical measurements

Cyclic voltammetry (CV) was carried out with an EC Epsilon potentiostat (C-3 cell stand) purchased from BASi Analytical Instruments (West Lafayette, IN). A glassy carbon (GC) electrode from BASi (MF-2012), 3 mm in diameter was polished on a white nylon pad (BASi MF-2058) with different sized diamond polishes (15, 6, 1 μm) to ensure a mirror-like finish. Between each measurement, the GC electrode was polished with the three diamond polishes. A three-electrode cell configuration was used with GC as the working electrode, an Ag wire (0.5 mm dia.) quasi reference electrode housed in a glass tube (7.5 cm x 5.7 mm) with a Porous CoralPor™ tip, and a Pt wire (7.5 cm) as the counter electrode (BASi MW-1032). All solutions were bubbled with nitrogen gas for at least 15 min. prior to experimentation and were kept under a humidified nitrogen gas blanket. All potentials in this chapter are reported vs. Fc/Fc^+ ($E_{1/2} = 0 \text{ V}$). For each electrochemical analysis, 3.0 mg of each complex was dissolved in 3.0 mL of anhydrous DMF containing 0.1 M tetrabutylammonium perchlorate (TBAP) as the supporting electrolyte.

2.9.11. Equilibrium measurements

The chemicals (MCl_2 salts) used in these studies were of the highest analytical grade obtained from Millipore Sigma, Alfa Aesar, or Strem Chemicals Inc. companies. The concentration of the stock solutions ($\approx 50 \text{ mM}$) was determined by complexometric titration using a standardized $\text{Na}_2\text{H}_2\text{EDTA}$ solution and appropriate indicators. Eriochrome Black T (CaCl_2 , MnCl_2 , and ZnCl_2), xylenol orange (CoCl_2), 4-(2-pyridylazo)resorcinol (known as PAR) (CuCl_2), and murexide (NiCl_2).²¹¹

The pH-potentiometric titrations were carried out with a Metrohm 888 Titrando titration workstation, using a Metrohm 6.0234.100 combined electrode. The titrated solutions (6.00 mL) were thermostated at 25 °C, and samples were stirred and kept under an inert gas atmosphere (N_2) to avoid the effect of CO_2 . The calibration of the electrode was performed using a two-point calibration with KH-phthalate (pH = 4.005) and borax (pH = 9.177) buffers.

The concentration of the $H_4L_4^{2+}$ (where L_4 represents **L4**) was determined by pH-potentiometric titration. The protonation constants of L_4^{2-} and the stability and protonation constants of Mn(II), Zn(II), Co(II), and Ca(II) complexes were also determined by pH-potentiometric titration. The metal-to-ligand concentration ratios were 1:1 (the concentration of the ligand was generally 2-3 mM). In the pH-potentiometric titrations 200 – 360 mL:pH data pairs were recorded in the pH range of 1.6 – 12.0. The calculation of $[H^+]$ from the measured pH values was performed with the use of the method proposed by Irving *et al.*²¹² by titrating a 0.01 M HCl solution ($I = 0.15$ M NaCl) with a standardized NaOH solution. The differences between the measured (pH_{read}) and calculated pH ($-\log [H^+]$) values were used to obtain the equilibrium H^+ concentrations from the pH data obtained in the titrations. The ion product of water was determined from the same experiment in the pH range of 11.8-12.0. The protonation and stability constants were calculated from the titration data with the HYPERQUAD program.²¹³

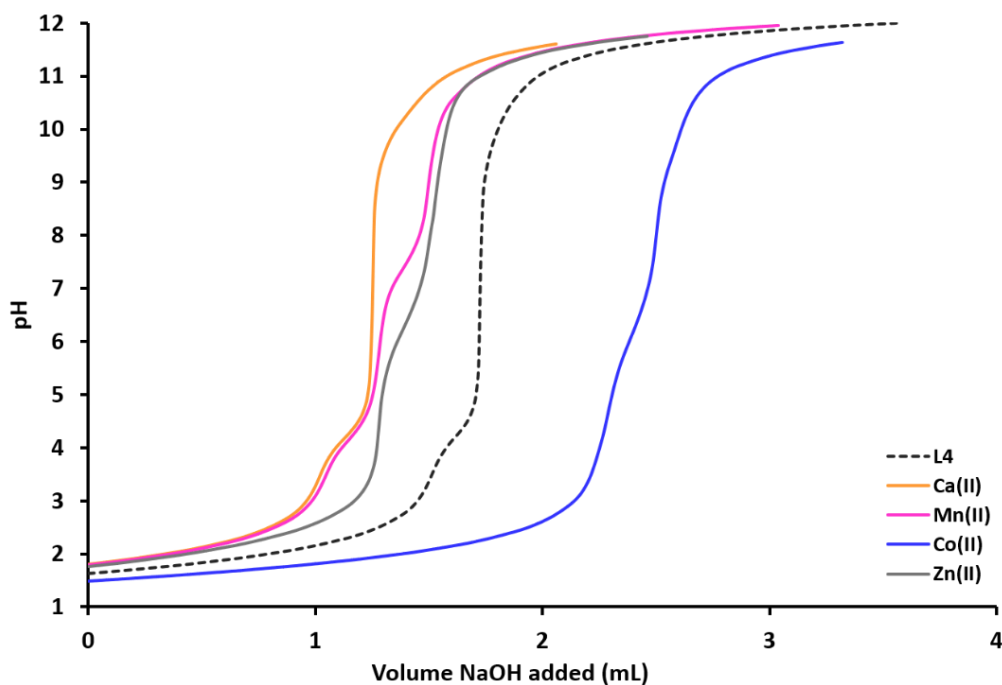


Figure 2.E1. pH-potentiometric titration curves of **L4** with and without the presence of an M(II) transition metal (Ca(II), Mn(II), Co(II), and Zn(II)). ($I = 0.15$ M NaCl, $T = 25$ °C).

2.9.12. DPPH radical quenching assay

A stock solution of the DPPH radical was prepared by dissolving 25.0 mg in 100 mL of absolute ethanol. The working radical solution was prepared by dilution with absolute EtOH to an absorbance of 1.3 ± 0.002 units at 515 nm. A solid sample of **L1**, **L2**, **L4**, or butylated hydroxytoluene (BHT) were dissolved in 10 mL of 95% EtOH, to an initial concentration of 5 mM and then diluted to 1 mM. Next, the stock solutions (1 mM) containing **L1**, **L2**, **L4** and BHT (positive control) were diluted in a series with 95% EtOH to obtain working concentrations ranging from 1000 μL to 0.112 μL . The serial dilutions were done by taking 5 mL of the preceding sample and 5 mL of the 95% EtOH. The blank used was 1 mL absolute EtOH + 1 mL 95% EtOH. Each final sample for analysis was prepared by mixing 2 mL of **L1**, **L2**, **L4** or BHT with 2 mL of the DPPH radical solution to obtain the final concentrations (500 μL , 250 μL , 125 μL , 62.5 μL , 31.25 μL , 15.625 μL , 7.81 μL , 3.91 μL , 1.95 μL , 0.977 μL , 0.488 μL , 0.244 μL , 0.122 μL , and 0.061 μL). An aliquot of the DPPH stock solution (2 mL) was mixed with 95% EtOH (2 mL) and was used as a negative control. The samples were incubated in the dark for 24 h, at room temperature. For analysis, 1 mL of each sample and 1 mL of absolute ethanol were transferred to a 3-mL quartz cuvette, and the absorbance at 515 nm of each sample was measured on an 8453 UV-vis spectrophotometer (Agilent). Each experiment was performed in triplicate ($n = 3$). The final absorbance values have been normalized to the average ($n = 3$) absorbance of the negative control DPPH sample and are expressed as the % DPPH radical remaining in solution.

2.9.13. CCA redox cycling assay

All solutions were prepared in $\text{KH}_2\text{PO}_4/\text{NaCl}$ (1X) buffer containing Desferal [$1 \mu\text{M}$]^{171, 214} except $\text{CuSO}_4 \cdot 6\text{H}_2\text{O}$, which was dissolved and diluted in Milli-Q water. Final sample volume = 3 mL. Each experiment was performed in triplicate ($n = 3$). Hydroxyl radical production was followed by measuring the conversion of CCA into 7-hydroxy-CCA ($\lambda_{\text{ex}} = 395 \text{ nm}$, $\lambda_{\text{em}} = 450 \text{ nm}$). General order of addition: CCA [$100 \mu\text{M}$], molecule **L2** or **L4** ($\frac{1}{2}$ eq. = $5 \mu\text{M}$; 1 eq. = $10 \mu\text{M}$), or Cu(II) [$10 \mu\text{M}$], then ascorbate [$300 \mu\text{M}$].

2.9.14. Cell studies

Mouse hippocampal cells (HT-22) and breast cancer cells (MCF-7) were grown in Dulbecco's Modified Eagle's Medium-high glucose (DMEM) supplemented in 10% fetal bovine serum (Sigma) and penicillin (10 μ /mL)/streptomycin (0.1 mg/mL) (Sigma), 2 mM glutamine (Sigma) and MEM non-essential amino acids (1x) (Sigma), at 37 °C, 5% CO₂, 95% air.

Cytotoxicity studies were carried out using the MTT assay. Briefly, cells were plated at a density of 5000 cells per well in a 96 well tray. Following the overnight incubation, the cells were treated with the indicated concentrations of drug and further incubated for 16 hours under normal growing conditions. Following this, the medium and drug were removed and 100 μ L per well of MTT (Thiazolyl Blue Tetrazolium Bromide, Sigma) was added at a concentration of 1 mg/mL in serum-free DMEM. Cells were incubated in this solution for 4 hours under normal growing conditions. Next, the MTT solution was removed and the precipitate generated was solubilized in 100 μ L of 100% DMSO for 5 min., RT, whilst shaking. The absorbance was measured at 540 nm in an Omega FLUOstar microplate reader (BMG Labtech). Results are presented as the average of 8 replicates per concentration of drug. GraphPad Prism was used to calculate EC₅₀ values and generate the graphs shown at the end of chapter 2.

2.9.15. Experimental acknowledgements

We would like to thank Dr. Akkaraju and Olivia Kinsinger for running the cell cytotoxicity studies. Thank you to Kristof Póta for running some of the pH-potentiometric titrations and generating protonation and stability constants for **L4** as well as the species distribution diagrams. Thank you to Dr. Gyula Tircsó and his group for running pH-potentiometric titrations of **L1-L3**. Additionally, we would like to thank Maddie Barnett for running both the DPPH and CCA assays.

Chapter 3: Spectroscopic and solid state evaluations of tetraazamacrocyclic cobalt complexes with parallels to the classic cobalt(II) chloride equilibrium

3.1. Introduction

From crown ethers to N-heterocyclic amines, macrocycles are integral to the field of coordination chemistry, and can bind to a multitude of transition metal ions.²¹⁵ Along with having a variety of donor atoms, these ligands have a range of sizes. The smallest macrocycles have as few as 3 donor atoms forming rings with 9 atoms in the macrocycle, while larger macrocycles can have as many as 11 donor atoms forming rings with 33 atoms.²¹⁵ However, more common examples are synthetic 12- to 16-membered rings which are often utilized to mimic biologically important and naturally occurring macrocycles, such as porphyrins and corrins.^{5, 55, 215-219} The vast array of macrocyclic transition metal complexes have numerous potential uses; applications range from use as biomimetic models, therapeutic agents, and catalysts in various organic reactions.^{5, 55, 215-223} The kinetic and thermodynamic stabilities of these diverse ligands have played a large role in their popularity within the fields of inorganic and bioinorganic chemistry. Macrocyclic complexes exhibit enhanced kinetic and thermodynamic stability when compared to noncyclic analogues; Margerum and Cabiness term this large increase in stability the *macrocyclic effect*.^{31, 215, 217, 220, 223} The large number and inherent stability of complexes derived from macrocycles have made these ligands ubiquitous in the field of coordination chemistry, as described in chapter 1.

Transition metal ions incorporated in the Irving-Williams series, based on the increasing stability of metal complex formed, (Mn(II) < Fe(II) < Co(II) < Ni(II) < Cu(II) > Zn(II)) are particularly popular choices for forming macrocyclic metal complexes.²⁰⁰ The Green group has explored the complexes of Fe(III), Ni(II), Cu(II), and Zn(II) with 12-membered pyridine- and pyridol- containing tetraazamacrocycles; these complexes have been characterized and studied in depth.^{55-56, 62, 85-86} In continuation with the studies on macrocyclic complexes of first-row late transition metal ions, a fundamental characterization of 12-membered pyridine-containing tetraaza macrocyclic cobalt(III) complexes has been conducted.⁶²

Surprisingly, cobalt(III) complexes with 12-membered tetraazamacrocycles are not prevalent in the literature, but there are a few examples.^{220, 224-225} The majority of the chemical literature is dominated by 12-membered Co(II) tetraaza macrocyclic complexes or planar 14-membered Co(II)/Co(III) tetraaza macrocyclic complexes.^{5, 216, 219, 221-222, 226-227} Although examples of Co(III) tetraaza macrocyclic complexes are sparse, there are many Co(II)/Co(III) coordination complexes derived from monodentate and open chain chelates that are both historically significant and ubiquitous in chemical literature.²²⁵ Several examples include, historically significant 'Werner' complexes; the in-depth analysis of these Co(III) complexes by Alfred Werner (for whom they are named) led to the development of the field of coordination chemistry.^{29, 228}

3.1.1. Werner complexes: the foundation of coordination chemistry

Before the development of Werner's coordination theory, inorganic chemists tried to explain bonding in coordination compounds using existing theories for organic molecules and salts.²⁹ Unfortunately, all other previously established theories fell short of explaining the bonding within coordination compounds. For an example complex, hexaamminecobalt(III) chloride ($[\text{Co}(\text{NH}_3)_6]\text{Cl}_3$), some early theories only allowed three atoms to be attached to the Co(III) center due to its 'valence' (charge) of 3.²⁹ Blomstrand and Jørgensen theorized that the nitrogen atoms could form chains and that the chloride ions bound directly to the Co(III) were more strongly bound than the chloride ions bonded to the nitrogen atoms; this theory is aptly named 'Blomstrand's Chain Theory'.^{29, 229-230} In contrast, Werner hypothesized that all six of the ammonia molecules were bound directly to the Co(III) center and that the chloride ions were bound more 'loosely' (which we now know are independent ions).^{29, 231-236} Table 3.1 shows a comparison of the two theories for various cobalt complexes.²⁹ Blomstrand's chain theory predicts the dissociation of chloride ions attached to ammonia, but not those attached to cobalt.^{29, 229-230} Similarly, Werner's coordination theory consisted of two types of chloride ions; those attached directly to the Co(III) and the 'other chlorides', which were less firmly bound to permit dissociation. From table 3.1,

it can be observed that except for the last entry both theories predict the same number of ions upon dissociation. Werner and Jørgensen debated their two theories for years.²⁹ Ultimately, their debate forced Werner to develop his theory more fully, because Jørgensen staunchly defended his chain theory.²⁹

Table 3.1. Comparison of Blomstrand's Chain Theory and Werner's Coordination Theory.

Werner Formula (modern form)	Number of ions predicted	Blomstrand Chain Formula	Number of ions predicted
$[\text{Co}(\text{NH}_3)_6]\text{Cl}_3$	4		4
$[\text{Co}(\text{NH}_3)_5\text{Cl}]\text{Cl}_2$	3		3
$[\text{Co}(\text{NH}_3)_4\text{Cl}_2]\text{Cl}$	2		2
$[\text{Co}(\text{NH}_3)_3\text{Cl}_3]$	1		2

*The italicized chlorides dissociate in solution, according to the two theories.²⁹

Eventually, Werner proposed octahedral structures for such compounds as $[\text{Co}(\text{NH}_3)_4\text{Cl}_2]^+$ and $[\text{Co}(\text{en})_2\text{Cl}_2]^+$ (en = ethylenediamine) (Figure 3.1(a)).^{29, 228, 231-236} He synthesized many isomers of coordination compounds, such as green and violet isomers of $[\text{Co}(\text{en})_2\text{Cl}_2]^+$.^{29, 228} Werner claimed that within these two isomers of $[\text{Co}(\text{en})_2\text{Cl}_2]^+$ the chloride ions were arranged *cis* and *trans* to one another (Figure 3.1(a)).²⁹ Jørgensen tried to offer alternative isomeric structures using his chain theory, but finally had to accept Werner's coordination theory in 1907. Blomstrand and Jørgensen's chain theory could not account for two different isomers with the same compound formula.^{29, 229-230}

Although Werner had convinced Jørgensen of his coordination theory and the existence of optically active, carbon-free, coordination complexes, other chemists were weary to accept it.²⁹ Some scientists suspected that the chirality of Werner's isomeric complexes was due to undetected carbon

atoms.²⁹ Finally, Werner was able to validate his hypothesis by separating a racemic mixture of $[\text{Co}(\text{Co}(\text{NH}_3)_4(\text{OH})_2)_3]\text{Br}_6$ into two optically active isomers (Figure 3.1(b)).^{29, 228} The definitive proof of an optically active coordination complex without the presence of carbon allowed Werner's coordination theory to finally be accepted by the scientific community.^{29, 228}

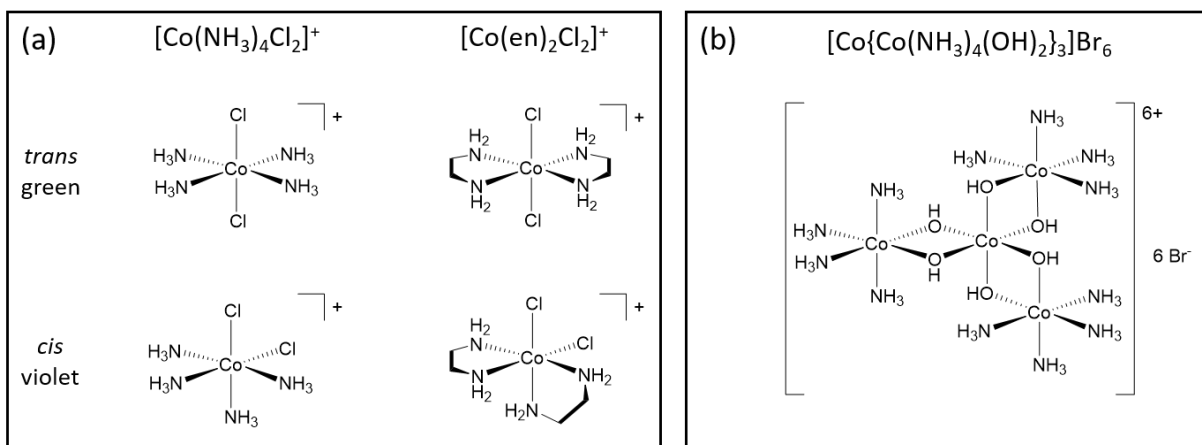


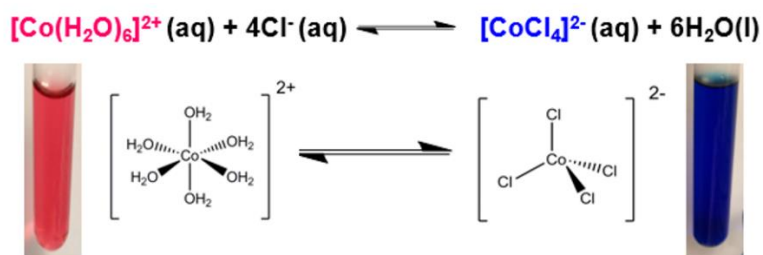
Figure 3.1. (a) *cis* and *trans* isomers of Werner complexes; (b) Werner's carbon-free optically active compound.^{29, 228}

Werner's study of Co(III) complexes ultimately led to the development modern coordination chemistry.^{29, 228, 231-236} He proposed that in a coordination compound up to six ligands could be attached to the metal center, forming an octahedron; this was in opposition to Blomstrand and Jørgensen's previously established chain theory.²²⁹⁻²³⁰ Some slight updates to Werner's coordination theory have been applied, but ultimately his theory of coordination compounds is still in use today.

3.1.2. Illustration of Le Châtelier's Principle using the classic CoCl_2 equilibrium

When new macrocycles are synthesized, the complexes formed with Co(II)/Co(III) ions can be compared to classic coordination compounds, (such as the Co(III) Werner complexes described above) in order to delineate the observed reactivity.²²⁵ A specific example of a classic Co(II) coordination complex (in contrast to the Co(III) containing Werner complexes) is the equilibrium between pink cobalt(II) hexahydrate and blue cobalt(II) tetrachloride (Scheme 3.1); this well-characterized demonstration is often used to illustrate Le Châtelier's Principle.²³⁷⁻²⁴³ Le Châtelier's Principle states that when a chemical system

at equilibrium is disturbed, the system shifts in a direction to minimize the disturbance.²⁴⁴ This principle is visualized by the introduction of different ‘disturbances’ that cause a shift between two different colored Co(II) species in aqueous solution. When CoCl₂ is dissolved in water, it forms cobalt(II) hexahydrate ([Co(H₂O)₆]²⁺), which is characteristically pink-red in color. Pink cobalt(II) hexahydrate can be converted into cobalt(II) tetrachloride ([CoCl₄]²⁻) (which is characteristically dark-blue) by shifting the equilibrium to the favor Co(II) tetrachloride formation. The equilibrium between these two species can easily be shifted by changing concentration, temperature, solvent, etc. For example, addition of excess chloride ions (in the form of HCl) to an aqueous solution of [Co(H₂O)₆]²⁺ ions shifts the equilibrium to the right, forming blue [CoCl₄]²⁻ ions. The stark color difference of the pink [Co(H₂O)₆]²⁺ vs. blue [CoCl₄]²⁻ allows for easy visualization of the equilibrium shift between the two species, which is why this reaction has been utilized frequently to demonstrate Le Châtelier’s Principle.



Scheme 3.1. Equilibrium reaction between cobalt(II) hexahydrate and cobalt(II) tetrachloride used to demonstrate Le Châtelier’s Principle.^{237, 239-243, 245}

3.1.3. Macrocyclic Co(III) complexes with parallels to the classic CoCl₂ equilibrium

Through solid state and spectroscopic methods, the characterization of the 12-membered tetraaza macrocyclic Co(III) compounds, provided solution behavior like the classic CoCl₂ equilibrium demonstration. The color change in organic vs. aqueous solvents, as well as the presence of a cobalt metal center, led to the examination of the classic CoCl₂ equilibrium to determine if there were any parallels to the Green group ligand systems.²³⁷⁻²⁴³

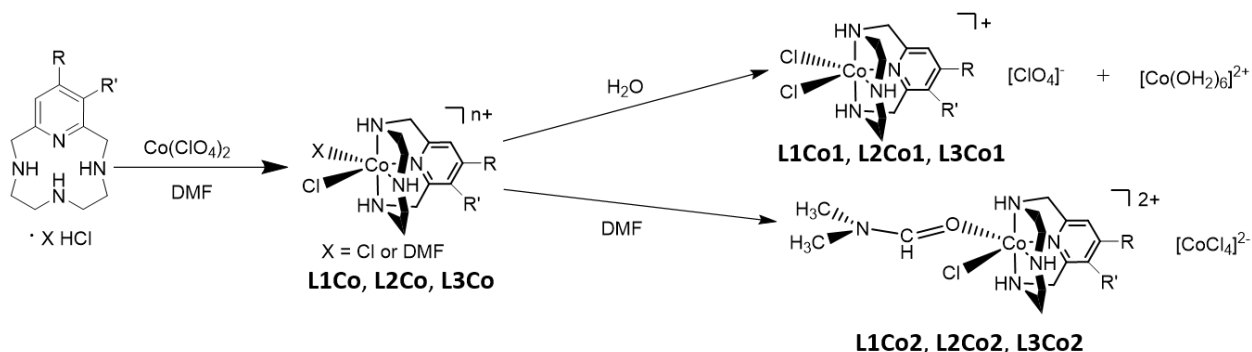
Electronic absorption spectra of CoCl_2 in both water and DMF lead to an important parallel that helped to confirm our system was undergoing a similar equilibrium in these two solvents. Electronic absorption spectroscopy and X-ray diffraction measurements were obtained to further investigate this phenomenon. Through this work, it was observed that solvent choice could be used to produce two derivatives of **L1Co**, **L2Co**, and **L3Co** (**L1Co1/L1Co2**; **L2Co1/L2Co2**; **L3Co1/L3Co2**). Depending on solvent choice one of the *cis*-bound ligands of complex (**L1Co**, **L2Co**, or **L3Co**) changes (Cl^- or DMF) as well as the overall complex charge (+1 or +2) and counter-ion ($[\text{ClO}_4]^-$ or $[\text{CoCl}_4]^{2-}$). The spectroscopic and solid state characteristics of these systems and the parallels to the classic CoCl_2 demonstration used to illustrate Le Châtelier's principle will be discussed.

In addition to fundamental characterization, ion exchange reactions were performed on **L1Co**, **L2Co**, and **L3Co**. Chloride ions present when the ligand is isolated as an HCl salt were exchanged using AgBF_4 , to prevent formation of a $[\text{CoCl}_4]^{2-}$ counter-ion during metalation. Upon isolation, the ion-exchanged cobalt complexes **L1Co3**, **L2Co3**, and **L3Co3** were tested as catalysts in several C-C coupling reactions.

3.2. Synthesis of **L1Co**, **L2Co**, and **L3Co** and equilibrium behavior in organic and aqueous solvents

Complexation between cobalt(II) perchlorate hexahydrate and the hydrochloride salt of **L1**, **L2**, **L3** in DMF yielded $[\text{L1Co}^{\text{III}}\text{ClX}]^{n+}$ (**L1Co**), $[\text{L2Co}^{\text{III}}\text{ClX}]^{n+}$ (**L2Co**), and $[\text{L3Co}^{\text{III}}\text{ClX}]^{n+}$ (**L3Co**) ($\text{X} = \text{Cl}^-$ or DMF; $n = 1$ or 2) (Scheme 3.2). Upon addition of the ligand to the stirred $\text{Co}(\text{ClO}_4)_2 \cdot 6\text{H}_2\text{O}$ solution, the color changed immediately from bright pink to deep blue (Figure 3.2). After reaction completion, **L1Co**, **L2Co**, and **L3Co** were isolated as light blue or purple solids. In order to characterize these ligand-cobalt complexes, **L1Co**, **L2Co**, and **L3Co** were dissolved in several different solvents, including DMF and water. Upon complex dissolution in DMF, the solutions remained blue in color. Conversely, when the complexes were dissolved in water, the resulting solutions were pink. The observed color changes suggested the cobalt coordination

was modified in DMF vs. H₂O solutions. Electronic absorption spectroscopy was utilized to further investigate this phenomenon in solution.



Scheme 3.2. Synthesis of **L1Co**, **L2Co**, and **L3Co**; equilibrium of **L1Co1/L1Co2**, **L2Co1/L2Co2**, and **L3Co1/L3Co2** in aqueous and organic solvents (**L1**: R = H, R' = H; **L2**: R = OH, R' = H; **L3**: R = H, R' = OH).

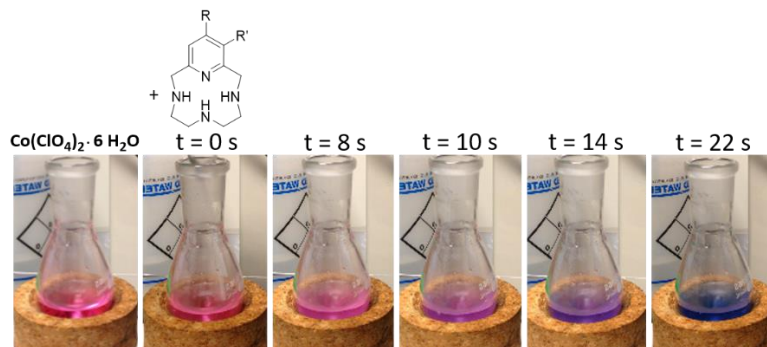


Figure 3.2. Images of the complexation reaction of Co(II) + ligand in DMF. Co(ClO₄)₂ is bright pink when dissolved in DMF, upon addition of **L1**, **L2**, or **L3** the solution color changes to deep blue (**L1**: R = H, R' = H; **L2**: R = OH, R' = H; **L3**: R = H, R' = OH).

3.3. Electronic absorption spectroscopy of **L1Co**, **L2Co**, and **L3Co**

The electronic absorption spectra of **L1Co**, **L2Co**, and **L3Co** were measured in DMF and H₂O to investigate the color changes observed upon complex dissolution (Figure 3.3). The following discussion focuses on (**L1Co**), but similar results were obtained for (**L2Co**) and (**L3Co**) (Figure 3.3). A comparison of the spectra in DMF vs. H₂O confirmed that cobalt coordination was dependent upon the nature of the solvent (i.e. organic vs. aqueous). For instance, in H₂O, the solution of (**L1Co**) is bright pink and contains two absorbance bands at 376 and 535 nm (Figure 3.4(b), Table 3.2). When **L1Co** is dissolved in H₂O the solution is bright pink and it exists as **L1Co1** ([**L1Co**^{III}Cl₂][ClO₄]) and cobalt(II) hexahydrate. Whereas, when

L1Co is dissolved in DMF the solution is deep blue and it exists as **L1Co2** ($[\text{L1Co}^{\text{III}}\text{Cl}(\text{DMF})][\text{Co}^{\text{II}}\text{Cl}_4]$). The following spectroscopic results support these assignments.

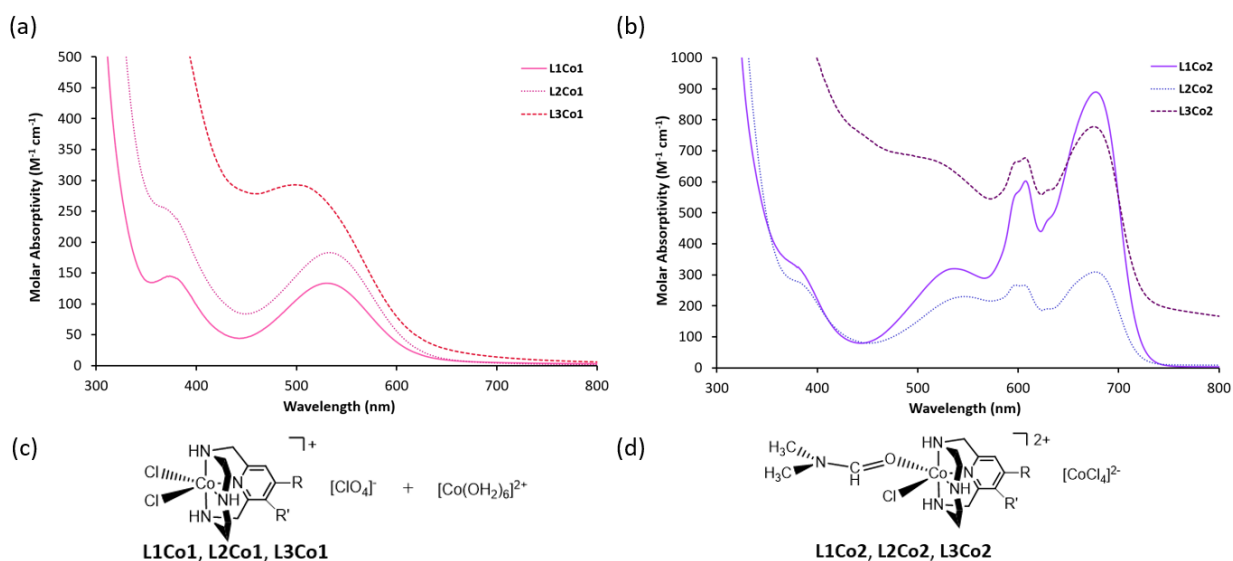


Figure 3.3. Comparison of the electronic absorption spectra of (a) **L1Co1**, **L2Co1**, and **L3Co1** with (b) **L1Co2**, **L2Co2**, and **L3Co2** in water vs. DMF. The observed species in (a) and (b) are noted in (c) and (d), respectively (**L1**: R = H, R' = H; **L2**: R = OH, R' = H; **L3**: R = H, R' = OH).

Most known octahedral cobalt(III) complexes are diamagnetic and have a ground state of $^1A_{1g}$. The visible absorption spectra of these octahedral cobalt(III) complexes consist of two spin allowed transitions, $^1A_{1g} \rightarrow ^1T_{1g}$ and $^1A_{1g} \rightarrow ^1T_{2g}$.^{30, 202, 246-247} In a perfectly symmetric octahedral complex $[\text{Co}^{\text{III}}\text{X}_6]$, there is no splitting observed in the $^1A_{1g} \rightarrow ^1T_{1g}$ transition, but in asymmetric octahedral complexes $[\text{Co}^{\text{III}}\text{X}_4\text{Y}_2]$ there can be splitting of the $^1T_{1g}$ state.³⁰ The magnitude of $^1T_{1g}$ splitting is dependent upon the nature of $[\text{Co}^{\text{III}}\text{X}_4\text{Y}_2]$, which can exist in both the *cis* and *trans* configurations.³⁰ *Trans*- $[\text{Co}^{\text{III}}\text{X}_4\text{Y}_2]$ complexes have large splitting in the $^1T_{1g}$ state, resulting in an electronic absorption spectrum with three absorbance bands.^{30, 202} In contrast, *cis*- $[\text{Co}^{\text{III}}\text{X}_4\text{Y}_2]$ complexes have a lesser degree of splitting in the $^1T_{1g}$ state, resulting in only two observed absorbance bands, with one absorbance band being slightly asymmetric in shape.^{30, 202} **L1Co1** has a geometry consistent with a *cis*- $[\text{Co}^{\text{III}}\text{X}_4\text{Y}_2]$ complex. In water, the absorption band at 376 nm is assigned to the higher energy transition, $^1A_{1g} \rightarrow ^1T_{2g}$. The absorption band observed at 535 nm is assigned to the lower energy transition, $^1A_{1g} \rightarrow ^1T_{1g}$.

In DMF, the solution of **L1Co2** is deep blue with a shoulder at 380 nm, and two absorbance bands at 535 and 680 nm. The lower energy absorbance at 680 nm has multiple shoulders due to spin-orbit coupling (Figure 3.4(b), Table 3.2). The absorbance bands at 380 nm and 535 nm can once again be assigned to the transitions ${}^1A_{1g} \rightarrow {}^1T_{2g}$ and ${}^1A_{1g} \rightarrow {}^1T_{1g}$, respectively, of the octahedral diamagnetic Co(III) complex. Upon careful examination of the additional absorbance band (680 nm), it was determined that it resembled the spectrum of a cobalt(II) chloride species in solution.^{238, 243} The electronic absorption spectrum of cobalt(II) chloride hexahydrate was obtained under the same experimental conditions (Figure 3.4(a)) because of this intriguing similarity of the absorbance band to **L1Co2** in DMF solution. It is established that cobalt(II) chloride dissolved in H₂O, or aqueous solvents, exists as the complex ion, cobalt(II) hexahydrate. Alternatively, when cobalt(II) chloride is dissolved in DMF (or organic solvents) it exists as cobalt(II) tetrachloride. Expectedly, the cobalt(II) chloride dissolved in DMF exhibited a complex absorbance band at 680 nm; this solution behavior is consistent with a cobalt(II) tetrachloride ion present in solution^{238, 243}; this absorbance band is in agreement with the higher energy band observed in the spectrum of the deep blue DMF solution containing **L1Co2**.

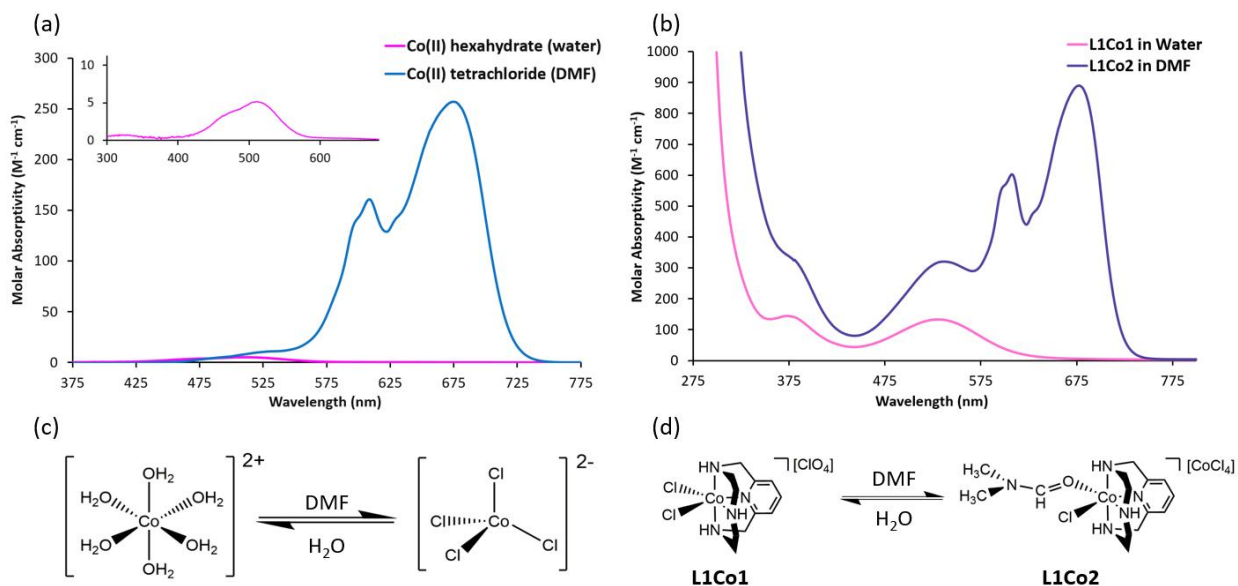


Figure 3.4. Comparison of the electronic absorption spectra of (a) CoCl₂ and (b) **L1Co1** and **L1Co2** in DMF vs. water. The conversion process observed for (a) and (b) are noted in (c) and (d), respectively.

Table 3.2. Electronic absorption bands and transition assignment for L1Co in DMF and H ₂ O, $\lambda_{\text{max}}/\text{nm}$ ($\epsilon/\text{M}^{-1} \text{cm}^{-1}$)			
DMF	Transitions in DMF	H ₂ O	Transitions in H ₂ O
380 (236)	O _h Co(III): $^1A_{1g} \rightarrow ^1T_{2g}$	376 (144)	O _h Co(III): $^1A_{1g} \rightarrow ^1T_{2g}$
535 (320)	O _h Co(III): $^1A_{1g} \rightarrow ^1T_{1g}$	535 (133)	O _h Co(III): $^1A_{1g} \rightarrow ^1T_{1g}$
680 (886)	T _d Co(II): $^4A_2 \rightarrow ^4T_1(P)$	530 (5)	O _h Co(II): $^4T_{1g}(F) \rightarrow ^4T_{1g}(P)$

The cobalt(II) tetrachloride ion has been well characterized using electronic absorption spectroscopy.^{30, 202, 238, 246-247} Because this complex has a tetrahedral geometry, with no center of symmetry, the absorption transitions are able to overcome LaPorte selection rules, resulting in very intense absorbance bands when compared to the octahedral cobalt(II) hexahydrate complex.²⁹ Assigning transitions for cobalt(II) tetrachloride can be somewhat difficult. In the visible region, the absorbance band that encompasses 680 nm can be assigned to the highest energy transition $^4A_2 \rightarrow ^4T_1(P)$.^{30, 202, 247} This absorbance band is very complex, (containing multiple shoulders and peaks) due to other transitions to doublet excited states that occur in the same region of wavelengths.^{30, 202}

Based on the parallel between the electronic absorption spectra of CoCl₂ and **L1Co** it was postulated that the DMF solution (Figure 3.4(b)) contained **L1Co2** with [Co^{II}Cl₄]²⁻ and the H₂O solution contained **L1Co1** with [Co^{II}(OH₂)₆]²⁺. EPR methods were in agreement with a 4-coordinate Co(II) in DMF and six coordinate Co(II) in water as well (Figure 3.E1). Solid state methods were employed to verify this hypothesis and determine the exact nature of the cobalt coordination sphere.

3.4. Solid state evaluation of **L1Co1**, **L2Co1**, **L3Co1**, and **L1Co2**

Following spectroscopic evaluation, crystallizations of **L1Co**, **L2Co**, and **L3Co** were carried out separately in H₂O and DMF yielding X-ray quality crystals of **L1Co** (**L1Co1** and **L1Co2**), **L2Co** (**L2Co1**), and **L3Co** (**L3Co1**), respectively (Figure 3.5). Although there were multiple attempts to grow crystals of **L2Co** and **L3Co** in both H₂O in DMF, only crystals of **L2Co** and **L3Co** grown from H₂O were suitable for XRD analysis. Two crystal growth methods were used in order to continue the investigation of how solvent type changed cobalt coordination. Through evaluation of the solid state structure, the exact nature of the cobalt coordination sphere was identified.

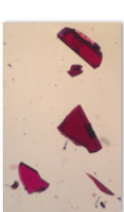
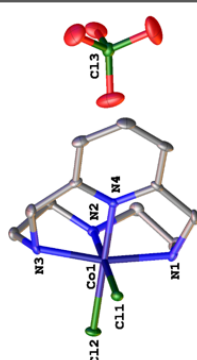
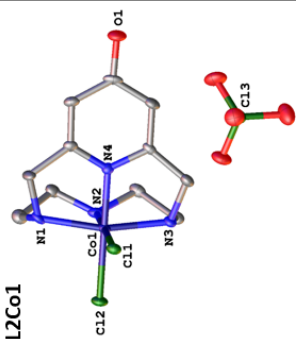
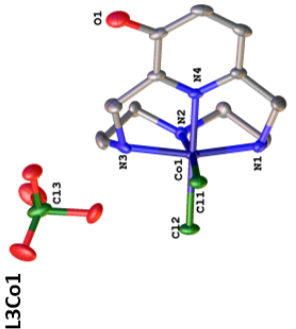
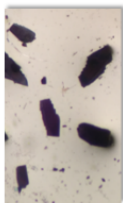
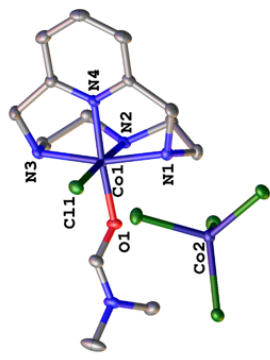
(a)	<p>[L1Co^{III}Cl₂][ClO₄] (L1Co1), [L2Co^{III}Cl₂][ClO₄] (L2Co1), and [L3Co^{III}Cl₂][ClO₄] (L3Co1)</p> 	<p>Crystal growth method: slow evaporation of water</p> <p>L1Co1</p>  <p>L2Co1</p>  <p>L3Co1</p> 
(b)	<p>[L1Co^{III}Cl(DMF)][Co^{II}Cl₄] (L1Co2)</p> 	<p>Crystal growth method: vapor diffusion of DMF/ether</p> <p>L1Co2</p> 

Figure 3.5. Comparison of L1Co1, L2Co1, L3Co1, and L1Co2 growth methods, crystal morphology, and solid state structures (ORTEP views 50% probability; hydrogen atoms were omitted for clarity).

Table 3.3. Crystal data, intensity collections, and structure refinement parameters for **L1Co1**, **L2Co1**, **L3Co1**, and **L1Co2**

Complex	L1Co1	L2Co1	L3Co1	L1Co2
Simplified formula	[L1Co ^{III} Cl ₂] ₃ [ClO ₄] ₃	[L2Co ^{III} Cl ₂] ₂ [ClO ₄][Cl]	[L3Co ^{III} Cl ₂][ClO ₄]	[L1Co ^{III} Cl(DMF)][Co ^{III} Cl ₄]
Empirical formula	C ₃₃ H ₅₄ Cl ₉ Co ₃ N ₁₂ O ₁₂	C ₂₂ H ₃₆ Cl ₆ Co ₂ N ₈ O ₆	C ₁₁ H ₁₈ Cl ₃ CoN ₄ O _{5.22}	C ₁₄ H ₂₅ Cl ₅ Co ₂ N ₅ O
Formula weight	1306.72	839.16	455.05	574.50
Temperature/K	100.0	100.0	100.0	100.0
Crystal system	Monoclinic	Monoclinic	Monoclinic	Orthorhombic
Space group	P2 ₁ /c	P2 ₁ /c	P2 ₁ /c	Pbca
a/Å	6.9187(9)	6.8468(4)	6.8377(3)	13.042(2)
b/Å	26.505(4)	18.3028(13)	13.1085(7)	16.735(3)
c/Å	25.212(3)	28.2684(17)	17.9970(9)	20.520(4)
α/°	90	90	90	90
β/°	94.664(4)	94.762(5)	91.150(2)	90
γ/°	90	90	90	90
Volume/Å ³	4608.1(10)	3530.2(4)	1612.78(14)	4478.7(14)
Z	4	4	4	8
ρ _{calc} /g/cm ³	1.884	1.5788	1.874	1.704
μ/mm ⁻¹	1.664	1.441	1.595	2.093
F(000)	2664.0	1718.9	927.0	2328.0
Crystal size/mm ³	0.303 × 0.262 × 0.101	0.165 × 0.144 × 0.084	0.176 × 0.077 × 0.073	0.464 × 0.272 × 0.086
Radiation	Mo Kα (λ = 0.71073)	Mo Kα (λ = 0.71073)	Mo Kα (λ = 0.71073)	Mo Kα (λ = 0.71073)
2θ range for data collection/°	5.754 to 77.27	4.68 to 50.5	6.616 to 60.216	6.116 to 70.13
Index ranges	-12 ≤ h ≤ 11 -46 ≤ k ≤ 46 -44 ≤ l ≤ 38	-8 ≤ h ≤ 8 -23 ≤ k ≤ 23 -36 ≤ l ≤ 36	-9 ≤ h ≤ 9 -18 ≤ k ≤ 18 -25 ≤ l ≤ 25	-21 ≤ h ≤ 20 -26 ≤ k ≤ 26 -33 ≤ l ≤ 33
Reflections collected	139761 26110	46094 5883	43444 4742	59090 9867
Independent reflections	[R _{int} = 0.0672] [R _{sigma} = 0.0588]	[R _{int} = 0.0801] [R _{sigma} = 0.0884]	[R _{int} = 0.1066] [R _{sigma} = 0.0880]	[R _{int} = 0.0426] [R _{sigma} = 0.0323]
Data/restraints/parameters	26110/0/630	5883/0/401	4742/0/271	9867/0/258
Goodness-of-fit on F ²	1.078	1.063	1.041	1.046
Final R indexes [I>=2σ(I)]	R ₁ = 0.0869 wR ₂ = 0.2028	R ₁ = 0.0529 wR ₂ = 0.1595	R ₁ = 0.0588 wR ₂ = 0.0951	R ₁ = 0.0329 wR ₂ = 0.0673
Final R indexes [all data]	R ₁ = 0.1325 wR ₂ = 0.2255	R ₁ = 0.0727 wR ₂ = 0.1652	R ₁ = 0.1184 wR ₂ = 0.1116	R ₁ = 0.0542 wR ₂ = 0.0746
Largest diff. peak/hole / e Å ⁻³	4.58/-1.44	1.17/-1.27	0.83/-0.57	0.99/-0.40

Pink crystals of **L1Co1**, **L2Co1**, and **L3Co1** suitable for X-ray analysis were obtained by dissolving **L1Co**, **L2Co**, and **L3Co** in H₂O followed by slow evaporation at room temperature. As shown in figure 3.5(a), compounds **L1Co1**, **L2Co1**, and **L3Co1** provide a Co(III) ion coordinated in a pseudo-octahedral geometry. The Co(III) cation is ligated by four N-donors derived from **L1**, **L2**, or **L3** and two *cis*-bound chloride ions completing the six-coordinate system. The cationic species [L1Co^{III}Cl₂]⁺ and [L3Co^{III}Cl₂]⁺ are balanced by anionic [ClO₄]⁻ counter-ions. Conversely, the cationic species [L2Co^{III}Cl₂]⁺ is balanced by two different anionic species; [ClO₄]⁻ and Cl⁻ serve as counter-ions to two separate cationic species. The asymmetric unit of **L1Co1** consists of three independent [L1Co^{III}Cl₂][ClO₄] species, the asymmetric unit of **L2Co1** consists of two independent [L2Co^{III}Cl₂][ClO₄] and [L2Co^{III}Cl₂][Cl] species, and the asymmetric unit of **L3Co1** consists of one independent [L3Co^{III}Cl₂][ClO₄] species. Analysis of the solid state structure of

L1Co1 revealed that orientations of the three $[\text{ClO}_4]^-$ counter-ions relative to the cationic species $[\text{L1Co}^{\text{III}}\text{Cl}_2]^+$ were slightly different, but that bond lengths and angles were similar between all three species and varied by less than 0.006 Å and 0.78°. Therefore, one representative unit of the cationic $[\text{L1Co}^{\text{III}}\text{Cl}_2]^+$ species' bond lengths and angles are reported (Table 3.4). Additionally, the two independent cationic species of **L2Co1** differed only slightly, the bond lengths and angles varied by less than 0.0132 Å and 0.79°; therefore, one representative unit of the cationic $[\text{L2Co}^{\text{III}}\text{Cl}_2]^+$ species' bond lengths and angles are also reported in table 3.4. The resulting structures for **L1Co1**, **L2Co1**, and **L3Co1** are derived from a monoclinic $P2_1/c$ system.

Alternatively, deep-blue crystals of **L1Co2** suitable for X-ray analysis were obtained via vapor diffusion of diethyl ether into DMF (Figure 3.5(b)). The asymmetric unit of **L1Co2** consisted of one independent $[\text{L1Co}^{\text{III}}\text{Cl}(\text{DMF})][\text{Co}^{\text{II}}\text{Cl}_4]$ species. The resulting structure was derived from an orthorhombic *Pbca* system. **L1Co2** also has a pseudo-octahedral geometry; the cobalt(III) ion is ligated by four N-donors of (**L1**), a *cis*-bound chloride ion, and a *cis*-bound DMF molecule, resulting in a six-coordinate complex. In contrast to **L1Co1**, **L2Co1**, and **L3Co1**, the cationic species $[\text{L1Co}^{\text{III}}\text{Cl}(\text{DMF})]^{2+}$ is balanced by an anionic $[\text{Co}^{\text{II}}\text{Cl}_4]^{2-}$ counter-ion. The second cobalt metal center present in the counter-ion is Co(II). It is this $[\text{Co}^{\text{II}}\text{Cl}_4]^{2-}$ anionic coordination complex that is responsible for the solvent dependent-equilibrium behavior of **L1Co** in solution.

The $[\text{L1Co}^{\text{III}}\text{ClX}]^{n+}$ ($X = \text{Cl}^-$ or DMF, $n = 1$ or 2) units of **L1Co1**, **L2Co1**, **L3Co1** and **L1Co2** show little deviation in the cobalt(III) coordination environment. It is interesting to note that the Co(III)-N bonds between the pyridine or pyridol nitrogen atom and the Co(III) metal center (Co(1)-N(4)) are the shortest Co(III)-N bonds within the complexes (Table 3.4). This is due to the additional electron density from the pyridine or pyridol ring stabilizing the bonding interactions, thus shortening those bond distances. Additionally, if the Co(1)-N(4) bond length is compared for only **L1Co1**, **L2Co1**, and **L3Co1** an interesting trend is observed. **L1Co1** has the shortest Co(1)-N(4) bond length (1.856 Å), followed by **L2Co1** (1.858 Å)

and then **L3Co1** (1.864 Å). This suggests that addition of the hydroxyl group on the pyridine ring weakens the bonding interaction between N(4) and Co(1) slightly. Moreover, the hydroxyl group in the *meta* position (**L3Co1**) weakens the bonding interaction between N(4) and Co(1) more than the hydroxyl group in the *para* position (**L2Co1**). When comparing the Co(1)-Cl(1) bond distances another interesting observation can be made; the Co(1)-Cl(1) distance decreases from 2.2823 Å, to 2.2765 Å, followed by 2.2680 Å, and 2.2412 Å in **L1Co1**, **L2Co1**, **L3Co1** and **L1Co2**. This is consistent with the change in Cl⁻ vs. DMF donors to the Co(III) center. The bond angles change very little (Table 3.4) between **L1Co1**, **L2Co1**, **L3Co1**, and **L1Co2**.

Table 3.4. Selected bond lengths (Å) and angles (°).

Bond lengths (Å)	L1Co1	L2Co1	L3Co1	L1Co2	3.1
Co(1)-N(1)	1.992(2)	1.995(4)	1.963(3)	1.9703(12)	2.020(9)
Co(1)-N(2)	1.945(3)	1.946(4)	1.935(3)	1.9326(12)	1.942(9)
Co(1)-N(3)	1.982(3)	1.978(4)	1.968(3)	1.9882(12)	1.995(9)
Co(1)-N(4)	1.856(2)	1.858(4)	1.864(3)	1.8536(11)	1.953(9)
Co(1)-Cl(1)	2.2823(8)	2.2765(13)	2.268(7)	2.2411(5)	2.274(4)
Co(1)-Cl(2)	2.2478(8)	2.2470(13)	2.2333(9)	-	2.274(3)
Co(1)-O(1)	-	-	-	1.9250(10)	-
Bond angles (°)					
N(1)-Co(1)-Cl(2)	95.99(8)	96.23(12)	95.26(9)	-	92.4(3)
N(2)-Co(1)-Cl(2)	88.40(8)	88.61(13)	87.85(9)	-	91.8(3)
N(3)-Co(1)-Cl(2)	94.99(8)	96.04(12)	96.05(8)	-	95.7(3)
N(4)-Co(1)-Cl(2)	178.19(8)	178.60(12)	177.48(9)	-	179.1(3)
Cl(1)-Co(1)-Cl(2)	90.51(3)	89.58(5)	90.03(17)	-	87.9(1)
N(1)-Co(1)-Cl(1)	94.25(8)	94.38(12)	99.66(13)	94.33(4)	96.4(3)
N(2)-Co(1)-Cl(1)	178.85(9)	178.14(13)	174.12(13)	176.97(4)	179.3(3)
N(2)-Co(1)-N(1)	85.49(11)	85.34(17)	86.00(12)	85.80(5)	84.3(4)
N(2)-Co(1)-N(3)	85.01(11)	84.95(17)	85.35(12)	85.46(5)	87.7(4)
N(3)-Co(1)-Cl(1)	95.46(8)	95.72(12)	89.43(13)	95.02(4)	91.7(3)
N(3)-Co(1)-N(1)	165.25(11)	164.14(16)	165.48(12)	165.33(5)	168.8(4)
N(4)-Co(1)-Cl(1)	87.69(8)	89.05(12)	87.50(19)	88.46(4)	93.0(3)
N(4)-Co(1)-N(1)	84.39(11)	84.20(17)	84.71(12)	84.78(5)	87.5(4)
N(4)-Co(1)-N(2)	93.40(11)	94.75(17)	94.66(12)	94.56(5)	87.2(4)
N(4)-Co(1)-N(3)	84.94(11)	83.77(17)	84.40(12)	84.19(5)	84.3(4)
N(4)-Co(1)-O(1)	-	-	-	176.29(5)	-
O(1)-Co(1)-Cl(1)	-	-	-	92.66(3)	-
O(1)-Co(1)-N(1)	-	-	-	91.61(5)	-
O(1)-Co(1)-N(2)	-	-	-	84.32(5)	-
O(1)-Co(1)-N(3)	-	-	-	99.22(5)	-

Complexes with a similar coordination environment to **L1Co1**, **L2Co1**, **L3Co1** and **L1Co2** are limited in number.^{220, 224-225} One particular Co(III) complex synthesized by Hubin *et al.* (denoted **3.1**)²²⁵ offered connectivity parallels to complexes **L1Co1**, **L2Co1**, **L3Co1**, and **L1Co2**. **3.1** is a 12-membered ethylene cross-bridged macrocycle bound to a Co(III) ion and is shown in figure 3.6. This complex, like **L1Co1**, **L2Co1**, **L3Co1**, and **L1Co2**, is a 5-5-5-5 ring structure with Co(III) ligated by four N-donors, as well as two *cis*-bound species to complete the octahedron. When comparing **L1Co1**, **L2Co1**, **L3Co1** and **L1Co2** with **3.1**, some distinguished differences in bond angles were noted, specifically when comparing axial vs. equatorial bond angles (Table 3.4). In **L1Co1**, **L2Co1**, **L3Co1**, and **L1Co2** the N(3)-Co(1)-N(1) bond angles are 165.25°, 164.14°, 165.48°, and 165.33°, but in **3.1** the N(3)-Co(1)-N(1) bond angle is 168.80°. This axial bond angle in **3.1** is much more linear than **L1Co1**, **L2Co1**, **L3Co1**, and **L1Co2** (Figure 3.6, Table 3.4).²²⁵ The equatorial bond angles N(4)-Co(1)-N(2) in **L1Co1**, **L2Co1**, **L3Co1**, and **L1Co2** are 93.40°, 94.75°, 94.66°, and 94.56°, respectively, while this same bond angle is only 87.24° in **3.1** (Figure 3.6, Table 3.4)²²⁵. Inspecting the axial and equatorial bond angles of these structures revealed that **L1Co1**, **L2Co1**, **L3Co1**, and **L1Co2** give rise to delineation from octahedral geometry in the axial coordination, whereas **3.1** modifies the equatorial Co(III) interactions. The slight difference in axial and equatorial bond angles is due to the structures of the two ligands. **L1**, **L2**, and **L3** are 12-membered pyridine- and pyridol-containing tetraazamacrocycles; the presence of the pyridine or pyridol ring constrains the axial N(3)-Co(1)-N(1) bond angle causing more deviation from linearity in **L1Co1**, **L2Co1**, **L3Co1**, and **L1Co2** than in **3.1**. In contrast, **3.1** contains a 12-membered ethylene cross-bridged tetraazamacrocycle; this ethylene cross-bridge restrains the equatorial N(4)-Co(1)-N(2) bond angle in **3.1** compared to **L1Co1**, **L2Co1**, **L3Co1**, and **L1Co2**.



Figure 3.6. Comparison of solid state structure of **L1Co1**, **L2Co1**, **L3Co1**, **L1Co2**, and **3.1** (hydrogen atoms have been omitted for clarity).²²⁵ (**3.1** CCDC #: 199072)

3.5. Equilibrium behavior of **L1Co**, **L2Co**, and **L3Co**

When dissolved in DMF, or organic solvents, **L1Co**, **L2Co**, and **L3Co** exist as **L1Co2**, **L2Co2**, and **L3Co2** ($[\text{L1-3Co}^{\text{III}}\text{Cl}(\text{DMF})][\text{Co}^{\text{II}}\text{Cl}_4]$), but when dissolved in H_2O , or aqueous solvents, they exist as **L1Co1**, **L2Co1**, and **L3Co1** ($[\text{L1-3Co}^{\text{III}}\text{Cl}_2][\text{ClO}_4]$). One important observation is that the solid state structure of **L1Co2** contains cobalt in two different oxidation states, (II) and (III); whereas, the solid state structure of **L1Co1** contains only cobalt(III). This indicates that **L1Co** (and **L2Co/L3Co** based on the electronic spectra) remains intact throughout. Although in the solid state **L1Co1**, **L2Co1**, and **L3Co1** contain only one cobalt ion, when **L1Co1**, **L2Co1**, or **L3Co1** are in solution there is another source of cobalt ions present, in the form of $[\text{Co}^{\text{II}}(\text{OH}_2)_6]^{2+}$. This complex ion is not observed in the solid state, because it does not balance the charge of the ligand-cobalt complex $[\text{L1-3Co}^{\text{III}}\text{Cl}_2]^+$, instead $[\text{ClO}_4]^-$ is observed as the anionic counter-ion (Scheme 3.2). Upon realizing that along with the ligand-cobalt complex, cobalt(II) tetrachloride was present in DMF and cobalt(II) hexahydrate was present in H_2O , it was made obvious how the solution behavior of these macrocyclic ligand complexes incorporates the classic cobalt(II) chloride equilibrium. This was further confirmed when the spectra of **L1Co2** and cobalt(II) chloride were obtained in concentrated HCl and compared (Figure 3.7). Although neither complex was dissolved in an organic solvent, both exhibited the characteristic cobalt(II) tetrachloride absorbance bands. Because chloride ions were present in such excess the equilibrium was shifted from cobalt(II) hexahydrate to cobalt(II) tetrachloride. The same complex ions present in this classic demonstration, were also present in within the coordination sphere of the cobalt-macrocyclic ligand complexes (Scheme 3.2). There are several

instances reported in literature where ligand-cobalt complexes have changed color drastically upon dissolution, but never before has this unique equilibrium been thoroughly investigated in the depth described here.²²⁵

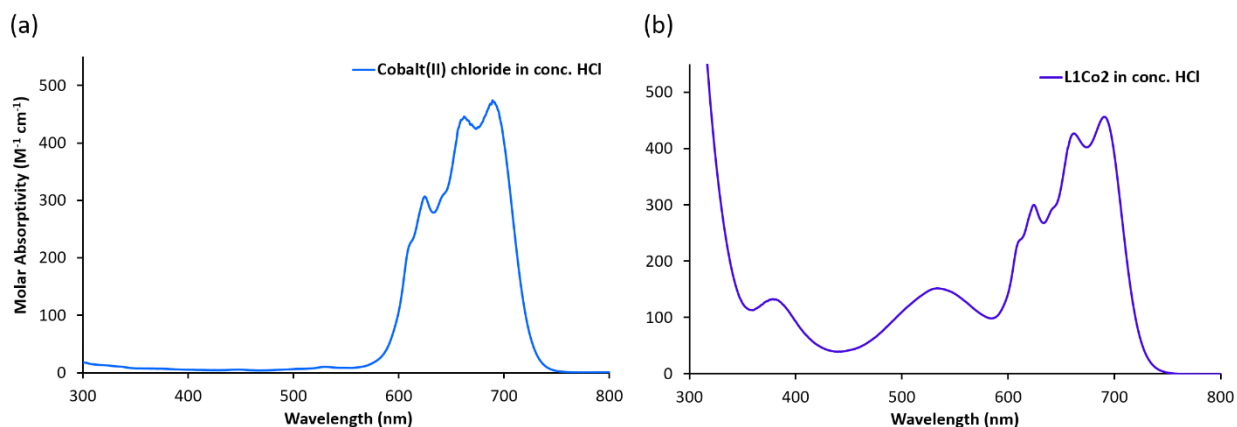


Figure 3.7. Comparison of the electronic absorption spectra of (a) CoCl_2 and (b) L1Co2 in concentrated hydrochloric acid; both contain the anionic species $[\text{Co}^{\text{II}}\text{Cl}_4]^{2-}$.

3.6. Electrochemistry of L1Co , L2Co , and L3Co

In addition to X-ray crystallography, complexes L1Co , L2Co , and L3Co were characterized using cyclic voltammetry. Analyses were performed in DMF solutions meaning the complexes were present as L1Co2 , L2Co2 , and L3Co2 . Two waves (oxidation and reduction) were observed for each complex when scanning from cathodic to anodic potentials (Figure 3.8). When the scan direction was reversed from anodic to cathodic potentials no oxidation event was observed indicating that the two redox events are related. Although the two events are related, the oxidation and reduction of the complex are irreversible (slow electron transfer) based on the separations of roughly 1.00 V (Table 3.5, Figure 3.8). Reduction of the metal center from $\text{Co(III)} \rightarrow \text{Co(II)}$ (-0.959 to -1.05 V for L1Co2-L3Co2) could result in the loss of *cis*-bound ligands in a weakly coordinating solvent, like DMF, thus producing CoCl_2 .²⁰³ Upon reversal of the scan directions the Co(II) 4-coordinate complex (resulting from loss of ligands upon cobalt reduction) is re-oxidized to Co(III) , at much higher potentials and the 6-coordinate Co(III) complex is reformed in quick succession.²⁰³ In addition, based on the $E_{1/2}$ values for each complex, the order of stability of the Co(III)

species is **L2Co2** (-0.552 V) > **L3Co2** (-0.489 V) > **L1Co2** (-0.423 V), with **L2Co2** being the most negative (Table 3.5, Figure 3.8). This data indicates that **L2** is the most electron donating ligand and stabilizes the Co(III) species to the greatest degree. The findings of the electrochemical analysis of complexes **L1Co2**, **L2Co2**, and **L3Co2** agree with previously reported conclusions related to the donor capacity of **L1-L3** from studies of other ligand-metal complexes.⁵⁶

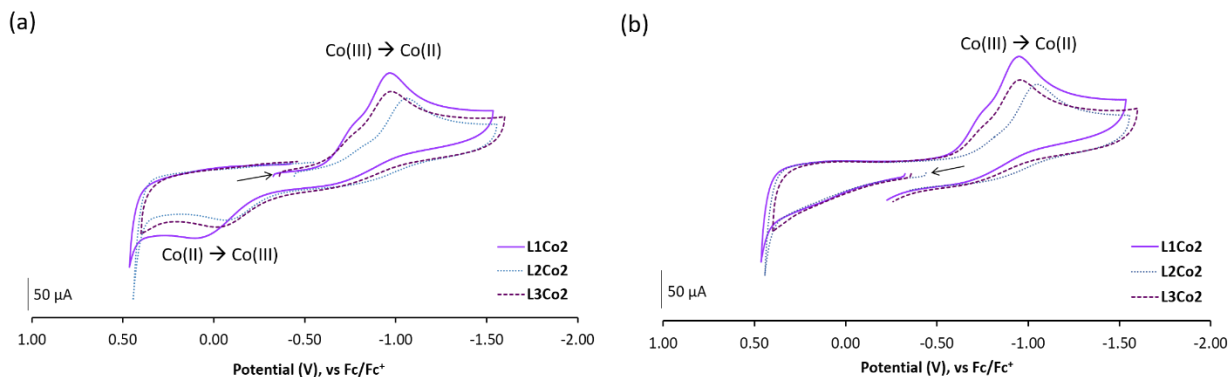


Figure 3.8. Cyclic voltammograms recording in 10 mL of DMF containing 10 mg (**L1Co**, **L2Co**, or **L3Co**; 0.01 mmol) + 0.1 TBAP with a glassy carbon working electrode, Ag wire *quasi*-reference electrode, and platinum wire auxiliary electrode. All voltammograms were referenced to Fc/Fc⁺ ($E_{1/2} = 0.00$ V). Arrows indicated direction of scans performed at 100 mV/s; (a) scanning from cathodic to anodic potentials and (b) scanning from anodic to cathodic potentials.

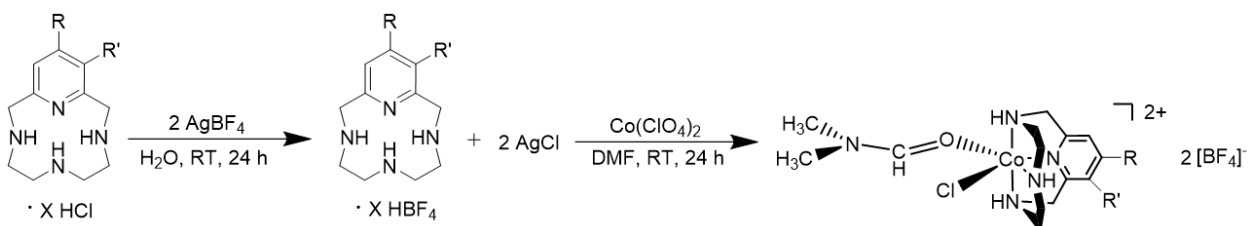
Table 3.5. Electrochemical values for **L1Co2**, **L2Co2**, and **L3Co2**

	E_{pc} (V)	E_{pa} (V)	$E_{1/2}$ (V)	ΔE_p (V)
L1Co2	-0.959	0.113	-0.423	1.07
L2Co2	-1.05	-0.053	-0.552	0.997
L3Co2	-0.967	-0.0115	-0.489	0.955

3.7. Ion exchange reactions with **L1Co**, **L2Co**, and **L3Co**

In order for **L1Co**, **L2Co**, and **L3Co** to be considered for catalytic chemistry, ion exchanges with silver tetrafluoroborate were performed to prepare complexes without $[\text{Co}^{\text{II}}\text{Cl}_4]^{2-}$. To accomplish this, ion-exchange reactions were performed with the ligand salt *sans* metal. Chloride ions present upon ligand synthesis were exchanged for tetrafluoroborate ions via precipitation and filtration of AgCl. Upon metathesis of the ligand, complexation was achieved using cobalt(II) perchlorate hexahydrate as described in section 3.2. A color change from pink to red was observed as an indication of ligand

complexation with cobalt. Complexation of the ligand with cobalt(III) was confirmed using UV-visible spectroscopy (Figure 3.9) and elemental analysis. The electronic spectra of **L1Co**, **L2Co**, and **L3Co** are the same in both H₂O and DMF, confirming that [CoCl₄]²⁻ ions are not present within the coordination sphere (Figure 3.9). Based on these characterization techniques it is hypothesized that in solution **L1Co**, **L2Co**, and **L3Co** exist as **L1Co3**, **L2Co3**, and **L3Co3** ([**L1Co**^{III}Cl(DMF)]₂[BF₄]₂, [**L2Co**^{III}Cl(DMF)]₂[BF₄]₂, [**L3Co**^{III}Cl(DMF)]₂[BF₄]₂) (Scheme 3.3).



Scheme 3.3. Metathesis reaction with AgBF₄ and subsequent complexation reaction to form **L1Co3**, **L2Co3**, and **L3Co3** (**L1**: R = H, R' = H; **L2** R = OH, R' = H; **L3**: R = H; R' = OH).

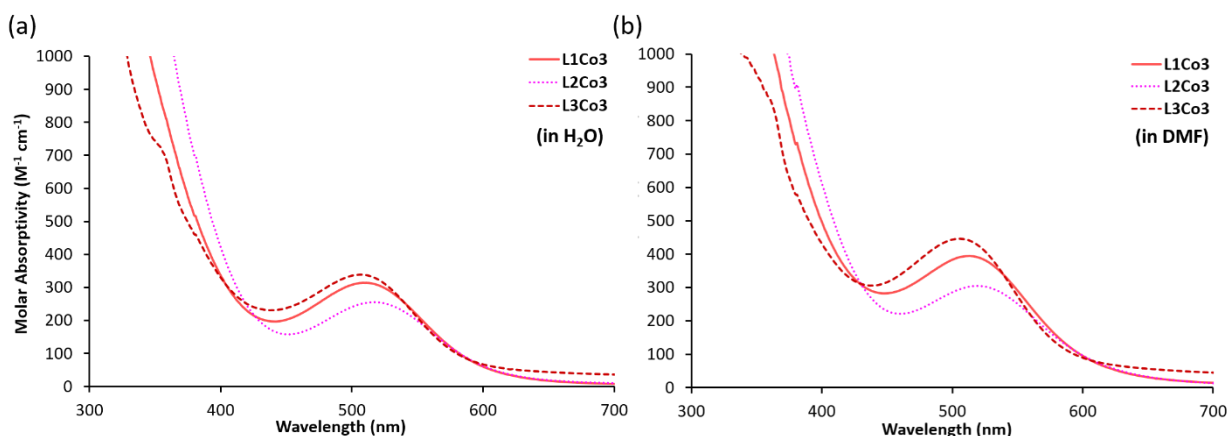


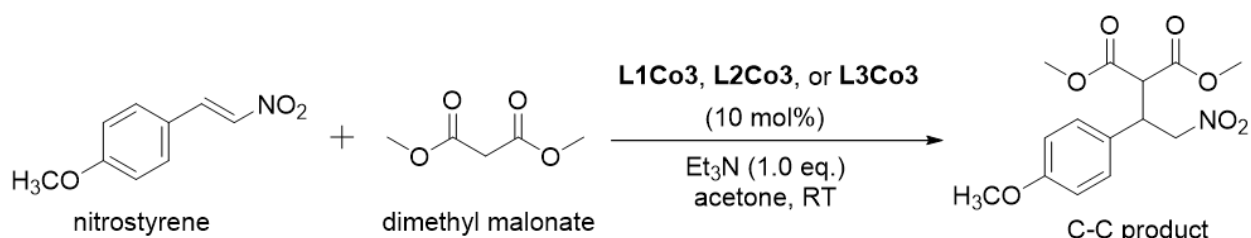
Figure 3.9. Electronic absorption spectra of **L1Co3**, **L2Co3**, and **L3Co3** in (a) H₂O and (b) DMF. No characteristic [CoCl₄]²⁻ absorbance band is present.

3.8. Exploration of catalytic activity

3.8.1. Michael-Addition C-C coupling

Upon performing metathesis reactions to exchange the counter-ion of the ligand-cobalt complexes (i.e. the second cobalt metal center) several catalysis reactions were tested using **L1Co3**, **L2Co3**, and **L3Co3**. Gladysz and coworkers have utilized modified Werner complexes (containing Co(III)) for

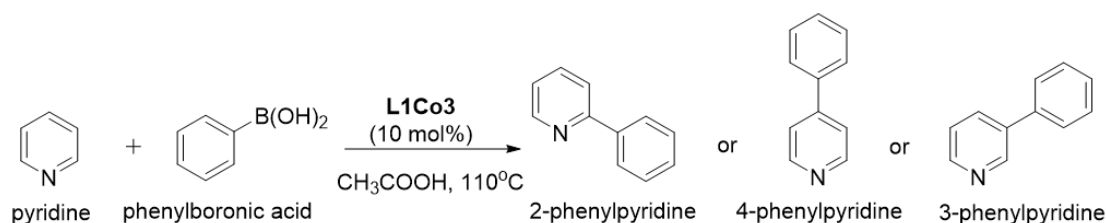
the enantioselective Michael-Addition reaction between various nitro-olefins and malonate esters (Scheme 3.4).²⁴⁸ The rationale for utilizing the ligand-cobalt complexes synthesized in the Green group was that the cobalt was in the same oxidation state and a similar ligand environment to the modified Werner complexes.²⁴⁸ Upon investigation into the catalytic ability of **L1Co3**, **L2Co3**, and **L3Co3** it was discovered that the Michael-Addition reaction proceeds without catalyst present, which was not indicated in the literature (Table 3.E1.).²⁴⁸ Yields suitable for enantiomeric selectivity testing (enantiomeric excess) were not obtained so this investigation was halted in favor of exploring other potential catalytic reactions.



Scheme 3.4. Michael-Addition C-C coupling reaction between nitrostyrene and dimethyl malonate.²⁴⁸

3.8.2. Suzuki-Miyaura type C-C coupling

Yu *et al.* have shown that Suzuki-Miyaura type C-C coupling can be achieved with the use of tetraazamacrocycles and iron salts as catalysts.²⁴⁹ The Green group has investigated the catalyst ability of ligand-iron(III) complexes on this reaction, with varying degrees of success.⁸⁵⁻⁸⁶ Out of curiosity, the catalyst ability of the ligand-cobalt complexes was also tested on the C-C coupling between phenylboronic acid and pyridine to yield phenylpyridine (Scheme 3.5). Unfortunately, no product was detected via ¹H NMR with or without the presence of ligand-cobalt catalyst (Table 3.E2). These results and those from colleague, Samantha Brewer, indicate that the metal choice (Fe) and ligand should be considerations for the catalysis described.



Scheme 3.5. Suzuki-Miyaura type catalyzed C-C coupling reaction.²⁴⁹

3.9. Conclusions

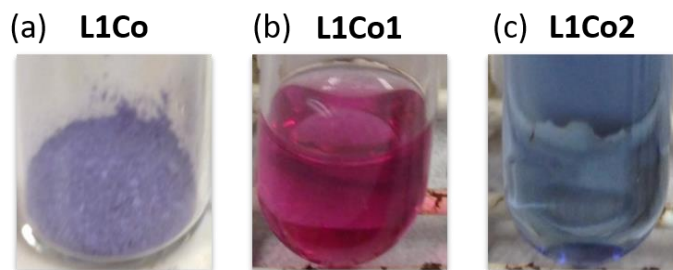


Figure 3.10. (a) **L1Co** isolated as a blue powder; (b) **L1Co** dissolved in H₂O exists as **L1Co1**; (c) **L1Co** dissolved in DMF exists as **L1Co2** (this solvent dependent behavior is also observed for **L2Co** and **L3Co**).

Various spectroscopic and solid state techniques were used to identify the coordination of the **L1-L3** cobalt complexes. In different solvents, ions bound to the Co(III) center, and counter-ions underwent a unique equilibrium (Scheme 3.2). When dissolved in DMF, complexes **L1Co**, **L2Co**, and **L3Co** are observed as **L1Co2**, **L2Co2**, or **L3Co2** with two cobalt metal centers: one Co(III) metal center bound to **L1**, **L2**, or **L3**, Cl⁻, and DMF and the other metal center (Co(II)) bound to four chlorides ($[\text{L1Co}^{\text{III}}\text{Cl}(\text{DMF})][\text{Co}^{\text{II}}\text{Cl}_4]$, $[\text{L2Co}^{\text{III}}\text{Cl}(\text{DMF})][\text{Co}^{\text{II}}\text{Cl}_4]$, $[\text{L3Co}^{\text{III}}\text{Cl}(\text{DMF})][\text{Co}^{\text{II}}\text{Cl}_4]$) (Scheme 3.2, Figure 3.3, 3.10). This $[\text{Co}^{\text{II}}\text{Cl}_4]^{2-}$ species serves as the counter-ion. In contrast, when complexes **L1Co**, **L2Co**, and **L3Co** are dissolved in water, they exist as **L1Co1**, **L2Co1**, or **L3Co1** consisting of a Co(III) metal center bound to **L1**, **L2**, or **L3** and two *cis*-chloride ions with a perchlorate or chloride counter-ion to balance the complex charge ($[\text{L1Co}^{\text{III}}\text{Cl}_2][\text{ClO}_4]$, $[\text{L2Co}^{\text{III}}\text{Cl}_2][\text{ClO}_4]$, $[\text{L3Co}^{\text{III}}\text{Cl}_2][\text{ClO}_4]$) (Scheme 3.2, Figure 3.3, 3.10). Investigation of this phenomenon utilizing electronic absorption spectroscopy and solid state methods showed that this ligand cobalt complex parallels the behavior of the classic cobalt(II) chloride equilibrium. The electrochemistry of these complexes was also explored; CV experiments revealed two related redox events, a reduction of Co(III) to Co(II) followed by subsequent re-oxidation to Co(III) (Figure 3.8). Additionally, ion-exchange reactions were performed, to isolate a macrocyclic Co(III) metal complex without the presence of $[\text{Co}^{\text{II}}\text{Cl}_4]^{2-}$ ions in the coordination sphere (Scheme 3.3, Figure 3.9). Metathesis reactions with AgBF₄ and subsequent metalation reactions led to the isolate of **L1Co3**, **L2Co3**, and **L3Co3** ($[\text{L1Co}^{\text{III}}\text{Cl}(\text{DMF})][\text{BF}_4]_2$,

[**L2Co^{III}**Cl(DMF)][BF₄]₂, and [**L3Co^{III}**Cl(DMF)][BF₄]₂). Finally, complexes **L1Co3**, **L2Co3**, and **L3Co3** were tested as catalysts in several C-C coupling reactions (Michael-Addition (Scheme 3.4) and Suzuki-Miyaura type (Scheme 3.5)), but no catalytic abilities were observed.

3.10. Experimental (methods and materials)

Caution! Perchlorate salts are explosive and should be handled with care; such compounds should never be heated as solids. All chemical reagents were purchased from either Millipore Sigma or Alfa Aesar and used without further purification. The 12-membered tetraazamacrocycles **L1**, **L2**, and **L3** were isolated as the hydrochloride salts prior to metal ion complexation in accordance with standard practices (syntheses are reported in the experimental section of chapter 2). The yields reported for **L1Co**, **L2Co**, and **L3Co** ([**L1Co^{III}**CIX]ⁿ⁺, [**L2Co^{III}**CIX]ⁿ⁺, [**L3Co^{III}**CIX]ⁿ⁺ X = Cl⁻ or DMF, n = 1 or 2) were calculated from an average of three trials and based on elemental analysis results; each reaction was carried out in DMF. Additionally, the yields for **L1Co3**, **L2Co3**, and **L3Co3** ([**L1Co^{III}**Cl(DMF)][BF₄]₂, [**L2Co^{III}**Cl(DMF)][BF₄]₂, [**L3Co^{III}**Cl(DMF)][BF₄]₂) were calculated based on elemental analysis results as well; each of these metathesis reactions was carried out in H₂O. Elemental analyses were performed by Canadian Microanalytical Services Ltd.

3.10.1. Physical measurements

¹H NMR and ¹³C NMR spectra were carried out in deuterated solvents at 25 °C. All spectra reported were obtained on a Bruker Avance III (400 MHz) High Performance Digital NMR Spectrometer. Electronic absorption spectra were collected between 190 nm and 1100 nm using an 8453 UV-vis spectrophotometer (Agilent) and a 3-mL quartz cuvette with a path length of 1.0 cm. Molar extinction coefficients were calculated utilizing the Beer-Lambert law ($A = \epsilon bc$).

3.10.2. Preparation of [L1Co^{III}CIX]ⁿ⁺ (L1Co)

Cobalt(II) perchlorate hexahydrate (89.0 mg, 0.243 mmol) was dissolved in 10 mL of DMF, resulting in a bright pink solution. Subsequently, **L1** (100 mg, 0.317 mmol) was added in one portion. The solution color changed immediately from bright pink to deep blue (Figure 3.2) upon addition of **L1**. This reaction mixture stirred at room temperature for 24 h. The resulting deep blue solution was filtered through a 0.45 μm filter syringe to remove excess unreacted ligand. Excess diethyl ether was added to the filtered solution, causing a deep blue powder to precipitate out of solution. The powder and diethyl ether mixture was transferred to Eppendorf tube(s) and centrifuged for 5 min. at 4000 rpm. The supernatant was decanted, and more diethyl ether was added to the blue powder in the Eppendorf tube; this process was repeated four to six times to remove traces of the solvent DMF. Finally, the blue powder, along with a small amount of diethyl ether, was transferred to a 6-mL vial and dried by vacuum on a Schlenk line to afford **L1Co** as a light blue solid (106 mg, 0.122 mmol, 39% yield). Crystals of **L1Co1** suitable for X-ray analysis were obtained via slow evaporation of water at room temperature and crystals of **L1Co2** suitable for X-ray analysis were obtained via vapor diffusion of diethyl ether into DMF. Electronic absorption $\lambda_{\text{max}}/\text{nm}$ ($\epsilon/\text{M}^{-1} \text{cm}^{-1}$); water: 376 (144), 535 (133); DMF: 380 (318), 535 (320), 680 (886). Elemental Analysis for **L1Co**; [L1CoCl:DMF][CoCl₄] \cdot 2HCl \cdot 3DMF Found (Calculated): C, 31.89 (31.87); H, 4.57 (5.58); N, 12.78 (12.93); O 7.95 (7.38) %.

3.10.3. Preparation of [L2Co^{III}CIX]ⁿ⁺ (L2Co)

Compound **L2Co** was prepared in a similar manner to that described above for **L1Co**. Compound **L2Co** was isolated as a light blue solid (113 mg, 0.135 mmol, 45% yield). Although a crystallization mixture was set-up, no crystals of **L2Co2** were obtained. Crystals of **L2Co1** suitable for X-ray analysis were obtained via slow evaporation of water at room temperature. Electronic absorption, $\lambda_{\text{max}}/\text{nm}$ ($\epsilon/\text{M}^{-1} \text{cm}^{-1}$); water: 376 (236), 535 (182); DMF: 380 (278), 545 (230), 680 (308). Elemental Analysis for **L2Co**;

[**L2CoCl**:DMF][CoCl₄]•HCl•2H₂O•HClO₄•DMF Found (Calculated): C, 25.33 (24.41); H, 4.00 (4.58); N, 9.45 (10.05); O, 17.22 (17.21) %.

3.10.4. Preparation of [**L3Co**^{III}CIX]ⁿ⁺ (**L3Co**)

Cobalt(II) perchlorate hexahydrate (85.0 mg, 0.232 mmol) was dissolved in 10 mL of DMF, resulting in a bright pink solution. Subsequently, 100 mg of **L3** (100 mg, 0.302 mmol) was added in one portion. The solution color changed immediately from bright pink to deep blue upon addition of **L3**. This reaction mixture stirred at room temperature for 24 h. The resulting indigo solution was filtered through a 0.45 µm filter syringe to remove excess unreacted ligand. Upon filtration the DMF, solvent was removed under reduced pressure. Toluene was added to aid in solvent removal. Excess diethyl ether and ethanol were added to the resulting deep purple oil; this mixture was stirred overnight, at which time a purple precipitate had formed. The powder and diethyl ether/ethanol mixture was transferred to Eppendorf tube(s) and centrifuged for 5 min. at 4000 rpm. The supernatant was decanted and additional diethyl ether (10 mL) was added to the purple powder in the Eppendorf tubes; this process was repeated several times to remove traces of ethanol and DMF. Finally, the purple powder along with a small amount of diethyl ether was transferred to a 6 mL vial and dried by vacuum on a Schlenk line to afford **L3Co** as a pale purple solid. (111 mg, 0.108 mmol, 36% yield). Although a crystallization mixture was set-up, no crystals of **L3Co2** were obtained. Crystals of **L3Co1** suitable for X-ray analysis were obtained via slow evaporation of water at room temperature. Electronic Absorption $\lambda_{\text{max}}/\text{nm}$ ($\epsilon/\text{M}^{-1} \text{cm}^{-1}$); water: 510 (291); DMF: 510 (674), 680 (772). Elemental Analysis for **L3Co**; [**L3CoCl**:DMF][CoCl₄]•HCl•2H₂O•HClO₄•EtOH•3DMF Found (Calculated): C, 29.16 (29.19); H, 4.53 (5.68); N, 11.66 (10.89); O 18.96 (18.66) %.

3.10.5. Preparation of $[\text{L1Co}^{\text{III}}\text{Cl}(\text{DMF})][\text{BF}_4]_2$ (**L1Co3**)

L1 (200 mg, 0.630 mmol) was dissolved in ~20 mL of H_2O , resulting in a clear pale-yellow solution. Subsequently, AgBF_4 (444 mg, 2.33 mmol) was added in one portion, which resulted in the immediate precipitation of AgCl . The solution, now cloudy, was shielded from light (to prevent AgCl photo-degradation) and stirred open to air at room temperature for 24 h. The resulting opaque white mixture was filtered through a 0.2 μm filter syringe to remove AgCl . Upon filtration the H_2O was removed under reduced pressure. To the resulting yellow oily residue diethyl ether and absolute ethanol were added; this mixture was stirred for 12 h. The oily residue was now a flaky off-white powder. The powder and diethyl ether/ethanol mixture was transferred to Eppendorf tube(s) and centrifuged for 5 min. at 4000 rpm. The supernatant was decanted and additional diethyl ether (10 mL) was added to the off-white powder in the Eppendorf tubes; this process was repeated several times to remove traces of ethanol. Finally, the off-white powder along with a small amount of diethyl ether was transferred to a 6 mL vial and dried by vacuum on a Schlenk line to afford **L1**•3 HBF_4 (298 mg, 0.71 mg, quantitative).

Cobalt(II) perchlorate hexahydrate (59.9 mg, 0.164 mmol) was dissolved in 10 mL of DMF, resulting in a bright pink solution. Subsequently, 100 mg of **L1**•3 HBF_4 (100 mg, 0.213 mmol) was added in one portion. There was no immediate color change of the solution. This reaction mixture stirred at room temperature for 24 h. The resulting red solution was filtered through a 0.45 μm filter syringe to remove excess unreacted ligand. Upon filtration the DMF solvent was removed under reduced pressure. Toluene was added to aid in solvent removal. Excess diethyl ether and ethanol were added to the resulting deep red oil; this mixture was stirred overnight, at which time a bright red powder had formed. The powder and diethyl ether/ethanol mixture was transferred to Eppendorf tube(s) and centrifuged for 5 min. at 4000 rpm. The supernatant was decanted and additional diethyl ether (10 mL) was added to the red powder in the Eppendorf tubes; this process was repeated several times to remove traces of ethanol and DMF. Finally, the red powder along with a small amount of diethyl ether was transferred to a 6 mL vial

and dried by vacuum on a Schlenk line to afford **L1Co3** as a pale red solid (104 mg, 0.116 mmol, 53%). Crystallizations of **L1Co3** were set up in both DMF and water, but no crystals suitable for X-ray analysis were obtained. Electronic Absorption $\lambda_{\text{max}}/\text{nm}$ ($\epsilon/\text{M}^{-1} \text{cm}^{-1}$); water: 505 (313); DMF: 516 (436). Elemental Analysis for **L1Co3**; [**L1CoCl**:DMF][BF₄]₂•H₂O•HClO₄•HBF₄•3DMF Found (Calculated): C, 27.39 (26.70); H, 4.36 (4.82); N, 11.16 (10.90); Co 7.08 (6.55) %.

3.10.6. Preparation of [**L2Co**^{III}Cl(DMF)][BF₄]₂ (**L2Co3**)

Compound **L2Co3** was prepared in a similar manner to that described above for **L1Co3**. Compound **L2Co3** was isolated as a light red solid (95 mg, 0.119 mmol, 56% yield). Electronic Absorption $\lambda_{\text{max}}/\text{nm}$ ($\epsilon/\text{M}^{-1} \text{cm}^{-1}$); water: 518 (256); DMF: 525 (302). Crystallizations of **L2Co3** were set up in both DMF and water, but no crystals suitable for X-ray analysis were obtained. Elemental Analysis for **L2Co3**; [**L2CoCl**:DMF][BF₄]₂•HBF₄•AgCl Found (Calculated): C, 20.78 (21.16); H, 3.26 (3.30); N, 8.54 (8.81); Co 7.55 (7.42) %.

3.10.7. Preparation of [**L3Co**^{III}Cl(DMF)][BF₄]₂ (**L3Co3**)

Compound **L3Co3** was prepared in a similar manner to that described above for **L1Co3** and **L2Co3**. Compound **L3Co3** was isolated as a light red solid (105.2 mg, 0.117 mmol, 63% yield). Crystallizations of **L3Co3** were set up in both DMF and water, but no crystals suitable for X-ray analysis were obtained. Electronic Absorption $\lambda_{\text{max}}/\text{nm}$ ($\epsilon/\text{M}^{-1} \text{cm}^{-1}$); water: 510 (337); DMF: 506 (446). Elemental Analysis for **L3Co3** [**L3CoCl**:DMF][BF₄]₂•HClO₄•HBF₄•3DMF Found (Calculated): C, 27.59 (26.76); H, 4.26 (4.60); N, 11.01 (10.92); Co 6.49 (6.56) %.

3.10.8. X-ray crystallography

A Leica MZ 75 microscope was used to identify samples suitable for analysis. A Bruker APEX-II CCD diffractometer was employed for crystal screening, unit cell determination, and data collection; which was obtained at 100 K. The Bruker D8 goniometer was controlled using the either the APEX2 software

suite (v2014.11-0)²⁵⁰ or the APEX3 software suite (v1).²⁰⁵ The samples were optically centered with the aid of video camera so that no translations were observed as the crystal was rotated through all positions. The X-ray radiation employed was generated from a MoK α sealed X-ray tube ($\lambda = 0.71076$) with a potential of 50 kV and a current of 30 mA; fitted with a graphite monochromator in the parallel mode (175 mm collimator with 0.5 mm pinholes).

3.10.8.1. [L1Co^{III}Cl₂]₃[ClO₄]₃ (L1Co1) structure determination

Crystals of **L1Co1** suitable for X-ray analysis were obtained by dissolving several mg of the blue powder of **L1Co** in H₂O to provide a pink solution. Slow evaporation, of this solution, at room temperature afforded a translucent dark red-pink plate-like crystal of **L1Co1** (0.101 x 0.262 x 0.303 mm³) which was mounted on a 0.5 mm cryo-loop and used for X-ray crystallographic analysis. The crystal-to-detector distance was set to 50 mm, and the exposure time was 10 s per degree for all data sets at a scan width of 0.5°. A total of 1304 frames were collected, and the data collection was 99.8% complete. The frames were integrated with the Bruker SAINT Software package²⁵⁰ using a narrow frame algorithm. The integration of the data using a monoclinic unit cell yielded a total of 139,761 reflections to a maximum ϑ angle of 38.63° (0.57 Å resolution) of which 26,110 were independent with the $R_{\text{int}} = 6.72\%$. Data were corrected for absorption effects using the multi-scan method SADABS.²⁰⁷ Structural refinements were performed with XShell (v. 6.3.1) by the full-matrix least-squares method.²⁵¹ All hydrogen and non-hydrogen atoms were refined using anisotropic thermal parameters. Two of the Co(III) metal centers in the asymmetric unit were disorder over two positions, demonstrating a 50/50 ratio between the components. The thermal ellipsoid molecular plots (50%) were produced using Olex2.²⁵²

3.10.8.2. [L2Co^{III}Cl₂]₂[ClO₄][Cl] (L2Co1) structure determination

Crystals of **L2Co1** suitable for X-ray analysis were obtained by dissolving several mg of the blue powder of **L2Co** in H₂O to provide a pink solution. Slow evaporation, of this solution, at room temperature afforded a translucent dark red-pink block-like crystal of **L2Co1** (0.54 x 0.33 x 0.10 mm³) which was

mounted on a 0.5 mm cryo-loop and used for X-ray crystallographic analysis. The crystal-to-detector distance was set to 50 mm, and the exposure time was 10 s per degree for all data sets at a scan width of 0.5°. X-ray diffraction data was collected using a Bruker APEXII single crystal X-ray diffractometer. Reflections were collected at 100(2) K using Mo K_{α1} radiation ($\lambda = 0.71073 \text{ \AA}$) using a data collection strategy determined by APEXII. Inspection of the collected diffraction images demonstrated the sample to be twinned. Using CrysAlisPRO, the data were processed as a four-component twin once the unit cell was determined by analysis of systematic absences from the experimental images. Data reduction and final twin refinement were also achieved using CryAlisPRO.²⁵³ Multi-scan absorption corrections were performed using the SCALE3 ABSPACK scaling algorithm implemented within CrysAlisPRO.²⁵³ The structure was solved via direct methods using ShelXT²⁵⁴, refined using ShelXL²⁵⁵ in the Olex2 graphical user interface²⁵² and had its space groups unambiguously verified via PLATON.²⁵⁶ Fourier recycling of the reflection data for **L2Co1** resulted in the identification of electron density peaks attributable to at least five highly-disordered water molecules present in solvent accessible voids of 538 Å³ that could not be satisfactorily modeled. The data was treated using the SQUEEZE routine in PLATON and then refined on F^2 to acceptable levels.²⁵⁷ The final structural refinement included anisotropic temperature factors on all non-hydrogen atoms. All hydrogen atoms were attached via the riding model at calculated positions using appropriate HFIX commands. The chlorine anion present in the asymmetric unit was disordered over two positions, demonstrating a 70/30 ratio between the components. The thermal ellipsoid molecular plots (50%) were produced using Olex2.²⁵²

3.8.10.3. [L3Co^{III}Cl₂][ClO₄] (**L3Co1**) structure determination

Crystals of **L3Co1** suitable for X-ray analysis were obtained by dissolving several mg of blue powder of **L3Co** in H₂O to provide a pink solution. Slow evaporation of this solution at room temperature afforded a translucent dark purple-pink block-like crystal of **L3Co1** (0.176 x 0.077 x 0.073 mm³), which was mounted on a 75 μm cryo-loop and used for X-ray crystallographic analysis. The crystal-to-detector

distance was set to 50 mm, and the exposure time was 10 s per degree for all data sets at a scan width of 0.5°. A total of 1,824 frames were collected, and the data collection was 100% complete. The frames were integrated with the Bruker SAINT Software package²⁰⁶ using a narrow frame algorithm. The integration of the data used a monoclinic unit cell yielding a total of 43,444 reflections to a maximum ϑ angle of 30.11° (0.71 Å resolution) of which 4,742 reflections were independent with the $R_{\text{int}} = 10.66\%$. Data were corrected for absorption effects using the multi-scan method SADABS.²⁰⁷ Using Olex2²⁰⁸ the structure was solved with the ShelXS²⁰⁹ structure solution program using Direct Methods and refined with the SHELXL²¹⁰ refinement package using Least Squares minimization. All hydrogen and non-hydrogen atoms were refined using anisotropic thermal parameters. The chlorine (Cl(1)) bound to the metal center present in the asymmetric unit was disordered over two positions, demonstrating a 50/50 ratio between the components. Additionally, the perchlorate anion present in the asymmetric unit was disorder over two positions, demonstrating a 50/50 ratio (for 2 O atoms) and 80/20 (for 2 O atoms) ratio between the components. The thermal ellipsoid molecular plots (50%) were produced using Olex2.²⁰⁸

3.10.8.4. [L1Co^{III}Cl(DMF)][Co^{II}Cl₄] (L1Co2) structure determination

Crystals of **L1Co2** suitable for X-ray analysis were obtained via vapor diffusion of diethyl ether into DMF. An intense dark blue-purple plate-like crystal of **L1Co2** (0.086 x 0.272 x 0.464 mm³) was mounted on a 0.5 mm cryo-loop and used for X-ray crystallographic analysis. The crystal-to-detector distance was set to 50 mm, and the exposure time was 10 s per degree for all data sets at a scan width of 0.5°. A total of 772 frames were collected, and the data collection was 99.6% complete. The frames were integrated with the Bruker SAINT Software package²⁵⁰ using a narrow frame algorithm. The integration of the data using a monoclinic unit cell yielded a total of 59,090 reflections to a maximum ϑ angle of 35.06° (0.62 Å resolution) of which 9,867 were independent with the $R_{\text{int}} = 4.26\%$. Data were corrected for absorption effects using the multi-scan method SADABS.²⁰⁷ Structural refinements were performed with XShell (v. 6.3.1) by the full-matrix least-squares method.²⁵¹ All hydrogen and non-hydrogen atoms were refined

using anisotropic thermal parameters. The thermal ellipsoid molecular plots (50%) were produced using Olex2.²⁵²

3.10.9. Electrochemical measurements

Cyclic voltammetry (CV) was carried out with an EC Epsilon potentiostat (C-3 cell stand) purchased from BASi Analytical Instruments (West Lafayette, IN). A glassy carbon (GC) electrode from BASi (MF-2012), 3 mm in diameter was polished on a white nylon pad (BASi MF-2058) with different sized diamond polishes (15, 6, 1 μm) to ensure a mirror-like finish. Between each measurement, the GC electrode was polished with the three diamond polishes. A three-electrode cell configuration was used with GC as the working electrode, an Ag wire (0.5 mm dia.) quasi reference electrode housed in a glass tube (7.5 cm x 5.7 mm) with a Porous CoralPorTM Tip, and a Pt wire (7.5 cm) as the counter electrode (BASi MW-1032). All solutions were bubbled with nitrogen gas for at least 15 min. prior to experimentation and were kept under a humidified nitrogen gas blanket. All potentials in this work are reported vs. Fc/Fc⁺ ($E_{1/2} = 0$ V). For electrochemical analysis, 10.0 mg of each complex was dissolved in 10 mL of anhydrous DMF containing 0.1 M tetrabutylammonium perchlorate (TBAP) as the supporting electrolyte.

3.10.10. X-band EPR spectroscopy and quantitative simulations

X-band (9 GHz) EPR spectra were recorded on a Bruker EMX Plus spectrometer equipped with a bimodal resonator (Bruker model 4116DM). Low-temperature measurements were made using an Oxford ESR900 cryostat and an Oxford ITC 503 temperature controller. A modulation frequency of 100 kHz was used for all EPR spectra. All experimental data used for spin-quantitation were collected under non-saturating conditions. Analysis of the EPR spectra utilized the general spin Hamiltonian,

$$\hat{H} = D \left(\hat{S}_z^2 - \frac{S(S+1)}{3} \right) + E \left(\hat{S}_x^2 + \hat{S}_y^2 \right) + \beta \mathbf{B} \cdot \mathbf{g} \cdot \mathbf{S} + \mathbf{SAI} \quad \text{Equation [3.1]}$$

where D and E are the axial and rhombic zero-field splitting parameters and g is the g -tensor.²⁵⁸ Nuclear hyperfine interactions (\mathbf{A}) are treated with second-order perturbation theory. EPR spectra were simulated

and quantified using Spin Count (ver. 5.5.5749.20032), written by Professor M. P. Hendrich at Carnegie Mellon University. The simulations were generated with consideration of all intensity factors, both theoretical and experimental, to allow concentration determination of species. The only unknown factor relating the spin concentration to signal intensity was an instrumental factor that depended on the microwave detection system. However, this was determined by the spin standard, Cu(EDTA), prepared from a copper atomic absorption standard solution purchased from Sigma–Aldrich.

3.10.10.1 EPR results of L1Co in H₂O and DMF (Carried out at UTA with Brad Pierce and co-workers)

As illustrated in figure 3.E1., below, EPR samples of **L1Co** were prepared in both water (**L1Co1**) (trace **1**) and DMF (**L1Co2**) (trace **2**) to complement electronic absorption results and verify the (II) oxidation state and coordination geometry of Co-coordination sphere. The EPR spectrum of aqueous samples of **L1Co1** (5 mM) is designated by trace **1**. This spectrum is consistent with a nearly axial $S = 3/2$ spin state ($E/D = 0.05$) with observed g -values at 5.5 and 2.04. The line width of this spectrum is dominated by both g -strain and unresolved hyperfine from the ^{59}Co ($I = 7/2$) nucleus. The simulation parameters (*dashed line*) for this species is typical of 5- or 6-coordinate Co(II).²⁵⁹⁻²⁶³ The temperature-normalized signal intensity for **1** decreases with increasing temperature indicating that the $m_s = \pm 1/2$ doublet is the ground state within the $S = 3/2$ spin system. The magnitude of the zero-field splitting parameter ($D = 10 \pm 3 \text{ cm}^{-1}$) was determined by plotting the EPR signal intensity of this signal versus $1/T$ and fitting the data to a Boltzmann population distribution for a 2-level system. The EPR simulation (*dashed lines*) for **1** shown in figure 3.E1. was calculated using this D -value. For analytical purposes, all data was recorded under non-saturating conditions.

An equivalent sample of **L1Co2** (5 mM) prepared in DMF is shown in figure 3.E1. (trace **2**). Unlike the sample prepared in water, additional features are observed at g -values of 6.40, 5.33, 2.81, 2.04, and 1.70. Additionally, a multiline hyperfine splitting [8.3 mT, 230 MHz] is observed in within the $6.4 < g$ -value < 4.4 region. These features are reasonably simulated (**S2**) by assuming contributions from two species (i

and *ii*) differing in their rhombicity (E/D -values) of 0.09 and 0.23, respectively. While slightly more rhombic ($E/D = 0.09$ versus 0.05), the simulation parameters for (*i*) are like those obtained for **S1**. Therefore, it can be concluded that this species is also a 5- or 6-coordinate Co(II) center. Alternatively, the increased rhombicity ($E/D = 0.23$) and resolved hyperfine of (*ii*) is **more** consistent with properties reported for tetrahedral Co(II) sites.²⁵⁸⁻²⁶³

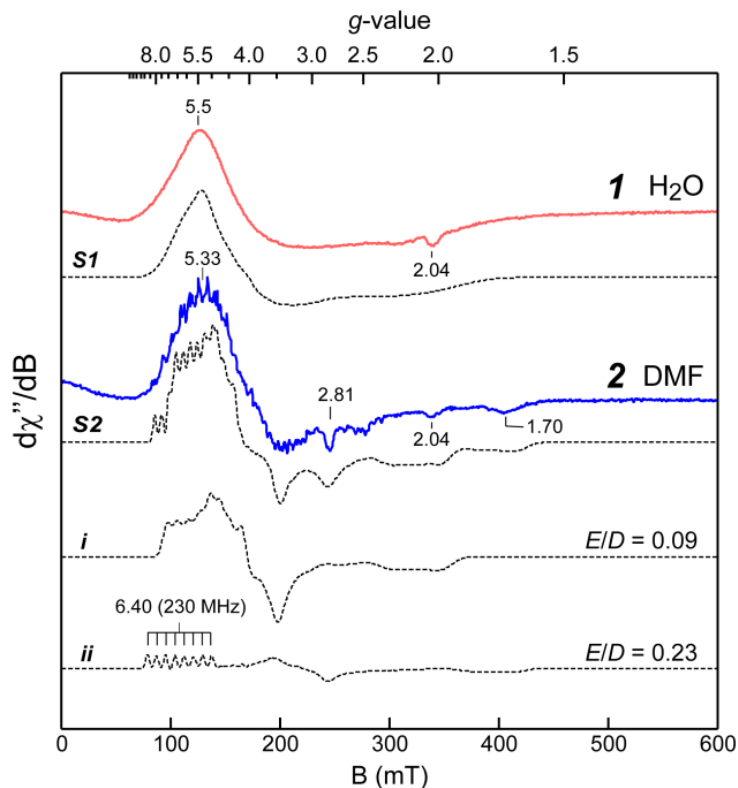


Figure 3.E1. 10 K X-band EPR spectra of L1-Co and in water (**1**) and DMF (**2**). Quantitative simulations (*dashed lines*) for each spectrum are included for comparison. Instrumental parameters: microwave frequency, 9.643 GHz; microwave power, 100 μ W for each spectrum arc, 0.9 mT; temperature, 10 K. Simulation parameters for each $^{59}\text{Co(II)}$ $S = 3/2$ ($I = 7/2$) site: **S1**, $g_{x,y,z}$ (2.01, 2.69, 2.15), $\sigma g_{x,y,z}$ (0.09, 0.08, 0.09), A_{iso} , (250 MHz), $D = 10 \pm 5 \text{ cm}^{-1}$, $E/D = 0.05$; **S2 (i)**, $g_{x,y,z}$ (2.38, 2.34, 2.17), $\sigma g_{x,y,z}$ (0.05, 0.05, 0.05), A_{iso} , (250 MHz), $D = 10 \pm 5 \text{ cm}^{-1}$, $E/D = 0.09$; **(ii)**, $g_{x,y,z}$ (2.46, 2.48, 2.04), $\sigma g_{x,y,z}$ (0.01, 0.02, 0.03), A_{iso} , (230 MHz), $D = 10 \pm 5 \text{ cm}^{-1}$, $E/D = 0.23$, 0.1 mT. All simulations utilize a uniform line width (σ_B) of 0.1 mT.

3.10.11. Michael-Addition C-C coupling²⁴⁸

An NMR tube was charged with catalyst (either **L1Co3**, **L2Co3**, or **L3Co3**) (8.99 mg (**L1Co3**), 7.95 mg (**L2Co3**), 8.97 mg (**L3Co3**), 0.010 mmol, 0.1 equiv.), dimethyl malonate (13.8 μ L, 0.120 mmol, 1.2 equiv.), nitro-olefin (17.9 mg, 0.10 mmol, 1.0 equiv.) and Ph_2SiMe_2 (0.0020 mL, internal standard) in

acetone- d_6 (0.70 mL). An ^1H NMR spectrum was recorded to measure the initial ratio of the nitroolefin to the standard. Et_3N (14 μL , 0.0101 mmol, 1.0 equiv.) was added to the vessel and the reactions stirred at room temperature. The reaction was monitored by ^1H NMR and TLC. The reaction mixture was filtered through glass wool and solvent was removed under reduced pressure. The resulting orange-yellow oil was taken up in dichloromethane.

Table 3.E1. Reaction conditions for Michael Addition experiments

nitrostyrene	dimethyl malonate	triethylamine	catalyst	C-C product
0.10 mmol, 1.0 eq.	0.120 mmol, 1.2 eq.	0.0101 mmol, 1.0 eq.	0.010 mmol, 0.1 eq.	Isolated or not
17.918 mg	13.8 μL	14.0 μL	n/a	Y
17.918 mg	13.8 μL	14.0 μL	8.99 mg (L1Co3)	Y
17.918 mg	13.8 μL	14.0 μL	7.95 mg (L2Co3)	Y
17.918 mg	13.8 μL	14.0 μL	8.97 mg (L3Co3)	Y

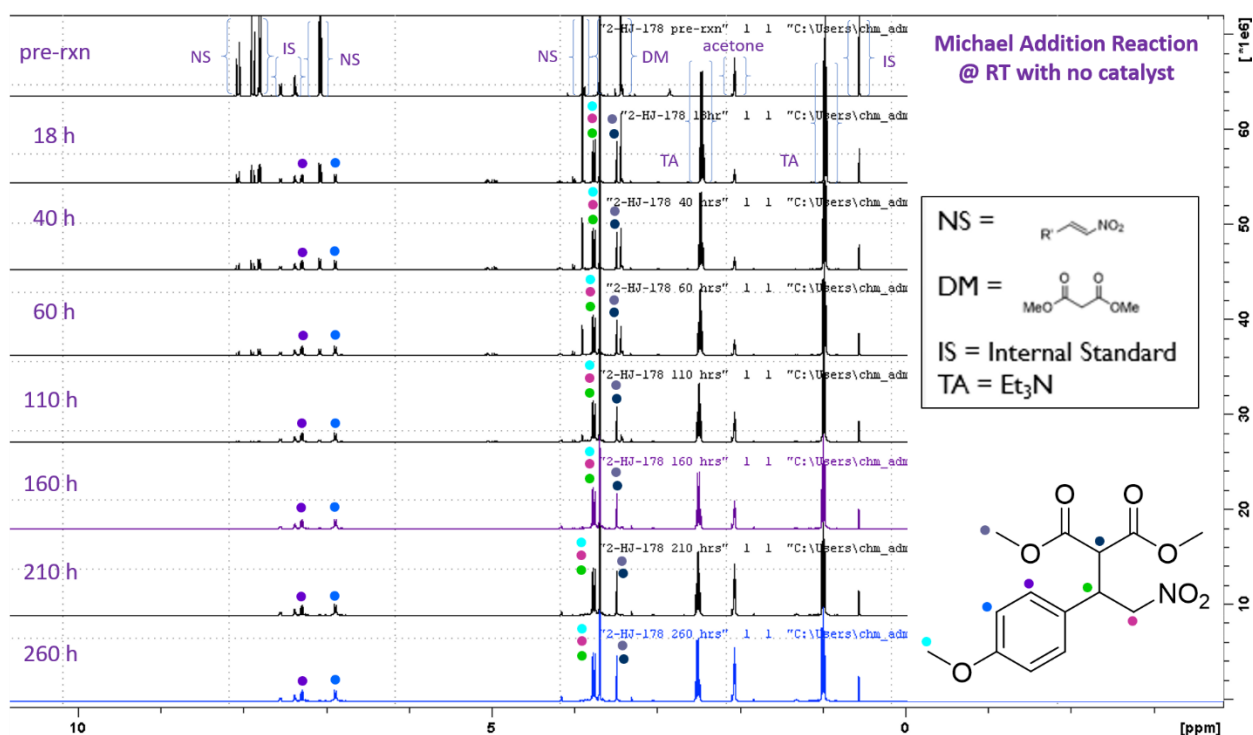


Figure 3.E2. Michael-Addition reaction *sans* catalyst monitored by ^1H NMR; product formation is observed without catalyst present (at RT).

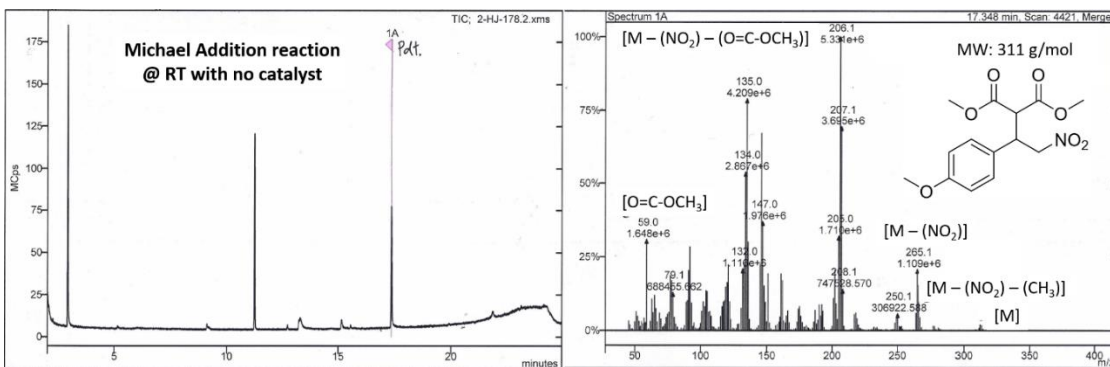


Figure 3.E3. GC-MS data for C-C coupling product of the Michael-Addition reaction (without catalyst).

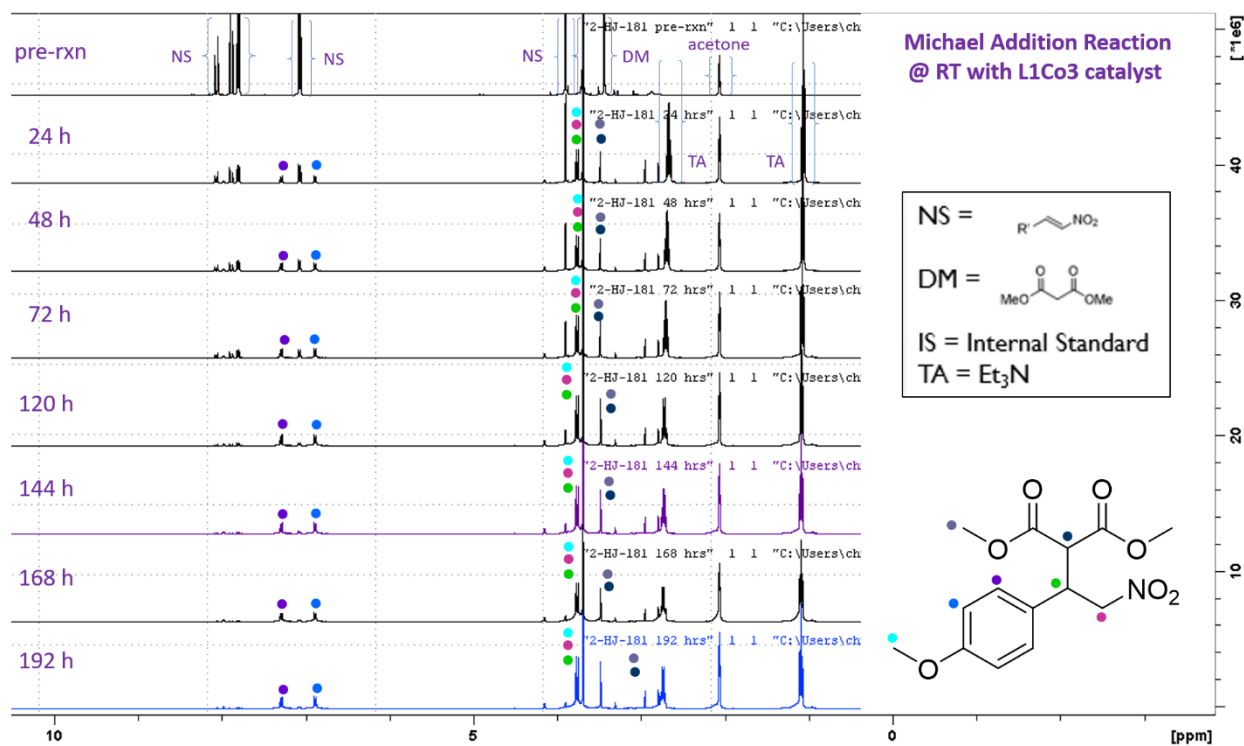


Figure 3.E4. Michael-Addition reaction with L1Co3 catalyst, monitored by ¹H NMR.

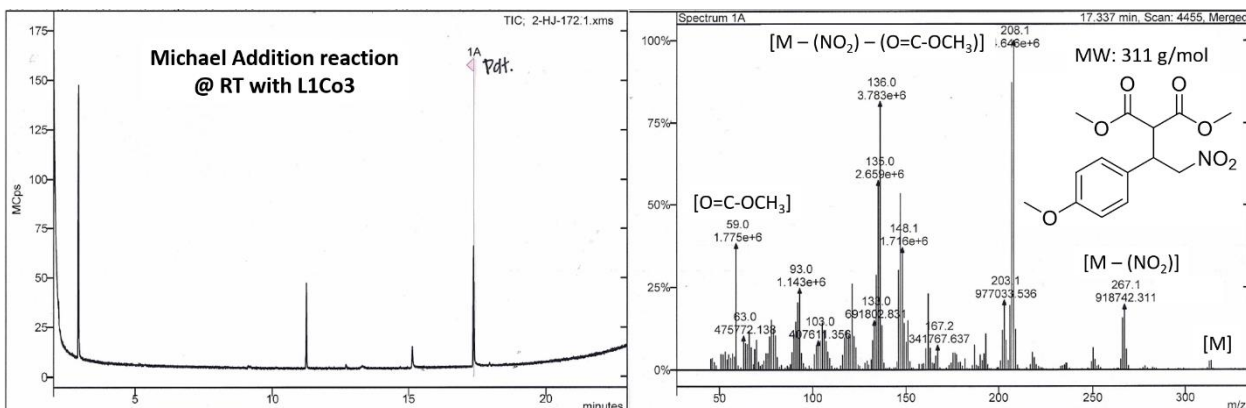


Figure 3.E5. GC-MS data for C-C coupling product of the Michael-Addition reaction with L1Co3 catalyst.

3.10.12. Suzuki-Miyaura type C-C coupling²⁴⁹

A reflux tube equipped with a magnetic stir bar was charged with phenylboronic acid (24.4 mg, 0.2 mmol, 1.0 equiv.), **L1Co3** (8.9 mg, 0.010 mmol, 0.1 equiv.), pyridine (1 mL), and acetic acid (1 mL). The reaction vessel was placed in a 110 °C oil bath and stirred for 12 h. Afterwards, the reaction mixture was cooled to room temperature and diluted with ethyl acetate. The resulting solution was filtered through a pad of silica and concentrated *in vacuo*. This “crude product” was then characterized using ¹H NMR.

Table 3.E2. Reaction conditions for Suzuki-Miyaura type experiments.

pyridine excess	phenylboronic acid 0.2 mmol, 1.0 eq.	acetic acid excess	catalyst 0.01 mmol, 0.1 eq.	2-phenylpyridine Isolated or not	3-phenylpyridine Isolated or not	4-phenylpyridine Isolated or not
1 mL	24.4 mg	1 mL	n/a	no product	no product	no product
1 mL	24.4 mg	1 mL	8.99 mg (L1Co3)	no product	no product	no product

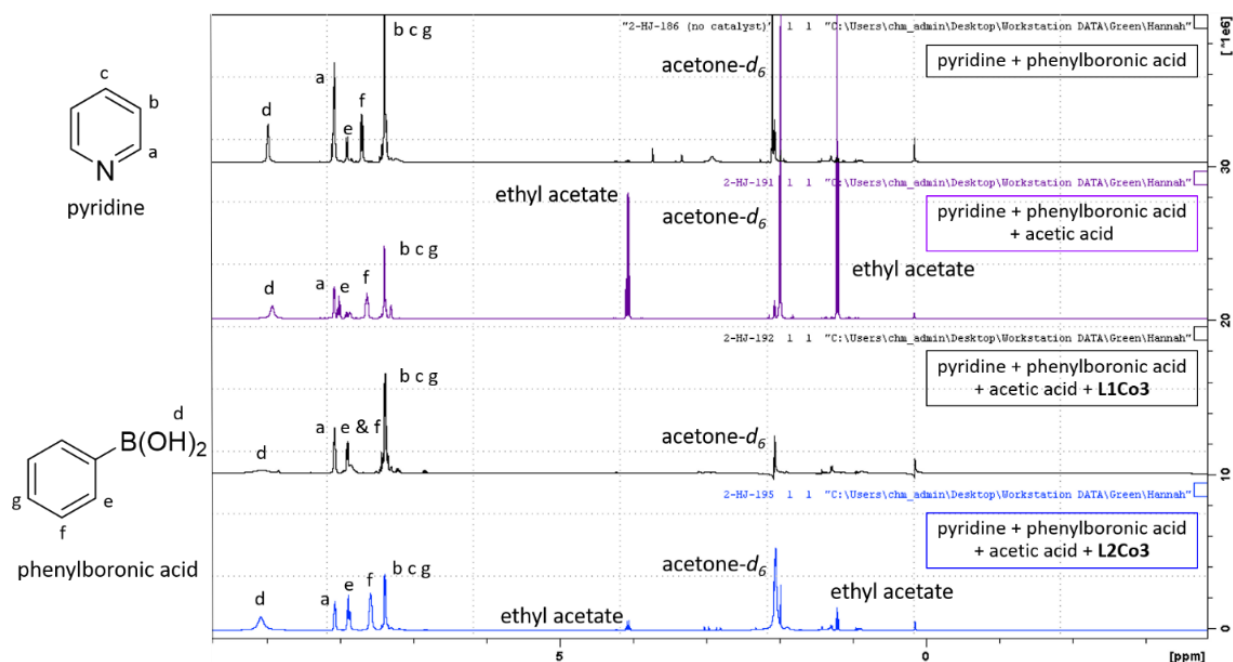


Figure 3.E6. ¹H NMR spectra of control and catalyst reactions of Suzuki-Miyaura type C-C coupling. Starting materials were conserved with no product formation observed by ¹H NMR.

3.10.13. Experimental acknowledgments

We thank Dr. Brad Pierce and co-workers at UT Arlington for performing EPR measurements on the ligand-cobalt complexes. We also thank Dr. Eric Reinheimer at Rigaku for his help with the analyses of the twinning and disorder of the **L2Co1** solid state structure.

Chapter 4: Synthesis and characterization of novel manganese monomers and dimers with tetraazamacrocyclic ligands

4.1. Introduction

Manganese can access many different oxidation states, from -3 up to +10 (+2, +4, and +7 are the most common oxidation states).²⁶⁴⁻²⁶⁵ This transition metal is used in a variety of different applications, because of its unique reactivity. Manganese can be utilized in practical applications such as metallurgy²⁶⁶, batteries²⁶⁷, and redox catalysis²⁶⁸, but it is also prevalent in nature.²⁶⁹ Because of the large range of oxidation states accessible to manganese, it is an ideal cofactor for a variety of metalloproteins with many diverse redox functions.²⁶⁵ Manganese plays an essential role in a multitude of biological systems and it can be found in numerous oxidation states and nuclearities within the active sites of metalloenzymes.²⁷⁰⁻²⁷¹ Examples of several manganese containing enzymes include, but are not limited to, superoxide dismutase, manganese catalase, and the oxygen-evolving complex within photosystem II. Superoxide dismutase (SOD) is a manganese containing enzyme that catalyzes the dismutation of superoxide into either oxygen or hydrogen peroxide.²⁷² The antioxidant capacity of Mn-SOD is a vastly important defense against the superoxide radical, which is a by-product of the oxygen metabolism of living cells exposed to oxygen. The active site of Mn-SOD is composed of a mononuclear manganese center with trigonal bipyramidal coordination geometry.^{270, 273} Another important manganese containing enzyme, manganese catalase (Mn-catalase), catalyzes the disproportionation (or decomposition) of hydrogen peroxide, a reactive oxygen species, into water and molecular oxygen.²⁷⁰ The active site of Mn-catalase contains a dinuclear manganese center that is bridged by two oxygen atoms from water or hydroxide.²⁷⁰ Additionally, the dinuclear manganese center is also anchored by a bridging carboxylate from a glutamate residue.²⁷⁰ Finally, the oxygen-evolving complex (OEC) within photosystem II (PSII) of green plants catalyzes the

oxidation of water during photosynthesis. The OEC active site is known to be composed of a tetranuclear manganese cluster, with several of the manganese atoms connected through μ -oxo bridges.²⁷⁰

To understand and study the active sites of these manganese containing enzymes, scientists have developed small molecule mimics to elucidate key information such as: number of manganese ions present, spatial arrangement, coordination number, and oxidation states of manganese ions.²⁷⁴ For example, pentaazamacrocyclic ligands have been used to synthesize Mn(II) complexes that can serve as mimics for the active site of superoxide dismutase and multidentate nitrogen-containing ligands have been used to synthesize Mn(III,IV) complexes with di- μ -oxo bridges to mimic the OEC in PSII.²⁷⁵ In addition to SOD and OEC mimics, macrocyclic complexes with manganese in higher oxidation states (III, IV, etc.) have been shown to be useful for catalytic oxidation reactions.²⁷⁴

Recently, the Green group has synthesized a small library of novel tetraazamacrocyclic manganese complexes with various oxidation states using pyclen (**L1**) (**L1** = 1,4,7,10-tetraaza-2,6-pyridinophane), and two novel pyridol-containing tetraazamacrocyclics (**L2** and **L3**) (**L2** = 1,4,7,10-tetraaza-2,6-pyridinophane-14-ol), (**L3** = 1,4,7,10-tetraaza-2,6-pyridinophane-13-ol). Two different sets of manganese complexes were synthesized, a set of Mn(III) mononuclear complexes and a set of Mn(III,IV) di- μ -oxo bridged dinuclear complexes. The two different types of complexes were synthesized by changing the order of addition of ligand and metal salt to a pH adjusted aqueous solution. In addition, the two types of complexes can be interconverted between one another. To our knowledge there is only one other report showing the synthesis of two different manganese complexes (a mononuclear Mn(III) complex and a dinuclear Mn(III,IV) complex) using the same macrocyclic ligand, within the same paper.²⁷⁶ The library of new complexes derived from **L1-L3** was characterized using traditional inorganic techniques including, X-ray diffraction (XRD), UV-visible spectroscopy (UV-vis), cyclic voltammetry (CV), infrared spectroscopy (IR), electronic paramagnetic resonance (EPR), and elemental analysis.

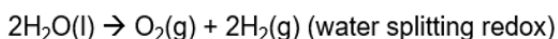
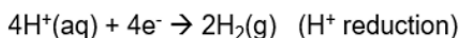
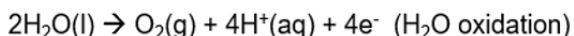
Before discussing the synthesis and characterization of each novel macrocyclic complex performed by the Green group, a brief review of other Mn(III) macrocyclic mononuclear complexes and Mn(III,IV) μ -oxo bridged dinuclear complexes will be presented. Manganese can form a plethora of coordination complexes with a variety of ligand sets, but in this review, we wish to highlight the manganese complexes which parallel the coordination environment observed in our own complexes. This work will be divided into three main sections, the first section of this review will focus on the synthesis, characterization, and applications of macrocyclic Mn(III,IV) di- μ -oxo bridged dinuclear complexes; which have a rich history within the chemical literature. The second section of this review will focus on the synthesis, characterization, and applications of Mn(III) mononuclear complexes; which are much less prevalent in the chemical literature. Following the review of these two types of manganese coordination complexes, the third section will discuss the small library of manganese complexes synthesized by the Green group and reported for the first time herein. As a disclaimer, this review is not comprehensive. We have discussed only manganese complexes relevant to our own studies. While many manganese complexes are covered within this review we apologize to the authors of works that were not included.

General Notes: Complexes are labelled based on a combination of the year they were synthesized, what ligand they were synthesized with, and what type of complex was formed. For example, a Mn(III,IV) dinuclear complex with cyclam is labelled as a different number than a Mn(III) mononuclear complex with cyclam. Different letters after the number indicate different counterions associated with each complex; complexes **4.1a** and **4.1b** are both comprised of the bipy ligand, but the counterions for each complex are different. If a number is written in the text without a letter after it, this is referring to only the cation of the complex not including counterions or solvent molecules, **4.1** = $[(\text{bipy})_4\text{Mn}^{\text{III,IV}}_2\text{O}_2]^{3+}$. For several ligands, such as bispicen and tmpa, researchers synthesized ligand derivatives and made metal complexes with the derivatives, these are labelled with a decimal number after the main number, **4.3.1**, **4.3.2**, etc.

4.2. History of Mn(III,IV) di- μ -oxo bridged dimer complexes

4.2.1. Photosystem II and water oxidation

Photosynthesis, or light-driven water splitting, is one of the most important chemical processes in nature. Nearly all 21% of the O₂ present in the Earth's atmosphere is generated and maintained by this essential process.²⁷⁷⁻²⁷⁸ Several membranes and organelles within plants, algae, and cyanobacteria are responsible for performing the reactions (both light-dependent and light-independent) required for photosynthesis. These light-dependent reactions, which take place in the thylakoid membranes of green plants, are essentially carried out by four major protein complexes: photosystem II (PSII), cytochrome b6f complex, photosystem I (PSI), and ATP synthase.²⁷⁹ The first protein in this series, PSII, is essential, because it contains the oxygen-evolving complex (OEC) which is responsible for water oxidation in plants. Water oxidation is not only a critical step in the photosynthetic process, but also a hot pursuit to understand and mimic among many researchers. The conversion of water into oxygen is an energy intensive process that nature has perfected over millions of years of evolution.



Scheme 4.1. Water splitting redox reactions (water oxidation + proton reduction)

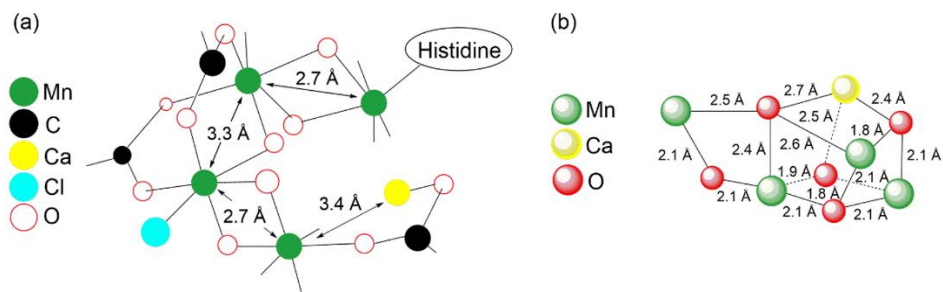
Water oxidation, when paired with proton reduction results in the water splitting redox reaction (Scheme 4.1). If a synthetic water oxidation catalyst (WOC) was combined with a hydrogen evolution catalyst (HEC) and a photosensitizer, scientists could build a device capable of artificial photosynthesis. A device that performs light-driven water splitting has the potential to revolutionize the energy industry. One such device could offer the ability to transform solar radiation into usable energy, in the form of hydrogen.²⁸⁰ Hydrogen could be utilized as an alternative fuel or even as a means reduce the greenhouse gas, carbon dioxide.²⁸⁰ Unfortunately, one of the largest obstacles for building such a device is finding an

efficient WOC. Water oxidation is sometimes referred to as the bottleneck of the water splitting redox reaction, because it (1) requires coupling of 4 e⁻ and H⁺ transfers, (2) has a high activation energy, and (3) requires formation of an O=O bond.²⁸¹⁻²⁸³ Scientists are currently trying to overcome the bottleneck of water splitting to make it a worthwhile endeavor for solar energy storage; the search for the ideal WOC is well underway.²⁸⁰

Fortunately, nature has already designed a highly efficient WOC. The OEC located in PSII performs water oxidation in green plants. This highly efficient WOC has a turnover number (TON) of 180,000 molecules of O₂ per site and a turnover frequency (TOF) of 100-400 s⁻¹; it is by far the most efficient and robust WOC known to date.²⁸⁴ If scientists can mimic the structure of the OEC using small molecular models, this could offer the ability to effectively oxidize water on command.

4.2.2. The oxygen evolving complex (OEC)

The OEC in PSII has been studied by numerous scientists attempting to elucidate the structure of this highly efficient water-oxidation catalyst. During the last century scientists often disagreed about the predicted structure of the OEC. In 1970, Joliot and Kok established a theory, known today as the Kok cycle, that the OEC exists in 5 different oxidation states (S₀ – S₄).²⁸⁵⁻²⁸⁷ Some of the first evidence for multiple manganese atoms in different oxidation states came from low temperature EPR measurements derived from work related to the Kok cycle. In the stable S₂ state, the OEC exhibited a multiline EPR signal, due in part to an exchange coupled multinuclear manganese structure.^{285, 287-289} Additionally, EXAFS data of the OEC in both the S₁ and S₂ states indicated Mn—Mn distances of 2.7 Å.^{285, 287, 289} These pieces of evidence, along with several other observations, seemed to be diagnostic of a di-μ-oxo bridged manganese cluster within the OEC.²⁸⁵ In 1993, Yachandra *et al.* proposed a model for the OEC in PSII based upon the culmination of gathered evidence suggesting multiple manganese centers connected through oxo-bridges (Scheme 4.2(a)).^{287, 289} Not all scientists agreed with the proposed model, based on differing interpretations of the data relating to the S states.²⁸⁷



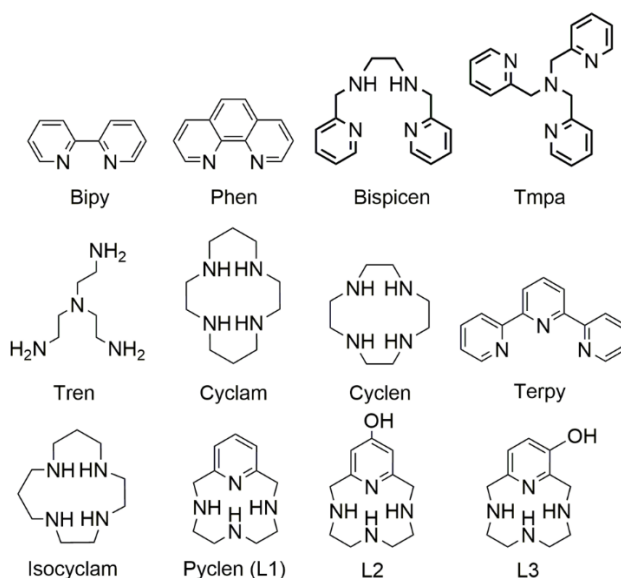
Scheme 4.2. (a) Proposed model of OEC published in 1994^{287, 289} (b) Crystal structure of OEC at resolution of 1.9 Å, published in 2011.²⁹⁰

A huge step toward determining the structure of the OEC came in 1998, when Rhee *et al.* published a crystal structure of PSII fragments at a resolution of 8 Å.²⁹¹ This initial crystal structure of inactive PSII fragments was followed by an influx of PSII crystal structures from 2000 up to 2011. Each newly solved PSII structure offered a higher resolution than what was previously reported, with some structures only differing by 0.1 Å.²⁸⁹⁻²⁹⁸ Finally, in 2011, Umena *et al.* reported the crystal structure of PSII contained within the thermophilic cyanobacteria *Thermosynechococcus vulcanus* at a resolution of 1.9 Å, the highest reported resolution of PSII reported to date.²⁹⁰ At this resolution, the electron densities of four manganese atoms and a single calcium atom were distinguishable. Additionally, five oxygen atoms that serve as oxo-bridges linking the five metal atoms were identified. The arrangement of the metal and oxygen atoms within the OEC gives rise to a cubane-like structure (Mn_3CaO_4). Three manganese atoms and a calcium atom are in four corners of the cubane. The fourth manganese atom is not within the cubane structure but linked to it through a di- μ -oxo bridge. Umena *et al.* describe the structure of the OEC as a “distorted chair” with the cubane serving as the seat base and the isolated manganese atom and oxygen as the chair back (Scheme 4.2(b)).²⁹⁰

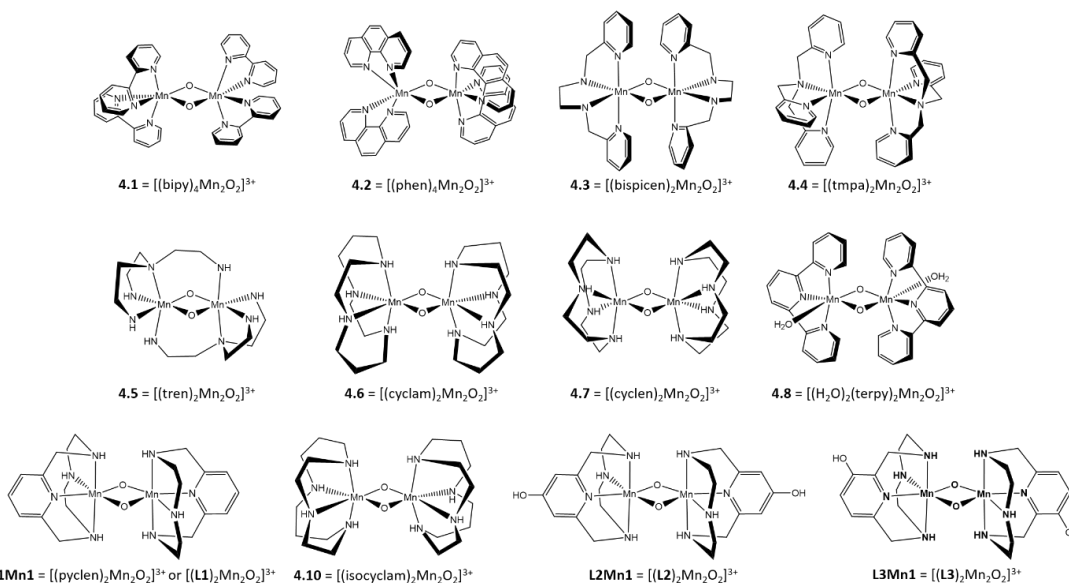
Until recently the complete structure of the OEC had not been determined, but early data gathered on PSII, using EXAFS and EPR, indicated a di- μ -oxo bridged manganese complex contained within the OEC. Many researchers believed that the OEC contained a “dimer” of dimers.²⁶⁵ Based on this early evidence, small molecule di- μ -oxo bridged manganese dimers have been produced to mimic the structure of the OEC. There is a rich history of these dimers within the chemical literature.²⁹⁹⁻³⁰⁶ While these di- μ -

oxo bridged manganese dimers may be rudimentary they still offer the ability to catalyze water oxidation. The following section will discuss the synthesis, characterization, and applications of these historically significant Mn(III,IV) dimers (refer to schemes 4.3 and 4.4 for the range of ligands utilized and resulting complexes).

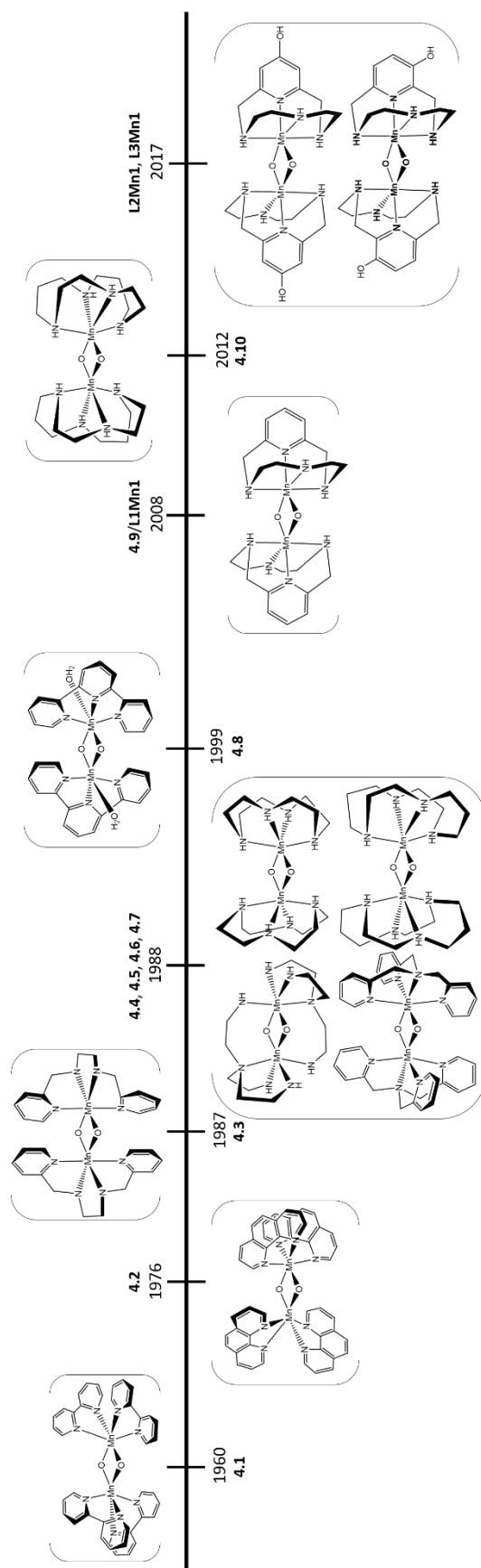
4.2.3. Schemes and tables related to historic Mn(III,IV) dimer complexes



Scheme 4.3. Parent ligands for Mn(III,IV) dimer complexes.



Scheme 4.4. Historically significant di- μ -oxo bridged Mn(III,IV) dimers.



Scheme 4.5. Synthesis timeline of Mn(III,IV) di- μ -oxo bridged dimers.

Table 4.1. Di- μ -oxo-bridged Mn(III,IV) dimers reported in literature.

	Complex	Year reported	Reference
4.1a	$[(\text{bipy})_4\text{Mn}_2\text{O}_2][\text{S}_2\text{O}_8]_{1.5}$	1960	1
4.1b	$[(\text{bipy})_4\text{Mn}_2\text{O}_2][\text{ClO}_4]_3 \cdot 2 \text{H}_2\text{O}$	1960, 1977	2
4.1c*	$[(\text{bipy})_4\text{Mn}_2\text{O}_2][\text{ClO}_4]_3$	1972	3
4.1d*	$[(\text{bipy})_4\text{Mn}_2\text{O}_2][\text{ClO}_4]_3 \cdot 3 \text{H}_2\text{O}$	1986	4
4.2a*	$[(\text{phen})_4\text{Mn}_2\text{O}_2][\text{PF}_6]_3 \cdot \text{CH}_3\text{CN}$	1976, 1986	5
4.2b	$[(\text{phen})_4\text{Mn}_2\text{O}_2][\text{ClO}_4]_3 \cdot \text{CH}_3\text{COCH}_3$	1977	6
4.2c*	$[(\text{phen})_4\text{Mn}_2\text{O}_2][\text{ClO}_4]_3 \cdot 2\text{C}_2\text{H}_3\text{O}_2 \cdot 2\text{H}_2\text{O}$	1994	7
4.3a*	$[(\text{bispicen})_2\text{Mn}_2\text{O}_2][\text{ClO}_4]_3 \cdot 3 \text{H}_2\text{O}$	1987	8
4.3b	$[(\text{bispicen})_2\text{Mn}_2\text{O}_2][\text{ClO}_4]_3$	1990	9
4.4a*	$[(\text{tmpa})_2\text{Mn}_2\text{O}_2][\text{S}_2\text{O}_6]_{3/2} \cdot 7 \text{H}_2\text{O}$	1988	10
4.4b	$[(\text{tmpa})_2\text{Mn}_2\text{O}_2][\text{ClO}_4]_3 \cdot 3 \text{H}_2\text{O}$	1988	11
4.4c*	$[(\text{tmpa})_2\text{Mn}_2\text{O}_2][\text{ClO}_4]_3$	2007, 2014	12
4.5a*	$[(\text{tren})_2\text{Mn}_2\text{O}_2][\text{CF}_3\text{SO}_3]_3 \cdot \text{EtOH}$	1988	13
4.6a*	$[(\text{cyclam})_2\text{Mn}_2\text{O}_2][\text{ClO}_4]_3 \cdot 2 \text{H}_2\text{O}$	1988, 1989	14
4.6b*	$[(\text{cyclam})_2\text{Mn}_2\text{O}_2][\text{Br}]_3 \cdot 4 \text{H}_2\text{O}$	1990	15
4.6c*	$[(\text{cyclam})_2\text{Mn}_2\text{O}_2][\text{S}_2\text{O}_6]_{1.37}[\text{S}_2\text{O}_3]_{0.13}$	1990	16
4.6d	$[(\text{cyclam})_2\text{Mn}_2\text{O}_2][\text{ClO}_4]_3$	2014	17
4.7a	$[(\text{cyclen})_2\text{Mn}_2\text{O}_2][\text{ClO}_4]_3 \cdot 2 \text{H}_2\text{O}$	1988	18
4.7b*	$[(\text{cyclen})_2\text{Mn}_2\text{O}_2][\text{Cl}]_3 \cdot \text{LiCl} \cdot 5 \text{H}_2\text{O}$	1992	19
4.7c	$[(\text{cyclen})_2\text{Mn}_2\text{O}_2][\text{NO}_3]_3$	1992	20
4.8a*	$[(\text{H}_2\text{O})_2(\text{terpy})_2\text{Mn}_2\text{O}_2](\text{NO}_3)_3$	1999	21
4.9a*	$[(\text{pyclen})_2\text{Mn}_2\text{O}_2][\text{Cl}]_3 \cdot 6 \text{H}_2\text{O}$	2008	22
L1Mn1*	$[(\text{L1})_2\text{Mn}_2\text{O}_2][\text{ClO}_4]_3 \cdot 4 \text{H}_2\text{O}$	2017	This work
4.10a	$[(\text{isocyclam})_2\text{Mn}_2\text{O}_2][\text{ClO}_4]_3 \cdot 2\text{H}_2\text{O}$	2012	23
L2Mn1*	$[(\text{L2})_2\text{Mn}_2\text{O}_2][\text{ClO}_4] \cdot 4 \text{H}_2\text{O}$	2017	This work
L3Mn1	$[(\text{L3})_2\text{Mn}_2\text{O}_2]^{3+}$	2017	This work

*Solid state structure has been reported in literature. 1: ref. ²⁹⁹; 2: ref. ^{299, 302}; 3: ref. ³⁰⁰; 4: ref. ³⁰⁷; 5: ref. ^{301, 307}; 6: ref. ³⁰²; 7: ref. ³⁰⁸; 8: ref. ³⁰³; 9: ref. ³⁰⁹; 10: ref. ²⁶⁸; 11: ref. ³⁰⁶; 12: ref. ^{270, 310}; 13: ref. ³⁰⁵; 14: ref. ^{265, 304}; 15: ref. ³¹¹; 16: ref. ³¹¹; 17: ref. ³¹²; 18: ref. ³⁰⁴; 19: ref. ³¹³; 20: ref. ³¹³; 21: ref. ³¹⁴; 22: ref. ³¹⁵; 23: ref. ²⁷⁶.

Table 4.2. Mn—Mn bond distances within di- μ -oxo bridged Mn(III,IV) dimers.

Complex	Mn ^{III} —Mn ^{IV} (Å)	Reference
4.1c	2.716	1
4.1d	2.716	2
4.2a	2.700	3
4.3a	2.659	4
4.4a	2.643	5
4.4c	2.624 & 2.626*	6
4.5a	2.679	7
4.6a	2.731	8
4.6b	2.741	9
4.6c	2.729 & 2.738*	10
4.7b	2.694	11
4.8a	2.723	12
4.9a	2.6814	13
L1Mn1	2.712	This work
L2Mn1	2.709	This work

*Contains two Mn₂O₂ species within asymmetric unit, both Mn—Mn distances are reported. 1: ref. ³⁰⁰; 2: ref. ³⁰⁷; 3: ref. ^{301,307}; 4: ref. ³⁰³; 5: ref. ²⁶⁸; 6: ref. ²⁷⁰; 7: ref. ³⁰⁵; 8: ref. ²⁶⁵; 9: ref. ³¹¹; 10: ref. ³¹¹; 11: ref. ³¹³; 12: ref. ³¹⁴; 13: ref. ³¹⁵.

Table 4.3. Mn₂O₂ vibrational frequencies of di- μ -oxo bridged Mn(III,IV) dimers.

Complex	Mn ₂ O ₂ (cm ⁻¹)	Reference
4.1b	688	1
4.2b	686	2
4.5a	694	3
4.6a	680	4
4.7a	689	5
L1Mn1	676	This work
4.10a	684	6
L2Mn1	676	This work

1: ref. ³⁰²; 2: ref. ³⁰²; 3: ref. ³⁰⁵; 4: ref. ³⁰⁴; 5: ref. ³⁰⁴; 6: ref. ²⁷⁶.

Table 4.4. Electronic spectra of di- μ -oxo bridged Mn(III,IV) dimers.

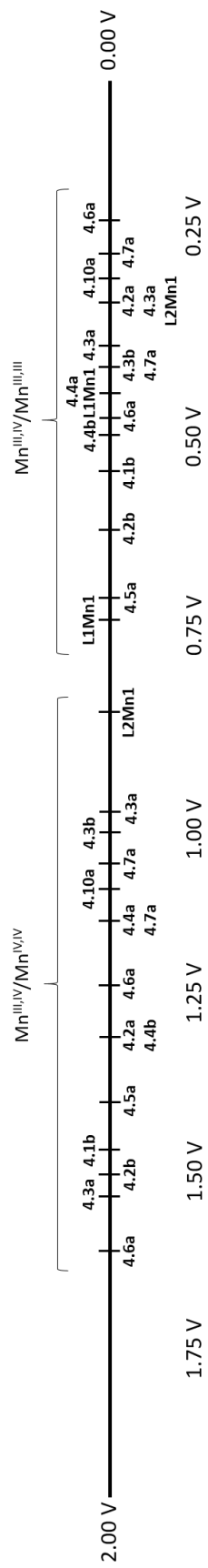
Complex	λ_{\max} (nm), (ϵ , Mol ⁻¹ cm ⁻¹)	Solvent	Reference
4.1b	525 (530), 555 (455), 684 (561)	bipy buffer	1
4.2a	523 (580), 550 (460), 680 (550), 800 (sh)	solid state	2
4.2b	525 (509), 555 (427), 684 (553)	phen buffer	3
4.3b	386 (1355), 432 (1270), 553 (569), 655 (526), 805 (250)	water	4
4.4b	443 (1490), 561 (760), 658 (620)	acetonitrile	5
4.5a	380 (1170), 428 (sh), 526 (sh), 548 (440), 590 (sh), 638 (sh), 680 (570)	acetonitrile	6
4.6a	550 (760), 650 (780) 556 (750), 560 (sh), 646 (760), 800 (125)	water acetonitrile	7
4.6b	550 (750), 644 (770), 800 (sh)	N-methylformamide	8
4.7a	556 (700), 650 (890), 740 (880)	water	9
4.7b	381 (1741), 430 (sh 1275), 554 (535), 658 (676), 696 (666) 379 (1769), 430 (sh 1289), 554 (550), 652 (678), 697 (667)	water N-methylformamide	10
L1Mn1	382(652), 555(181), 665(211), 800 (sh)	Water	This work
4.10a	548, 562(760), 652(750)	Water	11
L2Mn1	382(536), 554(119), 658(107), 800(sh)	Water	This work
L3Mn1	383(446), 554(119), 659(123), 800(sh)	Water	This work

1: ref. ³⁰²; 2: ref. ³⁰⁷; 3: ref. ³⁰²; 4: ref. ³⁰⁹; 5: ref. ³⁰⁶; 6: ref. ³⁰⁵; 7: ref. ^{265, 304}; 8: ref. ³¹¹; 9: ref. ³⁰⁴; 10: ref. ³¹³; 11: ref. ²⁷⁶

Table 4.5. Electrochemistry of di- μ -oxo bridged Mn(III,IV) dimers.

Complex	Mn ^{III,IV} /Mn ^{IV,IV} (V) vs. NHE	Mn ^{III,IV} /Mn ^{III,III} (V) vs. NHE	Solvent and Electrolyte	Reference
4.1b	1.49	0.53	CH ₃ CN, 0.3 M TEAP	1
4.2a	1.28	0.34	CH ₃ CN, 0.1 M TBAP	2
4.2b	1.50	0.58	CH ₃ CN, 0.3 TEAP	3
4.3a	0.99	0.38	H ₂ O (pH 7.0), 0.1 M NaClO ₄	4
	1.51	0.34	CH ₃ CN, 0.1 M NaClO ₄	
4.3b	1.00	0.39	H ₂ O (pH 7.4), 0.1 M NaClO ₄	5
4.4a	1.14	0.44 (E _{pc} only)	H ₂ O (pH 6.9)	6
4.4b	1.28	0.48	CH ₃ CN, 0.1 M TBAP	7
4.5a	1.42	0.68	No information	8
4.6a	1.24	0.24	CH ₃ CN, 0.1 M TBAP	9
	1.59	0.47	CH ₃ CN, 0.1 M TBAPF ₆	
4.7a	1.14	0.39	CH ₃ CN, 0.1 M TBAP	10
	1.04	0.27	CH ₃ CN, 0.1 M TBAP	
L1Mn1	-	0.70	CH ₃ CN, 0.1 M TBAP	This work
	-	0.44 (E _{pc} only)	H ₂ O (pH 7.0), 0.1 M NaClO ₄	
4.10a	1.09	0.29	H ₂ O (pH 7.0), 0.1 M KCl	11
L2Mn1	0.85	0.35 (E _{pc} only)	H ₂ O (pH 7.0), 0.1 M NaClO ₄	This work

1: ref. ^{299, 302}; 2: ref. ^{301, 307}; 3: ref. ³⁰²; 4: ref. ³⁰³; 5: ref. ³⁰⁹; 6: ref. ²⁶⁸; 7: ref. ³⁰⁶; 8: ref. ³⁰⁵; 9: ref. ^{265, 304}; 10: ref. ^{304, 313}; 11: ref. ²⁷⁶.



Scheme 4.6. Oxidation and reduction values for various di- μ -oxo bridged Mn(III,IV) dimers in literature.

4.2.4. Bipy and phen Mn(III,IV) dimers

As shown in Scheme 4.5, the first di- μ -oxo bridged manganese dimer $[(\text{bipy})_4\text{Mn}^{\text{III,IV}}_2\text{O}_2][\text{S}_2\text{O}_8]_{1.5}$ (**4.1a**) (bipy = 2,2-bipyridine) (Schemes 4.3, 4.4, 4.5; Table 4.1) was chemically synthesized in 1960 by Nyholm and Turco by adding molten bipy and solid $\text{K}_2\text{S}_2\text{O}_8$ (an oxidizing agent) to a suspension of $\text{MnSO}_4 \cdot 4\text{H}_2\text{O}$ in warm water.²⁹⁹ The product, which was isolated as large greenish-black crystals was postulated to contain two manganese centers in different high valent oxidation states (III, IV).²⁹⁹ In addition to the synthesis of **4.1a** which contained a persulfate counterion, Nyholm and Turco also performed a metathesis reaction to obtain the corresponding perchlorate $[(\text{bipy})_4\text{Mn}^{\text{III,IV}}_2\text{O}_2][\text{ClO}_4]_3 \cdot 2\text{H}_2\text{O}$ (**4.1b**) (Table 4.1). Later, in 1972 Plaksin *et al.* chemically synthesized a similar di- μ -oxo bridged manganese dimer containing bipy ligands $[(\text{bipy})_4\text{Mn}^{\text{III,IV}}_2\text{O}_2][\text{ClO}_4]_3$ (**4.1c**) (Table 4.1).³⁰⁰ They reported the solid state structure for the novel bimetallic complex **4.1c** and confirmed the manganese centers were in two different oxidation states (III, IV) based on bond lengths and the significant Jahn-Teller distortion exhibited by the Mn(III) atom.³⁰⁰ The Mn—Mn bond distance reported for **4.1c** was 2.716 Å (Table 4.2), which is similar to the Mn—Mn bond distance observed in the OEC (2.7 Å).³⁰⁰

In 1977, Cooper and Calvin were able to chemically synthesize another di- μ -oxo bridged manganese dimer $[(\text{phen})_4\text{Mn}^{\text{III,IV}}_2\text{O}_2][\text{ClO}_4]_3 \cdot \text{CH}_3\text{COCH}_3$ (**4.2b**) (phen = 1,10-phenanthroline) (Schemes 4.3, 4.4, 4.5; Table 4.1) which was originally synthesized by Uson as $[(\text{phen})_4\text{Mn}^{\text{III,IV}}_2\text{O}_2][\text{PF}_6]_3 \cdot \text{CH}_3\text{CN}$ (**4.2a**), in 1976 (Table 4.1).³⁰¹⁻³⁰² The green powder (**4.2b**) was synthesized by adding KMnO_4 (an oxidizing agent) in H_2O , dropwise, to a solution of $\text{Mn}(\text{OAc})_2 \cdot 4\text{H}_2\text{O}$ and phen.³⁰² In addition to synthesizing the new phen Mn(III,IV) dimer, Cooper and Calvin examined both **4.1b** and **4.2b** using IR, CV, and UV-vis, (Table(s) 4.3, 4.4; Schemes 4.5, 4.6).³⁰² These characterization techniques offered insight into how the two manganese centers were interacting in solution. Cooper and Calvin utilized IR and isotopic substitution to identify the Mn_2O_2 vibration mode. Prior to recrystallization in H_2^{18}O a stretching frequency of 688 cm^{-1} was observed for the bipy dimer (Table 4.3), but upon recrystallization in H_2^{18}O at 80°C a new band (shoulder) appeared

at 676 cm^{-1} .³⁰² The stretching frequencies of 688 cm^{-1} (**4.1b**) and 686 cm^{-1} (**4.2b**) were assigned as the vibrational modes of the Mn_2O_2 core; no other bands were shifted.³⁰² Additionally, based on the electronic spectra and previously obtained crystal structure of **4.1b**, Cooper and Calvin concluded that both **4.1b** and **4.2b** were Class II compounds in the classification scheme of Robin and Day for mixed valent compounds.^{302, 316} Class II compounds have weak interactions between the metal ions, meaning that in addition to the typical absorbances observed from each metal ion, the electronic spectrum also exhibits a new absorption due to a photon-driven electron transfer (intervalence transfer or IT) between the metal ions.^{302, 316} In contrast, Class I compounds have almost no interaction between the metal ions and Class III compounds are considered fully delocalized and resonance stabilized compounds.^{302, 316} The electronic spectra for both **4.1b** and **4.2b** exhibited absorbance bands at 525, 555, and 684 nm.³⁰² Cooper and Calvin assigned the 525 and 555 nm absorbance bands as d-d bands, based on small extinction coefficient values; the 684 nm absorbance band had been previously assigned as a ligand to metal charge transfer band (LMCT) from the oxygen to the Mn(III) metal center.^{302, 317} This lower energy band was later reassigned by Suzuki *et al.* as the ligand to metal charge transfer from the oxygen to the Mn(IV) metal center.³⁰⁶ In addition to these absorbance bands, an 830 nm shoulder off of the 684 nm absorbance band was observed; this would later be identified as an IT band by Stebler *et al.*³⁰⁷ Cooper and Calvin also investigated **4.1b** and **4.2b** using CV. For both complexes, they observed two redox events, a reversible anodic wave corresponding the oxidation of $\text{Mn}^{\text{III,IV}}/\text{Mn}^{\text{IV,IV}}$ ($E_{1/2} = 1.49\text{ V vs. NHE}$ for **4.1b** and $E_{1/2} = 1.50\text{ V vs. NHE}$ for **4.2b**) (Table 4.4, Scheme 4.6) and a reversible cathodic wave corresponding to the reduction of $\text{Mn}^{\text{III,IV}}/\text{Mn}^{\text{III,III}}$ ($E_{1/2} = 0.53\text{ V vs. NHE}$ for **4.1b** and $E_{1/2} = 0.58\text{ V vs. NHE}$ for **4.2b**) (Table 4.4, Scheme 4.6).³⁰² The following year, in 1978, Cooper and Calvin published EPR investigations of **4.1b** and **4.2b** which exhibited a 16-line spectrum at 18 K and average g values of 2.003.³¹⁸ The small g anisotropy suggested that the ground state of the Mn(III) (d^4) ion was high-spin.³¹⁸ Subsequent, EPR studies on **4.1b** and **4.2b** confirmed that the manganese ions were inequivalent in solution.

Although the initial synthesis of **4.2a** was reported in 1976 (Scheme 4.5, Table 4.1), a complete solid state structure of a phen Mn(III,IV) dimer was not published until 1986. Stebler *et al.* reported the crystal structure for a $[(\text{phen})_4\text{Mn}^{\text{III,IV}}_2\text{O}_2][\text{PF}_6]_3 \cdot \text{CH}_3\text{CN}$ (**4.2a**) complex with static disorder between the two manganese centers.³⁰⁷ The measured bond distance between the Mn—Mn atoms was 2.700 Å (100 K) and 2.695 Å (200 K) (Table 4.2). At both temperatures, the bond distances are slightly shorter than the Mn—Mn distance in **4.1c** or **4.1d** but still comparable to Mn—Mn distances found in the OEC.³⁰⁷ In addition to the solid state structure, Stebler *et al.* also performed UV-vis, and CV measurements on **4.2a**.³⁰⁷ The electronic spectrum and cyclic voltammogram of the newly synthesized phen dimer were remarkably similar to those previously reported by Cooper and Calvin (Tables 4.4, 4.5; Scheme 4.6). After the initial reports in the 1970s and 1980s regarding the synthesis and characterization of novel phen Mn(III,IV) dimers another report in 1994, focused on a new and improved synthesis.³⁰⁸ Manchanda *et al.* reported a different method for obtaining a phen Mn(III,IV) dimer $[(\text{phen})_4\text{Mn}^{\text{III,IV}}_2\text{O}_2][\text{ClO}_4]_3 \cdot 2\text{C}_2\text{H}_3\text{O}_2 \cdot 2\text{H}_2\text{O}$ (**4.2c**) and subsequently reported the crystal structure of this newly synthesized complex. Unlike the crystal structure reported by Stebler *et al.* for **4.2a**, which contained static disorder between the two manganese centers, Manchanda *et al.* obtained data that showed crystallographically distinct Mn(III) and Mn(IV) ions and a Mn—Mn bond distance of 2.711 Å (Table 4.2).³⁰⁸

4.2.4.1. Catalytic ability of bipy and phen Mn(III,IV) dimers

After synthesis and extensive characterization of complexes **4.1** and **4.2** (remember that **4.1** and **4.2** refer to the cation of the Mn(III,IV) complex only, shown in scheme 4.4); several groups investigated the catalytic abilities of these novel complexes. The first activity report by Gref *et al.*, in 1984 showed that the redox couples of complexes **4.1** and **4.2** (Scheme 4.4) could catalyze the anodic oxidation of benzyl ethers and benzyl alcohols with high selectivity.³¹⁹ Later in 1986 and for the first time, Ramaraj *et al.* reported evidence of complexes **4.1** and **4.2** performing water oxidation.³²⁰ They found that when the di- μ -oxo bridged manganese dimers were suspended heterogeneously in water, with the presence of a

chemical oxidant (Ce^{IV}) these complexes could oxidize water; as evidenced by the visible formation of oxygen bubbles.³²⁰ In contrast, when complexes **4.1** or **4.2** were completely dissolved in water (i.e. in a homogeneous solution), addition of Ce^{IV} resulted in no oxygen formation, as confirmed by analysis of the gas phase above the solution.³²⁰ Additional investigation of this heterogeneous water oxidation revealed that stirring the reaction mixture led to more O_2 formation and that the pH of the solution did not affect the water oxidation process.³²⁰ Ramaraj *et al.* also found that complex **4.1** was a more efficient catalyst than complex **4.2**; which was consistent with complex **4.1** being easier to oxidize, as evidenced by CV.³²⁰ This was the first report of water oxidation by Mn(III,IV) dimer complexes, and the first confirmation of their heterogeneous water oxidation ability.

The year following this initial report, Ramaraj *et al.* published an additional report on the investigation of complex **4.1** adsorbed onto clay and its water oxidation ability as a heterogeneous catalyst.³²¹ The heterogeneous catalyst was prepared by mixing complex **4.1** with Kaolin clay in water. Findings for this heterogeneous catalyst were similar to what was observed previously by Ramaraj *et al.* When complex **4.1** was adsorbed onto clay, O_2 bubbles formed on the surface of the clay in the presence of Ce^{IV} .³²¹ Ramaraj *et al.* did observe decomposition of complex **4.1** if too much catalyst was adsorbed onto the clay surface; increase of complex **4.1** on the clay surface led to an increase in oxygen evolution, but once a certain threshold was reached decomposition was observed. The decomposition product, MnO_4^- , was detected by UV-vis analysis of the solution after catalysis.³²¹ Overall, the findings of this second report by Ramaraj *et al.* complimented what had been discovered in the original report.³²⁰ Following the discovery that di- μ -oxo bridged manganese dimers had the potential to act as water oxidation catalysts, there was a large increase in the number of publications dedicated to manganese dimers in the late 1980s.^{265, 268, 303-305, 322-323}

4.2.5. Bispicen Mn(III,IV) dimers

After the discovery, synthesis, and characterization of the novel di- μ -oxo bridged manganese dimer complexes with phen and bipy ligands more groups began to synthesize Mn(III,IV) dimers with different multidentate nitrogen containing ligands. In 1987, Collins *et al.* synthesized a novel bispicen dimer complex $[(\text{bispicen})_2\text{Mn}^{\text{III,IV}}_2\text{O}_2][\text{ClO}_4]_3 \cdot 3\text{H}_2\text{O}$ (**4.3a**) (bispicen = *N,N'*-bis(2-pyridylmethyl)-1,2-diaminoethane) (Schemes 4.3, 4.4, 4.5; Table 4.1) by combining $\text{MnCl}_2 \cdot 4\text{H}_2\text{O}$, bispicen $\cdot 4\text{HCl}$, sodium bicarbonate, and hydrogen peroxide.³⁰³ As shown in scheme 4.4, complex **4.3a** deviated from the previously synthesized complexes **4.1** and **4.2** based on number of ligands comprising the complex. Both **4.1** and **4.2** contained four individual bidentate ligands (two ligands bound to each individual manganese atom), whereas **4.3** contained two individual tetradentate ligands (one ligand bound to each individual manganese atom). Collins *et al.* obtained a solid state structure of the bispicen dimer as well as CV measurements.³⁰³ Within the solid state structure of **4.3a**, the Mn—Mn bond distance in the bispicen dimer was measured to be 2.659 Å; this distance was considerably shorter than the Mn—Mn bond distances of complex **4.1a/4.1d** (2.716 Å) and **4.2a** (2.700 Å) (table 4.2).³⁰³ Additionally, the CV of the bispicen dimer **4.3a** in both water and acetonitrile showed two *quasi*-reversible redox events, similar to **4.1** and **4.2**, these corresponded to the *quasi*-reversible anodic oxidation of $\text{Mn}^{\text{III,IV}}/\text{Mn}^{\text{IV,IV}}$ ($E_{1/2} = 0.99$ V vs. NHE in water; $E_{1/2} = 1.51$ vs. NHE in acetonitrile) and the *quasi*-reversible cathodic reduction of $\text{Mn}^{\text{III,IV}}/\text{Mn}^{\text{III,III}}$ ($E_{1/2} = 0.38$ vs. NHE in water; $E_{1/2} = 0.34$ vs. NHE in acetonitrile) (Table 4.5).³⁰³ In contrast to the previously synthesized dimers, Collins *et al.* found **4.3a** was easier to oxidize to the Mn(IV,IV) form, based on more negative anodic waves of **4.3a** compared to either complex **4.1** or **4.2**.³⁰³

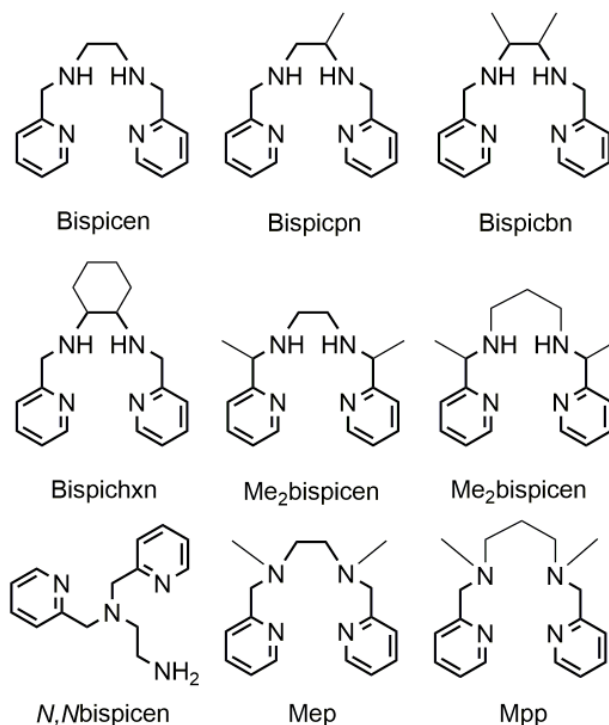
In 1990, Goodson *et al.* synthesized another bispicen dimer $[(\text{bispicen})_2\text{Mn}^{\text{III,IV}}_2\text{O}_2][\text{ClO}_4]_3$ (**4.3b**) (Table 4.1) and performed additional characterization techniques.³⁰⁹ They acquired the electronic spectrum, additional CV measurements, and EPR measurements for this bispicen complex (Tables 4.4, 4.5; Scheme 4.6). The electronic spectrum of **4.3b** was similar to complexes **4.1** and **4.2**, with absorbance

bands at 386, 432, 655, and 805 nm (Table 4.4). The CV measurements obtained by Goodson *et al.* were congruent to those taken initially by Collins *et al.* Two *quasi*-reversible waves were observed for the complex corresponding to the reduction and oxidation of the Mn(III,IV) dimer ($E_{1/2} = 0.99$ V vs. NHE (oxidation); $E_{1/2} = 0.39$ V vs. NHE (reduction) in water) (Table 4.5, Scheme 4.6).³⁰⁹ EPR studies of **4.3b** exhibited a 16-line hyperfine pattern, which was now assigned as two antiferromagnetically coupled manganese ions.

Table 4.6. Bispicen derived Mn(III,IV) dimer complexes.

Complex	Coordinating Ligand	Metal Complex	Reference
4.3a	<i>N,N'</i> -bis(2-pyridylmethyl)-1,2-diaminoethane (bispicen)	$[(\text{bispicen})_2\text{Mn}_2\text{O}_2][\text{ClO}_4]_3 \cdot 3 \text{H}_2\text{O}$	1
4.3b	<i>N,N'</i> -bis(2-pyridylmethyl)-1,2-diaminoethane (bispicen)	$[(\text{bispicen})_2\text{Mn}_2\text{O}_2][\text{ClO}_4]_3$	2
4.3.1a	<i>N,N'</i> -bis(2-pyridylmethyl)-1,2-propanediamine (bispicpn)	$[(\text{bispicpn})_2\text{Mn}_2\text{O}_2][\text{ClO}_4]_3 \cdot 5 \text{H}_2\text{O}$	
4.3.2a	<i>N,N'</i> -bis(2-pyridylmethyl)-2,3-butanediamine (bispicbn)	$[(\text{bispicbn})_2\text{Mn}_2\text{O}_2][\text{ClO}_4]_3 \cdot 4 \text{H}_2\text{O}$	
4.3.3a	<i>N,N'</i> -bis(2-pyridylmethyl)-1,2-cyclohexanediamine (bispichxn)	$[(\text{bispichxn})_2\text{Mn}_2\text{O}_2][\text{ClO}_4]_3 \cdot 5 \text{H}_2\text{O}$	3
4.3.4a	<i>N,N'</i> -bis(1-(2-pyridyl)ethyl)-1,2-ethanediamine (Me_2 bispicen)	$[(\text{Me}_2\text{bispicen})_2\text{Mn}_2\text{O}_2][\text{ClO}_4]_3 \cdot \text{H}_2\text{O}$	
4.3.5a	<i>N,N'</i> -bis(1-(2-pyridyl)ethyl)-1,3-propanediamine (Me_2 bispicpn)	$[(\text{Me}_2\text{bispicpn})_2\text{Mn}_2\text{O}_2][\text{ClO}_4]_3$	
4.3.6a	<i>N,N</i> -bis(2-pyridylmethyl)-1,2-diaminoethane (<i>N,N</i> bispicen)	$[(\text{N,Nbispicen})_2\text{Mn}_2\text{O}_2][\text{ClO}_4]_3 \cdot \text{CH}_3\text{CN}$	4
4.3.7a	<i>N,N'</i> -dimethyl- <i>N,N'</i> -bis(2-pyridylmethyl)ethane-1,2-diamine (mep)	$[(\text{mep})_2\text{Mn}_2\text{O}_2][\text{ClO}_4]_3$	5
4.3.8a	<i>N,N'</i> -dimethyl- <i>N,N'</i> -bis(2-pyridylmethyl)propane-1,3-diamine (mpp)	$[(\text{mpp})_2\text{Mn}_2\text{O}_2][\text{ClO}_4]_3$	

1: ref. ³⁰³; 2: ref. ³⁰⁹; 3: ref. ³²⁴; 4: ref. ³²⁵; 5: ref. ³²⁶.



Scheme 4.7. Bispicen and derivatized ligands.

The following year, in 1991, Goodson *et al.* published an additional report describing the synthesis and characterization of a library of bispicen derived di- μ -oxo bridged manganese dimers (**4.3.1a-4.3.5a**) (Table 4.6, Scheme 4.7).³²⁴ The complexes were synthesized utilizing a similar approach to Collins *et al.*³⁰³ As stated in the report, the goal for synthesizing this library of bispicen derived dimers was to bring about stereochemical and electronic changes to the manganese centers.³²⁴ Spectroscopic (UV-vis) and electrochemical (CV) characterization methods were utilized in the attempt to analyze each complex's ability to serve as a redox catalyst. Goodson *et al.* observed only small changes in the redox potentials of the bispicen derivative complexes compared to the original bispicen complex with maximum shifts in redox potentials of 49 mV.³²⁴

Yet another bispicen derivative complex was reported in 1998, by Horner *et al.* $[(N,N\text{bispicen})_2\text{Mn}^{\text{III,IV}}\text{O}_2][\text{ClO}_4]_3 \cdot \text{CH}_3\text{CN}$ (**4.3.6a**) (Table 4.6, Scheme 4.7).³²⁵ Although technically an isomer of bispicen, *N,N*bispicen is a tripodal ligand that is similar to ligands such as tmpa (tmpa = tris(2-methylpyridyl)amine) or tren (tren = tris(2-aminoethyl)amine).³²⁵ Horner *et al.* found an unusual feature of this novel *N,N*bispicen dimer. The crystal structure of complex **4.3.6a** indicated that the *N,N*bispicen ligands were in the *cis* configuration relative to the Mn_2O_2 core, meaning that the two primary amino groups from the ligand were situated on the same side of the Mn_2O_2 plane. Technically, this meant that both a *cis* and *trans* di- μ -oxo bridged manganese dimer could be synthesized, although only the *cis* isomer was isolated. Despite this interesting feature the characterization of complex **4.3.6a** was quite similar to previously reported bispicen derivatives.³²⁵

Almost 20 years after the original synthesis of a bispicen Mn(III,IV) dimer, Hureau *et al.* reported a method for electrochemically converting Mn(II) monomer complexes into Mn(III,IV) dimers (**4.3.7a** and **4.3.8a**) (Table 4.6, Scheme 4.7).³²⁶ It should be noted that prior to 2005 every di- μ -oxo bridged manganese dimer was chemically synthesized. In the presence of 2,6-dimethylpyridine and the absence of chloride ions, *cis*[(mep)Mn^{II}Cl₂] and *cis*[(mpp)Mn^{II}Cl₂] were electrochemically oxidized to [(mep)₂Mn^{III,IV}O₂]³⁺

(**4.3.7a**) and $[(mpp)_2Mn^{III,IV}_2O_2]^{3+}$ (**4.3.8a**) using bulk electrolysis.³²⁶ Hureau *et al.* noted that in the absence of base no such Mn(III,IV) dimer complexes were observed after bulk electrolysis. It was hypothesized the 2,6-dimethylpyridine acted to neutralize the protons generated by the formation of the oxo bridges, which originated from the water molecules, thus facilitating formation of the Mn(III,IV) dimer in solution.³²⁶ The newly synthesized species were confirmed with EPR, CV, UV-vis, and XRD (complex **4.3.8a** only). Each characterization method exhibited characteristic signs of a Mn(III,IV) dimer in solution. This was the first report of electrochemically synthesized di- μ -oxo bridged manganese dimers to date.

4.2.6. Tmpa Mn(III,IV) dimers

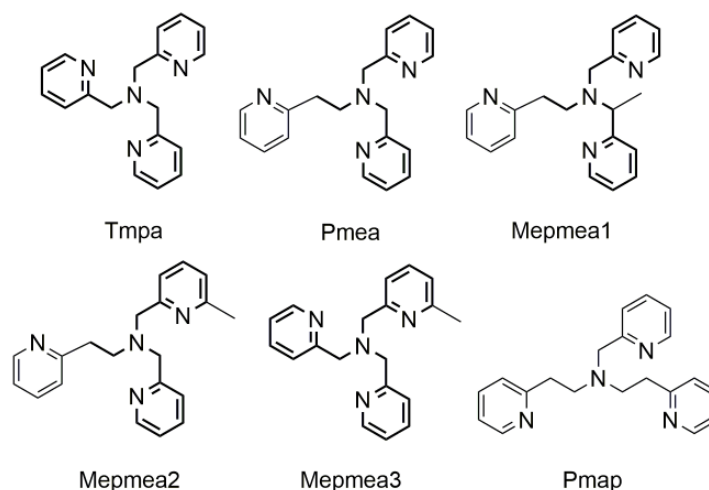
Tris(2-methylpyridyl)amine) or tmpa is a popular choice for use in biomimetic complexes because it is easily synthesized and exhibits a versatile coordination chemistry.^{270, 327} In 1988, both Suzuki *et al.* and Towle *et al.* independently synthesized two tmpa dimers. Complex **4.4a** ($[(tmpa)_2Mn^{III,IV}_2O_2][S_2O_6]_{3/2} \cdot 7H_2O$) was synthesized by Towle *et al.* and complex **4.4b** ($[(tmpa)_2Mn^{III,IV}_2O_2][ClO_4]_3 \cdot 3 H_2O$) was synthesized by Suzuki *et al.* (tmpa = tris(2-methylpyridyl)amine) (Schemes 4.3, 4, 4.5; Table 4.1).^{268, 306} The two tmpa dimers were also only composed of two tetradentate ligands (one tmpa ligand bound to each individual manganese atom), similar to complex **4.3**.^{268, 306} Both groups synthesized the tmpa Mn(III,IV) dimer complexes in a similar manner by combining an Mn(II) salt, $MnSO_4 \cdot H_2O$, (for Towle *et al.*) or $Mn(ClO_4)_2 \cdot 6H_2O$ (for Suzuki *et al.*) with the ligand and adding H_2O_2 .^{268, 306} Suzuki *et al.* performed CV, UV-vis, EPR, and tested for catalytic activity. Additionally, Towle *et al.* were also able to obtain the solid state structure through single crystal X-ray diffraction, and additional CV measurements for the determination of the complex's ability to serve as an electroactive redox catalyst.²⁶⁸ Cyclic voltammograms performed by Suzuki *et al.* (in CH_3CN) revealed two independent sets of reversible redox events. The couple that occurred at lower potentials was assigned as the reduction of $Mn^{III,IV}/Mn^{III,III}$ ($E_{1/2} = 0.48$ V vs. NHE) (Table 4.5, Scheme 4.6) whereas the higher potential wave was assigned to the oxidation of $Mn^{III,IV}/Mn^{IV,IV}$ ($E_{1/2} = 1.28$ V vs. NHE) (Table 4.5, Scheme 4.6).³⁰⁶ The electronic spectrum once

again revealed similar bands to previously established di- μ -oxo bridged manganese dimers. Absorbance bands were found at 442, 562, and 658 nm. Unlike complexes **4.1** and **4.2**, complex **4.4b** did not exhibit a shoulder near 830 nm, which had previously been assigned as an IT band (Table 4.4).³⁰⁶ Suzuki *et al.* hypothesized this was because the degree of delocalization within **4.4b** was smaller than either **4.1** or **4.2**.³⁰⁶ The EPR spectrum exhibited the classic 16-line hyperfine pattern which was expected for an antiferromagnetically coupled Mn(III,IV) dimer with two inequivalent manganese ions.³⁰⁶ The water oxidation ability of complex **4.4b** was tested in similar conditions to Ramaraj *et al.*, but no water oxidation occurred with this complex. Towle *et al.* obtained the solid state structure of the tmpa dimer **4.4a** and the Mn—Mn bond distance was measured to be 2.643 Å, which was considerably shorter than previously synthesized di- μ -oxo bridged manganese dimers (Table 4.2).²⁶⁸ Additionally, the cyclic voltammogram revealed a *quasi*-reversible oxidation wave corresponding to Mn^{III,IV}/Mn^{IV,IV} ($E_{1/2}$ = 1.14 V vs. NHE) (Table 4.5, Scheme 4.6) and an irreversible reduction from Mn^{III,IV}/Mn^{III,III} (E_{peak} = 0.44 V vs. NHE) (Table 4.5, Scheme 4.6).²⁶⁸ Towle *et al.* hypothesized that because of the presence of a dithionate ion the reduction was not reversible, unlike the tmpa complex **4.4b**, synthesized by Suzuki *et al.*^{268, 306}

Table 4.7. Tmpa derived Mn(III,IV) dimer complexes.

Complex	Coordinating Ligand	Metal Complex	Reference
4.4a	tris(2-methylpyridyl)amine (tmpa)	[(tmpa) ₂ Mn ₂ O ₂][S ₂ O ₆] _{3/2} • 7 H ₂ O	1
4.4b	tris(2-methylpyridyl)amine (tmpa)	[(tmpa) ₂ Mn ₂ O ₂][ClO ₄] ₃ • 3 H ₂ O	2
4.4.1a	(2-(2-pyridyl)ethyl)bis(2-pyridylmethyl)amine (pmea)	[(pmea) ₂ Mn ₂ O ₂][ClO ₄] ₃	3
4.4.2a	(1-(2-pyridyl)ethyl)(2-(2-pyridyl)ethyl)(2-pyridylmethyl)amine (Mepmea1)	[(Mepmea1) ₂ Mn ₂ O ₂][ClO ₄] ₃	
4.4.3a	((6-methyl-2-pyridyl)methyl)(2-(2-pyridyl)ethyl)(2-pyridylmethyl)amine (Mepmea2)	[(Mepmea2)Mn ₂ O ₂][ClO ₄] ₃	
4.4.4a	((6-methyl-2-pyridyl)methyl)bis(2-pyridylmethyl)amine (Mepmea3)	[(Mepmea3)Mn ₂ O ₂][ClO ₄] ₃	
4.4.5a	(bis[2-(2-pyridyl)ethyl]-2-pyridylmethyl)amine (pmap)	[(pmap) ₂ Mn ₂ O ₂][ClO ₄] ₃ • CH ₃ CN	4

1: ref. ²⁶⁸; 2: ref. ³⁰⁶; 3: ref. ³²⁸; 4: ref. ³²⁷.



Scheme 4.8. Tmpa and derivatized ligands.

Following the independent reports by Towle and Suzuki *et al.* regarding the synthesis and characterization of novel Mn(III,IV) tmpa dimers, Oki *et al.* built upon the work of a report related to the synthesis and characterization of Mn(III,IV) dimers with several different tmpa derivatives. Their goal was to synthesize a library of chemically altered tmpa Mn(III,IV) complexes to modify the stereochemical and electronic properties of the metal centers.³²⁸ Complexes **4.4.1a-4.4.4a** (Table 4.7, Scheme 4.8) were synthesized in a similar manner to Towle *et al.*²⁶⁸ Oki *et al.* characterized the complexes using UV-vis, CV, EPR and XRD (for complex **4.4.1a** only). All methods confirmed the presence of an Mn₂O₂ core and were similar to those obtained for previous tmpa Mn(III,IV) complexes.^{268, 306} When examining the redox potentials of the chemically modified Mn(III,IV) tmpa derived complexes, the authors noted that substitution within the alkyl arms of the ligand had little impact on the redox potentials, but any substitution at the 6-position of the pyridine ring caused a significant shift (greater than 200 mV) in redox potentials.³²⁸ Upon complete characterization of the modified tmpa Mn(III,IV) dimer complexes Oki *et al.* investigated each dimer's ability to catalyze the epoxidation of cyclohexene by iodosobenzene; this had been an area of intense research with Mn(III) mononuclear complexes as noted in the report. All the complexes tested (**4.4.1a**, **4.4.3a**, and **4.4.4a**) exhibited preferential catalytic activity toward the epoxidation of cyclohexene.³²⁸ In addition, when a methyl group was introduced at the 6-position of the

pyridyl ring, a significant increase in the yield of epoxide was observed.³²⁸ Other groups have also investigated the effects of steric substitution on structural, spectroscopic, and electronic properties of Mn(III,IV) complexes with tmpa derived ligands.³²⁹

Many studies to date have utilized tmpa and tmpa derived ligands because they are versatile and easily modified. In 2000, Schindler *et al.* made modifications to the parent tmpa ligand by increasing the arm lengths of the alkyl chains connected to the pyridine units. Tmpa, the parent ligand utilized in many biomimetic models, contains three methylpyridyl moieties attached to a central nitrogen atom (Table 4.7, Scheme 4.8). Pmea, a derivative of the parent tmpa ligand, contains two methyl pyridyl moieties and one ethylpyridyl moiety attached to the central nitrogen (Scheme 4.8); Mn(III,IV) dimer complexes with this ligand have been well characterized by others (Table 4.7).³²⁸ Pmap and tepa are also derivatives of the parent tmpa ligand, but manganese complexes with these two ligands had not been synthesized to date.³²⁷ Pmap contains two ethylpyridyl moieties and one methylpyridyl moiety attached to a central nitrogen and tepa contains three ethylpyridyl moieties attached to central nitrogen (Table 4.7, Scheme 4.8). Increasing arm length of the alkyl chains leads to an increase in the size of the chelate rings attached to the metal center which was postulated to favor lower oxidation states for the metal ions attached, i.e. Mn(III,III) complexes. Schindler *et al.*; therefore, investigated the potential to form high valent Mn(III,IV) complexes with increased alkyl chain lengths, using the pmap and tepa ligands. An Mn(III,IV) dimer complex was successfully synthesized with the pmap ligand by reacting Mn(ClO₄)₂, pmap, and hydrogen peroxide yielding [(pmap)₂Mn^{III,IV}₂O₂][ClO₄]₃•CH₃CN (**4.4.5a**) (Table 4.7).³²⁷ The complex structure was confirmed by X-ray diffraction. Schindler *et al.* observed a considerable change in Mn—Mn bond lengths between the three different Mn(III,IV) dimers: complex **4.4a** (2.643 Å)²⁶⁸, complex **4.4.1a** (2.693 Å)³²⁸, and complex **4.4.5a** (2.738 Å).³²⁷ The increasing Mn—Mn bond distances directly correlate to the increase in chelate ring size within the Mn(III,IV) dimer complexes.³²⁷ Complex **4.4.5a** was also characterized utilizing traditional methods which served as confirmation of the presence of an Mn(III,IV) dimer.³²⁷ However,

attempts to synthesize a Mn(III,IV) dimer with the tpa were unsuccessful. Schindler *et al.* postulated that the Mn—Mn distance was too large for a μ -oxo bridge to form.³²⁷

In 2007, Shin *et al.* synthesized a $[(\text{tmpa})_2\text{Mn}_2(\mu\text{-Cl})_2]^{2+}$ dimer to model chloride-inhibited superoxidized Mn-catalase.²⁷⁰ In the superoxidized Mn(III,IV) oxidation state Mn-catalase is catalytically inactive. The H_2O_2 dismutation activity was tested against several other manganese containing complexes, including a $[(\text{tmpa})\text{Mn}^{\text{II}}\text{Cl}_2]^{2+}$ monomer and a $[(\text{tmpa})_2\text{Mn}^{\text{III,IV}}_2\text{O}_2][\text{ClO}_4]_3$ dimer (**4.4c**). The core complex $[(\text{tmpa})_2\text{Mn}^{\text{III,IV}}_2\text{O}_2]^{3+}$ (**4.4**) had been previously prepared by others, but Shin *et al.* were able to synthesize complex **4.4c** using slightly different methodology.^{268, 322} They found that catalytic activity of the conversion of H_2O_2 to O_2 was observed with all three complexes, $[(\text{tmpa})_2\text{Mn}_2(\mu\text{-Cl})_2]^{2+}$, $[(\text{tmpa})\text{MnCl}_2]^{2+}$, $[(\text{tmpa})_2\text{Mn}^{\text{III,IV}}_2\text{O}_2]^{3+}$ (**4.4c**).²⁷⁰ Although synthesis of a Mn(III,IV) tmpa dimer was not the focus of the report, it was included in this section, because of the modified $[(\text{tmpa})_2\text{Mn}^{\text{III,IV}}_2\text{O}_2][\text{ClO}_4]_3$ synthesis and investigation into its ability to catalyze H_2O_2 disproportionation. Shin *et al.* followed up this work by an investigation of the conversion of $[(\text{tmpa})_2\text{Mn}_2(\mu\text{-Cl})_2]^{2+}$ to $[(\text{tmpa})_2\text{Mn}^{\text{III,IV}}_2\text{O}_2]^{3+}$ by adding stoichiometric amounts of H_2O_2 and subsequent catalysis of H_2O_2 disproportionation.³³⁰

In 2014, Yatabe *et al.* developed a model for the water-oxidation and recovery systems of the OEC. They began by synthesizing an Mn(III,III) $[(\text{tmpa})_2\text{Mn}^{\text{III,III}}_2\text{O}_2]^{2+}$ dimer. They subsequently reduced this Mn(III,III) dimer by photo-irradiation with DTBBQ (3,5-di-*t*-butyl-1,2-benzoquinone) and NEt_3 (triethylamine) which formed an Mn(II)-semiquinonato complex ($[\text{Mn}^{\text{II}}(\text{tmpa})(\text{DTBSQ})]^+$) (DTBSQ = 3,5-di-*t*-butyl-1,2-semiquinonato).³¹⁰ When the Mn(II)-semiquinonato complex was exposed to O_2 the Mn(III,III) $[(\text{tmpa})_2\text{Mn}^{\text{III,III}}_2\text{O}_2]^{2+}$ dimer was regenerated. Yatabe *et al.* hypothesized that the cycle between the Mn(III,III) $[(\text{tmpa})_2\text{Mn}^{\text{III,III}}_2\text{O}_2]^{2+}$ dimer and Mn(II)-semiquinonato complexes would potentially be a good model for the photo-damaged OEC, based on several biological studies suggesting that the photodamaged OEC contains reduced Mn(II). In addition, Yatabe *et al.* also synthesized a Mn(III,IV) tmpa dimer based on the procedures described by both Towle *et al.* and Suzuki *et al.*^{268, 310, 322} This complex was one of several

di- μ -oxo bridged manganese dimers synthesized to model the water-oxidation of the OEC.³¹⁰ Along with the Mn(III,IV) dimer $[(\text{tmpa})_2\text{Mn}^{\text{III,IV}}_2\text{O}_2][\text{ClO}_4]_3$ (**4.4c**), the group also synthesized the previously discussed Mn(III,III) dimer $[(\text{tmpa})_2\text{Mn}^{\text{III,III}}_2\text{O}_2]^{2+}$, and a Mn(IV,IV) $[(\text{tmpa})_2\text{Mn}^{\text{IV,IV}}_2\text{O}_2]^{4+}$ dimer.³¹⁰ UV-vis, and EPR were utilized to characterize each different complex. In addition to performing characterization, Yatabe *et al.* adsorbed the Mn(III,III), Mn(III,IV), and Mn(IV,IV) complexes onto clay and tested for the ability to heterogeneously oxidize water using cerium ammonium nitrate as a chemical oxidant. All three dimer complexes catalytically evolved O_2 from H_2O , albeit in very modest amounts (turnover numbers ranging from 1.9-2.6 over 500 s).³¹⁰ The O_2 formation gradually plateaued due to the formation of MnO_4^- , which was confirmed with UV-vis spectroscopy.³¹⁰ Ultimately the various manganese complexes Yatabe *et al.* synthesized and studied individually were brought together to form a tandem reaction, modelling the photoinhibition, recovery, and water-oxidation that takes place within the OEC.³¹⁰

4.2.7. Tren Mn(III,IV) dimer

Another group, Hagen *et al.*, synthesized a novel di- μ -oxo bridged manganese dimer in 1988. This dimer was synthesized with tren ligands, $[(\text{tren})_2\text{Mn}^{\text{III,IV}}_2\text{O}_2][\text{CF}_3\text{SO}_3]_3 \cdot \text{EtOH}$ (**4.5a**) (tren = tris(2-aminoethyl)amine) (Schemes 4.3, 4.4, 4.5; Table 4.1) and was the first complex to be isolated with a ligand that did not contain pyridine moieties. Complex **4.5a** was synthesized by exposing a mixture of $\text{Mn}(\text{CF}_3\text{SO}_3)_2 \cdot \text{CH}_3\text{CN}$, tren, and CH_3CN to air for two hours, which resulted in a green solution that eventually turned brown.³⁰⁵ Interestingly, this may be the first time that an external oxidant was not utilized to form the Mn(III,IV) dimer complex in a report. Hagen *et al.* characterized this complex using XRD, IR, UV-vis, CV, and EPR; which had become standard for the characterization of these di- μ -oxo bridged manganese dimers (Table 4.2, 4.3, 4.4, 4.5). The complex crystallized as $[(\text{tren})_2\text{Mn}^{\text{III,IV}}_2\text{O}_2][\text{CF}_3\text{SO}_3]_3 \cdot \text{EtOH}$ (**4.5a**) and the Mn—Mn distance was found to be 2.679 Å (Table 4.1, 4.2). This bond distance was intermediate compared to its predecessors: shorter than both complexes **4.1** and **2**, but longer than Mn—Mn distance found in complexes **4.3** and **4.4**. IR revealed a Mn_2O_2 vibration at

694 cm^{-1} which was the highest vibrational frequency recorded to date for these di- μ -oxo bridged manganese dimers. The electronic spectrum of this tren complex in CH_3CN revealed maxima at 380, 428(sh), 526(sh), 548, 590, 638, and 680 nm.³⁰⁵ Unlike **4.1** and **4.2**, there was no broad band observed at 800 nm in the electronic spectrum of the tren complex, this might suggest the degree of delocalization between the two metal ions was lesser than either complex **4.1** or **4.2**.^{305, 322} Additionally, the cyclic voltammogram revealed two *quasi*-reversible redox couples corresponding to reduction of $\text{Mn}^{\text{III,IV}}/\text{Mn}^{\text{III,III}}$ ($E_{1/2} = 0.68$ V vs. NHE) and oxidation of $\text{Mn}^{\text{III,IV}}/\text{Mn}^{\text{IV,IV}}$ ($E_{1/2} = 1.42$ V vs. NHE). Interestingly, the values of these redox couples were significantly higher than either complex **4.1** or **4.2**, meaning that complex **4.5a** was easier to oxidize in solution.³⁰⁵ EPR of **4.5a** revealed the expected 16-line pattern.³⁰⁵

4.2.8. Cyclam and cyclen Mn(III,IV) dimers

In addition to the already summarized open chain ligand complexes, Brewer *et al.* synthesized two novel macrocyclic di- μ -oxo bridged manganese dimers in 1988.³⁰⁴ One dimer was composed of two cyclam ligands (cyclam = 1,4,8,11-tetraazacyclotetradecane) $[(\text{cyclam})_2\text{Mn}^{\text{III,IV}}_2\text{O}_2][\text{ClO}_4]_3 \cdot 2\text{H}_2\text{O}$ (**4.6a**) (Schemes 4.3, 4.4, 4.5; Table 4.1); the other dimer was composed of two cyclen ligands (cyclen = 1,4,7,10-tetraazacyclododecane) $[(\text{cyclen})_2\text{Mn}^{\text{III,IV}}_2\text{O}_2][\text{ClO}_4]_3 \cdot 2\text{H}_2\text{O}$ (**4.7a**) (Schemes 4.3, 4.4, 4.5; Table 4.1). These two novel Mn(III,IV) dimer complexes were synthesized by air oxidation of aqueous solutions containing the ligand (either cyclen or cyclam) and $\text{Mn}(\text{ClO}_4)_2$.³⁰⁴ Cyclam is a 14-membered macrocyclic ligand and cyclen is a 12-membered macrocyclic ligand. Although both cyclen and cyclam metalate in the same fashion (through the 4 nitrogen atoms contained in the backbone) the different cavity size of the 12- vs. 14-membered rings bring about slightly different characteristics for each metal complex. Brewer *et al.* characterized these novel complexes using IR, UV-vis, CV, and EPR; the techniques being standard in analysis of any novel di- μ -oxo bridged manganese dimer synthesized. The IR spectrum showed bands in the region now expected for an Mn_2O_2 vibration. **4.6a** showed a band at 680 cm^{-1} , in contrast **4.7a** showed a band at 689 cm^{-1} . Similarly, the UV-visible spectrum for both complexes were slightly different. Complex

4.6a exhibited absorbance bands at 550 and 650 nm (in water) and complex **4.7a** exhibited absorbance bands at 556, 650, and 740 nm (in water). No doubt that the slightly different electronic spectra are a result of the slight difference in ligand geometries. Additionally, both complex **4.6a** and **4.7a** exhibit two redox events, a reduction corresponding to $\text{Mn}^{\text{III,IV}}/\text{Mn}^{\text{III,III}}$ (cyclam $E_{1/2} = 0.24$ V vs. NHE; cyclen $E_{1/2} = 0.39$ V vs. NHE) and an oxidation corresponding to $\text{Mn}^{\text{III,IV}}/\text{Mn}^{\text{IV,IV}}$ (cyclam $E_{1/2} = 1.24$ V vs. NHE; cyclen $E_{1/2} = 1.14$ V vs. NHE) although, the $E_{1/2}$ values for each complex were very different (Table 4.5, Scheme 4.6). Based on the observed $E_{1/2}$ values for both Mn(III,IV) dimers, the cyclen complex **4.7a** is both easier to oxidize and easier to reduce than the cyclam dimer **4.6a**.³⁰⁴ Brewer *et al.* hypothesized that the electrochemical properties of each Mn(III,IV) dimer were influenced by steric factors, including the ability for the cyclam macrocycle to better accommodate the manganese metal center.³⁰⁴ Along with performing a complete characterization of the novel Mn(III,IV) dimers, Brewer *et al.* also investigated the catalytic ability of complex **4.6a**. Although the original electrochemical characterization of complex **4.6a** took place in rigorously dried acetonitrile, upon addition of water to the solution (1.5% v/v water-acetonitrile) the oxidative peak current (i_p^a) for the wave at 1.24 V (vs. NHE) increased markedly. To confirm this increase in oxidative peak current was indeed a result of complex **4.6a**, a CV was run with the mixed solvents in the absence of complex **4.6a**; no redox events were observed in the region. The observed peak current was much larger than what was expected for a one-electron oxidation of complex **4.6a**, therefore the authors concluded that this increase in the oxidative peak current was consistent with water oxidation in the chemical step at the electrode surface.³⁰⁴

A solid state structure for complex **4.6a** was reported a year later in 1989, by the same group.³²³ The Mn—Mn bond distance was measured to be 2.731 Å (Table 4.2). Additionally, Brewer *et al.* gathered evidence suggesting that water was the source of the bridging oxygens contained within the Mn_2O_2 core, which had not been established to date. Until this point, most Mn(III,IV) dimer complexes were synthesized using external oxidants, such as $\text{K}_2\text{S}_2\text{O}_8$, KMnO_4 , or H_2O_2 which could act as oxygen donors.²⁶⁵

By electrochemically synthesizing complex **4.6a** Brewer *et al.* were provided with evidence that H₂O was the source of the bridging oxygen atoms. An acetonitrile solution was prepared which contained 2% by volume water, 1 equivalent of Mn(CF₃SO₃)₂, 1 equivalent of cyclam, and 0.1 M TBAPF₆.²⁶⁵ Brewer *et al.* then deaerated the solution and applied a potential; they observed that the colorless solution developed a green color over 2 h, and the electronic spectrum of the solution was characteristic of an Mn(III,IV) dimer.²⁶⁵ In the solution, the only available source for the oxo bridges was the water; thus, the authors concluded that H₂O was the source of the oxo bridges within the Mn₂O₂ core. In addition to confirming the source of the oxo bridges, Brewer *et al.* characterized complex **4.6a** using spectroelectrochemistry, IR, CV, and EPR. A strong band was observed at 679 cm⁻¹ in the IR spectrum of **4.6a** which has been attributed to the Mn₂O₂ core by many other groups. When the synthesis of complex **4.6a** was performed in ¹⁸O-labelled water this band was split into two weaker peaks (681 cm⁻¹ and 679 cm⁻¹) thus confirming the 679 cm⁻¹ band was due to the vibration of the Mn₂O₂ core; Cooper and Calvin observed the same behavior with complex **4.1b**.^{265, 302}

The following year (1990) two additional Mn(III,IV) cyclam dimer structures were reported by Goodson *et al.* [(cyclam)₂Mn^{III,IV}₂O₂][Br]₃•4H₂O (**4.6b**) and [(cyclam)₂Mn^{III,IV}₂O₂][S₂O₆]_{1.37}[S₂O₃]_{0.13} (**4.6c**) (Table 4.1).³¹¹ Complex **4.6b** was measured to have an Mn—Mn bond distance of 2.741 Å and complex **4.6c** was measured to have Mn—Mn bond distances of 2.729 and 2.738 Å (with the crystal having two independent dimers within the unit cell) (Table 4.2).³¹¹ It wasn't until 1992 that a solid state structure of a Mn(III,IV) cyclen dimer was reported by Goodson *et al.*, [(cyclen)₂Mn^{III,IV}₂O₂][Cl]₃•LiCl•5 H₂O (**4.7b**) (Table 4.1).³¹³ The Mn—Mn bond distance in the cyclen complex was measured to be 2.694 Å, much smaller compared to the Mn(III,IV) cyclam complexes (Table 4.2). The shorter Mn—Mn bond distance within the cyclen complex is consistent with the different ring sizes of cyclam and cyclen. Cyclam, a 14-membered ring, is larger, allowing for a better fit within the macrocyclic cavity for the manganese ion, whereas, cyclen, a 12-membered ring, has a smaller cavity size which is not as accommodating to the size

of the manganese ion. Hence, the manganese ions sit more out of plane in the complex **4.7**, and “closer together” than in the cyclam complex. UV-vis, CV, and IR also revealed slight differences between the two complexes (Tables 4.3, 4.4, 4.5; Scheme 4.6).

Several other groups synthesized Mn(III,IV) cyclen and cyclam dimers in the early 2000s.³³¹⁻³³³ In 2014, Nakamori *et al.* reported the synthesis of a monomeric Mn(II)-semiquinonato complex as a model for elucidating the function of the OEC in PSII.³¹² This Mn(II)-semiquinonato complex was synthesized by the reaction of an Mn(III,IV) cyclam dimer[(cyclam)₂Mn^{III,IV}₂O₂][ClO₄]₃ (**4.6d**) with *p*-hydroquinone (Table 4.1). Complex **4.6d** could be regenerated by oxygenating the Mn(II)-semiquinonato complex. Nakamori *et al.* conducted several in depth isotopic labeling studies on the source of the oxo bridges when the Mn(II)-semiquinonato complex was oxygenated to complex **4.6d**. In one experiment, they utilized ¹⁸O₂ as an oxidation source instead of ¹⁶O₂, ESI-MS results indicated that two ¹⁸O atoms (from the ¹⁸O₂) were incorporated into the μ-oxo bridge within complex **4.6d**.³¹² Nakamori *et al.* also performed a cross-over experiment in which they carried out the oxygenation process using 50% ¹⁶O₂ and 50% ¹⁸O₂, ESI-MS results showed that complexes with cores consisting of Mn₂¹⁶O₂, Mn₂¹⁶O¹⁸O, and Mn₂¹⁸O₂ were formed in a 1:2:1 ratio.³¹² Finally, complexes of **4.6d** were exchanged for H₂O oxygen atoms, which was confirmed by additional isotopic labelling experiments using H₂¹⁸O. When an excess amount of H₂¹⁸O was added to complex **4.6d** in CH₃CN the ¹⁶O atoms incorporated into the μ-oxo bridge were exchanged for ¹⁸O atoms derived from the H₂¹⁸O.³¹² Evidence from the isotopic labelling studies lead Nakamori *et al.* to contradict what Brewer *et al.* had hypothesized about the source of the bridging oxygens.^{265, 312} Nakamori *et al.* stated that the source of the bridging oxygen atoms within Mn(III,IV) dimer complexes originated with O₂, not H₂O as was previously thought.^{265, 312} Although it was noted that because of the fast exchange of the oxo ligands with H₂O oxygen atoms this was an easy assignment for Brewer *et al.* to make.

4.2.9. Terpy Mn(III,IV) dimers

In 1999, Limburg *et al.* developed a model complex for the O—O bond formation that takes place in the OEC of PSII.³¹⁴ It was the first reported di- μ -oxo bridged Mn(III,IV) dimer that served as a structural model of the OEC by catalytically forming O—O bonds.^{314, 334} Previously it had been postulated that an Mn=O species was formed as an intermediate during photosynthetic water oxidation; the terminal oxo ligand within the OEC was thought to be formed by the abstraction of O atoms from a water molecule bound to a manganese ion.³¹⁴ Therefore, Limburg *et al.* designed and synthesized a model di- μ -oxo bridged Mn(III,IV) dimer with available sites for solvent coordination that provided a place for the formation of an Mn=O intermediate.³¹⁴ $[(\text{H}_2\text{O})_2(\text{terpy})_2\text{Mn}^{\text{III,IV}}\text{O}_2][\text{NO}_3]_3 \cdot 6\text{H}_2\text{O}$ (**4.8a**) (Schemes 4.4, 4.5; Table 4.1) was synthesized by reacting potassium peroxomonosulfate (K oxone) with Mn(II) or Mn(III) complexes containing the terpy ligand (terpy = 2,2':6',2''-terpyridine) (Scheme 4.3).³¹⁴ Limburg *et al.* obtained a crystal structure of the complex and observed an Mn—Mn bond distance of 2.723 Å (Table 4.2).³¹⁴ Of course, the most notable feature of complex **4.8a** were the exchangeable aqua ligands coordinated to each of the manganese ions (Scheme 4.4); this unique configuration was a result of using meridionally coordinating terpy ligands. Upon adding complex **4.8a** to an aqueous solution of sodium hypochlorite Limburg *et al.* observed O₂ formation with an initial rate of 12 ± 2 mol/h per mole of complex **4.8a**.³¹⁴ Limburg *et al.* followed the O₂ evolution by using ¹⁸O labeling and subsequent analysis with mass spectrometry, their findings were consistent with a mechanism involving a Mn=O intermediate. The catalytic reaction stopped after complex **4.8a** was completely disproportionated to permanganate over several hours; Limburg *et al.* followed the formation of MnO₄⁻ by UV-vis and observed isosbestic points at 497 and 583 nm.³¹⁴ Based on the gathered evidence Limburg *et al.* proposed a reaction mechanism for the formation of O₂ by the reaction of complex **4.8a** with sodium hypochlorite. Several years after the initial report of this novel Mn(III,IV) dimer **4.8a** Limburg *et al.* published a paper comparing the mechanisms of O₂-evolving reactions of **4.8a**, potassium oxone, and hypochlorite.³³⁴

Following the original synthesis of complex **4.8a**, Yagi *et al.* reported the ability of the complex to evolve O₂ when adsorbed onto clay.³³⁵ Whereas Limburg *et al.* designed and synthesized a homogeneous water oxidation catalyst with complex **4.8a**, Yagi *et al.* modified complex **4.8a** by adsorbing onto clay, thus making it a heterogeneous water oxidation catalyst. Before complex **4.8a** was adsorbed onto clay, Yagi *et al.* tested its water oxidation ability using Ce^{IV} (cerium ammonium nitrate) as an oxidant; no O₂ evolution was observed using this oxidant. This finding contrasted with what Limburg *et al.* had previously reported regarding O₂ evolution being observed using **4.8a** and sodium hypochlorite or potassium peroxymonosulfate as oxidants. Conversely, when Yagi *et al.* adsorbed complex **4.8a** onto Kaolin or Montmorillonite clay and Ce^{IV} was added to the aqueous suspension, a significant amount of O₂ was produced, at a turnover number of 13.5±1.1.³³⁵ Yagi *et al.* conducted ¹⁸O-labeling experiments to determine an oxygen atom source for the O₂ evolution; the labelling experiments revealed that the O₂ evolved was derived exclusively from water, thus confirming water oxidation.³³⁵ To further investigate a potential mechanism for the catalytic water oxidation, the authors characterized the **4.8a**/clay mixture. The diffuse reflectance spectrum of **4.8a**/clay seemed to indicate an Mn(IV,IV) species rather than an Mn(III,IV) species, meaning that upon adsorption onto the clay complex **4.8a** was most likely oxidized to Mn(IV,IV). In addition to confirming the oxidation state of complex **4.8a** when adsorbed onto clay, Yagi *et al.* evaluated the mechanism of O₂ evolution by comparing two different complexes, **4.8a** and **4.1** (recall a [(bipy)₄Mn^{III,IV}₂O₂]³⁺ complex). Complex **4.1** was comparable to complex **4.8a** but contained no terminal water ligands attached to the metal centers. Analysis of each complex's initial O₂ evolution rates (νO₂ mol/s) suggested that the terminal water ligands were involved in the catalytic water oxidation of complex **4.8a**.³³⁵ Following this report of the first heterogeneous water oxidation catalyst utilizing an Mn(III,IV) terpy complex, other groups reported additional studies with Mn(III,IV) dimers adsorbed onto clay with the ability to catalyze water oxidation.³³⁶

4.2.10. Additional macrocyclic Mn(III,IV) dimers with pyclen and isocyclam

After the burst of research articles surrounding the synthesis of novel di- μ -oxo bridged manganese dimers, the number of articles published on these Mn(III,IV) complexes diminished slightly during the late 1990s and onward. In 2008, a crystal structure of a pyclen di- μ -oxo bridged manganese dimer $[(\text{pyclen})_2\text{Mn}^{\text{III,IV}}_2\text{O}_2][\text{Cl}]_3 \cdot 6\text{H}_2\text{O}$ (**4.9a**) (Schemes 4.4, 4.5; Table 4.1) was deposited onto the Cambridge crystallographic database (CCDC #: 675326) by Alcock *et al.*³¹⁵ Pyclen is a congener of cyclen that contains a pyridine ring within the macrocycle (pyclen = 1,4,7,10-tetraaza-2,6-pyridinophane) (Scheme 4.3). However, no further attempts to characterize this Mn(III,IV) complex or compare it to the other previously synthesized macrocyclic di- μ -oxo bridged manganese dimers were carried out. The Green group successfully replicated the pyclen Mn(III,IV) dimer and were able to fully characterize and compare the complex to previously synthesized dimers.

In 2012, Tomczyk *et al.* reported the synthesis of two novel manganese complexes with the macrocycle isocyclam, one was a di- μ -oxo bridged dinuclear complex and one was a Mn(III) mononuclear complex (isocyclam = 1,4,7,11-tetraazacyclotetradecane) (Scheme 4.3).²⁷⁶ This appears to be one of the only reports where both a Mn(III) mononuclear complex and Mn(III,IV) dinuclear complex were obtained within the same publication, aside from this work.

One of the aims of the report by Tomczyk *et al.* was to investigate whether a macrocyclic ligand (isocyclam) with lower symmetry than cyclam could form similar dinuclear complexes. They were able to synthesize an Mn(III,IV) dinuclear complex, $[(\text{isocyclam})_2\text{Mn}^{\text{III,IV}}_2\text{O}_2][\text{ClO}_4]_3 \cdot 2\text{H}_2\text{O}$ (**4.10a**) (Table 4.1), by adding a solution of $\text{Mn}(\text{ClO}_4)_2 \cdot 6\text{H}_2\text{O}$ in ethanol, dropwise to a solution of isocyclam. The mixture was stirred and left open to the air for several days, upon which dark green crystals of complex **4.10a** were isolated. Tomczyk *et al.* used UV-vis, IR, and CV to confirm the presence of complex **4.10a**, after synthesis. UV-vis of complex **4.10a** was taken in water; the spectrum exhibited several absorption bands at 548, 562, and 652 nm (Table 4.4). The absorbance band at 548 nm was attributed to the d-d transition of a Mn(III)

ion within a mixed-valence complex. In addition, the absorbance band at 562 nm corresponded to the d-d transition of the Mn(IV) ion, and the absorbance band at 652 nm was a characteristic feature of a LMCT from oxo→Mn(IV) (as previously assigned by others).^{276, 306} Tomczyk *et al.* also observed a broad absorption band of low energy in the visible and near IR range; they concluded that this was due to intervalence transfer between the Mn(III) and Mn(IV) ions. The IR spectrum of complex **4.10a** exhibited a strong band at 684 nm⁻¹, which corresponded to the vibration of the Mn₂O₂ core (Table 4.3).²⁷⁶ CV measurements of complex **4.10a** revealed two *quasi*-reversible redox couples, although both were somewhat ill-defined. The first redox couple corresponded to the reversible reduction of Mn^{III,IV}/Mn^{III,III} ($E_{1/2} = 0.29$ V vs. NHE) and the second redox couple corresponded to the reversible oxidation of Mn^{III,IV}/Mn^{IV,IV} ($E_{1/2} = 1.09$ V vs. NHE) (Table 4.5, Scheme 4.6).²⁷⁶ These values are slightly more negative compared to the redox couples of previously synthesized Mn(III,IV) cyclam dimers, which may indicate that complex **4.10a** is easier to oxidize than complexes with cyclam.

4.3. History of mononuclear Mn(III) complexes

The biomimetic complexes synthesized with macrocyclic ligands and Mn(II) are numerous in the chemical literature, because such complexes can be utilized to model the structure and function of superoxide dismutase. However, Mn(III) macrocyclic complexes are much less prevalent, especially mononuclear complexes. Upon oxidation of manganese to higher valencies, the complexes tend to disproportionate to the thermodynamically stable MnO₂ species.³³⁷⁻³³⁸ This thermodynamic sink often limits the ability to isolate stable coordination complexes with high valent manganese, especially in aqueous media.³³⁷ Despite this, there are a few examples of mononuclear Mn(III) macrocyclic complexes within the chemical literature. Several of these complexes were designed to mimic the OEC within PSII. Before details about the actual structure of the OEC were discovered, it was clear that high valent manganese in the (III) and (IV) oxidation states was present within the OEC.^{274, 338-339} With this knowledge, several groups designed mononuclear Mn(III) macrocyclic complexes to mimic the OEC. In addition to the

pursuit of biomimetic structures, Mn(III) macrocyclic complexes were found to be useful in catalytic oxidation reactions.³³⁹ The pursuit of oxidation catalysts, lead to the synthesis of several Mn(III) complexes using cyclam and derivatives.

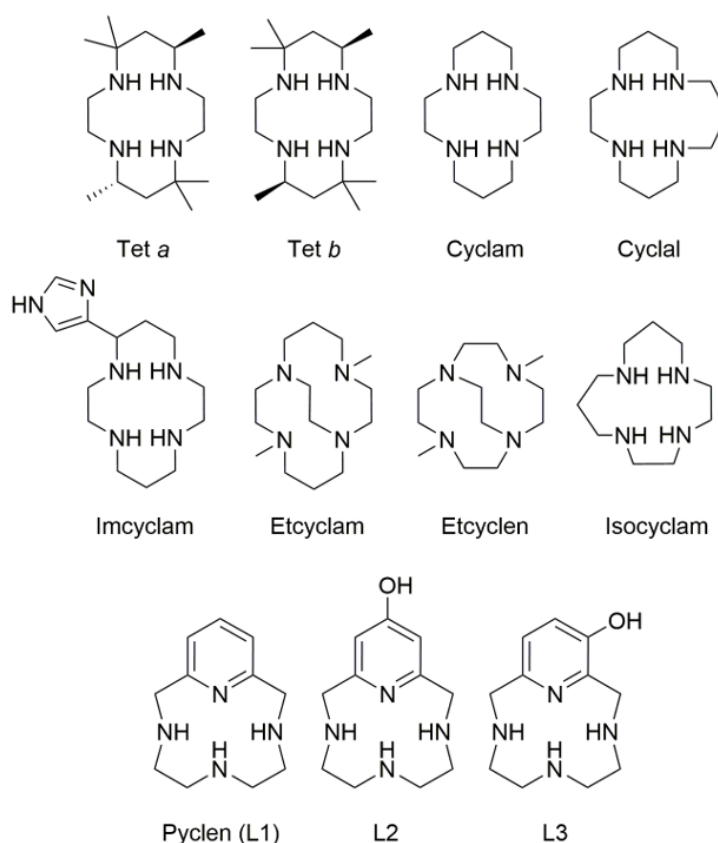
4.3.1. Description of tetraazamacrocyclic ligands discussed

The complexes covered in portion of the chapter consist of several different tetraazamacrocyclic ligands, cyclal (cyclal = 1,4,8,12-tetraazacyclopentadecane), cyclam (and derivatives), and cyclen (and derivatives). Although many other types of nitrogen containing ligands exist these ligands were the most pertinent to Mn(III) complexes related to our interests and the focus of this review. Cyclal is a 15-membered macrocyclic ligand, cyclam is a 14-membered macrocyclic ligand, and cyclen is a 12-membered macrocyclic ligand. Although cyclal, cyclam, and cyclen metalate in the same fashion (through 4 nitrogen atoms contained in the backbone) the different cavity size of the 15- vs. 14- vs. 12-membered rings bring about slightly different characteristics for each metal complex. Typically, cyclal and cyclam coordinate the metals in a planar/*trans* fashion, because the macrocyclic cavities are large enough to accommodate metal ions. In contrast, cyclen coordinates to metals in a folded/*cis* fashion, because the macrocyclic cavity is not quite large enough to fit the entire metal ion.

Table 4.8. Mn(III) monomeric complexes with various tetraazamacrocyclic ligands.

	Coordinating Ligand	Metal Complex	Reference
4.13a	<i>meso</i> -5,5,7,12,12,14-hexamethyl-1,4,8,11-tetraazacyclotetradecane (tet <i>a</i>)	[Mn ^{III} (tet <i>a</i>)Cl ₂][PF ₆]	
4.13b	<i>meso</i> -5,5,7,12,12,14-hexamethyl-1,4,8,11-tetraazacyclotetradecane (tet <i>a</i>)	[Mn ^{III} (tet <i>a</i>)Cl ₂][BF ₄]	
4.13c	<i>meso</i> -5,5,7,12,12,14-hexamethyl-1,4,8,11-tetraazacyclotetradecane (tet <i>a</i>)	[Mn ^{III} (tet <i>a</i>)Br ₂][PF ₆]	1
4.13d	<i>meso</i> -5,5,7,12,12,14-hexamethyl-1,4,8,11-tetraazacyclotetradecane (tet <i>a</i>)	[Mn ^{III} (tet <i>a</i>)(NCS) ₂][NCS]	
4.13e	<i>meso</i> -5,5,7,12,12,14-hexamethyl-1,4,8,11-tetraazacyclotetradecane (tet <i>a</i>)	[Mn ^{III} (tet <i>a</i>)Cl ₂][Cl]•3H ₂ O	
4.13f*	<i>meso</i> -5,5,7,12,12,14-hexamethyl-1,4,8,11-tetraazacyclotetradecane (tet <i>a</i>)	[Mn ^{III} (tet <i>a</i>)Cl ₂][Cl]•1.5H ₂ O	2
4.14a	<i>rac</i> -5,7,7,12,12,14-hexamethyl-1,4,8,11-tetraazacyclotetradecane (tet <i>b</i>)	[Mn ^{III} (tet <i>b</i>)Cl ₂][PF ₆]	
4.14b	<i>rac</i> -5,7,7,12,12,14-hexamethyl-1,4,8,11-tetraazacyclotetradecane (tet <i>b</i>)	[Mn ^{III} (tet <i>b</i>)Br ₂][PF ₆]	3
4.14c^	<i>rac</i> -5,7,7,12,12,14-hexamethyl-1,4,8,11-tetraazacyclotetradecane (tet <i>b</i>)	[Mn ^{III} (cyclam)Cl ₂][Cl]•4H ₂ O	4
4.15a	1,4,8,11-tetraazacyclotetradecane (cyclam)	[Mn ^{III} (cyclam)Cl ₂][Cl]	5
4.15b*	1,4,8,11-tetraazacyclotetradecane (cyclam)	[Mn ^{III} (cyclam)Br ₂][Br]	
4.15c*	1,4,8,11-tetraazacyclotetradecane (cyclam)	[Mn ^{III} (cyclam)(NCS) ₂][NCS]	6
4.15d	1,4,8,11-tetraazacyclotetradecane (cyclam)	[Mn ^{III} (cyclam)(N ₃) ₂][ClO ₄]	7
4.15e	1,4,8,11-tetraazacyclotetradecane (cyclam)	[Mn ^{III} (cyclam)Br ₂][PF ₆]	
4.15f	1,4,8,11-tetraazacyclotetradecane (cyclam)	[Mn ^{III} (cyclam)Cl ₂][BF ₄]	8
4.15g	1,4,8,11-tetraazacyclotetradecane (cyclam)	[Mn ^{III} (cyclam)Cl ₂][CF ₃ SO ₃]	9
4.15h*	1,4,8,11-tetraazacyclotetradecane (cyclam)	[Mn ^{III} (cyclam)(NO ₃) ₂][NO ₃]	10
4.15i*	1,4,8,11-tetraazacyclotetradecane (cyclam)	[Mn ^{III} (cyclam)Cl ₂][NO ₃]	
4.15j*	1,4,8,11-tetraazacyclotetradecane (cyclam)	[Mn ^{III} (cyclam)Cl ₂][Cl]•5H ₂ O	11
4.15k	1,4,8,11-tetraazacyclotetradecane (cyclam)	[Mn ^{III} (cyclam)(CN) ₂][ClO ₄]	12
4.15l^	1,4,8,11-tetraazacyclotetradecane (cyclam)	[Mn ^{III} (cyclam)Br ₂][Br]•H ₂ O	
4.15m^	1,4,8,11-tetraazacyclotetradecane (cyclam)	[Mn ^{III} (cyclam)Cl ₂][Cl]•0.33CH ₃ OH	13
4.15n	1,4,8,11-tetraazacyclotetradecane (cyclam)	[Mn ^{III} (cyclam)(OH ₂) ₂][CF ₃ SO ₃] ₃ •H ₂ O	
4.15o	1,4,8,11-tetraazacyclotetradecane (cyclam)	[Mn ^{III} (cyclam)] ₂ [I]	
4.15p	1,4,8,11-tetraazacyclotetradecane (cyclam)	[Mn ^{III} (cyclam)(ONO) ₂][ClO ₄]	
4.15q	1,4,8,11-tetraazacyclotetradecane (cyclam)	[Mn ^{III} (cyclam)(OCIO ₃) ₂][ClO ₄]	14
4.15r	1,4,8,11-tetraazacyclotetradecane (cyclam)	[Mn ^{III} (cyclam)(CH ₃ COO)(CH ₂ COOH)][ClO ₄] ₂	
4.15s	1,4,8,11-tetraazacyclotetradecane (cyclam)	[Mn ^{III} (cyclam)(N ₃) ₂][CF ₃ SO ₃]	
4.16a	1,4,8,12-tetraazacyclotetradecane (cyclal)	[Mn ^{III} (cyclal)Br ₂][PF ₆]	15
4.16b	1,4,8,12-tetraazacyclotetradecane (cyclal)	[Mn ^{III} (cyclal)Cl ₂][Cl]•H ₂ O	16
4.17a	5-imidazole-1,4,8,11-tetraazacyclotetradecane (imcyclam)	[Mn ^{III} (imcyclam)(ClO ₄)] ₂ [ClO ₄] ₂	17
4.17b*	5-imidazole-1,4,8,11-tetraazacyclotetradecane (imcyclam)	[Mn ^{III} (imcyclam)Cl][ClO ₄] ₂	
4.18a*^	4,11-dimethyl-1,4,8,11-tetraazabicyclo[6.6.2]hexadecane (etcyclam)	[Mn ^{III} (etcyclam)Cl ₂][PF ₆]	
4.18b*^	4,11-dimethyl-1,4,8,11-tetraazabicyclo[6.6.2]hexadecane (etcyclam)	[Mn ^{III} (etcyclam)(N ₃) ₂][PF ₆]	
4.18c*^	4,11-dimethyl-1,4,8,11-tetraazabicyclo[6.6.2]hexadecane (etcyclam)	[Mn ^{III} (etcyclam)(OH)(OAc)][PF ₆]	18
4.18d*^	4,11-dimethyl-1,4,8,11-tetraazabicyclo[6.6.2]hexadecane (etcyclam)	[Mn ^{III} (etcyclam)(OMe) ₂][PF ₆]	
4.19a*^	4,10-dimethyl-1,4,7,10-tetraazabicyclo[5.5.2]tetradecane (etcyclen)	[Mn ^{III} (etcyclen)Cl ₂][PF ₆]	
4.20a	1,4,7,11-tetraazacyclotetradecane (isocyclam)	[Mn ^{III} (isocyclam)Cl ₂][Cl]•2H ₂ O	19
L1Mn2*^	1,4,7,10-tetraaza-2,6-pyridinophane (pyclen or L1)	[Mn ^{III} (L1)Cl ₂][ClO ₄]	This work
L2Mn2^	1,4,7,10-tetraaza-2,6-pyridinophane-14-ol (L2)	[Mn ^{III} (L2)Cl ₂][ClO ₄]	This work
L3Mn3^	1,4,7,10-tetraaza-2,6-pyridinophane-13-ol (L3)	[Mn ^{III} (L3)Cl ₂][ClO ₄]	This work

*Solid state structure reported in literature. ^Indicates complex is in the *cis*- geometry, all others are in the *trans*- geometry. 1: ref. ³³⁹; 2: ref. ³³⁸; 3: ref. ³⁴⁰; 4: ref. ³³⁸; 5: ref. ³⁴¹; 6: ref. ³⁴¹⁻³⁴²; 7: ref. ³⁴¹; 8: ref. ³⁴³; 9: ref. ³³⁸; 10: ref. ³⁴²; 11: ref. ^{274, 342}; 12: ref. ³⁴²; 13: ref. ²⁷⁴; 14: ref. ³⁴⁴; 15: ref. ³⁴³; 16: ref. ³⁴⁵; 17: ref. ³⁴⁶; 18: ref. ³³⁷; 19: ref. ²⁷⁶.



Scheme 4.9. Tetraazamacrocyclic ligands described in table 4.8.

4.3.2. Mn(III) mononuclear complexes with tetraazamacrocycles

Examples of the first Mn(III) monomeric complexes with cyclam were reported in the mid-1970s.³³⁹⁻³⁴⁰ Initially, these complexes were investigated to show how manipulation of the cyclam backbone brought about different properties to each Mn(III) complex. Bryan *et al.* published back-to-back reports on several Mn(III) complexes with hexamethyl cyclam derivatives, *meso*-5,5,7,12,12,14-hexamethyl-1,4,8,11-tetraazacyclotetradecane (tet *a*) and *rac*-5,7,7,12,12,14-hexamethyl-1,4,8,11-tetraazacyclotetradecane (tet *b*) (Scheme 4.9).³³⁸⁻³⁴⁰ [Mn^{III}(tet *a*)Cl₂][PF₆] (**4.13a**), [Mn^{III}(tet *a*)Cl₂][BF₄] (**4.13b**), [Mn^{III}(tet *a*)Br₂][PF₆] (**4.13c**), [Mn^{III}(tet *a*)(NCS)₂][NCS] (**4.13d**), [Mn^{III}(tet *a*)Cl₂][Cl]•3H₂O (**4.13e**), [Mn^{III}(tet *b*)Cl₂][PF₆] (**4.14a**), and [Mn^{III}(tet *b*)Br₂][PF₆] (**4.14b**) (Table 4.8) were all synthesized in a similar manner, by first making the corresponding Mn(II) complexes with each ligand and subsequently reacting each with an oxidizing agent such as NOPF₆ or NOBF₄ to obtain the desired Mn(III) complexes (**4.13a-e** and

4.14a-b). In addition to the original Mn(III) complexes reported as PF₆⁻ or BF₄⁻ salts, Bryan *et al.* also conducted metathesis reactions to obtain corresponding NCS⁻, Cl⁻, and Br⁻ complexes. Each complex was six-coordinate, with Mn(III) coordinated to the four nitrogen atoms from the ligand and two *trans* axial ligands (which vary depending on the synthetic route), giving the complex an octahedral geometry. The manganese within the complexes was metalated in a planar fashion, consisting of two six-membered chelate rings and two five-membered chelate rings (5-6-5-6 coordination). The six-membered rings adopted a chair confirmation and the two five-membered chelate rings adopted two different enantiomeric confirmations, λ and α .³³⁹⁻³⁴⁰ It was noted that these Mn(III) complexes could withstand large pH changes compared to the Mn(II) counterparts.³³⁹⁻³⁴⁰

Following the synthesis of Mn(III) complexes with hexamethyl cyclam derivatives, Chan *et al.* reported Mn(III) mononuclear complexes with cyclam, in 1976 (Scheme 4.9, Table 4.8).³⁴¹ In their report, Chan *et al.* stated that because of the excess methyl substitutions present in the complexes synthesized previously by Bryan *et al.*, there were concerns with serious steric effects.³⁴¹ Therefore, the authors synthesized mononuclear Mn(III) complexes with the unsubstituted/unsaturated cyclam ligand, forming complexes [Mn^{III}(cyclam)Cl₂][Cl] (**4.15a**), [Mn^{III}(cyclam)Br₂][Br] (**4.15b**), [Mn^{III}(cyclam)(NCS)₂][NCS] (**4.15c**), and [Mn^{III}(cyclam)(N₃)₂][ClO₄] (**4.15d**) (Table 4.8). Complexes **4.15a-4.15d** were obtained by bubbling air through solutions containing equimolar amounts of ligand and metal salt. The magnetic moments (μ_{eff}) of samples derived from these methods indicated that Mn(III) was high spin within the cyclam complexes.³⁴¹

In 1977, Bryan *et al.* synthesized additional Mn(III) complexes, this time with cyclam and cyclal; this was the first time a Mn(III) cyclal complex had been reported (Table 4.8, Scheme 4.9).³⁴³ Bryan *et al.* followed similar methods for metalation as they did in previous reports; combining equimolar amounts of ligand and metal salt, then adding an oxidizing agent (i.e. bromine or chlorine) to obtain the Mn(III) complexes, [Mn^{III}(cyclam)Br₂][PF₆] (**4.15e**), [Mn^{III}(cyclam)Cl₂][BF₄] (**4.15f**), and [Mn^{III}(cyclal)Br₂][PF₆] (**4.16a**) (Table 4.8). The absorption spectra of each Mn(III) complex was obtained in both acetonitrile and

the solid state. Based on these spectral results and previous work by Busch *et al.*, the authors concluded that the cyclam ligand provided a better match of “hole size” or cavity size for the Mn(III) radius than the cyclal ligand.^{218, 343}

It wasn't until 1987 that a crystal structure of a Mn(III) hexamethyl cyclam complex ($[\text{Mn}^{\text{III}}(\text{tet}a)\text{Cl}_2][\text{Cl}]\cdot 1.5\text{H}_2\text{O}$ (**4.13f**) was published by Hambley *et al.*³³⁸ Three different complexes were synthesized by the group, $[\text{Mn}^{\text{III}}(\text{cyclam})\text{Cl}_2][\text{CF}_3\text{SO}_3]$ (**4.15g**), $[\text{Mn}^{\text{III}}(\text{tet}a)\text{Cl}_2][\text{Cl}]\cdot 1.5\text{H}_2\text{O}$ (**4.13f**), and $[\text{Mn}(\text{tet}b)\text{Cl}_2][\text{Cl}]\cdot 4\text{H}_2\text{O}$ (**4.14c**) (Table 4.8). The crystal structure of **4.13f** shows the geometry of the Mn(III) is close to octahedral, with the tet *a* ligand coordinated to four equatorial sites and chloride ions coordinated in *trans* axial sites. Similar to a previously report complex by Bryan *et al.*,³³⁹⁻³⁴⁰ the five-membered chelate rings adopted skewed conformations and the six-membered chelate rings adopted distorted chair geometries. Bond distances for this complex, particularly Mn—N and Mn—Cl are shorter than bond lengths observed in non-macrocyclic ligand complexes.³⁴⁷ The observed Mn—N bond distances were 2.074 Å and 2.043 Å, whereas the Mn—Cl bond distance was 2.549 Å.³³⁸ In addition to the crystal structure, Hambley *et al.* reported CV measurements for each of the three complexes synthesized. Each complex exhibited a Mn^{III}/Mn^{II} couple at slightly different potentials (**4.15g** $E_{1/2} = 0.087$ V vs. NHE; **4.13f** $E_{1/2} = 0.317$ V vs. NHE; **4.14c** $E_{1/2} = -1.403$ V vs. NHE).³³⁸

After the initial reports describing the synthesis and characterization of monomeric Mn(III) cyclam complexes, other groups modified the ligands to obtain desired reactivity. In 1991, Kimura *et al.* modified cyclam by appending an imidazole moiety onto the ligand (Scheme 4.9).³⁴⁶ This was explored to test if a Mn(III) cyclam complex could parallel the catalytic activity of previously studied Mn(III) porphyrin complexes toward olefin epoxidations. Additionally, the Mn(III) cyclam complex was tested for activation by a proximal donor, such as imidazole. Two different imidazole modified Mn(III) cyclam complexes were synthesized, $[\text{Mn}^{\text{III}}(\text{imcyclam})(\text{ClO}_4)][\text{ClO}_4]_2$ (**4.17a**) and $[\text{Mn}^{\text{III}}(\text{imcyclam})\text{Cl}][\text{ClO}_4]_2$ (**4.17b**) (Table 4.8).³⁴⁶ The electronic spectra of complex **4.17a** was consistent with other reported Mn(III) complexes in

tetragonally distorted environments, with a LMCT band at 268 nm and a d-d band at 350 nm in water.³⁴⁶ The crystal structure of complex **4.17b** was also reported.; Mn(III) was bound in a square planar fashion by the cyclam ligand with the proximal imidazole and chloride ion bound in axial positions. The average equatorial Mn—N bond distance was 2.06 Å, but the axial Mn—N bond distance (from the imidazole group) was 2.277 Å.³⁴⁶ The difference in bond lengths between axial and equatorial sites is consistent with Jahn-Teller distortion for a high-spin d⁴ Mn(III) ion. Kimura *et al.* conducted CV measurements of complex **4.17a** and found that at scan rates of 500 mV/s a *quasi*-reversible redox event was observed ($E_{1/2} = 0.3312$ V vs. NHE) corresponding to Mn^{III}/Mn^{II}.³⁴⁶ Additionally, Kimura *et al.* tested the catalytic ability of complex **4.15a** for olefin epoxidations. The addition of the proximal imidazole onto the cyclam complex increased the catalytic turnover, similar to porphyrins previously tested.^{346, 348}

In the same year Daugherty *et al.* synthesized seven new cyclam Mn(III) mononuclear complexes, with a variety of axial ligands and counterions: [Mn^{III}(cyclam)Br₂][Br] (**4.15b**), [Mn^{III}(cyclam)(NCS)₂][NCS] (**4.15c**), [Mn^{III}(cyclam)(NO₃)₂][NO₃] (**4.15h**), [Mn^{III}(cyclam)Cl₂][NO₃] (**4.15i**), [Mn^{III}(cyclam)Cl₂][Cl]•5H₂O (**4.15j**), [Mn^{III}(cyclam)(CN)₂][ClO₄] (**4.15k**), and [Mn^{III}(cyclam)Br₂][Br]•H₂O (**4.15l**) (Table 4.8).³⁴² All but one of the complexes were isolated in the *trans* configuration. *Cis*-[Mn^{III}(cyclam)Br₂][Br]•H₂O (**4.15l**) was produced by adding a small amount of HBr to the previously reported/synthesized dimeric compound [(cyclam)₂Mn^{III,IV}₂O₂][Br₃]•5H₂O (**4.6b**).³¹¹ When HBr was added to the dinuclear complex the green crystals immediately turned dark red, unfortunately complex **4.15l** was unstable in all solvents.³⁴² Daugherty *et al.* also reported crystal structures for complexes **4.15b**, **4.15c**, **4.15h**, and **4.15i**. Which all exhibited roughly *trans* octahedral geometry around each Mn(III) center. The magnetic properties of all the complexes, except one, were consistent with high-spin d⁴ Mn(III) ions. Complex **4.15k**, which contained two *trans*-cyano groups coordinated to Mn(III), had magnetic properties consist with a low-spin d⁴ Mn(III) ion.

Several years later (in 1998), Létumier *et al.* published a detailed report on the *cis-trans* isomerization of two Mn(III) mononuclear cyclam complexes.²⁷⁴ Although there had already been many

reports on *trans*-cyclam Mn(III) complexes, *cis*-cyclam Mn(III) complexes were relatively rare in the chemical literature. Létumier *et al.* utilized a one-pot synthesis to obtain both the *trans* and *cis* isomer complexes. First, MnCl₂ was added to a solution of cyclam in methanol. The solvent was evaporated to one-fourth volume and filtered. The precipitate was identified as the *trans*-Mn(III) complex [Mn^{III}(cyclam)Cl₂][Cl]•5H₂O (**4.15j**) (Table 4.8). The filtrate contained the di-μ-oxo bridged Mn(III,IV) dimer complex [(cyclam)₂Mn^{III,IV}₂O₂]³⁺ (**4.6**), concentrated HCl was added to this mixture to give a red precipitate which was the *cis*-Mn(III) complex [Mn^{II}(cyclam)Cl₂][Cl]•0.33CH₃OH (**4.15m**) (Table 4.8). Létumier *et al.* observed a drastic color change upon addition of the concentrated HCl, as the solution of the dinuclear Mn(III,IV) complex changed from olive green to red. It was also noted that upon addition of the HCl, which seemed to break apart the μ-oxo bridges within the dinuclear complex, the complex maintained its *cis* arrangement. Létumier *et al.* also observed that the *cis* complex was converted irreversibly to the *trans*-Mn(III) complex upon dissolution in aqueous media. Although there were numerous attempts to grow crystalline material of complex **4.15m**, only the crystal structure of complex **4.15j** is reported. Mn—N and Mn—Cl bond distances are similar to those reported previously in the literature.^{338, 342, 346} In addition to synthesizing these two complexes, Létumier *et al.* conducted CV measurements and observed the *cis*-*trans* isomerization electrochemically. Starting with complex **4.15m** an irreversible reduction of the *trans*-Mn(III) isomer to Mn(II) (*trans*-Mn^{III}/*trans*-Mn^{II}) was observed in the CV. Only after the complex was reduced to Mn(II) did another redox wave appear, which corresponded to the reversible oxidation of a *cis*-Mn(II) complex (*cis*-Mn^{II}/*cis*-Mn^{III}).

It wasn't until 2001, that a crystal structure of a *cis*-Mn(III) mononuclear complex was reported. Hubin *et al.* reported several crystal structures for *cis*-Mn(III) mononuclear complexes.³³⁷ These complexes, which were synthesized with ethylene cross-bridged macrocycles, exhibit coordination chemistry most like the Mn(III) complexes synthesized by the Green group. Hubin *et al.* synthesized several different ethylene cross-bridged macrocycles etcyclam and etcyclen (etcyclam = 4,11-dimethyl-

1,4,8,11-tetraazabicyclo[6.6.2]hexadecane; etcyclen = 4,10-dimethyl-1,4,7,10-tetraazabicyclo[5.5.2]tetradecane) (Scheme 4.9) with the intent to form kinetically stable, mononuclear metal complexes in high valent states.³³⁷ Initial attempts at synthesizing Mn(III) complexes in aprotic or protic solvents with hydrated metal salts were unsuccessful; therefore, Hubin *et al.* prepared anhydrous Mn(II) complexes with the ligands, Mn(etcyclam)Cl₂ and Mn(etcyclen)Cl₂. To form the corresponding Mn(III) complexes, Mn(etcyclam)Cl₂ or Mn(etcyclen)Cl₂ in methanol with NH₄PF₆ was prepared and Br₂ was added as an oxidizing agent. This procedure yielded complexes [Mn^{III}(etcyclam)Cl₂][PF₆] (**4.18a**) and [Mn^{III}(etcyclen)Cl₂][PF₆] (**4.19a**) (Table 4.8). Hubin *et al.* also performed a metathesis reaction to obtain complex [Mn^{III}(etcyclam)(N₃)₂][PF₆] (**4.18b**) and additional modified procedures to obtain complexes [Mn^{III}(etcyclam)(OH)(OAc)][PF₆] (**4.18c**) and [Mn^{III}(etcyclam)(OMe)₂][PF₆] (**4.18d**) (Table 4.8). Additionally, crystal structures for all the complexes listed above (**4.18a-d** and **4.19a**) were obtained by Hubin *et al.* (Table 4.8).

All the *cis*-Mn(III) complexes (**4.18a-d** and **4.19a**) adopted a pseudo-octahedral geometry with the ligand occupying two axial and two *cis* equatorial sites. The two adjacent sites not occupied by the ligand were left open to be occupied by chloride, azide, hydroxide, acetoxy, or methoxy (depending on the complex). Although most of the complexes were formed with cyclam derived ligands, which typically adopt a *trans* geometry when metalated, the short ethylene cross-bridge within the macrocycle forced each complex to adopt a folded conformation. Within each complex Jahn-Teller distortion were observed based on the large difference in bond distances between Mn—N_{ax} and Mn—N_{eq}. In complex **4.19a** the Mn—N_{ax} bond distances were reported to be 2.202 and 2.211 Å, whereas the Mn—N_{eq} bond distances were reported to be 2.087 and 2.111 Å, the difference between the bond distances is over 0.1 Å.³³⁷ Complex **4.19a** also exhibited distortions between Mn—N_{ax} and Mn—N_{eq} bond distances, although to a slightly lesser extent (difference of less than 0.09 Å between the two bond distances).

Hubin *et al.* not only obtained crystal structures for the newly synthesized *cis*-Mn(III) complexes, but they also conducted UV-vis, and CV experiments to further explore the nature of these new complexes. Both complex **4.18a** and **4.19a** exhibited several charge transfer bands in solution ($\lambda_{\text{max}} = 220, 297 \text{ nm}$ (**4.18a**); $219, 294 \text{ nm}$ (**4.19a**)), as well as a d-d band ($\lambda_{\text{max}} = 534 \text{ nm}$ (**4.18a**); 530 nm (**4.19a**)) (Table 4.9).³³⁷ CV measurements revealed two *quasi*-reversible redox events for both complex **4.18a** and **4.19a**. The first redox event, which occurred at more negative potentials corresponded to the *quasi*-reversible reduction of Mn^{III}/Mn^{II} ($E_{1/2} = 0.582 \text{ V vs. NHE}$ (**4.18a**); $E_{1/2} = 0.400 \text{ V vs. NHE}$ (**4.19a**)).³³⁷ The second of the two reversible events corresponded to the *quasi*-reversible oxidation of Mn^{III}/Mn^{IV} ($E_{1/2} = 1.343 \text{ V vs. NHE}$ (**4.18a**); $E_{1/2} = 1.177 \text{ V vs. NHE}$ (**4.19a**)).³³⁷ Hubin *et al.* noted that the smaller macrocyclic complex **4.19a** was easier to oxidize, based on the shift in potentials. They hypothesized that this was because the smaller cavity size fit the smaller oxidized manganese ion better. The authors also characterized additional complexes **4.18b-d** using the same techniques, the results were like those obtained for complexes **4.18a** and **4.19a**.

More cyclam Mn(III) complexes were synthesized in 2005. Mossin *et al.* synthesized six additional *trans*-Mn(III) complexes $[\text{Mn}^{\text{III}}(\text{cyclam})(\text{OH}_2)_2][\text{CF}_3\text{SO}_3]_3 \cdot \text{H}_2\text{O}$ (**4.15n**), $[\text{Mn}^{\text{III}}(\text{cyclam})\text{I}_2][\text{I}]$ (**4.15o**), $[\text{Mn}^{\text{III}}(\text{cyclam})(\text{ONO})_2][\text{ClO}_4]$ (**4.15p**), $[\text{Mn}^{\text{III}}(\text{cyclam})(\text{OCIO}_3)_2][\text{ClO}_4]$ (**4.15q**), $[\text{Mn}^{\text{III}}(\text{cyclam})(\text{CH}_3\text{COO})(\text{CH}_3\text{COOH})][\text{ClO}_4]_2$ (**4.15r**), and $[\text{Mn}^{\text{III}}(\text{cyclam})(\text{N}_3)_2][\text{CF}_3\text{SO}_3]$ (**4.15s**) (Table 4.8). Crystal structures were obtained for five out of the six complexes (**4.15n-r**). All five of the complexes were high spin and in the *trans* configuration, which is the most energetically favorable conformation for cyclam metal complexes. Axial bond distances of Mn—X_{ax} (X = O, I) differed widely, depending on the attached ion (OH₂, I⁻, ONO⁻, OClO₃⁻, CH₃COO⁻, or CH₃COOH). In contrast, the Mn—N_{eq} bond distances were relatively similar between all the complexes, $2.03 \pm 0.01 \text{ \AA}$.

As previously discussed in the earlier chapter covering Mn(III,IV) dinuclear complexes, Tomczyk *et al.* reported the synthesis of two novel manganese complexes with the macrocycle isocyclam (Scheme

4.9), in 2012, one was a di- μ -oxo bridged dinuclear complex and one was a Mn(III) mononuclear complex. In this section, the Mn(III) mononuclear complex will be discussed. Tomczyk *et al.* synthesized *trans*-[Mn^{III}(isocyclam)Cl₂][Cl]•2H₂O (**4.20a**) (Table 4.8) by addition of MnCl₂•4H₂O in ethanol, to a solution of isocyclam. Upon complete addition of the metal salt and after stirring for 1.5 h, concentrated HCl was added to the solution; this resulted in a red solid which quickly turned into a clear green precipitate (complex **4.20a**). Tomczyk *et al.* theorized that the red precipitate was a *cis*-[Mn^{III}(isocyclam)Cl₂][Cl] complex, but unfortunately this unstable complex only persisted in solution for about 30 s before it was converted to stable *trans*-[Mn^{III}(isocyclam)Cl₂][Cl]•2H₂O (**4.20a**). UV-visible spectroscopy was utilized to confirm the presence of a Mn(III) mononuclear complex. In aqueous solution, three absorbance bands were observed at 274, 382, and 696 nm. The absorbance bands at 382 and 696 nm confirmed the *trans* nature of the complex and correspond to the d-d transitions of Mn(III) in a weak ligand field. The absorbance band at 274 nm, which had a higher molar absorptivity, was evidence of a LMCT from the ligand nitrogen to Mn(III). It is interesting to note that the molar absorptivity of the d-d transitions observed for complex **4.20a** were slightly higher compared to other cyclam complexes (**4.15g**); this is caused by the lower symmetry of the isocyclam complex versus the cyclam complexes.

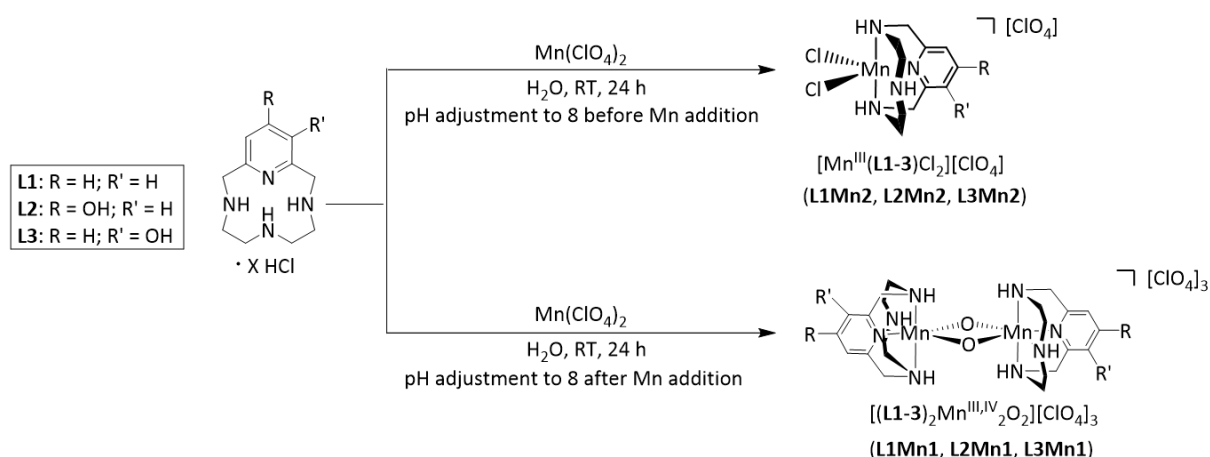
4.4. Novel library of high valent manganese complexes derived from pyridine- and pyridol-based tetraazamacrocyclic ligands

Herein, a small library of manganese tetraazamacrocyclic complexes derived from **L1-L3** is reported. As stated earlier in the report, two types of complexes were synthesized from this ligand library, a Mn(III) mononuclear complex and an Mn(III,IV) dinuclear complex. Each complex has been characterized and will be compared to other similar complexes found within the chemical literature. One unique feature of these complexes, particularly in the Mn(III) mononuclear complexes, is that the tetraazamacrocyclic utilized is a 12-membered ring. This forces the manganese ion to metalate in a *cis* fashion, because the macrocyclic ring is not large enough to accommodate the entire metal ion. Only one other Mn(III)

tetraazamacrocyclic complex with a 12-membered ring has been reported to date.³³⁷ Almost all the Mn(III) tetraazamacrocyclic complexes reported in the literature contain *cyclam* (or variations) metalated in a *trans* planar fashion. Due to a lack of *cis*-Mn(III) mononuclear complexes akin to those reported herein, several comparisons will be made to *trans*-Mn(III) mononuclear complexes in the literature.

In contrast, Mn(III,IV) dinuclear complexes are prevalent in the chemical literature, because of their history as molecular mimics for the OEC. However, pyridol- containing macrocyclic Mn(III,IV) dimer complexes (such as the ones reported here) have not been reported, to date. A pyridine-containing macrocyclic Mn(III,IV) dimer (**4.9a**) was deposited by Alcock *et al.* in the CCDC database, but no attempts to characterize this complex were made. Therefore, the three Mn(III,IV) dimer complexes with **L1-L3** are reported in this chapter, with comparisons to historically significant Mn(III,IV) dimers in the literature.

4.4.1. Synthesis of novel Mn(III) monomers and Mn(III,IV) dimers



Scheme 4.10. Different methods for synthesis and isolation of Mn(III) monomers vs. Mn(III,IV) dimers.

Two different types of high valent manganese complexes with tetraazamacrocyclic ligands were synthesized by slight modification of a traditional metalation procedure.⁵⁶ As previously reported by the Green group, metal complexes with **L1-L3** are best formed by dissolving the ligand in a small amount of water, adjusting to basic pH values, and then adding the corresponding metal perchlorate salt. Typically, the pH of the solution drops upon metalation and a drastic color change occurs. The *cis*-Mn(III) complexes

with **L1-L3** were formed using this traditional method with a pH adjustment to 8 prior to addition of the metal salt (Scheme 4.10). Initially, no stark color change occurred, but after several hours (and overnight) the solution darkened to a deep brown color. After filtration and drying, the crude solid was dissolved in CH₃CN to separate the salts formed during pH adjustment from the metal complex. Upon filtration of the pink (or red) CH₃CN solution and drying, the clean *cis*-Mn(III) products were isolated as pink/red/beige solids [**L1Mn**^{III}Cl₂][ClO₄] (**L1Mn2**), [**L2Mn**^{III}Cl₂][ClO₄] (**L2Mn2**), and [**L3Mn**^{III}Cl₂][ClO₄] (**L3Mn2**), respectively (Table 4.8, Scheme 4.10). These powders were re-dissolved in CH₃CN, filtered, and set out for crystallization via slow-evaporation. X-ray quality crystals of complex **L1Mn2** were obtained using this method. No materials suitable for XRD were isolated for complexes **L2Mn2** and **L3Mn2**. The *cis* geometry of these complexes was confirmed with UV-visible spectroscopy, and the solid state structure of complex **L1Mn2**. In addition to UV-visible spectroscopy, and X-ray diffraction, each complex was also electrochemically characterized using CV.

It is interesting to note that complexes **L1Mn2-L3Mn2** were synthesized with Mn^{II}(ClO₄)₂, but no outside oxidants were used to oxidize the Mn(II) to Mn(III) within the metal complexes. Several previous reports of the synthesis of mononuclear macrocyclic Mn(III) complexes utilized oxidizing agents, such as NOBF₄ or Br₂, to convert divalent manganese to trivalent manganese within the complex.^{337, 339-340} However, at least one group, Chan *et al.* used only atmosphere to aid in manganese oxidation, by bubbling air through solutions of ligand and metal salt.³⁴¹ Based on the slow darkening of the ligand/metal salt solution that was observed the oxidation from Mn(II) to Mn(III) is a gradual process. Although atmosphere certainly aided in the oxidation divalent manganese, another possibility is the ClO₄⁻ ions present within the solution. ClO₄⁻ ions are known oxidizers and could certainly have aided in oxidizing the manganese within the metalation solutions.

Complexes **L1Mn2-L3Mn2** were synthesized separately from the di-μ-oxo bridged Mn(III,IV) dinuclear complexes described herein. Within the literature, Mn(III) mononuclear complexes are typically

synthesized one of two ways: (1) synthesis of the Mn(II) complex followed by addition of an oxidizing agent to obtain the corresponding Mn(III) complex^{337, 339-340}, or (2) breaking apart a Mn(III,IV) dimer complex with acid.^{274, 276, 342} The latter method, was used successfully by several groups to obtain *cis*-Mn(III) complexes.^{274, 276, 342} Reports describe that upon addition of acid (such as HCl or HBr) to a green solution of a dimeric Mn(III,IV) complex the color changes to red, which is characteristic of the presence of a *cis*-Mn(III) complex.^{274, 276, 342} Although this synthetic method was not employed to synthesize complexes **21-L3Mn2**, a similar behavior was observed when acid was added to Mn(III,IV) dimers synthesized by the Green group.

A slight modification to the traditional metalation procedure was made to synthesize the di- μ -oxo bridged manganese(III,IV) dinuclear complexes. Instead of dissolving the ligand, adjusting the pH, and then adding the metal salt, both the ligand and Mn(ClO₄)₂ were dissolved at the same time followed by adjustment of the pH to 8 (Scheme 4.10). The resulting solution gradually darkened over several hours and turned a deep green color, which is characteristic of Mn(III,IV) dimers.^{337, 349} The solution was filtered, dried, and the crude solid was taken up in CH₃CN, as previously described. The CH₃CN solution was dark green and the solids resulting from evaporation of the CH₃CN were similarly colored, [(**L1**)₂Mn^{III,IV}₂O₂][ClO₄]₃ (**L1Mn1**) and [(**L2**)₂Mn^{III,IV}₂O₂][ClO₄] (**L2Mn1**) (Table 4.1). Both the isolated powders of **L1Mn1** and **L2Mn1** were dissolved in water, filtered, and X-ray quality crystals of **L1Mn1** and **L2Mn1** were obtained by slow evaporation. Characterization of these complexes was achieved using UV-vis, IR, XRD, CV, and EPR spectroscopy. Unfortunately, the Mn(III,IV) complex with **L3** (**L3Mn1**) was not isolable utilizing the method described above. Repeated synthesis and crystallization attempts resulted only in isolation of a brown powder that is most likely MnO₂.³³⁷⁻³³⁸ In fact, the only evidence of the existence of [(**L3**)₂Mn^{III,IV}₂O₂]³⁺ (**L3Mn1**) is found upon dissolution of complex **L3Mn2** [(**L3Mn**^{III}Cl₂)[ClO₄]] in water, as evidenced by UV-visible spectroscopy. However, this behavior is not unique to just the **L3** complex; all the *cis*-Mn(III) complexes (**L1Mn2-L3Mn2**) exhibit this feature.

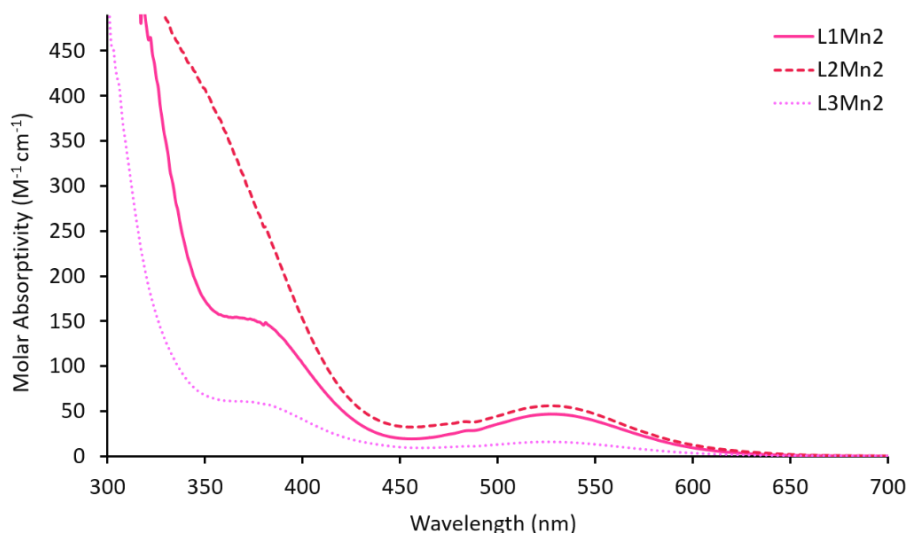
When complexes **L1Mn2-L3Mn2** are dissolved in CH₃CN or other organic solvents they exist as the *cis*-Mn(III) mononuclear complexes, but upon dissolution in water they are converted to di- μ -oxo bridged manganese(III,IV) dinuclear complexes **L1Mn1**, **L2Mn1**, and **L3Mn1**, which is confirmed by the characteristic deep green color of each solution. This behavior has been observed before by others, Hubin *et al.* describe the air oxidation of a cross-bridged macrocyclic Mn(II) complex which resulted in the characteristic deep green solution evidencing formation of an oxo-bridged dimer.³⁴⁹

4.4.2. UV-visible spectroscopy of Mn(III) monomers and Mn(III,IV) dimers

UV-visible spectroscopy was utilized to characterize complexes **L1Mn2-L3Mn2** and to confirm the unique *cis* configuration of each complex. As stated previously, relatively few examples of *cis*-Mn(III) mononuclear complexes exist in the chemical literature. In fact, only one other group obtained the electronic spectra of a *cis*-Mn(III) complex similar to complexes **L1Mn2-L3Mn2** (Table 4.9).³³⁷ Complexes **L1Mn2-L3Mn2** were dissolved in CH₃CN, each solution exhibiting the characteristic red/pink color of *cis*-Mn(III) mononuclear complexes. For each complex, two absorbance bands were observed at ~370 and ~527 nm (averaged between the three complexes **L1Mn2-L3Mn2**) (Table 4.9, Figure 4.1). The higher energy absorbance band at ~370 nm is most likely a LMCT. The lower energy band at ~527 nm is a d-d band. The characteristic red/pink color of the solution can be attributed to this absorbance band.³⁰ The d-d band observed at this wavelength is confirmatory of a high-spin Mn(III) complex, and is assigned as the only spin-allowed transition, ${}^5E_g \rightarrow {}^5T_{2g}$, expected within the visible region of this electronic spectrum.³⁰²⁰² Hubin *et al.* observed similar absorbance bands for complexes **4.18a** and **4.19a**, but no formal assignments were made in their report.³³⁷

Table 4.9. Electronic spectra of selected monomeric *cis*-Mn(III) tetraazamacrocyclic complexes in CH₃CN.

	Complex	λ_{\max} (nm), (ϵ , Mol ⁻¹ cm ⁻¹)	Reference
4.18a	[Mn ^{III} (etcyclam)Cl ₂][PF ₆]	220(7230), 297(7670), 534(540)	1
4.19a	[Mn ^{III} (etcyclen)Cl ₂][PF ₆]	219(4790), 294(4070), 530(190)	
L1Mn2	[Mn ^{III} (L1)Cl ₂][ClO ₄]	370(sh, 153), 525(46)	This work
L2Mn2	[Mn ^{III} (L2)Cl ₂][ClO ₄]	360(sh, 361), 530(56)	This work
L3Mn2	[Mn ^{III} (L3)Cl ₂][ClO ₄]	380(sh, 58), 525(16)	This work

1: ref. ³³⁷.**Figure 4.1.** Electronic spectra of *cis*-Mn(III) complexes of **L1Mn2**, **L2Mn2**, and **L3Mn2**.

In contrast to *cis*-Mn(III) mononuclear complexes, Mn(III,IV) dimeric complexes are prevalent in the chemical literature and there are many electronic spectra to compare with complexes **L1Mn1**, **L2Mn1**, and **L3Mn1** (Table 4.4). Complexes **L1Mn1**, **L2Mn1**, and **L3Mn1** were dissolved in water and each complexes' electronic spectrum exhibits absorbance bands that are characteristic of di- μ -oxo bridged Mn(III,IV) dimers (Table 4.4, Figure 4.2). The first, highest energy, feature of the electronic spectra is a ligand-to-metal charge transfer (LMCT) at 382 nm (for all three complexes **L1Mn1**, **L2Mn1**, and **L3Mn1**) which has been well documented by others.^{305, 309, 313} Although this particular absorbance band is not present within every Mn(III,IV) dimer complex reported, it is present in complexes **4.3b** (with bispicen), **4.5a** (with tren), and **4.7b** (with cyclen).^{305, 309, 313} The next feature of the electronic spectrum is a sharp

absorbance band at 555 nm (Table 4.4, Figure 4.2). This absorbance band corresponds to the d-d transition of the Mn(III) ion within the complex. Every previously reported Mn(III,IV) dimer has this feature in the electronic spectrum, with the band often observed from 548-561 nm.^{265, 276, 302, 304-307, 309, 311, 313} The next lower energy feature in the spectrum is a broad absorbance band at ~660 nm (averaged for complexes **L1Mn1**, **L2Mn1**, and **L3Mn1**) and is assigned as a ligand-to-metal charge transfer band from the oxo-bridge to the Mn(IV) ion within the complex (Table 4.4, Figure 4.2). This band was previously mis-assigned as a LMCT from the oxo-bridge to the Mn(III) ion in complexes **4.1b** and **4.2b**, but was later correctly re-assigned, in 1988.^{306, 317} Finally, tailing into the near-IR region a small shoulder is observed at ~800 nm (for all three complexes **L1Mn1**, **L2Mn1**, and **L3Mn1**) (Table 4.4, Figure 4.2). This shoulder corresponds to an intervalence transfer between the two metal ions. As such, complexes **L1Mn1**, **L2Mn1**, and **L3Mn1** can be categorized as Class II complexes, based on the classification scheme of Robin and Day.³¹⁶ Class II compounds have electronic spectra that exhibit typical absorbance bands expected for each metal ion, as well as some new features that arise from the weak interactions between the two metal ions.³¹⁶ Many previously synthesized Mn(III,IV) dimers exhibit this same IT band, although several notable complexes such as complex **4.4b**, do not. Suzuki *et al.* stated that the absence of an IT band suggested that complex **4.4b** had a lesser degree of delocalization between the two metal centers.³⁰⁶

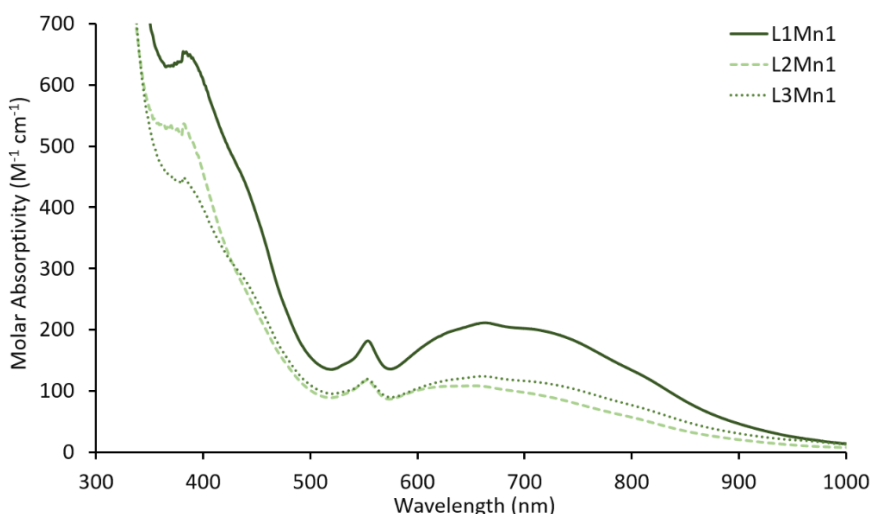


Figure 4.2. Electronic spectra of di- μ -oxo bridged Mn(III,IV) complexes **L1Mn1**, **L2Mn1**, and **L3Mn1**.

4.4.3. Solid state structures of Mn(III) monomer and Mn(III,IV) dimers.

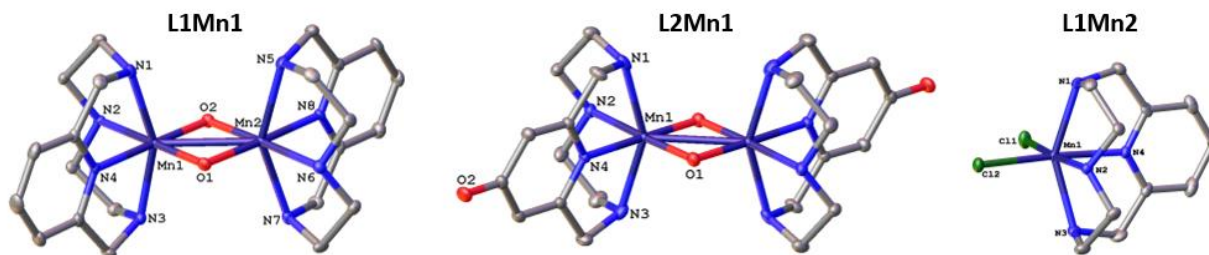


Figure 4.3. Solid state structures of complexes **L1Mn1**, **L2Mn1**, and **L1Mn2** (hydrogen atoms have been omitted for clarity).

Three solid state structures were obtained for **L1Mn1**, **L2Mn1**, and **L1Mn2** (Figure 4.3). Pink blade-like crystals of **L1Mn2** were evaluated by X-ray diffraction and provided data that resulted in the structure shown in figures 4.3 and 4.4. The macrocycle, **L1** (pyclen), is bound to the Mn(III) ion in a *cis*-fashion, with two nitrogen atoms bound in the equatorial plane and two nitrogen atoms bound in the axial plan. The coordination environment is completed by two chloride ions bound in a *cis*-fashion (Figure 4.3, 4.4). The resulting complex is a 5-5-5 ring structure. The distances within the complex are typical for a Mn(III) high-spin complex. Jahn-Teller distortion is observed (and expected) due to the d^4 Mn(III) ion present within the complex. The axial bond distances of Mn(1)—N_{ax}(1) and Mn(1)—N_{ax}(3), 2.247 and 2.241 Å, are significantly longer than the equatorial bond distances of Mn(1)—N_{eq}(2) and Mn(1)—N_{eq}(4), 2.076 and 2.059 Å, differing by almost 0.2 Å (0.1765 Å actual) (Table 4.10). The axial elongation observed in complex **L1Mn2** has been observed in other Mn(III) complexes, as well.³³⁷ For instance, complex **4.19a**, a 12-membered ethylene-cross bridged macrocyclic Mn(III) complex, synthesized by Hubin *et al.*, also exhibits Jahn-Teller distortions, although to a lesser extent than complex **L1Mn2** (Table 4.10, Figure 4.4). The observed axial bond distances of Mn(1)—N_{ax}(1) (2.211 Å) and Mn(1)—N_{ax}(3) (2.202 Å) differ by only about ~0.1 Å (0.1075 Å actual) from the equatorial bond distances of Mn(1)—N_{eq}(2) (2.111 Å) and Mn(1)—N_{eq}(4) (2.087 Å) (Table 4.10).

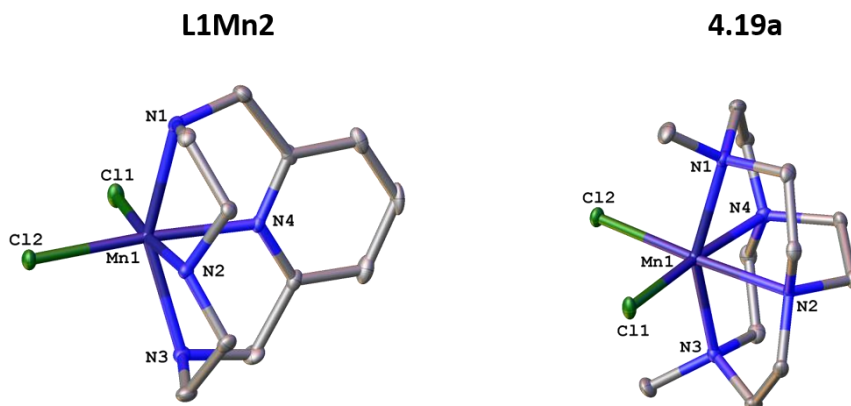


Figure 4.4. Comparison of the solid state structures of **L1Mn2** and **4.19a**.³³⁷

In addition to differences in elongation of the axial bond distances, there are some distinguishing differences in the bond angles of complexes **4.19a** and **L1Mn2**, specifically when comparing axial vs. equatorial bond angles (Table 4.11). In **L1Mn2** the axial bond angle N(1)-Mn(1)-N(3) is 149.22°, whereas, in **4.19a** the N(1)-Mn(1)-N(3) bond angle is 155.01°. The axial bond angle in complex **L1Mn2** is about 5° smaller than the same angle in **4.19a**. In contrast, the inverse is observed when comparing the equatorial bond angles of each complex. For **L1Mn2** the equatorial bond angle N(2)-Mn(1)-N(4) is 87.33°, but for **4.19a** the N(2)-Mn(1)-N(4) bond angle is 82.73°, making the equatorial bond angle of **L1Mn2** about 5° larger than the same angle in **4.19a**. Both differences between equatorial and axial angles of complexes **L1Mn2** and **4.19a** can be explained by a slight difference in the structure of the two ligands. Complex **L1Mn2** gives rise to delineation from octahedral geometry in the axial coordination, whereas complex **4.19a** modifies the equatorial Mn(III) interactions. The presence of the pyridine ring, within the 12-membered **L1** macrocycle, constrains the axial bond angle N(1)-Mn(1)-N(3) causing more deviation from linearity in complex **L1Mn2** than is observed in complex **4.19a**. In contrast, complex **4.19a** contains a 12-membered ethylene cross-bridged tetraazamacrocycle. The ethylene cross-bridge constrains the equatorial bond angle N(2)-Mn(1)-N(4) more in complex **4.19a** than compared to complex **L1Mn2**.

Table 4.10. Selected bond distances (Å) for complexes **4.9a**, **L1Mn1**, **L2Mn1**, **4.19a**, and **L1Mn2**

Bond Distances (Å)	4.9a	L1Mn1	L2Mn1	4.19a	L1Mn2
Mn(1)-N(1)	2.191(5)	2.086(3)	2.193(15)	2.211(3)	2.247(2)
Mn(1)-N(2)	2.127(4)	2.091(3)	2.104(13)	2.111(3)	2.076(2)
Mn(1)-N(3)	2.191(5)	2.090(3)	2.185(15)	2.202(3)	2.241(3)
Mn(1)-N(4)	2.090(6)	1.991(3)	2.00(12)	2.087(3)	2.059(2)
Mn(1)-Cl(1)	-	-	-	2.281(10)	2.248(9)
Mn(1)-Cl(2)	-	-	-	2.303(10)	2.249(9)
Mn(1)-O(1)	1.797(5)	1.809(2)	1.834(12)	-	-
Mn(1)-O(2)	1.792(4)	1.800(2)	1.830(11)	-	-
Mn(1)-Mn(2)	2.681(10)	2.712(7)	2.709(4)	-	-
Mn(2)-O(1)	1.847(4)	1.861(2)	-	-	-
Mn(2)-O(2)	1.842(4)	1.849(2)	-	-	-
Mn(2)-N(5)	2.146(4)	2.246(3)	-	-	-
Mn(2)-N(6)	2.041(4)	2.110(3)	-	-	-
Mn(2)-N(7)	2.146(4)	2.266(3)	-	-	-
Mn(2)-N(8)	2.000(6)	2.058(3)	-	-	-

Table 4.11. Selected bond angles (°) for complexes **4.19a** and **L1Mn2**

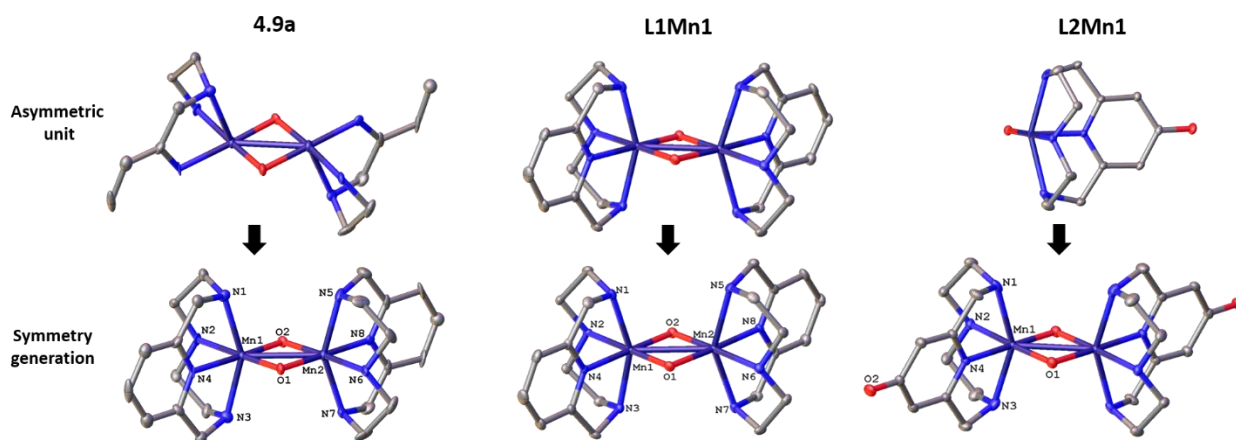
Bond Angles (°)	4.19a	L1Mn2
N(1)-Mn(1)-N(2)	81.29(11)	80.18(9)
N(1)-Mn(1)-N(3)	155.01(11)	149.22(9)
N(1)-Mn(1)-N(4)	78.61(11)	77.56(9)
N(2)-Mn(1)-N(3)	81.98(11)	80.81(9)
N(2)-Mn(1)-N(4)	82.73(11)	87.33(10)
N(3)-Mn(1)-N(4)	78.89(11)	77.58(1)
N(1)-Mn(1)-Cl(1)	96.32(8)	97.22(7)
N(1)-Mn(1)-Cl(2)	100.64(8)	104.44(7)
N(2)-Mn(1)-Cl(1)	174.11(9)	174.76(8)
N(2)-Mn(1)-Cl(2)	96.32(8)	88.60(7)
N(3)-Mn(1)-Cl(1)	99.91(9)	99.62(7)
N(3)-Mn(1)-Cl(2)	97.79(9)	99.06(7)
N(4)-Mn(1)-Cl(1)	92.88(8)	87.67(7)
N(4)-Mn(1)-Cl(2)	175.36(8)	175.09(7)
Cl(1)-Mn(1)-Cl(2)	91.76(4)	96.48(3)

Table 4.12. Selected bond angles (°) for **4.9a**, **L1Mn1**, and **L2Mn1**

Bond Angles (°)	4.9a	L1Mn1	L2Mn1
N(1)-Mn(1)-N(2)	80.65(12)	81.90(13)	80.79(5)
N(1)-Mn(1)-N(3)	151.51	153.83(11)	150.40(5)
N(1)-Mn(1)-N(4)	78.73(3)	80.16(14)	78.37(5)
N(2)-Mn(1)-N(3)	80.65	81.49(13)	80.85(5)
N(2)-Mn(1)-N(4)	86.10(2)	89.60(11)	88.84(5)
N(3)-Mn(1)-N(4)	78.73	79.65(14)	78.24(5)
Mn(1)-O(1)-Mn(2)	94.76(16)	95.26(11)	95.38(5)
Mn(1)-O(2)-Mn(2)	95.10(2)	95.97(11)	-
O(1)-Mn(1)-O(2)	86.50(2)	85.81(11)	-
O(1)-Mn(2)-O(2)	83.66(2)	82.96(10)	84.62(5)
N(1)-Mn(1)-O(1)	100.90(14)	100.68(14)	99.89(5)
N(1)-Mn(1)-O(2)	99.71(11)	100.36(14)	102.17(5)
N(2)-Mn(1)-O(1)	178.10(3)	176.48(12)	176.60(5)
N(2)-Mn(1)-O(2)	91.50(2)	91.37(11)	91.98(5)
N(3)-Mn(1)-O(1)	99.71	96.90(14)	99.81(5)
N(3)-Mn(1)-O(2)	100.90	100.11(14)	101.48(5)
N(4)-Mn(1)-O(1)	94.90(2)	93.20(11)	94.56(5)
N(4)-Mn(1)-O(2)	177.61(18)	178.96(12)	179.08(5)
N(5)-Mn(2)-N(6)	80.72	80.29(14)	-
N(5)-Mn(2)-N(7)	148.63	148.37(11)	-
Mn(5)-Mn(2)-N(8)	77.17	77.98(13)	-
N(5)-Mn(2)-O(1)	102.85	102.96(13)	-
N(5)-Mn(2)-O(2)	100.22	100.86(13)	-
N(6)-Mn(2)-N(7)	80.73(10)	79.57(14)	-
N(6)-Mn(2)-N(8)	88.20(2)	88.39(11)	-
N(6)-Mn(2)-O(1)	92.00(2)	95.38(11)	-
N(6)-Mn(2)-O(2)	175.60(2)	178.14(12)	-
N(7)-Mn(2)-N(8)	77.19(14)	77.32(13)	-
N(7)-Mn(2)-O(1)	102.84(13)	102.99(13)	-
N(7)-Mn(2)-O(2)	100.21(9)	99.97(13)	-
N(8)-Mn(2)-O(1)	179.84(18)	176.21(11)	-
N(8)-Mn(2)-O(2)	96.19(18)	93.27(11)	-

Solid state structures of the Mn di- μ -oxo bridged complexes **L1Mn1** and **L2Mn1** were also explored. Crystallizations of both complex **L1Mn1** and **L2Mn1** were carried out in H₂O. Slow evaporation of deep green aqueous solutions afforded block-like dark green/black crystals of **L1Mn1** and **L2Mn1**. Although multiple attempts were made to crystallize complex **L3Mn1** no crystals suitable for X-ray analysis were obtained. Both complexes consist of the ligand (either **L1** or **L2**) bound in a *cis*-fashion to a manganese ion, bridged to another ligand-bound manganese ion through a di- μ -oxo bridge (Figure 4.3).

The crystal structure of the **L1** Mn(III,IV) dimer complex has been previously deposited into the Cambridge crystallographic database (CCDC #:675326) and will be referred to as complex **4.9a** ($[(\text{pyclen})_2\text{Mn}^{\text{III,IV}}_2\text{O}_2][\text{Cl}]_3 \cdot 6\text{H}_2\text{O}$) (Table 4.1). There are several interesting differences when comparing **4.9a** and **L1Mn1**, although they share the Mn di- μ -oxo core structure. Complex **4.9a** was modeled in the monoclinic *Cm* space group, while complex **L1Mn1** was modeled in the monoclinic *C2/c* space group. As such, the asymmetric units of the two complexes are very different. **L1Mn1** contains the entire Mn(III,IV) dimer in the asymmetric unit, whereas **4.9a** contains only half of each ligand bound to manganese ions, (Scheme 4.11). The overall data of complex **L1Mn1** is better than complex **4.9a**.



Scheme 4.11. Asymmetric units and symmetry generated dimers for the solid state structure of **4.9a**, **L1Mn1**, **L2Mn1** (Hydrogen atoms omitted for clarity). (**4.19a** CCDC #: 675326)

Complexes **L1Mn1** (with **L1**) and **L2Mn1** (with **L2**), are both Mn(III,IV) di- μ -oxo bridged dinuclear complexes, but the crystal structure of each complex is unique. Complex **L1Mn1** and **L2Mn1** crystallize in

different space groups, as stated previously **L1Mn1** was modeled in the monoclinic $C2/c$ space group; whereas, complex **L2Mn1** was modeled in the monoclinic $P2_1$ space group. The asymmetric unit of **L1Mn1** contains the entire Mn(III,IV) dimer molecule. In contrast, the asymmetric unit of **L2Mn1** only contains one-half of the dinuclear complex and one bridging-oxygen atom; therefore, the second half of the complex is symmetry generated (Scheme 4.11). Because the asymmetric unit of **L1Mn1** contains the entire molecule, the crystal structure contains two crystallographic distinct manganese centers, whereas the crystal structure of **L2Mn1** contains two crystallographically equivalent manganese centers. The crystallographic equivalence of the two manganese centers in complex **L2Mn1** does not necessarily mean that the manganese ions are identical in nature (i.e. the same charge), it is merely a consequence of how the system crystallizes in the solid state. In fact, UV-visible spectroscopy and EPR spectroscopy of complex **L2Mn1** confirm that the complex contains two inequivalent manganese centers ((III) and (IV)). Several other previously reported Mn(III,IV) dimer complexes crystallize in a similar manner with two crystallographically equivalent metal centers.³⁰⁷

Evidence for two crystallographically distinct metal centers within complex **L1Mn1** can be found by observing the Mn—N bond lengths of Mn(1) vs. Mn(2). Mn(1) is a d^3 Mn(IV) ion and the axial and equatorial bond distances surrounding the metal ion are relatively similar to one another (Mn^{IV}—N_{ax} = 2.086 and 2.090 Å; Mn^{IV}—N_{eq} = 2.091 and 1.991 Å). In contrast, Mn(2) is a d^4 Mn(III) ion that experiences Jahn-Teller distortions; this can be observed in the lengthening of the Mn^{III}—N_{ax} bond distances (2.266 and 2.246 Å) vs. the Mn^{III}—N_{eq} distances (2.110 and 2.058 Å). In addition, the Mn—O bond distances are different for each metal center, indicating an inequivalence of charge (Table 4.10). Contrastingly, the Mn—N and Mn—O bond distances in complex **L2Mn1** are of intermediate length between an Mn(III) and Mn(IV) ion (Table 4.10). A small indication of Jahn-Teller distortion is observed between the axial and equatorial bound nitrogen atoms (Mn—N_{ax} = 2.195 and 2.185 Å; Mn—N_{eq} = 2.104 and 2.00 Å), but the distortion is much less pronounced compared to complex **L1Mn1**.

For many years, the bond distance of greatest interest within Mn(III,IV) complexes was the distance between the two di- μ -oxo bridged Mn—Mn atoms. Early studies of the OEC within PSII using EXAFS indicated an Mn—Mn bond length of 2.7 Å.^{285, 287-289} Complexes **L1Mn1** and **L2Mn1** exhibit Mn—Mn bond lengths of 2.712 and 2.709 Å, respectively. Compared to several other Mn(III,IV) dimers, the lengths observed in these complexes are intermediate in range (Table 4.2). For example, the Mn—Mn distance within complex **4.4c** (2.643 Å) with tmpa ligands, was the shortest Mn—Mn bond distance recorded to date vs. complex **4.6b** (2.741 Å) with cyclam ligands, which is the greatest Mn—Mn bond distance reported to date (Table 4.2).

Table 4.13. Crystal data, intensity collections, and structure refinement parameters for **L1Mn1**, **L2Mn1**, **L1Mn2**

	L1Mn1	L2Mn1	L1Mn2
Simplified Molecular Formula	$[(L1)_2Mn_2O_2][ClO_4]_3 \cdot 4H_2O$	$[(L2)_2Mn_2O_2][ClO_4] \cdot 6H_2O$	$[(L1)MnCl_2][ClO_4]$
Empirical formula	$C_{22}H_{44}Cl_3Mn_2N_8O_{18}$	$C_{11}H_{22.2}Cl_{0.5}MnN_4O_{6.94}$	$C_{11}H_{18}Cl_3MnN_4O_4$
Formula weight	924.88	394.25	431.58
Temperature/K	100.(2)	100.02	100.(2)
Crystal system	monoclinic	monoclinic	monoclinic
Space group	$P2_1$	$C2/c$	$P2_1/c$
a/Å	10.1199(6)	16.8774(6)	7.0070(4)
b/Å	16.2239(10)	11.4034(6)	12.7983(7)
c/Å	11.8583(8)	16.7065(6)	18.8563(11)
$\alpha/^\circ$	90	90	90
$\beta/^\circ$	114.402(2)	99.844(2)	90.618(2)
$\gamma/^\circ$	90	90	90
Volume/Å³	1773.02(19)	3168.0(2)	1690.89(17)
Z	2	8	4
ρ_{calc}/cm^3	1.732	1.653	1.695
μ/mm^{-1}	1.026	0.960	1.277
F(000)	954.0	1642.0	880.0
Crystal size/mm³	$0.273 \times 0.175 \times 0.067$	$0.457 \times 0.289 \times 0.274$	$0.362 \times 0.078 \times 0.052$
Radiation	Mo K α ($\lambda = 0.71073$)	Mo K α ($\lambda = 0.71073$)	Mo K α ($\lambda = 0.71073$)
2θ range for data collection/$^\circ$	6.28 to 66.48	6.256 to 60.298	6.36 to 60.24
Index ranges	$-15 \leq h \leq 15$ $-24 \leq k \leq 24$ $-18 \leq l \leq 18$	$-23 \leq h \leq 23$ $-16 \leq k \leq 16$ $-23 \leq l \leq 23$	$-9 \leq h \leq 9$ $-18 \leq k \leq 18$ $-26 \leq l \leq 26$
Reflections collected	33419	41977	28307
Independent reflections	13522 [$R_{int} = 0.0435$, $R_{sigma} = 0.0791$]	4682 [$R_{int} = 0.0237$, $R_{sigma} = 0.0123$]	4963 [$R_{int} = 0.0829$, $R_{sigma} = 0.0804$]
Data/restraints/parameters	13522/1/490	4682/0/265	4963/0/208
Goodness-of-fit on F²	0.991	1.100	1.063
Final R indexes [$I > 2\sigma(I)$]	$R_1 = 0.0499$, $wR_2 = 0.0970$	$R_1 = 0.0362$, $wR_2 = 0.0937$	$R_1 = 0.0520$, $wR_2 = 0.0894$
Final R indexes [all data]	$R_1 = 0.0829$, $wR_2 = 0.1087$	$R_1 = 0.0390$, $wR_2 = 0.0956$	$R_1 = 0.1045$, $wR_2 = 0.1039$
Largest diff. peak/hole / e⁻³	1.31/-0.49	0.60/-0.93	1.25/-0.55

4.4.4. Electrochemical studies of Mn(III) monomers and Mn(III,IV) dimers

Cyclic voltammograms of complexes **L1Mn2-L3Mn2** in CH₃CN offer insight into the stability of these unique *cis*-Mn(III) complexes. For all three complexes a *quasi*-reversible redox wave was observed and has been assigned to the Mn^{III}/Mn^{IV} couple (Figure 4.5, Table 4.14). The E_{1/2} values will not be compared to determine the relative electrochemical stability of each complex, because of the *quasi*-reversible nature of each couple. Based on the observed E_{pc} values for each complex, the order of stability of the Mn(III) species is **L2Mn2** (841 mV vs. NHE) > **L1Mn2** (852 mV vs. NHE) > **L3Mn2** (856 mV vs. NHE), **L2Mn2** being the most negative (Table 4.14, Figure 4.5). This data indicates that **L2** is the most electron donating ligand and stabilizes the Mn(III) species to the greatest degree. The findings of the electrochemical analysis of complexes **L1Mn2-L3Mn2** agree with previously reported conclusions related to donor capacity of **L1-L3** from studies of other ligand-metal complexes.⁵⁶

Table 4.14. Electrochemical data for complexes synthesized by the Green group (all reported vs. NHE).

Complex	Redox Couple	E _{pc} (V)	E _{pa} (V)	E _{1/2} (V)	ΔE (V)	Solvent	Electrolyte
L1Mn1	Mn ^{III,IV} /Mn ^{III,III}	0.295	0.379	0.702	0.084	CH ₃ CN	0.1 M TBAP
	Mn ^{III,IV} /Mn ^{III,III}	0.444	-	-	-	H ₂ O	0.1 M NaClO ₄
L2Mn1	Mn ^{III,IV} /Mn ^{III,III}	0.349	-	-	-	H ₂ O	0.1 M NaClO ₄
	Mn ^{III,IV} /Mn ^{IV,IV}	0.937	0.769	0.853	0.168		
L1Mn2	Mn ^{IV} /Mn ^{III}	0.852	1.045	0.948	0.193	CH ₃ CN	0.1 M TBAP
L2Mn2	Mn ^{IV} /Mn ^{III}	0.841	1.082	0.962	0.241	CH ₃ CN	0.1 M TBAP
L3Mn2	Mn ^{IV} /Mn ^{III}	0.856	0.967	0.912	0.111	CH ₃ CN	0.1 M TBAP

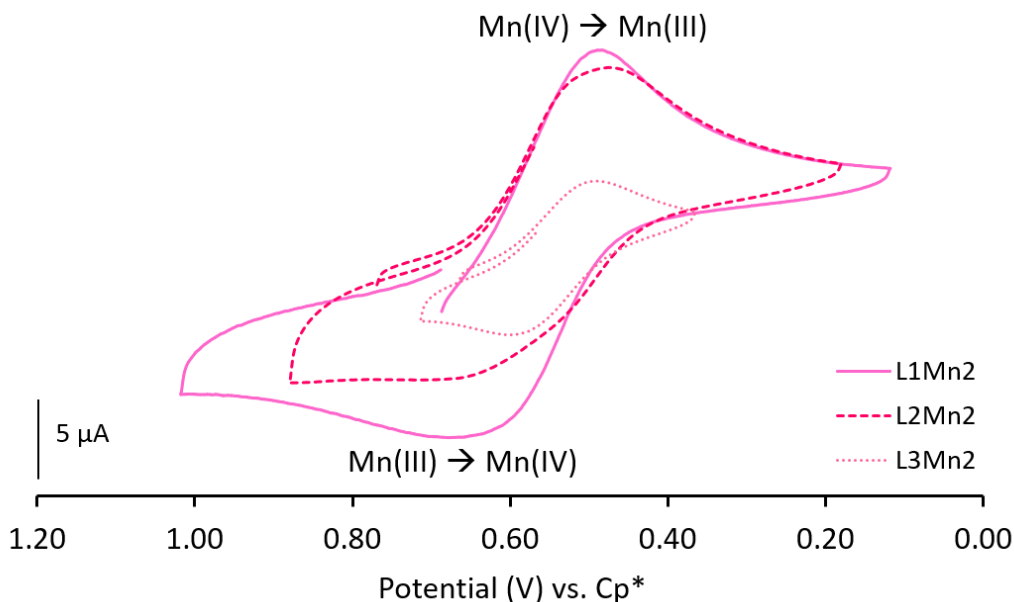


Figure 4.5. Cyclic voltammograms of *cis*-Mn(III) complexes **L1Mn2**, **L2Mn2**, **L3Mn2**. CV recording in 10.0 mL of DMF containing 10 mg complex + 0.1 M TBAP with a glassy carbon working electrode, Ag wire quasi-reference electrode, and a platinum wire auxiliary electrode.

Additionally, the cyclic voltammograms of complexes **L1Mn2-L3Mn2** can be compared with other *cis*-Mn(III) complexes. Hubin *et al.* obtained electrochemical measurements on a complex similar to those described here. As stated previously, complex **4.19a** is a rare *cis*-Mn(III) mononuclear complex that contains a 12-membered ethylene-cross bridged macrocycle. The electrochemistry of this complex consists of two redox couples, a Mn^{III}/Mn^{II} couple ($E_{1/2} = 400$ mV vs. NHE) and a Mn^{IV}/Mn^{III} couple ($E_{1/2} = 1177$ mV vs. NHE). The lack of an Mn^{III}/Mn^{II} couple in the CV of **L1Mn2-L3Mn2** is an obvious difference compared to complex **4.19a**. It is hypothesized that the Mn(II) oxidation state is not stabilized by the macrocyclic ligands (**L1-L3**), therefore no Mn^{III}/Mn^{II} couple is observed. However, the CV of complex **4.19a** and complexes **21-L3Mn2** both exhibit a Mn^{III}/Mn^{IV} couple. This anodic couple appears at much higher redox potentials for complex **4.19a** ($E_{1/2} = 1177$ mV vs. NHE) than for complexes **L1Mn2-L3Mn2** ($E_{1/2} = 948, 962, 912$ mV vs. NHE), suggesting that the manganese ions in complexes **L1Mn2-L3Mn2** are much easier to oxidize than complex **4.19a**.

The cyclic voltammograms of complexes **L1Mn1** (in H₂O and CH₃CN) and **L2Mn1** (in CH₃CN) offer insight into the stabilities of the Mn(III,IV) dimeric complexes synthesized to date. Historically, most Mn(III,IV) dimeric complexes with nitrogen-containing ligands exhibit two *quasi*-reversible redox events, one at more cathodic potentials that corresponds to a Mn^{III,IV}/Mn^{III,III} couple and another at more anodic potentials that corresponds to a Mn^{III,IV}/Mn^{IV,IV} couple (Table 4.5, Scheme 4.6)^{265, 268, 276, 299, 301-307, 309, 313}

The Mn(III,IV) dimeric complexes **L1Mn1** and **L2Mn1** exhibit electrochemical behavior that can be compared to other Mn(III,IV) dimers in the chemical literature. Complex **L1Mn1** exhibits solvent dependent redox behavior. In CH₃CN, complex **L1Mn1** exhibits a *quasi*-reversible redox couple that corresponds to the *quasi*-reversible reduction of Mn^{III,IV}/Mn^{III,III} ($E_{1/2} = 0.700$ V vs. NHE). In contrast, when complex **L1Mn1** is dissolved in H₂O only an irreversible reduction to Mn(III,III) is observed ($E_{pc} = 0.440$ V vs. NHE). Irreversibility of the reduction of Mn^{III,IV}/Mn^{III,III} has been observed before by others.²⁶⁸ When compared to other Mn(III,IV) dimeric complexes in the chemical literature the Mn^{III,IV}/Mn^{III,III} couple of complex **L1Mn1** (in CH₃CN) exhibits the most positive redox potential published to date.^{265, 268, 276, 299, 301-307, 309, 313}

Another unique aspect related to the redox behavior of **L1Mn1** is that no Mn^{III,IV}/Mn^{IV,IV} redox couple was observed. If the potential of the Mn^{III,IV}/Mn^{III,III} redox event is shifted to very positive redox potentials then it would be expected that the Mn^{III,IV}/Mn^{IV,IV} couple would also be shifted to higher redox potentials. Therefore, it is hypothesized that no anodic couple is observed because it is shifted to potentials outside the solvent window allowed by CH₃CN and H₂O experiments. In contrast, the electrochemical behavior of complex **L2Mn1** exhibits a *quasi*-reversible redox wave that corresponds to the Mn^{III,IV}/Mn^{IV,IV} couple ($E_{1/2} = 0.85$ V vs. NHE) and an irreversible reduction which is assigned as the reduction of Mn^{III,IV} to Mn^{III,III} ($E_{pc} = 0.35$ V vs. NHE). To the best of our knowledge, the anodic redox wave of complex **L2Mn1** is the most negative $E_{1/2}$ reported to date (Table 4.5, Scheme 4.6). Electrochemical analysis of **L2Mn1** was not conducted in CH₃CN, due to a lack of solubility. Electrochemical analysis was also attempted on complex **L3Mn1** as well. As discussed earlier, when complex **L3Mn2** is dissolved in H₂O

it is converted to **L3Mn1**. No redox waves were observed possibly because they are shifted to potentials that were outside the solvent window.

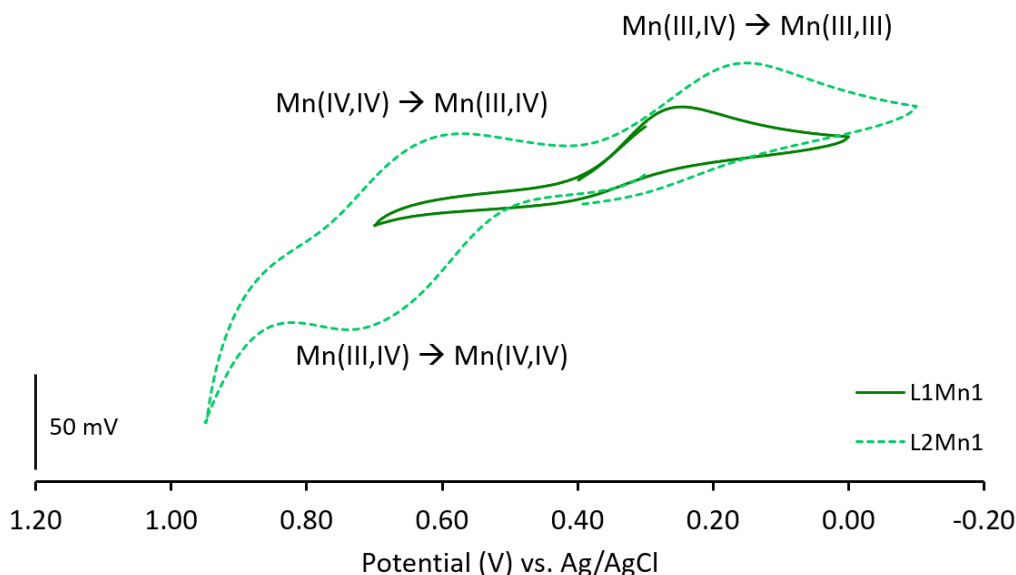


Figure 4.6. Cyclic voltammograms of Mn(III,IV) dimer complexes **L1Mn1**, **L2Mn1**. CV recorded in 3.0 mL of H₂O containing 3 mg complex + 0.1 M NaClO₄ with a glassy carbon working electrode, Ag/AgCl reference electrode, and a platinum wire auxiliary electrode.

4.4.5. Infrared spectroscopy of Mn(III,IV) dimers

IR spectroscopy was used to study complexes **L1Mn1** and **L2Mn1**. In the chemical literature, IR spectroscopy was utilized to monitor the Mn₂O₂ core vibrational modes. Generally, the Mn₂O₂ has been observed at an average value of 686 cm⁻¹ (Table 4.3).^{276, 302, 304-305} A Mn₂O₂ vibrational mode is observed for both **L1Mn1** (~676 cm⁻¹) and **L2Mn1** (~676 cm⁻¹). The Mn₂O₂ stretching frequency for complexes **L1Mn1** and **L2Mn1** is shifted to lower wavenumbers compared to previously synthesized Mn(III,IV) dimeric complexes, which is consistent with previous data indicating that **L1** and **L2** are stronger electron donors than the other ligands utilized in the chemical literature.

4.4.6. Conclusions

A small library of high-valent manganese complexes was synthesized from **L1-L3** by slight modification of metalation procedures in the current literature.⁵⁶ When an Mn(II) salt was added to a pH adjusted solution of ligand, *cis*-Mn(III) monomeric complexes resulted (**L1Mn2**, **L2Mn2**, and **L3Mn2**). In contrast, when an Mn(II) salt and ligand were dissolved together and then the pH was adjusted a di- μ -oxo bridged Mn(III,IV) dimeric complex resulted (**L1Mn1** and **L2Mn1**). X-ray quality crystals of **L1Mn1**, **L2Mn1**, and **L1Mn2** validated connectivity within the complexes. The crystal structure of complex **L1Mn1** is consistent with a high-spin Mn(III) ion; Jahn-Teller distortion is observed with the Mn—N_{ax} bond distances. The crystal structures of complexes **L1Mn1** and **L2Mn1** confirmed the presence of a di- μ -oxo bridged Mn(III,IV) dimer, although the two different complexes crystallize in different space groups. In addition to X-ray diffraction, complexes were also characterized using UV-vis, IR, CV, and EPR spectroscopy. The electronic spectra of complexes **L1Mn2-L3Mn2** confirmed the presence of a high-spin Mn(III) metal center; each spectrum exhibited only one spin-allowed transition in the visible region corresponding to $^5E_g \rightarrow ^5T_{2g}$.³⁰ In contrast, the electronic spectra of complexes **L1Mn1**, **L2Mn1**, and **L3Mn1** exhibited multiple absorbance bands; each band having been previously confirmed in the chemical literature.^{302, 304-305, 307, 313} Electrochemical studies of both the monomeric and dimeric complexes offered insight into the redox behavior of each complex. Complexes **L1Mn2-L3Mn2** all exhibited a redox event corresponding to the *quasi*-reversible oxidation of Mn^{III}/Mn^{IV}.³⁰⁴ Whereas, complexes **L1Mn1** and **L2Mn1** exhibited slightly different redox behavior that was comparable to electrochemical studies conducted by others. Complexes **L1Mn2-L3Mn2** are particularly unique because they are only the 2nd and 3rd examples of *cis*-Mn(III) macrocyclic complexes that have been reported in the chemical literature to date. Most previously synthesized Mn(III) macrocyclic complexes reported were isolated as the *trans* isomers. Complexes **L1Mn1**, **L2Mn1**, and **L3Mn1** were also compared to a group of historically significant Mn(III,IV) dimers.

4.5. Experimental (methods and materials)

Caution! Perchlorate salts are explosive and should be handled with care; such compounds should never be heated as solids. All chemical reagents were purchased from either Millipore Sigma or Alfa Aesar and used without further purification. The 12-membered tetraazamacrocycles **L1**, **L2**, and **L3** were isolated as the hydrochloride salts prior to metal ion complexation in accordance with standard practices; synthetic procedures are described in chapter 2. The yields reported for **L1Mn1**, **L2Mn1**, **L1Mn2**, **L2Mn2**, and **L3Mn2** were calculated based on solid state structures or elemental analysis results; each reaction was carried out in H₂O. Elemental analyses were performed by Canadian Microanalytical Services Ltd.

4.5.1. Physical measurements

Electronic absorption spectra were collected between 190 nm and 1100 nm using an 8453 UV-vis spectrophotometer (Agilent) and a 3-mL quartz cuvette with a path length of 1.0 cm. Molar extinction coefficients were calculated utilizing the Beer-Lambert law ($A = \epsilon bc$). Infrared spectra were collected using an ATR Pro One attachment on a JASCO FT-IR 4600 spectrometer.

4.5.2. Preparation of [L1MnO]₂[ClO₄]₃ (L1Mn1)

L1 (100 mg, 0.317 mmol) and Mn(ClO₄)₂ (80 mg, 0.317 mmol) were dissolved in 12 mL of H₂O. The pH of this solution was adjusted to 8 with a dilute solution of KOH. The resulting mixture was stirred at room temperature for 12 h; the solution color gradually darkened from pale yellow to dark brown to deep forest green. After 12 h, this green solution was filtered and pumped down under reduced pressure to afford a dark green/brown solid. The resulting solid was taken up in CH₃CN (20 mL) and stirred, open to air, for 12 h. The resulting solution, which was a dark green color, was filtered. The supernatant was pumped down under reduced pressure to afford a dark green powder. (90.0 mg, 0.097 mmol, 60% yield). The dark green powder was dissolved in H₂O and filtered, slow evaporation of the aqueous solution yielded X-ray quality crystals. Electronic absorption, λ_{\max}/nm ($\epsilon/\text{M}^{-1} \text{cm}^{-1}$); H₂O: 382 (652), 555(181), 665

(211), 800 (sh). Elemental Analysis for **L1Mn1**; [**L1MnO**]₂[ClO₄]₃•5H₂O Found (Calculated): C, 28.37 (28.03); H, 4.53 (4.92); N, 11.86 (11.88) %.

4.5.3. Preparation of [**L2MnO**]₂[ClO₄]₂ (**L2Mn1**)

This complex was synthesized in a similar manner to **L1Mn1** (instead of **L1**, **L2** was used). A dark green powder was isolated (60.0 mg, 0.073 mmol, 48% yield). The green powder was dissolved in H₂O, slow evaporation of the aqueous solution yielded X-ray quality crystals (it should be noted that the oxygen atoms of the coordinated **L2** ligand were deprotonated in the solid state structure). Electronic absorption, λ_{\max}/nm ($\epsilon/\text{M}^{-1} \text{cm}^{-1}$); H₂O: 382 (536), 554(119), 658 (107), 800 (sh). Elemental Analysis for **L2Mn1**; [**L2MnO**]₂[ClO₄]₂•2H₂O•4CH₃OH•HCl•KCl Found (Calculated): C, 32.23 (32.56); H, 5.63 (5.78); N, 11.66 (11.68) %.

4.5.4. Preparation of [**L1MnCl**]₂[ClO₄]₂ (**L1Mn2**)

L1 (100 mg, 0.317 mmol) was dissolved in 12 mL of H₂O. The pH of this solution was adjusted to 8 with a dilute solution of KOH. Mn(ClO₄)₂ (80 mg, 0.317 mmol) was then added to the pH adjusted solution. This mixture was stirred at room temperature for 12 h; the solution color gradually darkened from pale yellow to dark brown. After 12 h, this brown solution was filtered and pumped down under reduced pressure to afford a dark brown/red tinged solid. The resulting solid was taken up in CH₃CN (20 mL) and stirred, open to air, for 12 h. The resulting solution, which was red-pink, was filtered. The supernatant was pumped down under reduced pressure to afford a pale pink-red powder. (40.2 mg, 0.085 mmol, 57% yield). The bright pink-red powder was dissolved in CH₃CN and filtered, slow evaporation of the CH₃CN solution yielded X-ray quality crystals. Electronic absorption, λ_{\max}/nm ($\epsilon/\text{M}^{-1} \text{cm}^{-1}$); CH₃CN: 370 (sh, 153), 525 (46). Elemental Analysis for **L1Mn2**; [**L1MnCl**]₂[ClO₄]₂•2H₂O Found (Calculated): C, 28.10 (28.25); H, 3.70 (4.74); N, 11.73 (11.98) %

4.5.5. Preparation of [L2MnCl₂][ClO₄] (L2Mn2)

This complex was synthesized in a similar manner to **L1Mn2** (instead of **L1**, **L2** was used). A dark red powder was isolated (85.0 mg, 0.114 mmol, 75% yield). Electronic absorption, $\lambda_{\text{max}}/\text{nm}$ ($\epsilon/\text{M}^{-1} \text{cm}^{-1}$); CH₃CN: 360 (sh, 361), 530 (56). Elemental Analysis for **L2Mn2**; [L2MnCl₂][ClO₄]•MnCl₂•2MnO₂ Found (Calculated): C, 17.74 (17.68); H, 2.42 (2.43); N, 7.41 (7.50) %.

4.5.6. Preparation of [L3MnCl₂][ClO₄] (L3Mn2)

This complex was synthesized in a similar manner to **L1Mn2** (instead of **L1**, **L3** was used). A pale pink-brown powder was isolated (130 mg, 0.086 mmol, 57% yield). Electronic absorption, $\lambda_{\text{max}}/\text{nm}$ ($\epsilon/\text{M}^{-1} \text{cm}^{-1}$); CH₃CN: 380 (sh, 58), 525 (16). Elemental Analysis for **L3Mn2**; [L3MnCl₂][ClO₄]•2MnCl₂•3MnO₂•2Mn(ClO₄)₂ Found (Calculated): C, 17.74 (17.68); H, 2.42 (2.43); N, 7.41 (7.50) %.

4.5.7. X-ray crystallography

A Leica MZ 75 microscope was used to identify samples suitable for analysis. A Bruker APEX-II CCD diffractometer was employed for crystal screening, unit cell determination, and data collection; which was obtained at 100 K. The Bruker D8 goniometer was controlled using the APEX2 software suite, v2014.11-0.²⁵⁰ The samples were optically centered with the aid of video camera so that no translations were observed as the crystal was rotated through all positions. The X-ray radiation employed was generated from a MoK_α sealed X-ray tube ($\lambda = 0.71076$) with a potential of 50 kV and a current of 30 mA; fitted with a graphite monochromator in the parallel mode (175 mm collimator with 0.5 mm pinholes).

4.5.7.1. [L1MnO]₂[ClO₄]₃ (L1Mn1) structure determination

Crystals of **L1Mn1** suitable for X-ray analysis were obtained by dissolving several mg of dark green powder of **L1Mn1** in H₂O to provide a dark green solution. Slow evaporation of this solution at room

temperature afforded an opaque dark green block-like crystal of **L1Mn1** (0.273 x 0.175 x 0.067 mm³), which was mounted on a 100 µm cryo-loop and used for X-ray crystallographic analysis. The crystal-to-detector distance was set to 50 mm, and the exposure time was 10 s per degree for all data sets at a scan width of 0.5°. A total of 1,104 frames were collected, and the data collection was 100% complete. The frames were integrated with the Bruker SAINT Software package²⁰⁶ using a narrow frame algorithm. The integration of the data used a monoclinic unit cell yielding a total of 33,419 reflections to a maximum ϑ angle of 33.24° (0.65 Å resolution) of which 13,522 reflections were independent with the $R_{\text{int}} = 4.35\%$. Data were corrected for absorption effects using the multi-scan method SADABS.²⁰⁷ Using Olex2²⁰⁸ the structure was solved with the ShelXS²⁰⁹ structure solution program using Direct Methods and refined with the SHELXL²¹⁰ refinement package using Least Squares minimization. All hydrogen and non-hydrogen atoms were refined using anisotropic thermal parameters. The thermal ellipsoid molecular plots (50%) were produced using Olex2.²⁰⁸

4.5.7.2. [L2MnO]₂[ClO₄]₂ (**L2Mn1**) structure determination

Crystals of **L2Mn1** suitable for X-ray analysis were obtained by dissolving several mg of dark green powder of **L2Mn1** in H₂O to provide a dark green solution. Slow evaporation of this solution at room temperature afforded an opaque dark green block-like crystal of **L2Mn1** (0.457 x 0.289 x 0.274 mm³), which was mounted on a 200 µm cryo-loop and used for X-ray crystallographic analysis. The crystal-to-detector distance was set to 50 mm, and the exposure time was 10 s per degree for all data sets at a scan width of 0.5°. A total of 1,852 frames were collected, and the data collection was 100% complete. The frames were integrated with the Bruker SAINT Software package²⁰⁶ using a narrow frame algorithm. The integration of the data used a monoclinic unit cell yielding a total of 41,977 reflections to a maximum ϑ angle of 30.15° (0.71 Å resolution) of which 4,682 reflections were independent with the $R_{\text{int}} = 2.37\%$. Data were corrected for absorption effects using the multi-scan method SADABS.²⁰⁷ Using Olex2²⁰⁸ the structure was solved with the ShelXS²⁰⁹ structure solution program using Direct Methods and refined with

the SHELXL²¹⁰ refinement package using Least Squares minimization. All hydrogen and non-hydrogen atoms were refined using anisotropic thermal parameters. The thermal ellipsoid molecular plots (50%) were produced using Olex2.²⁰⁸

4.5.7.3. [L1MnCl₂][ClO₄] (L1Mn2) structure determination

Crystals of **L1Mn2** suitable for X-ray analysis were obtained by dissolving several mg of pink powder of **L1Mn2** in H₂O to provide a dark pink solution. Slow evaporation of this solution at room temperature afforded a translucent bright pink plate-like crystal of **L1Mn2** (0.362 x 0.078 x 0.052 mm³), which was mounted on a 75 μm cryo-loop and used for X-ray crystallographic analysis. The crystal-to-detector distance was set to 50 mm, and the exposure time was 10 s per degree for all data sets at a scan width of 0.5°. A total of 1,104 frames were collected, and the data collection was 100% complete. The frames were integrated with the Bruker SAINT Software package²⁰⁶ using a narrow frame algorithm. The integration of the data used a monoclinic unit cell yielding a total of 28,307 reflections to a maximum θ angle of 30.12° (0.71 Å resolution) of which 4,963 reflections were independent with the $R_{\text{int}} = 8.29\%$. Data were corrected for absorption effects using the multi-scan method SADABS.²⁰⁷ Using Olex2²⁰⁸ the structure was solved with the ShelXS²⁰⁹ structure solution program using Direct Methods and refined with the SHELXL²¹⁰ refinement package using Least Squares minimization. All hydrogen and non-hydrogen atoms were refined using anisotropic thermal parameters. The thermal ellipsoid molecular plots (50%) were produced using Olex2.²⁰⁸

4.5.8. Electrochemical measurements

Cyclic voltammetry (CV) was carried out with an EC Epsilon potentiostat (C-3 cell stand) purchased from BASi Analytical Instruments (West Lafayette, IN). A glassy carbon (GC) electrode from BASi (MF-2012), 3 mm in diameter was polished on a white nylon pad (BASi MF-2058) with different sized diamond polishes (15, 6, 1 μm) to ensure a mirror-like finish. Between each measurement, the GC electrode was polished with the three diamond polishes. For electrochemical analysis of **L1Mn1** and **L2Mn1**, a three-

electrode cell configuration was used with GC as the working electrode, an Ag/AgCl reference electrode, and a Pt wire (7.5 cm) as the counter electrode (BASi MW-1032). For electrochemical analysis of **L1Mn2**, **L2Mn2**, and **L3Mn2**, a three-electrode cell configuration was used with GC as the working electrode, an Ag wire (0.5 mm dia.) quasi reference electrode housed in a glass tube (7.5 cm x 5.7 mm) with a Porous CoralPor™ tip, and a Pt wire (7.5 cm) as the counter electrode (BASi MW-1032). All solutions were bubbled with nitrogen gas for at least 15 min. prior to experimentation and were kept under a humidified nitrogen gas blanket. **L1Mn1** and **L2Mn1** potentials are reported vs. Ag/AgCl ($E_{1/2} = 0$ V); whereas, **L1Mn2**, **L2Mn2**, and **L3Mn2** potentials are reported vs. Cp* ($E_{1/2} = 0$ V). For each electrochemical analysis, the concentration was 1 mg analyte per 1 mL solvent (varying from 1.5 mL up to 10.0 mL). **L1Mn1** and **L2Mn1** were dissolved in H₂O containing 0.1 M NaClO₄ as the supporting electrolyte. **L1Mn2**, **L2Mn2**, and **L3Mn2** were dissolved in anhydrous CH₃CN containing 0.1 M tetrabutylammonium perchlorate (TBAP) as the supporting electrolyte.

Equations used to convert between references³⁵⁰

$$E(\text{NHE}) = E(\text{Cp}^*) + 0.366 \text{ V}$$

$$E(\text{NHE}) = E(\text{SCE}) + 0.2412 \text{ V}$$

$$E(\text{NHE}) = E(\text{Ag}/\text{AgCl}) + 0.197 \text{ V}$$

$$E(\text{SCE}) = E(\text{Ag}/\text{AgCl}) - 0.045 \text{ V}$$

$$E(\text{SCE}) = E(\text{Ag}/\text{Ag}^+) + 0.35 \text{ V}$$

$$E(\text{SCE}) = E(\text{NHE}) - 0.241 \text{ V}$$

Chapter 5: Synthesis, characterization, and applications of a novel 30-membered pyridine/piperazine-based decaazamacrocycle (L5)

5.1. Introduction

The novel 30-membered decaazamacrocycle (**L5**) discussed in the following chapter was originally designed as an Mn(II)-based imaging agent. Considering this, the introduction portion of this chapter will briefly discuss: (i) background information on imaging agents (such as MRI contrast agents); (ii) why there is a need for transition metal-based contrast agents; (iii) current approaches to designing Mn(II)-based imaging agents; and (iv) the design rationale for a rigid Mn(II)-based imaging agent proposed by the Green group. Following the introduction, the synthesis and characterization of the proposed novel macrocyclic Mn(II)-based imaging agent will be discussed, which had some unexpected results. Finally, metalation attempts of **L5** with Cu(II) ions as well as the protonation and stability constants of **L5** will be discussed.

5.1.1. Magnetic resonance imaging (MRI) and use of contrast agents (CA)

Magnetic resonance imaging (MRI) is a very powerful diagnostic tool used in clinical medicine.⁹¹ It has a wide range of applications in medical diagnosis including (but not limited to): neuroimaging, cardiovascular imaging, musculoskeletal imaging, and hepatobiliary imaging. Contrast agents are sometimes used, because of the inherently low sensitivity of MRI.⁹¹ In fact, 40% of MRI examinations are carried out with the use of a contrast agent.⁹¹ Currently, most clinically approved contrast agents utilize the paramagnetic Gd(III) ion, which has 7 unpaired electrons. Paramagnetic metal ions help to enhance the longitudinal ($1/T_1$) relaxation of water protons within body tissues, which results in a positive contrast in T_1 weighted magnetic resonance images.⁹⁰⁻⁹¹ Contrast agent efficiency can be described by its proton relaxivity (r_1), in which proton relaxivity (r_1) is defined as the paramagnetic enhancement of the longitudinal relaxation rate of water protons in 1 mM solution of a particular contrast agent.⁹⁰⁻⁹¹ The proton relaxivity originates from inner- and outer-sphere mechanisms.^{90-91, 351} Inner-sphere relaxivity is influenced by the number water molecules directly coordinated to the contrast agent (hydration number,

q), the water exchange rate (k_{ex}), residence time (τ_M ; $\tau_M = 1/k_{ex}$), the rotational correlation time (τ_R), and the electron spin relaxation (T_{ie} , $i=1,2$).⁹⁰⁻⁹¹ Additionally, the inner-sphere relaxivity is linearly proportional to the number of coordinated water molecules.⁹¹ The water molecules present in the first coordination sphere of a paramagnetic ion (such as Gd(III)) exchange with surrounding water molecules, which transmits the paramagnetic effect of the metal ion to the bulk of the solution.⁹¹ In contrast, the outer-sphere relaxivity originates from random translational diffusion of water molecules near the paramagnetic metal ion.⁹¹

5.1.2. Alternatives to the paramagnetic Gd(III) metal ion.

Gd(III)-based contrast agents represent the majority of CAs used in a clinical setting.^{89-91,352} Gd(III) offers the advantage of being highly paramagnetic, which is necessary to give rise to the contrast for MRI.³⁵² Unfortunately, there are also some disadvantages to using Gd(III)-based contrast agents. Gadolinium, a rare earth metal, is relatively expensive (GdCl₃ \$585/25 g, Millipore Sigma).³⁵² Additionally, gadolinium salts are highly toxic.³⁵² Although Gd(III) used within CAs is bound tightly to chelating ligands that prevent leaching within the body, there are increasing concerns about the safety of these contrast agents.³⁵² Nephrogenic systemic fibrosis (NSF) is a systemic disorder that involves fibrosis of the skin, joints, eyes, and internal organs.³⁵³ Evidence suggests that this disorder is caused by exposure to Gd(III) used in Gd(III)-based CAs in patients with kidney disease or dysfunction and it is thought to affect around 5% of patients who receive Gd(III)-based CAs.³⁵²⁻³⁵³ Patients with kidney disease retain these CAs and the Gd(III) bound to the chelates slowly leaches from the ligand framework into tissues causing Gd(III) deposition and severe damage to internal organs.³⁵²⁻³⁵³ These concerns have prompted multiple government organizations to fund research to find alternatives to Gd(III)-based CAs.³⁵⁴⁻³⁵⁹

Although Gd(III) is highly paramagnetic and currently dominates the field of metal-based CAs, there are other alternatives to this expensive, rare earth metal. One very promising alternative to Gd(III) is the paramagnetic transition metal ion Mn(II).^{90-91, 352, 360-363} Mn(II) has 5 unpaired electrons and a slow

electronic relaxation rate.⁹⁰⁻⁹¹ Complexes with Mn(II) generally have water exchange rates allowing for higher relaxivities to be obtained, which can be a limiting factor for Gd(III)-based complexes.⁹⁰⁻⁹¹ Moreover, Mn(II) is earth-abundant and relatively cheap (MnCl₂ \$42.25/100 g, Millipore Sigma) compared to the rare-earth metal, gadolinium.

In addition to the advantages discussed above, Mn(II) is also a biogenic element.^{90-91, 360, 362} For example, Mn(II) is an essential cofactor in several enzymes such as superoxide dismutase (SOD)³⁶⁴ and glutamine synthetase.^{90-91, 360, 362, 365} Mn(II) also competes with Ca(II) in many biological processes, because it is similarly sized to Ca(II).^{90-91, 366} This allows for detection of calcium influx and distribution within the central nervous system using a technique called manganese enhanced magnetic resonance imaging (MEMRI).^{90-91, 361, 366-367} MEMRI utilizes free Mn(II) to trace neuronal pathways and provide detailed monitoring of brain and/or heart structures.^{90-91, 361, 366} Unfortunately, the concentrations of Mn(II) salts necessary for sufficient contrast (matching Gd(III) systems) are toxic, thus limiting this method to animal studies.⁹⁰⁻⁹¹ In the brain for example, high concentrations of free Mn(II) can lead to manganism (or manganese poisoning), which resembles Parkinson's disease.

Currently, there is only one Mn(II)-based CA utilized as a clinical diagnostic tool. [Mn(DPDP)]⁴⁻ (DPDP⁶⁻ = *N,N'*-dipyridoxylethylenediamine-*N,N'*-diacetate-5,5'-bis(phosphate)) (Figure 5.1(a)) is used in liver and cardiac imaging.^{363, 368} Technically, the relaxation effect (contrast) *in vivo* is due to the free Mn(II) released from the complex, because the complex itself has no coordinated water molecules (to give inner-sphere relaxivity).⁹⁰⁻⁹¹ Indeed, the presence of the DPDP⁶⁻ ligand is only necessary to ensure the Mn(II) ions are released slowly, to prevent the toxicity observed from use of Mn(II) salts.⁹⁰⁻⁹¹

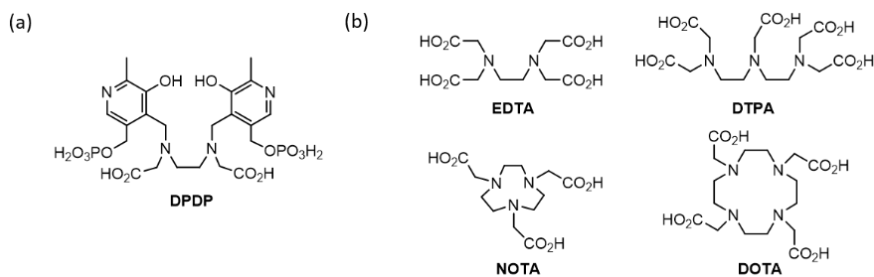


Figure 5.1. (a) Ligand framework for only clinically approved Mn(II)-based contrast agent; (b) Common ligand frameworks used in Gd(III)-based contrast agents.^{88, 90-91}

5.1.3. Previously designed ligand frameworks for Mn(II)-based contrast agents

The development of MEMRI and use of $[\text{Mn}(\text{DPDP})]^{4-}$ as a CA offer a proof-of-concept for applicability of Mn(II) ions as paramagnetic ions, but research on Mn(II)-based contrast agents has far to come. Designing proper ligand frameworks for housing Mn(II) ions is critical. Key features of Mn(II) complexes must include: (i) high thermodynamic/redox stability; (ii) high kinetic inertness; and (iii) the presence of water molecule(s) directly coordinated to Mn(II).^{90-91, 352} High stability and kinetic inertness of Mn(II)-based CAs are essential for safe *in vivo* use. There is a lack of ligand-field stabilization energy associated with these metal ions because of the electron configuration of high-spin Mn(II) (d^5).⁹⁰⁻⁹¹ The lack of ligand-field stabilization energy and the smaller charge of Mn(II) ions result in complexes with lower thermodynamic stability compared to other transition metal ions or Gd(III) complexes.⁹⁰⁻⁹¹ Although most noncyclic Mn(II) coordination complexes are technically considered kinetically labile, there have been recent studies conducted with the Mn(II) complexes of NOTA and DOTA (Figure 5.1(b)) that show these complexes are kinetically inert.^{88, 90}

Regrettably, high complex stability and kinetic inertness are often at odds with the necessity for inner-sphere water molecules bound directly to the Mn(II) ion, which are necessary to increase the inner-sphere relaxivity (contrast). These contradictory requirements for Mn(II)-based CAs offer a significant challenge to designing an ideal ligand framework.

Mn(II) complexes that have been studied previously, for contrast application, were formed with polydentate ligands originally designed for Gd(III), including: EDTA⁴⁻,³⁶⁹⁻³⁷² DTPA⁵⁻,^{371, 373} NOTA³⁻,³⁷⁴ and

DOTA⁴⁻³⁷⁵⁻³⁷⁶ (Figure 5.1(b)). Each of these complexes exhibit low inner-sphere relaxivities and only EDTA contains a water molecule bound to the Mn(II) ion.⁹⁰⁻⁹¹ Ideally, the appropriate ligand would form a bis-hydrated Mn(II) complex with adequate thermodynamic stability, but this offers a serious design challenge.

Recently, Éva Tóth and coworkers have designed and synthesized a family of novel macrocyclic ligand frameworks that form bis-hydrated Mn(II) complexes (Figure 5.2).^{87-88, 90-91} These researchers drew inspiration from extensively studied SOD mimics for designing ligand frameworks.⁹¹ While studying these new ligands, Tóth and coworkers developed some conclusions: (i) Mn(II) tends to prefer nitrogen donor atoms over oxygen donor atoms; (ii) Mn(II) complex stability increases with the size of the macrocyclic cavity (9 → 15-membered); (iii) an increase in ligand basicity leads to an increase in complex stability compared to previously designed ligands; (iv) the presence of a pyridine ring rigidifies the complex and increases complex stability; and (v) the relaxivity of the complexes evaluated is higher than typical low-molecular-weight Gd(III) complexes.⁹⁰ Although this family of macrocyclic ligands form stable Mn(II) complexes with remarkably high relaxivities, they are far from optimal.³⁵² Tóth and coworkers observed that variation of macrocycle size and the nature of donor atoms or pendant arms lead to significant modification of thermodynamic stability, redox potential, kinetic inertness, and hydration number of the Mn(II) complex.⁹⁰ Unfortunately, these parameters could not be optimized simultaneously; meaning that improvement of one parameter often came at the detriment of another parameter.⁹⁰ Tóth and coworkers suggested that future research should focus on the development of more rigid complexes to be used as highly stable and efficient Mn(II)-based CAs.⁹⁰

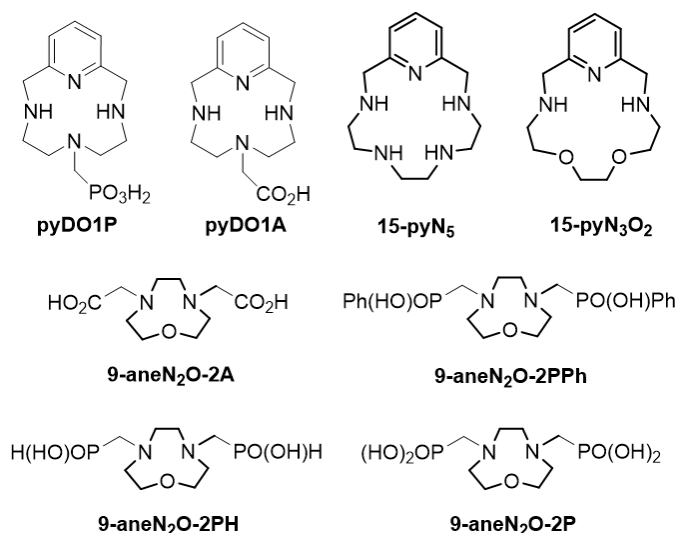


Figure 5.2. Ligand frameworks designed by Tóth and coworkers for Mn(II)-based contrast agents (names have previously been used in literature).^{88, 90-91}

5.1.4. Designing an ultra-rigid ligand framework for Mn(II)-based contrast agents

Based on the suggestions made by Tóth and coworkers and in collaboration with Gyula Tircsó at the University of Debrecen in Hungary, the Green group designed several novel ultra-rigid ligand frameworks for use as Mn(II)-based contrast agents (Figure 5.3). Each ligand, in addition to pyridine, incorporates either a phenyl ring or piperazine ring to maximize ligand rigidity. Tóth and coworkers hypothesized that by increasing the rigidity of the ligand frameworks, an increase in the kinetic inertness of the corresponding Mn(II) complexes would be observed. The ligand frameworks collaboratively designed by the Green and Tircsó groups would offer increased rigidity (and theoretically increased kinetic inertness) while keeping the thermodynamic stability and relaxivity of the complexes large enough to be utilized as future Mn(II)-based contrast agents.

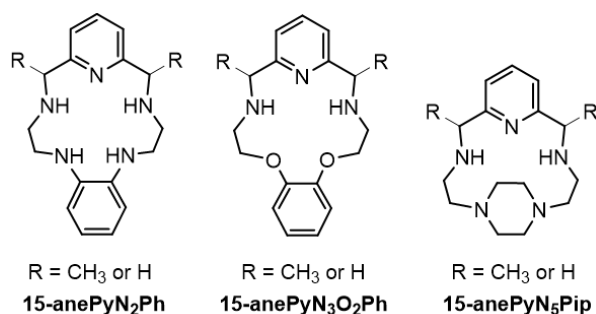


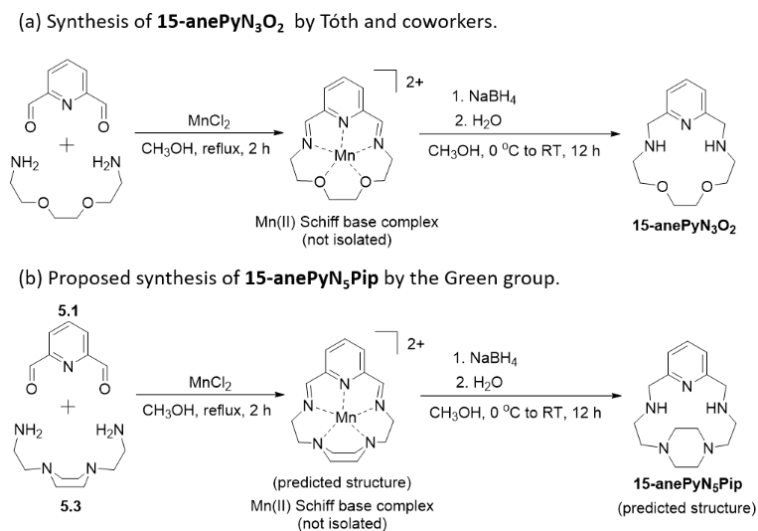
Figure 5.3. Novel ultra-rigid pentaazamacrocyclic ligand frameworks for Mn(II)-based contrast agents.

5.2. Synthesis of a novel 30-membered decaazamacrocyclic (L5)

The following discussion will focus on **15-anePyN₅Pip**, the other remaining ligands are the synthetic focus of colleague Kristof Póta. Following the design of the three novel ultra-rigid pentaazamacrocyclics (shown above in figure 5.3), a synthetic procedure for obtaining **15-anePyN₅Pip** was proposed. As discussed in chapter 1 (section 1.4.) there are two different methods for synthesizing macrocyclic ligands, non-metal templated and metal-templated. The direct/non-templated method involves cyclization of the ligand using conventional organic reactions without dependence on a metal ion.^{1, 3} A representative example for the non-templated synthesis of macrocycles is the Richman-Atkins method, described in chapter 1, section 1.4.1 (Schemes 1.2 and 1.3).⁴⁸ In contrast, metal-directed/metal-templated reactions utilize a metal ion to generate a cyclic product; the metal ion acts as a 'template' for the cyclization reaction to occur (Scheme 1.4).^{1, 3} Typically, for smaller macrocycles that cannot fully encompass a metal ion (such as 12-membered macrocycles **L1-L4**) the direct/non-templated methodology is adopted; whereas, for larger macrocycles the metal-directed/metal-templated method can be used. Therefore, because the proposed **15-anePyN₅Pip** ligand is a 15-membered pentaazamacrocyclic, a metal-templated synthetic method was applied.

Tóth and coworkers recently reported the synthesis of **15-pyN₅** and **15-pyN₃O₂** using a metal-templated method, the synthetic scheme is pictured in scheme 5.1(a). In this metal-templated synthesis a Mn(II) ion was complexed to a Schiff base derived from 2,6-pyridinedicarboxaldehyde and an aminoether. The Mn(II) Schiff base complex, which is not isolated, is then simultaneously reduced and demetalated to yield the saturated macrocyclic complex **15-pyN₃O₂**. The Green group, including visiting scholar Kristof Póta, adopted a similar strategy for the synthesis of **15-anePyN₅Pip**. The starting materials necessary for the proposed synthesis of **15-anePyN₅Pip** (2,6-pyridinedicarboxaldehyde (**5.1**) and 1,4-bis(2-aminoethyl)piperazine (**5.3**)) were prepared according to literature procedures (Schemes 5.E1, 5.E2, 5.E3).^{91, 377-381} (**5.3**) was added dropwise to a solution of (**5.1**) and MnCl₂ in CH₃OH and refluxed for several

hours to form the Mn(II) Schiff base complex. This imine complex was then reduced and de-metalated using NaBH₄ to yield a cyclized product. Scheme 5.1 depicts the predicted Mn(II) Schiff base and cyclic ligand product (**15-anePyN₅Pip**).



Scheme 5.1. (a) Synthesis of **15-anePyN₃O₂** published by Tóth and coworkers.⁹¹ (b) Predicted intermediate and products of the template reaction with (**5.1**), (**5.3**), and Mn(II).

Characterization of the cyclized product with NMR (¹H and ¹³C) and MS appeared to indicate formation of the predicted 15-membered pentaazamacrocyclic (**15-anePyN₅Pip**), the MS and NMR spectra are shown above in figure 5.4. Additionally, X-ray quality crystals of the cyclic product were obtained from the slow evaporation of chloroform. These crystals were analyzed using X-ray diffraction and the solid state structure offered some unexpected results that seemed to contradict the MS and NMR spectra. Based on the solid state structure it was determined that **15-anePyN₅Pip** had not been synthesized. Instead, what had been isolated was a dimeric congener of **15-anePyN₅Pip**, which is a completely symmetric 30-membered decaazamacrocyclic ligand (**L5**). The asymmetric unit of **L5** consists of half of the molecule; the remaining half of the molecule can be visualized by symmetry generation (Figure 5.5). The resulting structure of **L5** is derived from a triclinic P $\bar{1}$ system (Table 5.1). Additionally, to confirm the crystal that was initially isolated was not just a small side-product from the reaction, several different crystals from the same batch were analyzed with XRD. All the crystals analyzed gave the same dimeric congener (**L5**), confirming that the bulk of the crystals were all **L5**.

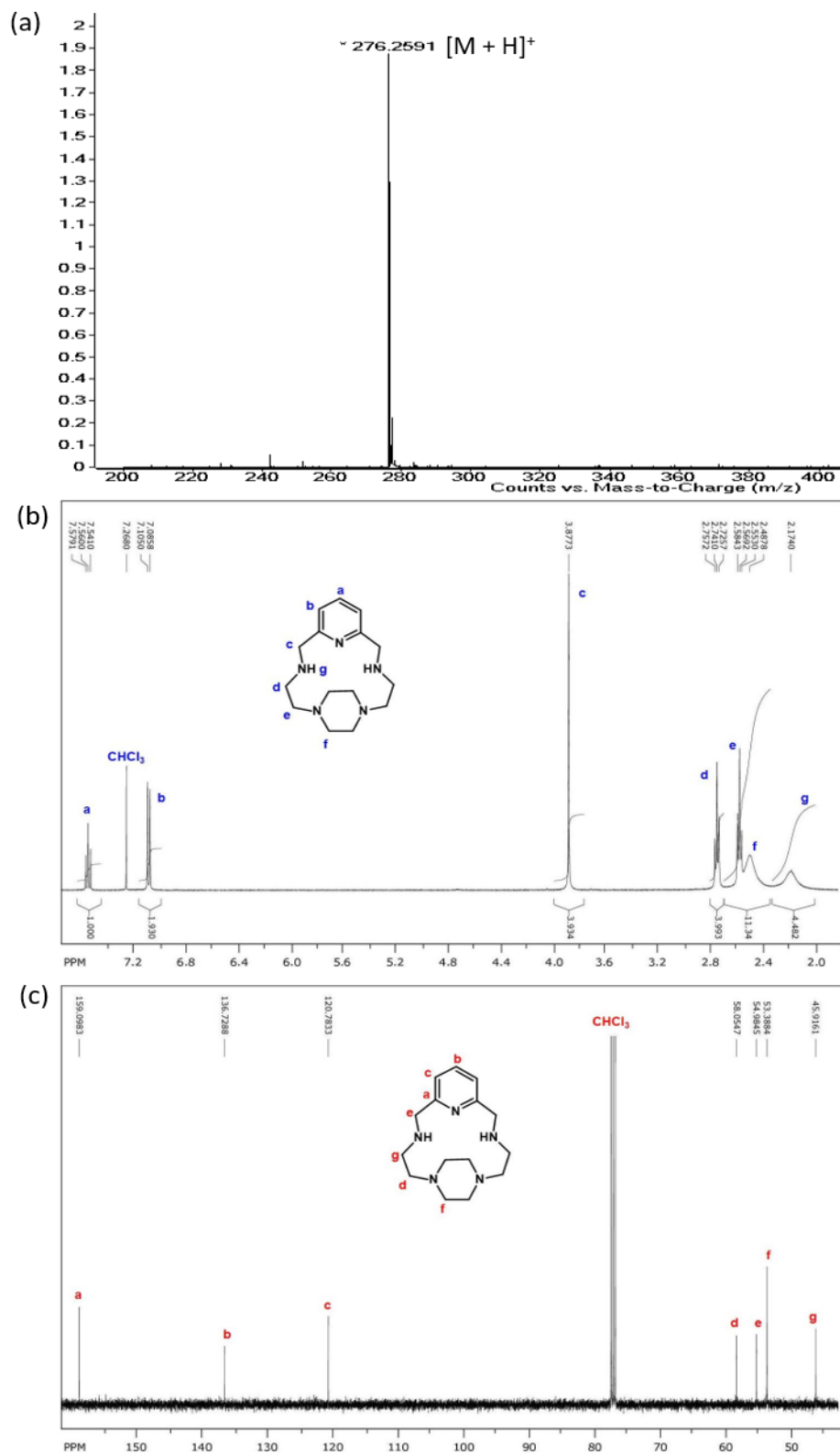


Figure 5.4. (a) Mass spectrum of predicted **15-anePyN₅Pip**; (b) ¹H NMR spectrum of predicted **15-anePyN₅Pip** with resonance assignments; (c) ¹³C NMR spectrum of predicted **15-anePyN₅Pip** with resonance assignments.

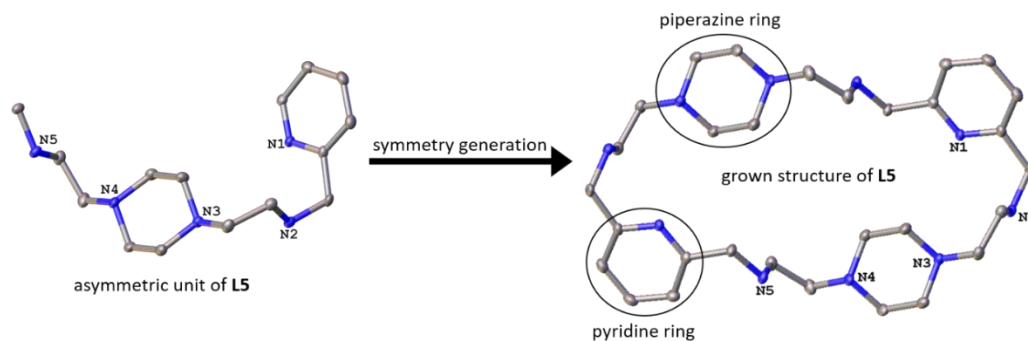


Figure 5.5. Solid state structure of **L5**; the asymmetric unit and grown structure are pictured above (hydrogen atoms have been omitted for clarity).

Table 5.1. Crystal data, intensity collections, and structure refinement parameters for **L5**.

Complex	L5
Simplified formula	$[C_{30}N_{10}H_{52}][Cl]_2 \cdot 2CHCl_3$
Empirical formula	$C_{8.13.5}H_{2.01}N_{2.5}$
Formula weight	216.06
Temperature/K	100.03
Crystal system	triclinic
Space group	P-1
a/Å	8.8978(4)
b/Å	11.3086(5)
c/Å	11.3231(5)
$\alpha/^\circ$	71.129(2)
$\beta/^\circ$	72.654(2)
$\gamma/^\circ$	84.049(2)
Volume/Å ³	1029.05(8)
Z	4
ρ_{calc}/cm^3	1.395
μ/mm^{-1}	0.588
F(000)	453.0
Crystal size, mm ³	0.274 x 0.190 x 0.073
Radiation	MoK α ($\lambda = 0.71073$)
2 θ range for data collection/ $^\circ$	5.738 to 60.284
Index ranges	-12 $\leq h \leq$ 12, -15 $\leq k \leq$ 15, -15 $\leq l \leq$ 15
Reflections collected	49846
Independent reflections	6071 [$R_{int} = 0.0540$, $R_{sigma} = 0.0417$]
Data/restraints/parameters	6071/0/256
Goodness-of-fit on F ²	1.044
Final R indexes [$I \geq 2\sigma(I)$]	$R_1 = 0.0858$, $wR_2 = 0.2380$
Final R indexes [all data]	$R_1 = 0.1232$, $wR_2 = 0.2679$
Largest diff. peak/hole / e Å ⁻³	0.71/-2.08

Based on the unexpected XRD results, re-analysis of the NMR and MS data, thus ensued. The highly symmetric nature of **L5** yielded the original misinterpretation. Based on the XRD analysis, amended assignments, shown in figure 5.6(a), (b), and (c), were obtained. Additionally, the window of the MS spectrum, in subsequent MS experiments, was expanded to account for the dimeric nature of **L5** (MW: 550.80 g/mol). The re-assigned MS and NMR spectra are shown below. The 276.26 m/z signal, observed

in both figure 5.4(a) and 5.6(a) is consistent with $[M + 2H]^{2+}$; whereas, the 551.54 m/z signal observed in figure 5.6(a) consistent with $[M + H]^+$. Considering the evidence provided by XRD, NMR, and MS spectroscopy, a new reaction scheme was proposed for the synthesis of **L5** (Scheme 5.7).

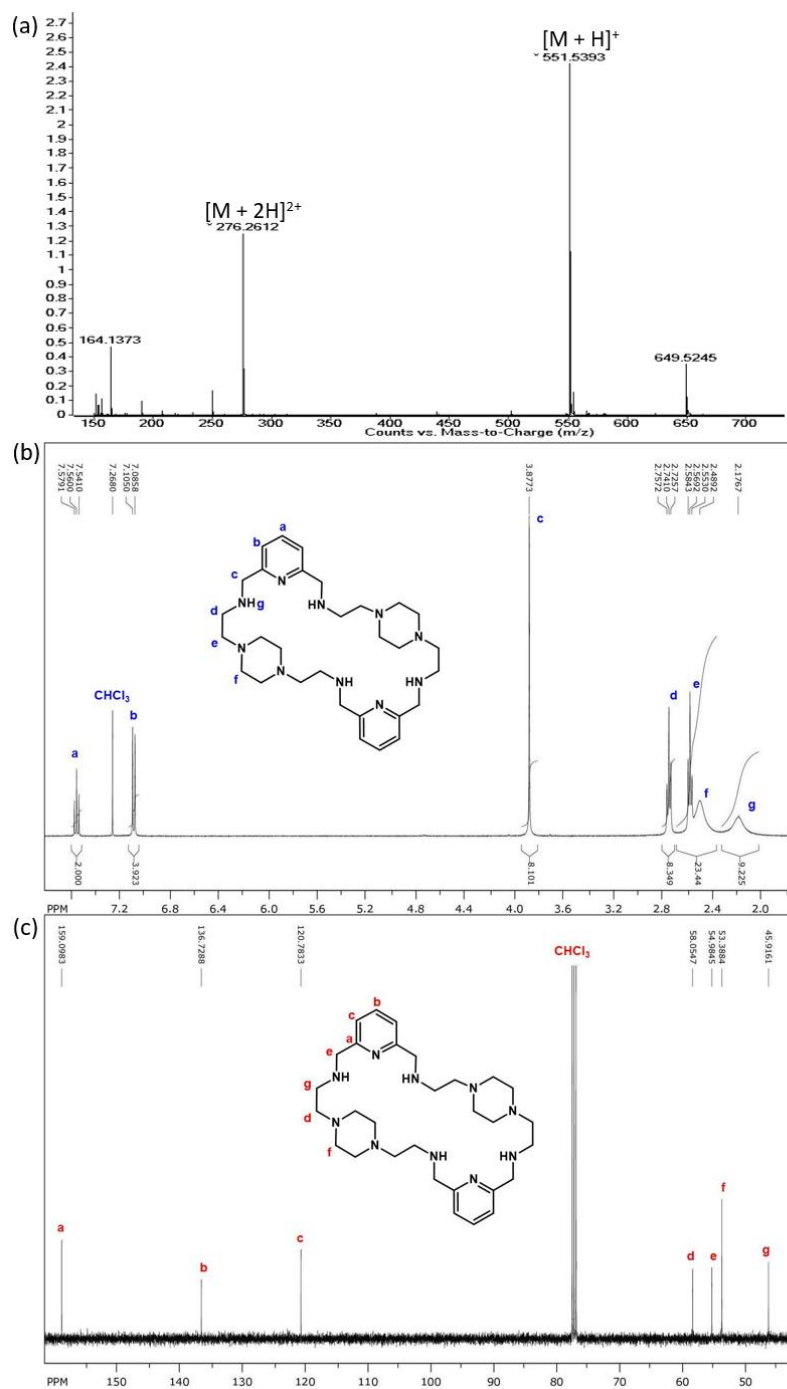
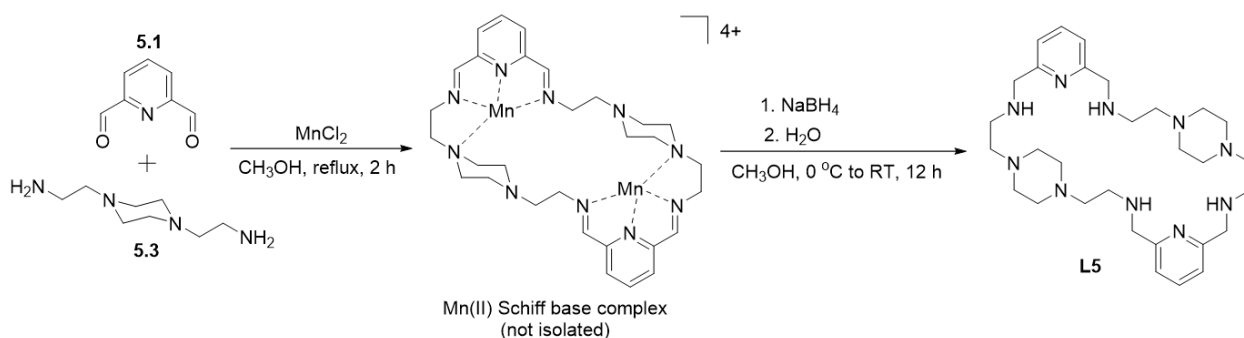


Figure 5.6. (a) Mass spectrum of **L5**; (b) ^1H NMR spectrum of **L5** with resonance assignments; (c) ^{13}C NMR spectrum of **L5** with resonance assignments.



Scheme 5.2. Mn(II) Schiff base complex and resulting product (**L5**) from the template reaction between (**5.1**) and (**5.3**).

The following discussion will analyze the reasoning for the formation of **L5** versus the expected 15-membered macrocycle. When Tóth and coworkers synthesized **15-anePyN₃O₂** the Mn(II) ion coordinated to donor atoms and pre-organized the intermediates into a conformation that resulted in the desired cyclic product (Scheme 5.1(a)).⁹¹ No rigidifying ring was incorporated into the aminoether, which allowed it to adopt a conformation favorable for the isolation of **15-anePyN₃O₂**.⁹¹ In contrast, the amine used by the Green group (**5.3**), contained a rigidifying piperazine ring. Therefore, the difference between the predicted **15-anePyN₃Pip** structure and the actual structure of **L5** can be explained by the conformations adopted by the piperazine ring. 6-membered rings such as piperazine (or cyclohexane) can exist in four distinct conformations: *chair*, *half-chair*, *twist-boat*, and *boat*.³⁸²⁻³⁸⁴ Of these four conformers, the *chair* conformation is the most thermodynamically favorable, followed by (in order of increasing energy) the *twist-boat*, *boat*, and *half-chair* conformers (Figure 5.7).³⁸²⁻³⁸⁴ In solution there is a conformational equilibrium between the four conformers where the molecule is rapidly interconverting between all its forms and inverting (Figure 5.7).³⁸²⁻³⁸³

It was predicted that the presence of a templating metal ion (such as Mn(II)) would allow the piperazine-containing amine (**5.3**) to adopt the *boat* conformation necessary to form a mononuclear Mn(II) Schiff base complex, and ultimately produce the 15-membered pentaazamacrocycle **15-anePyN₃Pip** (Scheme 5.1(b)). In this case, a 1:1 condensation between one di-aldehyde (**5.1**) molecule and one piperazine-containing amine molecule (**5.3**) was hypothesized. In reality, the piperazine-containing

amine (**5.3**) adopts the thermodynamically favorable *chair* conformation, thus resulting in a 2:2 condensation between (**5.3**) and (**5.1**) and the formation of a dimeric Mn(II) Schiff base complex (Scheme 5.2). Upon reduction and demetallation of the dimeric Mn(II) Schiff base complex, the 30-membered decaazamacrocycle (**L5**) is isolated (Scheme 5.2).

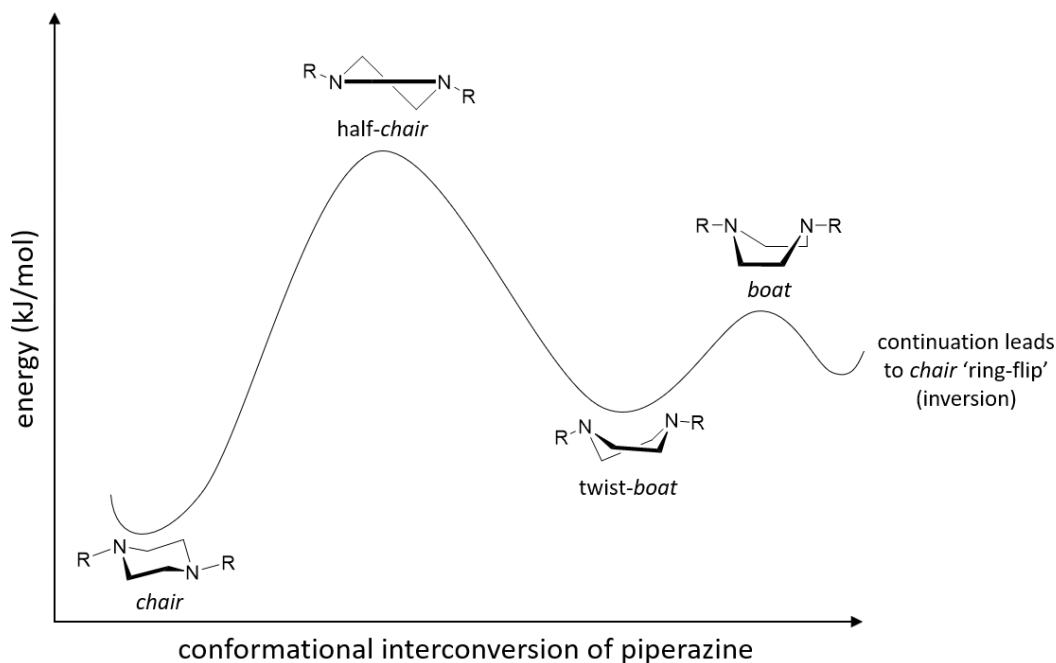
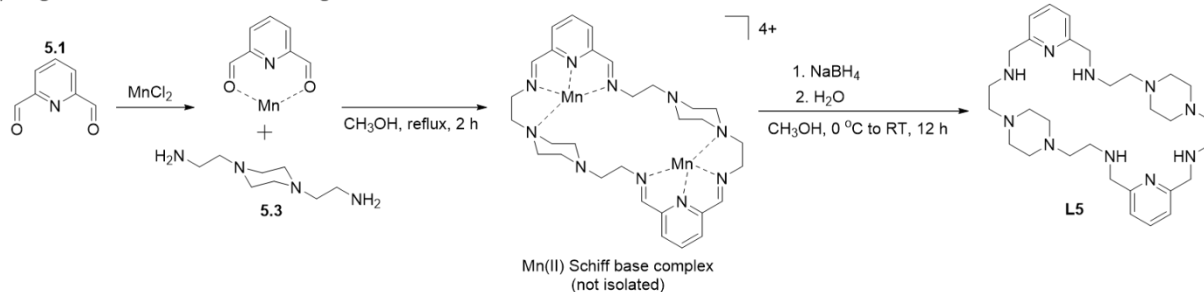


Figure 5.7. Conformational changes of piperazine in solution eventually leading to inversion, which is reminiscent of cyclohexane. (R = H for piperazine; R = CH₂CH₂NH₂ for (**5.3**))³⁸²⁻³⁸⁴

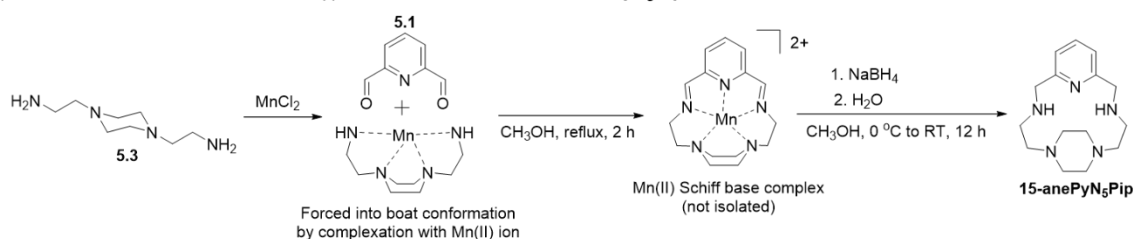
5.2.1. Procedure modifications for the attempted isolation of **15-anePyN₅Pip**

Although **L5** is a unique ligand that may be utilized for applications other than Mn(II)-based contrast agents, continued effort was put forth to try and isolate the originally designed **15-anePyN₅Pip** ligand. The template reaction was performed several times with slight variations in the reaction conditions to favor the formation of **15-anePyN₅Pip** vs. the dimeric **L5**. Modifications to the procedure included: (i) changing the order of addition of the starting materials; (ii) varying the temperature of the reaction; and (iii) replacing the original templating Mn(II) ion with a Zn(II) metal ion (Figure 5.8).

(a) Original order of addition resulting in the isolation of dimeric **L5**.



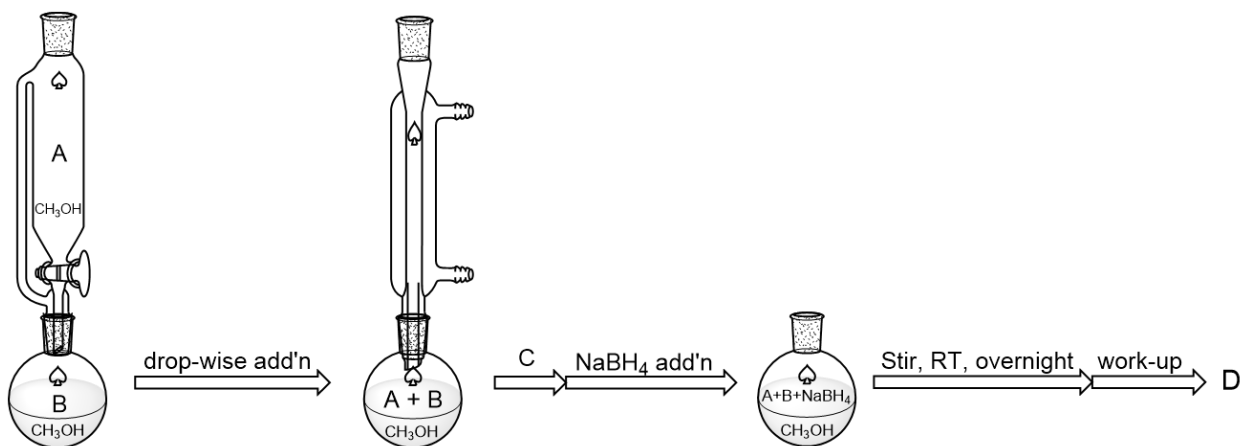
(b) Reversed order of addition with hypothesized isolation of **15-anePyN₅Pip**.



Scheme 5.3. (a) Original starting material order of addition, resulting in isolation of **L5**; (b) Hypothesized isolation of **15-anePyN₅Pip** upon reversal of starting material order of addition.

In the original procedure, the amine was added dropwise to a solution of the di-aldehyde and MnCl_2 in CH_3OH . When the di-aldehyde and Mn(II) salt are combined, a weak coordination complex results from the Mn(II) ion binding to the carbonyl oxygen atoms (Scheme 5.3(a)). It was hypothesized that if the order of addition was reversed and the di-aldehyde was added to a solution of the amine and MnCl_2 , this may result in the desired cyclic product. The Mn(II) ion could potentially coordinate to the amine forcing it into the *boat* conformation necessary for the isolation of **15-anePyN₅Pip** (Scheme 5.3(b)). In addition, the original templating reaction was performed under reflux conditions. It was also postulated that lowering the temperature of the reaction may favor the formation of **15-anePyN₅Pip**. Finally, in the last modification to the original procedure, the MnCl_2 salt was replaced with ZnCl_2 (Figure 5.8). Zn(II) ions have a slightly smaller ionic radius than Mn(II) ions and it was hypothesized that reducing the size of the templating metal ion could result in isolation of **15-anePyN₅Pip**. Unfortunately, after performing the synthesis with all the modifications listed above no **15-anePyN₅Pip** ligand was isolated. Instead, **L5** was synthesized with varying yields (Figure 5.8). Despite the lack of success isolating **15-anePyN₅Pip**, it was determined that the conditions utilized for reaction #3 (Figure 5.8) gave the best yield for **L5**. In this

optimization run, the di-aldehyde (**5.1**) was added dropwise to a solution of the amine (**5.3**) and MnCl₂. This mixture was stirred at room temperature, overnight. Following this, NaBH₄ was added on ice and the reaction stirred at room temperature for an additional twelve hours. After the reaction workup the 'crude' product was sufficiently pure, based on NMR analysis, that no column was needed; this resulted in the isolation of 330 mg of clean **L5** (41% yield).



Reaction #	Add'n funnel contents (A)	Flask contents (B)	Temperature/Time (C)	Product/Yield (D)	Column needed
1	(5.3)	(5.1) + MnCl ₂	reflux, 2 h	L5 , 208 mg (26%)	Y
2	(5.1)	(5.3) + MnCl ₂	reflux, 2 h	L5 , 117 mg (15%)	Y
3	(5.1)	(5.3) + MnCl ₂	RT, overnight	L5 , 330 mg (41%)	N
4	(5.3)	(5.1) + MnCl ₂	RT, overnight	L5 , 262 mg (32%)	N
5	(5.1)	(5.3) + ZnCl ₂	reflux, 2 h	L5 , <50 mg (6%)	Y

Figure 5.8. Modifications to reaction conditions of metal-template synthetic procedure for **L5**.

5.3. Overview of large macrocyclic and/or piperazine-containing ligands

The isolation of a 30-membered decaazamacrocycle was unexpected, but this novel ligand has many potential applications. In this section, applications for large polyazamacrocycles such as **L5** will be discussed. For the purpose of this brief overview, a large polyazamacrocycle is defined as a cyclic ligand containing at least 18-members and 6 donor nitrogen atoms. In addition to discussing applications of large polyazamacrocycles, a brief survey of piperazine-containing macrocycles and corresponding metal complexes will be presented.

5.3.1. Applications of large polyazamacrocycles

In recent years, large polyazamacrocyclic ligands have garnered attention because of their ability to form mononuclear/dinuclear metal complexes and act as hosts for organic anions and cations.³⁸⁵ Numerous reviews have described the design, synthesis, and applications of large polyazamacrocyclic ligands.³⁸⁶⁻³⁸⁷ Within the chemical literature, large polyazamacrocycles and corresponding metal complexes are mainly used for three applications including: (i) structural/functional models of active sites within bimetallic metalloenzymes (both homonuclear and heteronuclear); (ii) catalysts; and (iii) molecular recognition of cations and anions.³⁸⁶⁻⁴⁰⁴ Figure 5.9, below, shows some representative examples of large polyazamacrocycles. The denticities of these ligands range from hexadentate to octadentate and the ring sizes range from 18- to 26-membered. Additionally, some of these macrocyclic ligands only form mononuclear metal complexes (**5.4**, **5.7**, **5.9**, and **5.10**)⁴⁰⁵⁻⁴⁰⁸; whereas others are able to bind two transition metal ions (**5.8**, **5.14**, and **5.15**).^{385, 388, 393, 396-397, 409} Moreover, ligands such as **5.7** and **5.9** can be modified with pendant arms so that dinuclear complexes can be obtained.^{404, 410} In the following section(s) these representative ligands and corresponding metal complexes will be discussed in relation to the three applications stated above.

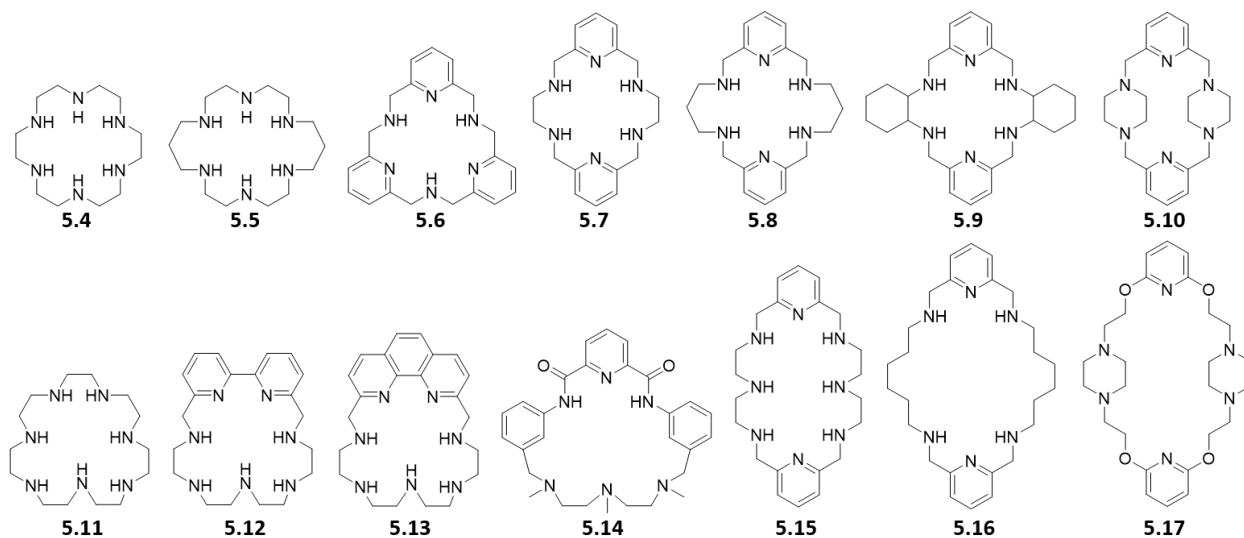


Figure 5.9. Selected large polyazamacrocyclic ligands.^{385, 388, 393, 396, 399-400, 402-406, 408-413}

5.3.1.1. Large polyazamacrocycles as metalloenzyme models

The idea of utilizing macrocyclic metal complexes as models for metalloenzymes can be traced back to the inception of the field of macrocyclic chemistry, when metalloporphyrins were used to model the active sites of hemoglobin, cobalamin, and chlorophyll (see chapter 1, section 1.2.1).^{1, 3-4, 6} Many metalloenzyme models can only incorporate one metal ion within the macrocyclic cavity, but there are numerous metalloenzymes with bimetallic active sites.^{6, 392, 396} Dinuclear metalloenzyme active sites can be homo- or heteronuclear and common examples include: FeNi carbon monoxide dehydrogenase, CuZn superoxide dismutase, FeCu cytochrome *c* oxidase, FeZn purple acid phosphatase, urease, dopamine β -monooxygenase, and peptidylglycine α -hydroxylating monooxygenase.^{6, 391-393, 396-397} Large polyazamacrocycles offer the ability to bind multiple metal ions within a macrocyclic cavity, thus making these ligands ideal for use as models for metalloenzyme bimetallic active sites.^{386-388, 391-393, 396}

Ligands **5.14** and **5.15** (Figure 5.9) have both been utilized as metalloenzyme models to study the structure and function of bimetallic active sites.^{388, 393, 396-397} **5.14** and its congeners were complexed with Ni(II) and Fe(II) in an effort to elucidate more structural and mechanistic information about the active site of NiFe carbon monoxide dehydrogenase.^{393, 397} The unique hexadentate ligand **5.14** was designed with two different metal binding moieties; the amide nitrogen groups bind the Ni(II) ion while the lower triamine portion binds Fe(II).^{393, 397} Additionally, the two metal ions are linked through a hydroxy bridge which further mimics the active site of NiFe carbon monoxide dehydrogenase.^{393, 397} **5.15** was complexed to Zn(II) to gain structural insight into the active site of several Zn(II) containing metalloenzymes.³⁸⁸ Moreover, by varying the metal to ligand ratio both mononuclear and dinuclear Zn(II) complexes were isolated.³⁸⁸

5.3.1.2. Large polyazamacrocycles as catalysts

Large polyazamacrocycles are useful frameworks for stabilizing dinuclear or even polynuclear metal complexes; the ligand framework allows for well-defined metal-metal distances, which is very

important to catalyst design.³⁹⁴ The preparation of complexes with two metal ions separated by distances of 3-6 Å is of particular interest in catalytic design.³⁸⁶ At these distances, the metal ions should not directly interact, but a large polyazamacrocycle can bind/interact with both metal ions simultaneously.³⁸⁶ It has been shown that pairs of metal ions within a suitable distance of one another or with the appropriate ligand framework can give rise to chemical reactivity that is better or different than two isolated metal centers.³⁸⁶ In contrast, ligand frameworks can also be designed so that metal ions are close enough to interact with one another.³⁸⁷ If the two metals are paramagnetic, interaction could lead to ferromagnetic or antiferromagnetic coupling and unique chemical reactivity exhibited by the dinuclear metal complex.³⁸⁷ Several of the selected large polyazamacrocyclic metal complexes have been explored for catalytic properties, such as **5.14**.^{391, 396} Homonuclear mixed-valent copper and heteronuclear complexes (CuPd and CuPt) with **5.14** were recently synthesized in an effort to design new oxidation catalysts and gain mechanistic insights into oxidation catalysis.³⁹⁶

5.3.1.3. Large polyazamacrocycles as anion receptors

The design and synthesis of macrocyclic ligands for the recognition of anionic species has led to the development of 'anion coordination chemistry'.³⁹⁹ This interdisciplinary field has overarching applications due to the chemical and biological importance of anions.^{399, 403} Polyfunctional anions, which are anionic species with several different types of binding sites, are challenging recognition targets because they require polyfunctional receptors.³⁹⁹ Receptors that can bind and recognize polyfunctional anions are not readily available and can often be a challenge to design and synthesize.³⁹⁹ A majority of the large polyazamacrocyclic ligands pictured above were designed as anion receptors including: **5.4-5.8, 5.10, 5.11-5.12, and 5.16**.^{399-400, 402-403, 406, 410, 413} Nitrogen containing macrocycles are ideal for use as anion receptors. When these polyazamacrocycles are protonated, the positively charged ammonium groups can bind inorganic, organic, and biological anions via coulombic forces, hydrogen bonding and other weak

interactions.⁴⁰²⁻⁴⁰³ In the following paragraph(s), specific applications of anion recognition will be discussed.

Ligands **5.11**, **5.12**, and **5.13** were designed as polyfunctional receptors to detect and bind pyridinedicarboxylic acid derivatives (H₂PDC).³⁹⁹ Detection and recognition of pyridinedicarboxylic acids is an important analytical issue due to the potential use of *Bacillus anthracis* spores as a biological warfare agent.³⁹⁹ 2,6-pyridinedicarboxylic acid (H₂(2,6-PDC)) is a major component of *Bacillus anthracis* and is also considered diagnostic for the presence of these bacterial spores; therefore, many analytical methods based on detection of this molecule have been developed.³⁹⁹ **5.11**, **5.12**, and **5.13** form highly protonated species in solution that can bind the anionic forms of H₂PDCs through the formation of salt bridges and hydrogen bonds.³⁹⁹

Ligand **5.16** was designed as a carboxylate anion receptor.⁴⁰³ Carboxylate anions are important to organic, environmental, and biological processes.⁴⁰³ For example, carboxylate functions of enzymes are critical components of many biological processes.⁴⁰³ Carboxylate's role in biology makes it a relevant candidate for anion recognition. In this study, several features of the dicopper(II) complex of **5.16** were evaluated, such as the host-guest binding interactions with various biologically relevant dicarboxylate anions of different sizes and flexibilities.⁴⁰³

5.3.2. Azamacrocyclic piperazine-containing ligands and corresponding metal complexes

The use of piperazine rings within the macrocyclic ligand designed by the Green group gave some unexpected results when a dimeric 30-membered decaazamacrocyclic (**L5**) was isolated, instead of the hypothesized 15-membered pentaazamacrocyclic. It was established in section 5.2, that the thermodynamically favored *chair* conformation of the piperazine rings within the macrocyclic structure were responsible for the formation of a dimeric ligand. In an effort to understand more about the nature of this ligand and its ability to complex metal ions a brief survey of the chemical literature was conducted. It was discovered that piperazine moieties have been utilized in a variety of different macrocyclic ligand

frameworks, with varying degrees of success. Therefore, this section will give a brief overview of other piperazine-containing macrocyclic ligands and metal complexes found within the chemical literature.

5.3.2.1. A piperazine-containing macrocycle similar to **15-anePyN₅Pip**

One of the most interesting and structurally relevant sets of ligands was designed and synthesized by Alcock *et al.* in 1988, shown below in figure 5.10.⁴¹⁴ Interestingly, this macrocycle only differs from the ligand designed by the Green group (**15-anePyN₅Pip**, Figure 5.3) by one -CH₂- unit. **5.18** was designed with a rigidifying piperazine to prevent the macrocycle from folding upon metalation in order to study the size match selectivity of azamacrocycles.⁴¹⁴ **5.18** was synthesized using high dilution conditions and by slow addition of the reagents, dropwise over 12 h.⁴¹⁴ These conditions are typically used in a non-direct synthesis to achieve 1:1 condensation and to prevent polymerization or oligomerization of the starting materials.^{1, 3} Additionally, the synthesis of **5.18** was also attempted using the Richman-Atkins cyclization (described in chapter 1, section 1.4.1), which only requires moderate to low dilution conditions.^{1, 3, 48} This later synthetic strategy did not yield **5.18**; instead, a large octaazamacrocycle (shown in figure 5.10) was isolated due to the piperazine's preference to exist in the *chair* conformation.⁴¹⁴

The question remains, how was **5.18** (which is structurally similar to **15-anePyN₅Pip**) isolated, while synthetic attempts to isolate **15-anePyN₅Pip** proved futile? Although these two ligands are structurally similar, the presence of the extra -CH₂- unit in **5.18** makes a significant difference. The longer alkyl chains present within the amine (1,4-bis(3'-aminopropyl)piperazine) allow for a 1:1 condensation to occur to yield the desired product. The piperazine moiety within the amine still adopts a *chair* conformation, but because the amine arms are longer, no dimerization occurs. Additionally, **5.18** was synthesized with high dilution conditions and slow addition; whereas the attempted synthesis of **15-anePyN₅Pip** was conducted using metal-templating techniques.^{91, 414} Non-templated vs. templated synthetic methodology could also make a difference in the products isolated.

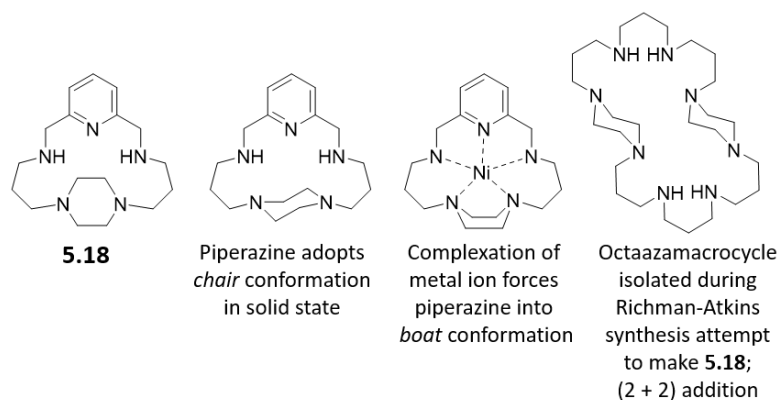


Figure 5.10. Ligand set and metal complex designed and synthesized by Alcock *et al.*⁴¹⁴

The solid state structure of the free ligand **5.18** confirmed that the piperazine moiety exists in the thermodynamically favored *chair* conformation in the solid state (Figure 5.10).⁴¹⁴ Alcock *et al.* also complexed **5.18** to several metal ions (Ni(II), Cu(II), and Zn(II)) in an attempt to elucidate the binding nature of the piperazine ring. X-ray quality crystals of the Ni(II) complex were analyzed and the solid state structure revealed that the piperazine ring within **5.18** adopts the *boat* conformation necessary to bind in a bidentate fashion to the Ni(II) ion.⁴¹⁴ In the *chair* conformation the lone pairs on the nitrogen atoms are oriented *trans* to one another (Figure 5.11).^{384, 414-415} In contrast, in the *boat* conformation, the lone pairs on the nitrogen atoms are oriented *cis* to one another allowing for bidentate chelation of a metal ion (Figure 5.11).^{384, 414-415} This phenomenon has also been observed in other small piperazine-containing azamacrocycles.⁴¹⁶⁻⁴²⁰ Typically, for relatively small (5 nitrogen atom donors or less) and flexible azamacrocycles, the piperazine ring adopts the thermodynamically stable *chair* conformation within the free ligand, but upon complexation to a metal ion the piperazine moiety adopts the less favored *boat* conformation, in order to bind the metal ion.

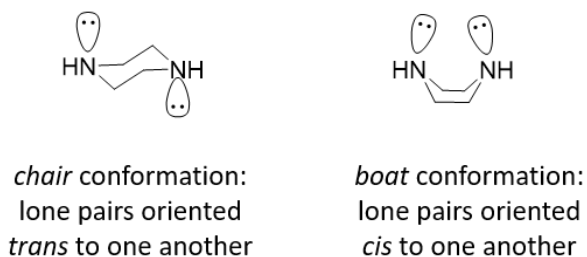


Figure 5.11. Positions of nitrogen atom lone pairs dependent on the conformation of piperazine.^{384, 415}

5.3.2.2. Piperazine-containing macrocycles similar to L5

5.18 is an example of an azamacrocyclic ligand that contains only one piperazine ring, but there are other examples in the literature where two piperazine rings are incorporated into a macrocyclic ligand, similar to **L5**. **5.10** and **5.17**, shown in figure 5.9, are examples of dimeric piperazine-containing azamacrocyclic ligands.^{400, 411, 413}

5.17 was reported in 1980 by Fronczek *et al.*⁴¹¹ This hexaazamacrocyclic dimer was originally designed as a tetradentate chelating agent for transition metal ions.⁴¹¹ The authors envisioned the piperazine rings adopting the *boat* conformation necessary for all four piperazine nitrogen atoms to bind to a metal ion, thus forming a stable metal complex.⁴¹¹ In reality, the piperazine rings prefer the more favored *chair* conformation in the solid state (Figure 5.12).⁴¹¹ Complexation of **5.17** with CoCl_2 was attempted, but no stable metal complex was formed. Treatment of **5.17** with $\text{CoCl}_2 \cdot 6\text{H}_2\text{O}$ led to the diprotonation of **5.17**, in which the acid responsible is most likely a hexaaquocobalt(II) complex ($[\text{Co}^{\text{II}}(\text{H}_2\text{O})_6]^{2+}$).⁴¹¹ The diprotonated ligand then crystallized out of solution with a cobalt(II) tetrachloride counterion ($[\text{Co}^{\text{II}}\text{Cl}_4]^{2-}$) (Figure 5.12).⁴¹¹ The lack of complexation of **5.17** with metal ions is due to the *trans* orientation of the lone pairs on the piperazine nitrogen atoms (Figure 5.11).^{384, 411, 415} The lone pairs are oppositely oriented because of the favored *chair* conformation adopted by the piperazine rings within the macrocycle. Moreover, **5.17** is a relatively inflexible ligand, which does not allow the piperazine rings to rotate or change orientation to bind metal ions.⁴¹¹

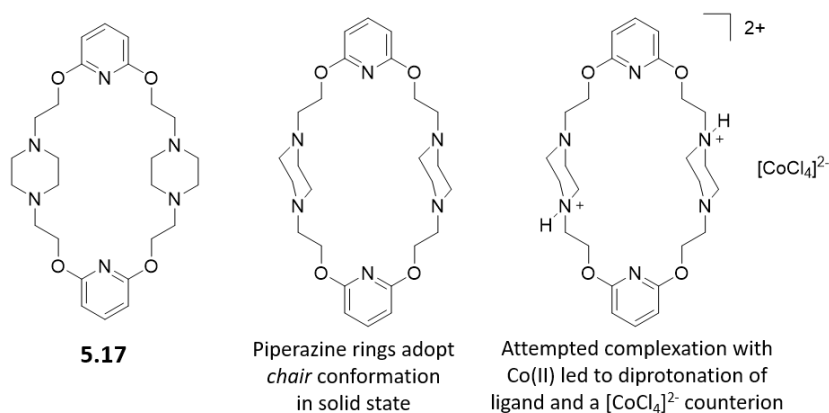


Figure 5.12. Hexaazamacrocyclic ligand **5.17** and related solid state structures.⁴¹¹

5.10 is another azamacrocyclic piperazine dimer found within the chemical literature. This ligand and corresponding mononuclear Cu(I) complex was reported by two different groups in the early 1990s (Rissanen *et al.* in 1994 and Fronczek *et al.* in 1996).^{400, 413} **5.10** was designed as a potential receptor for ions or uncharged organic molecules.⁴¹³ The piperazine rings were incorporated into the macrocycle because of the ability to act as both donors and spacers in large molecules.⁴¹³ Similar to **5.17**, the solid state structure of **5.10** indicated that the piperazine rings adopt the thermodynamically favored *chair* conformation in the solid state.^{400, 413} The ligand was then complexed with Cu(I) to yield a mononuclear Cu(I) complex (Figure 5.13).^{400, 413} Remarkably, upon protonation, one of the piperazine rings rotates 180°.^{400, 413} This rotation results in one lone pair being oriented into the macrocyclic cavity. Due to the rotation of one of the piperazine rings, three nitrogen atom lone pairs are oriented toward the macrocyclic cavity; one lone pair from the pyridine nitrogen atom and one lone pair from the each piperazine nitrogen atom (totaling two pairs). The orientation of the lone pairs is favorable for metal complexation, thus when this ligand is combined with a Cu(I) (or Cu(II)) salt, complexation occurs.^{400, 413} Interestingly, although the two groups obtained the same Cu(I) complex, one group started with a Cu(II) salt (Cu^{II}Cl₂) and the other started with a Cu(I) salt (Cu^ICl).^{400, 413} Although it was stated by Fronczek *et al.*, that the chemistry of Cu(II) reduction to Cu(I) upon complexation to **5.10** was not well understood.⁴⁰⁰

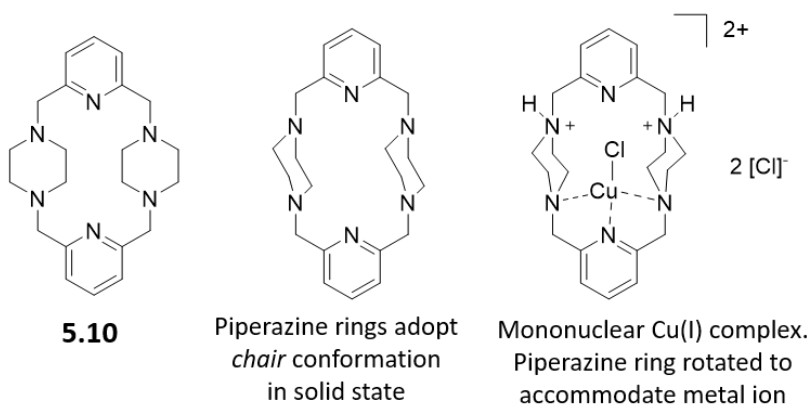


Figure 5.13. Ligand **5.10** and related solid state structures.^{400, 413}

5.4. Complexation studies of L5 with Cu(II)

Large polyazamacrocycles and corresponding metal complexes can be used for many different applications, such as biomimetic models, catalysts, and anion receptors. These unique ligands can form both mononuclear and dinuclear metal complexes, which is dependent upon the ligand design and reaction conditions. Copper was chosen to initially test the metal complexation ability of **L5**, because it typically forms the most stable complexes when compared to the other first-row transition metals (as predicted by the Irving-Williams series). As discussed in a previous chapter, the Irving-Williams series refers to the relative stabilities of complexes formed with divalent first-row transition metal ions.²⁰⁰ In this series the stabilities of transition metal complexes generally increases across the period to a maximum stability at copper: $\text{Mn(II)} < \text{Fe(II)} < \text{Co(II)} < \text{Ni(II)} < \text{Cu(II)} > \text{Zn(II)}$.²⁰⁰

Complexation reactions of **L5** with Cu(II) were performed in water using methodology previously reported by the Green group.⁵⁶ The first step in the complexation reaction is the dissolution of **L5** in a small amount of water and adjustment of the pH to around 6. After the pH adjustment, two equivalents of $\text{Cu}(\text{ClO}_4)_2$ were added dropwise to the ligand solution. Immediately upon addition of the blue Cu(II) salt, the solution color changed from pale yellow to blue-green; this solution stirred at room temperature overnight with no further color change. The following day, the solution was filtered and evaporated to yield a green powder. This green powder was then dissolved in CH_3OH , filtered, and evaporated to dryness. The resulting light green powder was dissolved in water and analyzed by mass spectrometry to validate complexation of the Cu(II) ion(s) and to determine if a mononuclear or dinuclear complex had resulted (the mass spectrum is shown in figure 5.14). As indicated by the mass spectrum, several different positively charged molecular fragments result upon ionization. It should be noted that assignments for the m/z base peaks were validated using an isotope distribution calculator to model the isotopic envelope; each experimentally determined isotopic distribution matches up with the predicted isotopic distribution (found vs. theoretical isotopic distribution diagrams are shown in the experimental section at the end of

this chapter). Interestingly, some molecular fragments consist of ligand only (highlighted in red), some fragments consist of ligand and one Cu(II) ion (highlighted in blue), and some fragments consist of ligand and two Cu(II) ions (highlighted in green). Most importantly, the mass spectrum does indicate that at least some of the analyzed sample consists of a potentially dinuclear **L5**-Cu(II) complex.

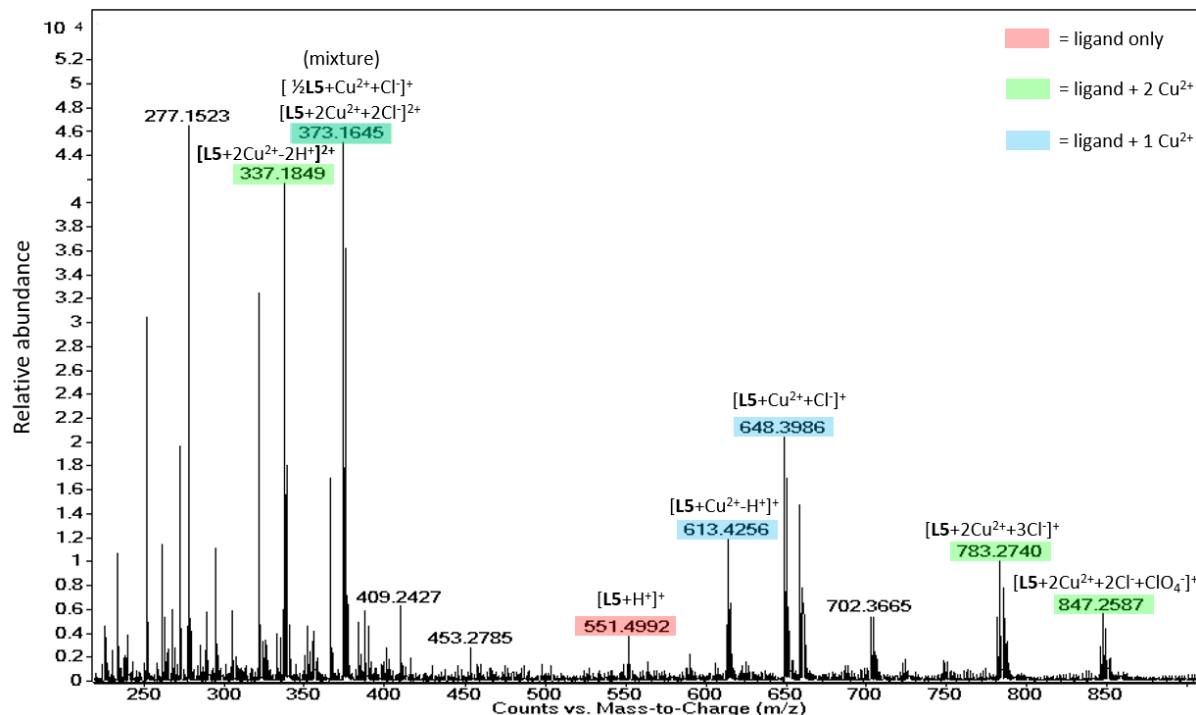


Figure 5.14. Mass spectrum of **L5** complexation reaction with 2 equivalents of Cu(II).

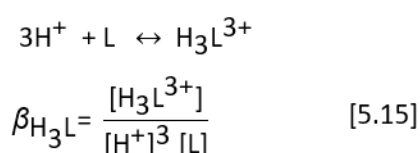
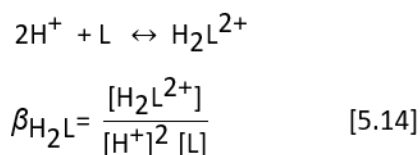
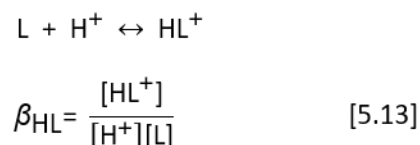
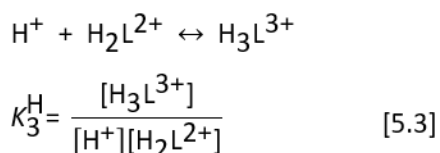
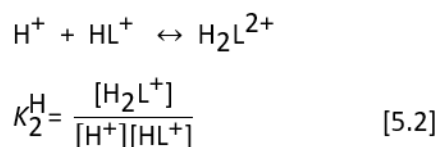
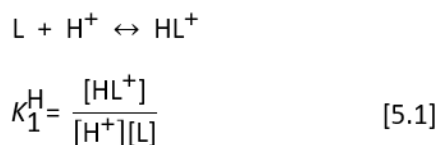
After initial analysis with MS, the light green powder was dissolved in water and set aside for crystallization via slow evaporation. Unfortunately, after multiple attempts to grow X-ray quality crystals, no crystalline material was isolated. It was hypothesized that the light green powder isolated during the complexation of **L5** with 2 equivalents of Cu(II) consisted of multiple species such as: salt(s), mononuclear **L5Cu**, and dinuclear **L5Cu**.

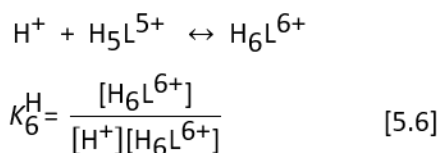
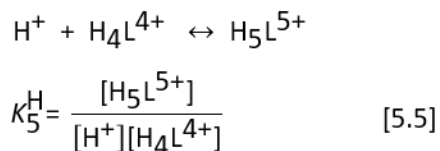
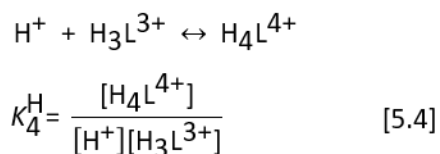
5.5. Protonation and stability constants of L5 with various divalent transition metals

In order to analyze the solution behavior of L5, the protonation and stability constants were determined using pH-potentiometric titrations. The potentiometric titrations and data fittings were performed by collaborator Gyula Tircsó in Hungary. Ultimately, these measurements offered insight into determining better metalation conditions to isolate both mononuclear and dinuclear metal complexes of L5. A brief overview of stability constants was previously discussed in chapter 2, section 2.4.1.

5.5.1. Relevant equations for the expression of the protonation and stability constants of L4

Like L4, the protonation and stability constants of L5 will be described in terms of Lewis acids and Lewis bases. Two different types of constants will be used to describe the protonation and complex formation equilibria, stepwise constants (K) and overall constants (β).¹⁸⁹ L5 is represented as L in the following equilibrium expressions. In solution and in the absence of metal ions, L5 can be modulated between seven different species: H_6L^{6+} , H_5L^{5+} , H_4L^{4+} , H_3L^{3+} , H_2L^{2+} , and HL^+ , based on solution pH. The seven-different species are related by six successive stepwise protonation constants, which are represented by equations [5.1]-[5.6]. Additionally, the stepwise protonation constants (K^H) are related to the overall protonation constants (β) through equations [5.7]-[5.12], where the overall protonation constants are the cumulative product of the stepwise protonation constants in equations [5.13]-[5.18].





$$\beta_{HL} = K_1^H \quad [5.7]$$

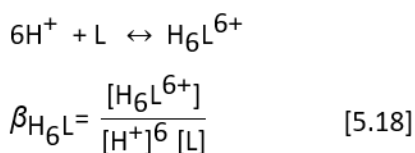
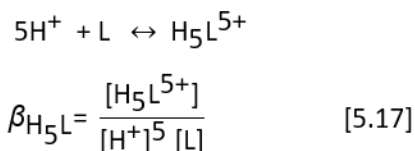
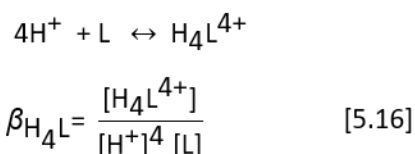
$$\beta_{H_2L} = K_1^H K_2^H \quad [5.8]$$

$$\beta_{H_3L} = K_1^H K_2^H K_3^H \quad [5.9]$$

$$\beta_{H_4L} = K_1^H K_2^H K_3^H K_4^H \quad [5.10]$$

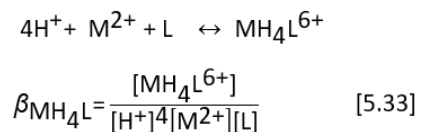
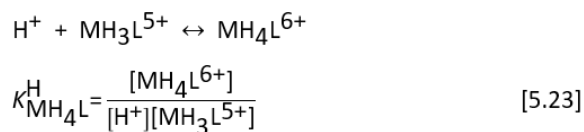
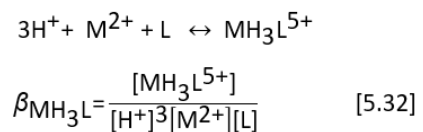
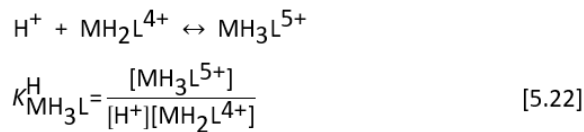
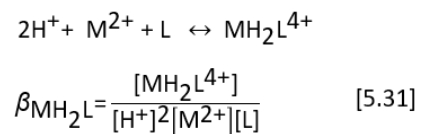
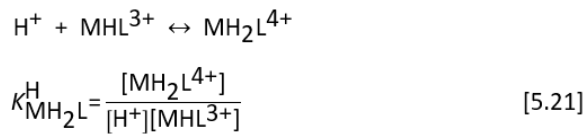
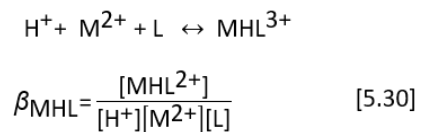
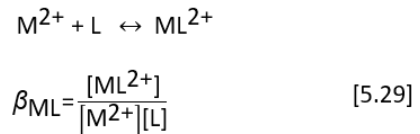
$$\beta_{H_5L} = K_1^H K_2^H K_3^H K_4^H K_5^H \quad [5.11]$$

$$\beta_{H_6L} = K_1^H K_2^H K_3^H K_4^H K_5^H K_6^H \quad [5.12]$$



The complex formation equilibria can be expressed in a similar manner to the protonation equilibria. Due to the ability of **L5** to bind two metal ions the equations used to describe this system are more complex and numerous. Additionally, complexes of **L5** (with certain metal ions) exhibit the ability to undergo hydrolysis reactions leading to the formation of several different ligand/metal-hydroxy species. In terms of metal and ligand (not including possible hydroxy species) nine different species are possible: ML^{2+} , MHL^{3+} , MH_2L^{4+} , MH_3L^{5+} , MH_4L^{6+} , M_2L^{4+} , M_2HL^{5+} , and $M_2H_2L^{6+}$ (where M represents a divalent metal ion); although not all species listed above are experimentally observed for each type of metal. The nine-different species are related by eight successive stepwise formation/protonation constants, which are represented by equations [5.19]-[5.23] and [5.34]-[5.36]. The stepwise formation/protonation constants (K^M and K^H) are related to the overall formation/protonation constants (β) through equations [5.24]-[5.28]

and [5.37]-[5.39], where the overall formation/protonation constants are the cumulative product of the stepwise formation/protonation constants in equations [5.29]-[5.33] and [5.40]-[5.42]. It should be noted that some of the species appearing in equations [5.1]-[5.6], [5.19]-[5.23], and [5.34]-[5.36] are not observed (not formed) within the system over various pH ranges (or in the absence of a metal ion), but a complete set of equations [5.1]-[5.42] are necessary to describe the equilibria in the pH range where hydrogen ion concentrations are measured.¹⁸⁹ In addition to the species listed within the equations [5.1]-[5.42], there can also be H⁺, M²⁺, and OH⁻ ions present within the solution.¹⁸⁹



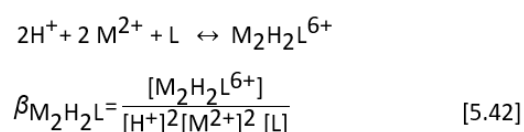
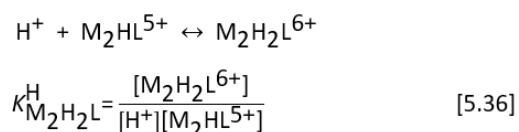
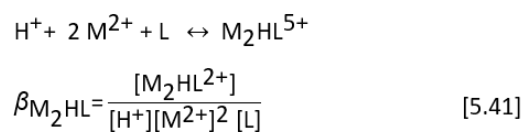
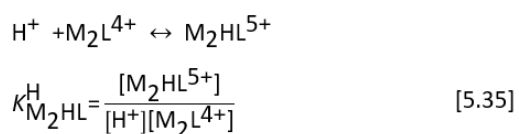
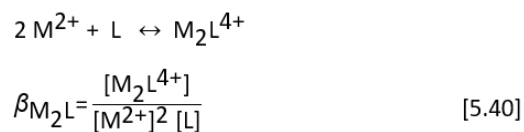
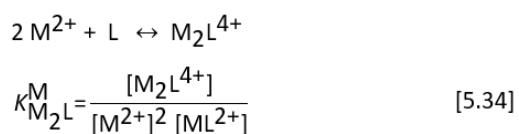
$$\beta_{ML} = K_{ML}^M \quad [5.24]$$

$$\beta_{MHL} = K_{ML}^M K_{MHL}^H \quad [5.25]$$

$$\beta_{MH_2L} = K_{ML}^M K_{MHL}^H K_{MH_2L}^H \quad [5.26]$$

$$\beta_{MH_3L} = K_{ML}^M K_{MHL}^H K_{MH_2L}^H K_{MH_3L}^H \quad [5.27]$$

$$\beta_{MH_4L} = K_{ML}^M K_{MHL}^H K_{MH_2L}^H K_{MH_3L}^H K_{MH_4L}^H \quad [5.28]$$



$$\beta_{M_2L} = K_{M_2L}^M \quad [5.37]$$

$$\beta_{M_2HL} = K_{M_2L}^M K_{M_2HL}^H \quad [5.38]$$

$$\beta_{M_2H_2L} = K_{M_2L}^M K_{M_2HL}^H K_{M_2H_2L}^H \quad [5.39]$$

5.5.2. Determination of protonation constants for L5

The step-wise protonation constants, $\log K_n^H$ ($n = 1, 2, 3, 4, 5, \text{ or } 6$), of **L5** as defined in equations [5.1]-[5.6] were determined by pH-potentiometric titrations at constant ionic strength (I) and temperature ($I = 0.15 \text{ M NaCl}$, $25 \text{ }^\circ\text{C}$) (Figure 5.15). The results are compiled in table 5.2; **L5** contains four secondary amines in the macrocyclic core and four tertiary amines within the pyridine and piperazine moieties. Interestingly, **L5** is observed to undergo only six (experimentally measurable) protonation equilibria, despite the ten amine groups present within the macrocycle. This is constant with the elemental analysis of **L5** which indicates the presence of 6 HCl molecules when **L5** is isolated as a hydrochloride salt **L5**•6HCl; see experimental section for complete elemental analysis of **L5**).

Table 5.2. Protonation constants for **L5** ($I = 0.15 \text{ M NaCl}$, $25 \text{ }^\circ\text{C}$)

$\log K_1^H$	8.77(6)	$\log \beta_{011}$	8.77(6)
$\log K_2^H$	8.24(4)	$\log \beta_{012}$	17.01(4)
$\log K_3^H$	7.77(6)	$\log \beta_{013}$	24.75(6)
$\log K_4^H$	7.26(3)	$\log \beta_{014}$	32.01(3)
$\log K_5^H$	4.74(7)	$\log \beta_{015}$	36.73(7)
$\log K_6^H$	4.39(7)	$\log \beta_{016}$	41.12(4)

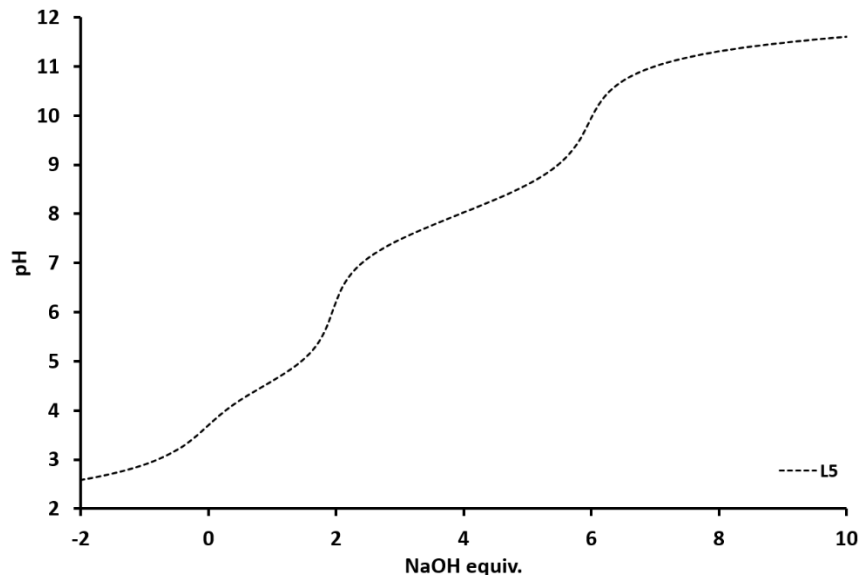
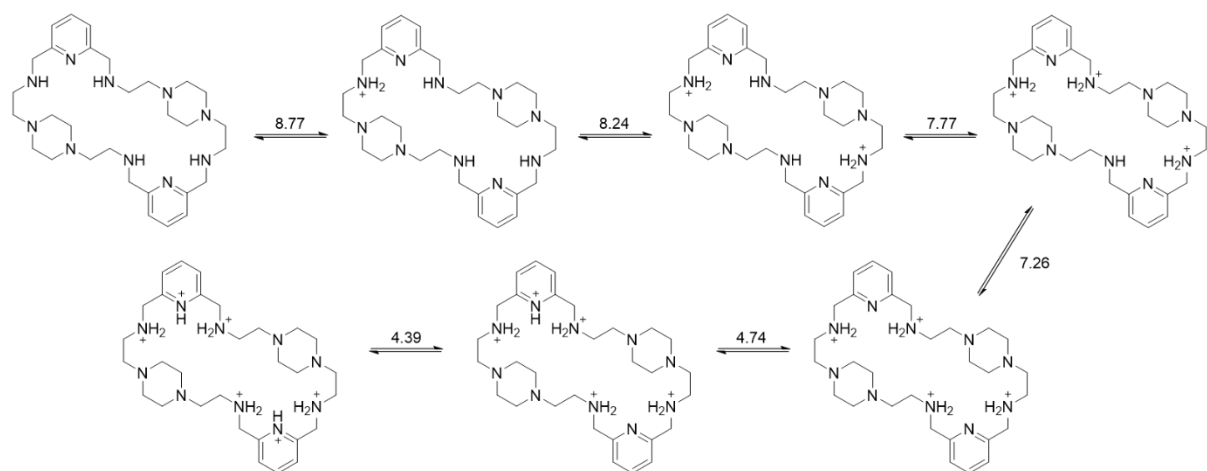


Figure 5.15. pH-potentiometric titration curve of H₆L⁶⁺ titrated with NaOH (*I* = 0.15 M NaCl, *T* = 25 °C) over pH range 2.0 – 12.0. (H₆L⁶⁺ represents the fully protonated **L5**).

Concrete assignments of the six protonation constants cannot be made without additional experimentation (such as UV-vis and/or NMR titrations), but speciation approximations can be made. Interestingly, the protonation constants seem to be ‘grouped’ together with two events occurring between pH 8-9, another two occurring between pH 7-8, and the final two occurring between pH 4-5. It can be postulated that the three ‘groups’ of protonation constants could be assigned to different types of amine groups within the ligand (i.e. secondary vs. tertiary amine groups). For visualization purposes only, a protonation scheme was generated for the six protonation events observed upon titrations with NaOH (Scheme 5.3). The occurrence of six protonation events is promising result for **L5** to be used as a potential anion receptor. As discussed in section 5.3.1.3. good anion receptors have many protonation events that allow for amine nitrogens to become positively charged; the positively charged amine moieties can then bind anions via coulombic forces, hydrogen bonding and other weak interactions.⁴⁰²⁻⁴⁰³



Scheme 5.4. Proposed protonation sequence of **L5** (for visualization purposes only).

Additionally, the protonation constants determined for **L5** were compared to several of the large macrocycles described in section 5.3 (Figure 5.9). Table 5.3 is a compilation of the protonation constants from several large polyazamacrocycles. It was noted that **L5** had the lowest $\log K_1^H$ value compared to the other polyazamacrocycles, meaning that it is the least basic ligand. An increase in ligand basicity is often used to predict the formation of thermodynamically stable metal-complexes.¹⁹⁴ Therefore, it is predicted (based on the pKas) that **L5** will form the least stable metal complexes compared to the other polyazamacrocycles compiled in table 5.3.

Table 5.3. Protonation constants ($\log K$) for various large polyazamacrocycles ($T = 25\text{ }^\circ\text{C}$)

Ligand	Members	N donors	$\log K_1^H$	$\log K_2^H$	$\log K_3^H$	$\log K_4^H$	$\log K_5^H$	$\log K_6^H$
L5 ^a	30	10	8.77(6)	8.24(4)	7.77(6)	7.26(3)	4.74(7)	4.39(7)
5.4 ^b	18	6	10.19	9.23	8.73	4.09	-	-
5.7 ^c	18	6	9.13	8.32	6.12	5.24	≈ 2	≈ 1
5.15 ^d	24	8	9.25	8.49	7.55	6.98	4.11	-
5.16 ^e	26	6	9.18	8.69	8.52	7.83	1.51	-

(a) This work; $I = 0.15\text{ M NaCl}$; (b) from ref.⁴⁰⁶; $I = 0.2\text{ M KCl}$; (c) from ref.⁴⁰⁶; $I = 0.2\text{ M NaClO}_4$; (d) from ref.⁴⁰⁹; (e) from ref.⁴⁰²; $I = 0.10\text{ M KNO}_3$; (-) species no observed.

5.5.3. Determination of stability (formation) constants for **L5** with various divalent transition metal ions

As previously stated, the applications of large polyazamacrocyclic ligands and their corresponding metal complexes include use as biomimetic models, catalyst, and anion receptors. To assess the

thermodynamic stability and applicability of **L5**, the metal binding constants were determined for biologically and/or catalytically relevant metal ions including: Mn(II), Fe(II), Cu(II), and Zn(II). pH-potentiometric titrations were carried out with one or two equivalents of the metals listed above (Figures 5.16, 5.17). As expected, the Cu(II) formed the most stable complex with the ligand (and the most stable dinuclear complex) compared to any other metal ion tested. The formation of dinuclear complexes with **L5** and Cu(II) can be seen by comparing the titration curves obtained at 1:1 and 1:2 metal-to-ligand ratio (Figure 5.17). The stability constants resulting from the pH-potentiometric titration of **L5** with different transition metals are shown in table 5.4.

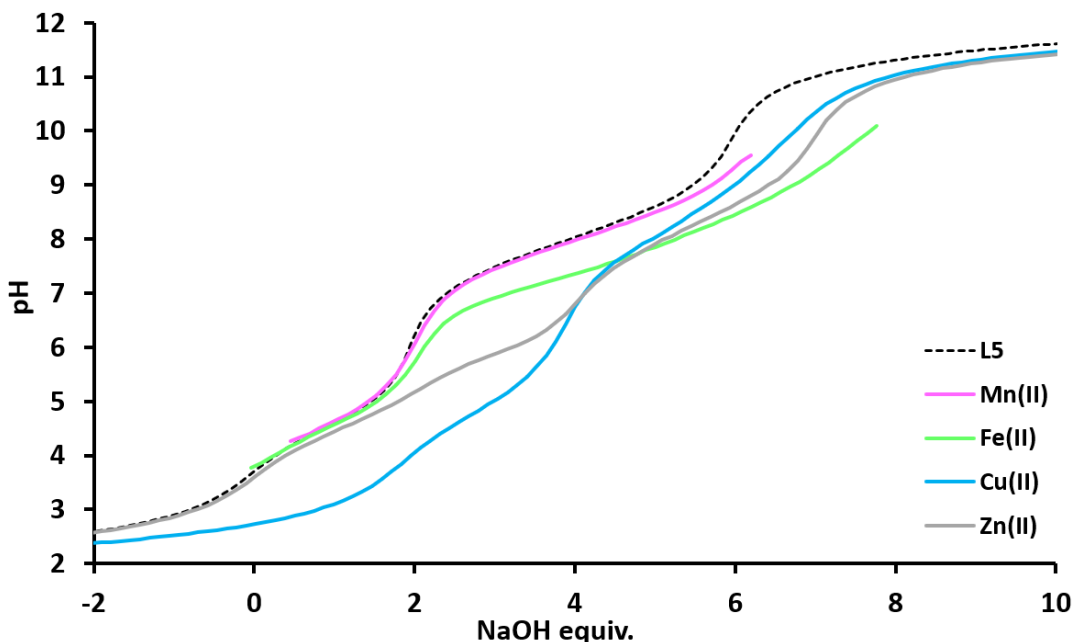


Figure 5.16. pH-potentiometric titration of solutions containing 1:1 equivalents of H_6L^{6+} in the presence of M(II) ($I = 0.15$ M NaCl, $T = 25$ °C). (M(II) is a divalent transition metal ion; M(II) was introduced in the form of a MCl_2 stock solution). *For Mn(II) and Fe(II) the titrations were halted due to formation of metal hydroxide species.

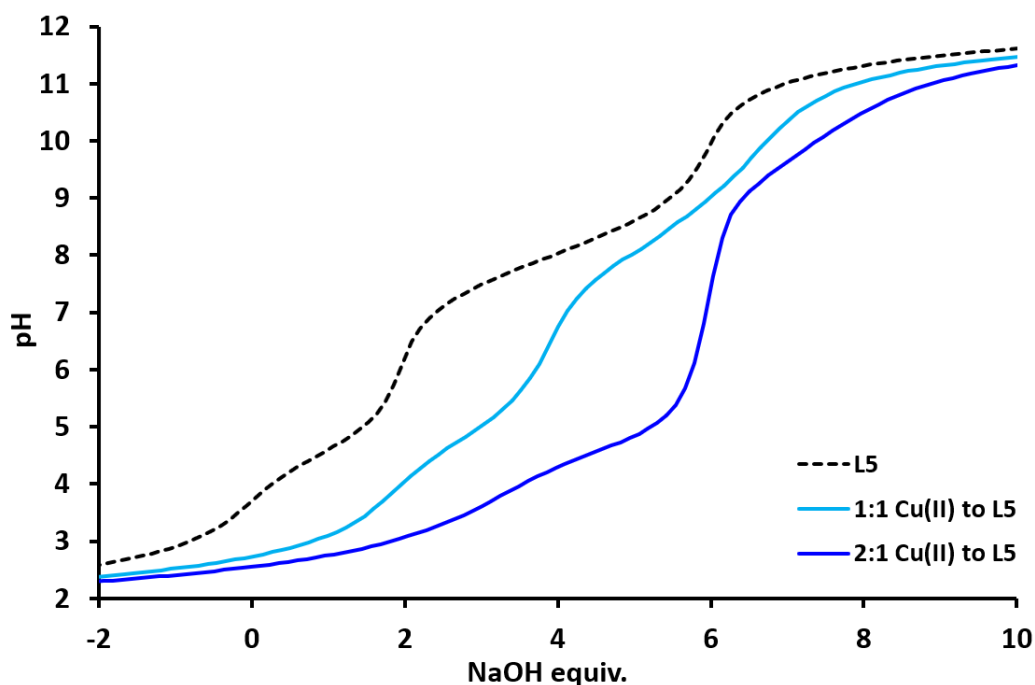


Figure 5.17. pH-potentiometric titration of solutions containing 1:1 and 1:2 equivalents of H_6L^{6+} in the presence of Cu(II) ($I = 0.15$ M NaCl, $T = 25$ °C). Cu(II) was introduced in the form of a $CuCl_2$ stock solution.

Table 5.4. Stability constants of the complexes formed with L5 and various metal ions ($I = 0.15$ M NaCl, 25 °C).

	Mn(II)	Fe(II)	Cu(II)	Zn(II)
$\log \beta_{ML}$	4.12(4)	7.02(5)	14.45(7)	7.72(5)
$\log \beta_{MHL}$	12.41(6)	15.00(5)	22.77(7)	15.94(6)
$\log \beta_{MH_2L}$	20.25(6)	21.72(10)	30.19(4)	25.58(3)
$\log \beta_{MH_3L}$	27.99(6)	29.24(5)	25.27(4)	29.10(9)
$\log \beta_{MH_4L}$	x	x	39.84(1)	x
* $\log \beta_{MH-1L}$	5.13	-1.39(4)	5.08(8)	-1.27(6)
* $\log \beta_{MH-12}$	x	-10.55(4)	-6.97(8)	-13.19(7)
$\log \beta_{M_2L}$	x	x	26.58(17)	14.49(3)
$\log \beta_{M_2HL}$	x	x	32.07(7)	x
$\log \beta_{M_2H_2L}$	x	x	x	x
* $\log \beta_{M_2H-1L}$	x	x	17.56(27)	5.92(1)
* $\log \beta_{M_2H-12}$	x	x	7.71(22)	-3.03

(*) $\log \beta_{MH-1L}$, $\log \beta_{MH-12}$, $\log \beta_{M_2H-1L}$, and $\log \beta_{M_2H-12}$ are the stability constants for $ML(OH)$, $ML(OH)_2$, $M_2L(OH)$, and $M_2L(OH)_2$ species, respectively; these species are ternary hydroxo complexes generated *in situ* hydrolysis reactions.

From the stability/protonation constants compiled in table 5.4, some observations and conclusions can be made about the complexation of **L5** with various transition metal ions. It was observed that the 1:1 stability constants follow the Irving-Williams series ($\text{Mn(II)} < \text{Fe(II)} < \text{Co(II)} < \text{Ni(II)} < \text{Cu(II)} > \text{Zn(II)}$).²⁰⁰ The 1:1 complex of **L5** with Cu(II) is the most stable, followed by the Zn(II), Fe(II), and Mn(II) complexes (Figure 5.18). Another noteworthy observation is that the stability constants of **L5** are all relatively small, especially for a macrocyclic ligand. In fact, the stability constants for **L5** are significantly smaller than those for **L1-L4** (Table 2.3). The stability constants of **L5** were also compared to several of the large macrocycles described in section 5.3 (Figure 5.9). Table 5.3 is a compilation of the stability constants from several large polyazamacrocycles. **L5** is a 30-membered decaazamacrocycle, **5.4** and **5.7** are 18-membered hexaazamacrocycles, and **5.16** is a 26-membered hexaazamacrocycle. Interestingly, the smaller membered macrocycles (18-membered) have much larger 1:1 stability constants than their larger counterparts. In contrast, the larger 26-membered macrocycle (**5.16**) has stability constants (1:1 and 2:1) that are comparable to **L5**. The larger polyazamacrocycles do not bind metal ions as well as smaller macrocyclic ligands; this may be because of a mismatch between the size of the macrocyclic cavity and metal ion radius. Additionally, the decrease in stability constants may also be a consequence of the larger steric energy required for conformational reorganization of the macrocyclic cavity to complex metal ions.⁴⁰²

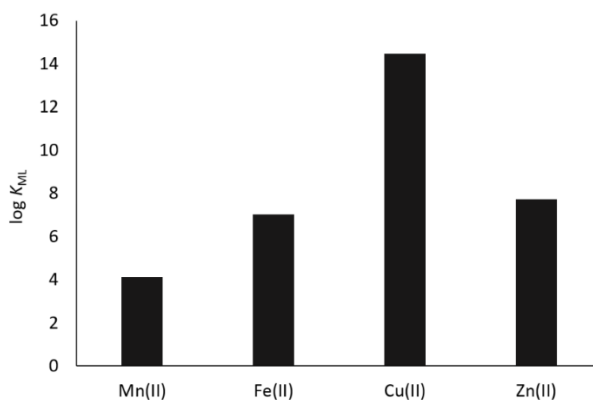


Figure 5.18. Plot of the first stability constants for 1:1 complex of **L5** with M(II) ions. Log K_{ML} values follow the Irving-Williams series ($\text{Mn(II)} < \text{Fe(II)} < \text{Co(II)} < \text{Ni(II)} < \text{Cu(II)} > \text{Zn(II)}$).²⁰⁰

Table 5.5. Overall stability constants and protonation constants of various polyazamacrocyclic M(II) complexes.

Metal ion	Log β	L5 ^a	5.4 ^b	5.7 ^c	5.16 ^d
Mn(II)	log β_{ML}	4.12(4)	-	12.5	-
	log β_{MHL}	12.41(6)	-	-	-
	log β_{MH2L}	20.25(6)	-	-	-
	log β_{MH3L}	27.99(6)	-	-	-
	log β_{MH-1L}	5.13	-	-	-
Cu(II)	log β_{ML}	14.45(7)	-	25.0	14.09(1)
	log β_{MHL}	22.77(7)	-	-	22.27(2)
	log β_{MH2L}	30.19(4)	-	-	29.49(4)
	log β_{MH3L}	25.27(4)	-	-	33.02(4)
	log β_{MH4L}	39.84(1)	-	-	x
	log β_{MH-1L}	5.08(8)	-	-	x
	log β_{MH-12}	-6.97(8)	-	-	x
	log β_{M2L}	26.58(17)	-	-	25.20(2)
	log β_{M2HL}	32.07(7)	-	-	29.38(2)
	log β_{M2H-1L}	17.56(27)	-	-	17.45(3)
	log β_{M2H-12}	7.71(22)	-	-	8.63(2)
Zn(II)	log β_{ML}	7.72(5)	17.8	21.1	8.27(4)
	log β_{MHL}	15.94(6)	-	-	16.07(4)
	log β_{MH2L}	25.58(3)	-	-	23.46(3)
	log β_{MH3L}	29.10(9)	-	-	29.80(9)
	log β_{MH-1L}	-1.27(6)	-	-	x
	log β_{MH-12}	-13.19(7)	-	-	x
	log β_{M2L}	14.49(3)	-	-	11.63(5)
	log β_{M2H-1L}	5.92(1)	-	-	x
	log β_{M2H-12}	-3.03	-	-	-4.63(9)

(a) This work; $I = 0.15$ M NaCl; (b) from ref.⁴⁰⁶; $I = 0.2$ M KCl; (c) from ref.⁴⁰⁶; $I = 0.2$ M NaClO₄; (d) from ref.⁴⁰², $I = 0.10$ M KNO₃; (x) species no observed; (-) not measured. (log β_{MH-1L} , log β_{MH-12} , log β_{M2H-1L} , and *log β_{M2H-12} are the stability constants for ML(OH), ML(OH)₂, M₂L(OH), and M₂L(OH)₂ species, respectively; these species are generated during a hydrolysis reaction.)

Finally, in addition to the titrations performed one and two equivalents of Cu(II) (Figure 5.17), species distribution diagrams were generated (by collaborator Gyula Tircsó) for the two different stoichiometric amounts of Cu(II) with **L5** (Figures 5.19, 5.20). The first of the two species distribution diagrams (Figure 5.19) shows the species in solution when both Cu(II) and **L5** are present in a 1:1 ratio (2 mM **L5** and 2 mM Cu(II)). It is observed that there are many different species in solution over a range of pH values, including several hydroxy species and very small amounts of a protonated dinuclear **L5Cu** complex. As pH is varied from 2 – 12, the solution components change from a majority of uncomplexed Cu(II) (at pH = 2), to CuH_4L (at pH = 2 – 4), to CuH_2L (at pH = 5 – 7), to CuL(OH) (at pH = 9 – 12). The second species distribution diagram (Figure 5.20) shows the species in solution when Cu(II) and **L5** are present in a 2:1 ratio (4 mM Cu(II) and 2 mM **L5**).

The second species distribution diagram is much less complex than the first diagram. As pH is varied from 2 – 12, the solution components change from a majority of uncomplexed Cu(II) (at pH = 2), to CuH_4L (at pH = 3), to Cu_2HL (at pH = 4 – 5), to Cu_2L (at pH = 6 – 9), to $\text{Cu}_2\text{L(OH)}_2$ (at pH = 10 – 12). The presence of a $\text{Cu}_2\text{L(OH)}_2$ species could be hypothesized to contain an OH bridge. Moreover, the species distribution diagram is in agreement with experimental data pertaining to a dinuclear complex of **L5** with Cu(II). According to the species distribution curve a dinuclear Cu_2L complex is observed around pH 6; this is the same pH that the complexation reaction of **L5** with Cu(II) was adjusted to promote metalation (discussed in the previous section) and in fact a dinuclear complex was observed in the mass spectrum (Figure 5.14).

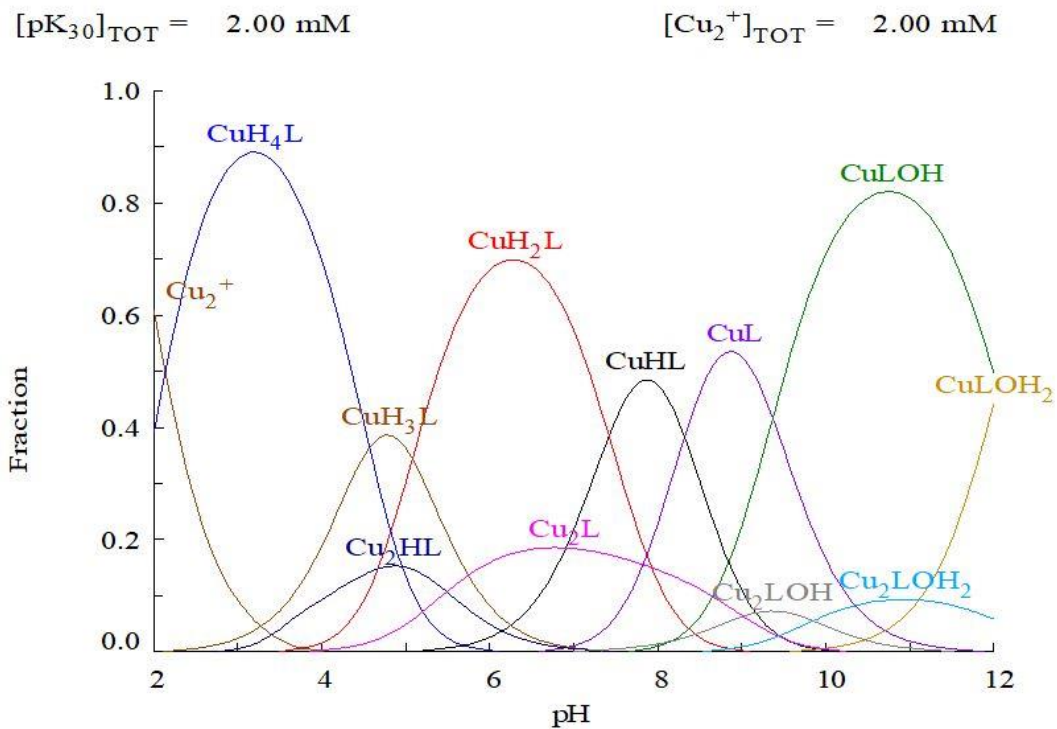


Figure 5.19. Species distribution diagram for the $\text{L5}:\text{Cu}^{2+}:\text{H}^+$ system ($[\text{Cu}^{2+}] = [\text{L5}] = 2.0 \text{ mM}$; $\text{pK}_{30} = \text{L5}$).

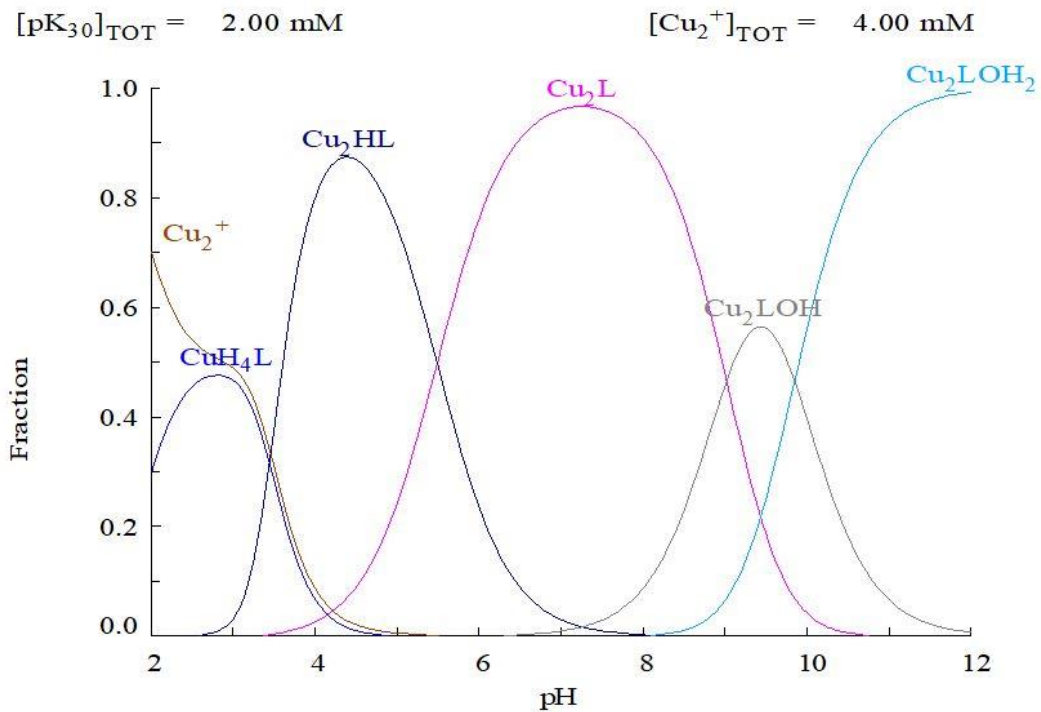


Figure 5.20. Species distribution diagram for the $\text{L5}:\text{Cu}^{2+}:\text{H}^+$ system ($[\text{Cu}^{2+}] = 4.0 \text{ mM}$, $[\text{L5}] = 2.0 \text{ mM}$; $\text{pK}_{30} = \text{L5}$).

5.6. Conclusions

L5 was originally designed as a novel ultra-rigid Mn(II)-based contrast agent, **15-anePyN₅Pip**. Increased rigidity was postulated to increase the kinetic inertness while keeping the thermodynamic stability and relaxivity of the corresponding complexes high enough to be utilized as future Mn(II)-based contrast agents. The ligand framework design was supposed to incorporate a rigidifying piperazine ring into a 15-membered pentaazamacrocycle. However, synthetic methodology utilizing templating Mn(II) and Zn(II) ions yielded a novel, dimeric 30-membered decaazamacrocycle. Due to the completely symmetric nature of **L5**, a solid state structure of the ligand offered the only direct confirmation of ‘dimer’ formation. Dimerization of the ligand occurred because of the thermodynamically preferred *chair* conformation adopted by the piperazine rings within the macrocyclic framework (Scheme 5.2, Figure 5.7). Several different modifications were made to the procedure to isolate **15-anePyN₅Pip**, attempts were unsuccessful, but increased yields and purity were obtained.

Through a brief review of the literature, it was determined that large polyazamacrocycles, such as **L5** can be used as biomimetic models, catalysts, and anion receptors. Therefore, **L5** was combined with Cu(II) to generate a mononuclear and/or dinuclear metal complex. Isolation of X-ray quality crystals proved unfruitful, but analysis with MS showed **L5** complexation to two Cu(II) ions. Additionally, protonation and stability constants were determined for **L5** with several divalent transition metal ions.

L5 undergoes six protonation events in solution and forms very weak complexes with the metal ions tested. This is most likely due to the size of the macrocycle and presence of rigidifying piperazine rings in the preferred *chair* conformation. Because the lone pairs on the nitrogen atoms are oriented *trans* from one another, this does not promote complexation with metal ions. Revisiting the solid state structure of **L5** offers insight into the orientation of the nitrogen atom lone pairs within the ligand framework (Figure 5.21). As shown in figure 5.21, the lone pairs on many of the nitrogen atoms are not oriented toward the macrocyclic cavity, thus making complexation with a metal ion difficult. The ligand must undergo a

conformational reorientation of the macrocyclic cavity to undergo complexation, but due to the presence of rigidifying piperazine rings this is somewhat difficult. This may explain why **L5** forms such weak complexes with metal ions; it is too large and too rigid. Even though **L5** only weakly coordinates metal ions, it has the potential to be an excellent anion receptor, due to its highly charged nature upon protonation. The ability for **L5** to bind biologically relevant anions will be investigated in the future.

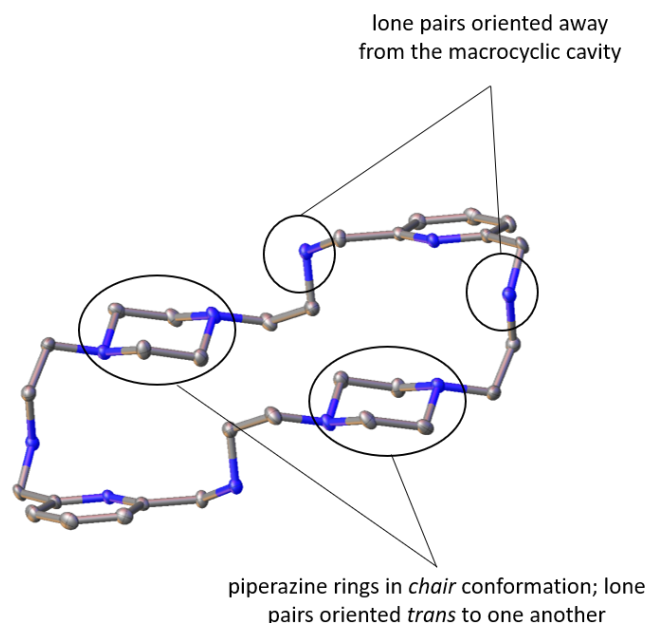


Figure 5.21. Solid state structure of **L5**, showing preferred *chair* conformation of piperazine rings and *trans* orientation of nitrogen atom lone pairs. (Hydrogen atoms have been omitted for clarity)

5.7. Experimental (materials and methods)

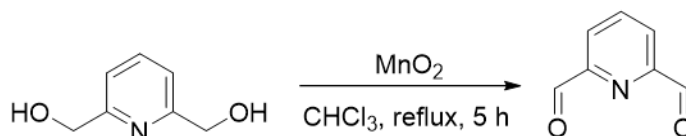
All chemical reagents were purchased from either Millipore Sigma or Alfa Aesar and used without further purification. The yield reported for **L5** were calculated based on elemental analysis results. Elemental analyses were performed by Canadian Microanalytical Services Ltd.

5.7.1. Physical measurements

ESI mass spectral analysis were obtained on an Agilent 1200 series 6224 TOF LC/MS spectrometer at 175 V (positive ESI scan) in H₂O, CH₃OH, CHCl₃, or CH₂Cl₂. ¹H NMR and ¹³C NMR spectra were carried out

in deuterated solvents at 25 °C. All spectra reported were obtained on a Bruker Avance III (400 MHz) High Performance Digital NMR Spectrometer.

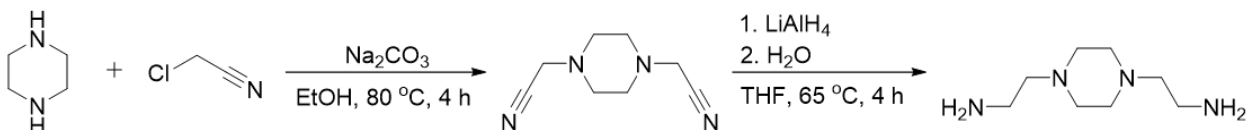
5.7.2. Preparation of L5



Scheme 5.E1. Synthesis of (5.1) using activated MnO₂.

Synthesis of 2,6-pyridinedicarboxaldehyde (5.1):

Activated MnO₂ was prepared by heating overnight at 110 °C. An excess of MnO₂ (21.272 g, 0.245 mol) and 2,6-bis(hydroxymethyl)pyridine (2.0585 g, 14.8 mmol) were refluxed with stirring for 5 h in CHCl₃ (100 mL). The oxide residue was separated from the solution by vacuum filtration and the black solid was rinsed with chloroform (4 x 20 mL). Solvent was removed from the solution by rotary evaporation, and then the crude product was purified by flash chromatography (SiO₂, CH₂Cl₂, R_f = 0.4). (5.1) was isolated as a white solid and was characterized with ¹H NMR. Yield: 0.753 g (38%). ¹H NMR (400 MHz, CDCl₃, 25 °C): δ = 10.81 (s, 2H), 8.19-8.17 (d, 2H), 8.09-8.07 (t, 1H).^{91, 378-380}



Scheme 5.E2. Synthesis of piperazine-based amine precursor (5.3) for cyclization.

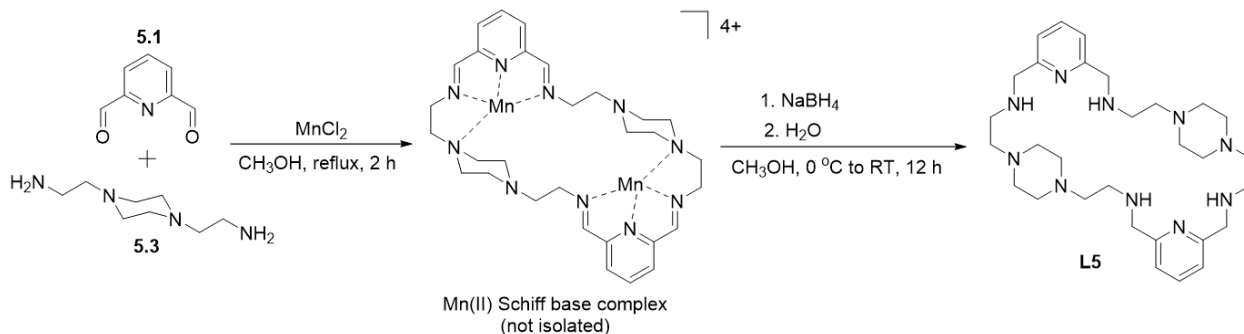
Synthesis of 1,4-bis(ethanenitrile)piperazine (5.2):

Anhydrous sodium carbonate, Na₂CO₃ (10.6 g, 0.10 mol) was added, in a single portion, to a solution of piperazine (2.15 g, 25 mmol) and chloroacetonitrile (4.53 g, 60 mmol) in absolute ethanol (100 mL). The whole mixture was then stirred under reflux conditions (80°C) for 4 h. The hot mixture was filtered, and the insoluble part was washed with hot absolute ethanol and filtered again. The combined

filtrate was condensed to 20 mL and then cooled on ice. **(5.2)** crystallized from the solution as white needles and was characterized with ^1H NMR. Yield: 3.47 g (85%). ^1H NMR (400 MHz, CDCl_3 , 25 $^\circ\text{C}$): δ = 3.54 (s, 4H), 2.68 (s, 8H). ^{13}C NMR (101 MHz, CDCl_3 , 25 $^\circ\text{C}$): δ = 114.4, 51.2, 45.8.^{377, 381}

Synthesis of 1,4-bis(2-aminoethyl)piperazine (**5.3**):

LiAlH_4 (3.23 g, 86 mmol) was cautiously weighed out in the hood and added portionwise to 120 mL of THF, which had been flushed with N_2 . **(5.2)** (3.00 g, 18 mmol) was dissolved in 120 mL of THF and added dropwise via addition funnel to the reaction mixture. Upon complete addition of **(5.2)**, the addition funnel was replaced with a condenser and the reaction was stirred under reflux conditions (65 $^\circ\text{C}$) for 4 h. Afterwards the reaction mixture was cooled on ice and was cautiously quenched with 3.0 mL of H_2O , 3.0 mL of 15% NaOH , and 9.0 mL of H_2O (in that order). The white precipitate that developed was vacuum filtered and washed with several portions of diethyl ether (4 x 50 mL). The resulting filtrate was pumped down under reduced pressure to yield **(5.3)** as an off-white viscous yellow oil, which was characterized with ^1H and ^{13}C NMR. Yield 1.81 g (57%). ^1H NMR (400 MHz, CDCl_3 , 25 $^\circ\text{C}$, TMS): δ = 2.78-2.75 (t, 4H), 2.46-2.39 (br+t, 12H). ^{13}C (101 MHz, CDCl_3 , 25 $^\circ\text{C}$): δ = 61.1, 53.3, 38.7.³⁷⁷



Scheme 5.E3. Template synthesis of **L5** ligand using MnCl_2 .

Synthesis of L5:

(**5.3**) (0.246 g, 1.465 mmol) and $\text{MnCl}_2 \cdot 4\text{H}_2\text{O}$ (0.291 g, 1.466 mmol) were dissolved in dry CH_3OH (25 mL). The solution of (**5.1**) (0.198 g, 1.460 mmol) in dry CH_3OH (15 mL) was added dropwise over 15 min. The reaction mixture was stirred under N_2 at room temperature, overnight. After cooling to $0\text{ }^\circ\text{C}$, NaBH_4 (0.763 g, 19.750 mmol) was added portionwise. The solution was left stirring overnight at RT. Water (15 mL) was slowly added, inducing the precipitation of $\text{Mn}(\text{OH})_2$ (which started to oxidize) and this suspension was stirred at RT for 1 h. CH_3OH and 10 mL of H_2O were removed *in vacuo*, and the remaining aqueous phase was vacuum filtered and rinsed with H_2O (3 x 25 mL). NaOH pellets were added to the filtrate, enough to make the solution 1 M and pH 14. The resulting basic solution was filtered again to get rid of additional $\text{Mn}(\text{OH})_2$ that had formed upon basification. The resulting basic aqueous phase was extracted with CH_2Cl_2 (9 x 25 mL). After these first extractions the aqueous phase was reduced in volume *in vacuo*. Following evaporation of part of the aqueous phase additional extractions were performed with CH_2Cl_2 (6 x 25 mL). The organic layer was dried with anhydrous Na_2SO_4 and the solvent was evaporated under reduced pressure to give **L5** as a yellow-white solid. **L5** was characterized with ^1H and ^{13}C NMR. Yield: 0.330 g (41%). ^1H NMR (400 MHz, CDCl_3 , $25\text{ }^\circ\text{C}$): $\delta = 7.58\text{--}7.54$ (t, 2 H), $7.10\text{--}7.09$ (d, 4H), 3.88 (s, 8H), $2.75\text{--}2.72$ (t, 8H), $2.57\text{--}2.52$ (t, 8H), 2.49 (br s, 16H), 2.18 (br s, 9NH). ^{13}C NMR (101 MHz, CDCl_3 , $25\text{ }^\circ\text{C}$): $\delta = 159.1, 136.7, 120.8, 58.1, 55.0, 53.4, 45.9$. ESI-MS (m/z): Found: 551.5393 (100%) [**L5**+H] $^+$, Theoretical: 551.4298 [**L5**+H] $^+$. Elemental Analysis for **L5** (basic); **L5**•1.5 H_2O Found (Calculated): C, 62.36 (62.36); H, 9.05 (9.25); N, 23.32 (24.24) %. Elemental Analysis for **L5** (acidic); **L5**•6HCl•2NaCl•3 H_2O Found (Calculated): C, 38.66 (38.31); H, 6.82 (6.65); N, 14.54 (14.89).

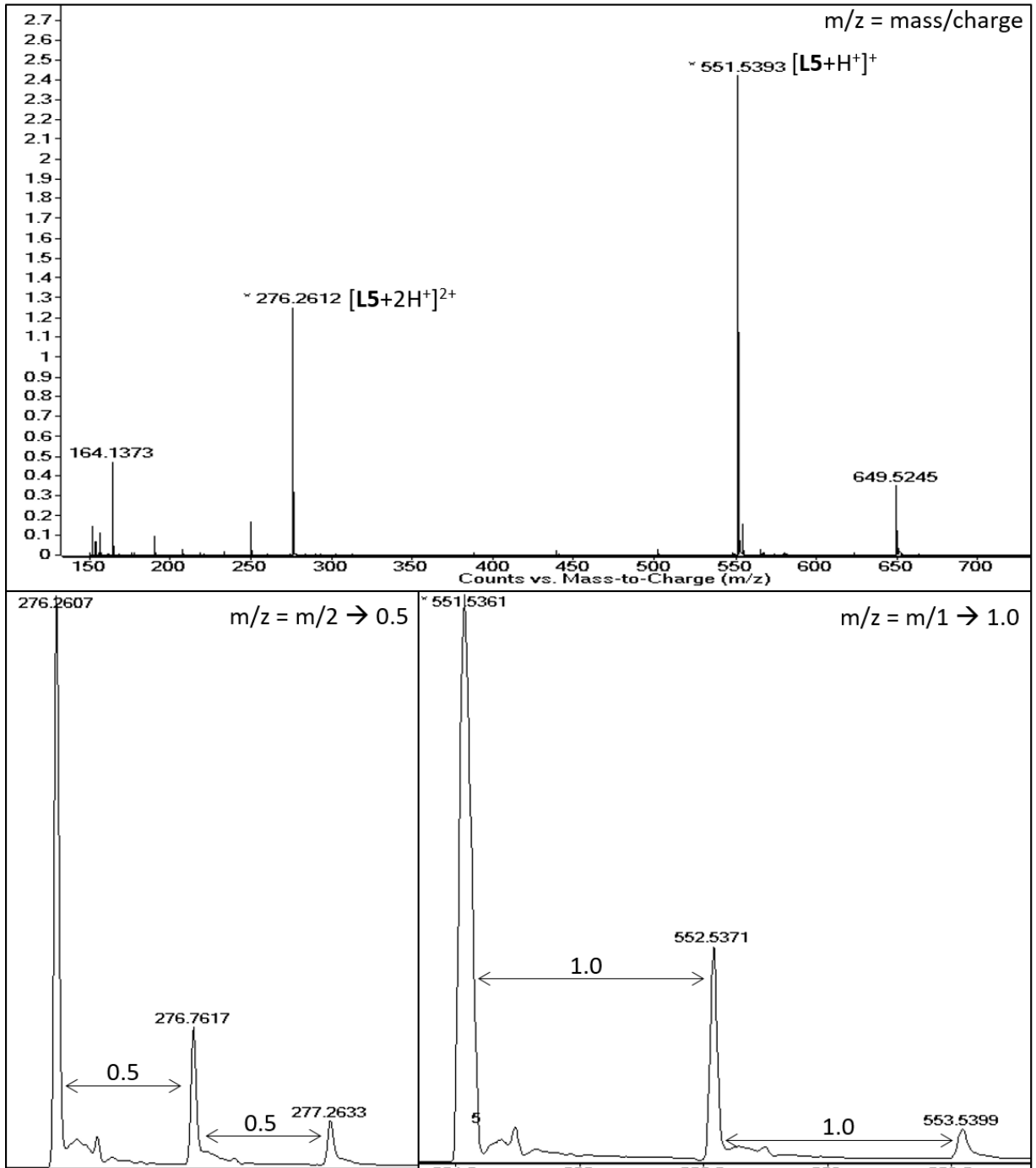


Figure 5.E1. MS of L5 with assignments and zoomed in isotopic envelopes of [$L5+2H^+]$ ²⁺ and [$L5+H^+$]⁺.

5.7.3. X-ray crystallography

A Leica MZ 75 microscope was used to identify samples suitable for analysis. A Bruker APEX-II CCD diffractometer was employed for crystal screening, unit cell determination, and data collection; which was obtained at 100 K. The Bruker D8 goniometer was controlled using the APEX3 software suite, v1.²⁰⁵ The samples were optically centered with the aid of video camera so that no translations were observed as the crystal was rotated through all positions. The X-ray radiation employed was generated from a MoK α sealed X-ray tube ($\lambda = 0.71076$) with a potential of 50 kV and a current of 30 mA; fitted with a graphite monochromator in the parallel mode (175 mm collimator with 0.5 mm pinholes).

5.7.3.1. [C₃₀H₅₀N₁₀] (L5) structure determination

Crystals of **L5** suitable for X-ray analysis were obtained by dissolving several mg of off-white powder of **L5** in CH₃Cl to provide a light-yellow solution. Slow evaporation of this solution at room temperature afforded a translucent light-yellow block-like crystal of **L5** (0.274 x 0.190 x 0.073 mm³), which was mounted on a 75 μ m cryo-loop and used for X-ray crystallographic analysis. The crystal-to-detector distance was set to 50 mm, and the exposure time was 10 s per degree for all data sets at a scan width of 0.5°. A total of 2,928 frames were collected, and the data collection was 100% complete. The frames were integrated with the Bruker SAINT Software package²⁰⁶ using a narrow frame algorithm. The integration of the data used a triclinic unit cell yielding a total of 49,846 reflections to a maximum ϑ angle of 30.14° (0.71 Å resolution) of which 6,071 reflections were independent with the $R_{\text{int}} = 5.40\%$. Data were corrected for absorption effects using the multi-scan method SADABS.²⁰⁷ Using Olex2²⁰⁸ the structure was solved with the ShelXS²⁰⁹ structure solution program using Direct Methods and refined with the SHELXL²¹⁰ refinement package using Least Squares minimization. All hydrogen and non-hydrogen atoms were refined using anisotropic thermal parameters. The thermal ellipsoid molecular plots (50%) were produced using Olex2.²⁰⁸

5.7.4. Preparation of L5Cu*

*Note: the solid isolated in this synthesis was not characterized with anything other than MS, due to the presence of both mononuclear and dinuclear Cu(II) species. Attempts to grow crystals of the complexes also failed because of the presence of multiple species.

L5 (20.0 mg, 0.036 mmol) was dissolved in H₂O (5 mL) and the pH was adjusted to 6.0 with dilute HCl (0.1 M) (as the pH of the solution dropped, the ligand became more soluble). 2 equivalents of Cu(ClO₄)₂•6H₂O (27.0 mg, 0.073 mmol) were dissolved in a small amount of H₂O (1 mL) and added dropwise to the ligand solution. Upon addition of the Cu(II) salt the solution color changed from light yellow to teal blue and the pH dropped to 2.4. This solution was stirred at RT, overnight. The H₂O was evaporated to yield a green powder. The green powder was dissolved in CH₃OH and subsequently filtered and evaporated to yield a bright green solid. A small amount of this solid was dissolved in H₂O and analyzed using MS. The rest of the green solid was dissolved in H₂O and set aside for crystal growth via slow evaporation. No X-ray quality crystals were isolated, and no yield is presented for this reaction due to the presence of mixed species. ESI-MS (m/z) Found (Theoretical): 337.1849 [L5+2Cu²⁺-2H⁺]²⁺ (337.14 [L5+2Cu²⁺-2H⁺]²⁺); 373.1645 [L5+2Cu²⁺+2Cl⁻]²⁺ and [½L5+Cu²⁺+Cl⁻]⁺ (373.11 [L5+2Cu²⁺+2Cl⁻]²⁺ and [½L5+Cu²⁺+Cl⁻]⁺); 551.4992 [L5+H⁺]⁺ (551.81 [L5+H⁺]⁺); 613.4256 [L5+Cu²⁺-H⁺]⁺ (613.34 [L5+Cu²⁺-H⁺]⁺); 648.3986 [L5+Cu²⁺+Cl⁻]⁺ (648.79 [L5+Cu²⁺+Cl⁻]⁺); 783.2740 [L5+2Cu²⁺+3Cl⁻]⁺ (783.27 [L5+2Cu²⁺+3Cl⁻]⁺); 847.2587 [L5+2Cu²⁺+2Cl⁻+ClO₄⁻]⁺ (847.23 [L5+2Cu²⁺+2Cl⁻+ClO₄⁻]⁺).

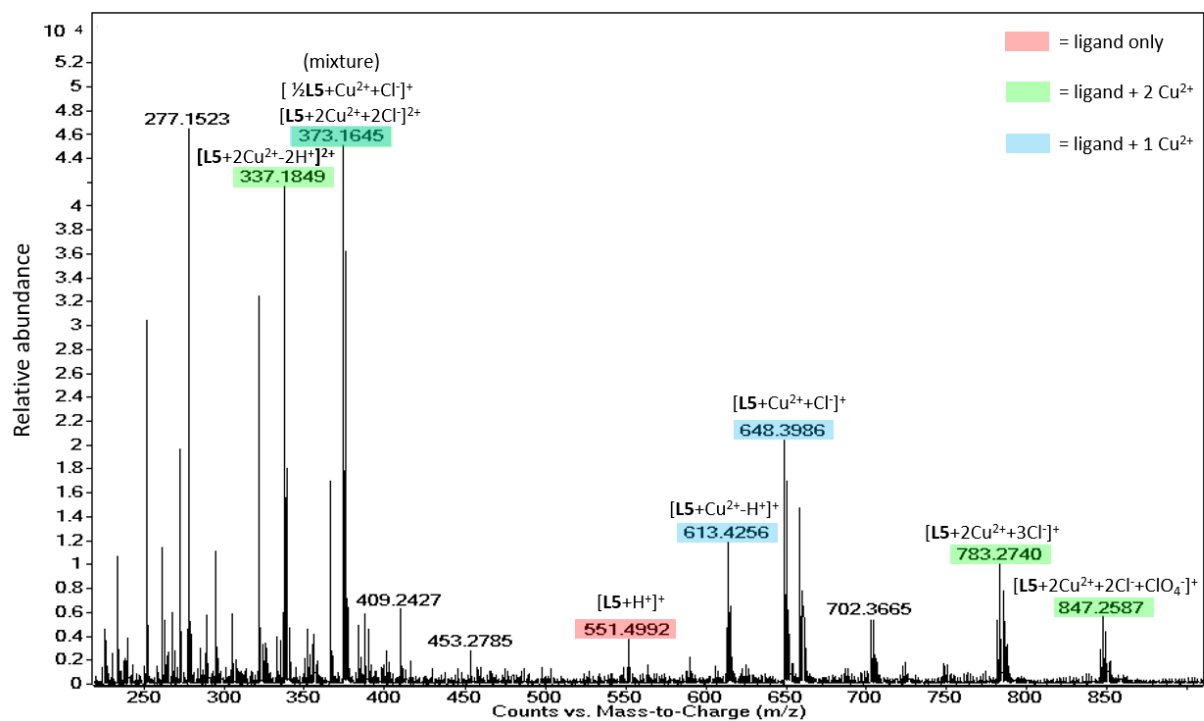


Figure 5.E2. Overall MS spectrum of L5Cu dissolved in H₂O (originally shown as figure 5.14).

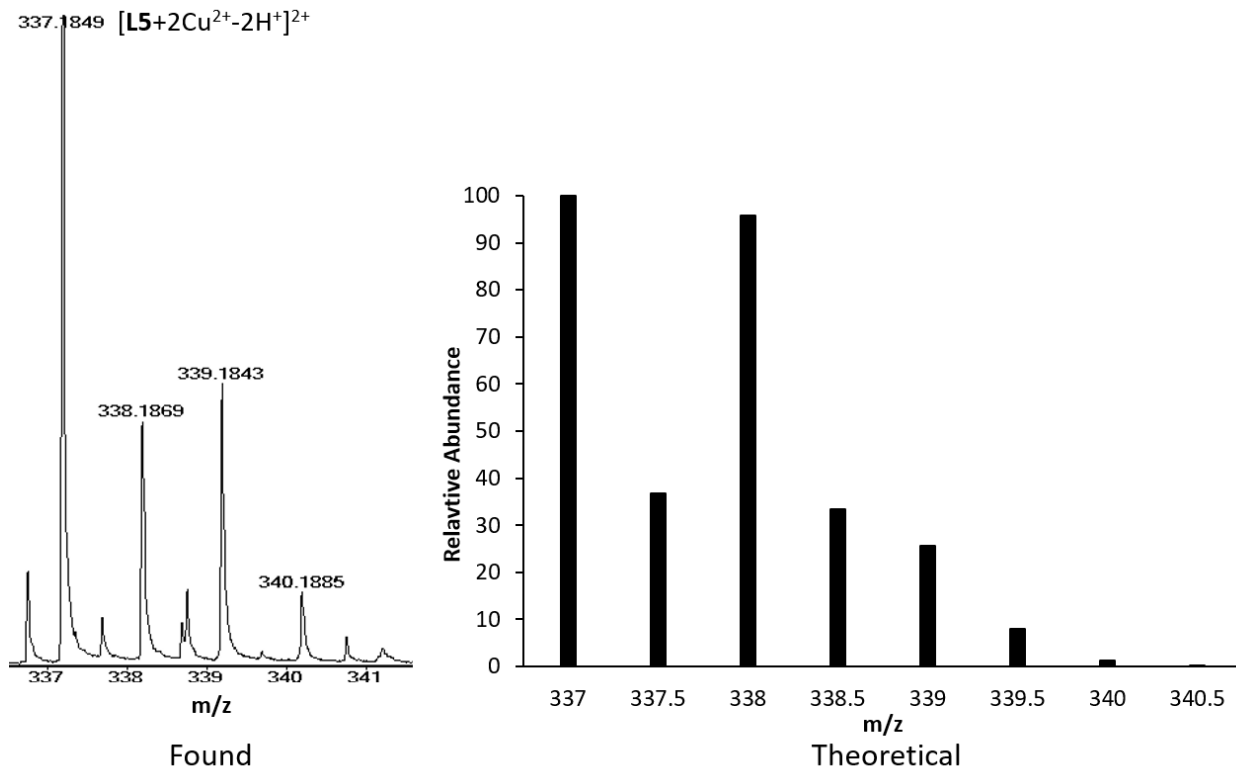


Figure 5.E3. Found vs. theoretical isotopic distribution of $[\text{L5}+2\text{Cu}^{2+}-2\text{H}^+]^{2+}$ fragment.

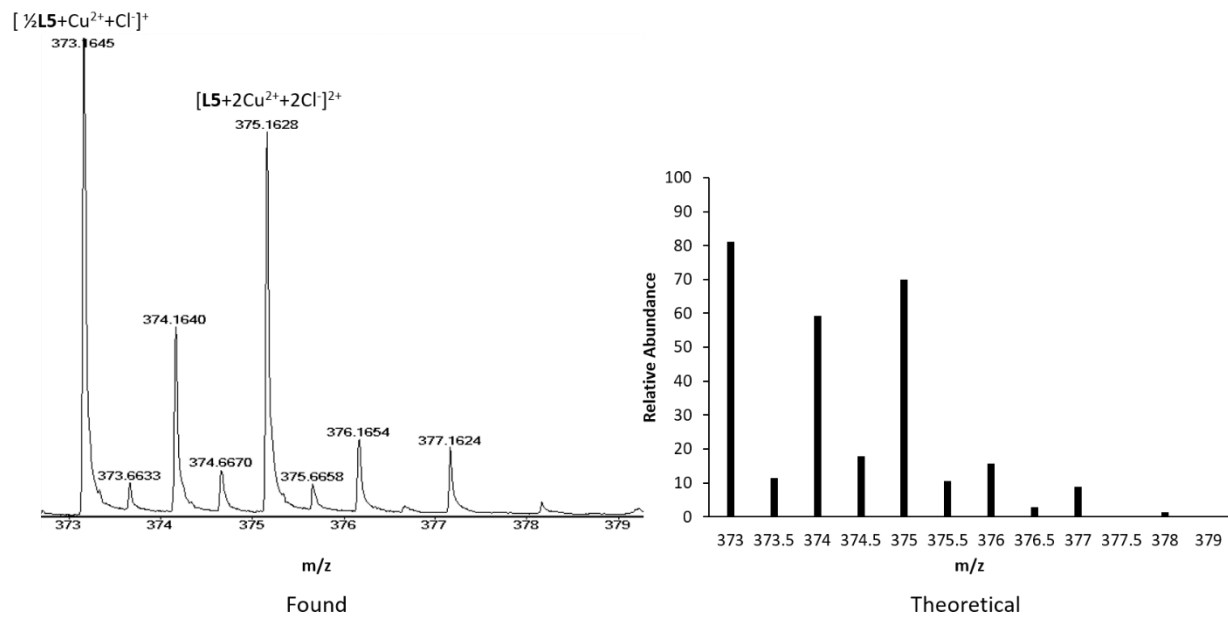


Figure 5.E4. Found vs. theoretical isotopic distribution of $[L5+2Cu^{2+}+2Cl]^{2+}$ and $[\frac{1}{2}L5+Cu^{2+}+Cl]^+$ fragments.

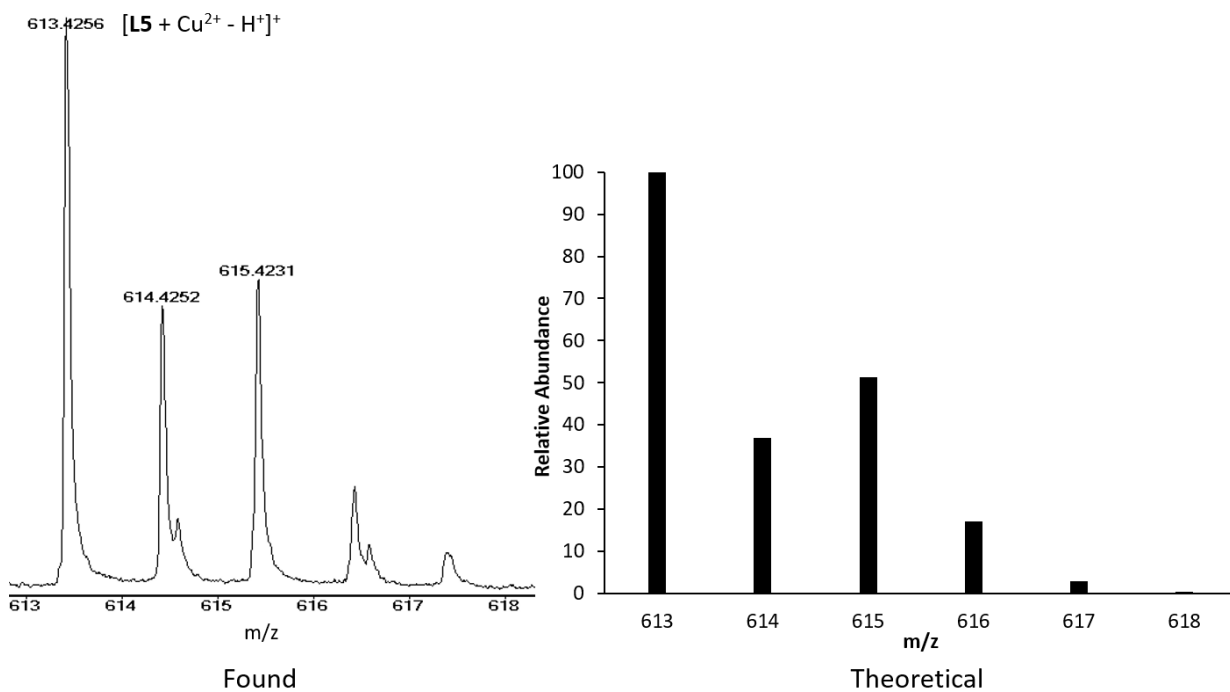


Figure 5.E5. Found vs. theoretical isotopic distribution of $[L5+Cu^{2+}-H]^+$ fragment.

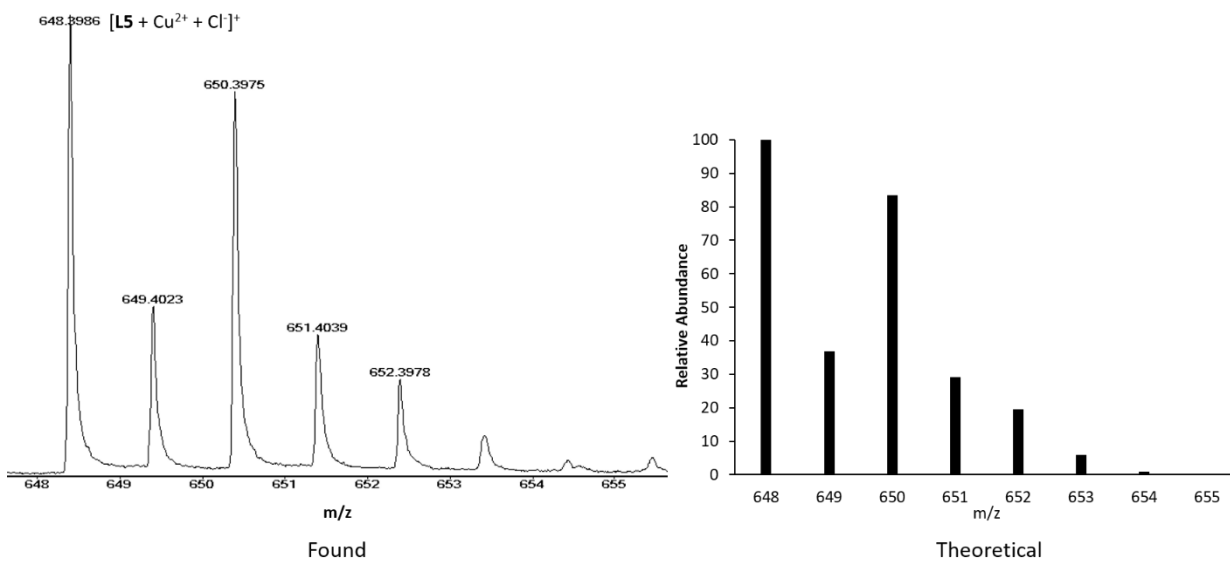


Figure 5.E6. Found vs. theoretical isotopic distribution of $[L5+Cu^{2+}+Cl]^+$ fragment.

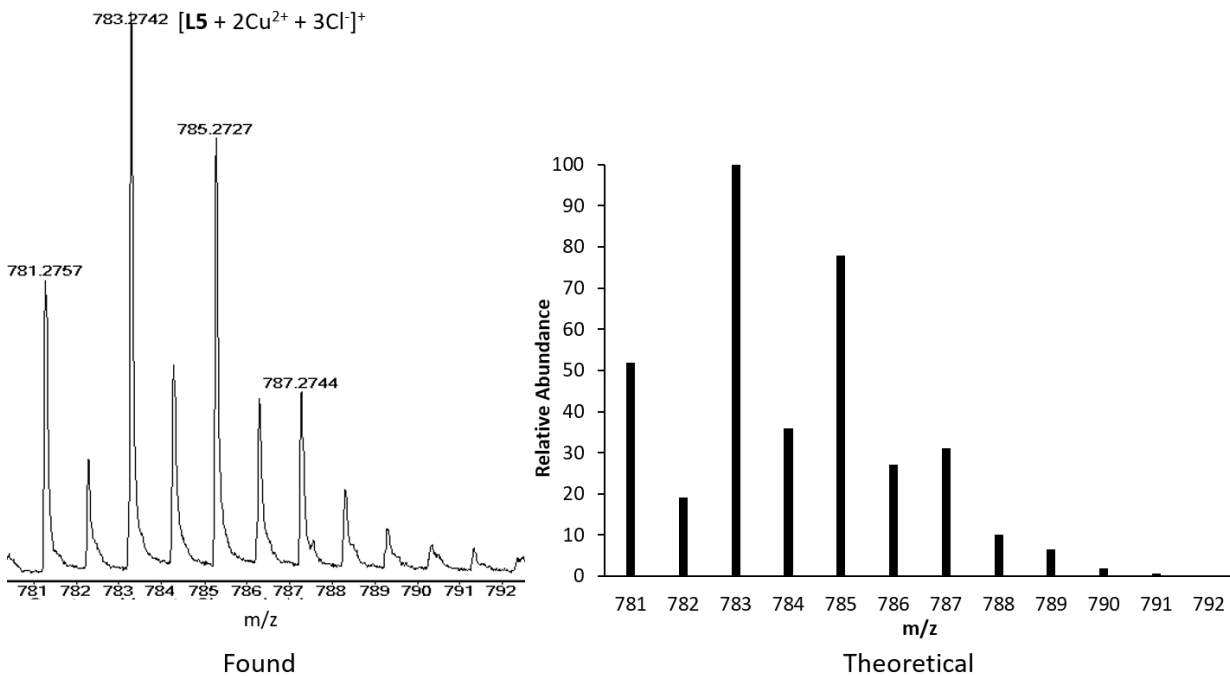


Figure 5.E7. Found vs. theoretical isotopic distribution of $[L5+2Cu^{2+}+3Cl]^+$ fragment.

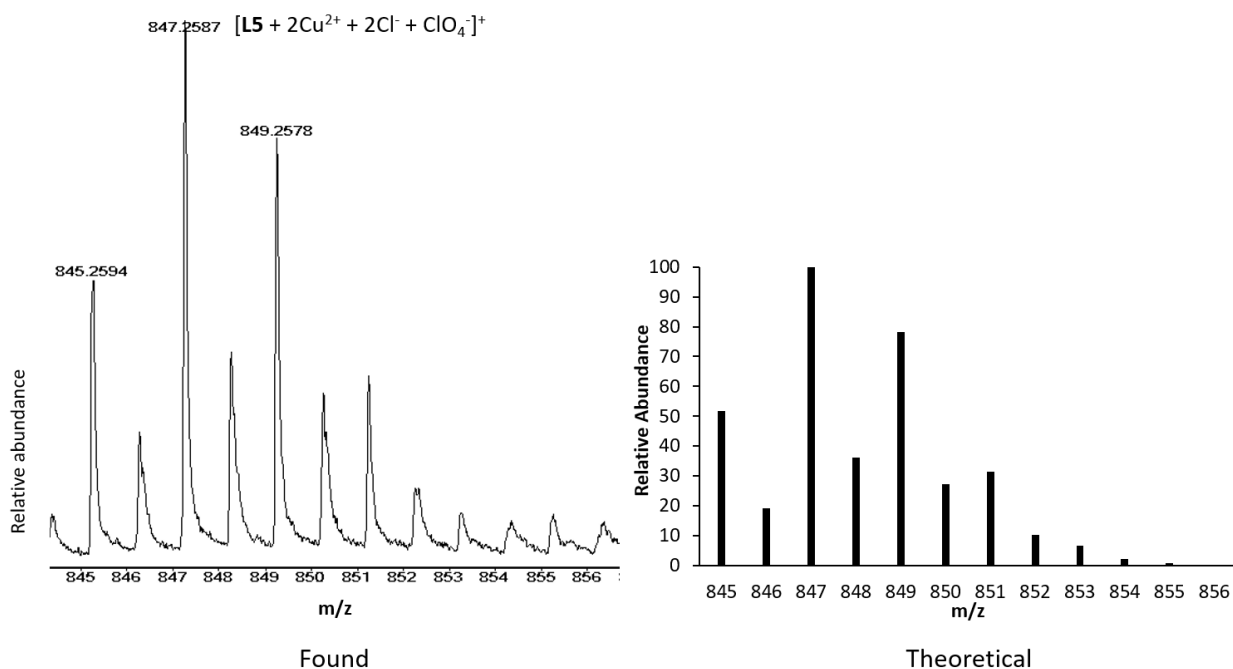


Figure 5.E8. Found vs. theoretical isotopic distribution of $[L5+2Cu^{2+}+2Cl^{-}+ClO_4^{-}]^{+}$ fragment.

5.7.5. Equilibrium measurements

The chemicals (MCl_2 salts) used in these studies were of the highest analytical grade obtained from Millipore Sigma, Alfa Aesar, or Strem Chemicals Inc. companies. The concentration of the stock solutions (≈ 50 mM) was determined by complexometric titration using a standardized Na_2H_2EDTA solution and appropriate indicators. Eriochrome Black T ($MnCl_2$, and $ZnCl_2$), 4-(2-pyridylazo)resorcinol (known as PAR) ($CuCl_2$).²¹¹

The pH-potentiometric titrations were carried out with a Metrohm 888 Titrando titration workstation, using a Metrohm 6.0233.100 combined electrode. The titrated solutions (6.00 mL) were thermostated at 25 °C, and samples were stirred and kept under an inert gas atmosphere (N_2) to avoid the effect of CO_2 . The calibration of the electrode was performed using a two-point calibration with KH-phthalate (pH = 4.005) and borax (pH = 9.177) buffers.

The concentration of the $H_6L_5^{6+}$ (where L_5 represents **L5**) was determined by pH-potentiometric titration. The protonation constants of L_5 , the stability and protonation constants of Mn(II), Fe(II), Cu(II),

and Zn(II) complexes were also determined by pH-potentiometric titration. The metal-to-ligand concentration ratios were 1:1 for Mn(II), Fe(II), Cu(II), and Zn(II) (the concentration of the ligand was generally 2-3 mM). Additionally, the metal-to-ligand concentration ratio for Cu(II) was 2:1 (the concentration of the ligand was generally 2-3 mM). In the pH-potentiometric titrations 50 – 410 mL:pH data pairs were recorded in the pH range of 1.8 – 12.0. The calculation of $[H^+]$ from the measured pH values was performed with the use of the method proposed by Irving *et al.*²¹² by titrating a 0.1 M HCl solution ($I = 0.15$ M NaCl) with a standardized NaOH solution. The differences between the measured (pH_{read}) and calculated pH ($-\log [H^+]$) values were used to obtain the equilibrium H^+ concentrations from the pH data obtained in the titrations. The ion product of water was determined from the same experiment in the pH range of 11.8-12.0. The protonation and stability constants were calculated from the titration data with the PSEQUAD program.⁴²¹

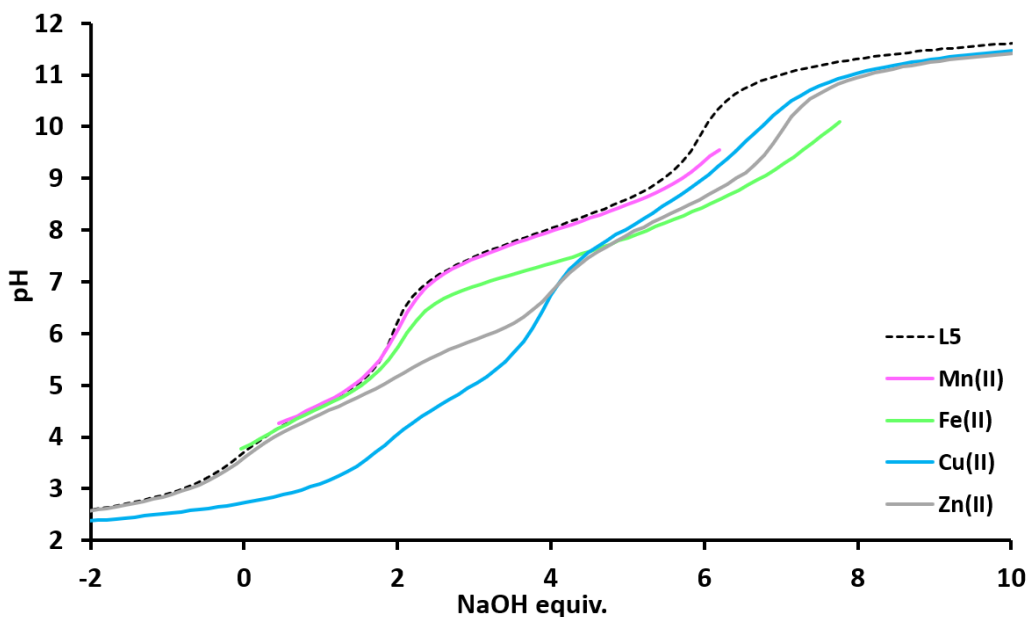


Figure 5.E9. pH-potentiometric titration curves of **L5** with and without the presence of 1 equiv. of transition metal **M(II)** (**M(II)** = Mn(II), Fe(II), Cu(II), or Zn(II)). ($I = 0.15$ M NaCl, $T = 25$ °C). Titrations in the presence of Mn(II) and Fe(II) were halted upon precipitation of metal-hydroxide species.

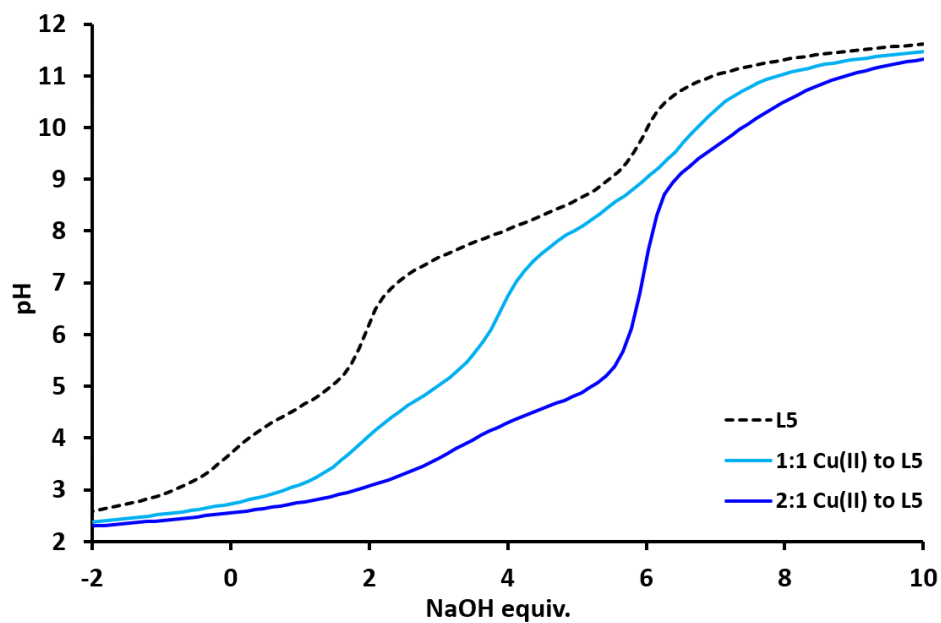


Figure 5.E10. pH-potentiometric titration curve of L5 with and without the presence of 1 or 2 equiv. of Cu(II). ($I = 0.15$ M NaCl, $T = 25$ °C).

Chapter 6: Conclusions

Macrocycles represent a broad family of unique ligands that can be utilized across many different chemical fields. Although macrocycles have many of the same attributes as their noncyclic counterparts, these ligands have exceptional coordination behavior (such as the *macrocyclic effect*) that places them in a unique ligand class.¹ Researchers have long studied the unique structural, kinetic, thermodynamic, spectral, and electrochemical properties of macrocycles and their corresponding macrocyclic complexes.^{1-4, 56, 62-63} These molecules can be utilized for various applications across many different fields, from use as biomimetic models, to catalysts, to therapeutic and diagnostic agents.

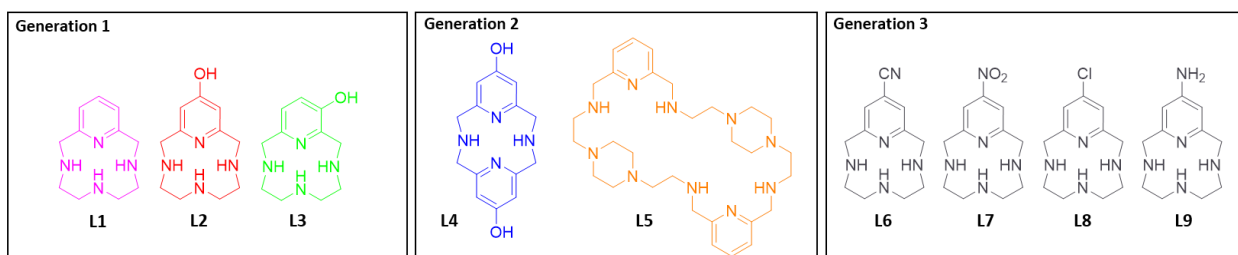
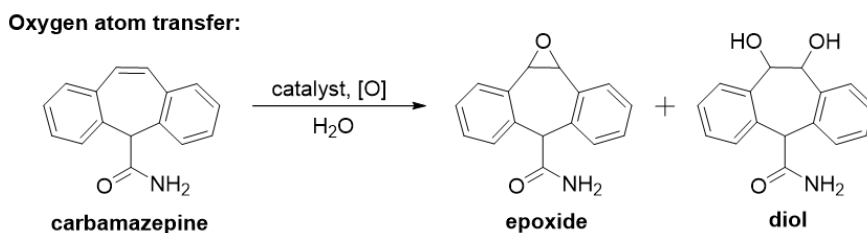


Figure 6.1. Macroyclic ligands synthesized by the Green group.^{55-56, 62, 72-73, 85-86, 422}

This work describes azamacrocycles and their corresponding transition metal complexes synthesized by the Green group (Figure 6.1). The first generation of ligands, 12-membered pyridine- and pyridol-based tetraazamacrocycles (**L1-L3**), were synthesized and complexed with first-row transition metals, including: Mn(III,IV), Fe(III), Co(III), Ni(II), Cu(II), and Zn(II).^{55-56, 62, 72-73, 85-86} The **L1-L3** macrocyclic complexes with Co(III) and Mn(III,IV) are described in chapters 3 and 4; whereas the complexes with Fe(III), Ni(II), Cu(II), and Zn(II) have been described and published elsewhere (coworker Samantha Brewer studied the Fe(III) complexes; coworker Kimberly Lincoln studied the Ni(II), Cu(II), and Zn(II) complexes).^{55-56, 72-73, 85-86} Chapter 2 and 5 report new macrocyclic ligands and the corresponding metal complexes synthesized by the Green group. The following discussion will focus on the broad conclusions from each study and highlight potential areas of future work.

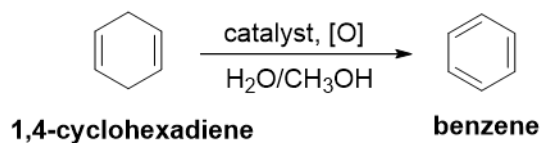
The ligand-cobalt complexes **L1Co**, **L2Co**, and **L3Co** were prepared and characterized using X-ray crystallography, UV-visible spectroscopy, and cyclic voltammetry. These complexes exhibit equilibrium behavior that parallels the classic CoCl_2 equilibrium. In water, **L1Co**, **L2Co**, and **L3Co** exist as $[\text{L1-3Co}^{\text{III}}\text{Cl}_2][\text{ClO}_4]$ (**L1Co1**, **L2Co1**, and **L3Co1**), but in DMF they exist as $[\text{L1-3Co}^{\text{III}}\text{Cl}(\text{DMF})][\text{Co}^{\text{II}}\text{Cl}_4]$ (**L1Co2**, **L2Co2**, and **L3Co2**). Ion exchange reactions were performed to eliminate the $[\text{Co}^{\text{II}}\text{Cl}_4]^{2-}$ counterions and the resulting complexes $[\text{L1-3Co}^{\text{III}}\text{Cl}(\text{DMF})][\text{BF}_4]_2$ (**L1Co3**, **L2Co3**, and **L3Co3**) were tested for catalytic abilities with several C-C coupling reactions. Results indicated that **L1Co3**, **L2Co3**, and **L3Co3** were not suitable catalysts for the reactions tested. Future studies with these ligand-cobalt complexes will focus on finding a suitable reaction to test the catalytic ability of these complexes.

Two different types of ligand-manganese complexes with **L1-L3** were synthesized: a series of monomeric Mn(III) complexes (**L1Mn2**, **L2Mn2**, and **L3Mn2**; $[\text{L1-3Mn}^{\text{III}}\text{Cl}_2][\text{ClO}_4]$) and a series of dimeric di- μ -oxo bridged Mn(III,IV) complexes (**L1Mn1**, **L2Mn1**, and **L3Mn3**; $[(\text{L1-3})_2\text{Mn}^{\text{III,IV}}\text{O}_2][\text{ClO}_4]_3$). These manganese complexes were characterized using traditional inorganic spectroscopic techniques. Additionally, these two sets of complexes were compared to structurally similar manganese complexes within the chemical literature. Di- μ -oxo bridged Mn(III,IV) complexes have historically been used to model the active site of photosystem II in plants and as water oxidation catalysts. Currently, the monomeric Mn(III) complexes **L1Mn2**, **L2Mn2**, and **L3Mn2** are being screened as oxidative catalysts in the two reactions shown in schemes 6.1 and 6.2, below. The two reactions represent two main classes of oxidation with great potential utility: oxygen atom transfer and hydrogen atom abstraction.⁴²³⁻⁴²⁵ 'Greener' catalysts (such as earth abundant transition metal complexes with manganese) may offer an alternative to expensive rare metal complexes that are typically utilized as catalysts.⁴²³⁻⁴²⁸ These catalytic studies are being conducted collaboratively with Tim Hubin at Southwestern Oklahoma State University.



Scheme 6.1. Oxygen atom transfer catalytic reaction to be studied with Mn(III) complexes.⁴²³

Hydrogen atom abstraction:



Scheme 6.2. Hydrogen atom abstraction catalytic reaction to be studied with Mn(III) complexes.⁴²³

The second generation of ligands designed and synthesized by the Green group (**L4** and **L5**; shown in figure 6.1) are discussed in chapters 2 (**L4**) and 5 (**L5**). **L4** encompasses two pyridol moieties within a tetraazamacrocyclic ring. The rationale behind this ligand design was to further enhance the antioxidant capacity exhibited by **L2** by doubling the pyridol moieties present within the molecule. **L4** was complexed to Cu(II) and Zn(II) and these metal complexes were characterized using X-ray crystallography and UV-visible spectroscopy. Protonation and stability constants of **L4** were obtained using pH-potentiometric titrations. Finally, several antioxidant assays and cell studies were performed with **L4** to determine its antioxidant capacity and therapeutic window. In the future, **L4** will be complexed with the remaining first-row transition metals (Co(III), Fe(III), Ni(II), and Mn(III)) previously studied by the Green group, to complete the series. These complexes will be characterized and compared to the Cu(II) and Zn(II) complexes with **L4**, reported in this document. Furthermore, more assays (such as the ABTS radical scavenging assay) and cell studies (with relevant cell lines) will be conducted with **L4** to continue to probe its use as a therapeutic agent. Eventually, **L4** will be used in animal studies. In addition, the catalytic activity of **L4** complexed to various transition metals will be tested. Pyridinophanes similar to **L4** (only differing in R groups) have been utilized for a variety of catalytic reactions from water oxidation with Mn(II) to C-C bond formation with

Ni(III) (Figure 6.2).⁴²⁹⁻⁴³⁷ These types of reactions will be pursued for testing the catalytic ability of **L4** transition metal complexes in the near future.

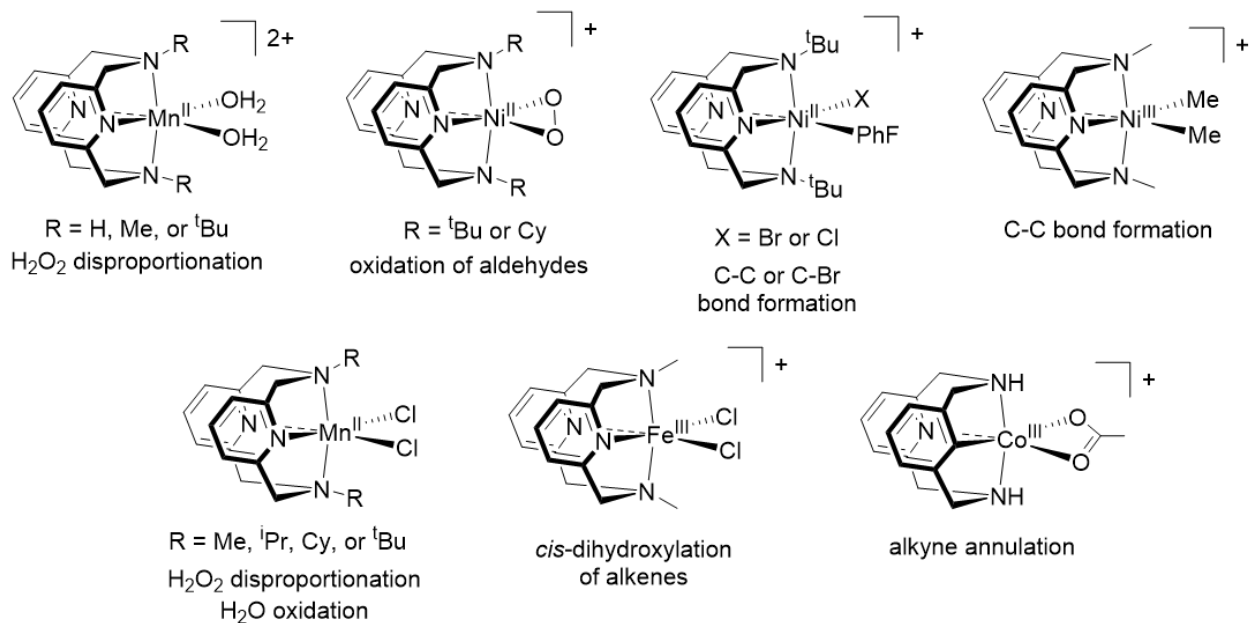
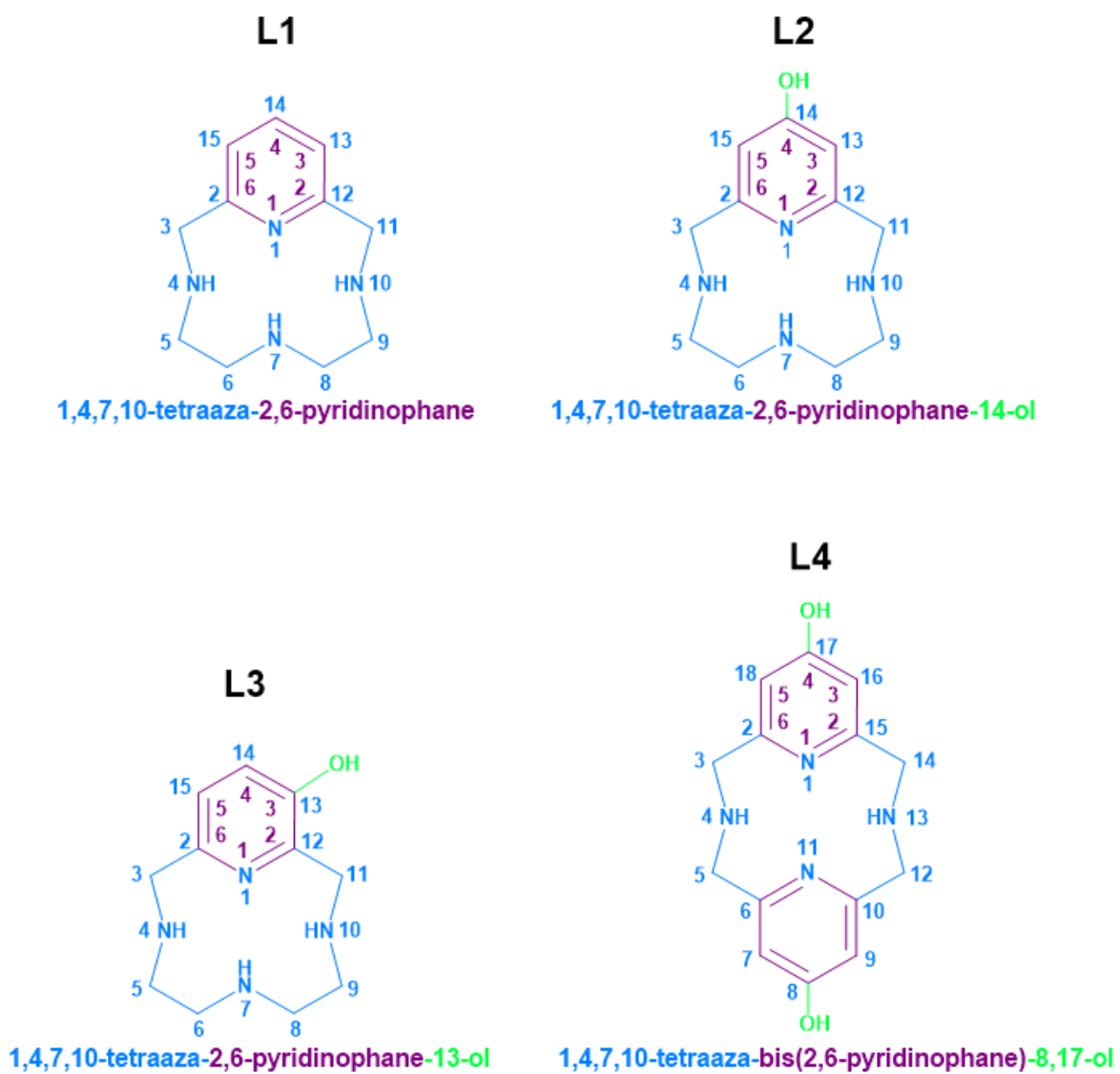


Figure 6.2. Pyridinophane-metal complexes that have been tested as catalysts in a variety of different reactions; the ligand framework and metal-binding modalities are similar to **L4**.⁴²⁹⁻⁴³⁷

Finally, **L5** was originally designed as an ultra-rigid ligand framework to be utilized as a Mn(II)-based contrast agent. Due to the presence of piperazine the ligand was isolated as a dimeric decaazamacrocycle (**L5**), which was confirmed with X-ray crystallography. pH-potentiometric titrations with **L5** indicate that it forms very weak complexes with transition metal ions. Additionally, potentiometric measurements also indicate that **L5** undergoes six protonation events in solution. The large number of protonation events indicate that **L5** may be an excellent anion receptor. Anion receptors are typically large polyazamacrocyclic rings that interact with anions (biological, inorganic, or organic) via electrostatic interactions and hydrogen bonding.^{388, 390, 399-404} Future work with this ligand will focus on finding an acceptable relevant target anion to detect in solution.

Appendix



Scheme A1. Naming scheme for pyridine- and pyridol-based tetraazamacrocycles **L1-L4**.

Complex	L1Co1	L2Co1	L3Co1	L1Co2
Simplified formula	[L1Co ^{III} Cl ₂] ₃ [ClO ₄] ₃	[L2Co ^{III} Cl ₂] ₂ [ClO ₄][Cl]	[L3Co ^{III} Cl ₂][ClO ₄]	[L1Co ^{III} Cl(DMF)][Co ^{II} Cl ₄]
Empirical formula	C ₃₃ H ₅₄ Cl ₉ Co ₃ N ₁₂ O ₁₂	C ₂₂ H ₃₆ Cl ₆ Co ₂ N ₈ O ₆	C ₁₁ H ₁₈ Cl ₃ CoN ₄ O _{5.22}	C ₁₄ H ₂₅ Cl ₅ Co ₂ N ₅ O
Formula weight	1306.72	839.16	455.05	574.50
Temperature/K	100.0	100.0	100.0	100.0
Crystal system	Monoclinic	Monoclinic	Monoclinic	Orthorhombic
Space group	P2 ₁ /c	P2 ₁ /c	P2 ₁ /c	Pbca
a/Å	6.9187(9)	6.8468(4)	6.8377(3)	13.042(2)
b/Å	26.505(4)	18.3028(13)	13.1085(7)	16.735(3)
c/Å	25.212(3)	28.2684(17)	17.9970(9)	20.520(4)
α/°	90	90	90	90
β/°	94.664(4)	94.762(5)	91.150(2)	90
γ/°	90	90	90	90
Volume/Å³	4608.1(10)	3530.2(4)	1612.78(14)	4478.7(14)
Z	4	4	4	8
ρ_{calc}/cm³	1.884	1.5788	1.874	1.704
μ/mm⁻¹	1.664	1.441	1.595	2.093
F(000)	2664.0	1718.9	927.0	2328.0
Crystal size/mm³	0.303 × 0.262 × 0.101	0.165 × 0.144 × 0.084	0.176 × 0.077 × 0.073	0.464 × 0.272 × 0.086
Radiation	Mo Kα (λ = 0.71073)	Mo Kα (λ = 0.71073)	Mo Kα (λ = 0.71073)	Mo Kα (λ = 0.71073)
2θ range for data collection/°	5.754 to 77.27	4.68 to 50.5	6.616 to 60.216	6.116 to 70.13
Index ranges	-12 ≤ h ≤ 11 -46 ≤ k ≤ 46 -44 ≤ l ≤ 38	-8 ≤ h ≤ 8 -23 ≤ k ≤ 23 -36 ≤ l ≤ 36	-9 ≤ h ≤ 9 -18 ≤ k ≤ 18 -25 ≤ l ≤ 25	-21 ≤ h ≤ 20 -26 ≤ k ≤ 26 -33 ≤ l ≤ 33
Reflections collected	139761	46094	43444	59090
Independent reflections	26110 [R _{int} = 0.0672] [R _{sigma} = 0.0588]	5883 [R _{int} = 0.0801] [R _{sigma} = 0.0884]	4742 [R _{int} = 0.1066] [R _{sigma} = 0.0880]	9867 [R _{int} = 0.0426] [R _{sigma} = 0.0323]
Data/restraints/parameters	26110/0/630	5883/0/401	4742/0/271	9867/0/258
Goodness-of-fit on F²	1.078	1.063	1.041	1.046
Final R indexes [I > 2σ (I)]	R ₁ = 0.0869 wR ₂ = 0.2028	R ₁ = 0.0529 wR ₂ = 0.1595	R ₁ = 0.0588 wR ₂ = 0.0951	R ₁ = 0.0329 wR ₂ = 0.0673
Final R indexes [all data]	R ₁ = 0.1325 wR ₂ = 0.2255	R ₁ = 0.0727 wR ₂ = 0.1652	R ₁ = 0.1184 wR ₂ = 0.1116	R ₁ = 0.0542 wR ₂ = 0.0746
Largest diff. peak/hole / e Å⁻³	4.58/-1.44	1.17/-1.27	0.83/-0.57	0.99/-0.40

Atom	Atom	Length/Å	Atom	Atom	Length/Å
C1	C2	1.382(4)	C31	N10	1.465(5)
C1	C11	1.502(4)	C32	N11	1.502(4)
C1	N4	1.350(4)	C33	N11	1.488(5)
C2	C3	1.391(5)	Cl1	Co1	2.2820(8)
C3	C4	1.390(5)	Cl2	Co1	2.2478(8)
C4	C5	1.389(4)	Cl3	O1	1.417(3)
C5	C6	1.502(5)	Cl3	O2	1.441(4)
C5	N4	1.339(4)	Cl3	O3	1.431(3)
C6	N1	1.497(4)	Cl3	O4	1.446(3)
C7	C8	1.520(5)	Cl4	Co2	2.3019(18)
C7	N1	1.495(4)	Cl4	Co4	2.261(2)
C8	N2	1.466(4)	Cl5	Co2	2.2828(18)
C9	C10	1.508(5)	Cl5	Co4	2.204(2)
C9	N2	1.469(4)	Cl6	O5	1.429(3)
C10	N3	1.502(4)	Cl6	O6	1.437(3)
C11	N3	1.491(4)	Cl6	O7	1.448(3)
C12	C13	1.392(5)	Cl6	O8	1.425(3)
C12	C22	1.486(5)	Cl7	Co3	2.327(2)
C12	N8	1.351(4)	Cl7	Co5	2.229(3)
C13	C14	1.378(6)	Cl8	Co3	2.207(3)
C14	C15	1.383(6)	Cl8	Co5	2.316(3)
C15	C16	1.393(5)	Cl9	O9	1.444(3)
C16	C17	1.503(5)	Cl9	O10	1.434(4)

C16	N8	1.339(4)	C19	O11	1.430(3)
C17	N5	1.497(5)	C19	O12	1.448(4)
C18	C19	1.504(5)	Co3	N9	2.034(4)
C18	N5	1.501(4)	Co3	N10	1.889(4)
C19	N6	1.467(5)	Co3	N11	1.947(4)
C20	C21	1.519(5)	Co3	N12	1.908(4)
C20	N6	1.468(5)	Co1	N1	1.992(2)
C21	N7	1.493(4)	Co1	N2	1.945(3)
C22	N7	1.491(5)	Co1	N3	1.982(3)
C23	C24	1.373(5)	Co1	N4	1.855(2)
C23	C33	1.489(5)	Co2	N5	2.070(3)
C23	N12	1.352(4)	Co2	N6	1.936(3)
C24	C25	1.385(6)	Co2	N7	1.905(3)
C25	C26	1.383(6)	Co2	N8	1.823(3)
C26	C27	1.398(5)	N5	Co4	1.896(3)
C27	C28	1.501(5)	N6	Co4	1.980(4)
C27	N12	1.336(4)	N7	Co4	2.105(3)
C28	N9	1.510(5)	N8	Co4	1.908(3)
C29	C30	1.516(5)	N9	Co5	1.952(4)
C29	N9	1.495(4)	N10	Co5	1.992(4)
C30	N10	1.463(4)	N11	Co5	2.027(4)
C31	C32	1.513(5)	N12	Co5	1.797(4)

Table A3. Bond angles (°) for [L1Co^{III}Cl₂]₃[ClO₄]₃(L1Co1).

Atom	Atom	Atom	Angle/°	Atom	Atom	Atom	Angle/°
C2	C1	C11	125.0(3)	N6	Co2	Cl5	87.61(11)
N4	C1	C2	120.3(3)	N6	Co2	N5	83.74(13)
N4	C1	C11	114.3(3)	N7	Co2	Cl4	96.12(11)
C1	C2	C3	118.1(3)	N7	Co2	Cl5	96.12(11)
C4	C3	C2	120.5(3)	N7	Co2	N5	166.93(15)
C5	C4	C3	118.9(3)	N7	Co2	N6	88.26(14)
C4	C5	C6	126.5(3)	N8	Co2	Cl4	87.98(11)
N4	C5	C4	119.5(3)	N8	Co2	Cl5	175.69(13)
N4	C5	C6	113.8(3)	N8	Co2	N5	83.06(14)
N1	C6	C5	110.7(2)	N8	Co2	N6	95.02(14)
N1	C7	C8	107.5(2)	N8	Co2	N7	87.39(14)
N2	C8	C7	104.5(3)	C6	N1	Co1	109.52(18)
N2	C9	C10	104.4(3)	C7	N1	C6	111.9(3)
N3	C10	C9	107.6(2)	C7	N1	Co1	106.81(19)
N3	C11	C1	109.7(2)	C8	N2	C9	118.2(3)
C13	C12	C22	124.9(3)	C8	N2	Co1	110.58(19)
N8	C12	C13	120.4(3)	C9	N2	Co1	110.6(2)
N8	C12	C22	114.5(3)	C10	N3	Co1	107.90(19)
C14	C13	C12	118.2(4)	C11	N3	C10	112.3(3)
C13	C14	C15	120.9(3)	C11	N3	Co1	109.09(18)
C14	C15	C16	118.7(4)	C1	N4	Co1	117.6(2)
C15	C16	C17	126.3(3)	C5	N4	C1	122.5(3)
N8	C16	C15	120.0(4)	C5	N4	Co1	119.3(2)
N8	C16	C17	113.5(3)	C17	N5	C18	112.3(3)
N5	C17	C16	110.5(3)	C17	N5	Co2	108.0(2)
N5	C18	C19	107.9(3)	C17	N5	Co4	110.3(2)
N6	C19	C18	105.1(3)	C18	N5	Co2	106.5(2)
N6	C20	C21	104.6(3)	C18	N5	Co4	107.5(2)
N7	C21	C20	107.6(3)	Co4	N5	Co2	3.48(10)
C12	C22	N7	110.1(3)	C19	N6	C20	118.8(3)
C24	C23	C33	124.9(3)	C19	N6	Co2	111.9(2)
N12	C23	C24	120.5(3)	C19	N6	Co4	107.9(2)
N12	C23	C33	114.4(3)	C20	N6	Co2	107.6(2)
C23	C24	C25	118.3(3)	C20	N6	Co4	113.7(2)
C26	C25	C24	120.6(3)	Co2	N6	Co4	6.07(8)
C25	C26	C27	119.1(3)	C21	N7	Co2	107.0(2)
C26	C27	C28	126.7(3)	C21	N7	Co4	107.3(2)

N12	C27	C26	118.9(3)	C22	N7	C21	111.7(3)
N12	C27	C28	114.3(3)	C22	N7	Co2	109.5(2)
C27	C28	N9	110.7(3)	C22	N7	Co4	111.0(2)
N9	C29	C30	107.3(2)	Co2	N7	Co4	1.99(10)
N10	C30	C29	104.7(3)	C12	N8	Co2	116.1(2)
N10	C31	C32	103.8(3)	C12	N8	Co4	121.7(2)
N11	C32	C31	107.7(3)	C16	N8	C12	121.7(3)
N11	C33	C23	110.3(3)	C16	N8	Co2	121.9(2)
O1	C13	O2	110.8(3)	C16	N8	Co4	116.0(2)
O1	C13	O3	111.6(2)	Co2	N8	Co4	5.97(9)
O1	C13	O4	109.8(2)	C28	N9	Co3	111.1(2)
O2	C13	O4	107.1(3)	C28	N9	Co5	107.7(2)
O3	C13	O2	107.8(2)	C29	N9	C28	111.5(3)
O3	C13	O4	109.7(2)	C29	N9	Co3	104.4(2)
Co4	C14	Co2	5.22(7)	C29	N9	Co5	108.2(2)
Co4	C15	Co2	5.02(7)	Co5	N9	Co3	4.21(12)
O5	C16	O6	109.1(2)	C30	N10	C31	118.2(3)
O5	C16	O7	110.71(19)	C30	N10	Co3	112.6(2)
O6	C16	O7	108.7(2)	C30	N10	Co5	109.3(2)
O8	C16	O5	109.9(2)	C31	N10	Co3	110.7(2)
O8	C16	O6	109.2(3)	C31	N10	Co5	111.4(2)
O8	C16	O7	109.2(2)	Co3	N10	Co5	3.90(14)
Co5	C17	Co3	3.42(12)	C32	N11	Co3	106.5(2)
Co3	C18	Co5	3.24(12)	C32	N11	Co5	109.8(2)
O9	C19	O12	109.7(2)	C33	N11	C32	112.1(3)
O10	C19	O9	111.2(2)	C33	N11	Co3	110.7(2)
O10	C19	O12	106.8(3)	C33	N11	Co5	106.6(2)
O11	C19	O9	109.4(2)	Co3	N11	Co5	4.25(13)
O11	C19	O10	110.2(3)	C23	N12	Co3	116.4(2)
O11	C19	O12	109.6(3)	C23	N12	Co5	118.6(3)
C18	Co3	C17	89.67(10)	C27	N12	C23	122.5(3)
N9	Co3	C17	93.04(12)	C27	N12	Co3	120.5(2)
N9	Co3	C18	96.62(13)	C27	N12	Co5	117.8(2)
N10	Co3	C17	178.50(17)	Co5	N12	Co3	3.90(14)
N10	Co3	C18	91.32(13)	C15	Co4	C14	92.23(8)
N10	Co3	N9	85.73(15)	N5	Co4	C14	98.63(12)
N10	Co3	N11	87.03(15)	N5	Co4	C15	101.61(13)
N10	Co3	N12	93.41(17)	N5	Co4	N6	87.31(15)
N11	Co3	C17	93.96(13)	N5	Co4	N7	161.57(17)
N11	Co3	C18	97.30(14)	N5	Co4	N8	85.74(15)
N11	Co3	N9	164.44(19)	N6	Co4	C14	173.64(13)
N12	Co3	C17	85.57(11)	N6	Co4	C15	88.79(12)
N12	Co3	C18	175.06(15)	N6	Co4	N7	81.74(13)
N12	Co3	N9	82.33(15)	N7	Co4	C14	91.93(11)
N12	Co3	N11	84.37(16)	N7	Co4	C15	92.97(11)
C12	Co1	C11	90.51(3)	N8	Co4	C14	87.19(11)
N1	Co1	C11	94.25(8)	N8	Co4	C15	172.62(12)
N1	Co1	C12	95.99(8)	N8	Co4	N6	91.00(15)
N2	Co1	C11	178.85(9)	N8	Co4	N7	79.71(13)
N2	Co1	C12	88.40(8)	C17	Co5	C18	89.43(10)
N2	Co1	N1	85.49(11)	N9	Co5	C17	98.43(13)
N2	Co1	N3	85.01(11)	N9	Co5	C18	95.53(14)
N3	Co1	C11	95.46(8)	N9	Co5	N10	85.23(16)
N3	Co1	C12	94.99(8)	N9	Co5	N11	164.9(2)
N3	Co1	N1	165.25(11)	N10	Co5	C17	174.14(16)
N4	Co1	C11	87.69(8)	N10	Co5	C18	85.65(12)
N4	Co1	C12	178.19(8)	N10	Co5	N11	82.19(15)
N4	Co1	N1	84.39(11)	N11	Co5	C17	94.80(14)
N4	Co1	N2	93.40(11)	N11	Co5	C18	91.74(13)
N4	Co1	N3	84.94(11)	N12	Co5	C17	91.22(13)
C15	Co2	C14	89.15(6)	N12	Co5	C18	176.72(18)
N5	Co2	C14	92.44(10)	N12	Co5	N9	87.56(16)
N5	Co2	C15	93.85(11)	N12	Co5	N10	93.51(17)

N6	Co2	Cl4	174.81(13)	N12	Co5	N11	85.00(17)
----	-----	-----	------------	-----	-----	-----	-----------

Table A4. Bond lengths (Å) for [L1Co^{III}Cl(DMF)][Co^ICl₄] (L1Co2).

Atom	Atom	Length/Å	Atom	Atom	Length/Å
C1	N4	1.3417(18)	C11	N3	1.4971(19)
C1	C2	1.380(2)	C12	O1	1.2609(17)
C1	C11	1.496(2)	C12	N5	1.3049(18)
C2	C3	1.385(2)	C13	N5	1.4553(19)
C3	C4	1.387(2)	C14	N5	1.462(2)
C4	C5	1.380(2)	Cl1	Co1	2.2411(5)
C5	N4	1.3424(17)	Cl2	Co2	2.2745(5)
C5	C6	1.494(2)	Cl3	Co2	2.2687(5)
C6	N1	1.4967(18)	Cl4	Co2	2.2942(5)
C7	N1	1.4921(18)	Cl5	Co2	2.2862(5)
C7	C8	1.516(2)	Co1	N4	1.8536(11)
C8	N2	1.4749(18)	Co1	O1	1.9250(10)
C9	N2	1.4741(18)	Co1	N2	1.9326(12)
C9	C10	1.514(2)	Co1	N1	1.9703(12)
C10	N3	1.4984(19)	Co1	N3	1.9882(12)

Table A5. Bond Angles (°) for [L1Co^{III}Cl(DMF)][Co^ICl₄] (L1Co2).

Atom	Atom	Atom	Angle/°	Atom	Atom	Atom	Angle/°
N4	C1	C2	120.29(13)	O1	Co1	Cl1	92.66(3)
N4	C1	C11	113.36(12)	N2	Co1	Cl1	176.97(4)
C2	C1	C11	125.99(13)	N1	Co1	Cl1	94.33(4)
C1	C2	C3	118.39(14)	N3	Co1	Cl1	95.02(4)
C2	C3	C4	120.54(14)	Cl3	Co2	Cl2	109.550(17)
C5	C4	C3	118.60(14)	Cl3	Co2	Cl5	111.076(16)
N4	C5	C4	120.06(13)	Cl2	Co2	Cl5	108.181(17)
N4	C5	C6	114.23(12)	Cl3	Co2	Cl4	108.54(2)
C4	C5	C6	125.49(13)	Cl2	Co2	Cl4	106.791(17)
C5	C6	N1	110.36(11)	Cl5	Co2	Cl4	112.588(16)
N1	C7	C8	107.20(11)	C7	N1	C6	112.36(11)
N2	C8	C7	104.56(11)	C7	N1	Co1	107.03(8)
N2	C9	C10	104.36(11)	C6	N1	Co1	110.24(9)
N3	C10	C9	108.40(11)	C9	N2	C8	118.23(11)
C1	C11	N3	109.90(11)	C9	N2	Co1	110.43(9)
O1	C12	N5	122.24(13)	C8	N2	Co1	110.88(9)
N4	Co1	O1	176.29(5)	C11	N3	C10	113.25(12)
N4	Co1	N2	94.56(5)	C11	N3	Co1	108.27(9)
O1	Co1	N2	84.32(5)	C10	N3	Co1	107.83(9)
N4	Co1	N1	84.78(5)	C1	N4	C5	122.04(12)
O1	Co1	N1	91.61(5)	C1	N4	Co1	118.79(9)
N2	Co1	N1	85.80(5)	C5	N4	Co1	118.67(10)
N4	Co1	N3	84.19(5)	C12	N5	C13	121.27(13)
O1	Co1	N3	99.22(5)	C12	N5	C14	121.90(12)
N2	Co1	N3	85.46(5)	C13	N5	C14	116.68(13)
N1	Co1	N3	165.33(5)	C12	O1	Co1	126.29(9)
N4	Co1	Cl1	88.46(4)				

Table A6. Bond lengths (Å) for [L2Co^{III}Cl₂]₂[ClO₄][Cl] (L2Co1).

Atom	Atom	Length/Å	Atom	Atom	Length/Å
Co1	Cl2	2.2765(13)	N8	C20	1.495(6)
Co1	Cl1	2.2470(13)	N5	C21	1.338(6)
Co1	N2	1.978(4)	N5	C14	1.337(6)
Co1	N1	1.858(4)	N6	C15	1.503(6)
Co1	N3	1.946(4)	N6	C16	1.499(6)
Co1	N4	1.995(4)	N3	C7	1.482(6)
Co2	Cl4	2.2549(14)	N3	C6	1.464(6)
Co2	Cl3	2.2449(14)	N4	C9	1.514(6)

Co2	N7	1.949(4)	N4	C8	1.498(6)
Co2	N8	2.002(4)	C10	C11	1.393(7)
Co2	N5	1.872(4)	C10	C9	1.471(7)
Co2	N6	1.963(4)	C11	C1	1.393(7)
Cl5	O4	1.437(4)	C5	C6	1.503(7)
Cl5	O3	1.452(4)	C13	C14	1.356(7)
Cl5	O5	1.443(4)	C13	C12	1.395(8)
Cl5	O6	1.432(4)	C21	C22	1.399(7)
O1	C1	1.336(6)	C21	C20	1.503(7)
N2	C5	1.497(6)	C14	C15	1.499(7)
N2	C4	1.501(6)	C4	C3	1.508(7)
O2	C12	1.327(6)	C12	C22	1.392(7)
N1	C10	1.370(6)	C1	C2	1.390(7)
N1	C3	1.340(6)	C19	C18	1.511(7)
N7	C17	1.481(6)	C3	C2	1.364(7)
N7	C18	1.468(6)	C8	C7	1.493(7)
N8	C19	1.500(6)	C17	C16	1.508(7)

Table A7. Bond angles (°) for [L2Co^{III}Cl₂]₂[ClO₄][Cl] (L2Co1).

Atom	Atom	Atom	Angle/°	Atom	Atom	Atom	Angle/°
Cl1	Co1	Cl2	89.58(5)	C20	N8	C19	111.7(4)
N2	Co1	Cl2	95.72(12)	C21	N5	Co2	119.0(3)
N2	Co1	Cl1	96.04(12)	C14	N5	Co2	118.7(4)
N1	Co1	Cl2	89.05(12)	C14	N5	C21	122.3(5)
N1	Co1	Cl1	178.60(12)	C15	N6	Co2	109.3(3)
N1	Co1	N2	83.77(17)	C16	N6	Co2	108.5(3)
N3	Co1	Cl2	178.14(13)	C16	N6	C15	112.2(4)
N3	Co1	Cl1	88.61(13)	C7	N3	Co1	109.9(3)
N3	Co1	N2	84.95(17)	C6	N3	Co1	110.6(3)
N3	Co1	N1	92.75(17)	C6	N3	C7	118.5(4)
N4	Co1	Cl2	94.38(12)	C9	N4	Co1	108.7(3)
N4	Co1	Cl1	96.23(12)	C8	N4	Co1	107.4(3)
N4	Co1	N2	164.14(16)	C8	N4	C9	111.7(4)
N4	Co1	N1	84.20(17)	C11	C10	N1	118.4(5)
N4	Co1	N3	85.34(17)	C9	C10	N1	113.8(4)
Cl3	Co2	Cl4	91.14(5)	C9	C10	C11	127.7(5)
N7	Co2	Cl4	178.42(13)	C1	C11	C10	119.8(5)
N7	Co2	Cl3	87.31(12)	C6	C5	N2	106.7(4)
N8	Co2	Cl4	94.97(12)	C12	C13	C14	119.2(5)
N8	Co2	Cl3	96.73(12)	C22	C21	N5	120.0(5)
N8	Co2	N7	85.57(17)	C20	C21	N5	114.0(4)
N5	Co2	Cl4	88.84(13)	C20	C21	C22	125.9(5)
N5	Co2	Cl3	179.18(14)	C13	C14	N5	120.5(5)
N5	Co2	N7	92.70(17)	C15	C14	N5	113.1(5)
N5	Co2	N8	84.09(17)	C15	C14	C13	126.2(5)
N6	Co2	Cl4	94.41(13)	C3	C4	N2	109.7(4)
N6	Co2	Cl3	94.86(13)	C13	C12	O2	117.3(5)
N6	Co2	N7	85.37(18)	C22	C12	O2	122.7(5)
N6	Co2	N8	164.92(17)	C22	C12	C13	120.0(5)
N6	Co2	N5	84.32(18)	C11	C1	O1	117.6(5)
O3	Cl5	O4	109.6(2)	C2	C1	O1	122.6(5)
O5	Cl5	O4	108.0(2)	C2	C1	C11	119.8(5)
O5	Cl5	O3	108.9(2)	C18	C19	N8	107.7(4)
O6	Cl5	O4	110.8(2)	C12	C22	C21	117.8(5)
O6	Cl5	O3	109.2(2)	C4	C3	N1	112.7(4)
O6	Cl5	O5	110.3(2)	C2	C3	N1	121.9(5)
C5	N2	Co1	108.0(3)	C2	C3	C4	125.3(5)
C4	N2	Co1	110.3(3)	C10	C9	N4	109.8(4)
C4	N2	C5	111.4(4)	C14	C15	N6	109.8(4)
C10	N1	Co1	118.4(3)	C7	C8	N4	108.5(4)
C3	N1	Co1	120.2(3)	C16	C17	N7	104.6(4)
C3	N1	C10	121.3(4)	C8	C7	N3	104.9(4)

C17	N7	Co2	109.8(3)	C5	C6	N3	105.6(4)
C18	N7	Co2	110.2(3)	C21	C20	N8	110.2(4)
C18	N7	C17	119.3(4)	C3	C2	C1	118.5(5)
C19	N8	Co2	106.2(3)	C17	C16	N6	106.9(4)
C20	N8	Co2	109.5(3)	C19	C18	N7	104.9(4)

Table A8. Bond lengths (Å) for [L3Co^{III}Cl₂][ClO₄] (L3Co1).

Atom	Atom	Length/Å	Atom	Atom	Length/Å
Co1	Cl1	2.268(7)	C4	C5	1.384(5)
Co1	Cl2	2.233(9)	C3	C2	1.384(5)
Co1	N4	1.865(3)	O1	C2	1.352(4)
Co1	N3	1.968(3)	N4	C5	1.341(4)
Co1	N2	1.935(3)	N4	C1	1.339(4)
Co1	N1	1.963(3)	N3	C11	1.495(4)
Co1	Cl3	2.298(7)	N3	C10	1.490(5)
Cl4	O4	1.389(3)	N2	C9	1.473(4)
Cl4	O7	1.556(5)	N2	C8	1.472(4)
Cl4	O5	1.437(5)	N1	C7	1.487(5)
Cl4	O9	1.606(7)	N1	C6	1.500(5)
Cl4	O2	1.327(7)	C5	C6	1.500(5)
Cl4	O3	1.325(5)	C2	C1	1.379(5)
Cl4	O6	1.515(18)	C1	C11	1.490(5)
Cl4	O8	1.32(2)	C10	C9	1.505(5)
C4	C3	1.386(5)	C8	C7	1.510(5)

Table A9. Bond angles (°) for [L3Co^{III}Cl₂][ClO₄] (L3Co1).

Atom	Atom	Atom	Angle/°	Atom	Atom	Atom	Angle/°
Cl2	Co1	Cl1	90.02(18)	O8	Cl4	O6	112(3)
N4	Co1	Cl1	87.50(19)	C5	C4	C3	119.3(3)
N4	Co1	Cl2	177.48(9)	C2	C3	C4	119.7(3)
N4	Co1	N3	84.39(12)	C5	N4	Co1	118.7(2)
N4	Co1	N2	94.66(12)	C1	N4	Co1	117.9(2)
N4	Co1	N1	84.71(12)	C1	N4	C5	122.6(3)
N4	Co1	Cl3	86.13(19)	C11	N3	Co1	110.2(2)
N3	Co1	Cl1	89.42(13)	C10	N3	Co1	107.5(2)
N3	Co1	Cl2	96.05(9)	C10	N3	C11	111.8(3)
N3	Co1	Cl3	99.99(13)	C9	N2	Co1	110.2(2)
N2	Co1	Cl1	174.12(13)	C8	N2	Co1	110.1(2)
N2	Co1	Cl2	87.85(9)	C8	N2	C9	118.9(3)
N2	Co1	N3	85.35(12)	C7	N1	Co1	107.4(2)
N2	Co1	N1	86.00(12)	C7	N1	C6	112.7(3)
N2	Co1	Cl3	174.65(13)	C6	N1	Co1	109.8(2)
N1	Co1	Cl1	99.66(13)	C4	C5	C6	126.8(3)
N1	Co1	Cl2	95.26(9)	N4	C5	C4	119.3(3)
N1	Co1	N3	165.48(12)	N4	C5	C6	113.5(3)
N1	Co1	Cl3	88.82(13)	O1	C2	C3	125.2(3)
O4	Cl4	O7	98.6(3)	O1	C2	C1	115.7(3)
O4	Cl4	O5	110.7(3)	C1	C2	C3	119.1(3)
O5	Cl4	O7	100.5(5)	N4	C1	C2	119.9(3)
O2	Cl4	O9	103.0(6)	N4	C1	C11	114.8(3)
O2	Cl4	O6	77.7(11)	C2	C1	C11	125.0(3)
O3	Cl4	O4	119.8(4)	C1	C11	N3	109.9(3)
O3	Cl4	O7	107.8(5)	N3	C10	C9	107.6(3)
O3	Cl4	O5	115.9(5)	N2	C9	C10	103.7(3)
O6	Cl4	O9	116.7(8)	N2	C8	C7	104.8(3)
O8	Cl4	O9	113.8(10)	N1	C7	C8	107.8(3)
O8	Cl4	O2	129(3)	C5	C6	N1	110.6(3)

Complex	L1Mn1	L1Mn2	L2Mn1
Simplified formula	$[(L1)_2Mn^{III,IV}_2O_2][ClO_4]_3 \cdot 4H_2O$	$[L1Mn^{III}Cl_2][ClO_4]$	$[(L2)_2Mn^{III,IV}_2O_2][ClO_4] \cdot 6H_2O$
Empirical formula	$C_{22}H_{44}Cl_3Mn_2N_8O_{18}$	$C_{11}H_{18}Cl_3MnN_4O_4$	$C_{11}H_{22.2}Cl_{0.5}MnN_4O_{6.94}$
Formula weight	924.88	431.58	394.25
Temperature/K	100.0(2)	100.0(2)	100.0(2)
Crystal system	Monoclinic	Monoclinic	Monoclinic
Space group	$P2_1$	$P2_1/c$	$C2/c$
a/Å	10.1199(6)	7.0070(4)	16.8774(6)
b/Å	16.2239(10)	12.7983(7)	11.4034(6)
c/Å	11.8583(8)	18.8563(11)	16.7065(6)
α/°	90	90	90
β/°	114.402(2)	90.618(2)	99.844(2)
γ/°	90	90	90
Volume/Å³	1773.02(19)	1690.89(17)	3168.0(2)
Z	2	4	8
ρ_{calc}/cm^3	1.732	1.695	1.653
μ/mm^{-1}	1.026	1.277	0.960
F(000)	954.0	880.0	1642.0
Crystal size/mm³	0.273 × 0.175 × 0.067	0.362 × 0.078 × 0.052	0.457 × 0.289 × 0.274
Radiation	Mo K α ($\lambda = 0.71073$)	Mo K α ($\lambda = 0.71073$)	MoK α ($\lambda = 0.71073$)
2θ range for data collection/°	6.28 to 66.48	6.36 to 60.24	6.256 to 60.298
Index ranges	-15 ≤ h ≤ 15 -24 ≤ k ≤ 24 -18 ≤ l ≤ 18	-9 ≤ h ≤ 9 -18 ≤ k ≤ 18 -26 ≤ l ≤ 26	-23 ≤ h ≤ 23 -16 ≤ k ≤ 16 -23 ≤ l ≤ 23
Reflections collected	33419	28307	41977
Independent reflections	13522 [$R_{int} = 0.0435$, $R_{\sigma} = 0.0791$]	4963 [$R_{int} = 0.0829$, $R_{\sigma} = 0.0804$]	4682 [$R_{int} = 0.0237$, $R_{\sigma} = 0.0123$]
Data/restraints/parameters	13522/1/490	4963/0/208	4682/0/265
Goodness-of-fit on F^2	0.991	1.063	1.100
Final R indexes [$I > 2\sigma(I)$]	$R_1 = 0.0499$, $wR_2 = 0.0970$	$R_1 = 0.0520$, $wR_2 = 0.0894$	$R_1 = 0.0362$, $wR_2 = 0.0937$
Final R indexes [all data]	$R_1 = 0.0829$, $wR_2 = 0.1087$	$R_1 = 0.1045$, $wR_2 = 0.1039$	$R_1 = 0.0390$, $wR_2 = 0.0956$
Largest diff. peak/hole / e Å⁻³	1.31/-0.49	1.25/-0.55	0.60/-0.93

Atom	Atom	Length/Å	Atom	Atom	Length/Å
Mn1	N4	2.059(2)	N3	C10	1.477(4)
Mn1	N2	2.076(2)	N2	C9	1.483(4)
Mn1	N3	2.241(3)	N2	C8	1.486(4)
Mn1	N1	2.247(2)	N1	C6	1.464(4)
Mn1	Cl1	2.2483(9)	N1	C7	1.488(4)
Mn1	Cl2	2.2496(9)	C5	C4	1.378(4)
Cl3	O3	1.421(2)	C5	C6	1.508(4)
Cl3	O1	1.431(3)	C4	C3	1.383(5)
Cl3	O2	1.445(2)	C3	C2	1.380(5)
Cl3	O4	1.445(2)	C2	C1	1.384(4)
N4	C1	1.342(4)	C1	C11	1.502(4)
N4	C5	1.344(4)	C10	C9	1.509(4)
N3	C11	1.475(4)	C8	C7	1.508(4)

Atom	Atom	Atom	Angle/°	Atom	Atom	Atom	Angle/°
N4	Mn1	N2	87.33(10)	C11	N3	C10	113.7(2)
N4	Mn1	N3	77.58(10)	C11	N3	Mn1	110.33(19)
N2	Mn1	N3	80.81(9)	C10	N3	Mn1	104.67(18)
N4	Mn1	N1	77.56(9)	C9	N2	C8	113.9(2)
N2	Mn1	N1	80.18(9)	C9	N2	Mn1	111.50(18)
N3	Mn1	N1	149.22(9)	C8	N2	Mn1	111.89(18)
N4	Mn1	Cl1	87.67(7)	C6	N1	C7	114.2(2)
N2	Mn1	Cl1	174.76(8)	C6	N1	Mn1	108.95(18)
N3	Mn1	Cl1	99.62(7)	C7	N1	Mn1	105.84(18)

N1	Mn1	Cl1	97.22(7)	N4	C5	C4	120.3(3)
N4	Mn1	Cl2	175.09(7)	N4	C5	C6	117.0(3)
N2	Mn1	Cl2	88.60(7)	C4	C5	C6	122.7(3)
N3	Mn1	Cl2	99.06(7)	C5	C4	C3	119.2(3)
N1	Mn1	Cl2	104.44(7)	C2	C3	C4	119.8(3)
Cl1	Mn1	Cl2	96.48(3)	C3	C2	C1	119.2(3)
O3	Cl3	O1	110.49(17)	N4	C1	C2	120.0(3)
O3	Cl3	O2	109.56(16)	N4	C1	C11	117.5(3)
O1	Cl3	O2	108.97(17)	C2	C1	C11	122.4(3)
O3	Cl3	O4	109.71(15)	N3	C11	C1	112.6(3)
O1	Cl3	O4	109.86(15)	N3	C10	C9	109.1(2)
O2	Cl3	O4	108.21(14)	N2	C9	C10	108.5(2)
C1	N4	C5	121.6(3)	N2	C8	C7	107.5(2)
C1	N4	Mn1	119.2(2)	N1	C7	C8	109.5(2)
C5	N4	Mn1	118.5(2)	N1	C6	C5	112.8(3)

Table A13. Bond lengths (Å) for [(L1)₂Mn^{III,IV}O₂][ClO₄]₃ (L1Mn1).

Atom	Atom	Length/Å	Atom	Atom	Length/Å
C1	N4	1.344(5)	C20	C21	1.522(6)
C1	C2	1.379(6)	C21	N7	1.482(5)
C1	C11	1.501(6)	C22	N7	1.480(5)
C2	C3	1.395(6)	Cl1	O3	1.430(3)
C3	C4	1.390(6)	Cl1	O4	1.434(3)
C4	C5	1.385(5)	Cl1	O5	1.446(3)
C5	N4	1.342(5)	Cl1	O6	1.450(3)
C5	C6	1.499(6)	Cl2	O13	1.427(4)
C6	N1	1.488(5)	Cl2	O14	1.429(3)
C7	N1	1.502(5)	Cl2	O11	1.436(3)
C7	C8	1.511(6)	Cl2	O12	1.454(4)
C8	N2	1.483(5)	Cl3	O9	1.433(3)
C9	N2	1.466(5)	Cl3	O8	1.440(3)
C9	C10	1.512(6)	Cl3	O7	1.445(3)
C10	N3	1.503(5)	Cl3	O10	1.452(3)
C11	N3	1.496(5)	Mn1	O2	1.800(2)
C12	N8	1.344(5)	Mn1	O1	1.809(2)
C12	C13	1.385(5)	Mn1	N4	1.997(3)
C12	C22	1.510(6)	Mn1	N1	2.086(3)
C13	C14	1.389(6)	Mn1	N3	2.090(3)
C14	C15	1.388(6)	Mn1	N2	2.091(3)
C15	C16	1.380(5)	Mn1	Mn2	2.7115(7)
C16	N8	1.344(5)	Mn2	O2	1.849(2)
C16	C17	1.507(6)	Mn2	O1	1.861(2)
C17	N5	1.483(5)	Mn2	N8	2.058(3)
C18	N5	1.477(5)	Mn2	N6	2.110(3)
C18	C19	1.516(6)	Mn2	N5	2.249(3)
C19	N6	1.501(5)	Mn2	N7	2.266(3)
C20	N6	1.473(5)			

Table A14. Bond angles (°) for [(L1)₂Mn^{III,IV}O₂][ClO₄]₃ (L1Mn1).

Atom	Atom	Atom	Angle/°	Atom	Atom	Atom	Angle/°
N4	C1	C2	120.3(4)	O2	Mn1	N2	91.37(11)
N4	C1	C11	114.5(3)	O1	Mn1	N2	176.48(12)
C2	C1	C11	125.1(4)	N4	Mn1	N2	89.60(11)
C1	C2	C3	119.0(4)	N1	Mn1	N2	81.90(13)
C4	C3	C2	120.0(3)	N3	Mn1	N2	81.49(13)
C5	C4	C3	118.3(4)	O2	Mn1	Mn2	42.71(8)
N4	C5	C4	120.9(4)	O1	Mn1	Mn2	43.10(7)
N4	C5	C6	114.2(3)	N4	Mn1	Mn2	136.30(8)
C4	C5	C6	124.8(4)	N1	Mn1	Mn2	104.42(10)
N1	C6	C5	111.2(3)	N3	Mn1	Mn2	101.66(10)
N1	C7	C8	108.9(3)	N2	Mn1	Mn2	134.04(8)

N2	C8	C7	105.9(3)	O2	Mn2	O1	82.96(10)
N2	C9	C10	106.5(3)	O2	Mn2	N8	93.27(11)
N3	C10	C9	107.9(3)	O1	Mn2	N8	176.21(11)
N3	C11	C1	110.7(3)	O2	Mn2	N6	178.14(12)
N8	C12	C13	120.6(4)	O1	Mn2	N6	95.38(11)
N8	C12	C22	116.6(3)	N8	Mn2	N6	88.39(11)
C13	C12	C22	122.7(4)	O2	Mn2	N5	100.86(13)
C12	C13	C14	119.4(4)	O1	Mn2	N5	102.96(13)
C15	C14	C13	119.0(3)	N8	Mn2	N5	77.98(13)
C16	C15	C14	119.3(4)	N6	Mn2	N5	80.29(14)
N8	C16	C15	121.0(4)	O2	Mn2	N7	99.97(13)
N8	C16	C17	116.3(3)	O1	Mn2	N7	102.99(13)
C15	C16	C17	122.7(4)	N8	Mn2	N7	77.32(13)
N5	C17	C16	113.0(3)	N6	Mn2	N7	79.57(14)
N5	C18	C19	109.8(3)	N5	Mn2	N7	148.37(11)
N6	C19	C18	108.2(3)	O2	Mn2	Mn1	41.32(7)
N6	C20	C21	109.1(3)	O1	Mn2	Mn1	41.64(8)
N7	C21	C20	109.8(3)	N8	Mn2	Mn1	134.58(8)
N7	C22	C12	112.0(3)	N6	Mn2	Mn1	137.01(8)
O3	C1	O4	109.7(2)	N5	Mn2	Mn1	105.97(9)
O3	C1	O5	110.6(2)	N7	Mn2	Mn1	105.40(9)
O4	C1	O5	110.11(19)	C6	N1	C7	113.0(3)
O3	C1	O6	109.2(2)	C6	N1	Mn1	109.6(2)
O4	C1	O6	108.4(2)	C7	N1	Mn1	108.5(2)
O5	C1	O6	108.78(19)	C9	N2	C8	116.0(3)
O13	C12	O14	108.9(2)	C9	N2	Mn1	110.9(2)
O13	C12	O11	110.8(2)	C8	N2	Mn1	109.9(2)
O14	C12	O11	108.8(2)	C11	N3	C10	113.4(3)
O13	C12	O12	110.8(2)	C11	N3	Mn1	111.3(2)
O14	C12	O12	108.7(2)	C10	N3	Mn1	107.8(2)
O11	C12	O12	108.8(2)	C5	N4	C1	121.5(3)
O9	C13	O8	110.75(19)	C5	N4	Mn1	118.7(3)
O9	C13	O7	110.82(18)	C1	N4	Mn1	119.7(3)
O8	C13	O7	109.39(19)	C18	N5	C17	114.4(3)
O9	C13	O10	109.97(19)	C18	N5	Mn2	106.2(2)
O8	C13	O10	108.4(2)	C17	N5	Mn2	108.5(2)
O7	C13	O10	107.44(19)	C20	N6	C19	112.2(2)
O2	Mn1	O1	85.81(11)	C20	N6	Mn2	112.0(3)
O2	Mn1	N4	178.96(12)	C19	N6	Mn2	111.1(2)
O1	Mn1	N4	93.20(11)	C22	N7	C21	114.6(3)
O2	Mn1	N1	100.36(14)	C22	N7	Mn2	108.2(2)
O1	Mn1	N1	100.68(14)	C21	N7	Mn2	107.0(2)
N4	Mn1	N1	80.16(14)	C12	N8	C16	120.7(3)
O2	Mn1	N3	100.11(14)	C12	N8	Mn2	119.6(3)
O1	Mn1	N3	96.90(14)	C16	N8	Mn2	119.7(3)
N4	Mn1	N3	79.65(14)	Mn1	O1	Mn2	95.26(11)
N1	Mn1	N3	153.83(11)	Mn1	O2	Mn2	95.97(11)

Table A15. Bond lengths (Å) for $[(L2)_2Mn^{III,IV}_2O_2][ClO_4]$ (L2Mn1).

Atom	Atom	Length/Å	Atom	Atom	Length/Å
Mn1	Mn1 ¹	2.7094(4)	C8	C7	1.515(2)
Mn1	O1 ¹	1.8301(11)	C6	C5	1.500(2)
Mn1	O1	1.8337(12)	C1	C11	1.510(2)
Mn1	N2	2.1044(13)	C10	C9	1.510(2)
Mn1	N1	2.1929(15)	C11	O5 ²	1.385(4)
Mn1	N4	2.0072(12)	Cl1	O5	1.385(4)
Mn1	N3	2.1853(15)	Cl1	O6	1.441(5)
C2	C1	1.376(2)	Cl1	O6 ²	1.441(5)
C2	C3	1.422(2)	Cl1	O4	1.514(5)
C4	C5	1.368(2)	Cl1	O4 ²	1.514(5)
C4	C3	1.422(2)	Cl1	O3	1.447(5)
O2	C3	1.2921(18)	Cl1	O3 ²	1.447(5)

O1	Mn1 ¹	1.8300(11)	O5	O6	1.616(7)
N2	C8	1.4791(19)	O5	O4	1.711(6)
N2	C9	1.479(2)	O5	O3 ²	1.598(7)
N1	C7	1.485(2)	O6	O4 ²	1.695(8)
N1	C6	1.480(2)	O6	O3	1.613(7)
N4	C5	1.3547(19)	O4	O6 ²	1.695(8)
N4	C1	1.3517(18)	O4	O3	1.801(9)
N3	C11	1.486(2)	O3	O5 ²	1.598(7)
N3	C10	1.487(2)			

(¹) 1/2-X,1/2-Y,2-Z (²) 1/2-X,3/2-Y,-Z

Table A16. Bond angles (°) for [(L2)₂Mn^{III,IV}₂O₂][ClO₄] (L2Mn1).

Atom	Atom	Atom	Angle/°	Atom	Atom	Atom	Angle/°
O1	Mn1	Mn1 ¹	42.26(3)	O5	Cl1	O6 ²	110.3(3)
O1 ¹	Mn1	Mn1 ¹	42.36(4)	O5	Cl1	O6	69.7(3)
O1 ¹	Mn1	O1	84.62(5)	O5 ²	Cl1	O6	110.3(3)
O1 ¹	Mn1	N2	91.98(5)	O5 ²	Cl1	O6 ²	69.7(3)
O1	Mn1	N2	176.60(5)	O5	Cl1	O4	72.2(2)
O1 ¹	Mn1	N1	102.17(5)	O5 ²	Cl1	O4 ²	72.2(2)
O1	Mn1	N1	99.89(5)	O5 ²	Cl1	O4	107.8(2)
O1	Mn1	N4	94.56(5)	O5	Cl1	O4 ²	107.8(2)
O1 ¹	Mn1	N4	179.08(5)	O5 ²	Cl1	O3 ²	111.3(3)
O1 ¹	Mn1	N3	101.48(5)	O5	Cl1	O3	111.3(3)
O1	Mn1	N3	99.81(5)	O5	Cl1	O3 ²	68.7(3)
N2	Mn1	Mn1 ¹	134.34(4)	O5 ²	Cl1	O3	68.7(3)
N2	Mn1	N1	80.79(5)	O6 ²	Cl1	O6	180.00(16)
N2	Mn1	N3	80.85(5)	O6	Cl1	O4 ²	70.0(4)
N1	Mn1	Mn1 ¹	104.99(4)	O6	Cl1	O4	110.0(4)
N4	Mn1	Mn1 ¹	136.82(4)	O6 ²	Cl1	O4 ²	110.0(4)
N4	Mn1	N2	88.84(5)	O6 ²	Cl1	O4	70.0(4)
N4	Mn1	N1	78.37(5)	O6	Cl1	O3	67.9(3)
N4	Mn1	N3	78.24(5)	O6	Cl1	O3 ²	112.1(3)
N3	Mn1	Mn1 ¹	104.46(4)	O6 ²	Cl1	O3	112.1(3)
N3	Mn1	N1	150.40(5)	O6 ²	Cl1	O3 ²	67.9(3)
C1	C2	C3	120.17(13)	O4	Cl1	O4 ²	180.0
C5	C4	C3	120.22(14)	O3	Cl1	O4 ²	105.1(4)
Mn1 ¹	O1	Mn1	95.38(5)	O3 ²	Cl1	O4 ²	74.9(4)
C8	N2	Mn1	110.38(9)	O3 ²	Cl1	O4	105.1(4)
C8	N2	C9	113.97(12)	O3	Cl1	O4	74.9(4)
C9	N2	Mn1	111.11(9)	O3	Cl1	O3 ²	180.0
C7	N1	Mn1	108.09(10)	Cl1	O5	O6	56.8(2)
C6	N1	Mn1	107.24(9)	Cl1	O5	O4	57.4(2)
C6	N1	C7	114.01(14)	Cl1	O5	O3 ²	57.5(2)
C5	N4	Mn1	119.42(9)	O6	O5	O4	93.4(4)
C1	N4	Mn1	121.65(10)	O3 ²	O5	O6	96.4(3)
C1	N4	C5	118.93(13)	O3 ²	O5	O4	90.4(3)
C11	N3	Mn1	111.00(10)	Cl1	O6	O5	53.5(2)
C11	N3	C10	113.41(14)	Cl1	O6	O4 ²	57.0(3)
C10	N3	Mn1	105.72(10)	Cl1	O6	O3	56.2(2)
N2	C8	C7	107.99(13)	O5	O6	O4 ²	90.1(4)
N1	C7	C8	110.90(12)	O3	O6	O5	92.8(4)
N1	C6	C5	111.32(13)	O3	O6	O4 ²	90.5(3)
C4	C5	C6	123.11(14)	Cl1	O4	O5	50.4(2)
N4	C5	C4	122.38(13)	Cl1	O4	O6 ²	53.0(3)
N4	C5	C6	114.49(13)	Cl1	O4	O3	50.9(3)
C2	C1	C11	123.36(13)	O5	O4	O3	83.5(4)
N4	C1	C2	122.10(14)	O6 ²	O4	O5	85.9(3)
N4	C1	C11	114.45(13)	O6 ²	O4	O3	86.4(4)
N3	C11	C1	111.74(13)	Cl1	O3	O5 ²	53.8(3)
N3	C10	C9	108.62(13)	Cl1	O3	O6	55.9(2)
N2	C9	C10	108.09(13)	Cl1	O3	O4	54.2(3)
C2	C3	C4	116.11(13)	O5 ²	O3	O6	92.5(3)

O2	C3	C2	122.24(14)	O5 ²	O3	O4	86.9(4)
O2	C3	C4	121.63(15)	O6	O3	O4	90.2(4)
O5 ²	C1	O5	180.0				

(¹) 1/2-X, 1/2-Y, 2-Z (²) 1/2-X, 3/2-Y, -Z

Table A17. Crystal data, intensity collections, and structure refinement parameters for (2.14)

Complex	(2.14)
Empirical formula	C ₂₁ H ₂₀ N ₂ O ₃ S
Formula weight	380.45
Temperature/K	99.97
Crystal system	Tetragonal
Space group	I4 ₁ /a
a/Å	21.742(2)
b/Å	21.742(2)
c/Å	16.3228(19)
α/°	90
β/°	90
γ/°	90
Volume/Å³	7715.8(19)
Z	16
ρ_{calc}/cm³	1.310
μ/mm⁻¹	0.191
F(000)	3200.0
Radiation	MoKα (λ = 0.71073)
2θ range for data collection/°	6.15 to 55.136
Index ranges	-23 ≤ h ≤ 28, -28 ≤ k ≤ 27, -21 ≤ l ≤ 21
Reflections collected	54710
Independent reflections	4437 [R _{int} = 0.3703, R _{sigma} = 0.2501]
Data/restraints/parameters	4437/0/245
Goodness-of-fit on F²	1.071
Final R indexes [I > 2σ (I)]	R ₁ = 0.1263, wR ₂ = 0.1621
Final R indexes [all data]	R ₁ = 0.2975, wR ₂ = 0.2042
Largest diff. peak/hole / e Å⁻³	0.40/-0.28

Table A18. Bond lengths (Å) for (2.14).

Atom	Atom	Length/Å	Atom	Atom	Length/Å
S1	O2	1.433(4)	C8	C9	1.397(7)
S1	O3	1.429(3)	C8	C21 ¹	1.378(7)
S1	N1	1.644(4)	C9	C10	1.356(7)
S1	C12	1.747(6)	C10	C11	1.517(7)
O1	C7	1.428(6)	C19	C20	1.505(7)
O1	C8	1.355(7)	C20	N2 ¹	1.345(6)
N1	C11	1.487(6)	C20	C21	1.373(7)
N1	C19	1.489(6)	C21	C8 ¹	1.378(7)
N2	C10	1.348(6)	C1	C2	1.386(10)
N2	C20 ¹	1.345(6)	C12	C18	1.401(7)
C3	C4	1.354(10)	C12	C13	1.392(7)
C3	C2	1.346(10)	C18	C17	1.377(8)
C4	C5	1.414(10)	C17	C15	1.382(8)
C5	C6	1.385(8)	C15	C14	1.397(7)
C6	C7	1.502(8)	C15	C16	1.500(8)
C6	C1	1.359(9)	C14	C13	1.370(7)

(¹) 2-X, 1/2-Y, +Z

Table A19. Bond angles (°) for (2.14).

Atom	Atom	Atom	Angle/°	Atom	Atom	Atom	Angle/°
O2	S1	N1	106.7(2)	N2	C10	C9	123.5(5)
O2	S1	C12	108.6(2)	N2	C10	C11	114.6(5)
O3	S1	O2	118.6(2)	C9	C10	C11	121.8(5)
O3	S1	N1	106.5(2)	N1	C11	C10	110.8(4)

O3	S1	C12	108.7(2)	N1	C19	C20	113.1(4)
N1	S1	C12	107.2(2)	N2 ¹	C20	C19	113.9(5)
C8	O1	C7	120.1(4)	N2 ¹	C20	C21	123.6(5)
C11	N1	S1	114.6(3)	C21	C20	C19	122.5(5)
C11	N1	C19	114.5(4)	C20	C21	C8 ¹	118.7(5)
C19	N1	S1	114.1(3)	C6	C1	C2	122.5(7)
C20 ¹	N2	C10	116.6(5)	C3	C2	C1	117.8(8)
C2	C3	C4	122.5(8)	C18	C12	S1	120.6(5)
C3	C4	C5	119.4(7)	C13	C12	S1	120.7(4)
C6	C5	C4	118.7(7)	C13	C12	C18	118.7(6)
C5	C6	C7	120.1(7)	C17	C18	C12	119.7(6)
C1	C6	C5	119.0(7)	C18	C17	C15	122.3(6)
C1	C6	C7	120.6(6)	C17	C15	C14	117.2(6)
O1	C7	C6	106.2(5)	C17	C15	C16	121.8(6)
O1	C8	C9	115.4(5)	C14	C15	C16	121.0(6)
O1	C8	C21 ¹	126.1(5)	C13	C14	C15	121.8(6)
C21 ¹	C8	C9	118.4(6)	C14	C13	C12	120.3(5)
C10	C9	C8	119.1(5)				

(¹) 2-X, 1/2-Y, +Z

Table A20. Crystal data, intensity collections, and structure refinement parameters for **L4Cu** and **L4Zn**

Complex	L4Cu	L4Zn
Simplified formula	[(L4) ₂ Cu ^{II} ₂ Cl ₂][Cl] ₂ •CH ₃ OH	[(L4) ₂ Zn ^{II} ₂ Cl ₂][Cl] ₂ •CH ₃ OH
Empirical formula	C ₁₅ H ₂₀ Cl ₂ CuN ₄ O ₃	C ₁₅ H ₂₀ Cl ₂ N ₄ O ₃ Zn
Formula weight	438.79	440.62
Temperature/K	293.15	293.15
Crystal system	Monoclinic	Monoclinic
Space group	P2 ₁ /c	P2 ₁ /c
a/Å	11.375(7)	11.346(5)
b/Å	12.294(7)	12.280(5)
c/Å	12.815(8)	13.065(5)
α/°	90	90
β/°	90.49(2)	92.509(13)
γ/°	90	90
Volume/Å³	1792.2(18)	1818.6(12)
Z	4	4
ρ_{calc}/cm³	1.626	1.609
μ/mm⁻¹	1.539	1.667
F(000)	900.0	904.0
Crystal size/mm³	0.279 × 0.16 × 0.126	0.469 × 0.244 × 0.176
Radiation	MoKα (λ = 0.71076)	MoKα (λ = 0.71076)
2θ range for data collection/°	5.808 to 60.268	5.886 to 60.198
Index ranges	-15 ≤ h ≤ 16 -17 ≤ k ≤ 17 -18 ≤ l ≤ 18	-15 ≤ h ≤ 16 -17 ≤ k ≤ 17 -18 ≤ l ≤ 18
Reflections collected	45954	45536
Independent reflections	5217 [R _{int} = 0.0499, R _{sigma} = 0.0350]	5341 [R _{int} = 0.0285, R _{sigma} = 0.0173]
Data/restraints/parameters	5217/0/236	5341/0/230
Goodness-of-fit on F²	1.169	1.096
Final R indexes [I >= 2σ(I)]	R ₁ = 0.0517, wR ₂ = 0.0891	R ₁ = 0.0259, wR ₂ = 0.0511
Final R indexes [all data]	R ₁ = 0.0656, wR ₂ = 0.0944	R ₁ = 0.0307, wR ₂ = 0.0530
Largest diff. peak/hole / e Å⁻³	0.62/-0.56	0.46/-0.29

Table A23. Bond lengths (Å) for [(L4)₂Cu^{II}₂Cl₂][Cl]₂ (**L4Cu**).

Atom	Atom	Length/Å	Atom	Atom	Length/Å
Cu1	Cl1	2.3152(14)	N1	C6	1.467(4)
Cu1	Cl1 ¹	2.3347(12)	O1	C3	1.346(3)
Cu1	N4	2.010(2)	O3	C15	1.419(4)
Cu1	N3	2.309(3)	C1	C14	1.512(4)
Cu1	N2	2.007(3)	C1	C2	1.378(4)

Cu1	N1	2.313(3)	C13	C12	1.507(4)
Cl1	Cu1 ¹	2.3347(12)	C12	C11	1.385(4)
O2	C10	1.336(3)	C8	C7	1.513(4)
N4	C1	1.343(3)	C8	C9	1.382(4)
N4	C5	1.341(4)	C6	C5	1.513(4)
N3	C14	1.466(4)	C5	C4	1.381(4)
N3	C13	1.463(4)	C4	C3	1.389(4)
N2	C12	1.343(3)	C3	C2	1.402(4)
N2	C8	1.346(3)	C9	C10	1.395(4)
N1	C7	1.471(4)	C10	C11	1.395(4)

(¹)-X,1-Y,2-Z

Table A24. Bond angles (°) for [(L4)₂Cu^{II}Cl₂][Cl]₂ (L4Cu).

Atom	Atom	Atom	Angle/°	Atom	Atom	Atom	Angle/°
Cl1	Cu1	Cl1 ¹	87.82(3)	C6	N1	C7	115.3(2)
N4	Cu1	Cl1 ¹	177.65(7)	N4	C1	C14	115.4(2)
N4	Cu1	Cl1	94.18(7)	N4	C1	C2	122.0(3)
N4	Cu1	N3	78.95(9)	C2	C1	C14	122.6(2)
N4	Cu1	N1	78.76(10)	N3	C14	C1	111.3(2)
N3	Cu1	Cl1 ¹	102.03(7)	N3	C13	C12	113.4(2)
N3	Cu1	Cl1	97.30(7)	N2	C12	C13	117.8(2)
N3	Cu1	N1	149.36(8)	N2	C12	C11	120.9(3)
N2	Cu1	Cl1	176.23(7)	C11	C12	C13	121.3(2)
N2	Cu1	Cl1 ¹	93.63(7)	N2	C8	C7	116.0(2)
N2	Cu1	N4	84.45(9)	N2	C8	C9	122.1(3)
N2	Cu1	N3	78.99(9)	C9	C8	C7	121.9(2)
N2	Cu1	N1	78.17(9)	N1	C7	C8	111.6(2)
N1	Cu1	Cl1	105.04(7)	N1	C6	C5	112.9(2)
N1	Cu1	Cl1 ¹	99.54(7)	N4	C5	C6	116.8(2)
Cu1	Cl1	Cu1 ¹	92.18(3)	N4	C5	C4	121.6(3)
C1	N4	Cu1	118.14(18)	C4	C5	C6	121.7(2)
C5	N4	Cu1	119.71(19)	C5	C4	C3	119.0(3)
C5	N4	C1	119.9(2)	O1	C3	C4	118.0(3)
C14	N3	Cu1	102.68(16)	O1	C3	C2	122.7(3)
C13	N3	Cu1	107.03(17)	C4	C3	C2	119.2(3)
C13	N3	C14	114.7(2)	C1	C2	C3	118.3(3)
C12	N2	Cu1	119.46(19)	C8	C9	C10	118.3(3)
C12	N2	C8	120.0(2)	O2	C10	C9	123.9(3)
C8	N2	Cu1	119.54(18)	O2	C10	C11	117.0(3)
C7	N1	Cu1	104.17(17)	C9	C10	C11	119.1(3)
C6	N1	Cu1	106.58(17)	C12	C11	C10	119.4(3)

(¹)-X,1-Y,2-Z

Table A25. Bond lengths (Å) for [(L4)₂Zn^{II}Cl₂][Cl]₂ (L4Zn).

Atom	Atom	Length/Å	Atom	Atom	Length/Å
Zn1	Cl1	2.4022(8)	O2	C10	1.3435(18)
Zn1	Cl1 ¹	2.4258(8)	C4	C5	1.3791(19)
Zn1	N4	2.0866(13)	C4	C3	1.399(2)
Zn1	N1	2.2407(13)	C5	C6	1.5159(19)
Zn1	N3	2.2520(14)	C1	C14	1.518(2)
Zn1	N2	2.0899(14)	C1	C2	1.382(2)
Cl1	Zn1 ¹	2.4259(8)	C8	C7	1.513(2)
O1	C3	1.3476(17)	C8	C9	1.383(2)
N4	C5	1.3402(18)	C3	C2	1.392(2)
N4	C1	1.3362(18)	C12	C13	1.517(2)
N1	C6	1.4784(18)	C12	C11	1.385(2)
N1	C7	1.4785(19)	C9	C10	1.394(2)
N3	C13	1.4821(19)	C11	C10	1.402(2)
N3	C14	1.4783(19)	O3	C15 ²	1.415(2)
N2	C8	1.3361(18)	C15	O3 ³	1.416(2)
N2	C12	1.3369(18)			

(¹) 1-X,1-Y,2-Z (²) -1+X,+Y,+Z (³) 1+X,+Y,+Z

Table A26. Bond angles (°) for [(L4)₂Zn^{II}₂Cl₂][Cl]₂ (L4Zn).

Atom	Atom	Atom	Angle/°	Atom	Atom	Atom	Angle/°
C11	Zn1	Cl1 ¹	87.33(2)	C12	N2	Zn1	118.88(9)
N4	Zn1	Cl1 ¹	175.16(3)	C5	C4	C3	117.95(13)
N4	Zn1	Cl1	95.16(4)	N4	C5	C4	122.08(13)
N4	Zn1	N1	78.38(5)	N4	C5	C6	114.15(12)
N4	Zn1	N3	77.98(5)	C4	C5	C6	123.76(12)
N4	Zn1	N2	84.49(5)	N1	C6	C5	110.72(11)
N1	Zn1	Cl1	94.78(4)	N4	C1	C14	115.05(12)
N1	Zn1	Cl1 ¹	105.59(4)	N4	C1	C2	121.76(13)
N1	Zn1	N3	147.12(4)	C2	C1	C14	123.18(12)
N3	Zn1	Cl1 ¹	97.28(4)	N2	C8	C7	116.04(12)
N3	Zn1	Cl1	109.80(4)	N2	C8	C9	121.41(13)
N2	Zn1	Cl1 ¹	93.59(4)	C9	C8	C7	122.54(13)
N2	Zn1	Cl1	172.52(3)	O1	C3	C4	122.50(13)
N2	Zn1	N1	77.81(5)	O1	C3	C2	117.81(13)
N2	Zn1	N3	77.47(5)	C2	C3	C4	119.66(13)
Zn1	Cl1	Zn1 ¹	92.67(2)	N2	C12	C13	114.49(12)
C5	N4	Zn1	117.19(9)	N2	C12	C11	121.84(13)
C1	N4	Zn1	118.89(10)	C11	C12	C13	123.67(13)
C1	N4	C5	120.00(12)	N1	C7	C8	112.43(11)
C6	N1	Zn1	105.28(8)	N3	C13	C12	111.66(12)
C6	N1	C7	113.86(11)	C8	C9	C10	118.73(13)
C7	N1	Zn1	109.78(9)	N3	C14	C1	112.34(11)
C13	N3	Zn1	106.21(8)	C1	C2	C3	118.38(13)
C14	N3	Zn1	108.72(9)	C12	C11	C10	117.97(14)
C14	N3	C13	114.49(11)	O2	C10	C9	116.72(14)
C8	N2	Zn1	119.07(10)	O2	C10	C11	123.90(15)
C8	N2	C12	120.48(12)	C9	C10	C11	119.34(13)

(¹) 1-X,1-Y,2-Z

Table A27. Crystal data, intensity collections, and structure refinement parameters for L5.

Complex	L5
Empirical formula	C ₈ H _{13.5} Cl _{2.01} N _{2.5}
Formula weight	216.06
Temperature/K	100.03
Crystal system	triclinic
Space group	P-1
a/Å	8.8978(4)
b/Å	11.3086(5)
c/Å	11.3231(5)
α/°	71.129(2)
β/°	72.654(2)
γ/°	84.049(2)
Volume/Å ³	1029.05(8)
Z	4
ρ _{calc} /cm ³	1.395
μ/mm ⁻¹	0.588
F(000)	453.0
Crystal size/mm ³	0.274 × 0.190 × 0.073
Radiation	MoKα (λ = 0.71073)
2θ range for data collection/°	5.738 to 60.284
Index ranges	-12 ≤ h ≤ 12, -15 ≤ k ≤ 15, -15 ≤ l ≤ 15
Reflections collected	49846
Independent reflections	6071 [R _{int} = 0.0540, R _{sigma} = 0.0417]
Data/restraints/parameters	6071/0/256
Goodness-of-fit on F ²	1.044
Final R indexes [I > 2σ (I)]	R ₁ = 0.0858, wR ₂ = 0.2380

Final R indexes [all data]	$R_1 = 0.1232$, $wR_2 = 0.2679$
Largest diff. peak/hole / e Å ⁻³	0.71/-2.08

Table A28. Bond lengths (Å) for C₃₀H₅₀N₁₀ (L5).

Atom	Atom	Length/Å	Atom	Atom	Length/Å
C15	C16	1.823(13)	C1	C15 ¹	1.510(4)
C13	C16	1.753(4)	C1	C2	1.392(5)
N1	C1	1.338(4)	C5	C6	1.518(5)
N1	C5	1.338(4)	C5	C4	1.385(5)
N3	C9	1.459(4)	C15	C1 ¹	1.509(4)
N3	C10	1.465(4)	C11	C10	1.512(5)
N3	C8	1.463(4)	C2	C3	1.378(5)
N4	C11	1.468(4)	C4	C3	1.397(5)
N4	C12	1.466(4)	C7	C8	1.518(5)
N4	C13	1.465(5)	C9	C12	1.505(5)
N5	C15	1.456(4)	C14	C13	1.512(5)
N5	C14	1.455(4)	C16	Cl4	1.57(3)
N2	C6	1.464(4)	C16	Cl2	1.758(4)
N2	C7	1.463(4)			

(¹) 1-X,2-Y,-Z

Table A29. Bond angles (°) for C₃₀H₅₀N₁₀ (L5).

Atom	Atom	Atom	Angle/°	Atom	Atom	Atom	Angle/°
C1	N1	C5	119.2(3)	N2	C6	C5	114.2(3)
C9	N3	C10	108.8(3)	C3	C2	C1	118.3(3)
C9	N3	C8	110.3(3)	C5	C4	C3	118.2(3)
C8	N3	C10	112.2(3)	N2	C7	C8	109.4(3)
C12	N4	C11	108.4(3)	C2	C3	C4	119.7(3)
C13	N4	C11	111.6(3)	N3	C9	C12	111.5(3)
C13	N4	C12	110.1(3)	N3	C10	C11	110.6(3)
C14	N5	C15	112.8(3)	N5	C14	C13	110.2(3)
C7	N2	C6	113.7(3)	N3	C8	C7	112.4(3)
N1	C1	C15 ¹	114.6(3)	N4	C12	C9	110.9(3)
N1	C1	C2	122.3(3)	N4	C13	C14	112.5(3)
C2	C1	C15 ¹	123.1(3)	Cl3	C16	Cl5	112.0(4)
N1	C5	C6	115.4(3)	Cl3	C16	Cl2	108.9(2)
N1	C5	C4	122.3(3)	Cl4	C16	Cl3	102.6(19)
C4	C5	C6	122.3(3)	Cl4	C16	Cl2	115.9(18)
N5	C15	C1 ¹	113.0(3)	Cl2	C16	Cl5	108.8(3)
N4	C11	C10	110.5(3)				

(¹) 1-X,2-Y,-Z

References

1. Constable, E. C., *Coordination Chemistry of Macrocyclic Compounds*. Oxford University Press: New York, NY, 1999.
2. McNaught, A. D.; Wilkinson, A., *IUPAC. Compendium of Chemical Terminology*. Blackwell Scientific Publications: Oxford, UK, 1997.
3. Lindoy, L. F., *The chemistry of macrocyclic ligand complexes*. Cambridge University Press: Cambridge, UK, 1989.
4. Lincoln, K. M. *Synthesis, Characterizations, and Applications of Pyridine- and Pyridol-Based Tetraaza Macrocycles*. Dissertation, Texas Christian University, Fort Worth, TX, 2015.
5. Busch, D. H. *Acc. Chem. Res.* **1978**, *11*, 392-400.
6. Voet, D.; Voet, J. G., *Biochemistry*. 4th ed.; John Wiley & Sons, Inc.: Hoboken, NJ, 2011.
7. Curtis, N. F. *J. Chem. Soc.* **1960**, 4409-13.
8. Meslon, G. A.; Busch, D. H. *J. Am. Chem. Soc.* **1964**, *86*, 4834-7.
9. McKeown, N. B., The Synthesis of Symmetrical Phthalocyanines. In *The Porphyrin Handbook*, 1st ed.; Kadish, K. M.; Smith, K. M.; Guillard, R., Eds. Academic Press: San Diego, CA, 2003; Vol. 15, pp 61-124.
10. Gregory, P. J. *Phorphyrins Phthalocyanines* **2000**, *4* (4), 432-437.
11. Lobbart, G., Phthalocyanines. In *Ullmann's Encyclopedia of Industrial Chemistry*, Wiley-VCH: 2000.
12. Blight, M. M.; Curtis, N. F. *J. Chem. Soc.* **1962**, 3016-20.
13. Blight, M. M.; Curtis, N. F. *J. Chem. Soc.* **1962**, 1204-7.
14. Curtis, N. F. *J. Chem. Soc.* **1964**, 2644-50.
15. Curtis, N. F.; Curtis, Y. M.; Powell, H. K. J. *J. Chem. Soc. A* **1966**, *0*, 1015-18.
16. Curtis, N. F.; House, D. A. *Chemistry and Industry* **1961**, 1708-9.
17. Curtis, N. F.; House, D. A. *J. Chem. Soc.* **1965**, 5502-8.

18. House, D. A.; Curtis, N. F. *J. Am. Chem. Soc.* **1964**, *86*, 1331-4.
19. House, D. A.; Curtis, N. F. *J. Am. Chem. Soc.* **1962**, *84*, 3248-50.
20. House, D. A.; Curtis, N. F. *J. Am. Chem. Soc.* **1964**, *86*, 223-5.
21. Martin, L. Y.; DeHayes, L. J.; Zompa, L. J.; Busch, D. H. *J. Am. Chem. Soc.* **1974**, *96* (12), 4046-8.
22. Bosnich, B.; Poon, C. K.; Tobe, M. L. *Inorg. Chem.* **1965**, *4* (8), 1102-8.
23. Bosnich, B.; Poon, C. K.; Tobe, M. L. *Inorg. Chem.* **1966**, *5* (9), 1514-7.
24. Bosnich, B.; Tobe, M. L.; Webb, G. A. *Inorg. Chem.* **1965**, *4* (8), 1109-12.
25. Martin, L. Y.; Sperati, C. R.; Busch, D. H. *J. Am. Chem. Soc.* **1977**, *99* (9), 2968-81.
26. Vallee, B. L.; Williams, R. J. P. *Proc. Natl. Acad. Sci.* **1968**, *59*, 498-505.
27. Cotton, F. A.; Wilkinson, A., *Advanced Inorganic Chemistry: A Comprehensive Text*. 2nd ed.; John Wiley & Sons: United States, 1966.
28. Martell, A. E. *Advances in Chemistry Series* **1967**, *62*, 272-94.
29. Miessler, G. L.; Fischer, P. J.; Tarr, D. A., *Inorganic Chemistry*. 5th Ed. ed.; Pearson: Upper Saddle River, NJ, 2014.
30. Cotton, F. A.; Wilkinson, G.; Murillo, C. A.; Bochmann, M., *Advanced Inorganic Chemistry*. 6th ed. ed.; John Wiley & Sons, Inc.: New York, NY, 1999.
31. Cabbiness, D. K.; Margerum, D. W. *J. Am. Chem. Soc.* **1969**, *91* (23), 6540-1.
32. Cabbiness, D. K.; Margerum, D. W. *J. Am. Chem. Soc.* **1970**, *92* (7), 2151-3.
33. Hinz, F. P.; Margerum, D. W. *Inorg. Chem.* **1974**, *13* (12), 2941-9.
34. Kodama, M.; Kimura, E. *J. C. S. Dalton* **1976**, 2341-5.
35. Kodama, M. *J. C. S. Chem. Comm.* **1975**, 326-7.
36. Clay, R. M.; Corr, S.; Micheloni, M.; Paoletti, P. *Inorg. Chem.* **1985**, *24*, 3330-6.
37. Anichini, A.; Fabbrizzi, L.; Paoletti, P. *J. Chem. Soc., Chem. Commun.* **1977**, (8), 244-5.
38. Gallori, E.; Martini, E.; Micheloni, M.; Paoletti, P. *J. C. S. Dalton* **1980**, (9), 1722-5.

39. Clay, R. M.; McCormac, H.; Micheloni, M.; Paoletti, P. *Inorg. Chem.* **1982**, *21*, 2494-6.
40. Clay, R. M.; Micheloni, M.; Paoletti, P.; Steele, W. V. *J. Am. Chem. Soc.* **1979**, *101* (15), 4119-22.
41. Micheloni, M.; Paoletti, P.; Sabatini, A. *J. Chem. Soc., Dalton Trans.* **1983**, 1189-91.
42. Drumhiller, J. A.; Montavon, F.; Lehn, J.-M.; Taylor, R. W. *Inorg. Chem.* **1986**, *25* (21), 3751-7.
43. Lin, C.-T.; Rorabacher, D. B.; Cayley, G. R.; Margerum, D. W. *Inorg. Chem.* **1975**, *14* (4), 919-25.
44. Margerum, D. W.; Cayley, G. R.; Weatherburn, D. C.; Pagenkopf, G. K. *ACS Monograph* **1978**, *174*, 1-220.
45. Billo, E. J. *Inorg. Chem.* **1984**, *23*, 236-8.
46. Barefield, E. K. *Inorg. Chem.* **1972**, *11* (9), 2273-4.
47. Busch, D. H. *Helv. Chim. Acta* **1967**, (S1), 174-206.
48. Richman, J. E.; Atkins, T. J. *J. Am. Chem. Soc.* **1974**, *96*, 2268-70.
49. Smith, W. L.; Ekstrand, J. D.; Raymond, K. N. *JACS* **1978**, *100* (11), 3539-44.
50. Burguete, M. I.; Escuder, B.; Luis, S. V.; Miravet, J. F.; Querol, M. *Tetrahedron Lett.* **1998**, *39*, 3799-802.
51. Bencini, A.; Fabbrizzi, L.; Poggi, A. *Inorg. Chem.* **1981**, *20* (8), 2544-9.
52. Sabatini, L.; Fabbrizzi, L. *Inorg. Chem.* **1979**, *18* (2), 438-44.
53. Fukuyama, T.; Jow, C.-K.; Cheung, M. *Tetrahedron Lett.* **1995**, *36* (36), 6373-4.
54. Favre-Reguillon, A.; Segat-Dioury, F.; Nait-Bouda, L.; Cosma, C.; Siaugue, J. M.; Foos, J.; Guy, A. *Synlett.* **2000**, (6), 868-70.
55. Lincoln, K. M.; Arroyo - Currás, N.; Johnston, H. M.; Hayden, T. D.; Pierce, B. S.; Bhuvanesh, N.; Green, K. N. *J. Coord. Chem.* **2015**, *68* (16), 2810-2826.
56. Lincoln, K. M.; Offut, M. E.; Hayden, T. D.; Saunders, R.; Green, K. N. *Inorg. Chem.* **2014**, *53*, 1406-16.
57. Nikac, M.; Brimble, M. A.; Crumbie, R. L. *Tetrahedron* **2007**, *63* (24), 5220-6.

58. Wang, T.; An, H.; Vickers, T. A.; Bharadwahj, R.; Cook, D. P. *Tetrahedron* **1998**, *54*, 7955-76.
59. Siaugue, J. M.; Segat-Dioury, F.; Sylvestre, I.; Favre-Reguillon, A.; Foos, J.; Madic, C.; Guy, A. *Tetrahedron* **2001**, *57*, 4713-18.
60. Thompson, M. C.; Busch, D. H. *J. Am. Chem. Soc.* **1964**, *86* (18), 3561-6.
61. Nelson, S. M. *Pure and Applied Chemistry* **1980**, *52* (11), 2461-76.
62. Johnston, H. M.; Palacios, P. M.; Pierce, B. S.; Green, K. N. *J. Coord. Chem.* **2016**, *69* (11-13), 1979-89.
63. Koch, W. O.; Kaiser, J. T.; Kruger, H.-J. *Chem. Commun.* **1997**, 2237-8.
64. Casitas, A.; Ribas, X. *Chem. Sci.* **2013**, *4*, 2301-19.
65. Raffard, N.; Carina, R.; Simaan, A. J.; Sainton, J.; Riviere, E.; Tchertanoc, L.; Bourcier, S.; Bouchoux, G.; Delroisse, M.; Banse, F.; Girerd, J. J. *Eur. J. Inorg. Chem.* **2001**, 2249-2254.
66. Wanhua, Y.; Ho, D. M.; Friedle, S.; Palluccio, T. D.; Rybak-Akimova, E. V. *Inorg. Chem.* **2012**, *51*, 5006-21.
67. Domagala, S.; Malecka, J.; Michalowicz, A.; Mames, I.; Kamienski, B.; Wozny, M.; Bilewicz, R.; Korybut-Daszkiwicz, B.; Wozniak, K. *Eur. J. Inorg. Chem.* **2012**, 3680-92.
68. Wen, J.; Qin, S.; Ma, L.-F.; Dong, L.; Zhang, J.; Liu, S.-S.; Duan, Y.-S.; Chen, S.-Y.; Hu, C.-W.; Yu, X.-Q. *Org. Lett.* **2010**, *12* (12), 2694-7.
69. Dorazio, S. J.; Tsitovich, P. B.; Gardina, S. A.; Morrow, J. R. *J. Inorg. Biochem.* **2012**, *117*, 212-19.
70. Green, K. N.; Viswanathan, S.; Rojas-Quijano, F. A.; Kovacs, Z.; Sherry, A. D. *Inorg. Chem.* **2011**, *50*, 1648-55.
71. Gonzalez, P.; da Costa, V. C.; Hyde, K.; Wu, Q.; Annunziata, O.; Rizo, J.; Akkaraju, G.; Green, K. N. *Metallomics* **2014**, *6* (11), 2072-82.
72. Lincoln, K. M.; Gonzalez, P.; Richardson, T. E.; Julovich, D. A.; Saunders, R.; Simpkins, J. W.; Green, K. N. *Chem. Commun.* **2013**, *49* (26), 2712-4.

73. Lincoln, K. M.; Richardson, T. E.; Rutter, L.; Gonzalez, P.; Simpkins, J. W.; Green, K. N. *ACS Chem. Neurosci.* **2012**, *3* (11), 919-27.
74. Crichton, R.; Ward, R., *Metal-based Neurodegeneration: From Molecular Mechanisms to Therapeutic Strategies*. 2nd ed.; John Wiley & Sons, Ltd.: Chichester, West Sussex, UK, 2014.
75. Dickens, M. G.; Franz, K. J. *ChemBioChem* **2010**, *11*, 59-62.
76. Hyman, L. M.; Stephenson, C. J.; Dickens, M. G.; Shimizu, K. D.; Franz, K. J. *Dalton Trans.* **2010**, *39*, 568-576.
77. Molina-Holgado, F.; Gaeta, A.; Francis, P. T.; Williams, R. J.; Hider, R. C. *J. Neurochem.* **2008**, *105*, 2466-7.
78. Perez, L. R.; Franz, K. J. *Dalton Trans.* **2010**, *39*, 2177-87.
79. Gaeta, A.; Molina-Holgado, F.; Kong, X. L.; Salvage, S.; Fakhri, S.; Francis, P. T.; Williams, R. J.; Hider, R. C. *Bioorg. Med. Chem.* **2011**, *19*, 1285-97.
80. Green, D. E.; Bowen, M. L.; Scott, L. E.; Storr, T.; Merkel, M.; Bohmerle, K.; Thompson, K. H.; Patrick, B. O.; Schugar, H. J.; Orvig, C. *Dalton Trans.* **2010**, *39* (1604-1615), 1604.
81. Hyman, L. M. *Inorg. Chim. Acta* **2012**, *380*, 125-134.
82. Santos, M. A.; Chand, K.; Chaves, S. *Coord. Chem. Rev.* **2016**, *327-328*, 287-303.
83. Schugar, H.; Green, D. E.; Bowen, M. L.; Scott, L. E.; Storr, T.; Bohmerle, K.; Thomas, F.; Allen, D. D.; Lockman, P. R.; Merkel, M.; Thompson, K. H.; Orvig, C. *Angew. Chem. Int. Ed.* **2007**, *46*, 1716-8.
84. Chen, T.; Wang, X.; He, Y.; Zhang, C.; Wu, Z.; Liao, K.; Wang, J.; Guo, Z. *Inorg. Chem.* **2009**, *48* (13), 5801-9.
85. Brewer, S. M.; Palacios, P. M.; Johnston, H. M.; Pierce, B. S.; Green, K. N. *Inorg. Chim. Acta* **2017**, *Accepted*.

86. Brewer, S. M.; Wilson, K. R.; Jones, D. G.; Su Turan, L.; Hubin, T. J.; Green, K. N. **2018**, *Manuscript in preparation*.
87. de Sa, A.; Bonnet, C. S.; Geraldés, C. F. G. C.; Toth, E.; Ferreira, P. M. T.; Andre, J. P. *Dalton Trans.* **2013**, *42* (13), 4522-32.
88. Drahos, B.; Pniok, M.; Havlickova, J.; Kotek, J.; Cisarova, I.; Hermann, P.; Lukes, I.; Toth, E. *Dalton Trans.* **2011**, *40* (39), 10131-46.
89. Viswanathan, S.; Kovacs, Z.; Green, K. N.; Ratnakar, S. J.; Sherry, A. D. *Chem. Rev.* **2010**, *110*, 2960-3018.
90. Drahos, B.; Kotek, J.; Cisarova, I.; Hermann, P.; Helm, L.; Lukes, I.; Toth, E. *Inorg. Chem.* **2011**, *50* (24), 12785-801.
91. Drahos, B.; Kotek, J.; Hermann, P.; Lukes, I.; Toth, E. *Inorg. Chem.* **2010**, *49* (7), 3224-38.
92. Kalman, F. K.; Vegh, A.; Regueiro-Figueroa, M.; Toth, E.; Platas-Iglesias, C.; Tirsco, G. *Inorg. Chem.* **2015**, *54* (5), 2345-56.
93. Ghandi, S.; Abramov, A. Y. *Oxid. Med. Cell. Longevity* **2012**, *2012*, 1-11.
94. Xu, J.; Church, S. J.; Patassini, S.; Begley, P.; Waldvogel, H. J.; Curtis, M. A.; Faull, R. L. M.; Unwin, R. D.; Cooper, G. J. S. *Metallomics* **2017**, *9*, 1106-19.
95. Barnham, K. J.; Bush, A. I. *Curr. Opin. Chem. Biol.* **2008**, *12*, 222-8.
96. Casadesus, G.; Smith, M. A.; Zhu, X. W.; Aliev, G.; Cash, A. D.; Honda, K.; Petersen, R. B.; Perry, G. *J. Alzheimer's Dis.* **2004**, *6*, 165-9.
97. Drew, S. C.; Barnham, K. J. *Acc. Chem. Res.* **2011**, *44*, 1146-55.
98. Duce, J. A.; Bush, A. I. *Prog. Neurobiol.* **2010**, *92*, 1-18.
99. Lovell, M. A.; Roberstons, J. D.; Teesdale, W. J. *J. Neurol. Sci.* **1998**, *158*, 47-52.
100. Maynard, C. J.; Bush, A. I.; Masters, C. L.; Cappai, R.; Li, Q. X. *Int. J. Exp. Pathol.* **2005**, *86*, 147-59.
101. Rauk, A. *Chem. Soc. Rev.* **2009**, *38*, 2698-2715.

102. Haas, K. L.; Franz, K. J. *Chem. Rev.* **2009**, *109*, 4921-60.
103. Kozlowski, H.; Luczkowski, M.; Remelli, M.; Valensin, D. *Coord. Chem. Rev.* **2012**, *256*, 2129-2141.
104. Gaggelli, E.; Kozlowski, H.; Valensin, D.; Valensin, G. *Chem. Rev.* **2006**, *106*, 1995-2044.
105. Atwood, C. S.; Huang, X.; Moir, R. D.; Tanzi, R. E.; Bush, A. I., *Metal Ions in Biological Systems*. Marcel Dekker, Inc.: New York, NY, 1999; Vol. 36.
106. Bush, A. I. *Trends Neurosci.* **2003**, *26*, 207-14.
107. Crouch, P. J.; Savva, M. S.; Hung, L. W.; Donnelly, P. S.; Mot, A. I.; Parker, S. J.; Geenough, M. A.; Volitakis, I.; Adlard, P. A.; A., C. R.; Masters, C. L.; Bush, A. I.; Barnham, K. J.; White, A. R. *J. Neurochem.* **2011**, *119*, 220-30.
108. Adlard, P. A.; Parncutt, J. M.; Finkelstein, D. I.; Bush, A. I. *J. Neurosci.* **2010**, *30*, 1631-6.
109. James, S. A.; Volitakis, I.; Adlard, P. A.; Duce, J. A.; Masters, C. L.; Cherny, R. A.; Bush, A. I. *Free Radical Biol. Med.* **2012**, *52*, 298-302.
110. Crouch, P. J.; Hung, L. W.; Adlard, P. A.; Cortes, M.; Lal, V.; Filiz, G.; Perez, K. A.; Nurjono, M.; Caragounis, A.; Du, T.; Loughton, K.; Volitakis, I.; Bush, A. I.; Li, Q. X.; Masters, C. L.; Cappai, R.; Cherny, R. A.; Donnelly, P. S.; White, A. R.; Barnham, K. J. *Proc. Natl. Acad. Sci. U.S.A.* **2009**, *106*, 381-6.
111. Miu, A. C.; Benga, O.; Adlard, P. A.; Bush, A. I. *Alzheimer's Dis.* **2006**, *10*, 145-63.
112. Jomova, K.; Vondrakova, D.; Lawson, M.; Valko, M. *Mol. Cell. Biochem.* **2010**, *345*, 91-104.
113. Barnham, K. J.; Masters, C. L.; Bush, A. I. *Nature Reviews Drug Discovery* **2004**, *3*, 205-14.
114. Rivera-Mancia, S.; Perez-Neri, I.; Rios, C.; Tristan-Lopez, L.; Rivera-Espinosa, L.; Montes, S. *Chemico-Biological Interactions* **2010**, *186*, 184-99.
115. Strozyk, D.; Launer, L. J.; Adlard, P. A.; Cherny, R. A.; Tsatsanis, A.; Volitakis, I.; Blennow, K.; Petrovitch, H.; White, L. R.; Bush, A. I. *Neurobiol. Aging* **2009**, *30*, 1069-77.
116. Anderson, J. K. *Nature Reviews Neuroscience* **2004**, *10*, S18-25.

117. Bebbington, D.; Monck, N. J. T.; Gaur, S.; Palmer, A. M.; Benwell, K.; Harvey, V.; Malcom, C. S.; Porter, R. H. P. *J. Med. Chem.* **2000**, *43*, 2779-82.
118. Bures, J.; Jansova, H.; Stariat, J.; Filipisky, T.; Mladenka, P.; Simunek, T.; Kucera, R.; Klimes, J.; Wang, Q.; Franz, K. J.; Kovarikova, P. *J. Pharm. Biomed. Anal.* **2015**, *105*, 55-63.
119. Charkoudian, L. K.; Dentchev, T.; Lukinova, N.; Wolkow, N.; Dunaief, J. L.; Franz, K. J. *J. Inorg. Biochem.* **2008**, *102*, 2130-5.
120. Charkoudian, L. K.; Pham, D. M.; Franz, K. J. *J. Am. Chem. Soc.* **2006**, *128*, 12424-5.
121. Charkoudian, L. K.; Pham, D. M.; Kwon, A. M.; Vangeloff, A. D.; Franz, K. J. *Dalton Trans.* **2007**, *43*, 4873-5092.
122. Fenton, H. J. H. *J. Chem. Soc., Trans.* **1894**, *65*, 899-910.
123. Franks, A. T.; Wang, Q.; Franz, K. J. *Bioorg. & Med. Chem. Lett.* **2015**, *25*, 4843-4847.
124. Halliwell, B.; Gutteridge, J. M. C., *Free Radicals in Biology and Medicine*. 5th ed.; Oxford University Press: New York, NY, 2015.
125. Jansova, H.; Bures, J.; Machacek, M.; Haskova, P.; Jirkovska, A.; Roh, J.; Wang, Q.; Franz, K. J.; Kovarikova, P.; Simunek, T. *Toxicology* **2016**, *350-352*, 15-24.
126. Jansova, H.; Machacek, M.; Wang, Q.; Haskova, P.; Jirkovska, A.; Potuckova, E.; Kielar, F.; Franz, K. J.; Simunek, T. *Free Radical Biol. Med.* **2014**, *74*, 210-221.
127. Kehrer, J. P. *Toxicology* **2000**, *149*, 43-50.
128. Kielar, F.; Helsel, M. E.; Wang, Q.; Franz, K. J. *Metallomics* **2012**, *4*, 899-909.
129. Leed, M. G. D.; Wolkow, N.; Pham, D. M.; Daniel, C. L.; Dunaief, J. L.; Franz, K. J. *J. Inorg. Biochem.* **2011**, *105*, 1161-72.
130. Oliveri, V.; Vecchio, G. *J. Inorg. Biochem.* **2016**, *162*, 31-43.
131. Santos, M. A.; Marques, S. M.; Chaves, S. *Coord. Chem. Rev.* **2012**, *256*, 240-59.

132. Adlard, P. A.; Bica, L.; White, A. R.; Nurjono, M.; Crouch, P. J.; Donnelly, P. S.; Cappai, R.; Finkelstein, D. I.; Bush, A. I. *PLoS One* **2011**, *6* (3), e17669.
133. Chen, T. W.; He, X.; Zhang, C.; Wu, Z.; Liao, K.; Wang, J.; Guo, Z. *Inorg. Chem.* **2009**, *48*, 5801-9.
134. Crichton, R. R.; Dexter, D. T.; Ward, R. J. *Coord. Chem. Rev.* **2008**, *252* (10-11), 1189-99.
135. Delgado, R.; Felix, V.; Lima, L. M. P.; Price, D. W. *Dalton Trans.* **2007**, 2734-45.
136. Hardeland, R. *Endocrine* **2005**, *27* (2), 119-30.
137. Lannfelt, L.; Blennow, K.; Zetterberg, H.; Batsman, S.; Ames, D.; Harrison, J.; Masters, C. L.; Targum, S.; Bush, A. I.; Murdoch, R.; Wilson, J.; Ritchie, C. W. *The Lancet Neurology* **2008**, *7*, 779-86.
138. Liang, X.; Sadler, P. J. *Chem. Soc. Rev.* **2004**, *33* (246-66), 246.
139. Lima, L. M.; Esteban-Gomez, R.; Delgado, R.; Platas-Iglesias, C.; Tripier, R. *Inorg. Chem.* **2012**, *51*, 6916-27.
140. Martins, A. F.; Oliveria, A. C.; Morfin, J.-F.; Laurents, D. V.; Toth, E.; Geraldos, C. F. G. C. *J. Biol. Inorg. Chem.* **2016**, *21*, 83-99.
141. Rodriguez-Rodriguez, D.; Telpoukhovskaia, M.; Orvig, C. *Coord. Chem. Rev.* **2012**, *256*, 2308-2332.
142. Rogolino, D.; Cavazzoni, A.; Gatti, A.; Tegoni, M.; Pelosi, G.; Verdolino, V.; Fumarola, C.; Cretella, D.; Petronini, P. G.; Carcelli, M. *Eur. J. Med. Chem.* **2017**, *128*, 140-53.
143. Yoon, M.-A.; Jeong, T.-S.; Park, D.-S.; Xu, M.-Z.; Oh, H.-W.; Song, K.-B.; Lee, W. S.; Park, H.-Y. *Biol. Pharm. Bull.* **2006**, *29*, 735-9.
144. Zambenedetti, P.; Schmitt, H. P.; Zatta, P. *J. Alzheimer's Dis.* **2002**, *4* (6), 459-66.
145. Adlard, P. A.; Cherny, R. A.; Finkelstein, D. I.; Gautier, E.; Robb, E.; Cortes, M.; Volitakis, I.; Liu, X.; Smith, J. P.; Perez, K.; Laughton, K.; Li, Q.-X.; Charman, S. A.; Nicolazzo, J. A.; Wilkins, S.; Deleva, K.; Lynch, T.; Kok, G.; Ritchie, C. W.; Rudolph, E.; Cappai, R.; Masters, C. L.; Barnham, K. J.; Bush, A. I. *Neuron* **2008**, *59* (1), 43-55.

146. Bush, A. I.; Tanzi, R. E. *Neurotherapeutics* **2008**, *5*, 421-32.
147. Crouch, P. J.; Harding, S.-M. E.; White, A. R.; Camakaris, J.; Bush, A. I. *Int. J. Biochem. Cell Biol.* **2008**, *40* (2), 181-98.
148. Gonzalez, P.; Pota, K.; Su Turan, L.; da Costa, V. C. P.; Akkaraju, G.; Green, K. N. *ACS Chem. Neurosci.* **2017**, *8*, 2414-23.
149. Safadi, M. E.; Bhadbhade, M.; Shimmon, R.; Baker, A. T.; McDonagh, A. M. *Inorg. Chim. Acta* **2017**, *467*, 343-50.
150. Cherny, R. A.; Atwood, C. S.; Xilinas, M. E.; Gray, D. N.; Jones, W. D.; McLean, C. A.; Barnham, K. J.; Volitakis, I.; Fraser, F. W.; Kim, Y.-S.; Huang, X.; Goldstein, L. E.; Moir, R. D.; Lim, J. T.; Beyreuther, K.; Zheng, H.; Tanzi, R. E.; Masters, C. L.; Bush, A. I. *Neuron* **2001**, *30*, 665-76.
151. Faux, N. G.; Ritchie, C. W.; Gunn, A.; Rembach, A.; Tsatsanis, A.; Bedo, J.; Harrison, J.; Lannfelt, L.; Blennow, K.; Zetterberg, J.; Ingelsson, M.; Masters, C. L.; Tanzi, R. E.; Cummings, J. L.; Herd, C. M.; Bush, A. I. *J. Alzheimer's Dis.* **2010**, *20*, 509-16.
152. Mikelens, R. W.; Jackson, J.; Blackman, J.; Whitcher, J.; Levinson, W. *Antimicrob. Agents Chemother* **1976**, *10* (2), 234-40.
153. Adlard, P. A.; Cherny, R. A.; Finkelstein, D. I.; Gautier, E.; Robb, E.; Cortes, M.; Volitakis, I.; Liu, X.; Smith, J. P.; Perez, K.; Laughton, K.; Li, Q.-X.; Charman, S. A.; Nicolazzo, J. A.; Wilkins, S.; Deleva, K.; Lynch, T.; Kok, G.; Ritchie, C. W.; Rudolph, E.; Cappai, R.; Masters, C. L.; Barnham, K. J.; Bush, A. I. *Neuron* **2008**, *59* (1), 43-55.
154. Moret, V.; Laras, Y.; Pietrancosta, N.; Garino, C.; Quilever, G.; Rolland, A.; Mallet, B.; Norreel, J.-C.; Kraus, J.-L. *Bioorg. & Med. Chem. Lett.* **2006**, *16*, 3298-3301.
155. Ritchie, C. W.; Bush, A. I.; Mackinnon, A.; Macfarlane, S.; Mastwyk, M.; MacGregor, L.; Kiers, L.; Cherny, R.; Li, Q. X.; Tammer, A.; Carrington, D.; Mavros, C.; Volitakis, I.; Xilinas, M.; Ames, D.; Beyreuther, K.; Tanzi, R. E.; Masters, C. L. *Arch. Neurol.* **2003**, *60*, 1685-91.

156. Tsubaki, T.; Honma, Y.; Hoshi, M. *Lancet* **1971**, *1*, 696-7.
157. Scott, L. E.; Page, B. D. G.; Patrick, B. O.; Orvig, C. *Dalton Trans.* **2008**, 6364-7.
158. Zhang, Z.; Rettig, S. J.; Orvig, C. *Inorg. Chem.* **1991**, *30*, 509-15.
159. Sherry, A. D.; Caravan, P.; Lenkinski, R. E. *J. Magn. Reson. Imaging* **2009**, *30* (6), 1240-8.
160. Rojas-Quijano, F. A.; Kovacs, Z.; Sherry, A. D., Synthesis and evaluation of PCTA derivatives as luminescent-CEST active molecular probes for soft tissue imaging. In *ACS National Meeting*, Abstr. Pap. Am. Chem. Soc.: San Francisco, CA, 2006; pp INOR-282.
161. Rojas-Quijano, F. A.; Benyo, E. T.; Tirscso, G.; Kalman, F. K.; Baranyai, Z.; Aime, S.; Sherry, A. D.; Kovacs, Z. *Chem. Eur. J.* **2009**, *15*, 13188-200.
162. Izatt, R. M.; Pawlak, K.; Bradshaw, J. S. *Chem. Rev.* **1991**, *91*, 1721-2085.
163. Hindo, S. S.; Mancino, A. M.; Braymer, J. J.; Liu, Y. H.; Vivekanandan, S.; Ramamoorthy, A.; Lim, M. *H. J. Am. Chem. Soc.* **2009**, *131*, 16663-5.
164. Scott, L. E.; Orvig, C. *Chem. Rev.* **2009**, *109*, 4885-910.
165. Amaro, M.; Birch, D. J. S.; Rolinski, O. J. *Phys. Chem. Chem. Phys.* **2011**, *13*, 6434-41.
166. Maji, S. K.; Amsden, J. J.; Rothschild, K. J.; Condrón, M. M.; Teplow, D. B. *Biochemistry* **2005**, *44*, 13365-76.
167. Rolinski, O. J.; Amaro, M.; Birch, D. J. S. *Biosens. Bioelectron.* **2010**, *25*, 2249-52.
168. Yang, C.-A.; Chen, Y.-H.; Ke, S.-C.; Chen, Y.-R.; Huang, H.-B.; Lin, T.-H.; Chen, Y.-C. *Int. J. Alzheimer's Dis.* **2011**, *2011*, 1-7.
169. Boligon, A. A.; Machado, M. M.; Athayde, M. L. *Med. Chem.* **2014**, *4* (7), 517-22.
170. Re, R.; Pellegrini, N.; Proteggente, A.; Pannala, A.; Yang, M.; Rice-Evans, C. *Free Radical Biol. Med.* **1999**, *26*, 1231-7.
171. Guilloureau, L.; Combalbert, S.; Sournia-Saquet, A.; Mazarguil, H.; Faller, P. *ChemBioChem* **2007**, *8*, 1317-25.

172. Yepremyan, A.; Mehmood, A.; Brewer, S. M.; Barnett, M. M.; Janesko, B. G.; Akkaraju, G.; Simanek, E. E.; Green, K. N. *RSC Advances* **2018**, *8*, 3024-35.
173. Steenken, S.; O'Neill, P. J. *Phys. Chem.* **1979**, *83* (18), 2407-12.
174. Koleckar, V.; Kubikova, K.; Rehakova, Z.; Kuca, K.; Jun, D.; Jahodar, L.; Opletal, L. *Mini-Reviews in Medicinal Chemistry* **2008**, *8* (5), 436-47.
175. Sharma, O. P.; Bhat, T. K. *Food Chem.* **2009**, *113*, 1202-5.
176. Wuts, P. G. M.; Greene, T. W., *Greene's Protective Groups in Organic Synthesis*. 4th ed.; John Wiley & Sons, Inc.: Hoboken, NJ, 2007.
177. Aime, S.; Botta, M.; Crich, S. G.; Giovenzana, G. B.; Jommi, G.; Pagliarin, R.; Sisti, M. *Inorg. Chem.* **1997**, *36*, 2992-3000.
178. Busto, E.; Gonzalez-Alvarez, A.; Gotor-Fernandez, V.; Alfonso, I.; Gotor, V. *Tetrahedron* **2010**, *66*, 6070-77.
179. Chessa, G.; Alberto, S. *J. Chem. Soc., Perkin Trans. 1* **1996**, (4), 307-11.
180. Froidevaux, P.; Harrowfield, J. M.; Sobolev, A. N. *Inorg. Chem.* **2000**, *39*, 4678-87.
181. Kan, T.; Fukuyama, T. *Chem. Commun.* **2004**, 353-9.
182. Mochizuki, K.; Sugita, T.; Kuroiwa, S.; Yamada, F.; Hayano, K.; Ohgami, Y.; Suzuki, M.; Kato, S. *Inorg. Chim. Acta* **2010**, *363*, 3151-57.
183. Bottino, F.; Di Grazia, M.; Finocchiaro, P.; Fronczek, F. R.; Mamo, A.; Pappalardo, S. *J. Org. Chem.* **1988**, *53*, 3521-9.
184. Pappalardo, S.; Bottino, F.; Di Grazia, M.; Finocchiaro, P.; Mamo, A. *Heterocycles* **1985**, *23* (8), 1881-4.
185. Wessel, A. J.; Schultz, J. W.; Tang, F.; Duan, H.; Mirica, L. M. *Org. Biomol. Chem.* **2017**, *15*, 9923-31.

186. Alpha, B.; Anklam, E.; Deschenaux, R.; Lehn, J.-M.; Pietraskiewicz, M. *Helv. Chim. Acta* **1988**, *71*, 1042-52.
187. Satou, T.; Shinmyozu, T. *J. Chem. Soc., Perkin Trans. 2* **2002**, 393-7.
188. Alonso, E.; Ramon, D. J.; Yus, M. *Polyhedron* **1997**, *53* (42), 14355-68.
189. Martell, A. E.; Motekaitis, R. J., *Determination and Use of Stability Constants*. 2nd ed.; VCH Publishers, Inc.: New York, NY, 1992.
190. Grossman, H. Z. *Anorg. Chem.* **1905**, *43*, 356-69.
191. Lewis, G. N.; Randall, M. *J. Am. Chem. Soc.* **1921**, *43* (5), 1112-54.
192. Tircso, G.; Davda, C.; Hyde, K.; Gonzalez, P.; Brewer, S. M.; Johnston, H. M.; Akkaraju, G.; Green, K. N. *Manuscript in preparation* **2018**.
193. Cabani, S.; Ceccanti, N.; Pardini, R.; Tine, M. *Polyhedron* **1999**, *18*, 3295-303.
194. Tircso, G.; Regueiro-Figueroa, M.; Nagy, V.; Garda, Z.; Garai, T.; Kalman, F. K.; Esteban-Gomez, D.; Toth, E.; Platas-Iglesias, C. *Chemistry* **2016**, *22* (3), 896-901.
195. Ruangpornvisuti, V. W.; Probst, M. M.; Rode, B. M. *Inorg. Chim. Acta* **1988**, *144* (1), 21-3.
196. Hancock, R. D.; Shaikjee, M. S.; Dobson, S. M.; Boeyens, J. C. A. *Inorg. Chim. Acta* **1988**, *154* (2), 229-38.
197. Thom, V. J.; Hancock, R. D. *J. Chem. Soc., Dalton Trans.* **1985**, 1877-80.
198. Thom, V. J.; Hosken, G. D.; Hancock, R. D. *Inorg. Chem.* **1985**, *24* (21), 3378-81.
199. Hancock, R. D.; Dobson, S. M.; Evers, A.; Wade, P. W.; Ngwenya, M. P.; Boeyens, J. C. A.; Wainwright, K. P. *J. Am. Chem. Soc.* **1988**, *110* (9), 2788-94.
200. Irving, H.; Williams, R. J. P. *J. Chem. Soc.* **1953**, 3192-3210.
201. Kruger, H.-J. *Chem. Ber.* **1995**, *128*, 531-9.
202. Lever, A. B. P., *Inorganic Electronic Spectroscopy*. Elsevier Publishing Company: Amsterdam, The Netherlands, 1968.

203. Bottcher, A.; Takeuchi, T.; Hardcastle, K. I.; Meade, T. J.; Gray, H. B.; Cwikel, D.; Kapon, M.; Dori, Z. *Inorg. Chem.* **1997**, *36*, 2498-2504.
204. Sayre, L. M.; Smith, M. A.; Perry, G. *Curr. Med. Chem.* **2001**, *8* (7), 721-38.
205. *APEX3*, Version 1; Bruker AXS Inc.: Madison, WI, 2016.
206. *SAINT*, Bruker AXS Inc.: Madison, WI, 2012.
207. *SADABS*, Bruker AXS Inc.: Madison, WI, 2001.
208. Dolomanov, O. V.; Bourhis, L. J.; Gildea, R. J.; Howard, J. A. K.; Puschmann, H. *J. Appl. Cryst.* **2009**, *42*, 339-41.
209. Sheldrick, G. M. *Acta Cryst.* **2008**, *A64*, 112-22.
210. Sheldrick, G. M. *Acta Cryst.* **2015**, *C71*, 3-8.
211. Schwarzenbach, G.; Flaschka, H. A., *Complexometric Titrations*. Methuen Young Books: London, UK, 1969.
212. Irving, H. M.; Miles, M. G. *Anal. Chim. Acta* **1967**, *38*, 475-88.
213. Gans, P.; Sabatini, A.; Vacca, A. *Talanta* **1996**, *43*, 1739-53.
214. Faller, P.; Hureau, C.; Dorlet, P.; Hellwig, P.; Coppel, Y.; Collin, F.; Alies, B. *Coord. Chem. Rev.* **2012**, *256*, 2381-96.
215. Constable, E. C., *Coordination Chemistry of Macrocyclic Compounds*. Oxford University Press: New York, NY, 1999; p 93.
216. Bakac, A.; Brynildson, M. E.; Espenson, J. H. *Inorg. Chem.* **1986**, *25*, 4108-14.
217. Hubin, T. J. *Coord. Chem. Rev.* **2003**, *241*, 27-46.
218. Martin, L. Y.; DeHayes, L. J.; Zompa, L. J.; Busch, D. H. *J. Am. Chem. Soc.* **1974**, *96* (12), 4046-8.
219. Sarther, C. M.; Blinn, E. L. *Inorg. Chem.* **1976**, *15* (12), 3083-86.
220. Bongard, J. E.; Hartsock, R. W.; Stegbauer, W. D.; Streich, F. C.; Barnum, R.; Chang, E. L.; Knight, D. *A. Synth. React. Inorg. M.* **2005**, *35* (9), 727-731.

221. Choi, K.-Y.; Lee, H.-K.; Kim, K.-J.; Ryu, H.; Lee, K.-C.; Ko, J.; Kim, M.-J. *Transition Met. Chem.* **2006**, *31* (8), 1093-1097.
222. Omar, H. A. A.; Moore, P.; Alcock, N. W. *J. Chem. Soc., Dalton Trans.* **1994**, 2631-5.
223. Ozay, H.; Baran, Y.; Ishii, Y. *Spectrochim. Acta A, Mol. Biomol. Spectrosc.* **2011**, *83* (1), 525-31.
224. Collman, J. P.; Schneider, P. W. *Inorg. Chem.* **1966**, *5* (8), 1380-4.
225. Hubin, T. J.; Alcock, N. W.; Clase, H. J.; Seib, L. L.; Busch, D. H. *Inorg. Chim. Acta* **2002**, *337*, 91-102.
226. Delgado, R.; Quintino, S.; Teixeira, M.; Zhang, A. *J. Chem. Soc., Dalton Trans.* **1996**, 55-63.
227. Tait, A. M.; Lovecchio, F. V.; Busch, D. H. *Inorg. Chem.* **1977**, *16* (9), 2206-12.
228. Greenaway, A. M.; Lancashire, R. J. *J. Chem. Ed.* **1982**, *59* (5), 419-20.
229. Blomstrand, C. W. *Berichte* **1871**, *4*, 40.
230. Jorgensen, S. M. *Z. Anorg. Chem.* **1899**, *19*, 109.
231. Werner, A. *Z. Anorg. Chem.* **1893**, *3*, 267.
232. Werner, A. *Berichte* **1907**, *40*, 4817.
233. Werner, A. *Berichte* **1911**, *44*, 1887.
234. Werner, A. *Berichte* **1914**, *47*, 3087.
235. Werner, A.; Miolati, A. *Z. Phys. Chem.* **1893**, *12*, 35.
236. Werner, A.; Miolati, A. *Z. Phys. Chem.* **1894**, *14*, 506.
237. Eberhardt, W. H. *J. Chem. Ed.* **1964**.
238. Koga, N.; Kimizu, T.; Sakamoto, M.; Furkawa, Y. *Chem. Educator* **2009**, *14*, 1-4.
239. Lever, A. B. P. *J. Chem. Ed.* **1974**, *51* (9), 612-16.
240. Martins, L. J. A.; da Costa, J. B. *J. Chem. Ed.* **1986**, *63* (11), 989.
241. Nguyen, V. D.; Birdwhistell, K. R. *J. Chem. Ed.* **2014**, *91*, 880-882.
242. Ophardt, C. E. *J. Chem. Ed.* **1980**, *57* (6), 453.

243. Spears Jr., L. G.; Spears, L. G. *J. Chem. Ed.* **1984**, *61* (3), 252-54.
244. Tro, N. J., *Chemistry: A Molecular Approach*. 3rd ed.; Pearson Education, Inc.: Upper Saddle River, NJ, 2014.
245. Zeltmann, A. H.; Matwiyoff, N. A.; Morgan, L. O. *J. Phys. Chem.* **1968**, *72* (1), 121-7.
246. Drago, R. S., *Physical Methods in Inorganic Chemistry*. Van Nostrand Reinhold Company: New York, NY, 1965.
247. Dunn, T. M.; McClure, D. S.; Pearson, R. G., *Some Aspects of Crystal Field Theory*. Harper & Row: New York, NY, 1965.
248. Lewis, K. G.; Ghosh, S. K.; Bhuvanesh, N.; Gladysz, J. A. *ACS Central Science* **2015**, *1* (1), 50-56.
249. Wen, J.; Qin, S.; L.-F., M.; Dong, L.; Zhang, J.; Liu, S.-S.; Duan, Y.-S.; Chen, S.-Y.; Hu, C.-W.; Yu, X.-Q. *Org. Lett.* **2010**, *12*.
250. *APEX2*, Version 2014.9-0; Bruker AXS Inc.: Madison, WI, 2007.
251. *XSELL*, Version 6.3.1; Bruker AXS Inc.: Madison, WI, 2004.
252. Dolomanov, O. V.; Bourhis, L. J.; Gildea, R. J.; Howard, J. A. K.; Puschmann, H. *J. Appl. Cryst.* **2009**, *42*, 339-41.
253. *CrysAlis PRO*, Agilent Technologies Ltd.: Oxfordshire, England, 2014.
254. Sheldrick, G. M. *Acta Cryst.* **2015**, *A71*, 3-8.
255. Sheldrick, G. M. *Acta Cryst.* **2015**, *C71*, 3-8.
256. Spek, A. L. *Acta Cryst.* **2009**, *D65*, 148-55.
257. Spek, A. L. *Acta Cryst.* **2009**, *C71*, 9-18.
258. Abragam, A.; Bleaney, B., *Electron Paramagnetic Resonance of Transition Ions (International Series of Monographs on Physics)*. 1970.
259. Bennett, B.; Holz, R. C. *Biochemistry* **1997**, *36*, 9837.
260. Bennett, B.; Holz, R. C. *J. Am. Chem. Soc.* **1997**, *119*, 1923.

261. Crawford, P. A.; Yang, K.-W.; Sharma, N.; Bennett, B. *Biochemistry* **2005**, *44*, 5168.
262. Periyannan, G. R.; Costello, A. L.; Tierney, D. L.; Yang, K.-W.; Bennett, B.; Crowder, M. W. *Biochemistry* **2006**, *45*, 1313.
263. Yang, H.; Aitha, M.; Marts, A. R.; Hetrick, A.; Bennett, B.; Crowder, M. W.; Tierney, D. L. *J. Am. Chem. Soc.* **2014**, *136*, 7273.
264. Brunning, A., The Transition Metals. Metals, E. I.-T., Ed. Compound Interest: 2013.
265. Brewer, K. J.; Clavin, M.; Lumpkin, R. S.; Otvos, J. W.; Spreer, L. O. *Inorg. Chem.* **1989**, *28*, 4446-51.
266. Verhoeven, J., *Steel Metallurgy for the Non-Metallurgist*. ASM International: Materials Park, OH, 2007.
267. Dell, R. M. *Solid State Ionics* **2000**, *134*, 139-58.
268. Towle, D. K.; Botsford, C. A. *Inorg. Chim. Acta* **1988**, *141*, 167-8.
269. Law, N.; Caudle, M.; Pecoraro, V., *Manganese Redox Enzymes and Model Systems: Properties, Structures, and Reactivity*. Academic Press: San Diego, CA, 1998; Vol. 46.
270. Shin, B.-K.; Kim, Y.; Kim, M.; Han, J. *Polyhedron* **2007**, *26*, 4557-66.
271. Horsburgh, M. J.; Wharton, S. J.; Karavolos, M.; Foster, S. J. *Trends Microbiol.* **2002**, *10* (11), 496-501.
272. Hayyan, M.; Hashim, M. A.; AlNashef, I. M. *Chem. Rev.* **2016**, *116*, 3029-3085.
273. Atzenhofer, W.; Regelsberger, G.; Jacob, U.; Peschek, G. A.; Furtmuller, P. G.; Huber, R.; Obinger, C. *J. Mol. Biol.* **2002**, *321* (3), 479-89.
274. Létumier, F.; Broeker, G.; Barbe, J.-M.; Guillard, R.; Lucas, D.; Dahaoui-Gindrey, V.; Lecomte, C.; Thouin, L.; Amatore, C. *J. Chem. Soc., Dalton Trans.* **1998**, (13), 2233-9.
275. Riley, D. P.; Weiss, R. H. *J. Am. Chem. Soc.* **1994**, *116*, 387-8.
276. Tomczyk, D.; Andrijewski, G.; Nowak, L.; Urbaniak, P.; Sroczynski, D. *Inorg. Chim. Acta* **2012**, *390*, 70-78.

277. Bryant, D. A.; Frigaard, N.-U. *Trends Microbiol.* **2006**, *14* (11), 488-96.
278. Armstrong, F. A. *Phil. Trans. R. Soc. B* **2008**, *363*, 1263-70.
279. Nocera, D. G. *Acc. Chem. Res.* **2012**, *45*, 767-76.
280. Barber, J. *Chem. Soc. Rev.* **2009**, *38*, 185-96.
281. Duan, L.; Bozoglian, F.; Mandal, S.; Stewart, B.; Privalov, T.; Llobet, A.; Sun, L. *Nat. Chem.* **2012**, *4* (5), 418-23.
282. Joya, K. S.; Vallés-Pardo, J. L.; Joya, Y. F.; Eisenmayer, T.; Thomas, B.; Buda, F.; de Groot, H. J. M. *ChemPlusChem* **2013**, *78* (1), 35-47.
283. Duan, L.; Araujo, C. M.; Ahlquist, M. S. G.; Sun, L. *PNAS* **2012**, *109* (39), 15584-88.
284. Singh, A.; Spiccia, L. *Coord. Chem. Rev.* **2013**, *257*, 2607-22.
285. Brudvig, G. W.; Crabtree, R. H., Bioinorganic Chemistry of Manganese Related to Photosynthetic Oxygen Evolution. In *Progress in Inorganic Chemistry*, Lippard, S. J., Ed. John Wiley & Sons: Hoboken, NJ, 1989; Vol. 37, pp 99-142.
286. Joliot, P.; Kok, B., Oxygen Evolution in Photosynthesis. In *Bioenergetics of Photosynthesis*, Govindjee, Ed. Academic Press Inc.: New York, New York, 1975; p 387.
287. Wieghardt, K. *Angew. Chem., Int. Ed.* **1994**, *33* (7), 725-8.
288. Dismukes, G. C.; Siderer, Y. *Proc. Natl. Acad. Sci.* **1981**, *78* (1), 274-8.
289. Yachandra, V. K.; DeRose, V. J.; Latimer, M. J.; Mukerji, I.; Sauer, K.; Klein, M. P. *Science* **1993**, *260*, 675-9.
290. Umena, Y.; Kawakami, K.; Shen, J.-R.; Kamiya, N. *Nature* **2011**, *473*, 55-61.
291. Rhee, K.-H.; Morris, E. P.; Barber, J.; Kuhlbrandt, W. *Nature* **1998**, *396*, 283-6.
292. Biesiadka, J.; Loll, B.; Kern, J.; Irrgang, K.-D.; Zouni, A. *Phys. Chem. Chem. Phys.* **2004**, *6*, 4733-6.
293. Ferreira, K. N.; Iverson, T. M.; Maghlaoui, K.; Barber, J.; Iwata, S. *Science* **2004**, *303*, 1831-8.

294. Guskov, A.; Kern, J.; Gabdulkhakov, A.; Broser, M.; Zouni, A.; Saenger, W. *Nat. Struct. Mo. Biol.* **2009**, *16*, 334-42.
295. Kamiya, N.; Shen, J.-R. *PNAS* **2003**, *100* (1), 98-103.
296. Loll, B.; Kern, J.; Saenger, W.; Zouni, A.; Biesiadka, J. *Nature* **2005**, *438*, 1040-4.
297. Nield, J.; Kruse, O.; Ruprecht, J.; de Fonseca, P.; Buchel, C.; Barber, J. *J. Biol. Chem.* **2000**, *275* (36), 27940-6.
298. Zouni, A.; Witt, H.-T.; Kern, J.; Fromme, P.; Krauß, N.; Saenger, W.; Orth, P. *Nature* **2001**, *409*, 739-43.
299. Nyholm, R. S.; Turco, A. *Chem. Ind. (London)* **1960**, 74-5.
300. Plaksin, P. M.; Stoufer, R. C.; Mathew, M.; Palenik, G. J. *J. Am. Chem. Soc.* **1970**, *94* (6), 2121-2.
301. Uson, R.; Riera, V.; Ciriano, M. *Transition Met. Chem.* **1976**, *1* (3), 98-9.
302. Cooper, S. R.; Clavin, M. *J. Am. Chem. Soc.* **1977**, *99* (22), 6623-30.
303. Collins, M. A.; Hodgson, D. J.; Michelsen, K.; Towle, D. K. *J. Chem. Soc., Chem. Commun.* **1987**, 1659-60.
304. Brewer, K. J.; Liegeois, A.; Otvos, J. W.; Calvin, M.; Spreer, L. O. *J. Chem. Soc., Chem. Commun.* **1988**, 1219-20.
305. Hagen, K. S.; Armstrong, W. H.; Hope, H. *Inorg. Chem.* **1988**, *27*, 967-9.
306. Suzuki, M.; Tokura, S.; Suhara, M.; Uehara, A. *Chem. Lett.* **1988**, 477-80.
307. Stebler, M.; Ludi, A.; Burgi, H.-B. *Inorg. Chem.* **1986**, *25*, 4743-50.
308. Manchanda, R.; Brudvig, G. W.; de Gala, S.; Crabtree, R. H. *Inorg. Chem.* **1994**, *33*, 5157-60.
309. Goodson, P. A.; Glerup, J.; Michelsen, K.; Pedersen, E. *Inorg. Chem.* **1990**, *29*, 503-8.
310. Yatabe, T.; Kikkawa, M.; Matsumoto, T.; Nakai, H.; Kaneko, K.; Ogo, S. *Dalton Trans.* **2014**, *43*, 3063-71.
311. Goodson, P. A.; Hodgson, D. J. *Inorg. Chim. Acta* **1990**, 49-57.

312. Nakamori, H.; Matsumoto, T.; Yatabe, T.; Yoon, K.-S.; Nakai, H.; Ogo, S. *Chem. Commun.* **2014**, *50*, 13059-61.
313. Goodson, P. A.; Hodgson, D. J.; Glerup, J.; Michelsen, K.; Weihe, H. *Inorg. Chim. Acta* **1992**, *197*, 141-7.
314. Limburg, J.; Vrettos, J. S.; Liable-Sands, L. M.; Rheingold, A. L.; Crabtree, R. H.; Brudvig, G. W. *Science* **1999**, *283*, 1524-27.
315. Alcock, N. W.; Busch, D. H.; Liu, C. Y., CCDC 675326: Experimental Crystal Structure Determination. Cambridge Crystallographic Data Centre, 2008.
316. Robin, M. B.; Day, P. *Adv. Inorg. Chem. Radiochem.* **1967**, *10*, 247-422.
317. Dingle, R. *Acta Chemica Scandinavica* **1966**, *20* (1), 33-44.
318. Cooper, S. R.; Dismukes, G. C.; Klein, M. P.; Calvin, M. J. *Am. Chem. Soc.* **1978**, *100* (23), 7248-52.
319. Gref, A.; Balavoine, G.; Riviere, H.; Andrieux, C. P. *Nouv. J. Chim.* **1984**, *8* (10), 615-18.
320. Ramaraj, R.; Kira, A.; Kaneko, M. *Angew. Chem., Int. Ed. Engl.* **1986**, *25* (9), 825-7.
321. Ramaraj, R.; Kira, A.; Kaneko, K. *Chem. Lett.* **1987**, 261-4.
322. Suzuki, M.; Senda, H.; Kobayashi, Y.; Oshio, H.; Uehara, A. *Chem. Lett.* **1988**, 1763-1766.
323. Goodson, P. A.; Hodgson, D. J. *Inorg. Chem.* **1989**, *28*, 3606-8.
324. Goodson, P. A.; Glerup, J.; Hodgson, D. J.; Michelsen, K.; Weihe, H. *Inorg. Chem.* **1991**, *30*, 4909-14.
325. Horner, O.; Charlot, M.-F.; Boussac, A.; Anxolabehere-Mallart, E.; Tchertanov, L.; Guilhem, J.; Girerd, J. J. *Eur. J. Inorg. Chem.* **1998**, 721-7.
326. Hureau, C.; Blondin, G.; Charlot, M.-F.; Philouze, C.; Nierlich, M.; Cersario, M.; Anxolaberhere-Mallart, E. *Inorg. Chem.* **2005**, *44*, 3669-83.
327. Schindler, S.; Walter, O.; Pederson, J. Z.; Toftlund, H. *Inorg. Chim. Acta* **2000**, *303*, 215-19.
328. Oki, A. R.; Glerup, J.; Hodgson, D. J. *Inorg. Chem.* **1990**, *29*, 2435-41.

329. Gultneh, Y.; Yisgedu, T. B.; Tesema, Y. T.; Butcher, R. J. *Inorg. Chem.* **2003**, *42*, 1857-67.
330. Shin, B.-K.; Kim, M.; Han, J. *Polyhedron* **2010**, 2560-8.
331. Panja, A.; Shaikh, N.; Banerjee, P.; Saha, B. *Int. J. Chem. Kin.* **2004**, *36* (2), 119-28.
332. Ren, Y.-W.; Li, J.; Zhang, F.-X.; Zhang, J.-H.; Guo, H. *Chin. J. Chem.* **2005**, *23*, 418-420.
333. Goswami, S.; Shaikh, N.; Panja, A.; Banerjee, P. *Int. J. Chem. Kin.* **2004**, *36*, 129-7.
334. Limburg, J.; Vrettos, J. S.; Chen, H.; dePaula, J. C.; Crabtree, R. H.; Brudvig, G. W. *J. Am. Chem. Soc.* **2001**, *123*, 423-430.
335. Yagi, M.; Narita, K. *J. Am. Chem. Soc.* **2004**, *126*, 8084-5.
336. Kurz, P. *Dalton Trans.* **2009**, 6103-08.
337. Hubin, T. J.; McCormick, J. M.; Alcock, N. W.; Busch, D. H. *Inorg. Chem.* **2001**, *40*, 435-44.
338. Hambley, T. W.; Lawrance, G. A.; Sangster, D. F.; Ward, C. B. *Aust. J. Chem.* **1987**, *40*, 883-93.
339. Bryan, P. S.; Dabrowiak, J. C. *Inorg. Chem.* **1975**, *14* (2), 296-9.
340. Bryan, P. S.; Dabrowiak, J. C. *Inorg. Chem.* **1975**, *14* (2), 299-302.
341. Chan, P.-K.; Poon, C.-K. *J. C. S. Dalton* **1976**, 858-62.
342. Daugherty, P. A.; Glerup, J.; Goodson, P. A.; Hodgson, D. J.; Michelsen, K. *Acta Chemica Scandinavica* **1991**, *45*, 244-53.
343. Bryan, P. S.; Calvert, J. M. *Inorg. Nucl. Chem. Letters* **1977**, *13*, 615-9.
344. Mossin, S.; Sorensen, H. O.; Weihe, H.; Glerup, J.; Sotofte, I. *Inorg. Chim. Acta* **2004**, *358*, 1096-1106.
345. Hay, R. W.; Fraser, I. *Polyhedron* **1997**, *16* (13), 2223-7.
346. Kimura, E.; Shionoya, M.; Yamauchi, T.; Shiro, M. *Chem. Lett.* **1991**, 1217-20.
347. Lis, T. *Acta Crystallogr., Sect. B* **1978**, *34*, 1342.
348. Meunier, B.; de Carvalho, M.-E.; Bortolini, O.; Momenteau, M. *Inorg. Chem.* **1988**, *27* (1), 161-4.

349. Hubin, T. J.; McCormick, J. M.; Collinson, S. R.; Alcock, N. W.; Clase, H. J.; Busch, D. H. *Inorg. Chim. Acta* **2003**, *346*, 76-86.
350. Bard, A. J.; Faulkner, L. R., *Electrochemical Methods: Fundamentals and Applications*. 2nd ed.; John Wiley & Sons, Inc.: Hoboken, NJ, 2001.
351. Toth, E.; Merbach, A. E., *The Chemistry of Contrast Agents in Medical Magnetic Resonance Imaging*. John Wiley & Sons: Chichester, U.K., 2001.
352. Green, K. N.; Tircso, G. *Original Research Proposal* **2016**, 1-5.
353. Thomsen, H. S. *Radiologic Clinics* **2009**, *47* (5), 827-31.
354. *ACR Manual on Contrast Media*. 10 ed.; American College of Radiology: 2017; Vol. 10.3.
355. Aguilera, C.; Agusti, A. *Med. Clin.-Barcelona* **2011**, *136* (14), 643-5.
356. Stratta, P.; Canavese, C.; Quaglia, M.; Fenoglio, R. *Rheumatology* **2010**, *49* (4), 821-3.
357. Jalandhara, N.; Arura, R.; Batuman, V. *Clin. Pharmacol. Ther.* **2011**, *89* (6), 920-3.
358. Kay, J. *Clin. Exp. Rheumatol.* **2010**, *28* (2), S79.
359. Kay, J.; Czirjak, L. *Ann. Rheum. Dis.* **2010**, *69* (11), 1895-7.
360. Dees, A.; Zahl, A.; Puchta, R.; van Eikema Hommes, N. J. R.; Heinemman, F. W.; Ivanovic-Burmazovic, I. *Inorg. Chem.* **2007**, *46*, 2459-70.
361. Koretsky, A. P.; Silva, A. C. *NMR Biomed.* **2004**, *17* (8), 527-31.
362. Liu, G.-F.; Filipovic, M.; Heinemann, F. W.; Ivanovic-Burmazovic, I. *Inorg. Chem.* **2007**, *46* (21), 8825-35.
363. Rocklage, S. M.; Cacheris, W. P.; Quay, S. C.; Hahn, F. E.; Raymond, K. N. *Inorg. Chem.* **1989**, *28*, 477-85.
364. Li, Y.; Huang, T.-T.; Carlson, E. J.; Melov, S.; Ursell, P. C.; Olson, J. L.; Noble, L. J.; Yoshimura, M. P.; Berger, C.; Chan, P. H.; Wallace, D. C.; Epstein, C. J. *Nat. Genet.* **1995**, *11*, 376-81.
365. Wedler, F. C.; Denman, R. B. *Curr. Top. Cell Regul.* **1984**, *24*, 153-69.

366. Aoki, I.; Naruse, S.; Tanaka, T. *NMR Biomed.* **2004**, *17*, 569-80.
367. Bock, N. A.; Silva, A. C. *Future Neurol.* **2007**, *2*, 297-205.
368. Murakami, T.; Baron, R. L.; Peterson, M. S.; Oliver, J. H., III; Davis, P. L.; Confer, S. R.; Federle, M. *P. Radiology* **1996**, *200* (1), 69-77.
369. Aime, S.; Anelli, P. L.; Botta, M.; Brocchetta, M.; Canton, S.; Fedeli, F.; Gianolio, E.; Terreno, E. *J. Biol. Inorg. Chem.* **2002**, *7* (1-2), 58-67.
370. Koenig, S. H.; Baglin, C.; Brown, R. D., III; Brewer, F. C. *Magn. Res. Med.* **1984**, *1* (4), 496-501.
371. Maigut, J.; Meier, R.; Zahl, A.; Van Eldik, R. *Inorg. Chem.* **2008**, *47*, 5702-19.
372. Troughton, J. S.; Greenfield, M. T.; Greenwood, J. M.; Dumas, S.; Wiethoff, A. J.; Wang, J.; Spiller, M.; McMurry, T. J.; Caravan, P. *Inorg. Chem.* **2004**, *43*, 6313-23.
373. Bertin, A.; Steibel, J.; Michou-Gallani, A.-I.; Gallani, J.-L.; Felder-Flesch, D. *Bioconjugate Chem.* **2009**, *20*, 760-7.
374. Balogh, E.; He, Z.; Hsieh, W.; Liu, S.; Toth, E. *Inorg. Chem.* **2007**, *46*, 238-50.
375. Bianchi, A.; Calabi, L.; Giorgi, C.; Losi, P.; Mariani, P.; Palano, D.; Paoli, P.; Rossi, P.; Valtancoli, B. *J. Chem. Soc., Dalton Trans.* **2001**, 917-22.
376. Wang, S.; Westmoreland, T. D. *Inorg. Chem.* **2009**, *48*, 719-27.
377. Filosa, R.; Peduto, A.; Micco, S. D.; Caprariis, P.; Festa, M.; Petrella, A.; Capranico, G.; Bifulco, G. *Bioorg Med Chem* **2009**, *17* (1), 13-24.
378. Garza-Oritz, A.; Maheswari, P. U.; Siegler, M.; Spek, A. L.; Reedijk, J. *Inorg. Chem.* **2008**, *47*, 6964-6973.
379. Papadopoulos, E. P.; Jarrar, A.; Issidorides, C. H. *J. Org. Chem.* **1966**, *31*, 615-6.
380. Vance, A. L.; Alcock, N. W.; Busch, D. H.; Heppert, J. A. *Inorg. Chem.* **1997**, *36*, 5132-4.
381. Wakelin, L. P. G.; Bu, X.; Eleftheriou, A.; Parmar, A.; Hayek, C.; Stewart, B. W. *J. Med. Chem.* **2003**, *46*, 5790-5802.

382. Clayden, J.; Greeves, N.; Warren, S., *Organic Chemistry*. 2nd ed.; Oxford University Press: New York, NY, 2012.
383. McMurry, J., *Organic Chemistry*. 7th ed.; Thomson Higher Education: Belmont, CA, 2008.
384. Paital, A. R.; Mandal, D.; Huang, X.; Li, J.; Aromi, G.; Ray, D. *Dalton Trans.* **2009**, 1352-62.
385. Martinez, S., J. M.; Bastida de la Calle, R.; Macias, A.; Perez-Lourido, P.; Matarranz, L. V. *Polyhedron* **2006**, *25*, 3495-500.
386. Vigato, P. A.; Tamburini, S. *Coord. Chem. Rev.* **2004**, *248*, 1717-2128.
387. Vigato, P. A.; Tamburini, S.; Bertolo, L. *Coord. Chem. Rev.* **2007**, *251*, 1311-492.
388. del Carmen Fernandez-Fernandez, M.; Bastida, R.; Macias, A.; Perez-Lourido, P.; Valencia, L. *Polyhedron* **2007**, *26*, 5317-23.
389. Lindahl, P. A. *J. Inorg. Biochem.* **2012**, *106*, 172-8.
390. Nunez, C.; Bastida, R.; Lexama, L.; Macias, A.; Perez-Lourido, P.; Valencia, L. *Inorg. Chem.* **2011**, *50*, 5596-604.
391. Salata, C. A.; Youinou, M.-T.; Burrows, C. J. *J. Am. Chem. Soc.* **1989**, *111* (26), 9278-9.
392. Salata, C. A.; Youinou, M.-T.; Burrows, C. J. *Inorg. Chem.* **1991**, *30*, 3454-61.
393. Zhang, X.; Huang, D.; Chen, Y.-S.; Holm, R. H. *Inorg. Chem.* **2012**, *51*, 11017-29.
394. Beattie, J. W.; SantaLucia, D. J.; White, D. S.; Groysman, S. *Inorg. Chim. Acta* **2017**, *460*, 8-16.
395. Cooper, B. G.; Napoline, J. W.; Thomas, C. M. *Catalysis Reviews* **2012**, *54* (1), 1-40.
396. Halvagar, M. R.; Neisen, B.; Tolman, W. B. *Inorg. Chem.* **2013**, *52*, 793-9.
397. Huang, D.; Holm, R. H. *J. Am. Chem. Soc.* **2010**, *132*, 4693-701.
398. Thomas, C. M. *Comm. Inorg. Chem.* **2011**, *32*, 14-38.
399. Bazzicuppi, C.; Bencini, A.; Bianchi, A.; Borri, C.; Danesi, A.; Garcia-Espana, E.; Giorgi, C.; Baltancoli, B. *J. Org. Chem.* **2008**, *73*, 8286-95.

400. Fronczek, F. R.; Schilling, P. J.; Watkins, S. F.; Majestic, V. K.; Newkome, G. R. *Inorg. Chim. Acta* **1996**, *246*, 119-23.
401. Jazwinski, J.; Lehn, J.-M.; Meric, R.; Vigneron, J.-P.; Caesario, M.; Guilhem, J.; Pascard, C. *Tetrahedron Lett.* **1987**, *28* (30), 3489-92.
402. Li, F.; Delgado, R.; Costa, J.; Drew, M. G. B.; Felix, V. *Dalton Trans.* **2005**, 82-91.
403. Li, F.; Delgado, R.; Felix, V. *Eur. J. Inorg. Chem.* **2005**, 4550-61.
404. Nunez, C.; Oliveira, E.; Giestas, L.; Valencia, L.; Macias, A.; Lima, J. C.; Bastida, R.; Lodeiro, C. *Inorg. Chim. Acta* **2008**, *361*, 2183-94.
405. Bligh, S. W. A.; Chio, N.; Evagorou, E. G.; Li, W.-S.; McPartlin, M. *J. Chem. Soc., Chem. Commun.* **1994**, 2399-400.
406. Rothermel, G. L.; Miao, L. J.; Hill, A. L.; Jackels, S. C. *Inorg. Chem.* **1992**, *31*, 4854-59.
407. Valencia, L.; Bastida, R.; del Carmen Fernandez-Fernandez, M.; Macias, A.; Vicente, M. *Inorg. Chim. Acta* **2005**, *358*, 2618-28.
408. Nunez, C.; Bastida, R.; Macias, A.; Mato-Iglesias, M.; Platas-Iglesias, C.; Valencia, L. *Dalton Trans.* **2008**, 3841-50.
409. Alarcon, J.; Teresa Albelda, M.; Belda, R.; Paz Clares, M.; Delgado-Pinar, E.; Frias, J. C.; Garcia-Espana, E.; Gonzalez, J.; Soriano, C. *Dalton Trans.* **2008**, 6530-8.
410. Nunez, C.; Bastida, R.; Macias, A.; Aldrey, A.; Valencia, L. *Polyhedron* **2010**, *29*, 126-33.
411. Fronczek, F. R.; Majestic, V. K.; Newkome, G. R. *J. Chem. Soc., Perkin Trans. II* **1980**, 331-5.
412. Nolan, C.; Gunnlaugsson, T. *Tetrahedron Lett.* **2008**, *49*, 1993-6.
413. Rissanen, K.; Breitenbach, J.; Huuskonen, J. *J. Chem. Soc., Chem. Commun.* **1994**, 1265-6.
414. Alcock, N. W.; Moore, P.; Reader, C. J.; Roe, S. M. *J. Chem. Soc., Dalton Trans.* **1988**, 2959-63.
415. Paital, A. R.; Nanda, P. K.; Das, S.; Aromi, G.; Ray, D. *Inorg. Chem.* **2006**, *45*, 505-7.
416. Massoud, S. S.; Mautner, F. A. *Inorg. Chem. Commun.* **2004**, *7* (4), 559-62.

417. Hancock, R. D.; Dobson, S. M.; Evers, A.; Wade, P. W.; Ngwenya, M. P.; Boeyens, J. C. A.; Wainwright, K. P. *J. Am. Chem. Soc.* **1988**, *110*, 2788-94.
418. Hancock, R. D.; Ngwenya, M. P.; Evers, A.; Wade, P. W.; Boeyens, J. C. A.; Dobson, S. M. *Inorg. Chem.* **1990**, *29*, 264-70.
419. Wade, P. W.; Hancock, R. D. *J. Chem. Soc., Dalton Trans.* **1990**, 1323-7.
420. Wade, P. W.; Hancock, R. D.; Boeyens, J. C. A.; Dobson, S. M. *J. Chem. Soc., Dalton Trans.* **1990**, 483-8.
421. Zekany, L.; Nagypal, I., Computational Method for Determination of Formation Constants. Legett, D. J., Ed. Plenum: New York, NY, 1985; p 291.
422. Green, K. N.; Johnston, H. M.; Burnett, M. E.; Brewer, S. M. *Comm. Inorg. Chem.* **2017**, *37* (3), 146-67.
423. Green, K. N.; Hubin, T. J. *Original Research Proposal* **2017**, 1-35.
424. Hubin, T. J.; McCormick, J. M.; Collinson, S. R.; Buchalova, M.; Perkins, C. M.; Alcock, N. W.; Kahol, P. K.; Raghunathan, A.; Busch, D. H. *J. Am. Chem. Soc.* **2000**, *122*, 2512-22.
425. Shircliff, A. D.; Wilson, K. R.; Cannon-Smith, D. J.; Jones, D. G.; Zhang, Z.; Chen, Z.; Yin, G.; Prior, T. J.; Hubin, T. J. *Inorg. Chem. Commun.* **2015**, *59*, 71-5.
426. He, Y.; Gorden, J. D.; Goldsmith, C. R. *Inorg Chem.* **2011**, *50*, 12651-60.
427. Sherry, B. D.; Furstner, A. *Acc. Chem. Res.* **2008**, *41* (11), 1500-11.
428. Ye, W.; Ho, D. M.; Friedle, S.; Palluccio, T. D.; Rybak-Akimova, E. V. *Inorg. Chem.* **2012**, *51*, 5006-21.
429. Chow, T. W.-S.; Wong, E. L.-M.; Guo, Z.; Liu, Y.; Huang, J.-S.; Che, C.-M. *J. Am. Chem. Soc.* **2010**, *132*, 13229-39.
430. Kim, J.; Shin, B.; Kim, H.; Lee, J.; Kang, J.; Yanagisawa, S.; Ogura, T.; Masuda, H.; Ozawa, T.; Cho, J. *Inorg. Chem.* **2015**, *54*, 6176-83.

431. Lee, W.-T.; Munoz III, S. B.; Dickie, D. A.; Smith, J. M. *Angew. Chem. Int. Ed.* **2014**, *53*, 9856-59.
432. Lee, W.-T.; Xu, S.; Dickie, D. A.; Smith, J. M. *Eur. J. Inorg. Chem.* **2013**, 3867-3873.
433. Planas, O.; Whiteoak, C. J.; Martin-Diaconescu, V.; Gamba, I.; Luis, J. M.; Parella, T.; Company, A.; Ribas, X. *J. Am. Chem. Soc.* **2016**, *138*, 14388-97.
434. Schultz, J. W.; Fuchigami, K.; Zheng, B.; Rath, N. P.; Mirica, L. M. *J. Am. Chem. Soc.* **2016**, *238*, 12928-34.
435. Tang, F.; Qu, F.; Khusnutdinova, J. R.; Rath, N. P.; Mirica, L. M. *Dalton Trans.* **2012**, *41*, 14046-50.
436. Xu, S.; Bucinsky, L.; Breza, M.; Krzystek, J.; Chen, C.-H.; Pink, M.; Telsner, J.; Smith, J. M. *Inorg. Chem.* **2017**, *56*, 14315-25.
437. Zheng, B.; Tang, F.; Luo, J.; Schultz, J. W.; Rath, N. P.; Mirica, L. M. *J. Am. Chem. Soc.* **2014**, *136*, 6499-504.

Vita

Personal	Hannah May Johnston
Background	Fort Worth, Texas Daughter of Mark and Tammy Johnston
Education	Diploma, Southwest Christian School, Fort Worth, TX, 2009 Bachelor of Science, Chemistry, Abilene Christian University Abilene, TX, 2013 Doctor of Philosophy, Chemistry, Texas Christian University Fort Worth, TX, 2018
Experience	Teaching Assistantship, Texas Christian University Fort Worth, TX 2013-2018 Graduate Research Assistant, Texas Christian University Fort Worth, TX, 2013-2018 Departmental Tutor, Texas Christian University Fort Worth, TX, 2013-2018
Professional	American Chemical Society

ABSTRACT

SYNTHESIS, CHARACTERIZATION, AND APPLICATIONS OF PYRIDINE- AND PYRIDOL-BASED AZAMACROCYCLIC TRANSITION METAL COMPLEXES

by Hannah May Johnston, Ph.D., 2018
Department of Chemistry and Biochemistry
Texas Christian University

Dissertation Advisor: Kayla N. Green, Associate Professor of Chemistry

The Green group has designed and synthesized a series of pyridine- and pyridol-based azamacrocycles, **L1-L9** (Figure 1). Azamacrocycles are a unique class of ligands that form exceptionally stable complexes with transition metals, due to the *macrocyclic effect*.¹⁻² The corresponding metal complexes have exceptional structural, kinetic, thermodynamic, spectral, and electrochemical properties that have long been studied by researchers.² Additionally, these macrocyclic metal complexes have a broad range of applications such as use as biomimetic models, catalysts, or therapeutic/diagnostic agents.

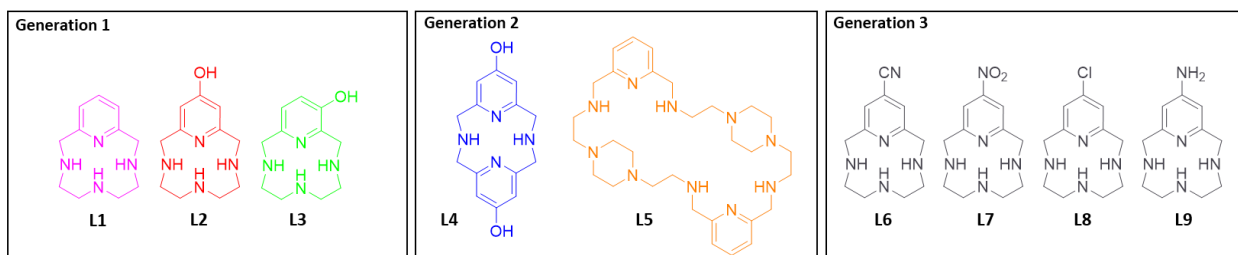


Figure 1. Macrocyclic ligands synthesized by the Green group.³⁻⁷

This work presents the synthesis, characterization, and applications of **L1-L5** (gen. 1 and 2) and corresponding transition metal complexes. Ligands **L1-L3** were complexed to manganese and cobalt; these complexes were studied using traditional inorganic spectroscopic techniques. Ligand-cobalt complexes exhibit a unique solvent-dependent equilibrium behavior similar to the classic CoCl_2 equilibrium, which is often used to illustrate Le Châtelier's Principle.⁸ The ligand-manganese complexes can be modulated between mononuclear or dinuclear depending on the pH of solution during synthesis. Mononuclear Mn(III) complexes offer the potential to be utilized as oxidation catalysts. Additionally,

resulting dinuclear di- μ -oxo bridged complexes offer connectivity to historically significant biomimetic model complexes. Within the literature, Mn(III,IV) di- μ -oxo bridged dimers have traditionally been used to model the active site of the oxygen evolving complex (OEC) with photosystem II (PSII).⁹

L4, was designed to enhance the radical scavenging abilities exhibited by **L2**, by doubling the number of pyridol-rings present within the ligand. These pyridol-based macrocycles offer the potential to be used as therapeutics for the treatment of neurodegenerative disorders by combating reactive oxygen species and sequestering misregulated metal ions. After synthesizing **L4**, it was complexed to several biologically relevant metal ions, Cu(II) and Zn(II). Additionally, radical scavenging assays were performed, as well as cell studies to determine the therapeutic window of **L4**.

Finally, **L5** was originally designed to be a rigid 15-membered pentaazamacrocyclic for use as a Mn(II)-based contrast agent. Due to the presence of piperazine-rings, a 30-membered decaazamacrocyclic 'dimer' was isolated instead. Although this ligand forms weak complexes with transition metal ions, it will be explored as a potential anion receptor in the future, due to its six protonation events.

References:

1. Constable, E. C., *Coordination Chemistry of Macrocyclic Compounds*. Oxford University Press: New York, NY, 1999.
2. Lindoy, L. F., *The chemistry of macrocyclic ligand complexes*. Cambridge University Press: Cambridge, UK, 1989.
3. Johnston, H. M.; Palacios, P. M.; Pierce, B. S.; Green, K. N. *J. Coord. Chem.* **2016**, *69* (11-13), 1979-89.
4. Lincoln, K. M.; Arroyo - Currás, N.; Johnston, H. M.; Hayden, T. D.; Pierce, B. S.; Bhuvanesh, N.; Green, K. N. *J. Coord. Chem.* **2015**, *68* (16), 2810-2826.
5. Lincoln, K. M.; Gonzalez, P.; Richardson, T. E.; Julovich, D. A.; Saunders, R.; Simpkins, J. W.; Green, K. N. *Chem. Commun.* **2013**, *49* (26), 2712-4.
6. Lincoln, K. M.; Offut, M. E.; Hayden, T. D.; Saunders, R.; Green, K. N. *Inorg. Chem.* **2014**, *53*, 1406-16.
7. Lincoln, K. M.; Richardson, T. E.; Rutter, L.; Gonzalez, P.; Simpkins, J. W.; Green, K. N. *ACS Chem. Neurosci.* **2012**, *3* (11), 919-27.
8. Ophardt, C. E. *J. Chem. Ed.* **1980**, *57* (6), 453.
9. Brudvig, G. W.; Crabtree, R. H., *Bioinorganic Chemistry of Manganese Related to Photosynthetic Oxygen Evolution*. In *Progress in Inorganic Chemistry*, Lippard, S. J., Ed. John Wiley & Sons: Hoboken, NJ, 1989; Vol. 37, pp 99-142.